

Los Alamos Science

LOS ALAMOS NATIONAL LABORATORY



LANSCE into the Future

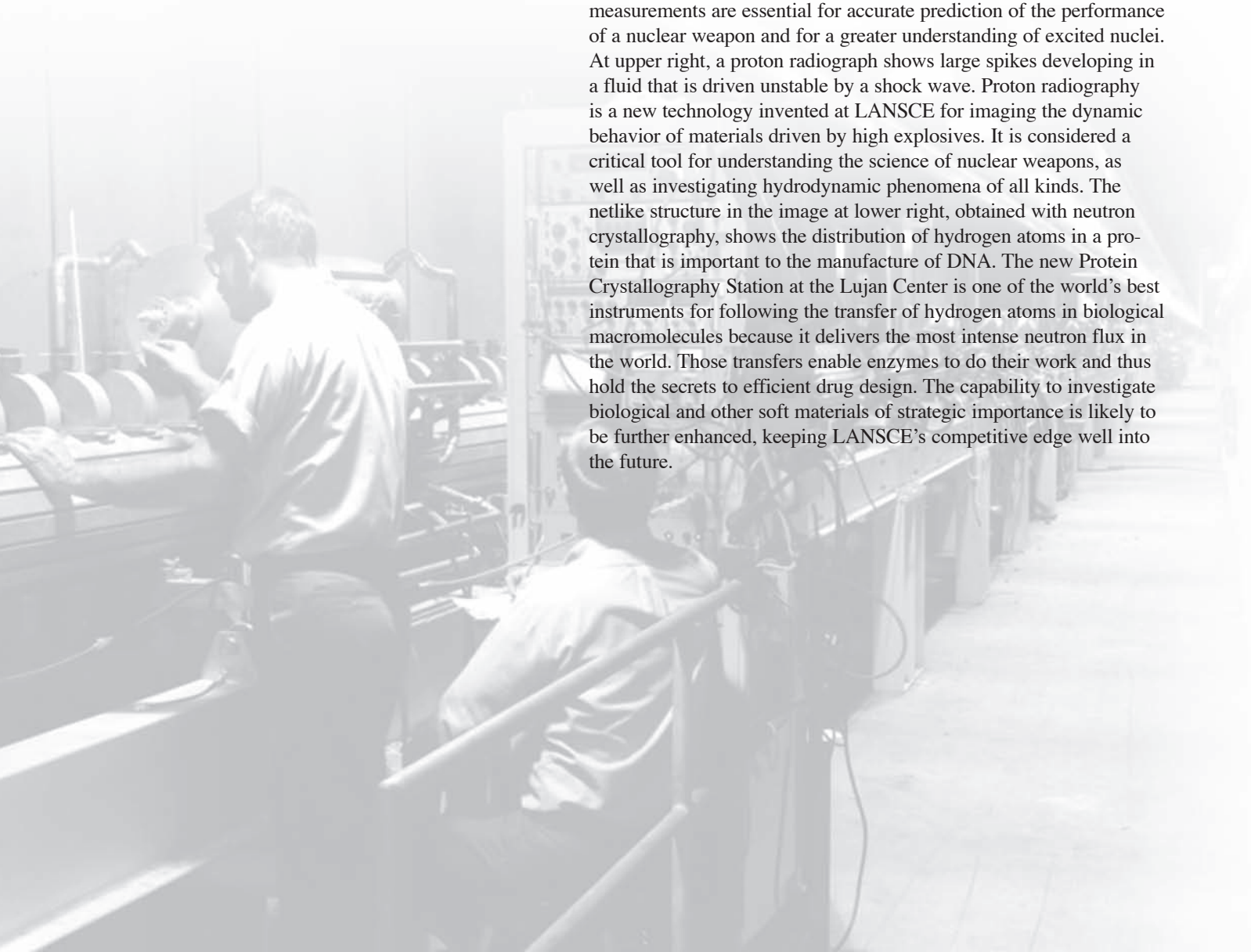
NUMBER 30



On the Cover

The Los Alamos Neutron Science Center (LANSCE) is a national user facility welcoming hundreds of visitors every year. The heart of LANSCE is the linear accelerator, or linac, which is shown stretching across a mesa top from the back cover to the front. The linac accelerates protons (a proton is the charged particle at the center of a hydrogen atom) to an energy of 800 million–electron volts. Remarkably, after 34 years of operation, it still produces one of the most intense sources of medium-energy protons in the world. The proton micro-pulses exiting the linac are shown entering the Proton Storage Ring (PSR), which stores and compresses the pulses, creating a much shorter and higher-intensity macropulse for research applications. When the PSR macropulses are allowed to collide with a heavy metal target, they produce neutrons through a process called nuclear spallation. Spallation neutrons are used for fundamental research on materials and biological structures at the Lujan Neutron Scattering Center (Lujan Center). Both protons and neutrons are used for experiments at LANSCE's five major facilities.

Shown within the ring are three images that illustrate exciting new technological innovations at LANSCE's three main user facilities. At left, two scientists use the GEANIE detector at the Weapons Neutron Research Facility. That detector is one of a brilliant set of new instruments at LANSCE that measure neutron reactions on a variety of nuclei, some of which have very short half-lives. These measurements are essential for accurate prediction of the performance of a nuclear weapon and for a greater understanding of excited nuclei. At upper right, a proton radiograph shows large spikes developing in a fluid that is driven unstable by a shock wave. Proton radiography is a new technology invented at LANSCE for imaging the dynamic behavior of materials driven by high explosives. It is considered a critical tool for understanding the science of nuclear weapons, as well as investigating hydrodynamic phenomena of all kinds. The netlike structure in the image at lower right, obtained with neutron crystallography, shows the distribution of hydrogen atoms in a protein that is important to the manufacture of DNA. The new Protein Crystallography Station at the Lujan Center is one of the world's best instruments for following the transfer of hydrogen atoms in biological macromolecules because it delivers the most intense neutron flux in the world. Those transfers enable enzymes to do their work and thus hold the secrets to efficient drug design. The capability to investigate biological and other soft materials of strategic importance is likely to be further enhanced, keeping LANSCE's competitive edge well into the future.



Editorial Advisor
Kurt F. Schoenberg

Editor
Necia Grant Cooper

Managing Editor
Ileana G. Buican

Science Writer
Brian H. Fishbine

Designer
Gloria E. Sharp

Cover Design
Gail E. Flower

Illustrator
Andrea J. Kron

Composition and Distribution
Joy E. Baker

Photographers
Robert W. Kramer
LeRoy N. Sanchez

Printing Coordinator
Guadalupe D. Archuleta

Address mail to
Los Alamos Science
Mail Stop M711
Los Alamos National Laboratory
Los Alamos, NM 87545

lascience@lanl.gov
Tel: 505-667-1447
Fax: 505-665-4408

<http://www.lanl.gov/science/>

LANSCCE

into the Future



Statement from the Associate Director for Weapons Physics

The history of Los Alamos National Laboratory is one of heroic accomplishment in a time of great danger. As midwife to the birth of the fission bomb and fusion bomb and as the leader of the miniaturization of both, the Laboratory's place in history is ensured. To continue to serve national security after World War II—optimally and convincingly—the Laboratory had to diversify. The element in diversification that has endured to the present emerged from a daring initiative, namely, the creation of the Los Alamos Neutron Science Center (LANSCE), formerly LAMPF. Notwithstanding pessimism on the part of most experts, the facility came online 34 years ago—on schedule and on budget—as the major interdisciplinary laboratory in the United States supporting both nuclear weapons technology and fundamental science (from medicine to astrophysics). It also contributed significantly to the reduction in international tensions by welcoming scientists from within and outside the United States in its unclassified programs.

LANSCE has remained a wellspring of new knowledge and applied technologies. Its contributions to the weapons program are steadily increasing through the new technology of proton radiography, the ultimate diagnostic tool for fission devices, and through the symbiotic relationship between LANSCE's Isotope Production Facility and Weapons Neutron Research Facility, which are producing the first results on the nuclear physics of short-lived isotopes. Those results provide essential data for predicting the nuclear performance of weapons, while results on materials aging from LANSCE's Lujan Center are solving essential questions on the lifetime of components in the stockpile.

The United States is still facing serious threats. Thus, our need to have strong, multidisciplinary national-security laboratories is no less, and may be greater, than it was when LAMPF was conceived. Critical investments are needed now so that LANSCE continues to drive the frontiers of science and technology for the benefit of national security.



Susan J. Seestrom

Introductory Note

Susan J. Seestrom v

Introduction to LANSCE

LANSCE—A Key Facility for National Science and Defense 2

Kurt F. Schoenberg and Paul W. Lisowski

LANSCE—Where Science Meets National Security 18

An interview with Founder Louis Rosen

Nuclear Weapons: Now and in the Future

LANSCE and the Nuclear Weapons Program 30

Phil Goldstone

Proton Radiography 32

Christopher Morris, John W. Hopson, and Philip Goldstone

A New “Camera on a Chip” for pRad Movies 46

Kris Kwiatkowski, Nicholas King, and Vincent M. Douence

Fundamental Nuclear Data for Pinning down the Performance of Nuclear Weapons 52

Robert C. Haight, Mark B. Chadwick, and David J. Vieira

Stardust and the Secrets of Heavy-Element Production 70

Rene Reifarth

Neutron Capture Physics for Nuclear Weapons and Nuclear Astrophysics 71

Francis X. Timmes

Aging and Deformation of Uranium-Niobium Alloys 78

Donald W. Brown, Robert E. Hackenberg, David F. Teter, and Mark A. Bourke

Plutonium under Pressure 84

Introduction 85

James L. Smith and George Chapline

Filling the Gap in Plutonium Properties—Studies at Intermediate Temperatures and Pressures 86

Albert Migliori, Alan J. Hurd, Yusheng Zhao, and Cristian Pantea

Plutonium Magic 90

Angus Lawson

Testing Electronics with Neutrons

The Ice House—Neutron Testing Leads to More-Reliable Electronics 96

Bruce E. Takala

Testing a Flight Control System for Neutron-Induced Disturbances 104

Celeste M. Belcastro, Kenneth Eure, and Richard Hess

Medicine

Accelerator Radioisotopes Save Lives—The Isotope Production Facility at Los Alamos 112

Eugene J. Peterson

Energy Security

The Role of LANSCCE in the Nuclear Energy Future 124

Michael W. Cappiello and Dana C. Christensen

Storing Hydrogen in Crystalline Molecular Cages of Water 138

Konstantin A. Lokshin and Yusheng Zhao

Materials and Bioscience Neutron-Scattering Research

Introduction to Materials and Bioscience Neutron-Scattering Research 146

Alan J. Hurd and Dale W. Schaefer

Unraveling the True Atomic Structures of Exotic Oxides 152

Thomas Proffen and Takeshi Egami

Pair Distribution Function for Nanoparticle Studies 161

Thomas E. Proffen, Katharine L. Page, Ram Seshadri, and Anthony Cheetham

The Hydrophobic Effect—Why Do Raindrops Slide off Leaves? 164

Dhaval A. Doshi, Erik B. Watkins, Jacob N. Israelachvili, and Jaroslaw Majewski

Anticorrosion Coatings—Can They Be Made without Chromium? 172

Dale W. Schaefer, Guirong Pan, and Wim van Ooij

Origins of Spin Coupling across Interfaces 178

Michael Fitzsimmons and Sunil K. Sinha

Giant Magnetoresistance (GMR) in a Hard-Drive Read Head 182

Brian H. Fishbine

Finding out How Enzymes Work 186

Paul A. Langan

How Single Hydrogen Atoms Came into View 196

Benno P. Schoenborn

Fundamental Physics at LANSCCE

Overview of Fundamental Physics at LANSCCE 204

Martin D. Cooper and W. Scott Wilburn

Electric Dipole Moment of the Neutron 208

Martin D. Cooper

The NPDGamma Experiment 211

W. Scott Wilburn

Neutron β -Decay and Precision Tests of the Standard Model 214

Takeyasu Ito and J. David Bowman

LANSCCE and the User Program

The User Program at LANSCCE—Serving the Nation and the Laboratory 220

Allen Hartford, Jr.

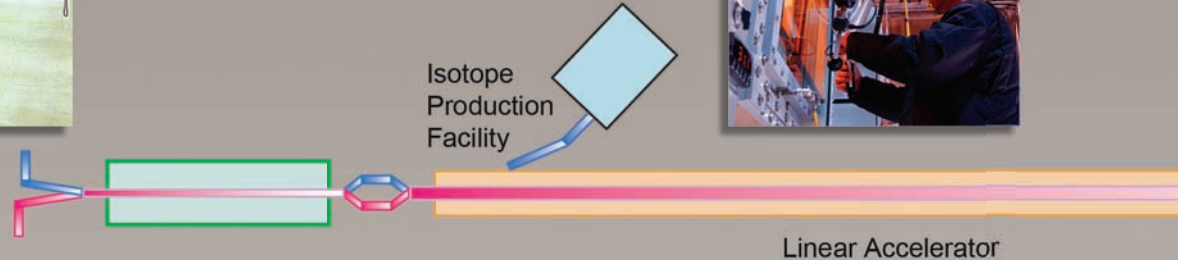




800 MeV
Proton
Accelerator



Isotope
Production
Facility



Linear Accelerator

LANSCE

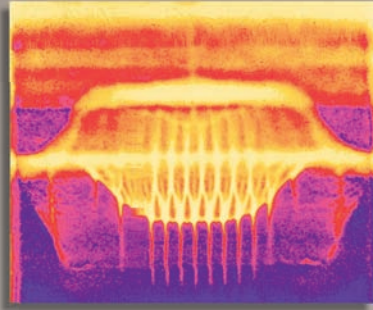
A Key Facility for National Science and Defense

Kurt F. Schoenberg and Paul W. Lisowski

For over thirty years, the Los Alamos Neutron Science Center (LANSCE) has been a premier accelerator-based user facility for national security and fundamental science. LANSCE has remained at the forefront of research because of its strength in technological innovation and its capacity to tailor its very intense proton beam and beam delivery modes to changing scientific and programmatic needs. Today, five state-of-the-art facilities operate simultaneously, contributing to the nuclear weapons program (including actinide and high explosives science), nuclear medicine, materials science and nanotechnology, biomedical research, electronics testing, fundamental physics, and many other areas. During eight months of the year, while the accelerator is operational, scientists from around the world work at LANSCE to execute an extraordinarily broad program of defense and civilian research. Over the 2004 operating period, more than 1100 users visited LANSCE, and over 350 experiments were performed. Because of its large user program, LANSCE is one of the Laboratory's most important "windows" into the academic community and a source for many of our brightest early-career scientists. LANSCE can claim no less than 1200 recruits to the Los Alamos National Laboratory's technical staff during the last 30 years, and it remains a magnet for the best and the brightest.

Plans to refurbish the facility and extend its role are in the works. The LANSCE refurbishment project is designed to sustain reliable facility operations well into the next decade for defense research and applications. A Materials Test Station delivering a very intense fast neutron flux has been designed for exploring advanced nuclear-energy options. A newly commissioned ultracold-neutron-source user facility will make high-precision tests of the standard model of elementary particle physics. Upgrades at the proton radiography facility will enable high-resolution high-speed imaging of hydrodynamic instabilities and detonation physics of importance to stockpile stewardship. Enhancements to the existing Lujan Neutron Scattering Center will ensure its pre-eminence in cold, long-wavelength neutron scattering for the foreseeable future. The development of a long-pulse neutron source prototype will explore techniques for achieving a hundredfold increase in neutron flux for designing the materials and pharmaceuticals of the future. These and other plans promise that LANSCE will support the nation's nuclear deterrent, energy security, health and welfare, and leadership in science for many decades to come.

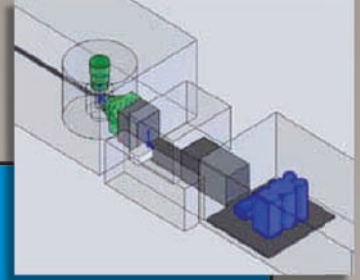
Proton Radiography



Proton Radiography

Nuclear Energy

Materials Test Station

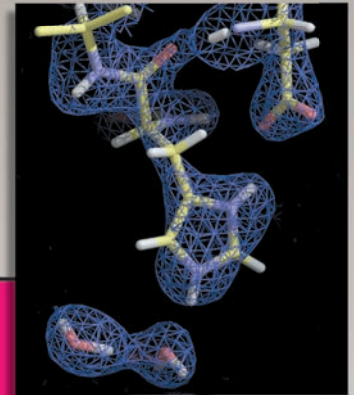


UltraCold Neutron Source

Fundamental Physics

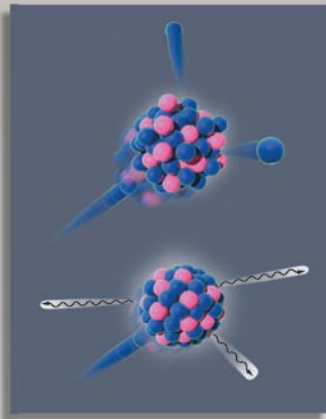
Drug Design

NATIONAL SECURITY



Proton Storage Ring

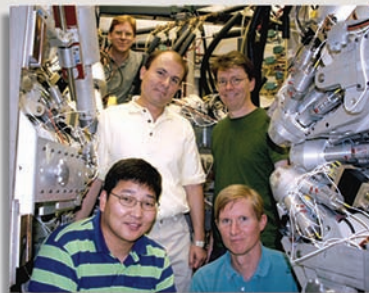
Lujan Center



Nuclear Data

Weapons Neutron Research Facility

ICE House



Aviation Safety

Nanomaterials



Figure 1. Aerial View of the LANSCE Facility

The heart of the Los Alamos Neutron Science Center (LANSCCE) is the high-intensity linear proton accelerator (linac), stretching eastward from the Laboratory along a narrow mesa top (Figure 1). Conceived in the 1960s by Louis Rosen, a veteran of both the Manhattan Project and the thermonuclear era, it was to be a world-class facility designed to extend the reach of the Los Alamos community into the international scientific arena. To complement the studies into the nature of elementary particles conducted at other institutions, the Los Alamos Meson Physics Facility (LAMPF) would produce the highest-intensity proton beam in the world to explore the fundamental forces of nature at medium energies. These are the energies at which pi mesons are

produced, and their role in holding together the protons and neutrons of ordinary nuclei could be studied.

LAMPF was an exciting project based on an innovative accelerator design, but a first-class meson physics facility was only one part of the total vision. Just as protons from the linac, traveling at 84 percent of the speed of light, would produce copious numbers of pi mesons when they crashed into a light-element target, the same protons, striking the neutron-rich nuclei of a heavy-metal target, would release copious numbers of neutrons through a process called spallation. Those neutrons would be perfect for studying the nuclear and materials physics that determines the performance of a nuclear weapon, as well as neutron radiation effects on reactor and weapons materials, and a neutron physics

facility would be especially needed if there ever were a moratorium or ban on nuclear weapons testing. The argument was presented, and the U.S. Congress saw its validity. Even before the 800-million-electron-volt (MeV) linac was complete, Congress had agreed to support a Weapons Neutron Research (WNR) Facility to complement the activities of LAMPF, thereby making LAMPF a world-class research facility for both science and national security.

Today, neutrons and protons have eclipsed mesons as the primary research tools provided at the facility; the name of the facility has been changed to the Los Alamos Neutron Science Center, or LANSCCE; and the research emphasis has shifted from medium-energy nuclear physics to material and nuclear science in sup-

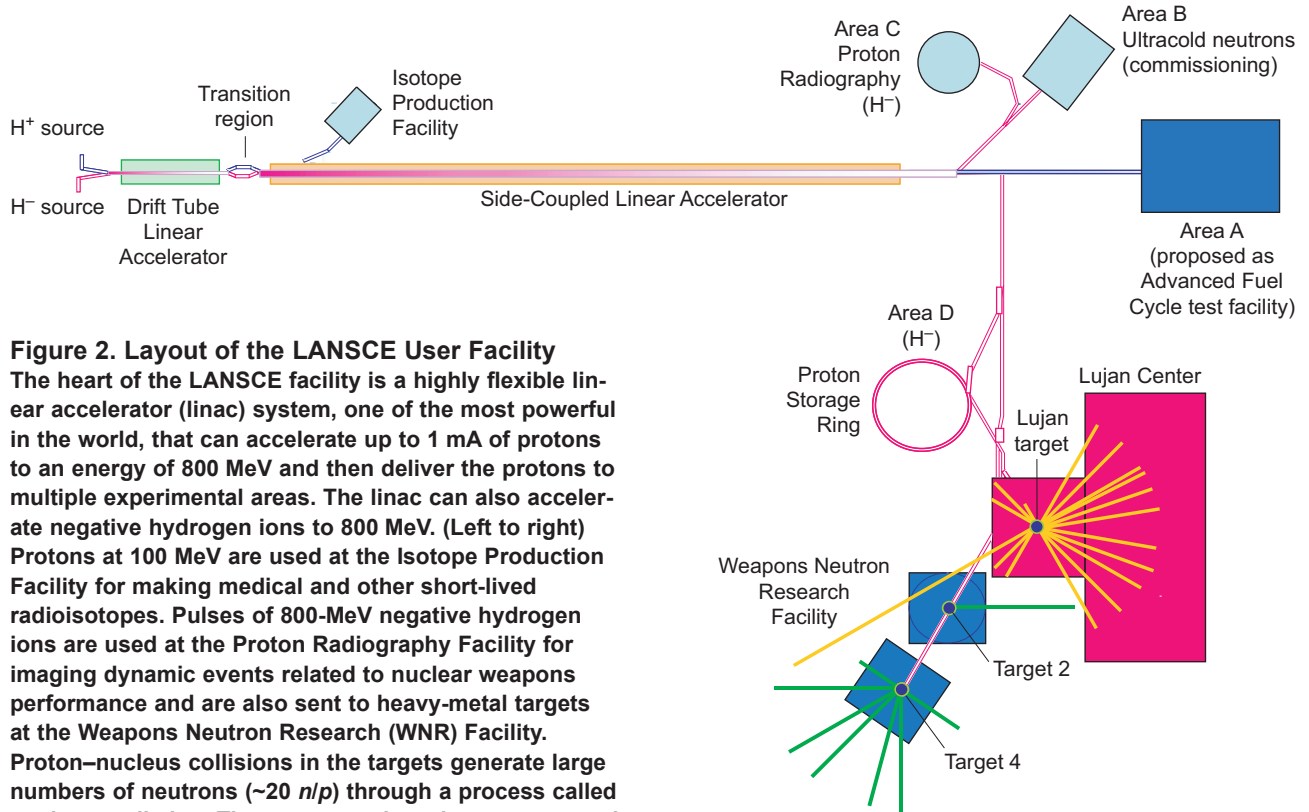


Figure 2. Layout of the LANSCE User Facility

The heart of the LANSCE facility is a highly flexible linear accelerator (linac) system, one of the most powerful in the world, that can accelerate up to 1 mA of protons to an energy of 800 MeV and then deliver the protons to multiple experimental areas. The linac can also accelerate negative hydrogen ions to 800 MeV. (Left to right) Protons at 100 MeV are used at the Isotope Production Facility for making medical and other short-lived radioisotopes. Pulses of 800-MeV negative hydrogen ions are used at the Proton Radiography Facility for imaging dynamic events related to nuclear weapons performance and are also sent to heavy-metal targets at the Weapons Neutron Research (WNR) Facility.

Proton-nucleus collisions in the targets generate large numbers of neutrons (~20 n/p) through a process called nuclear spallation. The neutron pulses, in turn, are used for materials irradiation and fundamental and applied nuclear physics research. The negative hydrogen ions are also injected into a 30-m-diameter Proton Storage Ring (PSR). The PSR converts a 625- μ s pulse of negative hydrogen ions into a 125-ns intense burst of protons. Those intense proton bursts produce, through nuclear spallation, short bursts of neutrons for neutron scattering studies of material properties at the Lujan Center and for nuclear physics research at the WNR. In addition, a newly commissioned ultracold-neutron research facility is beginning the exploration of fundamental nuclear physics with experiments designed to test the standard model of elementary particles.

port of Laboratory missions. The Lujan Neutron Scattering Center (Lujan Center) has become a major international user facility for studying the structure and dynamics of advanced materials and biological macromolecules. Semiconductor industries come to use the intense high-energy neutron flux at the WNR’s Irradiation of Chips and Electronics (ICE) House to test the vulnerability of their modern circuit designs to disturbances caused by atmospheric neutrons; and biomedical companies collaborate with staff at the new Isotope Production Facility to get the latest radioisotopes for nuclear medicine and research applications. (Figures 1 and 2 show the layout of the facility.)

The national security efforts at LANSCE have increased markedly over the past decade. Los Alamos scientists have developed an unmatched suite of precision instruments that exploit the intense, high-energy neutron source at the WNR, the highest-intensity source in the world, to supply essential nuclear data for predicting the performance of our nuclear deterrent from first principles and benchmarking the results against past tests. Proton radiography is a new technique invented at Los Alamos, in collaboration with Lawrence Livermore National Laboratory and other national laboratories, for imaging dynamic events with protons rather than x-rays. It is being used to

investigate the high-explosive detonation physics and hydrodynamic instabilities important to the weapons program. Instruments at the Lujan Center have been tailored to study material properties of high explosives, plutonium, uranium alloys, and other weapons materials under varying conditions of temperature and pressure. And the new Isotope Production Facility is producing the short-lived and rare isotopes needed for nuclear data experiments of interest to the nuclear weapons program. As Louis Rosen likes to say, “Technology is the child of science,” and that maxim could not be truer than at LANSCE.

The LANSCE Facilities

The Lujan Center. This facility (Figure 3) delivers the highest-peak neutron flux in the world for research on materials science and engineering, polymer science, chemistry, earth science and geology, structural biology, and condensed matter physics. High flux at low energies is at a premium in neutron scattering studies because low-energy neutrons, although essential both for penetrating bulk materials and for visualizing the hydrogen content of biological macromolecules, are hard to produce in great quantities and have a much lower scattering probability than x-rays.

Neutron scattering is used to determine where atoms are located in materials and how they move (diffuse or oscillate) collectively as a function of temperature. Elastic neutron scattering provides position information (structure), and inelastic neutron scattering provides information about motion (dynamics). Exactly how the position and motion of atoms affect properties such as strength, compressibility, density, heat capacity, and so forth is one of the grand challenges of materials science, known as the “structure–property relationship.” Understanding the connection between material structure at the atomic level or the nanoscale and macroscopic material properties promises both better use of existing materials and the ability to design new materials for specific applications (“designer materials”), a capability that will revolutionize manufacturing and technology in the future. Lujan Center users and researchers are engaged in this pursuit. They have discovered the nanoscale structure of high-temperature superconductors and are exploring its possible relationship to superconductivity, explored the role of strain in stabilizing nanometer-scale magnetic layers used in computer disk read heads and in future magnetic random-access-memory devices, and

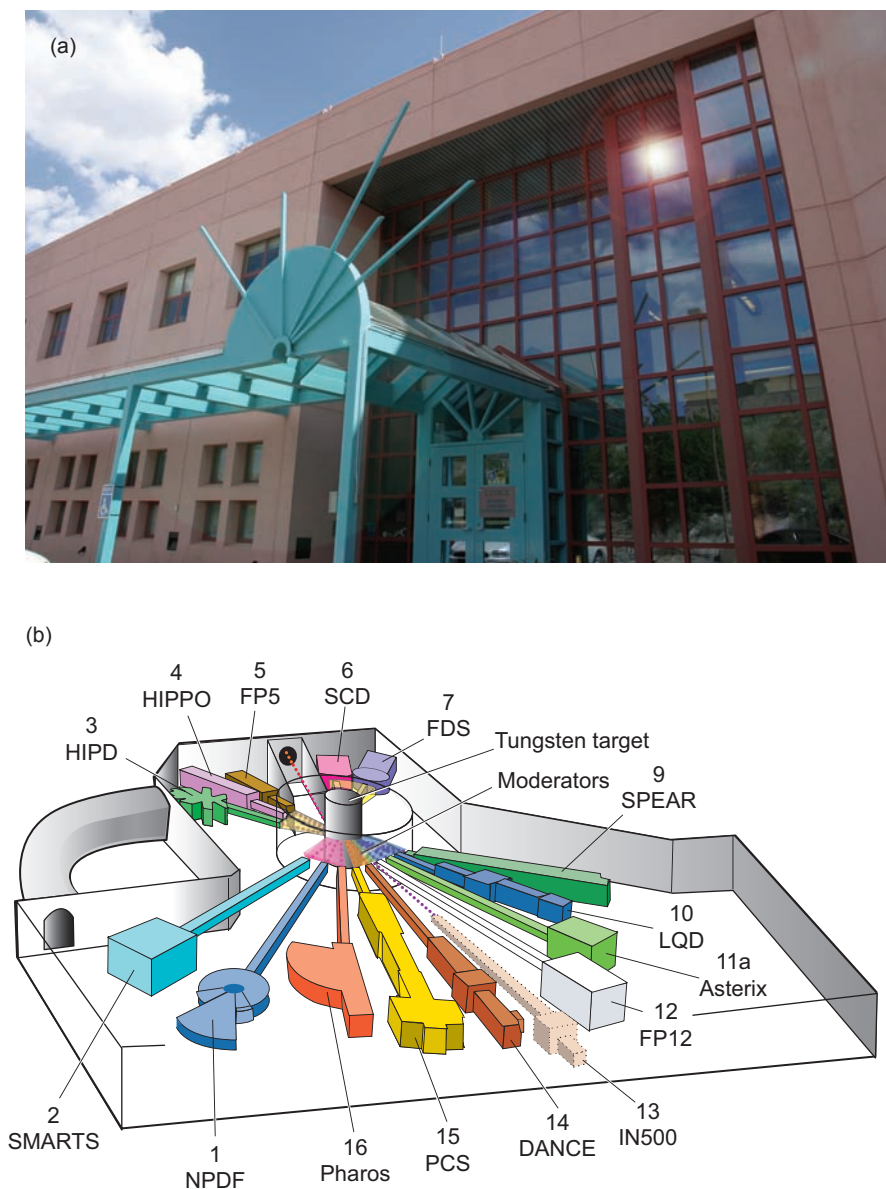


Figure 3. The Lujan Center

Short, intense pulses from the PSR are directed at the Lujan Center’s tungsten target, which is coupled to two different neutron moderators for the production of cold, thermal, and epithermal neutrons with energies that span the range from milli-electron volts to kilo-electron volts. The cold moderator, containing liquid hydrogen, is a first-of-its-kind design, featuring neutron coupling to the spallation target and neutron reflector materials; it is optimized for cold-neutron production and produces the most intense peak flux in the world. Neutrons from each moderator source are collimated to form beams for up to seventeen flight paths. These neutron flight paths are instrumented for different purposes, including powder diffraction, reflectometry, small-angle scattering, protein crystallography, inelastic scattering, single-crystal diffraction, and chemical spectroscopy. The entrance to the Lujan Center is shown in (a), and the experimental hall with target, moderators, and instrumented flight paths, in (b).

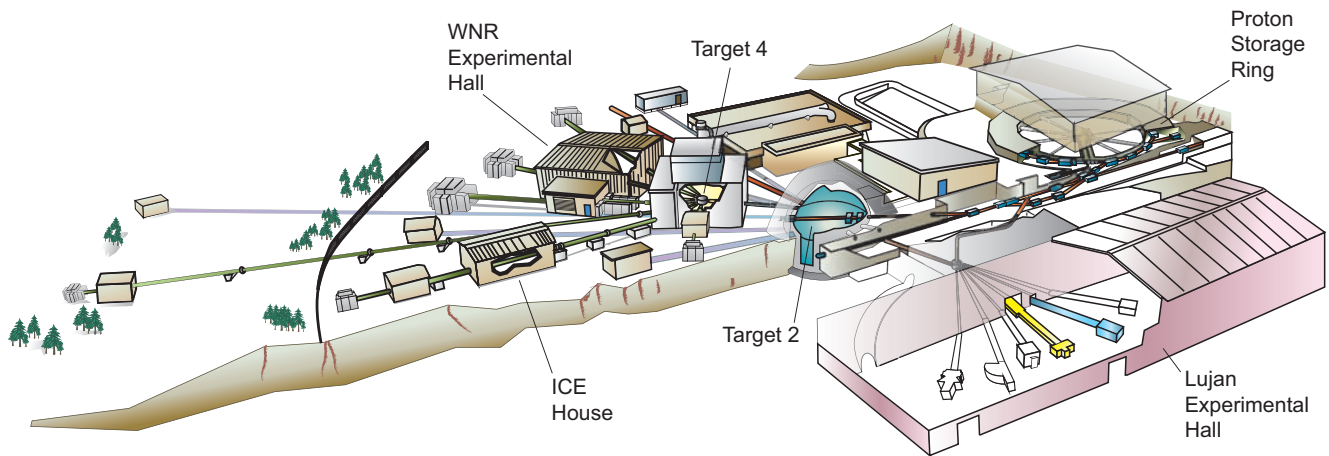


Figure 4. The Layout at WNR
 The WNR houses Targets 2 and 4. The latter provides pulses of energetic neutrons to a flexible array of instrumented flight paths.

located specific hydrogen atoms in enzymes and determined the role of those atoms in binding drugs or activating metabolic pathways. (See the articles “Unraveling the True Structure of Exotic Oxides,” “Origins of Spin Coupling across Interfaces,” and “Finding out How Enzymes Work” on pages 178 and 186, respectively.)

The Lujan Center has seventeen flight paths, twelve of which are instrumented for various neutron-scattering techniques to study materials. In addition, two flight paths are instrumented for neutron nuclear science, one is instrumented for transmission neutron spectroscopy, and two are currently available for future research activities.

The Weapons Neutron Research (WNR) Facility. The WNR houses a flexible array of instrumented flight paths to enable precise nuclear measurements for the weapons program and for fundamental nuclear physics research (Figure 4). This facility is the only sufficiently intense broad-spectrum neutron source for providing the nuclear data necessary for predicting nuclear weapons performance.

Developing this science-based predictive capability is crucial to certifying the present and future U.S. nuclear deterrent without testing.

New nuclear data are needed for two major aspects of stockpile stewardship: calculating precisely the nuclear energy production of a weapon as a function of time and benchmarking calculated nuclear performance against previous above-ground or underground test data. The unique research effort at the WNR, coupled to the Laboratory’s capabilities for fabricating and handling actinide and radioactive materials, provides an unmatched resource for meeting the requirements of stockpile stewardship. Among these requirements are measuring cross sections on isotopes and nuclear isomers with short half-lives in order to understand radiochemistry results of past nuclear tests (see Figure 5), determining cross sections for neutron-induced reactions on actinide isotopes and weapon materials, and improving our understanding of fission energy production in weapons systems. For example, techniques have recently been demonstrated that enable measuring the fis-

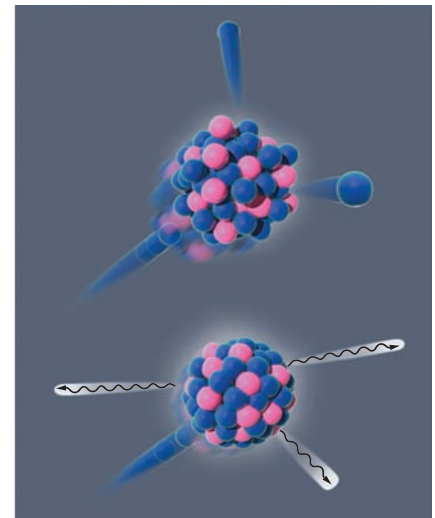


Figure 5. Neutron Reactions for Weapons Diagnostics
 (Top) An incoming neutron (blue) knocks out two neutrons from a nucleus. Using the GEANIE detector array at the WNR, this important $(n,2n)$ reaction on plutonium was measured accurately for the first time. (Bottom) An incoming neutron is captured by a nucleus, which then emits gamma rays. Neutron capture reactions are important for interpreting radiochemical data from past nuclear tests and are now being measured for the first time with the DANCE detector array at the Lujan Center.

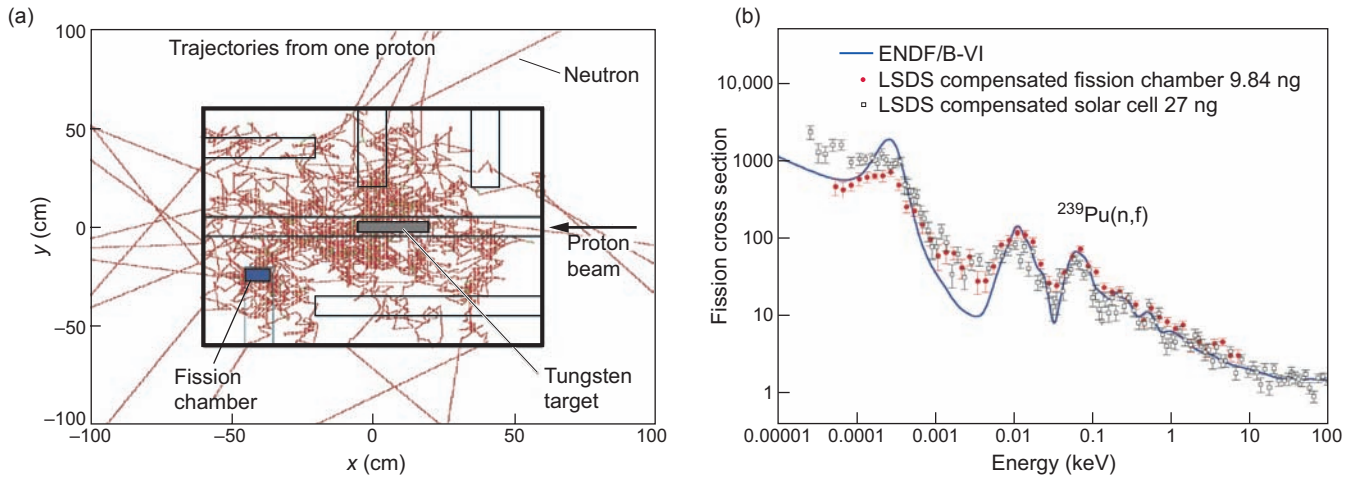


Figure 6. Measuring Fission Cross Sections on Ultrasmall Samples at the WNR

The Lead Slowing Down Spectrometer (LSDS) at the WNR can measure nuclear cross sections on extremely small, short-lived samples. (a) The LSDS consists of a tungsten spallation target surrounded by 1.2 m³ of high-purity lead with a fission chamber placed inside the lead cube. Protons striking the tungsten target produce a spectrum of high-energy neutrons that are concentrated in the spectrometer’s interior. Neutron trajectories (red) are from one proton and were calculated using Monte Carlo neutron transport codes. The intense neutron flux allows measuring nuclear cross sections with samples as small as 10 ng (the smallest sample ever used in a nuclear physics cross-section measurement). (b) Also shown are recent measurements of the plutonium-239 fission cross section with a 10-ng sample. The LSDS will be used in the near future to measure the fission cross section of uranium-235m, the isomer of uranium-235 with a half-life of 26 minutes.

sion cross section of samples as small as 10 nanograms and investigating fission cross sections of short-lived isotopes and isomers for defense science applications and nuclear astrophysics. (See Figure 6 and the article on nuclear data on page 58).

The Irradiation of Chips and Electronics (ICE) House. As electronic components continue to decrease in size, their vulnerability to single-event upsets (SEUs) by atmospheric neutrons has grown. A few years ago, the WNR began to provide the semiconductor electronics industry with an invaluable capability to irradiate semiconductor components and assemblies and quantify their vulnerability to neutron-induced SEUs. The neutron production spectrum at the WNR reproduces the naturally occurring neutron energy spectrum seen by aircraft electronics in flight, but at one million times the intensity. Recent studies by Honeywell and NASA of a flight control system (Figure 7) showed the benefits of a rollback recovery architecture in miti-



Figure 7. Testing Semiconductor Electronics at the ICE House
At the ICE House, Honeywell and NASA placed a flight control system in the neutron beam (inset) to determine how well the system would recover from upsets induced by atmospheric neutrons.

gating the effects of neutron-induced upsets. The WNR now provides the international standard for testing neutron-induced upsets in electronics, and in the 2004 run cycle, twenty-three

industrial companies, universities, and national laboratories used the facility for this purpose (see the articles “The ICE House” on page 96 and “Testing a Flight-Control System for Neutron-



Figure 8. The pRad Facility

For pRad, 50-ns-wide H^+ beam pulses with approximately 10^9 protons per pulse are spaced in time at intervals predetermined by experimental requirements. Transmitted and scattered protons are imaged by an electromagnetic lens system and recorded by cameras. This technique provides multiframe radiographs across a 10-cm field of view that spatially resolves features to an accuracy of approximately $150\ \mu\text{m}$ from samples with an areal density of up to $60\ \text{gm}/\text{cm}^2$. In addition, a permanent-magnet magnifier lens is available that provides a factor of 7 magnification for small systems with spatial resolution to roughly $15\ \mu\text{m}$.

Induced Disturbances” on page 104).

The Proton Radiography (pRad) Facility. The pRad facility provides a unique capability for the study of dynamic processes using 800-MeV protons and a magnetic-lens imaging system (Figure 8). Because protons interact with materials through both the strong nuclear force and the electromagnetic force, transmission measurements allow simultaneous imaging and determination of material properties.

Los Alamos National Laboratory, in collaboration with Lawrence Livermore National Laboratory and other national laboratories, developed and successfully applied pRad to meet the mission requirements of stockpile stewardship. Proton radiography is a powerful tool for elucidating basic principles of how nuclear weapons work. It is arguably the most valuable single tool available to interrogate the

hydrodynamic phase of a weapon. It is necessary to develop and validate quantitative models of material properties and hydrodynamics for this phase that can be implemented in new computer simulation codes from the Advanced Simulation and Computing (ASC) Program. These models must capture critical hydrodynamic behaviors with high accuracy, and achieving that goal sets the hydrodynamic-data requirements. Although many diagnostic tools have been developed to assess the hydrodynamic behavior of materials, most rely on surface measurements and are unable to interrogate the critical state variables and stress-strain response in the interior of the materials. Modeling depends on accurately capturing the time evolution of the hydrodynamics on a microsecond time scale (Figure 9). Proton radiography, with its ability to penetrate and accurately image the interior of highly compressed materi-

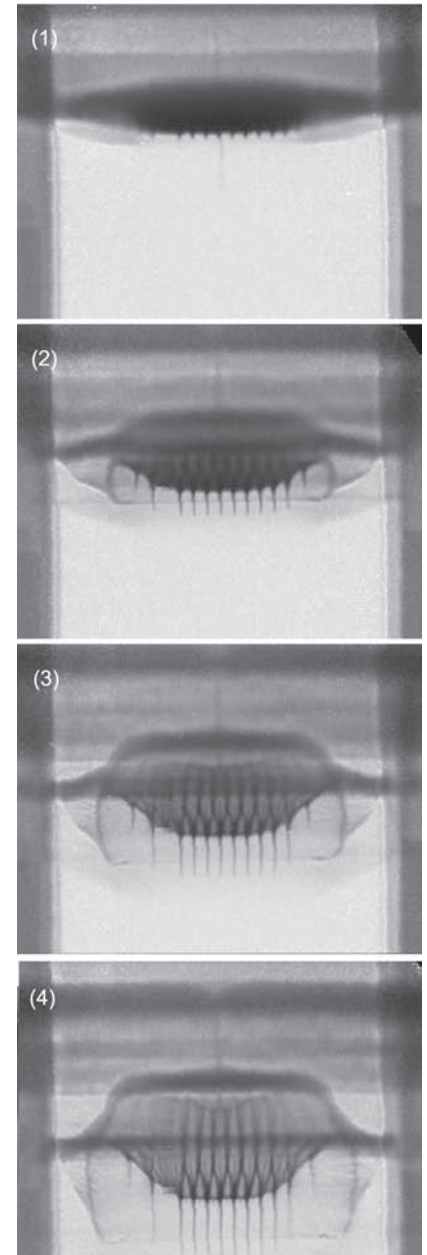


Figure 9. Proton Radiographs of Shock-Driven Ejecta

In this experiment, an explosively driven aluminum flyer plate impacts a solid tin target. The target’s surface was machined with a sinusoidal contour. The resulting nonlinear growth resulting from Richtmyer-Meshkov instabilities is clearly visible in the pRad images from (1) to (4). Such experiments are used to benchmark analytic theories and hydrodynamic simulation tools used for nuclear weapon certification.

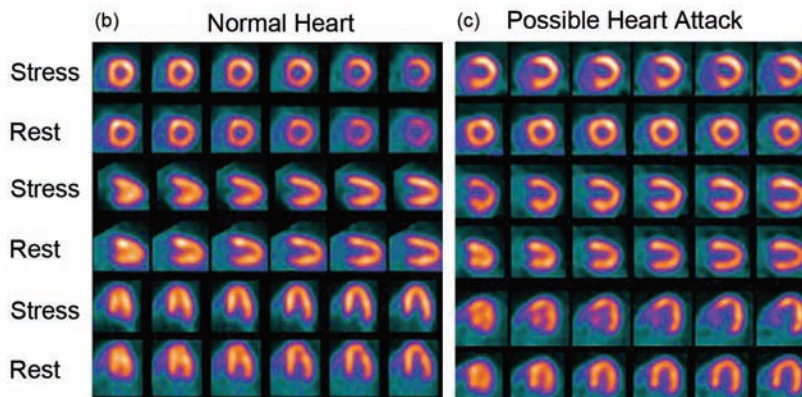


Figure 10. Producing Radioisotopes for Cardiac Scans

The radioisotope strontium-82 produced at the new Isotope Production Facility (IPF) at LANSCCE is the source of rubidium-82, an ideal tracer for scanning the heart. (a) A technician manipulates irradiated targets in the hot cell facility at the IPF. (b) and (c) Shown here are heart scans obtained by positron emission tomography. Alternating rows show images of the heart after stress and after a period of rest. Each pair of stress and rest images shows a different cross section of the heart.

als, as well as its highly flexible and precisely recordable pulse format, is uniquely suited to providing these necessary data for weapon certification codes and models.

The Isotope Production Facility (IPF). The new IPF continues a 30-year Los Alamos tradition of supplying advanced accelerator-produced radioisotopes for both research and nuclear medicine. Los Alamos and Brookhaven National Laboratories have the only such facilities in the United States. A new proton transport line delivers 100-MeV protons from the existing LANSCCE accelerator to the IPF target station. That station is designed specifically for the efficient production of radioisotopes. Targets of different materials are irradiated in a stacked configuration to allow varying the incident neutron energy and thereby optimize production of the desired radioisotopes. Some of those are distributed through pharmaceutical companies for use in cardiac scans and other medical diagnoses as well as medical treatment and research (Figure 10). Others are used for nuclear data experiments of importance to the weapons program, threat

reduction studies related to the dispersal of radioactive materials, and basic nuclear physics research. The IPF was designed to operate with minimal impact on scheduled beam delivery to other experimental areas at LANSCCE.

The Ultracold Neutron (UCN)

Source. The UCN source is being commissioned at LANSCCE. Ultracold neutrons have millikelvin temperatures and move at speeds of less than 8 meters per second. Because their wave functions are totally reflected from certain materials, they can be stored in a specially designed container, far from background radiation. Thus UCNs provide an ideal system for high-precision tests of the weak interaction as described in the Standard Model of particle physics. At a planned current of 4 microamperes, preliminary measurements indicate that the UCN source at LANSCCE will be the most intense one of its kind worldwide. Once the LANSCCE source becomes operational at full power, a series of fundamental physics measurements will be conducted, the first of which is a measurement of the β -decay asymmetry resulting from the decay of polarized UCNs. This exper-

iment could detect physics beyond the Standard Model, thereby changing our ideas of how the fundamental forces in the universe work. A future goal for the UCN facility is to operate as a fourth national user facility at LANSCCE for research that delves into the basic structure of matter.

The source uses solid deuterium at 5 kelvins to cool, or moderate, neutrons from a tungsten spallation target coupled to a set of graphite-beryllium and cold polyethylene moderators. The ultracold neutrons pass through guide tubes to nearby experiments.

National Security and Defense Science: The Stockpile Stewardship Program

The nuclear test moratorium era has led to fundamental changes in the way the weapons program certifies whether the U.S. stockpile will achieve its designed performance characteristics. When nuclear tests were conducted, the pedigree of a particular nuclear explosive package was evaluated experimentally with underground tests. The overall confidence in the continued performance of devices in the

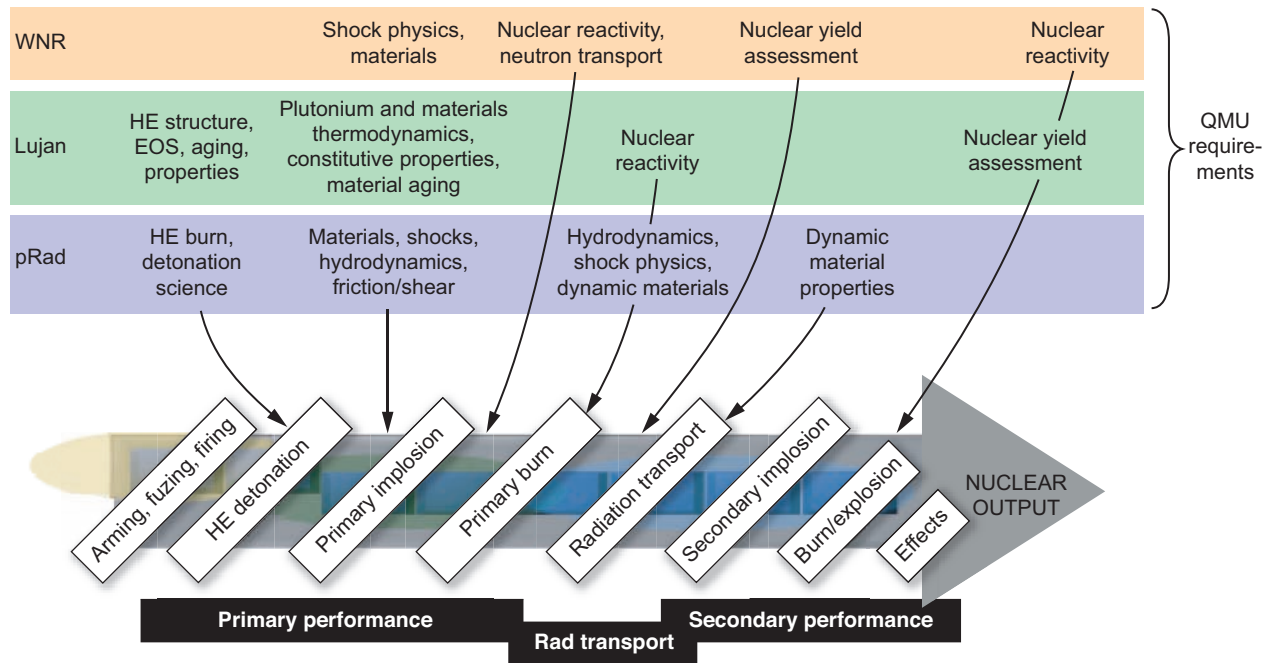


Figure 11. Supporting Science-Based Predictive Capability

As shown in this diagram, LANSCCE capabilities uniquely address science-based prediction, necessary for present and future weapons certification.

stockpile relied heavily on the expert judgment of designers with significant underground-test experience. In the absence of testing, a new certification methodology is required, namely, science-based prediction of weapon performance. Quantification of margins and uncertainties (QMU) provides this construct (Figure 11).

QMU is based on the capability to quantitatively predict the performance of a nuclear explosive package, including the performance margin and associated uncertainties, that is, how close the system is to the point at which it would begin to fail to perform as specified. This capability is firmly rooted in our ability to accurately model weapon performance across a broad range of physical conditions. LANSCCE facilities are presently used to meet this scientific grand challenge with research that explores many aspects of weapons science and behavior.

All three National Nuclear Security Agency (NNSA) laboratories, as well

as the Atomic Weapons Establishment in the United Kingdom, utilize LANSCCE's unique facilities to address issues related to weapons assessment and certification. In the past 5 years, LANSCCE research has produced high-explosive data underpinning the certification of the B61 nuclear warhead to meet specific performance requirements, nuclear data critical to revising the baseline performance of the W88 primary, and materials data validating the reuse of components in the W76 Lifetime Extension Program. Specific research areas in support of weapons certification include the following:

- Investigating the behavior of high-explosive (HE) materials, including the equation of state and constitutive properties affected by aging
- Assessing the effect of aging on stockpile materials and associated performance
- Resolving uncertainties in insen-

sitive-high-explosive burn and dynamic material properties under different environmental conditions

- Employing scaled experiments to quantify the hydrodynamics phase of a weapon and to test performance models
- Determining the constitutive properties of weapons metals, such as plutonium, at high temperature and pressure
- Quantifying the effects of manufacturing changes, such as changes in fabrication processes, on performance
- Providing high-accuracy nuclear cross sections for actinides and radiochemical isotope chains (including short-lived isotopes) to interpret archival underground nuclear tests and validate weapons performance predictions

In the future, our science-based predictive capabilities must continue to improve in order to ensure the

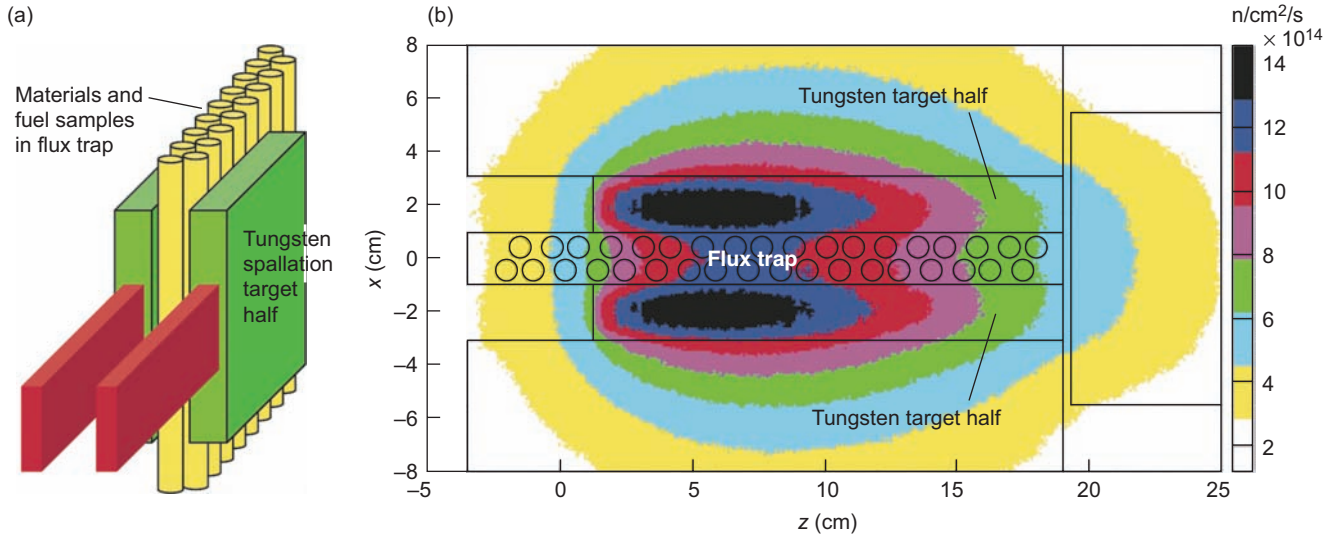


Figure 12. Testing Nuclear Fuels at the MTS

(a) At the MTS, nuclear fuel rods designed for a closed fuel cycle will be placed between a split tungsten target and irradiated by a fast neutron flux. (b) The plot shows the neutron flux intensity that the proton beam from the LANSCCE linac will produce when it strikes the tungsten target. The fast-neutron flux in the flux trap region between the tungsten halves will be nearly 10^{15} neutrons/cm²/s, equal to that of a typical fast reactor.

accuracy of our stockpile assessments as weapons age and components are refurbished or replaced. These capabilities will remain crucial to certification if and when a reliable replacement warhead is developed and fielded. LANSCCE is poised to meet these future challenges through capability enhancements and continued engagement with the best of the scientific community.

National Energy Security

Over the past fifty years, the development of commercial nuclear power has successfully relied on thermal reactors—mostly water-cooled reactors, which run at relatively low temperatures with thermal, or low-energy, neutrons driving the controlled-fission-chain reaction. However, inefficient use of nuclear fuel, risks of nuclear proliferation, and the problem of safely storing large quantities of nuclear waste in geologic repositories for thousands of years have revitalized interest in adding fast-neutron

fission systems to the nuclear fuel cycle. Fast, or high-energy, neutrons are much more efficient than thermal neutrons at transmuting long-lived actinides with half-lives of several hundred thousand years (plutonium, neptunium, americium, and curium), thereby eliminating them from nuclear waste and drastically reducing the long-term decay heat, radiotoxicity, and proliferation risks that make nuclear waste such a difficult problem.

To support the National Energy Policy, the Department of Energy (DOE) has initiated several programs focused on fast-spectrum reactor and fuel cycle concepts that can reduce the spent-fuel demands on geologic repositories by improving the utilization of nuclear fuels and the transmutation of long-lived transuranic waste products. These advanced concepts employ nontraditional fuels, structural materials, and coolants for which there is currently insufficient operating knowledge. Assessment of these concepts requires testing where fuels and materials are irradiated under

actual or prototypical fast-reactor flux conditions and operating environments. Currently, there are no fast-reactor or fast-flux test facilities in the United States that meet the required irradiation environment.

Because LANSCCE can reestablish full-power (1 milliampere) proton acceleration, it is poised to provide a new U.S. capability for the production of fast neutrons. The Materials Test Station (MTS) will achieve neutron intensity levels equivalent to a 100-megawatt fast-flux reactor. The neutron intensity will be sufficient to research and improve the next generation of materials and fuels necessary to deploy advanced fission systems for U.S. energy security (see Figure 12). The MTS irradiation capability, in concert with its post-irradiation examination capabilities, will provide necessary data for the validation of materials simulation models enhancing science-based prediction of materials behavior. This capability will be an integral component of the fast-reactor development program, serving as the nation's premier source of high-

intensity fast neutrons. In addition, the MTS at LANSCE will provide a world-class capability to help develop the advanced materials needed for fusion energy systems.

Role of LANSCE in Materials Science and Bioscience

Neutron scattering research began in the late 1940s as reactors that produce considerable neutron flux were built for nuclear energy research. Over the past few decades, with the advent of more-intense neutron sources and energy-discriminating time-of-flight techniques, neutron scattering has emerged as a major exploratory tool for understanding condensed matter. Neutron scattering data were seminal in understanding the structure and dynamics of the first high-temperature superconductors and have played a role since then in the discovery of many

unexpected and counterintuitive phenomena in electronic, magnetic, optical, and structural materials, as well as in biomaterials and nanomaterials.

The impact of neutron scattering is evident across the entire field of materials science. Recent examples of that impact at Los Alamos include understanding the anomalous thermal expansion of plutonium, elucidating the physics of new superconductors and magnetic materials, the discovery of water inclusions in DNA structure, and the identification of material failure modes in high-consequence accidents. Other examples are shown in Figures 13–15: predicting the lifetime of weapons parts, discovering new materials under pressure, and using the protein crystallography station to track the motive power of single hydrogen atoms during enzymatic reactions. The growing power of neutron sources and increasing sophistication of associated instrumentation

ensure an expanding role for neutrons in materials research, including the performance and aging of weapons materials and the development of new materials needed for threat reduction.

The Lujan Center is presently the premier U.S. spallation neutron source and produces the highest-peak flux for cold neutrons in the world. Cold (or long wave-length) neutrons are ideal for studying soft materials, biomaterials, and nanomaterials, which are predicted to be at the forefront of materials science for the next several decades. Biomaterials are among the coarsest and softest of materials classes while having the most complex properties. Both structure on larger scales and dynamics at lower energy become important in these materials. Neutron scattering studies of biomaterials with cold-neutron techniques are therefore essential to uncovering the scientific principles by which biomaterials exhibit

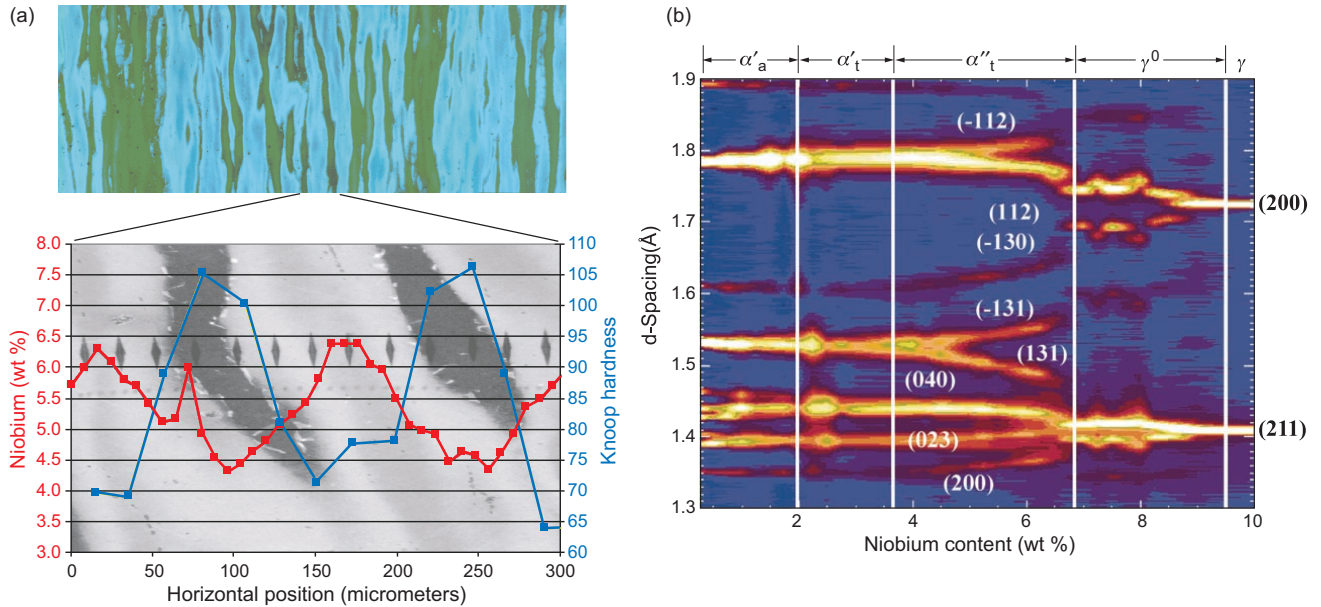


Figure 13. Predicting the Lifetimes of Uranium-Niobium Nuclear-Weapon Parts

(a) Rolled uranium-niobium parts exhibit a metastable striated structure (top) with large variations in niobium content and hardness (bottom). (b) Diffraction measurements at LANSCE identify the crystal phases present in homogeneous uranium-niobium alloy as the niobium content increases. Other diffraction measurements reveal that under stress, the crystal structure of uranium-niobium alloy with 6 weight-percent niobium deforms mainly by reorienting its crystalline “twins.” All these data can be used in computer models to accurately predict lifetimes and weapon performance.

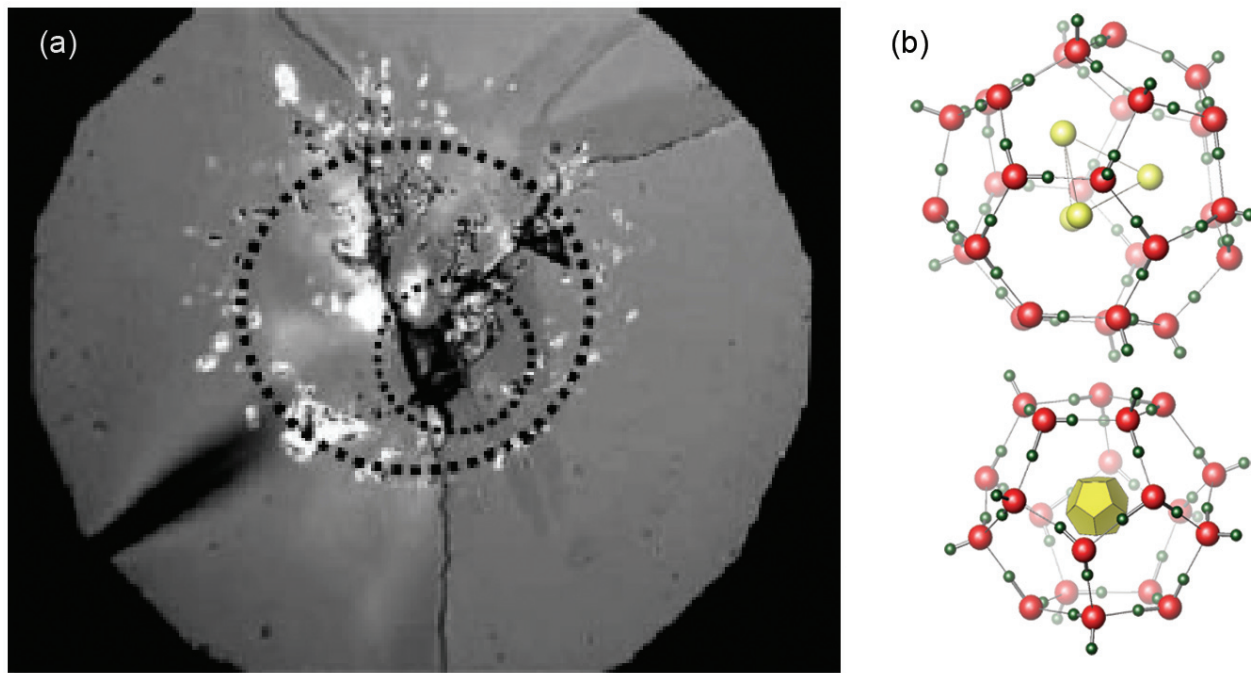


Figure 14. New Materials Discovered at High Pressures

(a) This indentation micrograph shows a new carbon phase whose density, hardness, and bulk modulus are at least as high as those of diamond. The new phase forms when carbon nanotubes are compressed to 75 GPa. (b) A new hydrogen clathrate formed from ordinary water traps hydrogen molecules (yellow) in large (top) and small (bottom) molecular cages at concentrations rivaling those of the best hydrogen-storage materials. The oxygen and hydrogen atoms in the cages' water molecules are shown in red and green, respectively.

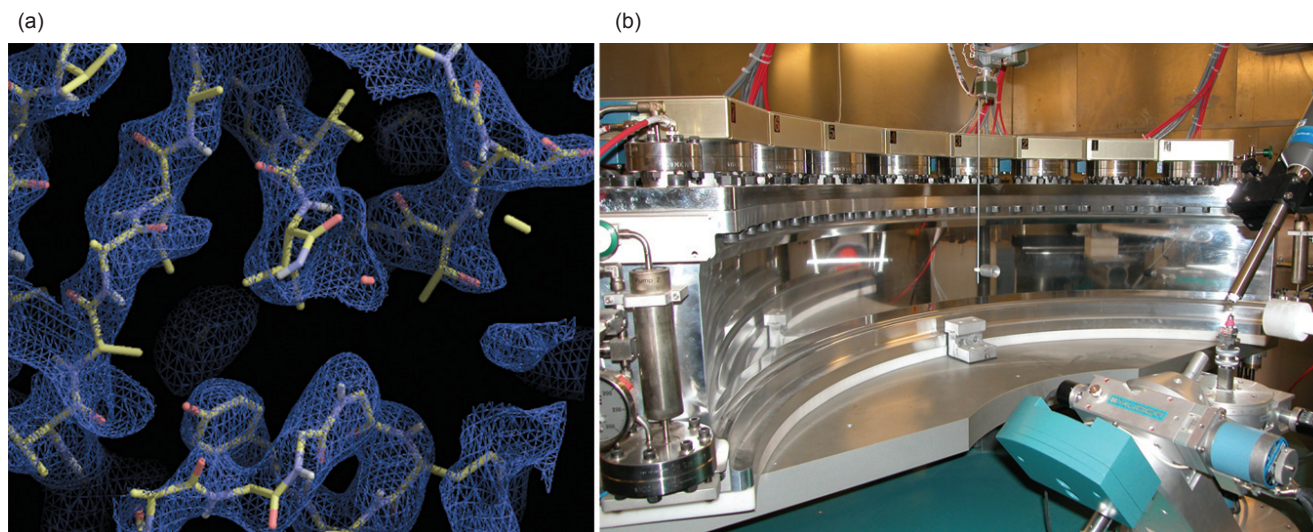


Figure 15. Improving Drug Design

(a) The antitumor drug methotrexate inhibits DNA from being produced by tight binding to a pocket in the cleft of the protein DHFR. The hydrogen density distribution of DHFR determined by neutron scattering is shown by the netlike structure. (b) Using the new protein crystallography station, scientists have identified the hydrogen bonds in DHFR responsible for binding methotrexate. That information will help them improve drug design.

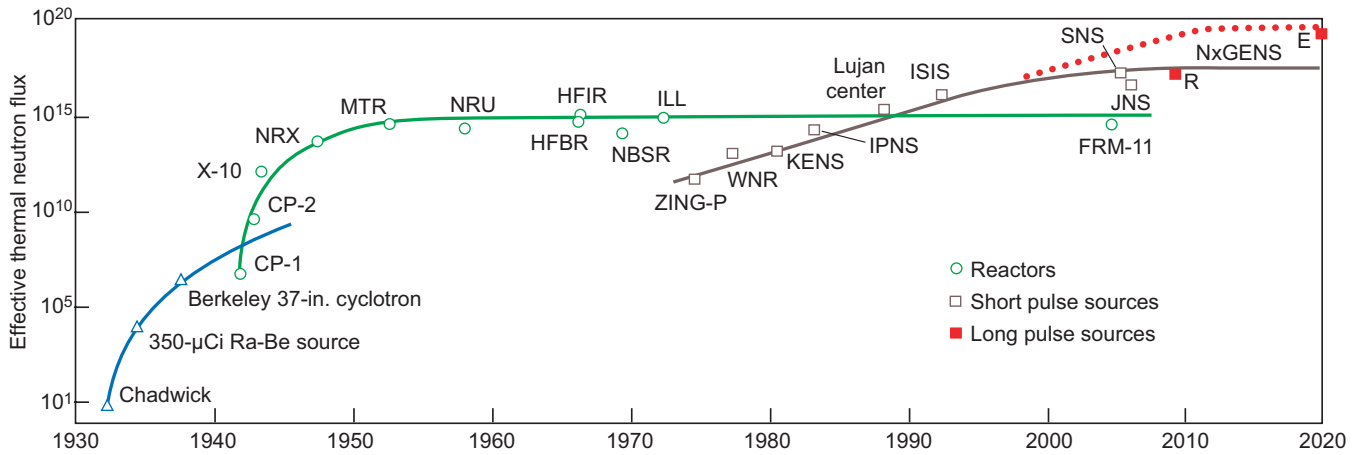


Figure 16. The Long-Pulse Spallation Source

Spallation sources that produce long pulses at low repetition rates are likely to achieve very-high-power, high-brightness cold neutrons for studying the properties of soft matter. Plotted on the graph are the effective fluxes of neutron sources worldwide and the dates the sources were commissioned. Reactor sources have increased in effective flux by only a factor of 4 since the first reactor for neutron scattering was built at Chalk River in the late 1950s. Further progress in creating higher fluxes relies on long-pulse sources. The proposed NxGENS long-pulse spallation source planned at LANSCCE would fully demonstrate long-pulse technology.

self-assembly, self-limited growth, healing, and adaptive emergent properties. Nanomaterials share many characteristics with soft materials; the essential structural features occur on supramolecular scales. The preferred synthesis path for soft nanomaterials is bottom-up self-assembly, whereby specific short-range interactions are engineered into complex precursor macromolecules that induce long-range order by cooperative physical interactions. Again, neutron scattering with cold-neutron techniques is essential to exploring nanostructure.

The evolution of materials science holds a very bright future for LANSCCE as plans develop to capitalize on the high-peak flux of cold neutrons and low pulse-repetition rate. Operating at a pulse repetition rate of 20 hertz, the Lujan Center is unique compared with other existing or planned facilities. For example, the Spallation Neutron Source (SNS) to be built in Oak Ridge, Tennessee, will operate at 60 hertz, and ISIS, the pulsed neutron and muon source in the United Kingdom, presently operates at 50 hertz. Low repetition

rate allows for the use of all the cold neutrons in a pulse and thus leads to efficiency. By fully using the neutron scattering instrumentation, the Lujan Center can take full advantage of its high-peak flux for cold-neutron-scattering research. This strategy will ensure that the Lujan Center maintains its preeminent role in cold-neutron scattering in partnership with the SNS and other future megawatt-class neutron scattering centers.

It is clear, however, that the future frontiers of structural biology and dynamic self-organization of materials will require neutron sources with at least ten times the cold-neutron flux presently planned or available. These so-called Generation III neutron sources are likely to utilize a long-pulse spallation source (LPSS)—see Figure 16. Future LANSCCE capabilities, associated with the Materials Test Station for nuclear energy research, will allow the United States to prototype a Generation III source with a single flight path at relatively modest cost. This prototype, called NxGENS, will be a cost-effective approach to complement the SNS capability. If

fully developed, NxGENS will substantially exceed SNS performance. The NxGENS prototype will assure U.S. leadership in Generation III neutron sources by offering unprecedented research opportunities in cold-neutron scattering.

As envisaged, the NxGENS prototype will operate with an 800-MeV beam at a power of 660 kilowatts and a repetition rate of 20 hertz. It will perform in short-wavelength applications (for example, diffraction and strain analysis) at about the same level as the current Lujan Center, and in cold-neutron-scattering applications, at about the same power level as the SNS. The cold-neutron applications include small-angle neutron scattering, reflectometry, protein crystallography, neutron spin-echo spectroscopy, and low- or variable-resolution time-of-flight spectroscopy. The NxGENS prototype could be further enhanced to accommodate multiple flight paths operating at 2.5 megawatts, thus promising an improvement in cold-neutron production greater than one order of magnitude over planned high-power



short-pulse sources. The NxGENS source would overcome intrinsic limitations of present and planned short-pulse sources and will be well suited to 21st century materials research for national security.

Role of LANSCE in Los Alamos Scientific Infrastructure

The success of an institution depends on the facilities, people, and purpose to which it is dedicated. For 30 years, LANSCE has created a unique scientific environment, attracting scientists from around the world to work together on high-stake issues related to global security, as well as on exciting challenges at the frontiers of knowledge. Today's national and global-security imperatives lend extra emphasis and meaning to research that already has high intellectual merit.

The last several years have seen a steady stream of new technologies come on line at the LANSCE user facilities: four new world-class instruments for high-precision nuclear physics measurements at the WNR and Lujan Center, high-resolution imaging devices for pRad, the first facility for ultracold-neutron research, and seven new instruments for materials science and bioscience on the floor at the Lujan Center. The Lujan Center, in combination with the new Center for Integrated Nanotechnology and the National High Magnetic Field Laboratory, makes Los Alamos a premier destination for materials scientists interested in materials structure and synthesis, nanoscience, structural biology, and high magnetic fields and pressure. The new LANSCE instruments and Los Alamos facilities were supported through investments by the NNSA Office of Defense Programs, the Office of Basic Energy Sciences in the Office of Science at DOE, the National Science Foundation, and the

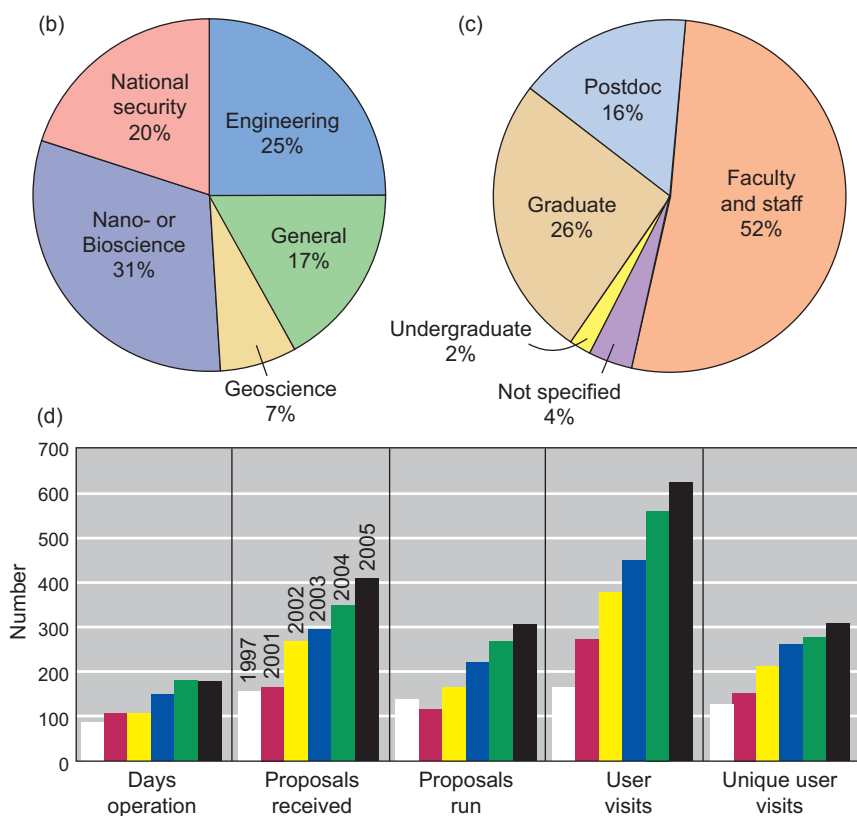


Figure 17. The User Program at the Lujan Center
 (a) Some of the students attending the 2004 LANSCE Neutron Scattering Winter School are pictured here with Jim Rhyne and Thomas Proffen of LANSCE. The pie chart in (b) shows the different areas of research in which Lujan Center users are involved, and the one in (c) shows the users' demographics. The bar chart in (d) shows the steady growth of the Lujan Center User Program between 2001 and 2005.

Laboratory-Directed Research and Development Program at Los Alamos.

Not surprisingly, this burst of creativity and investment was accompanied by a steady and dramatic increase in the number of experiments, users, and individual user visits, as well as in the level of user satisfaction every year since 2001. As illustrated in Figure 17, during the 2004 run cycle, for example, over 500 user visits were logged in at the WNR and another 500 at the Lujan Center, and that rate of growth continues unabated during the 2005 run cycle. The demographics are also impressive. At the Lujan Center, almost half the users are students and postdoctoral researchers conducting publishable research of a more fundamental nature, and nearly two-thirds are early-career scientists. A contributing factor to these healthy demographics is the LANSCE Neutron Scattering Winter School, a topical school started in 2004, which hosts 30 students for nine days of hands-on experimentation, as well as instruction by a dozen world-class lecturers. Thus, LANSCE continues to be a magnet facility for scientific talent. The Laboratory can point to well over 1200 people who have joined the Laboratory permanently after having been at LANSCE, and many of those have contributed significantly to the Laboratory's core mission.

LANSCE Futures

Future national missions will require enhanced LANSCE capabilities to support five principal research areas: (1) pRad to meet the mission-critical requirements of the Stockpile Stewardship Program for the next decade; (2) weapons nuclear science to meet Stockpile Stewardship Program and Homeland Security mission requirements and to provide an international standard for qualifying semiconductor components and sys-

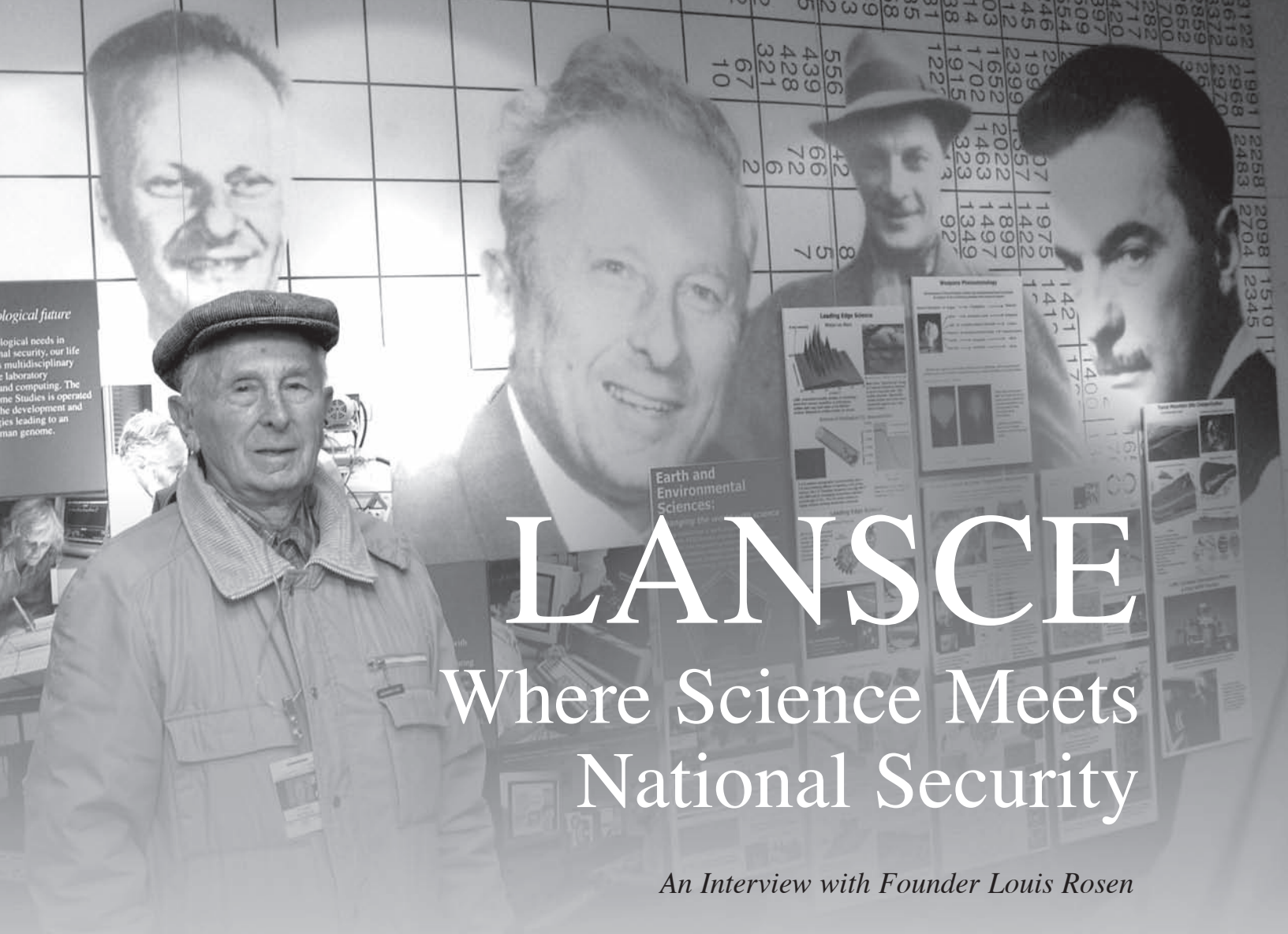
Major Benefits of LANSCE Enhancements

- Improving proton radiographic imaging at 800 MeV and exploring higher-energy, more-intense beams to fully resolve dense, full-scale systems for hydrotesting
- Enabling nuclear-cross-section measurements on short-lived isotopes for higher-fidelity weapons nuclear data and data relevant to nuclear astrophysics
- Enhancing burst production of neutrons for testing electronic components of weapons
- Improving the irradiation capability for materials testing with the MTS
- Upgrading the Lujan Center to achieve full scientific utilization with full-flight-path instrumentation serving 750 users per year
- Demonstrating the NxGENS neutron scattering source and flight path using the long-pulse format that will attain unprecedented cold-neutron scattering performance
- Developing the best-in-the-world ultracold-neutron source for fundamental nuclear-physics research

tems for performance during single-event upsets; (3) civilian nuclear science to enable operation of the Materials Test Station, meeting the needs of nuclear reactor research for future energy security; (4) materials science and bioscience to enhance neutron scattering performance at the Lujan Center for understanding the performance and aging of weapons materials, to support development of the broad spectrum of new materials needed for stockpile stewardship and threat reduction, and to develop NxGENS, a prototype Generation III long-pulse spallation neutron source, where future materials science and bioscience discoveries would be made; and (5) fundamental nuclear physics to enable the reliable production of cold and ultracold neutrons at unprecedented intensities and densities, which make it possible to conduct revolutionary research and thereby keep the United States at the forefront of fundamental nuclear physics.

Proposed LANSCE performance enhancements are focused to address specific mission requirements for multiple sponsors over the next 20 years. Our strategy is to start with enhancements to LANSCE facilities that fully exploit existing capabilities using 800-MeV protons and then to proceed with upgrades to accelerator energy and power that enable new and significant upgrades to facility performance. The enhancements will result in major benefits, some of which are summarized in the box above.

The LANSCE facility serves as a cornerstone in our national security and defense missions through its scientific excellence in research critical to those missions. Future LANSCE enhancements will ensure that this important role in national defense is maintained over the next two decades. ■



LANSCE

Where Science Meets National Security

An Interview with Founder Louis Rosen

Louis Rosen is standing near his friends; on the mural, from left to right, are Hans Bethe, Louis himself, Stan Ulam, and Nick Metropolis.

“When I testified before the Joint Congressional Committee on Atomic Energy to justify the 50 some million dollars we wanted for LAMPF/LANSCE, I still remember saying, ‘Los Alamos is emerging as a national security laboratory not only a national defense laboratory, but still our main focus has to do with nuclear energy. Whether nuclear energy is used for bombs, for generating electricity, or for any number of other purposes, the basic ingredient in the production of nuclear energy is neutrons. So one really needs to have a capability to maintain expertise and growing knowledge in neutron nuclear science and neutron technology. One thing this facility can do, as well as the basic research . . . , is provide the most-intense neutron source in the world for maintaining Laboratory expertise in nuclear physics and for training students and staff in this new field.’ I then asked the question, ‘How can you have a nuclear energy enterprise without strong support from nuclear science and from neutron science and neutron technology?’ Somewhat to my surprise, they understood this. They believed what I was telling them. They knew I wouldn’t dare try to mislead them even if I wanted to, and of course I didn’t want to.”

During the Manhattan Project, Louis Rosen learned from and worked side by side with the great scientists of the 20th century: Hans Bethe, Edward Teller, Stan Ulam, Nick Metropolis, John von Neumann and others. Louis' measurements turned out to be instrumental at Trinity, the first nuclear explosion on the planet. And later, at the George shot, Louis made the measurements that proved Teller's concept for a thermonuclear bomb would work. Steeped in the culture of those heroic times, Louis conceived of LANSCCE as an interdisciplinary facility that would keep Los Alamos as the world leader in nuclear technology. It would be a place for fundamental science, ranging from nuclear medicine to astrophysics, and for innovation in technologies critical to national security. In the following interview with *Los Alamos Science*, Louis recounts how he made that vision a reality and how relevant it is to the challenges of today.

Los Alamos Science: Louis, you have had such a strong influence at the Laboratory and at LANSCCE. It would be interesting to know where you grew up and how you became interested in physics.

Louis Rosen: I was born in New York City but I grew up in the Catskill Mountains. That move turned out to be very important because during the summers I was able to earn enough money to go to college by selling newspapers at the local hotels. I probably couldn't have worked in the City to earn the money. It was in the 30s, during the Great Depression, and it was very hard to find a job. I worked 12 or 14 hours a day selling newspapers and ice cream to vacationers, as did my brother, who went on to become executive director of the Civil Service Commission and a professor and author. Over the summer, each of us earned about \$400, which was just enough to attend the University of Alabama at that time, including tuition, room, and board—everything.

I had actually become interested in science in high school, thanks to a very good high school science teacher, who was also the school coach. He was very adept at making students understand the role of science in society, even way back then.

When I went to college, I started out in premed, but to be in premed you had to take a course in premed physics. In that course, I realized that

physics was really what I wanted to do, mainly, because it wouldn't take as much memory work as chemistry, biology, and all these medical courses. More important, you could figure things out from first principles. That was much more to my liking than to work cookbook style, no matter how important medical work is.



Louis Rosen at LANSCCE, 2006

I changed to being a physics major and got my bachelor's of science degree, and by the time the war had started, I was teaching at the University of Alabama while working on my master's degree. After that I went to Penn State in the Ph.D. program.

Los Alamos Science: Were you already interested in nuclear physics?

Louis Rosen: At that time, my work was in classical physics. My thesis was in using x-rays to study the effects of high hydrostatic pressures on materials. In those days, which tells you something about how old I am, there were no courses in nuclear physics even in some major universities like Penn State, which was (and still is) one of the largest universities. So, when I came to Los Alamos during the Manhattan Project, I had never had a nuclear physics course. Many of us were in the same boat and that was a godsend. In the late 1930s, Hans Bethe wrote three articles, two of them with coauthors Robert Bacher and Milton Livingston. Those became the nuclear physics bible and many of us learned nuclear physics just by studying that bible. However, when I first came to Los Alamos, I did not work in nuclear physics.

Los Alamos Science: How did you get invited to join the Manhattan Project?

Louis Rosen: In early 1944, I was a graduate student at Penn State. One day, there appeared on the campus an emissary from President Roosevelt's Office of Scientific Personnel. He was recruiting for the Manhattan Project, but we didn't know that at the time. His name was Dr. Tritten. I have a very bad memory, but some things just can't be forgotten. He was a well-known scientist. After he reviewed the credentials and records of all the

advanced graduate students, I was called to the dean's office. Here was this prominent scientist introducing himself and telling me, "I want you to join a project that can bring an end to the war." That was a very powerful statement. People were dying by the hundreds of thousands. Along with many others, I was trying to get into the Navy, but I was two pounds underweight. So when he said that he wanted me to join such a project, I immediately said okay. He wouldn't tell me where it was, what it was about, what I would be doing, or who I would be working for—just to come to 109 East Palace Avenue in Santa Fe, NM, for further instructions.

I was married by that time to my now sainted wife Mary, and we had a two-month old baby. They didn't have a house for us at the Project yet, so we got into my 1936 Ford and went to Tennessee, where Mary's father met us. He collected Mary and the baby and took them both to her family home in Tuscaloosa. Mary arrived in Los Alamos two months later. I, instead, went directly on to 109 East Palace Avenue in Santa Fe, NM. When I got to the Hill, they told me that they wanted me to join a group. I wasn't given a choice. They said this is the group you will join, and it was to work on implosion.

Los Alamos Science: Was that about the time it was discovered that the gun device wouldn't work?

Louis Rosen: Yes. It was early 1944, and by that time it was clear that there was a big, big problem here at the Project. When the Project started up, Oppenheimer thought all he would need to make a bomb were a couple of hundred scientists. The idea was that you would eventually collect enough fissionable material—uranium-235 at first and later plutonium-239—to make two nearly critical masses. Then, you'd just use explosives to fire one into the other, you'd get supercriticality, and you would

have your bomb. The questions were, "What would be the yield of this device?" and "What materials must one use?" That's why Oppenheimer thought this could be accomplished by, at the most, two hundred highly qualified scientists. But when Emilio Segrè, who had been a student of



The Trinity Tower

The bomb was in place on the tower. Everything was in readiness, awaiting the results of a pretest at Los Alamos involving a full-scale implosion but with a surrogate for the plutonium. The results were a cliffhanger.

Fermi in Italy, came to Los Alamos, his first job was to study plutonium. We had only microgram quantities at that time, and the first thing Segrè found out was that plutonium had some isotopes that fissioned spontaneously, producing neutrons to such an extent that a gun device could not be used to assemble two almost critical masses. If made with plutonium, it would predetonate, and that was the big problem they now had to solve.

Early in 1944, Oppenheimer began bringing many, many more scientific and technical engineering people to Los Alamos. A way had to be found

to assemble a subcritical mass of plutonium fast enough and uniformly enough to create a supercritical mass for a long enough time to provide a reasonable energy release. It was soon realized that the only possible method was explosive-driven compression—in other words, implosion. So, many groups were set up. My group leader was Ed McMillan, and my division leader was Bob Bacher. Those were pretty high-class people. McMillan achieved Nobel Laureate status, and Bacher became provost at CalTech. I had a lot of fun just being able to talk to people like that. I had never had that opportunity before.

My group was among those working on how to use high explosives to assemble a mass of metal under the conditions that we hoped, when the metal was replaced by plutonium, would ensure a proper energy release. The first metal we worked on was aluminum. Whenever we set off an implosion experiment, shards of red hot metal would fly into the canyons, setting fire to dry wood and leaves. We would have to stop everything, and everybody would fight fires. This was almost a daily occurrence. At one point, the shops ran out of aluminum, and without telling us, they substituted magnesium. It has about the same density, and you can't really see the difference, but magnesium is what you use for firebombs. Needless to say, we had quite a problem that day.

The magnetic method of studying implosions, which yield the collapse time and final density of the material being imploded, relied on electromagnetic signals produced by a conducting material moving in a magnetic field. These signals had to propagate through the explosive residue, which is ionizing. There was a question of whether the rise time of the signal would be distorted by the detonating explosive. Sometimes, when there were no new explosive designs to test, I took it upon myself to measure

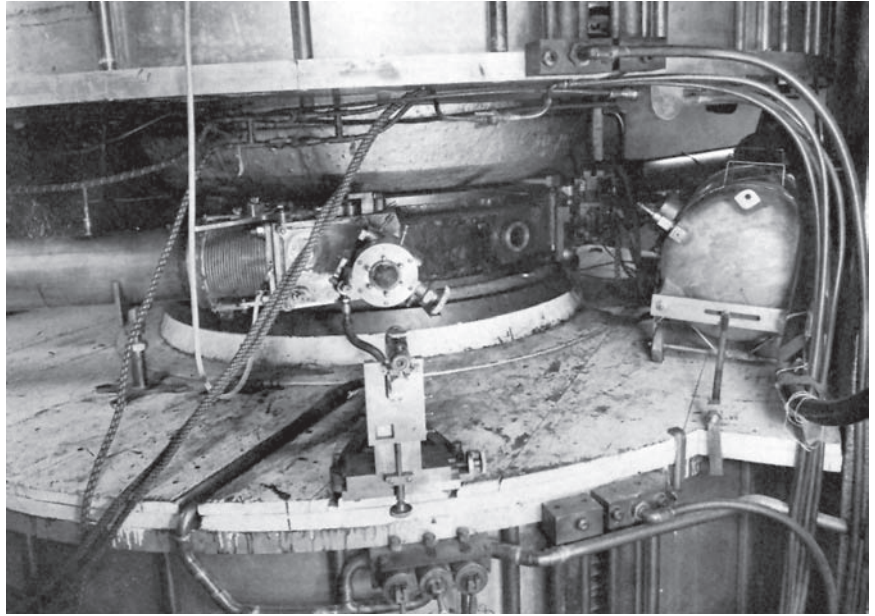
that effect. It was not a requirement; I was just interested in the results. I documented them in my reports, but I never knew that anyone noticed them, not until Hans Bethe kindly informed me of the following episode at the Trinity test.

Uncertainties about implosion continued to the very end, and the final hours before the test were no exception. The bomb was in place on the tower. Everything was in readiness, awaiting the results of a pretest at Los Alamos involving a full-scale implosion but with a surrogate for the plutonium. The results were a cliff-hanger. The electromagnetic signal looked different than expected, and everyone waited for Bethe to interpret them. Bethe looked at the curve and calculated the results from first principles, but he anchored his results in the experiments that, unbeknownst to me, he had seen written up in my reports. He concluded that all was well and the test went ahead.

The journey to Trinity was bumpy and very stressful, to the very last moment. But the experiment achieved the first violent release of nuclear energy on this planet.

Los Alamos Science: How do you view the impact of the Trinity test and your involvement in it?

Louis Rosen: The success of Trinity heralded the termination of World War II, with the saving of many lives on both sides and in occupied China. We now know that the emergence of nuclear energy and its utilization as a weapon, as well as for all manner of peaceful pursuits, was inevitable dictated by the laws of nature. That the development of nuclear weaponry was first mastered by a democracy, rather than by a Hitler or a Stalin or a Saddam Hussein, must certainly stand as one of the most fortuitous occurrences in all of history. In addition, Trinity opened the door to environmentally friendly and affordable energy at a



The Harvard Cyclotron

We now know that the emergence of nuclear energy and its utilization as a weapon, as well as for all manner of peaceful pursuits, was inevitable—dictated by the laws of nature. That the development of nuclear weaponry was first mastered by a democracy, rather than by a Hitler or a Stalin or a Saddam Hussein, must certainly stand as one of the most fortuitous occurrences in all of history.

time when we must plan for greatly diminished use of fossil fuels. This will hopefully help to contain international instability. That, to me, is the promise of Trinity and the validation of my modest contribution to the effort.

Los Alamos Science: Did you choose to stay at Los Alamos after the Manhattan Project?

Louis Rosen: Yes. Right after the war, people had a choice of what to do. I decided, after reading Bethe's bible, that nuclear energy was something the world would definitely need. Even back in high school in the 30s, we were being told that the world oil supplies were going to disappear eventually; they estimated about 50 years or so. Now, in 2005, it is starting to happen and so is global warming. What does one do? It seemed to me that nuclear energy was an obvious choice. I decided to become a nuclear physicist and joined the cyclotron group. During the Manhattan Project, Bob Wilson had come from Harvard to run the cyclotron. But after the war, most of the great people left, and we had to start rebuilding these groups. The cyclotron had been liberated from Harvard for the war effort, but they didn't want it back, and we didn't want to give it back, so we bought it from them.

It was a very temperamental machine, but Stan Hall—he's still here—was a sergeant during the war

and an expert on the cyclotron, and he could get a beam out when nobody else could. One day, Stan was working at the control desk, and he was having a beer, which was okay at that time. In comes a general on inspection, his eye catches this beer-drinking sergeant, and he says to him, "Soldier, is that necessary?" and Stan replies, "Sir, it won't run without it." The general graciously retreated.

After the war, I worked with the cyclotron, but it was still very temperamental. The first problem I tackled was to get certain fundamental scattering data between like nuclei. Almost nothing was known about the interactions of light nuclei with themselves and with each other. But you needed to take data at many angles, and it was so hard to get the machine to run long enough even for one angle. So I decided to develop a technology that would get data at all angles simultaneously. It became known as the nuclear multiplate camera. That was the beginning of the Laboratory's efforts to develop nuclear-detector technology, which turned out, as I will explain in a moment, to be a blessing in disguise. With this camera, we could get angular distributions for scattering reactions for deuterons with any target nucleus within a 30-minute run. It was marvelous, and I set up the first nuclear microscopy group. We hired young ladies, most of whom had a college degree and knew mathematics, and they became superb microscopists. It was hard work, and we would permit them to work only 4 hours a day. But that was all they wanted to work, so it was perfect.

Los Alamos Science: What were those nuclear plates?

Louis Rosen: The nuclear plates were glass plates covered with a high-density silver bromide emulsion—like you have in ordinary film, but with a much higher density of silver. The emulsions were very thick, hundreds of microns thick, and they would

record the tracks of the charged particles. From those tracks we could figure out the direction, energy, and charge of each particle going through. We developed that technique as did others in England and elsewhere.

I used that technique to measure nuclear cross sections (both neutron and charged-particle) for some years and published many papers. Everything one did in nuclear physics was brand new, so there was no problem publishing in refereed journals. The interesting thing is that, although originally I thought my work on basic research was without any practical



importance, I was wrong. It soon appeared that the thermonuclear program needed neutron energy spectra and cross sections for a host of materials. The electronics of that period could not give definitive energies of neutral particles that entered proportional or fission counters. So I decided to develop the nuclear-emulsion technique for neutron spectroscopy. We measured neutron spectra for essentially all the important materials related to fusion weapons. We had a Cockcroft-Walton accelerator, which provided 14-MeV neutrons from deuterium-tritium fusion reactions, and that was our chief neutron source.

Los Alamos Science: So, your measurements became very important

to the development of the hydrogen bomb.

Louis Rosen: Yes. At one point the theorists needed to know how 10-MeV neutrons would interact with materials because, if you have 14-MeV neutrons from fusion, they will degrade and you'll have neutrons at 10, 9, and 8 MeV. This presented a problem. We did not have any source of neutrons except at energies of a few million—electron volts and then 14 MeV. But, Professor Gregory Breit was here, and he said, "Look, if you will get me proton data at 10 MeV, I will calculate what the neutrons would do at that energy. But we didn't have 10-MeV protons. The cyclotron would give 10-MeV deuterons, but it wouldn't accelerate anything else at that time. So Norris Bradbury, our Lab Director, called E. O. Lawrence, and Bradbury said, "Look, we need to use your cyclotron for some experiments," and Lawrence said, "Absolutely." So they interrupted their programs, and we, with our multiplate camera, microscopes, and plate readers (those were people!), descended upon Berkeley. In order to extract the beam from the cyclotron, they had to cut a hole in one of the magnet pole pieces, which are made of very thick iron. At first, they were really upset to cut a hole in their beautiful cyclotron and wondered what that would do to the magnetic field. After we established that it wouldn't do anything to the magnetic field, they got the welders and cut a hole. We put in our beam pipe, got the beam out, and did experiments with 10-MeV protons on all the materials requested by the theorists. Then Gregory Breit calculated what 10-MeV neutrons would have done, and everything was okay. The Berkeley graduate student who ran the cyclotron was permitted to use our camera to do an experiment for his thesis. He later made his career at Los Alamos. His name was Tom Putnam.

But that's not the end of the story.

Finally, it was decided that the Teller Super wouldn't work. Teller wouldn't believe the calculations at first, but then Fermi did his own calculations and said, "Edward, it just won't work." It looked like there was no way to ignite the thermonuclear fuel. At that point, Stan Ulam suggested, "Why don't we use a fission bomb to heat up and ignite the thermonuclear fuel?" When Teller heard this, he immediately realized, "That's the answer, but how do you arrange a fission bomb so that it'll do what you want it to do?" How do you arrange things so that the energy from that bomb will be focused in the right way to make high-density thermonuclear fuel with a temperature of millions of degrees? Teller came up with the idea to use the radiation from the fission bomb. Everybody thought, "Wow, this may be the answer." But how do you know it's going to work?

It was decided to have a test. At that time, a large set of tests was being planned at Eniwetok—the Greenhouse series. The electronics were still not good enough to measure neutron spectra. However, to know whether the thermonuclear fuel ignited, you had to measure the number of high-energy neutrons coming out and their energy distribution. That measurement was especially important because the energy released would be too small to be distinguished from that released from the fission bomb. So, how does one determine whether Teller's idea really worked? Well, you had to measure the 14-MeV fusion neutrons. It was the only way. A large number of groups were set up to do electronic measurements detection. They didn't want to measure the energy; they just wanted to be sure that 14-MeV neutrons were produced. There was a big group from the National Naval Research Laboratory, a group from the University of California, and a number of groups from this laboratory, all

using electronic equipment. I made a proposal that we use nuclear emulsions. Everybody thought that had to be the craziest idea ever. Nuclear emulsions could only withstand a few hundred millirem of radiation before they would turn black. And how were the glass plates going to survive a several-hundred-kiloton bomb? Well, Bradbury called a big meeting with all the division leaders, and I was invited to the meeting to present the proposal for this experiment. People's eyes just glazed over. Only one person said, "I think we ought to try this other approach." That person was Bradbury,



The George Shot

and that was enough. One vote canceled all the others.

So, we started getting ready for this experiment, and we went down to Eniwetok to supervise the installation and alignment of these enormous multiton concrete collimators. It was a huge experiment. My first thesis student at Los Alamos, John Allred, had joined my group, and we were working together with a number of other people to mount this experiment. The explosion was set off one evening, as soon as it got dark, so you could take pictures. When the test went off, it was immediately known that all the electronic experiments had failed.

Not one of them provided a clue as to whether 14-MeV neutrons were produced. But because of the radiation fields, we couldn't collect our detectors for 24 hours.

The next evening, we went in to collect our film. We had a six-by-six truck and we had a lead cask to protect the film, but there was no protection for the people. The health division regulations allowed us to accumulate a few hundred millirem, but still we had to get in and out very fast to stay within that dose. John, I, and a radiation monitor went in, and as we were driving through this field of radiation with the detectors ticking continuously, the monitor said to John, who was driving, "What happens if this breaks down?" John replied, "I don't know, you just try and catch me." We finally arrived at the 400-meter collimator, quickly unbuttoned the shield, retrieved the plates, and put them in the lead cask. They were now safe. Off we went back to the lab.

We processed them that night. The next morning, just at daybreak, there was a pounding on the lab door. It was Edward Teller. Many of the experimentalists and theoreticians knew that the results of this experiment were crucial and that, if they were to have any data at all, the data would come from these emulsion plates. So, they stayed up all night playing poker and that's why Edward was up this early. He came in and said, "Louis, 'did we get 14-MeV neutrons?'" I said, "Edward, the plates are processed, but they are being washed, and then they have to dry." "Oh no, no. You can sacrifice one. Just take one out and see if it has the 14-MeV neutron signature." He was right; we could sacrifice one. So, I took it out, put it under the microscope, and this was one of the most exciting moments of my career. Here were these beautiful proton recoils, which had just the right energy to be from 14-MeV neu-

trons. We used absorbers to take out the proton recoils from fission neutrons. I had previously calibrated the microscope so I could determine from the number of proton tracks in a given field how many 14-MeV neutrons would have been generated. I looked at the plate not more than 20 seconds, and I said, “Edward, it’s okay. You’ve got 14-MeV neutrons, and many of them.” “How many?” Fortunately, I could tell him.

Then, much to my surprise, Edward, who usually walked with difficulty because of his artificial leg, went dashing out the door. I could not imagine where in the world he was going. Our lab was right next to the airstrip, and I watched Edward head for the airstrip and go out to the middle. A plane was taking off, and he waved for the plane to stop. It stopped, the door opened, and he handed something to whoever was in the plane. The door closed, Edward got out of the way, and the plane continued to take off. It was 15 years before I knew the end of the story. Edward and I had traveled to Albuquerque from Washington, and I offered him a ride to Los Alamos. It was hard for him to get into the little planes that flew to Los Alamos, so he was grateful for the ride. On the way home, it occurred to me to ask him, “What happened on that day that you came in and wanted to know whether you had 14-MeV neutrons?” Edward replied in his inimitable style, “All right, I’ll tell you.” He began by telling me that some months earlier he had been invited to give a colloquium for the students at the University of Texas, and when he finished his talk, a pretty young lady got up and said, “Professor Teller, did you ever commit a security breach?” Surprised by the question, he thought for a few seconds, and then he said, “Yes, once. But it was not my fault. It was the fault of Louis Rosen.” He continued with his story, telling me that he had

had a bet with E. O. Lawrence, a 5-dollar bet. And although the idea was his, he bet that it wouldn’t work—that there would be no significant burning of the thermonuclear fuel. But it did work, so he had paid Lawrence the 5 dollars and had done this in an uncleared area, which meant he was giving Lawrence classified information in an uncleared area. That was a security breach, but it was my fault because I gave him the data!

Bradbury recognized that the Laboratory had to diversify if it were to remain a world-class laboratory, which, . . . was absolutely essential for the security of this country. So Bradbury lassoed the Laboratory and morphed it from a national defense laboratory into a national security laboratory. Of course, national security includes national defense, but it has many other aspects. Environmental security, food security, energy security, economic security, and now antiterrorism,

Los Alamos Science: After being so involved with the nuclear weapons program, how did you get the idea to build LANSCE, or LAMPF as it was originally called?

Louis Rosen: Well, Los Alamos started as a national defense laboratory. It first invented the fission bomb, then it invented the fusion bomb, and

then it miniaturized both. What does one do for an encore? It was essential for the development of those weapons that we have very broad expertise in science and technology, not only in nuclear physics, not only in metallurgy, but in many fields. We had assembled the scientific staff to do that. And it had been a superb staff. After accomplishing your main mission as a weapons laboratory, how do you maintain the skills necessary to make sure that the weapons you stockpile remain safe, secure, and reliable? And how do you maintain the vitality of the Laboratory? And how do you maintain the skills to resume testing if necessary, in the almost certain event that there is a test ban? And how does the Laboratory position itself to contribute to national security in the broader sense?

By the middle of the 1950s, Bradbury recognized that the Laboratory had to diversify if it were to remain a world-class laboratory, which, he felt as did others at that time, was absolutely essential for the security of this country. So, Bradbury lassoed the Laboratory and morphed it from a national defense laboratory into a national security laboratory. Of course, national security includes national defense, but it has many other aspects. Environmental security, food security, energy security, economic security, and now antiterrorism, they all fall under national security. Norris set out to diversify the Laboratory, and several things were attempted—nuclear rocket propulsion, thermal neutron reactors, fast neutron reactors, high-temperature gas-cooled reactors, and fusion energy. Those programs achieved many technical successes, but for one reason or another, they did not become part of our main mission.

During the same period, nuclear physics was still classical nuclear physics. It ended at 10 MeV. The Laboratory had led the world in

nuclear physics for a while, but the details of nuclear physics being explored at that time didn't have too much to do with daily life, and interest in the field was diminishing. This presented both a problem and an opportunity. Another fortuitous thing then happened. My sainted wife Mary decided that we had to get away from Los Alamos for a while. I didn't want to leave as I was pioneering and publishing the results of new experiments, but I realized she was right. So, I applied for a Guggenheim Fellowship. The time for applications had passed, but I told Bethe and Teller, and they somehow arranged to get the deadline extended. I was awarded \$5000, which was a lot of money at that time, and I became one of the first people to go on a sabbatical from Los Alamos. The Laboratory paid half my salary. With that plus the \$5000, we could practically live like kings. We could have gone either to Paris, or Tokyo, or Oslo, and Mary chose Paris. We got an invitation to the Center for Nuclear Research at Saclay. They knew about my pioneering work on polarization and they wanted to start a polarization program there. So, off to Paris we went. During that year, I had time to think about how to rejuvenate nuclear physics and make Los Alamos once again a world leader in that area. It seemed to me that building an accelerator with not 10, but 1000 to 10,000 times the intensity that was available anywhere in the world (for energies above the pion production energy, at least 400 MeV) would open up new physics regimes. Students, faculty, and other scientists would be attracted to Los Alamos, maybe spending part of their time working with this facility and part on weapons physics.

When I got back to Los Alamos, I wrote a memo to Jerry Kellogg. He was Physics Division leader and a former student of I. I. Rabi. And I



(Left to right): Senator Clinton P. Anderson, Glenn Seaborg, and Louis Rosen at the Groundbreaking for LAMPF

It seemed to me that building an accelerator with not 10, but 1000 to 10,000 times the intensity that was available anywhere in the world would open up new physics regimes. Students, faculty, and other scientists would be attracted to Los Alamos, maybe spending part of their time working with this facility and part on weapons physics.

told him why I thought this new facility would be extremely important for the vitality of the Laboratory, for the nuclear weapons program, and for the health of nuclear physics. There was talk of building a nuclear energy economy at that time, which I hope will still happen. It's more likely now

than it has been for some time. But how do you build a nuclear energy economy if you don't have a basis in nuclear science to increase your understanding of nuclear phenomena and to train students in nuclear technology?

Kellogg thought I had a pretty good idea and sent the memo to Bradbury. Bradbury said, yes, he would support the proposal provided Louis Rosen would stop everything he was doing and devote all his time and effort to making this happen. Well, that was a big sacrifice for me, and it took me a little while before I decided that I was young enough to take the risk. If we failed, I could still go on to another career. It wasn't a sure thing that we were going to succeed, not at all.

Bradbury took money from the weapons program to support preparation of the proposal because he realized that this new facility was needed to maintain the health of the Laboratory as a weapons laboratory. It could do science for the sake of science, but also for the sake

of developing technologies for the broader aspects of national security. So that's how I became an advocate for LAMPF, the Los Alamos Meson Physics Facility, which has now become LANSCE.

Los Alamos Science:

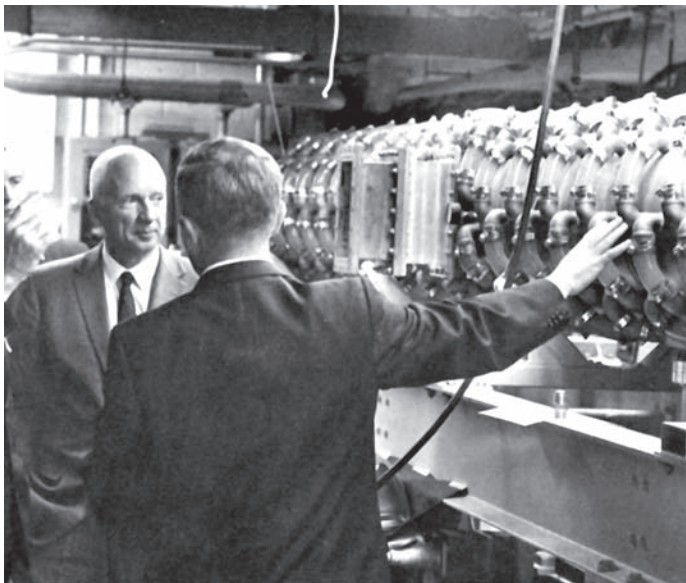
How did you manage to get the support for this new facility?

Louis Rosen: Well, before trying to sell the idea to Congress, we made sure that everybody in the Laboratory, especially the weapons people, saw this facility as an important contributor to their activity, and one of the things we built purposely for that work was the Weapons Neutron Research (WNR) Facility. We also had to get the scientific community to understand why the new facility

would be important for them as faculty and for their students. So, we set out on a campaign to talk at universities, and we set up a users group even before we had money for the accelerator. The nuclear physics community was worried that this facility would take money away from classical nuclear physics, so it took some doing to get the support of a very substantial fraction of that community.

Of course, the key to success was Congress. Here I was very lucky because the Atomic Energy Commission was made up of people who understood science. Glenn Seaborg was the chairman, and I knew Seaborg. He not only understood the science we were trying to address and that this would be the first multidisciplinary facility of its kind in the country, but he also understood how important it was for the maintenance of Los Alamos as a world-class laboratory to support world class steward-

ship of the nuclear stockpile. Seaborg also knew about some very important experiments that I had done having to do with weapons. The measurement of the 14-MeV neutrons was one, but



Director Norris Bradbury and Louis at the LAMPF Accelerator

then there were others—the neutron spectroscopy work, the neutron cross section work, and the problem that the second thermonuclear weapon ever tested yielded a much higher amount of energy than anticipated. It was almost a disaster. The questions were, “Where did this energy come from?” “Why were the theoretical estimates so wrong?” It turned out that I had done an experiment that indicated where this energy came from. Now, Seaborg knew this, and he told Congress how we had surmounted those problems.

So, when I testified before the Joint Congressional Committee on Atomic Energy to justify the 50 some million dollars we wanted for LAMPF, the Joint Committee knew me by the reputation that Seaborg had established. I was also very good friends with Senator Clinton P. Anderson, the chairman of the Joint Committee for Atomic Energy. I still remember say-

ing to them, “Los Alamos is emerging as a national security laboratory not only a national defense laboratory, but still our main focus has to do with nuclear energy. Whether nuclear

energy is used for bombs, for generating electricity, or for any number of other purposes, the basic ingredient in the production of nuclear energy is neutrons. So one really needs to have a capability to maintain expertise and growing knowledge in neutron nuclear science and neutron technology. One thing this facility can do, as well as the basic research with pions, neutrons, and neutrinos, and directly with protons, is provide the most intense neutron source in the world for maintaining Laboratory expertise in nuclear physics and for training students and

staff in this new field.” I then asked the question, “How can you have a nuclear energy enterprise without strong support from nuclear science and from neutron science and neutron technology?” Somewhat to my surprise, they understood this. They believed what I was telling them. They knew I wouldn't dare try to mislead them even if I wanted to, and of course I didn't want to. Although there was then, as now, a very difficult budgetary situation, they decided to go ahead with this facility, the most expensive nuclear physics facility ever proposed. They authorized and then allocated the funds to build LAMPF, which is now LANSCE.

Los Alamos Science: Didn't you make a rather audacious promise when you said that the new accelerator would produce a beam with an intensity much higher than had ever been achieved before?

Louis Rosen: Yes, the unique fea-

ture of the facility would be a beam of 800-MeV protons with an intensity at least a thousand times greater than anything on the planet. We were able to deliver on that promise because we were able to attract some of the very best people at the Laboratory. Three were in Project Sherwood (the fusion project), Darrah Nagle, Ed Knapp, and Don Hagerman; they were the creative and highly innovative people who invented the new accelerator—the side-coupled cavity—without which we couldn't have built the facility. They and their extraordinarily capable colleagues also led the design and construction effort. Standard linear accelerators—the type Louis Alvarez had invented—would only accelerate particles to a maximum energy of 200 MeV without becoming impossible from the standpoint of energy requirements. (We eventually used a 100-MeV Alvarez-type accelerator as the injector for the main accelerator in the LAMPF accelerator.) On the other hand, the beam loss in cyclotrons would be so great that it would be impossible to reach the intensity we wanted. Others who wanted to develop meson factories—the Canadians and the Swiss—realized as we did that technology was not at the stage where a circular machine could achieve such high currents. Eventually, they opted for a hundred microamperes in beam intensity. But we wanted a milliamperere, so we had to pin our hopes on a linear machine. We reached that goal with the side-coupled cavity of Knapp, Nagle, Hagerman, and their colleagues, and it has had profound consequences, not only permitting us to build LAMPF on schedule and

on budget, but every multihundred-million-electron-volt proton linac built today uses that design. It has made possible efficient and stable mega-voltage x-ray machines. All

companies that build mega-voltage x-ray machines now use that design. It's gotten more compact, it's more reliable, and it has helped hundreds of thousands of cancer patients, mil-



June 10, 1972—Achieving the Design Beam Energy of 800 MeV on Louis' birthday

lions probably, get better therapy than they otherwise could have got. So that's the way basic research works. It reaches out in ways that are unpredictable. It also stimulates technology. LAMPF was the first accelerator designed for complete control by computers. This is now standard practice.

Los Alamos Science:

In addition to delivering very high intensity, LANSCE seems to have many innovative features that make it a very flexible machine.

Louis Rosen: We were interested making the

machine as useful as possible. For example, LANSCE was the first dual-beam machine ever built. It uses both halves of the radio-frequency cycle to accelerate negative and positive ions simultaneously. That idea actually came from the Canadians. This makes possible twice as many experimental ports as you otherwise would have. But we did it for another reason. An important aspect of nuclear physics is identifying and exploring the different forces involved. One, which was very hard to understand, was what we call the spin-orbit force. This force comes from the fact that all nucleons (neutrons and protons) and most nuclei have net spin, clockwise (up) or counterclockwise (down). If the particles in a beam have all the same spin, the beam is said to be completely polarized. To study this spin orbit force required polarized nucleons, and with two beams, negative and positive, we could dedicate one to a polarized beam, which eventu-

We reached our goal with the side-coupled cavity . . . and it has had profound consequences . . . All companies that build mega-voltage x-ray machines now use that design. It's gotten more compact, it's more reliable, and it has helped hundreds of thousands of cancer patients, millions probably, get better therapy than they otherwise could have got. So that's the way basic research works. It reaches out in ways that are unpredictable.

ally had significance for the weapons program in the following sense. With the polarized beam it was possible to better parameterize the optical model for describing nucleon–nucleus interactions. By getting a better optical model one no longer had to measure nucleon–nucleus interactions for every angle and every energy and every nucleus. One could use this model to extrapolate between energies and angles, and it relieved a lot of the problems, providing data for the theorists to do their modeling of how nuclear weapons work. So, here was a purely basic research question that reflected on the practical applications of nuclear energy. Victor Weisskopf was the one who had a lot to do with the development of the optical model, and it is still used. It has better parameters now than it did when I was young. But it is still used, and it still gets its parameters from the same data.

Los Alamos Science: In addition to nuclear physics, isn't there a strong program in fundamental physics at LANSCE?

Louis Rosen: Yes, but there is also a lot going on now at LANSCE that was not considered nuclear physics 30 or 40 years ago—mainly because one didn't know how to access these questions. For example, at LANSCE they are planning for ultrahigh-precision neutron lifetime experiments and parity-violating experiments with ultracold neutrons. These do not have obvious practical applications; however, LANSCE is important as a magnet for recruiting people to the Laboratory. LANSCE brings to the Laboratory people with talent and ideas from all over the world. You cannot have world-class science if you don't interact with the world community of scientists, and LANSCE is a vehicle for promoting that interaction.

But LANSCE does one more thing that might not occur to everyone. It contributes to reducing international

tensions by inviting to LANSCE scientists from nations that are not particularly our friends. Even during the Cold War we gave access to Soviet scientists, and one of the most important things I ever did was to make it possible for scientists from the People's Republic of China to come to this Laboratory, work at LAMPF, and stay much longer than the canonical 8 days that were allowed at the time. And that has an interesting history.

Sometime in the 1980s, I received

People don't realize the close interplay between basic research and the emergence of national security technologies. LANSCE development was responsive to the fact that technology is truly the child of science.

an invitation from the Chinese Academy of Science to come to China with my wife under the following arrangement: If I provided three lectures, one of which had to be on energy, they would take us anywhere we wanted to go in China. When I mentioned this to Mary, it took her no time before she had an agenda of where we should go in China. I got permission from the Laboratory and Washington to go to China, and off we went. When we got to there they treated us like royalty. They told me where I would lecture, and I provided the lectures, but they also permitted me to visit any laboratory. I chose the major science laboratories. When our visit was almost at an end, a messenger from Fong Yi, the deputy premier in China at that time, told us that Fong Yi would like to talk to us in

the royal palace in the Forbidden City and asked whether we would be willing to meet with him. Of course we agreed, and the next morning we were taken to the Forbidden City in a black limousine. There, at the emperor's palace, we were confronted by a huge number of stairs leading up to the palace proper. Fong Yi and his entourage had come down halfway to meet us, and it was up to us to mount the stairs. But Mary already was having trouble walking as she had had polio and I wondered how in the world we were going to get her up those stairs. But I needn't have worried. They had arranged for two very stout Chinese officers to butterfly her up the stairs while I tagged along behind. We then introduced ourselves, went up the rest of the stairs to his office, Mary with her accomplices, and had an hour-and-a-half conversation.

He took half the time to tell me about the advances China had made during the great march. The other half I talked about what I had found out about his laboratories—the good and the bad. Then he said, “Now Professor Rosen, I do not have even a high school education, but I am in charge of all the science, technology, and education in all of China. If you were in my place, what would you do to catch up with the West in science and technology?” I had not anticipated the question (although I should have suspected something like this), but after thinking for a minute or two, I said, “Well, the first thing I would do is identify, every year, some hundreds of your brightest young scientists and engineers and send them to centers of excellence, not for a week or a month, but for a year or even two years. That way they can become engaged not only with the frontiers of science and technology but also with the environment that permits science and technology to flourish. He replied, “Yes, Professor Rosen, that's a very, very good idea. Now would you accept

some of them at your facility?” Now I understood the reason for our invitation and the reason for all the things that had happened before. My answer was, “Mr. Vice Premier, the rules of the government right now are that we can accept Chinese citizens at Los Alamos for only 8 days, but if you will nominate scientists whom we know by their reputation, I will do what I can to get that rule changed.” About 3 months later, a letter came from his deputy for science nominating three or four renowned people. One was director of their main nuclear physics laboratory, another was a group leader of the chemistry group, and a third was an expert on radioactive nuclei. Congress had already been persuaded that LAMPF must be an open facility if world-class science and technology was to continue at the Laboratory. I’m not sure that everyone in the present Congress understands that, but the Joint Committee on Atomic Energy did.

Now the monkey was on my back. Fortunately, if you’re lucky, you don’t have to be smart, and I have been lucky many times. This time, it turned out that a former neighbor of mine, Herman Roser, who had been the Atomic Energy Commission presence at Los Alamos, was made head of the Division of Military Applications in the Atomic Energy Program. It was up to him to decide what the security rules were. I went to see my friend Herman Roser and told him, “Look, if we could make friends with these people, one quarter of the people on Earth, it would be worth more than any number of aircraft carriers or bombers that we could possibly build.” He understood this. In a few months word came that “yes,” we could invite these scientists. They were marvelous visitors and worked all hours of the day and night. I suspect that our initiative was a factor in improving our relations with China at a critical time. Without LAMPF,

we couldn’t have done that, and now LANSCE serves a similar purpose. So, in addition to direct and unique contributions to national security, LANSCE also fosters an environment that encourages a symbiotic relationship among national laboratories, academia, and relevant industries.

Los Alamos Science: Isn’t LANSCE also important as a source of radioisotopes for medicine?

Louis Rosen: Yes, these are radioisotopes that cannot be produced by reactors. They are proton rich, whereas reactor radioisotopes are always neutron rich. Thus, we more or less double the radioisotopes available for medical diagnosis and treatment and for industrial purposes. In the original plans for the facility, I decided to include specifications for a radioisotope facility that would not interfere with anything else going on. It would be put at the end of the beam line, where the beam goes to a beam dump. That beam dump eventually became a neutrino source—even back then we used everything from the hog including the squeal. We built the radioisotope facility, and it functioned very well. Unfortunately, the accelerator is sometimes down for long periods, either for maintenance or because the budget will not support the electricity it demands. It uses 20 megawatts of power when it’s running full steam. But we had the foresight to do something that has only now come to pass. We provided a space between the 100-MeV section and the 700-MeV section of the accelerator, a space where a magnet could be installed to deflect the beam to the north into what we hoped would become a radioisotope facility to produce radioisotopes year round, whether the main machine is down or not. In addition, it could also use the negative ion beam to produce radioisotopes. It’s only in the last few years that funds became available to build an isotope production

facility at this juncture between the phase one linear accelerator and the main accelerator. And it’s marvelous for a lot of reasons—not just medical. You see, at WNR we measure neutron cross sections. That was one of the main reasons for establishing WNR in the first place, and those are still being measured because the weapons program is a black hole for neutron cross sections. It needs all it can get. Some of the needed cross sections are for short-lived radioisotopes that are made when a nuclear weapon detonates. They are so short lived that you can’t make them at Oak Ridge or Brookhaven and bring them here. There’s not enough time. With the new radioisotope facility, we can make the radioisotopes and quickly transport them to the WNR to make measurements. Again, that is a weapons measurement that the radioisotope facility uniquely makes possible.

Los Alamos Science: What do you see as the role of LANSCE in the future?

Louis Rosen: Today, national security, including economic security, involves characterizing, improving, and inventing materials as never before. Neutrons, including ultracold neutrons, are indispensable probes. With proper upgrades LANSCE can meet the civilian and military requirements far into the future.

People don’t realize the close interplay between basic research and the emergence of national security technologies. LANSCE development was responsive to the fact that technology is truly the child of science. It’s very important that those responsible for planning the future of the Laboratory understand the unique utility of LANSCE for both science and national security and how important it is for the nation that this facility be imbedded in a national security laboratory while being open to the world scientific community in its unclassified research activities. ■

LANSCE and the Nuclear Weapons Program

Philip D. Goldstone

In 1996, sponsorship of the Los Alamos Neutron Science Center (LANSCE), previously known as the Los Alamos Meson Physics Facility (LAMPF), was transferred to Defense Programs, and it was clear that neutrons provided a unique tool for understanding materials. It was also clear that improving physical models of materials and understanding materials issues related to aging or remanufacturing were going to be important for stockpile stewardship. However, although that vision could be broadly painted and some thrusts were well identified (for example, structural studies of plutonium), elements of that vision were not fully realized at the time.

The decade since 1996 has been remarkable for the nuclear weapons program and for LANSCE. Stockpile stewardship itself has moved to incorporate a more-coherent, sound methodological basis (the quantification of margins and uncertainties, QMU), and the technical details and priorities of the program have matured as a result of the successes and, especially, the challenges the program has identified and overcome. Some new tools have emerged. Proton radiography (pRad), in particular, which was not even in the minds of the “forefathers” of stockpile stewardship, has become a crucial element of the research program within a remarkably short time after key breakthroughs were first demonstrated at LANSCE. Further, understanding what is needed to reduce uncertainties in assessment resulted in a renewed appreciation at both Lawrence Livermore and Los Alamos National Laboratories of the importance of measuring certain neutron nuclear-reaction cross sections that only LANSCE can provide.

And although there is now a need to refurbish additional elements of the accelerator that powers the research capabilities at LANSCE’s several experimental areas, considerable investment was made over this decade to operate, maintain, and improve elements of the LANSCE infrastructure and scientific equipment, supported, as appropriate, by the National Nuclear Security Administration (NNSA) and the Office of Science sponsors and institutional funds. LANSCE is now a far more powerful and important facility in terms of the breadth of its scientific reach and its impact on stockpile stewardship than it was in 1996, when its sponsorship was transferred. LANSCE is also the Laboratory’s key world-class experimental user facility and science “magnet.” In 2001, LANSCE was designated a national user facility.

Strategic Role of LANSCE

Direct Mission Support through Science-Based Prediction and Assessment.

LANSCE contributes both directly and indirectly to the nuclear weapons program. The principal direct impacts are through pRad, nuclear data measurements, and structural information from neutron scattering on key materials. These measurements, most of which require the particular capabilities at LANSCE, are helping to reduce uncertainties in science-based predictive capability for weapon safety, reliability, and performance.

They are directly impacting weapon assessment and certification decisions and are essential for many identified program milestones. All NNSA laboratories rely on

LANSCE's capabilities.¹ The articles in this section will speak to a few examples of a broad set of contributions in three main areas:

pRad. Proton radiography at LANSCE is providing important data on detonation and burn properties of insensitive high explosives at controlled temperatures, shock-driven material damage and spall, ejecta transport, small implosion experiments, and dynamic loading of neutron generator components. Lawrence Livermore and Sandia National Laboratories and the Atomic Weapons Establishment in the United Kingdom have collaborated with us on, or led, many of these experiments. The results have been important for developing and validating physical models. Looking forward, we have identified work to be done with pRad using the 800-million-electron-volt beam at LANSCE that we estimate will take over a decade to complete at the rate of 20 to 30 experiments per year. Further, we continue to design and perform experiments that are immediately responsive to (and help resolve) unanticipated technical questions within the stewardship program. Experiments we have done have also demonstrated pRad's long-term value as a capability for stockpile stewardship. In the future, a 20-giga-electron-volt pRad capability for hydrotesting could potentially be based on the present LANSCE facility.

Nuclear data. Using the GEANIE detector at the Weapons Neutron Research Facility (WNR) and the DANCE detector at the Lujan Neutron Scattering Center (Lujan Center), LANSCE is providing key nuclear-cross-section data on actinides and radiochemical tracers, enabling important refinements in models and

better use of the historical nuclear-test database. The WNR recently enabled irradiation testing relevant to Sandia National Laboratories certification of the W76 arming, fuzing, and firing system. The neutron spectra available from LANSCE (including very high energies at the WNR) and the Laboratory's ability to handle short-lived isotopes, along with unique capabilities of a range of instruments, make LANSCE the only source for a variety of nuclear-cross-section data of interest.

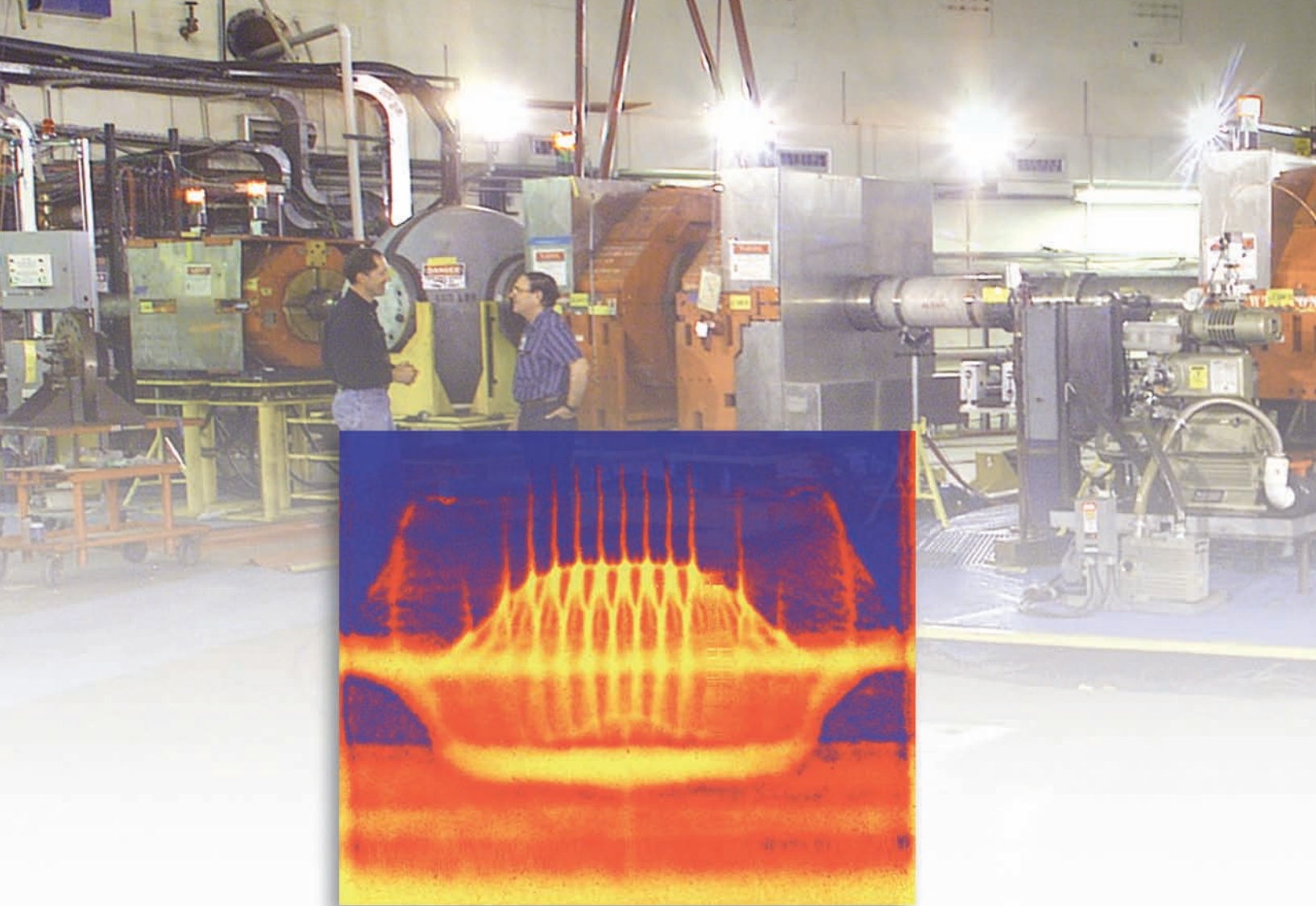
Materials. Unique instruments and sample environments at the Lujan Center, which is operated with Office of Science sponsorship as a user facility, are contributing to high-pressure data on plutonium, to understanding the constitutive properties of other weapon materials, to evaluation of the effects of fabrication processes on the characteristics of plutonium and uranium components and on neutron tubes, and to corrosion studies. Research at the Lujan Center is also determining underlying structural changes that occur in aging of uranium-niobium alloys, high explosives, and other materials.

Indirect Value to the Nuclear Weapons Mission through an Institutional Role. LANSCE also contributes to our national security missions indirectly by sustaining the Laboratory's scientific capabilities, which are essential to our ability as a national laboratory to address tomorrow's challenges. LANSCE's broad scientific reach in key areas that are important to national-security missions—materials science and engineering, nuclear science and nuclear energy, and structural biology—have made it integral to the scientific vital-

ity of the Laboratory. Synergy with the Center for Integrated Nanotechnologies and the National High Magnetic Field Laboratory not only provides distinguishing opportunities for scientists at LANSCE but makes the facility a central element of the Laboratory's materials strategy. LANSCE, as was LAMPF before it, is well established as a significant recruiting portal for mission activities across the Laboratory. Literally hundreds of Laboratory staff now engaged in other parts of the Laboratory in support of our missions initially came to Los Alamos through work at this facility. Research using LANSCE adds to contact with the best outside scientists in condensed matter and nuclear science; contact with the cutting edge of science is important to our continued technical excellence in these fields of importance to our weapons mission. Medical isotope production is a national service, and industry has made LANSCE a standard for single-event-upset testing of semiconductor devices.

To ensure that LANSCE remains a "magnet" for excellent scientists, we intend to maintain the facility's scientific vitality and productivity with an emphasis on condensed matter and biology, in addition to weapons program priorities. Feedback from the scientific community has indicated that, properly managed, LANSCE will maintain an important role as a complement to the Spallation Neutron Source for neutron scattering. At the same time, LANSCE offers unique nuclear-science capabilities at WNR, and with an operational Materials Test Station, it could become a unique U.S. capability for materials testing for advanced nuclear power. LANSCE continues to make important contributions to stockpile stewardship and to the scientific underpinnings that will enable the Laboratory to respond to national-security challenges in the future. ■

¹ In 2005, weapons program users from Los Alamos, Lawrence Livermore, and Sandia National Laboratories, as well as the Atomic Weapons Establishment, conducted 27 dynamic experiments at the pRad facility; 66 experiments using 20 percent of the beam time allocated to the user program at the Lujan Center (a 100 percent increase from 2004); and 51 experiments at the WNR and DANCE.



Proton Radiography

Christopher Morris, John W. Hopson, and Philip Goldstone

The United States stopped nuclear testing in 1992, and since then it has become increasingly important to develop predictive models for the behavior of materials driven by high explosives. The primary experimental tools to observe that dynamic behavior have been based on x-radiography, the imaging technique used during the earliest days of the Manhattan Project. Over the last decade, however, a new imaging technique has been developed that uses high-energy protons, rather than x-rays, to radiograph materials during dynamic experiments. Proton radiography allows researchers to make short movies and obtain much more detailed information on the motions and densities of materials when driven by shock compression than was ever possible before. The penetrating power, or long mean free path, of protons and the ability to focus them are opening up new opportunities for quantitative experiments, accurate model development, and designer training that will revolutionize how the U.S. nuclear stockpile is stewarded in the future.

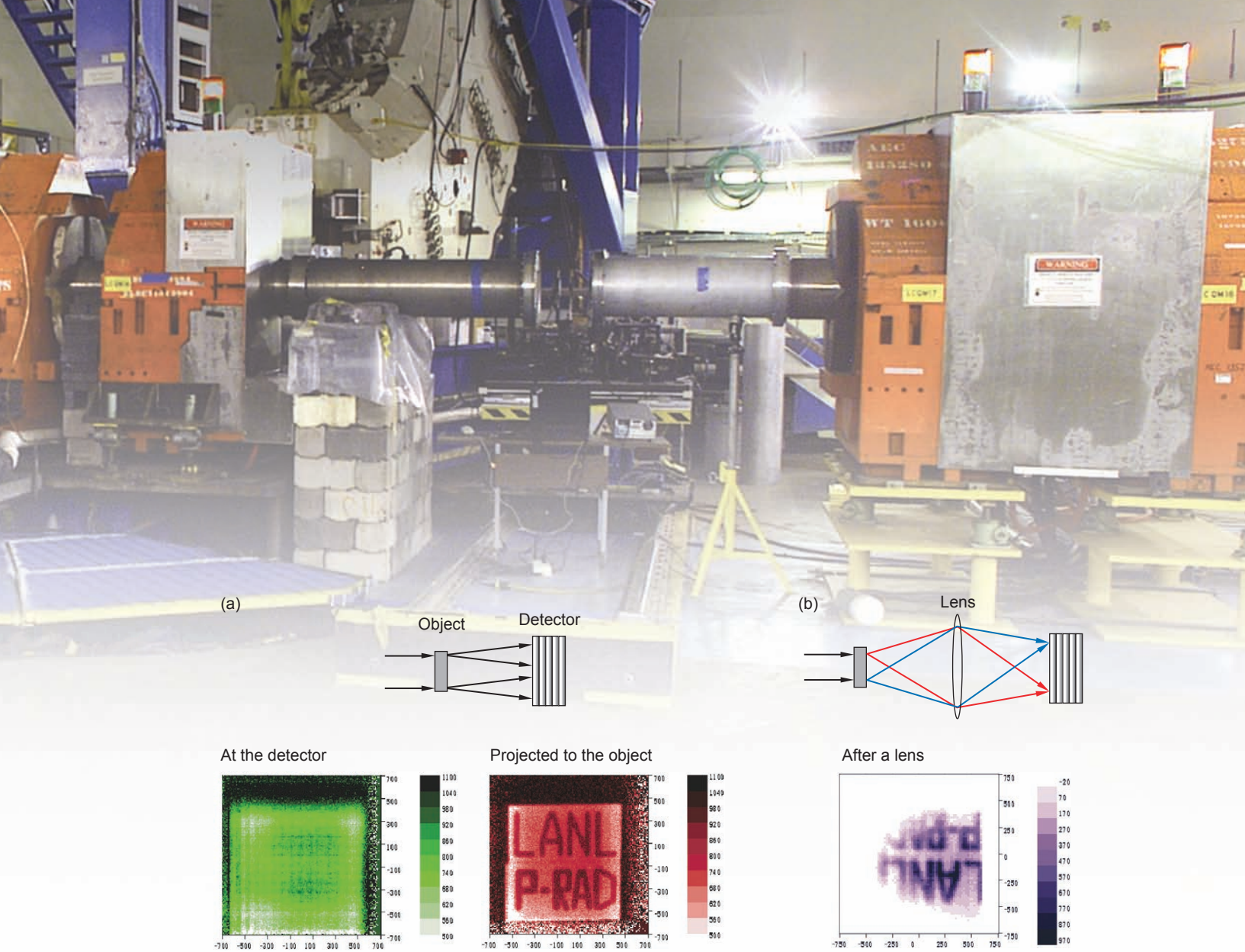


Figure 1. Demonstrating pRad with Magnetic Focusing

A beam of protons (188 MeV in energy) from the P3W channel at LAMPF was sent through an object—a 6-mm-thick steel plate with the words LANL P-RAD machined halfway through—and the positions and trajectories of the transmitted protons were recorded by a layered proton detector (see diagram). (a) With nothing between the object and the detector, we obtained a blurred radiograph (green) showing the positions of the protons as they entered the detector, but by projecting the proton trajectories recorded at the detector back to the object, the letters on the sign became visible (red radiograph). (b) The purple radiograph (inverted image) was obtained by placing a triplet of quadrupole magnets between the object and the detector and directly recording the positions of the protons entering the detector. Because the magnets act like a proton lens, focusing the protons at the detector, they allow a clear image to be recorded. Magnetic focusing makes flash radiography possible because each proton does not need to be individually measured.

The technique of focusing protons for radiography was first demonstrated in 1995 (Figure 1). The protons came from the P3W pion channel in the pion experimental area (Area-A) of the Los Alamos Neutron Science Center (LANSCE) linear accelerator. Since

then, major progress has been made in developing techniques for dynamic imaging that have made proton radiography (pRad) an important contributor to the weapons program. Approximately 30 small-scale dynamic experiments are performed per year using the line C facility at

LANSCE shown in the opening photograph. For the first time, movies of up to 32 frames can be made of explosively driven experiments, allowing new phenomena to be observed and quantified. (Just as visualization is a critical tool for designers using advanced simulation and computing,

seeing multiple frames adds a new dimension to understanding complex dynamic phenomena.) New capabilities are also being added to the line C facility continuously. Most recently, a powder gun drive has been commissioned, and a new magnifying lens is currently under construction.

In addition to the ongoing program at LANSCE, experiments with higher proton energies have been conducted at the Alternating Gradient Synchrotron (AGS) at Brookhaven National Laboratory (BNL). These experiments have shown that pRad could, in the future, enable a revolutionary improvement in data from hydrotests compared with the impressive capabilities of the dual-axis radiographic hydrotest facility (DARHT), the best flash x-ray machine in the world.

In this article, we discuss the contributions of pRad to stockpile stewardship and discuss how it emerged as a result of the interaction of basic science activities at LANSCE with nuclear weapons research.

Nuclear Weapons

Modern nuclear weapons in the U.S. stockpile use two stages to develop high yield-to-weight ratios. The first stage, the primary, works by using high explosives to compress a fissionable core, or “pit,” to a supercritical state in which it can sustain a chain reaction. The pit is filled with deuterium-tritium (d-t) gas, and the pit’s implosion, along with the onset of the fission reactions, heats the d-t gas to the point at which the d-t atoms undergo fusion reactions. In turn, neutrons released from the d-t fusion reactions produce additional fission reactions and amplify the energy released from the primary. This process of using fusion reactions to enhance the energy release is called “boost.”

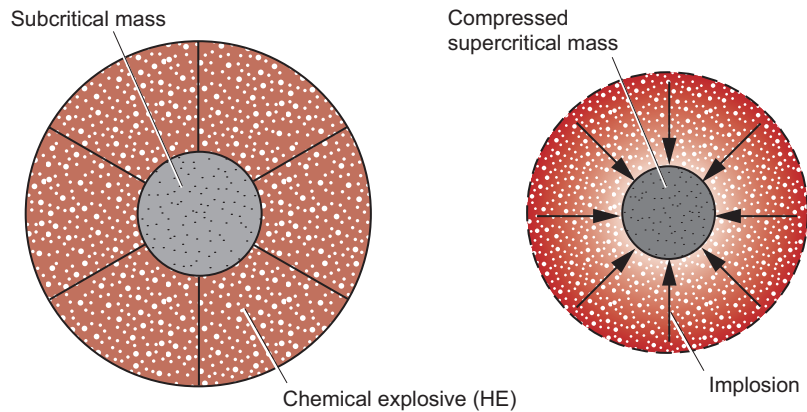


Figure 2. Schematic of an Implosion Assembly
 This schematic of implosion shows high explosives surrounding a fissile core. Detonation of the high explosive produces a converging shock wave that compresses the core to a supercritical state.

Although the basic physical processes involved are relatively straightforward, there are many subtleties that can lead to uncertainties in predicting the performance of a nuclear primary. The pressures generated in a convergent explosion far exceed those that are available for study in static laboratory experiments. The high pressures, forces, and accelerations involved drive instabilities at material interfaces that are difficult to predict with numerical simulations. The materials used in nuclear weapons are quite complicated in their behavior. For all these reasons, it is important to obtain data on the response of these materials in conditions and configurations that are close to the working conditions of a primary in order to develop and validate models and calculations. Obtaining such data will improve the predictive capability of our advanced simulation and computing models, reduce remaining uncertainties within those models, and help us ensure the safety and reliability of the stockpile without new nuclear tests.

A number of experiments must focus on isolating and closely studying individual processes or the combined effects of some of those

processes to improve the underlying physics models of materials response. Much of the work with pRad at LANSCE is along these lines. The results from such fundamental or semi-integrated experiments (sometimes called “small-scale”) help lead to validated science-based models that can be incorporated into the computer codes used to predict the entire weapons system. It is vital that the understanding embodied in these codes be accurate.

Other experiments must be more integral in nature and must more closely mock up the full set of processes and interactions that occur in a primary implosion (but, of course, without producing a nuclear explosion). One can obtain valuable data by replacing the fissile material with a surrogate, in a geometry that closely matches that of a primary (Figure 2). These large, integral implosion experiments are called hydrotests (hydrodynamic tests) because, at high pressures, the material flows like water. Electrical pins and flash x-ray radiography have been used to study hydrotest experiments since the development of the first plutonium weapons during World War II. The

most powerful x-ray machine ever built, DARHT, is the primary diagnostic for hydrotests in the United States. Results from hydrotests, along with past nuclear-test data, are vital for benchmarking and testing simulation models to ensure that the underlying science within these models is sufficiently accurate and complete. And although hydrotests use surrogate materials to prevent a nuclear explosion, precise data from these tests do allow direct inference of the initial conditions for the nuclear performance of a primary, including boost. That knowledge itself can significantly constrain predictions and can substantially increase designer confidence.

Current pRad experiments at LANSCE are playing an increasingly important role in developing the science for primary predictive capability. In addition, in the future, higher-energy pRad could provide a new, quantitative, and much more capable diagnostic for hydrotest experiments, meeting stringent requirements for establishing the initial conditions for boost.

pRad Principles

Radiographic information is obtained by measuring the intensity of the shadow of an object in a beam of penetrating radiation. If the radiation is attenuated over too short a distance, only the outer edges of the object can be measured, and if it is attenuated over too long a distance, there is no shadow. Indeed, during the Manhattan Project, flash x-radiography was used to measure the outside edge of an imploded core made of a heavy-metal surrogate in order to test the high-explosive drive for the implosion. X-rays have since been used in sophisticated hydrotests and “small-scale” research into shock- and high-explosive-driven phenomena.

However, high-energy proton beams offer an almost ideal radiographic probe for studying the physics related to primary implosion phenomena because their mean free path (or average distance traveled between collisions) can be tailored to allow seeing inside almost any experiment. Proton radiography offers new power and finesse for imaging such experiments.

Protons interact with matter in several ways. Each of these ways can be used to advantage for radiography. At high energies, protons interact with atomic nuclei primarily through the nuclear force (the short-range “strong” force that binds nuclei into a tight, compact shape) and less so through the Coulomb force (the long-range electrostatic force between charges). They also interact with electrons through the Coulomb force.

Because the cross section of the atomic nucleus is small (πr^2), high-energy protons travel a much longer distance in matter than even the most penetrating x-rays. This property makes them well suited for radiographing thick objects. High-energy protons that interact directly with a nucleus through the nuclear force are usually scattered through large angles. They are thus scattered out of the beam, and their energy is significantly reduced. In other words, protons undergo hard scattering much like x-rays in x-radiography, but they have a longer mean-free path than x-rays. This property makes them ideal for transmission radiography.

Every proton that passes by a given nucleus, even if not close to it, is given a push by the Coulomb force. The sum of all the small pushes from nuclei leads to changes in direction and therefore diffusion of the incident angle. A theory for how to treat this angle diffusion was developed by Enrico Fermi in the 1930s. Coulomb multiple scattering from nuclei can make the net mean-free path for protons shorter than

the nuclear mean-free path alone by using an angle collimator at a Fourier point (angle focus) in the lens, a feature that allows the mean free path to be adjusted to match nearly any experiment. It is this feature of proton interactions that has enabled the pRad program at LANSCE to address many different physics problems with protons of the same energy.

A Coulomb interaction also occurs between protons and electrons in the material. Because the electrons have very small mass compared with the protons, the interaction causes large changes in electron directions and velocities but only incremental changes in proton direction and energy. In the 1930s, Hans Bethe and Felix Bloch developed a theory that shows how the Coulomb interaction with electrons leads to a net force that results in a drag, slowing down and eventually stopping the protons.

Brief History of pRad

Although the motivation for developing pRad came from the weapons program, it is a remarkable fact that all the techniques, ideas, and equipment that were synthesized into this new technology are a legacy of the nuclear physics program at the Clinton P. Anderson Los Alamos Meson Physics Facility (LAMPF), the predecessor of LANSCE. Proton radiography would never have been developed had it not been for the collocation of basic research with classified, national-defense research and development. Strong basic-research efforts at the weapons laboratories can continue to provide personnel and feed innovative technologies that will be used for solving the difficult problems of stockpile stewardship in the future, and the emergence of pRad is just one of many important examples of how this outcome is achieved.

The basic idea behind pRad

goes back to Andreas Koehler from Harvard, who pointed out in the 1960s that the statistical fluctuations in proton range could be used to make very-high-contrast radiographs of objects if the proton beam energy was adjusted so that the proton range was just equal to the thickness of an object being radiographed. The range straggling in some conditions is only a few percent of the total range. Because of this narrow variation in range, the transmission of a proton beam can vary by 100 percent with just a few percent change in the thickness of an object. This high contrast meant that radiographs could be made using low radiation doses (beam intensities multiplied by irradiation times) when compared with conventional x-ray radiography, but the position resolution would be poor. Coulomb multiple scattering of protons leads to blur in the radiographs that is about an order of magnitude larger than that in radiographs made using x-rays because the latter travel on straight paths between interactions.

Ken Hanson implemented the idea of range radiography using proton beams at LAMPF. Hanson was able to extend the dynamic range over which this type of radiography could be applied by stopping the protons in a thick detector after the object rather than in the object itself and using the distances traveled in the detector to measure the energy remaining in the transmitted protons. In this way, variations in the thickness (areal density) of the object up to the detector thickness could be optimally radiographed. This energy-loss radiography provided better position resolution even using a low dose because the average proton energy in the object was higher, more protons were transmitted, and each transmitted proton provided radiographic information.

As one of us (Chris Morris) recalls, in the early 90s, the weapons program funded a study of neutron radiography

led by Victor Gavron. One important idea to come from that study was that the long mean-free path of high-energy protons, neutrons, and other hadrons (particles that interact through the nuclear force) made them ideal for performing radiography on objects typically encountered in the nuclear weapons program. Steve Sterbenz picked up on this idea and explored the possibility of using neutrons to radiograph hydrotests. However, the available neutron flux, even if the intense pulses from the Proton Storage Ring (PSR) were used to produce the neutrons, would be insufficient for obtaining images during the short timescales of a hydrotest. Gerry Garvey, then head of LAMPF, on hearing this argument, immediately asked, “Why not use protons?”

Because they are charged particles, protons bend as they move through magnetic fields, and they can therefore be focused by magnetic lenses. The technology of focusing and bending proton trajectories using magnets, or the optics of charged particles, is central to the operation of modern particle accelerators, and many physics experiments performed at LANSCE also required expertise in the optics of charged particles. For example, the high-resolution spectrometer (HRS) at LAMPF, one of the premier charged-particle spectrometers in the world, was tuned by optically imaging the low-intensity proton line in the focal plane using a phosphor and an intensified charge-coupled-device camera. Jerry Nolen, who developed this tuning technique, thus demonstrated that it was possible to image low intensities of protons with position resolution approaching 100 micrometers.

When one of us (Chris Morris) put all these ideas together, it became obvious that high-energy proton beams—within the existing state of the accelerator art—could provide a breakthrough in dynamic materials

experiments and hydrotest diagnostics. The final steps that led to the development of pRad occurred when Tom Mottershead and John Zumbro developed a magnetic lens design that provided good position resolution over the entire field of view required for radiography, and Nick King adapted a detector system based on fast imaging that had been developed for other weapons applications.

The development of pRad bears out the vision that Louis Rosen had more than forty years ago—by collocating basic research with programmatic work, LAMPF/LANSCE would be of great benefit to the Laboratory’s mission. Although over time, the LANSCE mission has increased its focus on national security, the importance of a clear engagement between defense research and the broad front of fundamental science has remained unchanged, and LANSCE continues to play an important role in that regard.

pRad and the Physics of Implosion

Proton radiography is arguably the most valuable and versatile single technique available to interrogate the hydrodynamic aspects of primary physics. Many physical regimes and processes become operative as a weapons implosion proceeds. They include the initiation and detonation of the chemical high explosive, the complex response of the metal components to intense shock waves, the extremely high rate of deformation and compression of the fissionable components during the supercritical assembly, and the fundamental hydrodynamics and hydrodynamic instabilities that are driven by these extreme conditions. For each condition, it is necessary to develop and validate explicit hydrodynamic physics models that can be implemented in new

simulation computer codes from the Advanced Simulation and Computing (ASC) Program. The physics models must capture critical hydrodynamic behaviors with high accuracy and are the main drivers for setting the design of most weapons physics experiments.

Though many techniques are (and must be) used, it remains experimentally challenging to interrogate the critical state variables and stress-strain response in the interior of materials under dynamic stress. Modeling of many processes depends on accurately capturing the time evolution of those state variables and stress-strain responses on a microsecond scale. With its ability to penetrate and accurately image the interior of highly compressed components, as well as its highly flexible and precisely recordable pulsed format, pRad is uniquely suited to providing the necessary data for weapon certification codes and models. At present, pRad is being applied to a number of key scientific questions that address stockpile stewardship goals. These include the detailed detonation behavior of insensitive high explosives; the dynamic material response to shock loading, including material failure; and experiments relating to understanding materials dynamics and conditions late in the process of implosion.

High-Explosive Detonations

Detonation fronts move through high explosives with velocities near 8 millimeters per microsecond ($\text{mm}/\mu\text{s}$). The combination of chemistry and shock physics needed to describe the detonation process is not completely understood and is difficult to model. Most calculations use parameterized geometric models to describe the detonation of high explosives. Proton radiography has been used to diagnose a number of experiments used to study the detonation process

in both conventional and insensitive high explosives.

The complex mix of shock physics and chemistry that occurs in a detonation front in high explosives has not yet been modeled from fundamental (atomic-scale) physics principles. However, physical models exist, and improvements continue to be developed that incorporate more complete (and complex) physics. For example, the pressure profile through the detonation front and the propagation of the front can be adequately described with some simplifying assumptions in a parameterized model. Movies made with pRad provide a way to establish parameters, as well as develop and check these models.

A number of pRad experiments on detonation physics performed by Eric Ferm are revealing in this regard. They include studies of a detonation front turning around a corner as it propagates from a narrow cylinder of high explosive into a wider one, rate sticks for measuring the velocity of the detonation front, colliding detonation fronts showing reflected shock waves propagating through detonation products, and failure cone experiments for determining the radius at which the detonation fails to propagate. Some time sequences from these experiments are shown in Figure 3. The failure cone and corner-turning experiments allow predictions of detonation front propagation to be checked, and the rate stick and colliding-wave experiments provide data on the equation of state of detonation products over a wide range of pressures. In particular, the velocity of the reflected shock waves in the detonation products determines a shock Hugoniot in the high-explosive products. The experimental results shown in Figure 3—for example, the dead zone in the corner-turning experiment—challenge even the best current models of high-explosive detonation.

Material Failure

When the pressure wave produced by a high-explosive detonation impacts a metal surface, the metal can be accelerated to velocities that exceed the sound speed in the metal. This phenomenon results in the formation and propagation of shock waves in the metal. The shock waves reflect from interfaces and surfaces putting the material alternately under compression and tension, and in many cases, under considerable shear. The pressures induced in these processes can exceed the strength of the metal and can lead to phase changes, as well as tensional and shear failure. These phenomena have been studied for well over a century. However, the richness of the physical processes involved and the complexity of the materials make it a challenge to develop microscopic models based on the fundamental forces of nature. We need data to guide and validate improvements to the various approaches to modeling these phenomena.

A set of experiments has been performed with pRad to study how shocked metals fail when a shock wave is reflected from a free metal surface and the resulting rarefaction wave puts material in tension. Experiments were driven with Taylor waves (the shape of a shock wave produced by high explosives) and with plane waves (waves produced by a high-explosive-driven flyer plate or a projectile from a gun). A composite of experiments showing the richness of metal failure from shock-induced tension is displayed in Figure 4.

Fragmentation, another form of material failure, occurs when metals are stretched (or strained) at very high rates. Figure 5 shows a series of experiments performed with pRad to study this phenomenon. Several sequences of metal failing in stretching modes are shown. In Figure 5(a), a half-cylinder of titanium is being

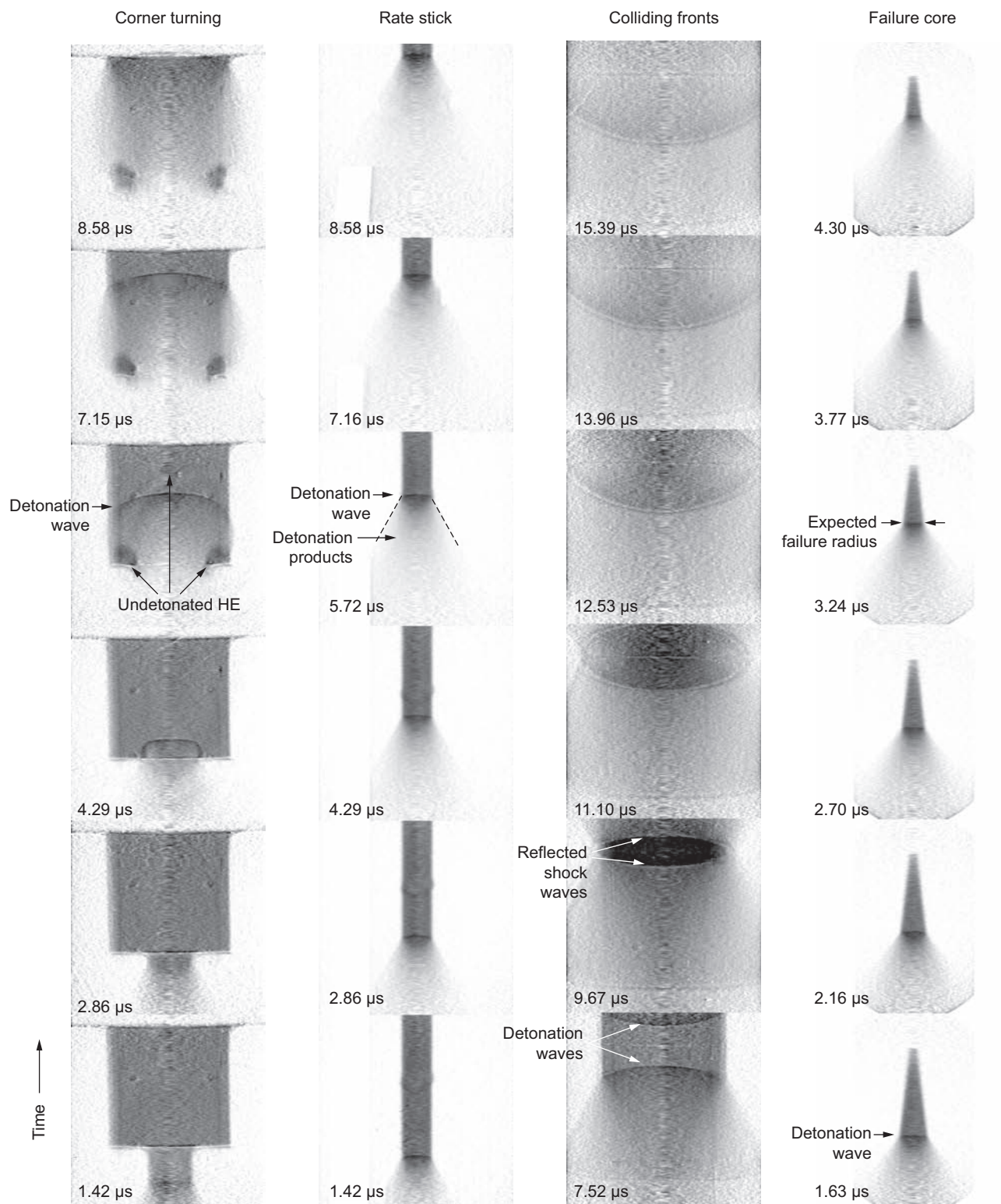


Figure 3. Studies of High-Explosive Detonation

These radiographic time sequences show a set of experiments aimed at studying the propagation of a detonation wave in a high-explosive and the densities and pressures of the detonation products. (Left to right) The images record detonation fronts turning a corner, traveling along a rate stick, colliding, and propagating in a failure cone, respectively. The images were enhanced by Abel inversion and therefore show volume densities (gm/cm^3). (This figure is courtesy of Eric Ferm.)

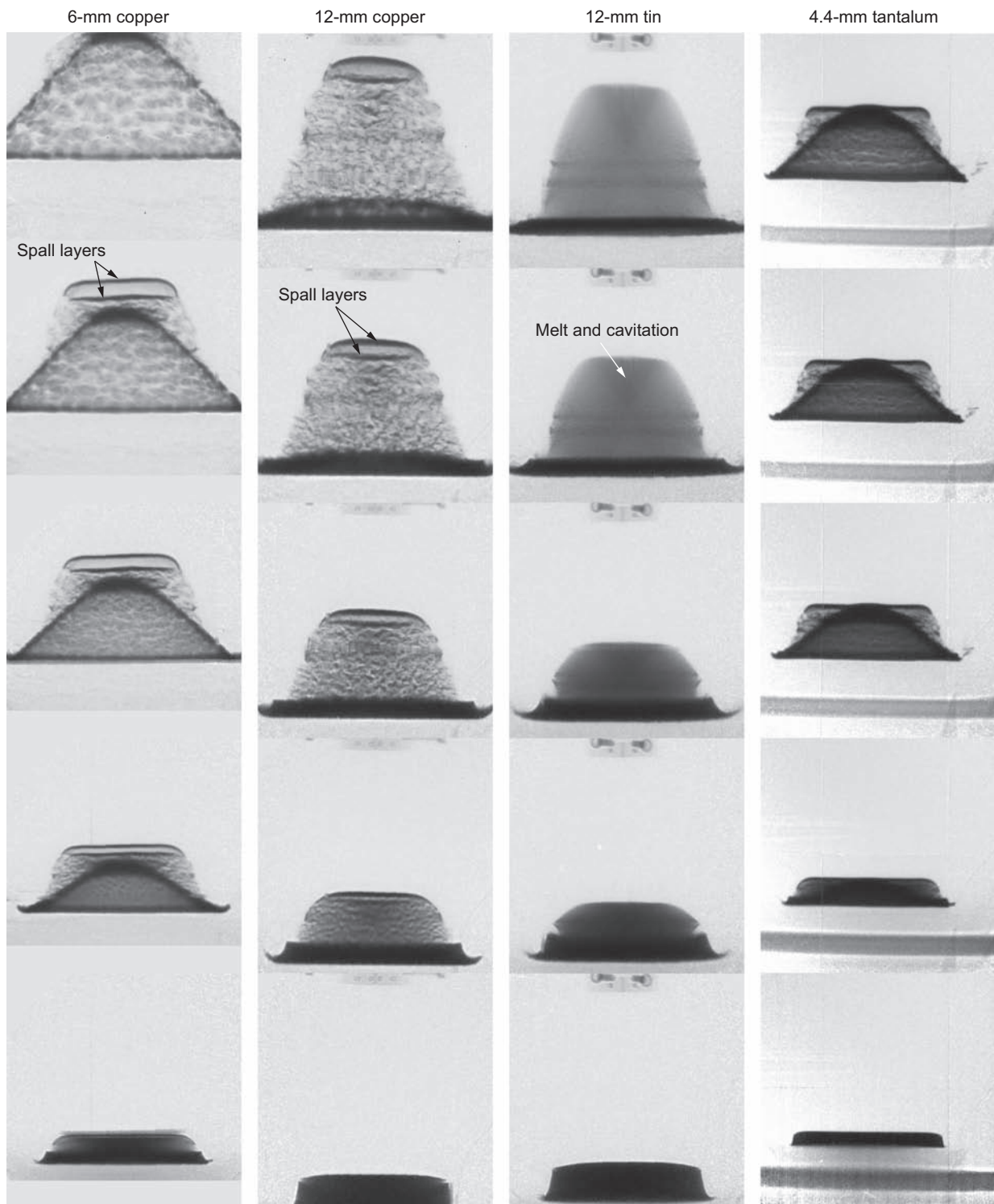


Figure 4. Spall from Metal Plates Driven by a Planar Shock Wave

These data, courtesy of D. Holtkamp, show the “spall” type of metal failure that occurs when metals are put in tension by shock waves that reflect from a free surface and produce rarefaction waves. (Left to right) The metal samples undergoing spall are 6-mm-thick copper, 12-mm-thick copper, 12-mm-thick tin, and 4.4-mm-thick tantalum. In the leading part of the experiment, layers break off from the free surface as a result of spall. Later these layers become disorganized and appear to be broken up. Each experiment was driven by a plane-wave high-explosive driver.

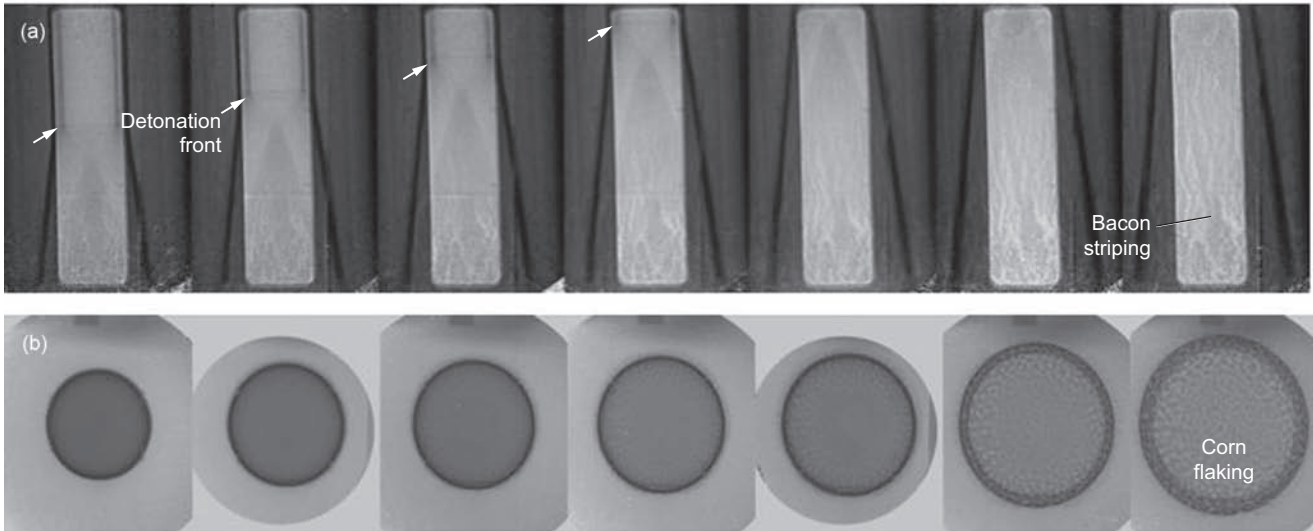


Figure 5. Fragmentation Failure of Metal Driven by Shock Waves from High-Explosive Charges
(a) Detonation of an explosive charge placed in a titanium half-cylinder causes rapid cylindrical expansion. The failure of the half-cylinder of titanium leads to bacon striping, or fragmentation along the axial direction of the cylinder (data are courtesy of P. Rightly). **(b) A hemispherical shell of uranium–6% niobium is being spherically expanded by detonation of a high-explosive charge** (data are courtesy of K. Prestrige). **The rapid expansion causes formation of a cornflake pattern of fragmentation.**

rapidly expanded by detonation of a cylindrical charge of high explosives placed inside the titanium cylinder. As the explosive expands radially, the cylinder fragments in a bacon strip pattern that seems to be characteristic of uniaxial (cylindrical) strain. In Figure 5b, a hemisphere of a uranium alloy is being expanded with a hemispherical high-explosive charge. Here, the failure results in irregular cornflake-shaped fragments.

These experiments demonstrate the richness and complexity of the response of real materials at high strain rate. These data are part of a program of model development aimed at a better understanding and predictive capability for the materials and conditions encountered in weapon systems.

Instabilities and Ejecta

Another very interesting field of research with important applications in weapons is the study of instabili-

ties. When a dense fluid is accelerated by a light fluid (Rayleigh-Taylor) or when an interface between two fluids is impulsively driven (Richtmyer-Meshkov), the interface is unstable. As the instability grows, the two fluids mix. Modeling instability growth in fluids is numerically difficult. For solid interfaces, even predicting the onset of instability growth becomes difficult because material strength stabilizes the surfaces.

Instability growth has been radiographed with pRad in several experiments. Two examples are shown in Figure 6. The first two time sequences in Figure 6a show different views of a jet growing vertically from a slot cut in an aluminum disc-shaped target as a shock wave from a high-explosive charge located underneath the disc propagates in orthogonal directions. The sequence in Figure 6b shows the development of a Richtmyer-Meshkov instability in a thin tin target containing a wavy, or sine-wave-shaped, free surface. That sine-wave-shaped perturbation was machined into the flat surface

as a seed for the growth of the instability. The tin plate was then struck by a flyer plate driven by a high explosive, and the rate of instability growth was then determined from the sequence of radiographs shown in the figure.

Small Implosion Experiments

In addition to these fundamental and semi-integral small-scale experiments, we have also performed some small implosion experiments with pRad at LANSCE, using experimental configurations and high-explosive charges suitable to the constraints of that facility. Although these integral experiments cannot be described in detail here, they have provided valuable and relevant information on the evolution of materials dynamics in implosions.

High-Energy pRad

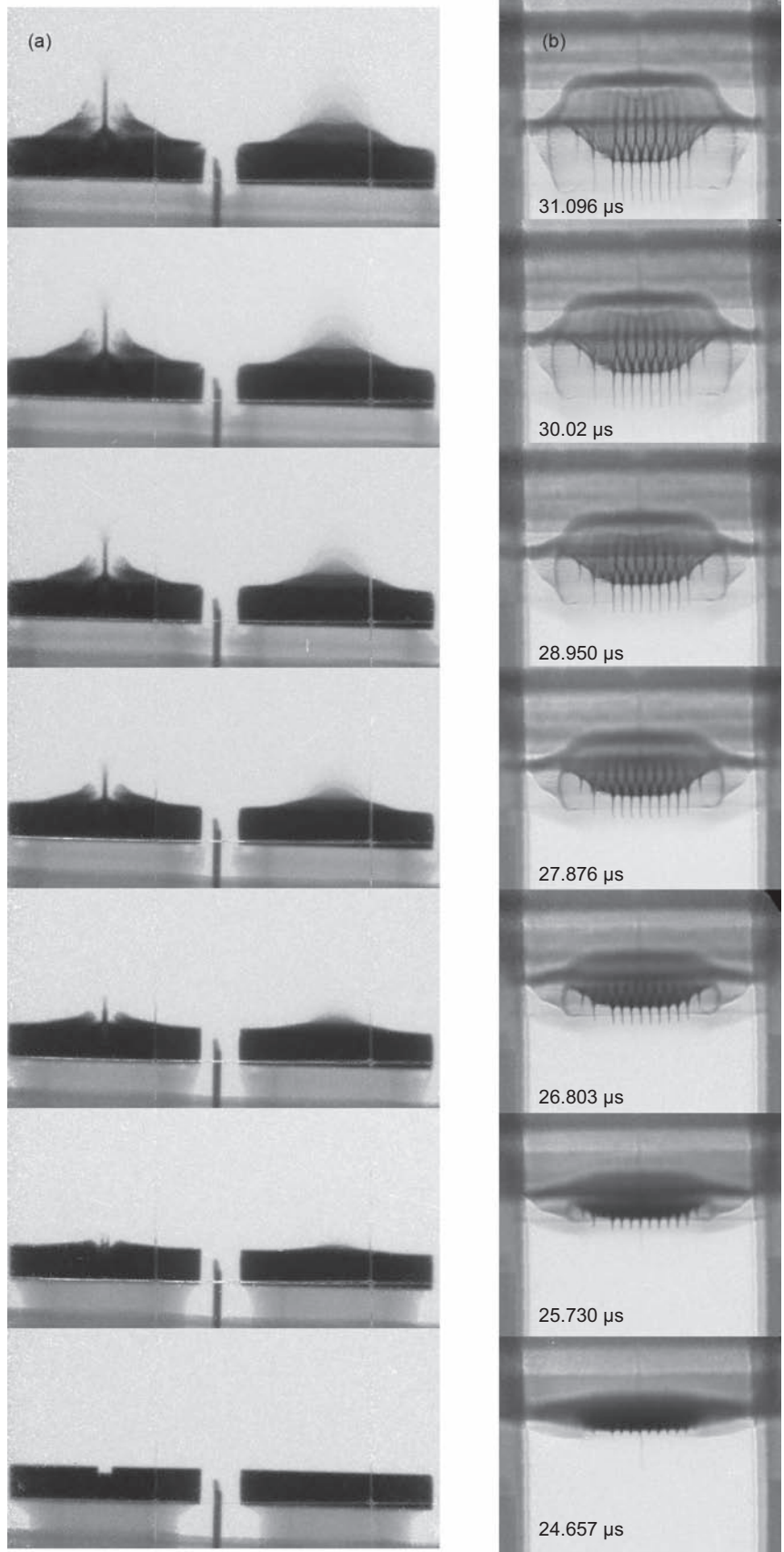
Planning done within the nuclear weapons program has shown that the

800-million-electron-volt (MeV) pRad facility at LANSCE is needed to support many of the long-term research goals of the weapons laboratories, and many years of experiments have already been identified to support specific stewardship deliverables. However, in addition to the need for the capability at 800 MeV, our colleagues are considering the potential—and potential need—for an extension to 20 giga-electron volts (GeV).

Full-scale hydrotest radiography with pRad requires higher energy than is available at LANSCE. A series of experiments has been performed using the high-energy protons available at the AGS at BNL with several goals in mind: developing the techniques needed for high-energy pRad, demonstrating the capabilities of pRad for interrogating full-scale hydrotests, and making some direct comparisons with DARHT. Much of this work is classified, but the conclusions are rather remarkable and can be given here. The quality of flash radiography with protons is so much better for thick hydrotest objects than even that obtained from DARHT that it would take about 100 times more x-ray dose than DARHT can currently deliver to

Figure 6. Ejecta and Instability Experiments

(a) These two sequences show the development of a metal jet from a slot in an aluminum target looking along the slot (left) and across the slot (right). The jet is driven by shock waves from a high-explosive charge located underneath the plate. (b) The growth of a “classic” Richtmyer-Meshkov instability from a tin target is shown. It contains a sinusoidally shaped free surface. The instability is driven by the impact of a high-explosive-driven flyer plate moving down in this figure. [The data in (a) are courtesy of K. Prestridge and in (b), courtesy of W. Buttler.]



obtain the same radiographic detail. Even more important than the quality is the quantitative nature of pRad.

A series of density reconstructions of an unclassified radiographic test object is shown in Figure 7. The radiographs have been calibrated to measure material densities using data taken on step wedges. In the set of tests shown, the uniformity and composition of the high-density material limited the precision of the density reconstructions to about 2 percent. In classified experiments done subsequently, an accuracy of better than 1 percent has been attained for density reconstructions from pRad. This level of precision for density measurements is nearly an order of magnitude better than that obtained from thick object radiography using x-rays and meets requirements established nearly a decade ago for a next generation of hydrotest radiography machines beyond DARHT.

The high effective dose, quantitative density reconstructions, submillimeter position resolution, and ease with which time sequences can be radiographed at frame rates in excess of 5 million frames per second make pRad the obvious choice for any next-generation flash-radiography machine beyond DARHT. This finding has led to the studies described below.

A 20-GeV Capability

Motivated by the success of the pRad experiments done at BNL, a recent study was made to examine the design parameters and estimate the costs of a proton synchrotron at an energy of 20 GeV that could be applied to quantitative radiography for the weapons stockpile. Siting options at both Los Alamos National Laboratory and the Nevada Test Site (NTS) were studied, and design feasibility and cost estimates were determined.

Table I. High-Energy Radiography Requirements

Number of pulses	>5
Minimum pulse spacing	~200 ns
Protons per pulse	2×10^{11}
Time format	Individual pulse extraction

If the mission requirement for such a capability were established, a choice of a Los Alamos site could take advantage of the existing accelerator infrastructure at LANSCE. The 800-MeV LANSCE linear accelerator could be used as an injector to the synchrotron ring, which would save the time and money needed to build and commission a new accelerator. In addition, the existing infrastructure of trained people and equipment would simplify commissioning a new accelerator. Studies indicate that a 20-GeV synchrotron ring would be smaller in its longest dimension than the existing kilometer-long linear accelerator that forms the core of LANSCE today.

Notional high-level requirements for a 20-GeV capability were synthesized from a combination of the results from the AGS experiments and from requirement studies carried out over the last decade. They are listed in Table I.

The number of pulses is driven by the need to measure density to infer criticality (as calculated for a hypothetical equivalent experiment that used nuclear material). Although large numbers of pulses are available with pRad, extensive studies by Kevin Buescher, John Hopson, and Wayne Slattery have shown that four pulses spaced at a minimum of 200 nanoseconds are sufficient (DARHT-2 is intended to produce four pulses, a new state of the art for x-ray machines). A fifth pulse was added to the design requirements so that early-time phenomena can be studied simultaneously with late-time

configurations. A 20-GeV ring can provide up to 10 pulses, limited by the circumference of the synchrotron. The proton dose in Table I is twice that used in the validation experiments described above. This increase is enough to allow a two-Gaussian imaging mode in which part of the beam would be used to image small radii in the object and the remainder would be used for full-field imaging.

Summary

Proton radiography is a highly versatile invention that was born from the interaction between defense mission research and basic science. Experiments similar to the examples described here and some others have added quantitative data that have impacted near-term nuclear weapons stockpile assessment and certification. They have also added qualitative insights that would have been hard to obtain without the resolution and multiple images pRad provides. This technology is an important complement to other dynamic materials research and to DARHT. Ensuring that pRad will continue to provide data for the next two decades is one of the key reasons that the Laboratory has proposed to refurbish LANSCE. We project a need for 20 to 30 pRad experiments annually based on outyear program planning, past experience in performing the required work, and the schedule that these experiments need to meet to deliver data for model validation and certification milestones.

Currently included within the LANSCE refurbishment proposal,

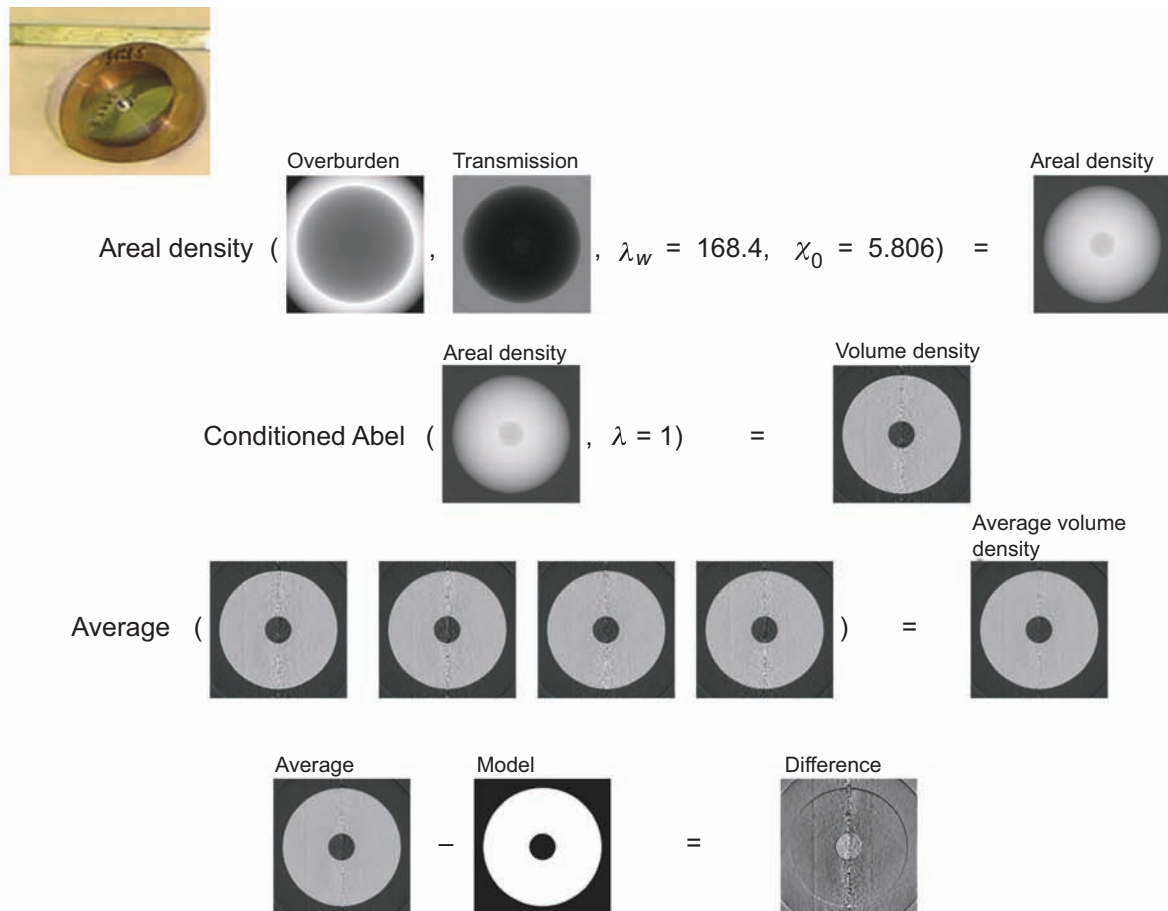


Figure 7. Analysis of 24-GeV/c Radiography of a Radiographic Test Object

This figure illustrates the analysis of 24 GeV/c radiography on the French test object. A photograph of the object is shown in the upper left. The raw data are first corrected for a number of experimental effects, such as beam shape and detector and camera response. Then, the transmission radiograph is inverted to give areal densities with data obtained from step wedges (λ_w is the nuclear mean free path for tungsten, and χ_0 is an empirical radiation length). A step wedge is a target with a set of constant thickness steps, which can be used to quantitatively calibrate the radiography. Volume densities are obtained from the areal densities by performing very simple tomography, which assumes symmetry around a central axis, called an Abel transform. The idea here is that, because of the symmetry, all views should look the same, so one needs data at only one angle rather than hundreds of angles, which are normally used in tomography. The results of many measurements have been combined to obtain an estimate of the uncertainties in each measurement. In the end, we have shown that it is possible to measure densities with a precision of better than 1% by using this straightforward procedure.

the H^- source intensity at LANSCE that feeds pRad can be increased by a factor of 2 in a cost-effective, straightforward manner. A doubling of H^- intensity would provide a factor of 2 improvement in image statistics and a commensurate improvement in quantitative density resolution for the scaled hydrolike experiments that are needed for current and future certification-related experiments.

LANSCE also provides the infra-

structure and a powerful injector that could be the basis for extending pRad to the higher energies needed for quantitative full-scale hydrotest radiography in the future. While not yet planned for development, such a capability could provide nuclear weapons modelers with quantitative data about the initial conditions for boost and could drastically increase the scope of challenges future stockpile stewards could address with high confidence.

Proton radiography is here to stay as a powerful tool for predictive capability and for addressing our national security missions. ■

Acknowledgments

The authors would like to acknowledge the enormous effort of the pRad team, assembled from the Physics, Dynamic Experimentation,

and Applied Physics Divisions, over the past decade. LANSCE has done an impressive job providing beam with 100 percent reliability for the 215 pRad shots that have been fired to date. We are also enormously grateful for the freedom to develop pRad and the funding that has been provided for the effort by the nuclear weapons program at the Laboratory.

Further Reading

- Alford, O. J., P. D. Barnes Jr., A. K. Chargin, W. D. Dekin, E. P. Hartouni, J. N. Hockman et al. 1999. The Scrounge-Atron: A Phased Approach to the Advanced Hydrotest Facility Utilizing Proton Radiography. In *Proceedings of the IEEE Particle Accelerator Conference*. Vol. 4, p. 2590. Piscataway, NJ: IEEE.
- Aufderheide, M. B., H.-S. Park, E. P. Hartouni, P. D. Barnes, D. M. Wright, R. M. Bionta et al. 1999. Proton Radiography as a Means of Material Characterization. In *AIP Conference Proceedings 9th International Symposium on Nondestructive Characterization of Materials*. Edited by R. E. Green. Vol. 497, p. 706. Melville, NY: AIP.
- Aufderheide, M. B., D. M. Slone, and A. E. Schach von Wittenau. 2001. HADES, a Radiographic Simulation Code. In *AIP Conference Proceedings on Review of Progress in Quantitative Nondestructive Evaluation*. Edited by D. O. Thompson and D. E. Chimenti. Vol. 557 (pt. A and B), p. 507. Melville, NY: AIP.
- Baker, S. A., L. J. Castellano, P. A. Flores, B. C. Frogget, W. Lewis, P. T. Nedrow et al. 1997. Large Format Imaging System. In *Proceedings of the SPIE - The International Society for Optical Engineering 22nd International Congress on High-Speed Photography and Photonics*. Edited by D. L. Paisley. Vol. 2869, p. 929. Bellingham, WA: SPIE.
- Charpak, G. 1978. Applications of Proportional Chambers to Some Problems in Medicine and Biology. *Nucl. Instrum. Methods* **156**: 1.
- Cochrane Jr., J. C., and P. J. Turchi. 2002. Design and Performance of a Current Transformer for Efficient Liner Implosions. *IEEE International Conference on Plasma Science*. p. 233. Piscataway, NJ: IEEE.
- Cookson, J. A., B. H. Armitage, and A. T. Ferguson. 1972. Proton Radiography. *Non-Destr. Test.* **5** (4):225.
- Cunningham, G., and C. Morris. 2003. The Development of Flash Radiography at Los Alamos National Laboratory. *Los Alamos Science* **28**: 76.
- Curry, J., and V. W. Steward. 1978. Establishment of a Beam Line at the Fermi National Accelerator Laboratory for Proton Radiography. *Med. Phys.* **5**: 188.
- Ellard, G. A., P. T. Gammon, H. S. Helmy, and R. J. W. Rees. 1972. Radiography with 160 MeV Protons. *Nature* **239** (5368): 157.
- Ferm, E. N., C. L. Morris, J. P. Quintana, P. Pazuchanic, H. Stacy, J. D. Zumbro et al. 2002. Proton Radiography Examination of Unburned Regions in PBX 9502 Corner Turning Experiments. In *AIP Conference Proceedings on Shock Compression of Condensed Matter*. Edited by M. D. Furnish, Y. Horie, and N. N. Thadhani. Vol. 620 (pt. 2), p. 966. Melville, NY: AIP.
- Gorbunov, V. I., V. P. Ivakin, B. A. Kononov, and A. L. Lukin. 1976. Flaw Detection with Medium-Energy Protons. *Defektoskopiya—Sov. J. Non-Destr. Test.* **12** (3): 338.
- Harms, A. A., and L. D. Molson. 1974. Nuclear Radiation Conversion Enhancement with Inhomogeneous Converters and Intensifiers. *Nucl. Instrum. Methods* **119**: 389.
- Hartouni, E., and C. L. Morris. 2000. Proton Radiography. *Beam Line* **30** (1): 20.
- Hogan, G. E. 1999. PC DAQ, A Windows-Based DAQ System. In *Proceedings of the IEEE Conference on Real-Time Computer Applications in Nuclear Particle and Plasma Physics*. Edited by S. C. Schaller. p. 160. Piscataway, NJ: IEEE.
- Hogan, G. E., K. J. Adams, K. R. Alrick, J. F. Amann, J. G. Boissevain, M. L. Crow et al. 1999. Proton Radiography. In *Proceedings of the IEEE Particle Accelerator Conference*. Edited by A. Luccio and W. MacKay. Vol. 1, p. 579. Piscataway, NJ: IEEE.
- Jones, D. T. L. 1982. Proposed Medical Applications of the National Accelerator Center Facilities. *S. Afr. J. Sci.* **78** (4): 149.
- King, N. S. P., E. Ables, K. Adams, K. R. Alrick, J. F. Amann, S. Balzar et al. 1999. An 800-MeV Proton Radiography Facility for Dynamic Experiments. *Nucl. Instrum. Methods Phys. Res. A, Accel. Spectrom. Detect. Assoc. Equip.* **424** (1): 84.
- King, N. S. P., S. Baker, S. Jaramillo, K. Kwiatkowski, S. Lutz, G. E. Hogan et al. 2003. Imaging Detector Systems for Soft X-Ray and Proton Radiography. In *Proceedings of the SPIE—The International Society for Optical Engineering 25th International Congress on High-Speed Photography and Photonics*. Edited by C. Cavailler, G. P. Haddleton, and M. Hugenschmidt. Vol. 4948, p. 610. Bellingham, WA: SPIE.
- Kleinfelder, S. 2004. High-Speed, High-Sensitivity, Low-Noise Scientific CMOS Image Sensors. In *Proceedings of the SPIE—Conference on Microelectronics: Design, Technology, and Packaging*. Edited by D. Abbott, K. Eshraghian, C. A. Musca, D. Pavlidis, and N. Weste. Vol. 5274, p. 194. Bellingham, WA: SPIE.
- Kleinfelder, S., K. Kwiatkowski, Y. Chen, and A. Shah. 2003. Multi-Million Frames/S Sensor Circuits for Pulsed-Source Imaging. *IEEE Nucl. Sci. Symp. Conf. Rec.* **3**: 1504.
- Koehler, A. M. 1968. Proton Radiography. *Science* **160**: 303.
- Koehler, A. M. 1970. Proton Radiography. *Phys. Med. Biol.* **15** (1): 181.
- Koehler, A. M. 1972. Medical Treatment and Diagnosis Using 160 MeV Protons. In *AIP Conference Proceedings*. Vol. 9, p. 586. Melville, NY: AIP.
- Kwiatkowski, K., J. F. Beche, M. T. Burks, G. Hart, G. E. Hogan, P. F. Manfredi et al. 2002. Development of Multi-Frame Detectors for Ultrafast Radiography with 800 MeV Protons. *IEEE Trans. Nucl. Sci.* **49** (1): 293.
- Kwiatkowski, K., N. S. P. King, J. Lyke, J. F. Beche, G. E. Hogan, C. Kapusta et al. 2003. Development of a Multi-Frame Optical Imaging Detector for Proton Radiography at LANL. In *Proceedings of the SPIE—The International Society for Optical Engineering 25th International Congress on High-Speed Photography and Photonics*. Vol. 4948, p. 616. Bellingham, WA: SPIE.

- Kwiatkowski, K., J. Lyke, R. Wojnarowski, C. Kapusta, S. Kleinfelder, and M. Wilke. 2003. 3-D Stacked Electronics Assembly for High-Performance Imaging Detectors. *IEEE Nucl. Sci. Symp. Conf. Rec.* 1: 63.
- Kwiatkowski, K., J. C. Lyke, R. J. Wojnarowski, J. F. Beche, R. Fillion, C. Kapusta et al. 2003. 3-D Interconnect Architecture for High-Bandwidth Massively Paralleled Imager. *Nucl. Instrum. Methods Phys. Res. A, Accel. Spectrom. Detect. Assoc. Equip.* **509** (1–3): 200.
- Martin, R., M. Foss, J. Moenich, and R. Lari. 1975. The Proton Diagnostic Accelerator. *IEEE Trans. Nucl. Sci.* **ns-22** (3): 1804.
- Mottershead, C. T., and J. D. Zumbro. 1998. Magnetic Optics for Proton Radiography. In *Proceedings of the IEEE Particle Accelerator Conference*. Edited by M. Comyn, M. K. Craddock, M. Reiser, and J. Thomson. Vol. 2, p. 1397. Piscataway, NJ: IEEE.
- Mottershead, T., D. Barlow, B. Blind, G. Hogan, A. Jason, F. Merrill et al. 2003. Design and Operation of a Proton Microscope for Radiography at 800 MeV. In *Proceedings of the IEEE Particle Accelerator Conference*. Edited by J. Chew, P. Lucas, and S. Webber. Vol. 1, p. 702. Piscataway, NJ: IEEE.
- Neri, F., H. A. Thiessen, and P. L. Walstrom. 1998. Synchrotrons and Beamlines for Proton Radiography. In *Proceedings of the IEEE Particle Accelerator Conference*. Edited by M. Comyn, M. K. Craddock, M. Reiser, and J. Thomson. Vol. 3, p. 3788. Piscataway, NJ: IEEE.
- Neri, F., and P. L. Walstrom. 2005. A Simple Empirical Forward Model for Combined Nuclear and Multiple Coulomb Scattering in Proton Radiography of Thick Objects. *Nucl. Instrum. Methods Phys. Res. Sect. B* **229**: (3–4): 425.
- Pedroni, E., R. Bacher, H. Blattmann, T. Bohringer, A. Coray, A. Lomax et al. 1995. The 200-MeV Proton Therapy Project at the Paul Scherrer Institute: Conceptual Design and Practical Realization. *Med. Phys.* **22**: 37.
- Prichard, B. A. 1993. A Proposed Proton Therapy Facility at the SSC. *Nucl. Instrum. Methods Phys. Res. Sect. B* **79** (1–4): 895.
- Saudinos, J. 1977. A New Medical Application: Radiography by Nuclear Scattering. *Bull. Info. Sci. Tech.* **224–225**: 175.
- Schneider, U., and E. Pedroni. 1994. Multiple Coulomb Scattering and Spatial Resolution in Proton Radiography. *Med. Phys.* **21** (11): 1657.
- . 1995. Proton Radiography as a Tool for Quality Control in Proton Therapy. *Med. Phys.* **22** (4): 353.
- . 1996. Quantitative Proton Radiography. In *Quantitative Imaging in Oncology: 19th L. H. Gray Conference on Quantitative Imaging in Oncology*. Edited by K. Faulkner, B. Carey, A. Crellin, and R. M. Harrison. p. 61. London: British Institute of Radiology.
- Schneider, U., J. Besserer, and P. Pemler. 2001. On Small Angle Multiple Coulomb Scattering of Protons in the Gaussian Approximation. *Z. Med. Phys.* **11**: 110.
- Schneider, U., M. Dellert, E. Pedroni, P. Pemler, J. Besserer, M. Moosburger et al. 2003. Quantitative Proton Radiography of an Animal Patient. In *Proceedings of the SPIE - The International Society for Optical Engineering*. Edited by M. K. Yaffe and L. E. Antonuk. Vol. 5030, p. 585. Bellingham, WA: SPIE.
- Schneider, U., and A. Tourovsky. 1998. Range-Uncertainty Imaging for Obtaining Dose Perturbations in Proton Therapy. *IEEE Trans. Nucl. Sci.* **45**: 2309.
- Schultz, J. H., T. Antaya, J. V. Minervini, A. L. Radovinsky, B. A. Smith, R. J. Camille et al. 2003. The Advanced Hydrotest Facility (AHF) Large Bore Quadrupole Focusing Magnet System. *IEEE Trans. Appl. Supercond.* **13** (2): 1343.
- Steward, V. W. 1976. Proton (and Other Heavy Charged Particle) Radiography in Medical Diagnosis. *IEEE Trans. Nucl. Sci.* **ns-23** (1): 577.
- . 1979. Proton (Heavy Ion) Radiography in Medical Diagnosis. *IEEE Trans. Nucl. Sci.* **ns-26** (2): 2257.
- Steward, V. W., and A. M. Koehler. 1973. Proton Radiography as a Diagnostic Tool. *Phys. Med. Biol.* **18** (4): 591.
- . 1974. Proton Radiography in the Diagnosis of Breast Carcinoma. *Radiology* **110** (1): 217.
- . 1974. Proton Radiography of a Human Brain Tumor Within Skull—Preliminary Report. *Surg. Neurol.* **2** (4): 283.
- West, D. 1975. The Potential of Proton Radiography. In *Proceedings of the 7th International Conference on Cyclotrons and Their Applications*. Edited by W. John. p. 503. Basel, Switzerland: Birkhäuser Verlag.
- Wilson, R. 1972. Medical Uses of the Harvard University Cyclotron: An Overall View. In *AIP Conference Proceedings*. Vol. 9, p. 578. Melville, NY: AIP.
- Yates, G. J., K. L. Albright, K. R. Alrick, R. A. Gallegos, J. Galyardt, N. T. Gray et al. 1998. An Intensified/Shuttered Cooled CCD Camera for Dynamic Proton Radiography. In *Proceedings of the SPIE—The International Society for Optical Engineering Conference on Digital Solid State Cameras: Designs and Applications*. Edited by G. M. Williams. Vol. 3302, p. 140. Bellingham, WA: SPIE.
- Ziock, H. J., K. J. Adams, K. R. Alrick, J. F. Amann, J. F. Boissevain, M. L. Crow et al. 1998. The Proton Radiography Concept. In *Proceedings of PIXEL98, International Pixel Detector Workshop*. Edited by D. Anderson and S. Kwan. p. 233. Batavia, IL: Fermi Nat. Accel. Lab.
- Ziock, H. J., K. R. Alrick, R. A. Gallegos, J. Galyardt, N. T. Gray, G. E. Hogan et al. 1998. Detector Development for Dynamic Proton Radiography. In *Proceedings of PIXEL98, International Pixel Detector Workshop*. Edited by D. Anderson and S. Kwan. p. 221. Batavia, IL: Fermi Nat. Accel. Lab.

A New “Camera on a Chip” for pRad Movies

*Kris Kwiatkowski, Nicholas King, and Vincent M. Douence**

* Rockwell Scientific Company



We have developed a camera that consists of two integrated circuits bonded together into a single “hybrid” chip. This camera can capture dynamic events in proton radiography movies with a minimum temporal resolution of 100 nanoseconds. The new camera's high light sensitivity also provides higher image quality than our current cameras. This improvement in image quality is equivalent to increasing the proton-beam intensity by a factor of 4. In addition to being able to capture multiple frames per camera, the new camera also has greater reliability, and lower cost per frame. It also takes up far less space and needs only a few external electrical connections. The new imager can also be used to study other ultrafast transient phenomena such as projectiles penetrating armor.

A proton radiography (pRad) movie records a series of images produced as protons transmitted through a dynamic experiment are focused on a scintillator screen; the scintillator material converts proton intensity to light intensity. Our current camera system allows us to capture and store a sequence of these images at rates of millions of frames per second for a fraction of a second. The system is

shown in Figure 1.

At present, we make 20-to-30-frame movies at up to 2.8 million frames per second; the minimum time between frames is thus about 360 nanoseconds. To capture each frame at this rate, the camera's electronic shutter must remain open for less than 360 nanoseconds. In the future, we plan to double or triple the number of frames per movie and increase the frame rate by a factor of

5 or more, which will require shutter speeds of 60 nanoseconds or less.

However, the current system's electronic shutter—a vacuum planar photodiode—cannot operate much below 300 nanoseconds.¹ In addition,

¹ The shutter speed is limited by the power supply producing the short, 12 kilovolt pulse required to briefly open the photodiode to incident light. To a lesser extent, it is also limited by the photodiode's capacitance-limited rise time.

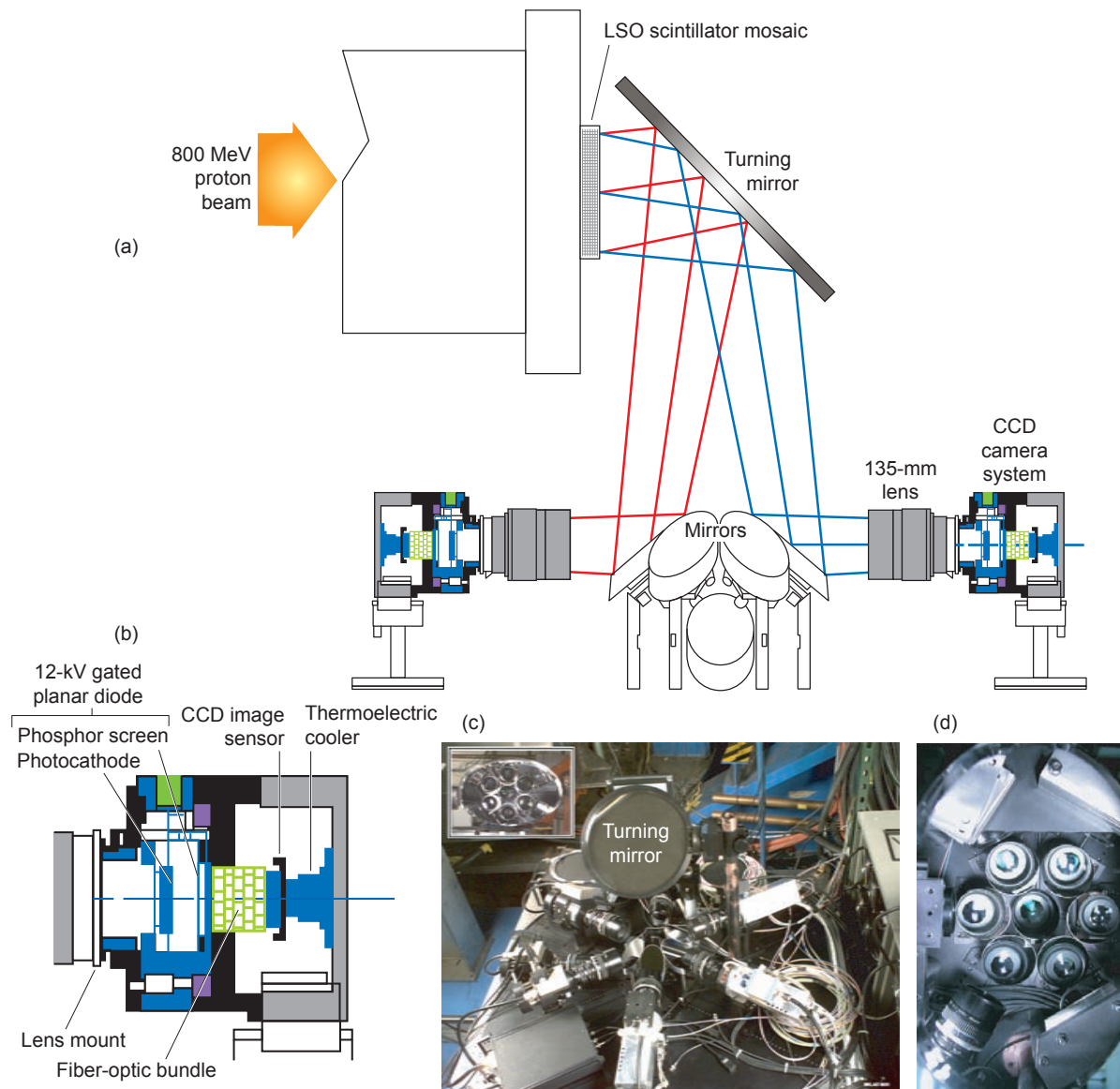


Figure 1. Proton Radiography Imaging System with Gated CCD Cameras

(a) Proton images are produced as protons transmitted through a dynamic experiment are focused on the 12-cm by 12-cm tiled LSO scintillator. The scintillator converts proton intensity to light intensity, and the “turning” mirror reflects these light images to seven smaller mirrors, which reflect the images to seven CCD cameras. (b) The gated CCD imager system consists of a CCD camera, which has no electronic shuttering capabilities, augmented by a 12-kV gated planar photodiode that acts as a fast optical shutter. A lens focuses the reflected light image onto the photodiode’s front plate, a photocathode that converts the light image to an electron image through the photoelectric effect. When the photodiode is activated by a 12-kV potential, the electrons are accelerated to the back plate, a scintillating screen that converts the electron image back to a light image. That image is transmitted through the fiberoptic bundle (to maximize light transmission) to a cooled 1600×1600 pixel CCD camera, which digitizes the image. The shutter speed of the photodiode is limited by the 100-ns rise and fall times for applying the 12-kV activating pulse. Although cumbersome, this shuttering method was the only high-speed electro-optic option available at the time. (c) The large gray circular object is the back of the turning mirror, beneath which are seven CCD cameras and some of the many cables and auxiliary electronics required to operate the cameras and process their outputs. Not shown is the equipment that generates the high-voltage pulses for the planar photodiodes. (d) All seven cameras are pictured from the scintillator screen’s point of view. Note the close packing of the cameras; there is little room for additional cameras. These cameras store one frame per camera—as opposed to the new camera’s three frames. Thus, the same number of new cameras will be able to capture three times the total number of frames as the old cameras. Moreover, the new hybrid cameras will reduce the total cost, real estate, and calibration time of the complete camera system.

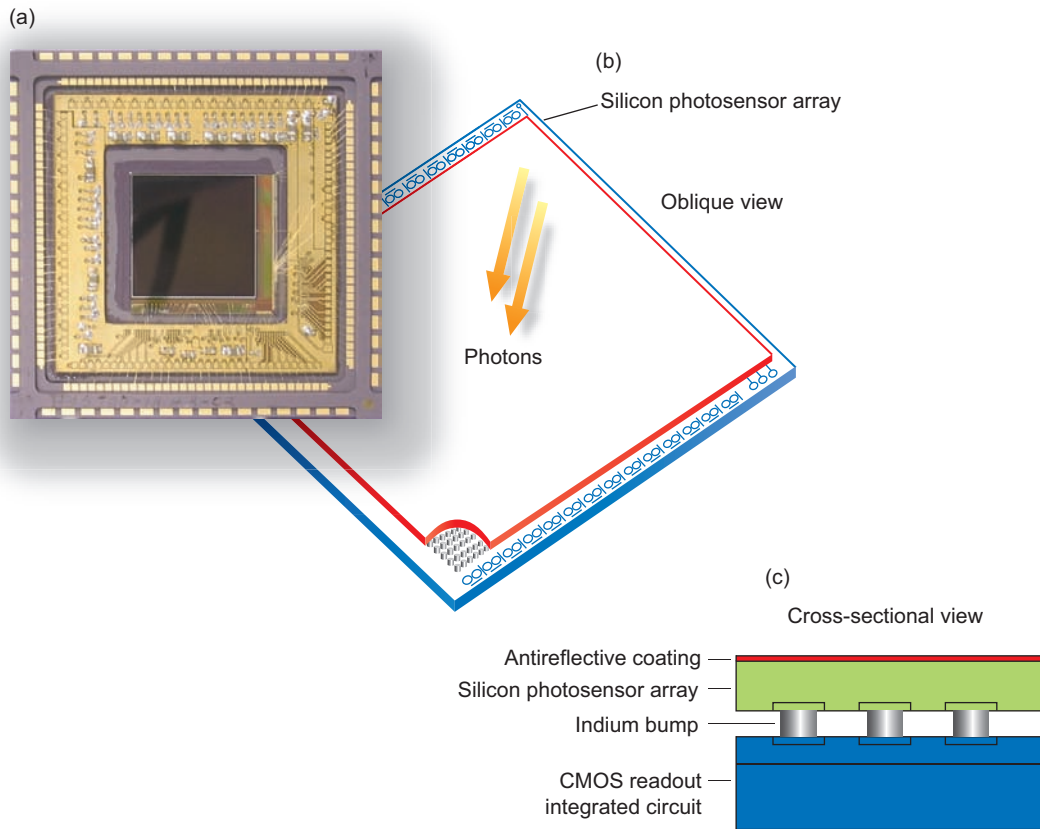


Figure 2. New High-Speed Camera on a Chip

The new chip consists of a 720×720 pixel array of fast silicon photosensors (with $26\text{-}\mu\text{m}$ pixel pitch) bonded to a CMOS integrated circuit that turns the signals from the photosensors on and off and processes their outputs. (a) In this photo, the photosensor array is the dark rectangle. Oblique (b) and side (c) views show how the two circuits are physically and electrically connected by indium bumps, much smaller than $10\ \mu\text{m}$ in diameter. The hybrid chip contains analog processing circuits, digital logic circuits, and a 12-bit analog-to-digital (A/D) converter. The only external connections required are for 2.5-, 3.3- and 14-V power supplies, clock and trigger (shutter) signals, and a digital-video output to transfer to the outside world the three frames acquired by the camera during an experimental run. This arrangement results in a "photons-to-bits" system on a chip. The hybrid chips can be butted on two sides, and thus a mosaic of 4 chips can form a (1440×1440) 2-megapixel imaging array.

the current system inefficiently converts light from the scintillator image to a digital image, which reduces the image quality. Finally, each of the system's charge-coupled device (CCD) cameras can store only one frame per experimental run, so many CCD cameras or lower resolution "framing cameras" are required to make a multiframe pRad movie.

To solve these and other problems, we have developed a new camera consisting of two silicon chips bonded together to form a "hybrid chip." The two circuits are a 720×720 array

of fast silicon photosensors and a complementary metal oxide semiconductor (CMOS) integrated circuit, which can turn the signals from the photosensors on and off to measure the intensity of the incident light in as little as 100 nanoseconds, although typically the camera is operated at an exposure time of 250 to 400 nanoseconds (Figure 2). The CMOS circuit then processes the photosensors' outputs and combines them into a frame; the new camera can capture three frames per experimental run. The photosensor array and all the control-

and-processing circuitry are contained in the $\sim 20 \times 20\ \text{mm}^2$ hybrid chip. As a result, the new camera is small, consumes only 2 watts of electrical power, needs few external electrical connections, and is highly reliable.

We chose to use advanced, but still "off-the-shelf" CMOS technology to design the large, complex circuit that both shutters the photosensors and processes their outputs, resulting in a "photons-to-bits" chip. CMOS is a mature but still-evolving technology used to produce the sophisticated microprocessors in personal computer

Figure 3. Silicon Photosensor Quantum Efficiency Compared with Scintillator Emission Spectrum

The silicon photosensors produce images with high signal-to-noise ratios because their quantum efficiency (green circles) is high at the scintillator's emission peak (black line). Quantum efficiency measures how efficiently a photodetector converts incident light to electrons. The new camera's quantum efficiency is about 85% at the emission peak (at about 415 nm), and due to the thin antireflective coating shown in Figure 2, little light is reflected at the interface between air and the photosensor's top layer. In contrast, the current CCD imaging system uses a cumbersome two-step process to convert light to electricity (as described in the caption to Figure 1), making it difficult to increase the current system's quantum efficiency much above its current 15%.

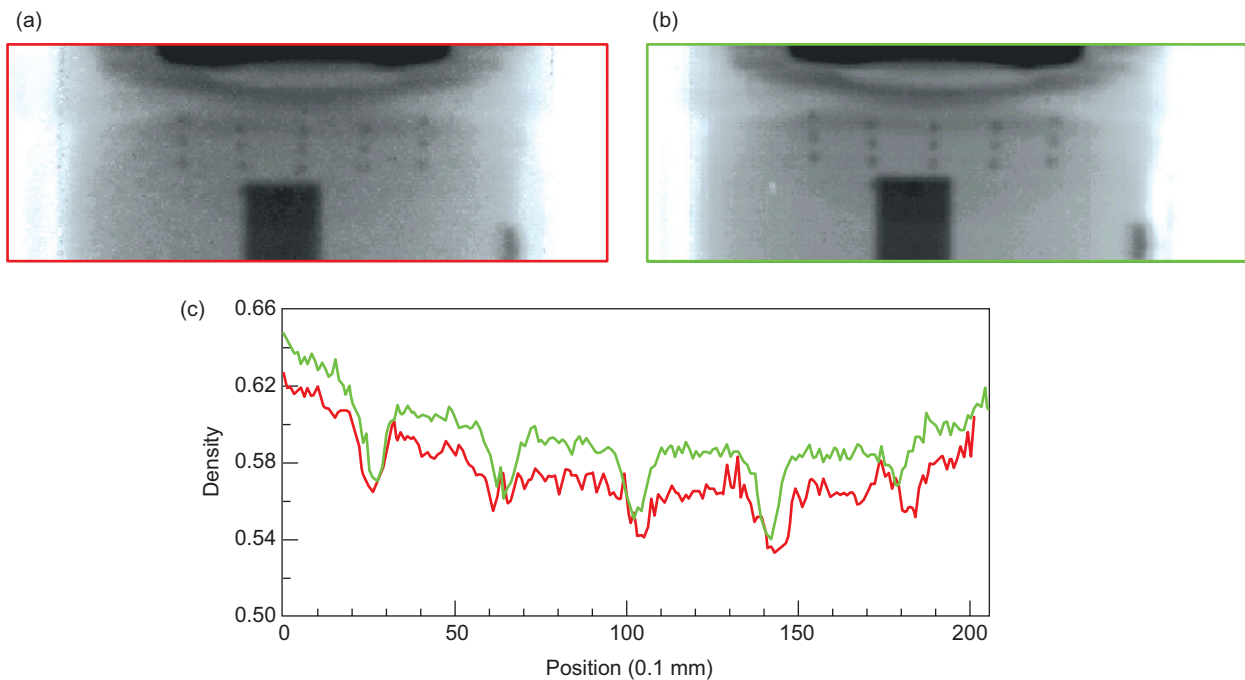
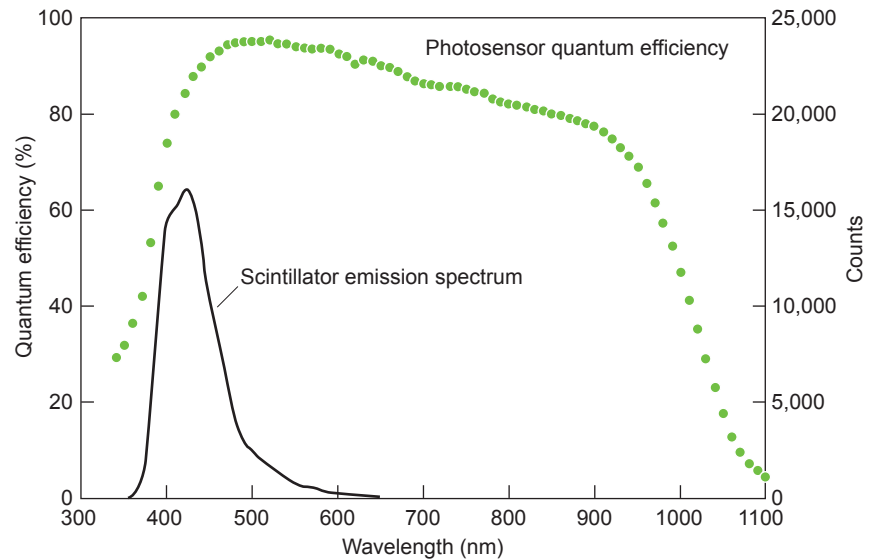


Figure 4. A Comparison of Signal-to-Noise Ratios and Position Resolutions for the Old and New Cameras
The small circles in the proton radiographs shown in (a) and (b) are gold spheres 0.635 mm in diameter. The spheres are sharper in (b), the image produced by the new hybrid CMOS camera, than in (a), the image produced by the old CCD camera because the new camera's silicon photosensors have high quantum efficiency, resulting in high signal-to-noise ratios in the images. (The improvement is even more impressive because the new camera's image contains about half a million pixels, about one-fourth the pixels in the old camera's image.) (c) Line scans of the radiographs through the center spheres quantitatively show the new camera's improved image resolution.

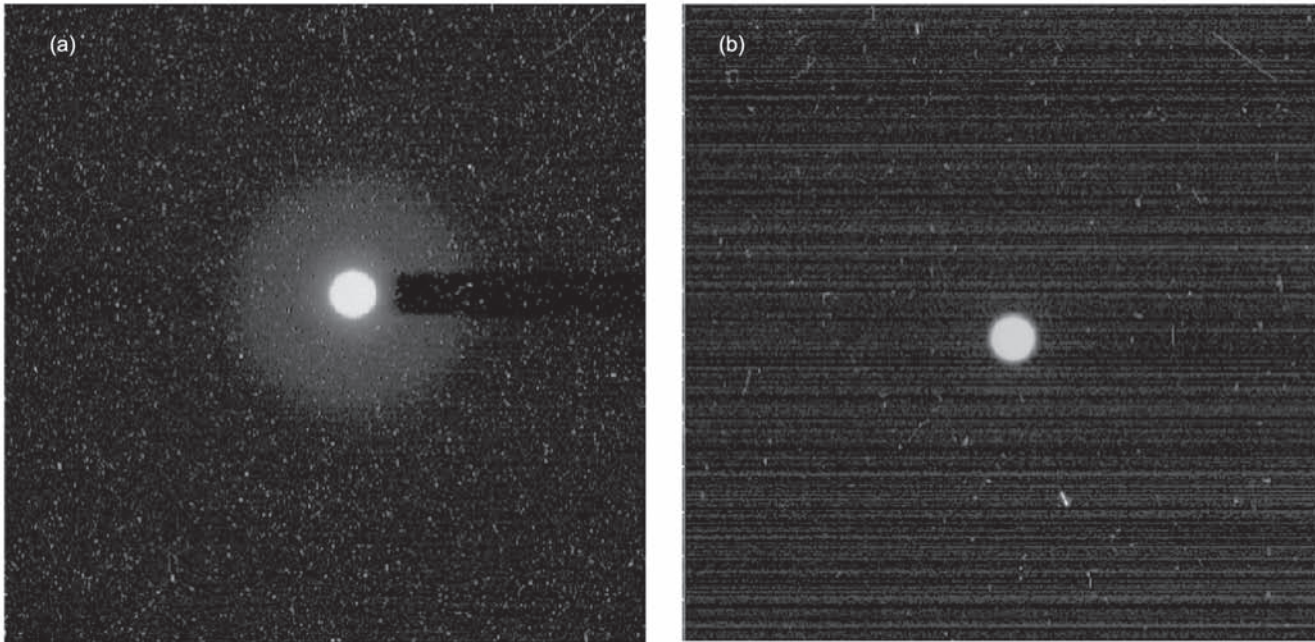


Figure 5. A Comparison of Camera Halos

These images were produced by exposing the old and new cameras for about 400 ns to a scene containing a bright circular spot. The large, bright halo around the spot in the old camera's image (a) was produced by the camera's planar-photodiode shutter. The new camera's image (b) has no halo because this camera is shuttered more directly and efficiently. The tiny white "stars" were produced by stray radiation, to which the new camera is clearly less susceptible. The horizontal lines in the right image are camera noise considered to be negligible because the intensities in these images are proportional to the logarithms of the intensities in the original images. The intensities of these lines are only about 0.05% of the maximum intensity.

and cell phone circuits; a microprocessor typically contains hundreds of millions of transistors. The new camera's CMOS chip contains over 10 million transistors. The hybrid chip containing both the photosensor array and the CMOS circuit was made at the Rockwell Scientific Company.

The 200-millimeter diameter wafers with 48 CMOS chips were fabricated at the United Microelectronics Corp. (UMC) silicon foundry in Taiwan, one of the largest facilities of this type in the world. Rockwell used its CMOS expertise to design the CMOS readout chip and its facilities to fabricate the photosensor arrays and to assemble the hybrid chips with minimal development costs.

The proton radiography team routinely operates the new camera in a

burst mode at 2.8 million frames per second but has successfully operated it as high as 4 million frames per second. The shutter control for the new camera is a fast 3-volt pulse, whose width determines the exposure time. This pulse is easy to generate and results in faster shutter times than those possible with the vacuum planar photodiode.

At wavelengths near the scintillator's light-emission peak, the new camera's quantum efficiency is 4 or 5 times that of our current camera system (Figure 3). Higher quantum efficiency means greater sensitivity to the scintillator light and therefore a higher "signal-to-noise" ratio in the images, allowing finer details to be seen (Figure 4). Although we could achieve higher image quality with our current camera system by increasing the proton beam intensity

by the same factor of 4 or 5, that would require upgrading the large, expensive accelerator that generates the 800-million-electron-volt protons that produce the radiographs.

Moreover, as shown in Figure 5, unlike the old camera, the new camera produces no "halo." The photos in Figure 5 also show the responses of the two cameras to stray radiation from the proton beam, which appears as tiny white spots (called "stars"). The lack of halos and the reduced response to stray radiation also improve the new camera's image quality.

The hybrid camera is also less susceptible to permanent damage from stray radiation. We typically replace each CCD camera in our current camera system every two to three years because of radiation dam-



Figure 6. The First Prototype of Our New Camera

The hybrid camera on a chip is mounted inside the solid-aluminum “camera body.” The red-striped gray cable shown is one of two such cables that provide all connections necessary to operate the camera, which consumes only 2 W of electrical power. The slotted-aluminum piece and black fan mounted on it comprise a cooling system that reduces thermal noise in the images (the hybrid imager is operated at 0°C). Five more prototypes are being made. In addition, hybrid-chip cameras that will provide images with 1440 × 1440 pixels could be developed by either building a mosaic of four hybrid chips or more efficiently by using the same basic design but “stitching” together four CMOS chips at the foundry to increase the pixel count by a factor of 4. (Stitching is a nonstandard CMOS process. That is why we did not use it for the first prototype.)

age. At about \$100,000 per single CCD-based camera system, the savings realized by using the new imagers will be considerable.

Finally, as mentioned above, the new camera stores three frames, but it has the potential, as CMOS technology advances, to store at least 10 frames in the near term and possibly hundreds of frames eventually. Thus, fewer of the new cameras will be required to capture the same total number of frames—reducing the cameras’ total cost, the time required to calibrate all of the cameras for each experiment, and the real estate of the cameras in the experimental area—where space is at a premium. The reduced space requirement also permits improved radiation shielding for the camera system. A prototype of the new camera is shown in Figure 6.

Although the new camera was designed specifically to make pRad movies, it can also be used to make visible-light and near-infrared movies of other fast dynamic phenomena, such as projectiles penetrating armor. It could also be used for multiframe flash x-ray imaging applications, possibly at the Los Alamos DARHT facility. The current 720 × 720 pixel array exceeds the array size and dynamic range of other visible-light, directly shuttered silicon-array cameras. Similar CMOS technology can also be used to measure much shorter, namely, nanosecond-scale changes, in light intensity for VISAR systems, which measure the velocity of an object’s surface by measuring the Doppler shift of light reflected from the surface. Alternatively, it can perform ultrafast shadowgraphy measure-

ments, or diagnostics of other ultrafast transient phenomena such as plasma fusion. In short, we see the new camera as the fast imaging technology of the future. ■

Further Reading

Douence, V. M., Y. B. Bai, H. Durmus, A. Joshi, P. O. Pettersson, D. Sahoo, K. Kwiatkowski, N. S. P. King, C. Morris, and M. D. Wilke. 2005. Hybrid Image Sensor with Multiple On-Chip Frame Storage for Ultra High-Speed Imaging. In *Proceedings of the SPIE—The International Society of Photo-Optical Instrumentation Engineers*. Edited by D. L. Paisley, S. Kleinfelder, D. T. Snyder, and B. J. Thompson. Vol. 5580, p. 226. Bellingham, WA: SPIE.

King, N. S. P., S. Baker, S. Jaramillo, K. Kwiatkowski, S. Lutz, G. E. Hogan, et al. 2003. Imaging Detector Systems for Soft X-Ray and Proton Radiography. In *Proceedings of the SPIE—The International Society for Optical Engineering 25th International Congress on High-Speed Photography and Photonics*. Edited by C. Cavallier, G. P. Haddleton, and M. Hugenschmidt. Vol. 4948, p. 610. Bellingham, WA: SPIE.

Kleinfelder, S., K. Kwiatkowski, and A. Shah. 2005. A Solid State Streak Camera. In *Proceedings of the SPIE—The International Society of Photo-Optical Instrumentation Engineers*. Edited by D. L. Paisley, S. Kleinfelder, D. T. Snyder, and B. J. Thompson. Vol. 5580, p. 235. Bellingham, WA: SPIE.



$n, 2n$

(neutron_{in}, 2 neutrons_{out})



Fission

(neutron_{in}, fission products_{out})

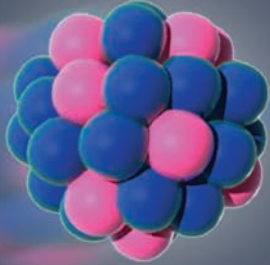
Neutron
Capture

(neutron_{in}, gammas_{out})




Fundamental Nuclear Data for Pinning down the Performance of Nuclear Weapons

Robert C. Haight, Mark B. Chadwick, and David J. Vieira



The cessation of nuclear-weapon testing and the new goal of predicting nuclear-weapon performance from first principles have put increased importance on the accuracy of fundamental data on neutron-induced nuclear reactions. These data are crucial both for calculating the energy yield of a nuclear detonation and for benchmarking those predictions against the telltale radiochemical evidence recorded in the debris from past aboveground and underground nuclear tests. They may also be needed to interpret the nuclear activities of rogue nations and terrorist groups. In the past, many of the relevant reactions, especially those involving radioactive nuclei, have been too difficult to measure or have not been measured in the detail needed for modern weapons codes. As part of the Stockpile Stewardship Program, we have developed an unmatched suite of instruments capable of measuring neutron reactions on samples as small as a billionth of a gram. Together with the intense neutron sources at the Los Alamos Neutron Science Center and the Los Alamos National Laboratory's capabilities to produce isotopic samples, these unique instruments fill in much of the missing nuclear data and thereby reduce uncertainties in predictions of device performance.



On the opposite page: The intense flux of neutrons in a nuclear device causes several types of nuclear reactions, which are illustrated here. In fission, an incident neutron (blue) splits a fissile nucleus into two smaller nuclei, which release a number of neutrons, and those can induce more fissions. In neutron capture, a neutron is captured by a nucleus, changing it to a heavier isotope of the same element. The new isotope is left in an excited state, which de-excites to the ground, or lowest-energy, state by emitting a cascade of gamma rays (white). In the $(n,2n)$ reaction, a neutron has high enough energy to knock out two neutrons, producing a lighter isotope of the same element.

In the sudden and gigantic release of energy by a thermonuclear weapon, two types of nuclear reactions are at work: the splitting of a very heavy fissile nucleus, typically uranium-235 or plutonium-239, and the fusion of two very light nuclei, deuterium and tritium. Both these reactions produce neutrons, and the exponential growth of the neutron population within a tiny fraction of a second, accompanied by an enormous release of energy, is the characteristic feature of a nuclear detonation. Predicting the history of neutron and energy production and the overall energy yield of a nuclear device from first principles is the goal of the Advanced Simulation and Computing (ASC) Program and of modern weapons codes. In this article, we outline the new and exciting approaches now being used at the Los Alamos Neutron Science Center (LANSCE) to achieve a much better understanding of the nuclear reactions that make weapons work and that give us insight into the performance of tested devices.

The importance of neutrons in nuclear weapons cannot be overstated. Neutrons induce fission, which is a major energy source in the explosion. Neutrons serve as the propagating vehicle for the supercritical chain reaction and the rapid, exponential amplification of energy. And neutrons can serve as essential diagnostic probes, either by escaping the device and entering external detectors or by transmuting materials placed in the device into radioactive nuclei. The product nuclei of the transmutations can be collected after the explosion and analyzed by radiochemical techniques to indicate the neutron flux in a specific region integrated over the history of the explosion (time-integrated flux is called “fluence”). Both these “prompt” and “radiochemical” (radchem) diagnostics give essential data that must be matched by calculations in order to benchmark the explo-

Table I. Neutron Reactions of Importance to Weapons Physics

Reaction	Properties	Importance
Fission	Cross section	Reaction rate
	Energy release	Energy produced
	Neutron production	Neutron economy, ^a neutron output
	Gamma-ray production	Heating and gamma-ray output
	Fission products	Radiochemical diagnostics
	Fission products	Neutron absorbers or multipliers
	Neutron capture	
	Cross section	Neutron economy
	Cross section	Radiochemical diagnostics
	Gamma-ray production	Heating and gamma-ray output
$(n,2n)$	Cross section	Radiochemical diagnostics
(n,p) , (n,α) and others	Cross section	Radiochemical diagnostics

^a Neutron economy refers to reactions that can increase or decrease the number of neutrons in the system

sion codes. To interpret these data correctly, one must know the basic nuclear transport and reaction data with high accuracy.

The need for improved understanding of basic nuclear reactions increased greatly with the cessation of underground nuclear tests in 1992. Whereas before that date weapons could be tested and a large database was accumulated of systematic performance, now the performance of a weapon is known only through calculation. These calculations are adjusted to reproduce previous test data, but their relevance as benchmarks can be questioned when conditions change because of aging materials, component modernization, or new designs. Our explosion models could be inappropriate for simulating completely different weapon concepts that might

be used by rogue nations or terrorists. Thus, it is critical to improve the models so that their application in new areas will give credible and accurate results. If the input neutron-reaction data are inaccurate, then the predictions of the models certainly will be so, and because of the high nonlinearity of the physical processes in a nuclear explosion, the models could be grossly in error. Thus, one of the most basic requirements in understanding previous test data to improve the models is highly accurate neutron-reaction data.

With the rapidly increasing power of computers, the actual nuclear properties can be used in modern weapons codes, rather than some convenient (and somewhat inaccurate) approximation to the data. A further increased need for nuclear data has been added

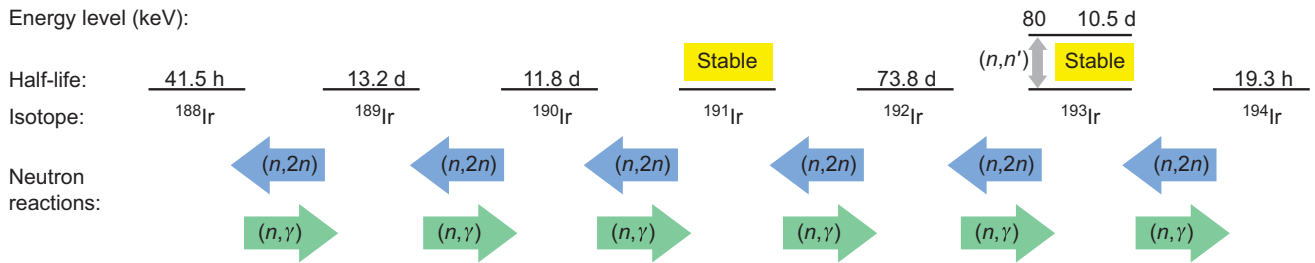


Figure 1. Chain of Neutron-Induced Reactions on Iridium Used in Radiochemical Analysis

Neutron-induced reactions on iridium isotopes are used to infer neutron fluence by radiochemical analysis of the amount of the radioactive isotopes produced. Natural iridium consisting of the stable isotopes 191 and 193 was placed in the device. The radioactive isotopes produced in the test live long enough so that they can be recovered by drill-back procedures and then analyzed in the laboratory. The $(n,2n)$ reactions have thresholds of approximately 6 MeV and therefore indicate the fluence of neutrons above this energy. The (n,γ) reactions have zero threshold and indicate the neutron fluence generally below 1 MeV. The (n,n') reaction on iridium-193 producing the 10.5-day excited state at 80 keV is sensitive to neutrons between 1 and 5 MeV, which is the major energy range for neutrons produced in fission.

recently as designers are now asked for uncertainties in the predicted performance. Quantification of margins and uncertainties (QMU) is now central to the weapons program. Fortunately, data from previous nuclear tests include extremely careful measurements of total energy yields, neutron and gamma-ray output, and the production of radioisotopes, which were extracted from weapon debris with radiochemical techniques. To interpret these data, we need precise fundamental nuclear data, rather than systematics of questionable accuracy, as input to these codes. The important nuclear reactions that must be quantified as accurately as possible are listed in Table I.

Nuclear explosions are unique among phenomena that happen on earth in that they obviously occur extremely fast and have a very large number of neutrons in a small volume driving up the rate of nuclear reactions. Only some astrophysical sites have similar conditions. With these special conditions of short time scales and very high reaction rates, nuclear reactions that are not important in systems such as nuclear reactors become very important in nuclear weapons. For example, new nuclei with short half-lives can be produced in the

explosion and then undergo additional reactions themselves before the explosion is over. In other cases, nuclei can be excited to states that live longer than the explosion, and these so-called “isomeric” states can have properties different from those of the ground state. In both cases, new opportunities arise to understand the performance of a nuclear weapon. Along with these opportunities, new challenges present themselves and require new, more-powerful techniques to take advantage of the opportunities.

Our nuclear-data research program at LANSCE has two components. One is to measure much more accurately reactions on stable (or at least long-lived) nuclei used as fuels, structural materials, or radiochemical detectors. Although many of these materials have been studied before, there are often large discrepancies in the literature that need to be resolved. And there are also many gaps in the literature data. The other component is a completely new challenge, namely, to study reactions on radioactive targets that have heretofore been impossible because of the short half-lives of the nuclei or the difficulty of producing or using these highly radioactive materials.

An example of basic nuclear

reactions used to infer the neutronic performance of a nuclear weapon is given in Figure 1. If iridium, a naturally occurring element that has two stable isotopes, is placed in the device, radioactive isotopes and long-lived excited nuclear states (isomers, for example, iridium-193m) are created by the intense neutron flux of the explosion. In the debris recovered in drill-backs hours or days later, these radioactive products can be separated and analyzed to indicate the neutron fluence and its energy spectrum at the location of the loaded iridium. Knowledge of the individual reaction rates is essential to the analysis, and our challenge is to improve this knowledge in key areas that have heretofore been inaccessible.

LANSCE, a Powerful Source of Neutrons

In the past, acquiring accurate nuclear-reaction data was limited by the lack of suitably intense neutron sources. To address the present-day requirement for more-accurate nuclear-reaction data, an advanced neutron source is essential. LANSCE is arguably the best facility in the

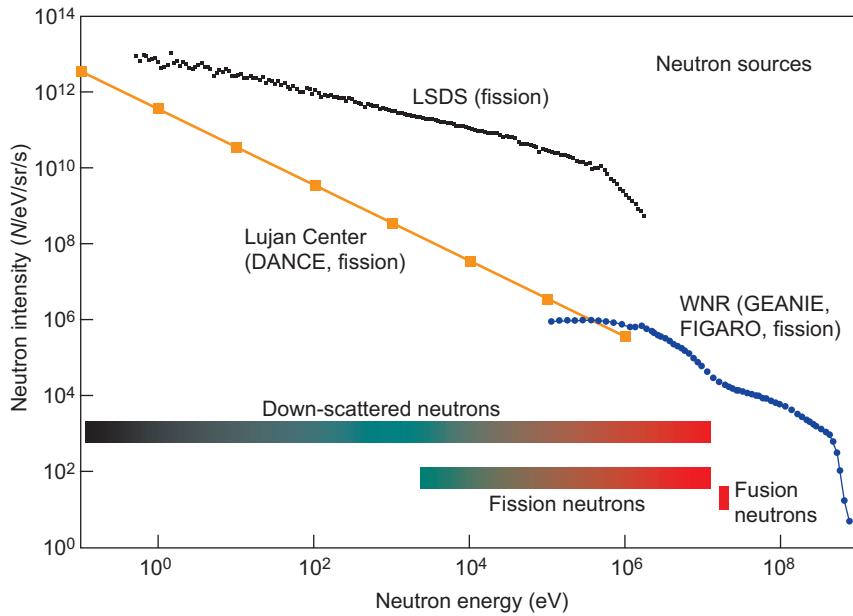


Figure 2. Energy Ranges of Neutron Sources at LANSCE
 The intensity and energy distributions of the neutrons produced at the WNR, Lujan Center, and LSDS show the very large range of energies covered in these facilities.

world to fill in the missing pieces of this nuclear puzzle. LANSCE is centered on a powerful 800-MeV proton linear accelerator used to produce intense neutron beams. The facility consists, in fact, of three neutron sources used for nuclear physics for the weapons program:

- The Weapons Neutron Research (WNR) source of fast neutrons from 100 kilo-electron volts (keV) to 800

- million-electron volts (MeV) in energy
- The Lujan Neutron Scattering Center (Lujan Center) source of moderated neutrons from subthermal energies to 500 keV
- The Lead Slowing-Down Spectrometer (LSDS) for specialized experiments with neutron energies from 1 electron volt to 200 keV

The relationship of the neutron ranges spanned by these three faci-

ties to the energy range of interest for weapons is shown in Figure 2. LANSCE produces the most intense source of neutrons in the world over the range of energies relevant to weapons. Future improvements are expected to increase the usable neutron flux in the important weapon regime of 1 keV to 5 MeV by a factor of 30 or so by stacking pulses in the Proton Storage Ring at LANSCE and transporting the stacked pulses to the WNR. At all these sources, neutron reactions are studied over a large range of energies all at once, using the time-of-flight method described below.

At LANSCE, neutrons are produced by spallation, which means that each time a proton pulse hits a heavy metal target, a pulse of neutrons having a wide range of energies boils off, or evaporates, from the target nuclei. Time-of-flight techniques are used to indicate the energy of the incident neutron. For the WNR and Lujan Center sources, the sample under study and the measuring instruments are placed at some distance (9 to 90 meters) from the source. Because the source is pulsed, neutrons with higher energy reach the measuring station before the slower neutrons (Figure 3), and the neutron time of flight can be measured to determine the incident-neutron energy. At the

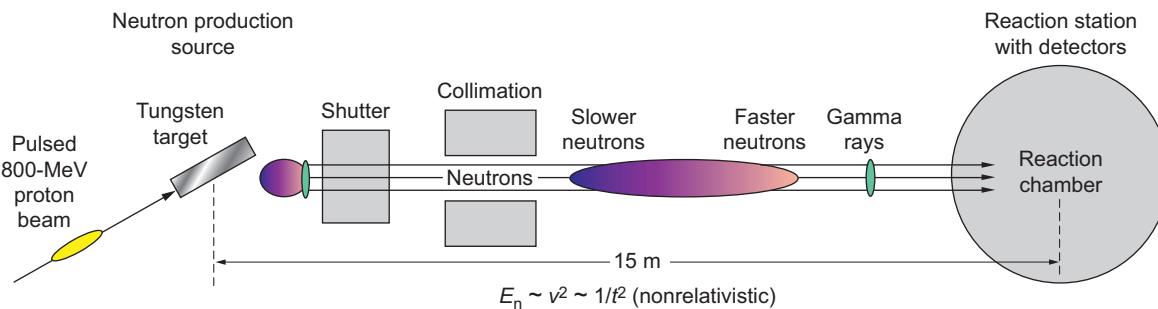


Figure 3. Determining Neutron Energies by Time-of-Flight Techniques
 Neutron energies initiating the reaction are determined by their time of flight (*t*) from the neutron source to the reaction station. The source is pulsed and the more-energetic (faster) neutrons arrive at the reaction station before those with lower energy, which travel more slowly.

LSDS, similar techniques are used although there is not a defined flight path (see below). This ability to study a given reaction simultaneously over a large energy range provides a consistent set of data over this range and therefore much more accurate information for the database.

Innovative Instruments at LANSCE

The second essential requirement in improved experimental capabilities is to be able to take advantage of these intense neutron sources. The challenge is to develop instruments that are sensitive to the desired signal and are not overwhelmed by high count rates or by backgrounds from unwanted sources. In this article, we describe unique high-precision experiments performed with several new LANSCE instruments—known as GEANIE, DANCE, FIGARO, and LSDS—to fill in significant gaps in the nuclear data. We outline several measurements to improve the interpretation of radchem results and also describe developments that are reducing uncertainties in the prediction of fission performance.

GEANIE—Reactions to Determine Neutron Fluence in Data from Weapon Tests

GEANIE (Germanium Array for Neutron-Induced Excitations) is an array of 26 high-resolution gamma- and x-ray detectors that view a sample bombarded with neutrons with energies from 0.1 to 200 MeV from the WNR source of fast neutrons (Figure 4). This unique array was constructed by a collaboration of researchers from Los Alamos and Lawrence Livermore National Laboratories specifically to investigate neutron reactions at the center of rad-



Figure 4. The GEANIE Detector
GEANIE is composed of 26 high-purity germanium detectors. The photo shows them viewing gamma rays from an encapsulated plutonium-239 sample bombarded with neutrons from the WNR source.

chem diagnostics, reactions that were tantalizingly difficult to study by any other means. The next two sections describe two of these experimental challenges: One is used to interpret radchem data for the neutron fluence in a weapon above 6 MeV, and the other is a unique probe into the fission neutron spectrum in the 1- to 5-MeV range.

First Accurate Data to Interpret Plutonium Radchem Results.

Isotopes produced during an explosion in the nuclear fuels, whether

uranium or plutonium, serve as a very useful radchem diagnostic of weapon performance. A neutron impacting a plutonium-239 nucleus can cause fission, but if the energy of the neutron is greater than 6 MeV, it can alternatively induce an $(n,2n)$ reaction that transforms plutonium-239 to plutonium-238. We write this reaction as $^{239}\text{Pu}(n,2n)^{238}\text{Pu}$. Thus, a measurement of the amount of plutonium-238 provides valuable information on the neutron energies in the device above 6 MeV, provided one knows the cross section for producing plutonium-238

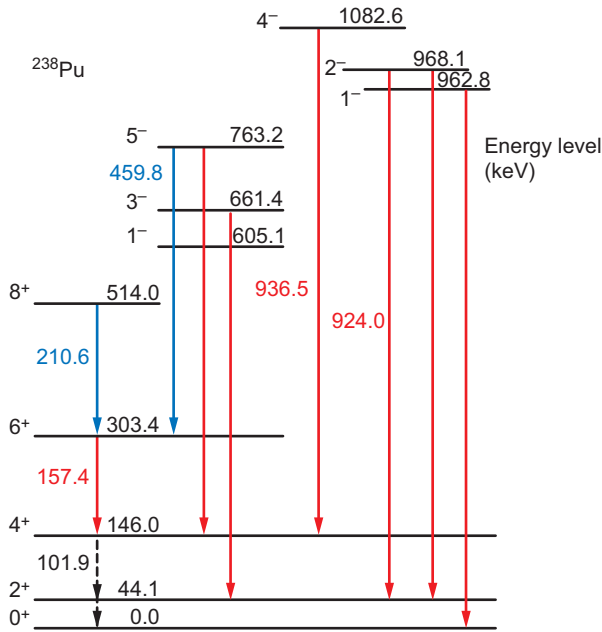


Figure 5. Gamma-Ray Transitions Observed in the $^{239}\text{Pu}(n,2n)^{238}\text{Pu}$ Reaction

The yields of the transitions shown in red were used to deduce the total cross section for this reaction with good confidence.

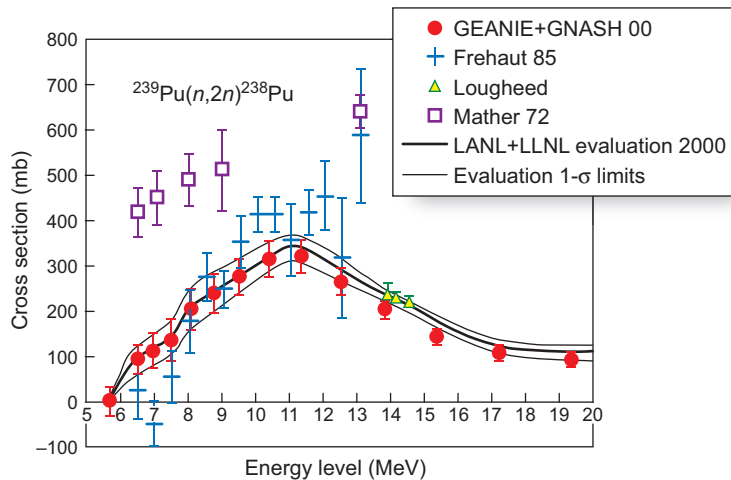


Figure 6. Measurement Results of $n,2n$ on Plutonium at GEANIE vs Previous Data

The $^{239}\text{Pu}(n,2n)^{238}\text{Pu}$ cross section results deduced from the GEANIE measurements are compared with previous data. Note that this cross section has a threshold at 6 MeV, and so the amount of plutonium-238 produced in a nuclear-weapon test is sensitive to neutrons above this energy.

as a function of energy.

Surprisingly, the first accurate measurements of the cross section (“rate”) for the $^{239}\text{Pu}(n,2n)^{238}\text{Pu}$ reaction over the neutron energy range of 6 to 20 MeV were not feasible until only a few years ago, when the new GEANIE detector at the WNR came online. The two previous approaches turned out to have insurmountable difficulties to yield anything that was close to an accurate result over the energy range of interest.

One would think that this reaction could be studied in the laboratory by bombarding a sample of plutonium-239 with monoenergetic neutrons and then measuring the amount of plutonium-238 produced. However, there is the very real problem that even the purest sample of plutonium-239 has some plutonium-238 contaminant. To overcome that background, one needs a very large total number of incident neutrons so that the buildup of plutonium-238 from the reaction is large enough to measure with radiochemical techniques. This direct approach was pursued many years ago with the intense 14-MeV neutron source at Lawrence Livermore. However, at other neutron energies, especially in the threshold region near 6 MeV, there has simply not been any neutron source intense enough for this measurement.

The other approach used previously was to detect the two neutrons emitted in the $(n,2n)$ reaction, but here another difficulty frustrated the researchers. The incident neutrons sometimes induce fission of plutonium-239 that is accompanied by the release of two neutrons, and those fission neutrons look just like the two neutrons coming from the $(n,2n)$ reaction. In fact, the fission neutrons are sufficiently numerous to introduce large uncertainties in the deduced cross section for the reaction $^{239}\text{Pu}(n,2n)^{238}\text{Pu}$.

In 1996, the GEANIE detector

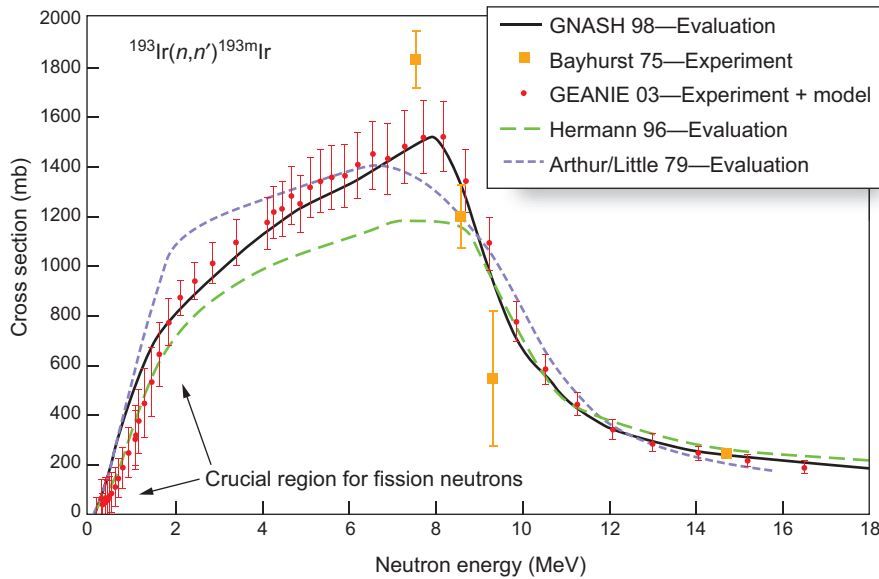


Figure 7. New Evaluated Production Cross Section for Iridium-193m
The new GEANIE/GNASH result for the 82-keV isomer production cross section in iridium-193 is shown here covering the incident-neutron energy range from the reaction threshold (80 keV) to 18 MeV. The $1\text{-}\sigma$ standard deviations come from uncertainties in both GEANIE data and GNASH reaction modeling. This new cross section is compared with the historical one by Edward Arthur and Robert Little (of the Theoretical and Applied Physics Divisions at Los Alamos), which was previously used at the Laboratory, with a more recent calculation by GNASH in 1998 and with another evaluation. The previous Los Alamos data by Bayhurst are also shown.

was completed at LANSCE, and its availability opened up a totally new approach. The plutonium-238 nucleus produced in the $^{239}\text{Pu}(n,2n)^{238}\text{Pu}$ reaction is most likely left in an excited state that quickly emits gamma rays as it decays to the ground state. In other words, the $(n,2n)$ reaction should be written as $^{239}\text{Pu}(n,2n + \text{gammas})^{238}\text{Pu}$. The GEANIE detector is an ideal instrument for measuring those gamma rays with high-energy resolution and high efficiency. The nuclear energy-level diagram in Figure 5 shows the transitions in the plutonium-238 nucleus that produce the gamma rays. Following the measurements at GEANIE carried out by a team from Lawrence Livermore and Los Alamos, model calculations were conducted in the Theoretical Division

at Los Alamos to relate the measured production of specific gamma rays produced in the $(n,2n)$ reaction cross section to the total production of plutonium-238. The larger the fraction of gamma rays detected by GEANIE, the better constrained is the theoretical model, and the lower is the resulting uncertainty in the deduced cross section. The results are shown in Figure 6, along with the previous Lawrence Livermore data at 14 MeV described above, the rather imprecise data from measuring the two neutrons, and a wide range of estimates of the cross section made before the GEANIE experiment.

The final results from this GEANIE project are crucial to inferring details of weapon performance through analysis of the measured

plutonium-238/plutonium-239 isotopic ratio in the debris of the explosion. This GEANIE measurement earned a National Nuclear Security Administration Award of Excellence for the Los Alamos and Lawrence Livermore collaboration.

First Accurate Data to Diagnose Fission Neutron Flux from Radchem Results. In a more recent study, the GEANIE detector was used to determine the cross section for another important radchem reaction—the inelastic neutron-scattering reaction $^{193}\text{Ir}(n,n')^{193\text{m}}\text{Ir}$, in which the incident neutron excites the iridium-193 nucleus to a so-called “isomeric excited state” with a half-life of 10.5 days. This isomer-producing reaction is particularly interesting because, unlike the $(n,2n)$ radchem detectors, such as $^{239}\text{Pu}(n,2n)^{238}\text{Pu}$, which are sensitive to high-energy neutrons (above 6 MeV), or the neutron capture detectors, which are sensitive to low-energy neutrons (below 1 MeV), isomer production via (n,n') reactions is sensitive to neutrons in the intermediate energy range of 1 to 5 MeV. Neutrons released in fission typically have energies of 1 to 5 MeV, and thus isomer production is a good measure of fission neutrons.

Surprisingly, accurate experimental data for the isomer production cross section were lacking for many years, and weapon designers had to rely almost completely on theory to interpret radchem results for iridium. Unfortunately, the predictions of the theory were acknowledged to be very imprecise because of poorly known nuclear-structure details in the (n,n') nuclear reaction. That situation has changed through the latest measurements at GEANIE.

In this case, as in the cross section measurements discussed in the previous section, direct laboratory experiments to measure the isomer production proved extremely difficult

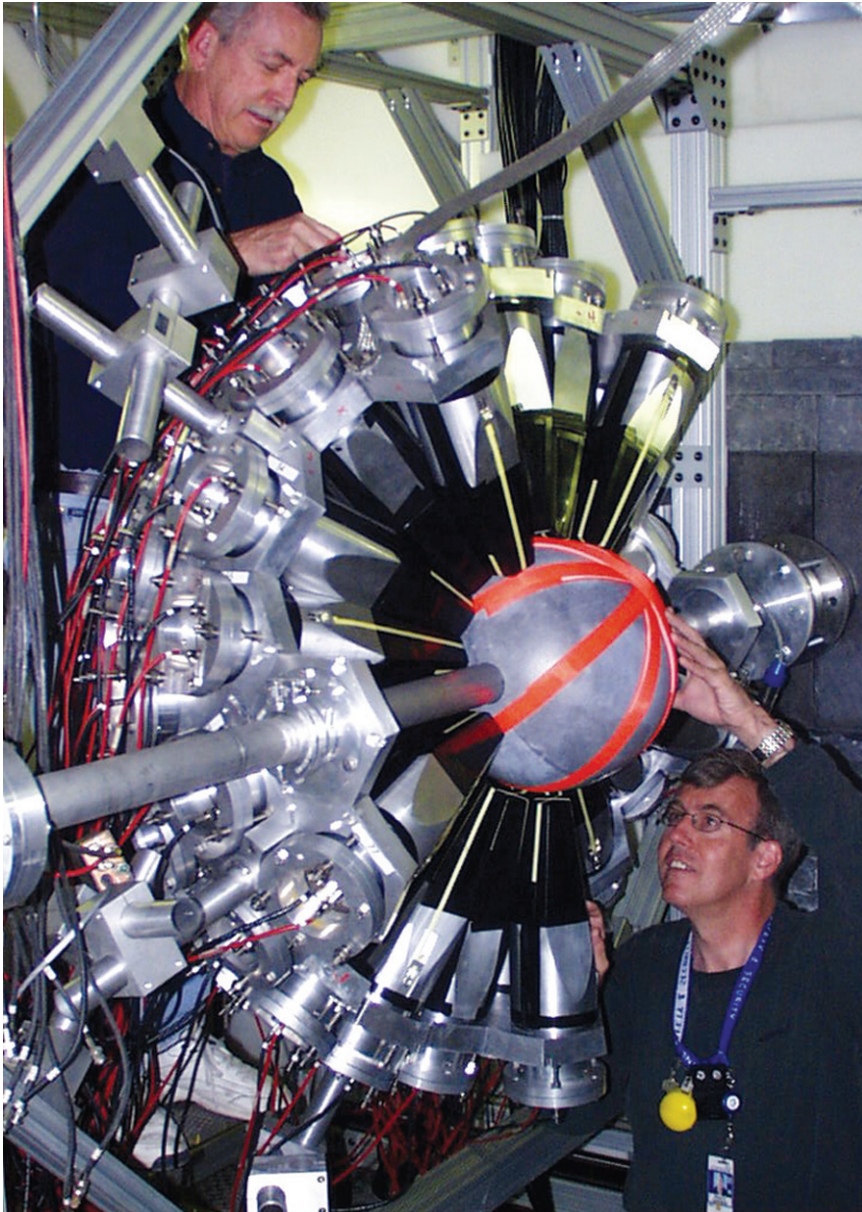


Figure 8. DANCE
 A photo of the DANCE detector shows only one-half of the array of barium fluoride (BaF_2) gamma-ray detectors and the spherical lithium hydride (^6LiH) neutron absorber surrounding the sample. When in use, the other half of the detector array is moved into place to make a spherical shell of gamma-ray detectors.

and gave results with huge error bars (Figure 7). The source of this difficulty was that the isomer decays mostly by a low-energy electron and low-energy x-rays, both of which are difficult to measure if only small quantities of the isomer are present.

Previously, there was only one set of data with large uncertainties at neutron energies of 7.6, 8.6, 9.3 and 14.7 MeV, and none in the region of most interest from 1 to 5 MeV.

As in the $(n,2n)$ measurements on plutonium, the advent of GEANIE

opened up an indirect approach to measuring isomer production, namely, through measuring the gamma rays emitted in the decay of excited states of iridium-193 to the isomer. The GEANIE/GNASH results resolved the long-standing question of what shape the cross section has as a function of incident-neutron energy, especially in the 1- to 5-MeV region that is so important for diagnosing fission neutrons.

DANCE: Unraveling Contributions from Complicating Reactions

DANCE, the Detector for Advanced Neutron-Capture Experiments (Figure 8), is shaped like a soccer ball with 160 equal-area pentagonal and hexagonal elements made from 15-centimeter-thick barium fluoride (BaF_2) scintillation material to capture nearly all the energy of gamma rays emitted in a nuclear reaction. Because of its high segmentation, the multiplicity (or number) of gamma rays in the reaction can also be measured. The sample is placed in the center of this spherical array and is bombarded with neutrons from the Lujan Center neutron source covering the energy range from thermal to approximately 200 keV. The most likely reaction on typical materials at these energies is neutron capture, whereby the neutron is added to the target isotope increasing its mass by one unit. The energy liberated in the capture process appears as one or more (typically 3 to 5) gamma rays. In this reaction, the total energy of all the gamma rays is characteristic of the sample under study, and this total energy is between 4 and 9 MeV. Thus, by energy selection and by the number of gamma rays detected, DANCE has good specificity for defining the particular neutron-capture reaction of interest. It also minimizes the back-

ground from scattered neutrons, as we have placed a lithium hydride (${}^6\text{LiH}$) shell around the sample to absorb these neutrons. Because this detector is so efficient and the neutron flux at the Lujan Center is so high, sample sizes can be very small—only about 1 milligram. With such small samples possible, a new world of reaction studies with radioactive samples is now open to investigation.

The DANCE instrument was developed to investigate reactions complementary to those studied at GEANIE. It is designed to quantify reactions that can confuse the interpretations of radchem results, such as from the neutron reactions just mentioned, by addressing the neutron energy range below 200 keV. The ultimate fate of weapon neutrons is often determined in this energy range because, once produced, these neutrons lose energy by reactions and scattering. Since radchem diagnostics are time integrated, the reactions produced by these slow neutrons must be taken into account in interpreting the test data correctly.

Neutron Capture Reactions.

Reactions used for weapon diagnostics such as those described above, ${}^{239}\text{Pu}(n,2n){}^{238}\text{Pu}$, and ${}^{193}\text{Ir}(n,n'){}^{193\text{m}}\text{Ir}$, produce radioactive products that can be assayed by radiochemical techniques. Many other reactions have also been used in nuclear tests, and the amount of each of the radioactive isotopes produced indicates both the fluence and the energy distribution of the neutrons at the location of the initial isotope. Now suppose that the radioactive isotope produced in the test undergoes further nuclear reactions in the dense neutron environment. Then the abundance of the radioactive isotope will be changed by second-order reactions, such as neutron capture reactions. These effects can provide useful information about the number

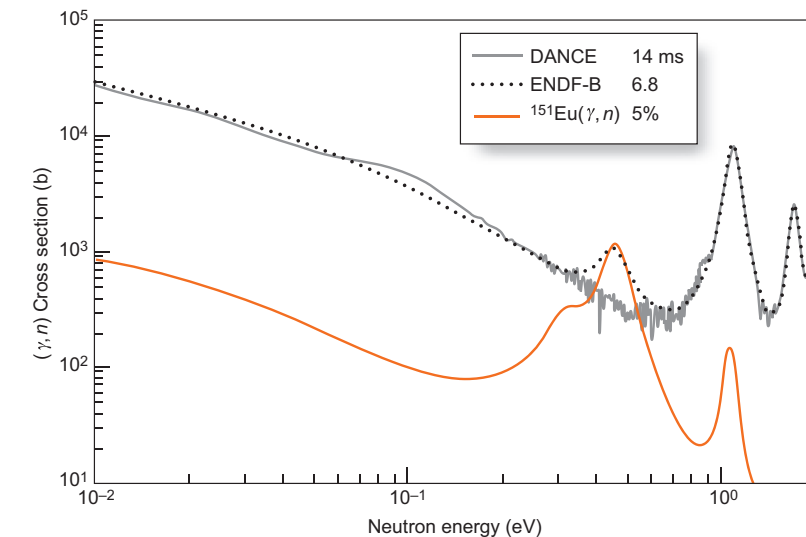


Figure 9. Neutron-Capture Cross Section of Samarium-151
DANCE data on the neutron-capture cross section on the radioactive nucleus samarium-151 show that the existing ENDF¹ evaluation incorrectly puts a resonance at 0.46 eV. This evaluation was guided by an experiment done elsewhere with a sample that was contaminated by a 5% impurity of europium-151, the decay product of samarium-151.

of low-energy neutrons, but they can also change the relative amounts of isotopes produced via $(n,2n)$ or (n,n') reactions in a weapon test and thereby complicate the analysis. Here follows an example based on the element thulium, in which both processes occur.

The rare-earth element thulium has been used as a neutron fluence detector in weapon tests. It has only one stable isotope, thulium-169, which, under intense neutron bombardment, makes a whole series of radioactive isotopes of the element, from masses 167 to 172. The chain of reactions is similar to that in Figure 1. The capture reaction ${}^{169}\text{Tm}(n,\gamma){}^{170}\text{Tm}$ gives data on low neutron energies, below 1 MeV, and we are remeasuring this cross section in order to resolve discrepancies between previous

measurements. The $(n,2n)$ reactions, especially ${}^{169}\text{Tm}(n,2n){}^{168}\text{Tm}$ and ${}^{168}\text{Tm}(n,2n){}^{167}\text{Tm}$, probe neutron energies above 6 MeV. The ratio of the amounts of two radioactive isotopes, such as thulium-167 and thulium-168, is often considered a reliable diagnostic of the neutron fluence above 6 MeV because isotopes of the same element undergo the same chemistry and fractionation in the underground environment. Although it is very difficult to measure the $(n,2n)$ reaction on the radioactive thulium-168 nucleus, systematics of nuclear reactions, together with a heroic point at 14 MeV from Livermore, can be used here rather reliably to estimate the cross section as a function of energy for this reaction. So, barring any complications,

¹ Evaluated nuclear data result from analyzing all available experiments, resolving discrepancies, and determining both the values and the uncertainties. They are kept in libraries known as ENDF, the Evaluated Nuclear Data File. ENDF data are freely available from the National Nuclear Data Center at Brookhaven National Laboratory (<http://www.nndc.bnl.gov>) and from the Los Alamos Web site (<http://t2.lanl.gov>).

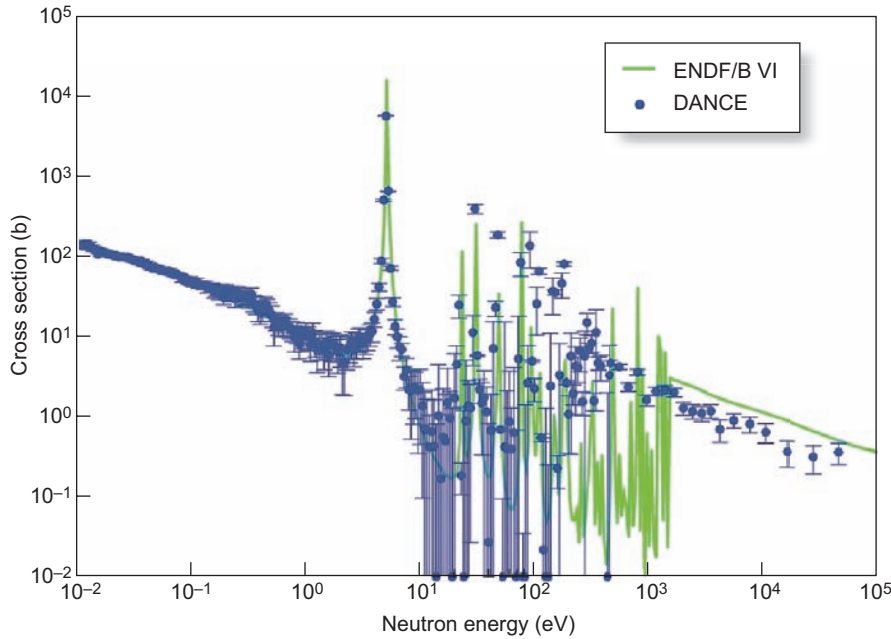


Figure 10. Neutron-Capture Cross Section of Uranium-234
 The important region above 1000 eV was never been measured before with good resolution. The data obtained at DANCE indicate that the evaluated data accepted for use in the United States, the ENDF/B-VI values, are significantly too high in this energy region.

the ratio of thulium-167 to thulium-168 gives good information on the neutron fluence above 6 MeV. Now, suppose, however, that another, second-order reaction comes into play, the $^{168}\text{Tm}(n,\gamma)^{169}\text{Tm}$ reaction, which decreases the amount of the originally produced thulium-168. The cross section for that reaction is not at all well known. Theory is not of much help because, where we have data, theory predicts capture rates only to a factor of 2 for stable nuclei. (However, more-precise predictions are sometimes feasible where nuclear modeling input parameters for a specific reaction are known from other nuclear physics studies.) In this neutron-capture reaction, the target nucleus thulium-168 is unstable, and there are no tests of the theory in this mass range for unstable nuclei. Similar issues come into play for the $^{170}\text{Tm}(n,\gamma)^{171}\text{Tm}$ reaction. For these reactions, experimental data are essential, and that is why DANCE

was constructed.

A series of radioactive isotopes of importance to radiochemical diagnostics is being prepared for experiments at DANCE. In preparation for this campaign, we have studied the available isotope samarium-151, which is of interest to astrophysicists in understanding the formation of elements in stars. These data are shown in Figure 9. Previous estimates were confirmed above 1 electron volt, and a significant correction was found near 0.46 electron volt.

DANCE is not limited to rare-earth nuclides and has already produced data on neutron capture for the important set of uranium isotopes uranium-234, -235, -236, and -238 and for neptunium-237. Neutron-capture data for uranium-234 are shown in Figure 10. These data are the first reliable ones for incident-neutron energies above a few electron volts. In a weapon environment, neutron reactions on the longer-lived isotope

uranium-235 create shorter-lived isotopes, which can subsequently participate in neutron reactions. Understanding neutron-capture cross sections on uranium-234 and -236 will improve the analysis of the radionuclide debris data after an explosion.

More generally, DANCE brings the unique capability to reduce many of the uncertainties that have been associated with nuclear reactions on short-lived isotopes, making a contribution crucial for an improved understanding of device performance.

With only very small samples required, DANCE has made it feasible to acquire adequate data on short-lived radioactive nuclei and rare nuclei. Reactions on these rare species are of interest beyond the nuclear-weapon community because they also occur in the interior of stars. In fact, there is now underway at LANSCE an exciting project to study neutron capture reactions that will help explain the dynamics of red giant stars and their synthesis of the heavy elements through slow neutron capture (see the sidebar “Star Dust and the Secrets of Heavy-Element Production” on page 70).

FIGARO: Mapping the Energy Dependence of Neutron Emission

FIGARO (Fast-Neutron-Induced Gamma-Ray Observer) is an array of 20 neutron detectors and two or three gamma-ray detectors (Figure 11), all of which look at a sample bombarded with fast neutrons (0.1–200 MeV) at the WNR neutron source. The gamma-ray detectors are rather close (15 centimeters) to the sample, but the neutron detectors are set back 1 to 2 meters from the sample in order to determine the outgoing neutron energy by time of flight from the sample. Two types of samples are used: active samples, such as fission chambers that produce a signal when

a nuclear interaction has taken place, and passive samples, which do not produce any signal. For the latter, gamma rays emitted in the reaction and detected by the gamma-ray detectors indicate the occurrence of the reaction. We need one or the other of these signals to measure the time of flight of the incident neutron from the source to the sample to deduce the incident-neutron energy of the event. We need the same signal as a “start” signal for time of flight of the neutrons emitted in the reaction from the sample to the neutron detectors. This latter time of flight gives the energy of the outgoing neutron. We call this setup a “double time-of-flight experiment,” which has been attempted at other laboratories but is now much easier to accomplish because of the intensity and pulse structure of the WNR neutron source. With this capability, we are able to map out the dependence of the neutron emission spectrum as a function of incident-neutron energy, all in one experimental run.

The importance of these neutron emission spectra is clear: Neutrons are the vector for nuclear chain reactions in a nuclear detonation. That is, when a neutron-induced fission takes place, more neutrons are emitted, and these can then induce further fissions. It is well known that both the number and energy spectrum of the emitted neutrons depend on the energy of the neutron inducing the fission. A model developed at Los Alamos (referred to as “the Los Alamos model”) for this spectrum is well known and used worldwide. Although the model has been tested several times at specific energies, it still needs to be validated for the whole range of incident-neutron energies for which it was originally intended (incident energies less than 20 MeV) and for extensions to higher incident energies. FIGARO enables comprehensive studies of these fission properties.

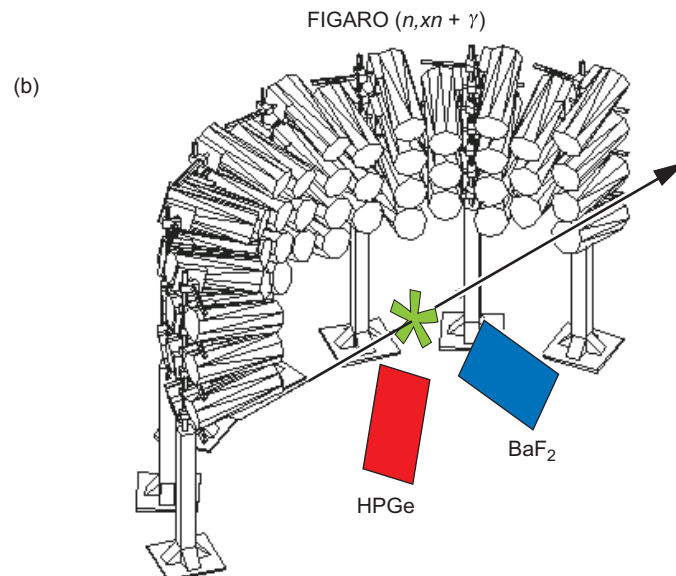


Figure 11. FIGARO

FIGARO, the Fast-Neutron-Induced Gamma Ray Observer at the WNR, is designed to measure neutron-induced reactions that result in the emission of neutrons and gamma rays. (a) The photograph shows the liquid scintillation neutron detectors, the fission chamber, and the location of the neutron beam. (b) The diagram shows a carefully collimated beam hitting the sample, which can be a fission chamber containing fissile material. The energies of the incident neutrons are determined by time of flight from the neutron source to the sample. Similarly, the energies of the fission neutrons are measured by time of flight from the sample to the array of neutron detectors (currently, there are 20 detectors) located 1 to 2 m from the sample.

The other application of FIGARO is to neutron emission in reactions on nonfissile nuclei such as structural materials. In many tests of nuclear weapons, the neutron spectrum emitted from the device was measured, and here, of course, the neutrons needed to penetrate through structural materials. These interactions need to be included in the calculations in order to relate the measured spectrum to that inside the device.

First Complete Data for Energy Spectrum of Uranium Fission Neutrons.

Together with scientists from the Commissariat à l'Énergie Atomique (CEA) at Bruyères-le-Châtel in France, we are using the FIGARO array of neutron detectors to measure the fission-neutron energy spectrum and the average neutron multiplicity for neutron-induced fission. Our first experiments were on uranium-238 and -235 for incident-neutron energies from 1 to 200 MeV. The results from 1 to 20 MeV are important for weapon applications, whereas those for higher energies are relevant to accelerator-driven systems or for irradiation facilities such as the Materials Test Station (MTS) to test the radiation effects in materials for the Advanced Fuel Cycle Initiative (AFCI)—see the article “The Role of LANSCE in the Nuclear Energy Future” on page 124. Measurements in progress are on neptunium-237. It is staggering that, to date, there are only very sparse data for the prompt-fission neutron energy spectrum of plutonium (a more difficult sample) for incident-neutron energies above a few million-electron volts. Such a measurement is urgently needed and will be carried out at FIGARO in the near future.

The average energy of the fission neutrons determined in this way shows the general trend and an essential physics feature (Figure 12). For uranium-238, for example, one

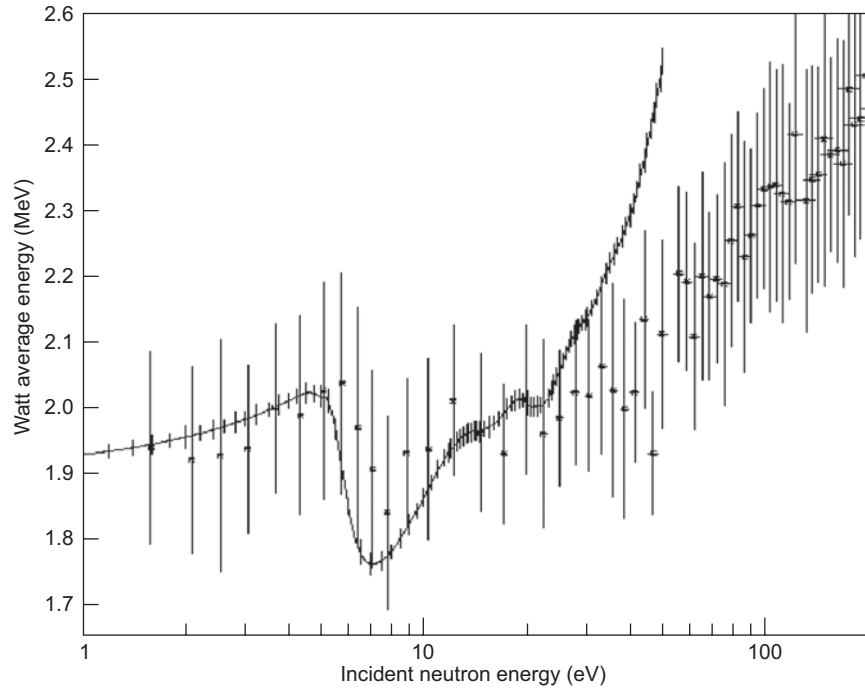


Figure 12. Average Energy of Fission Neutrons from Uranium-238
The average energy of fission neutrons from uranium-238 bombarded with neutrons was measured by FIGARO in the incident-neutron energy range of 1 to 200 MeV. Note the inflexion of the data and the model (solid curve) near 7 MeV, the energy at which “second-chance” fission begins.

sees a gradual increase in the average energy with incident-neutron energy except near 6 MeV, at which value a second fission channel opens up. That channel is the reaction $^{238}\text{U}(n, n + f)$ channel, or “second-chance fission,” in which a neutron is emitted before fission and carries off a significant amount of binding energy. These second-chance fission neutrons contribute to the chain reaction and thus can impact weapon performance. The energy distribution of the fission neutrons needs to be included in the calculations, as these neutrons are responsible for continuing the chain reaction. Our data validated very nicely the Los Alamos model in the region of importance to weapons, that is, below an incident-neutron energy of 20 MeV. At higher energies, which might be of importance to accelerator-driven fission systems, the Los

Alamos approach as implemented by our CEA colleagues does not do so well at predicting the average neutron energy.

Although the average number of neutrons emitted in each fission event is rather well known for very low incident-neutron energies, a complete mapping including the angular distribution of these neutrons has never been done, and the average number of emitted neutrons is not known for fission induced by high-energy neutrons. We have completed the multiplicity measurement, which showed interesting differences between the uranium-235 and -238 target nuclei (Ethvignot et al. 2005). Angular distribution information requires longer experimental runs, which have been carried out, and the data are now being analyzed. All of these data pertain to the basic understanding of the

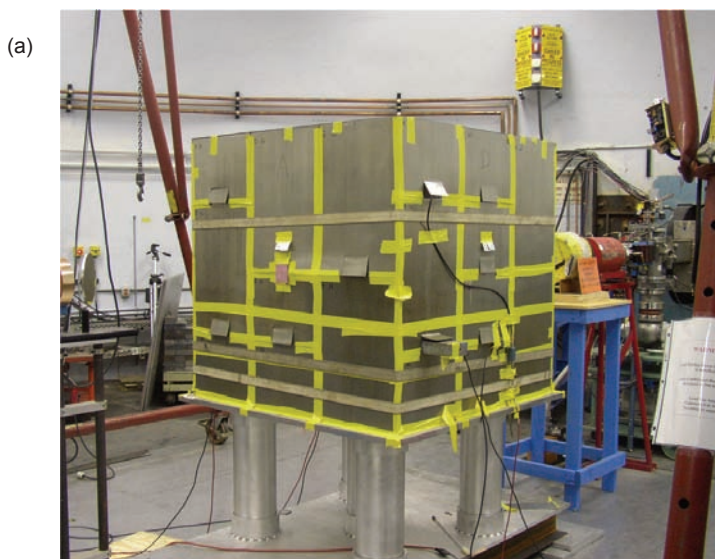
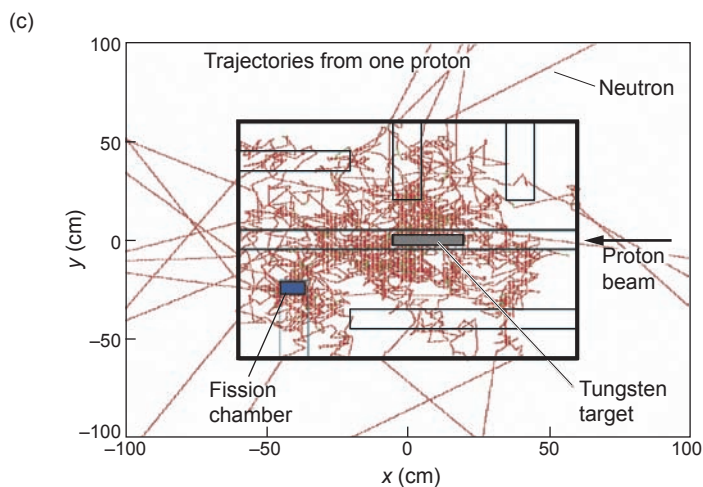
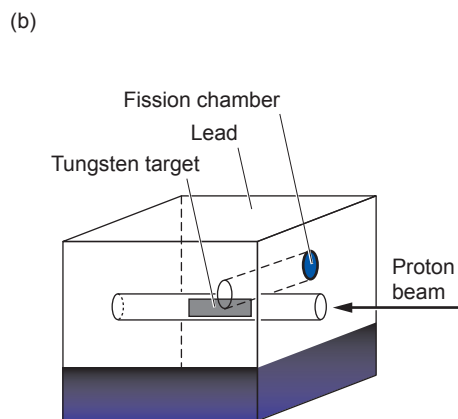


Figure 13. The LSDS

(a) The LSDS, the Lead Slowing-Down Spectrometer, is composed of 36 lead blocks, which are assembled into a cube 1.2 m on a side. (b) A pulsed proton beam from the LANSCE Proton Storage Ring hits a tungsten target in the center of the cube to produce a large number of neutrons, which then slow down by scattering from the lead nuclei. (c) The red trajectories, calculated with a Monte Carlo code, are an example of neutron trajectories resulting from one proton incident on the tungsten. A pulse of 1.5×10^{11} protons produces trajectories that fill the entire cube. Detectors are placed inside the channels, and reactions are recorded as a function of time after the proton pulse. The neutron energy inducing a reaction is directly related to this time interval.



fission process, which is still a very active area of research worldwide. Open questions include the following: (1) How does a nucleus undergo fission when it is highly excited? (2) For excited nuclei, how many neutrons are emitted before fission occurs? (3) When an energetic neutron interacts with a nucleus, does the system emit neutrons before coming to a state in thermal equilibrium, which then fissions? (4) What are the channels through which fission

occurs in terms of the time-dependent elongation, deformation, mass asymmetry, and other semiclassical shape parameters?

FIGARO is still in the developmental stage, and we plan to add additional detectors to increase the efficiency of measuring coincidences of fission events and fission neutrons, as well as coincidences of incident neutrons and emitted gamma rays. The latter are important for fundamental studies of the excited states of nuclei.

LSDS: Studying Fission Reactions on Ultrasmall Samples

The LSDS (Figure 13) is a unique instrument consisting of 36 very large lead bricks assembled into a 20-ton cube, 1.2 meters on a side, with a tungsten cylinder in the center and a path for the incident protons to hit the tungsten directly. Bunched and pulsed 800-MeV protons from the Proton Storage Ring (PSR) at LANSCE

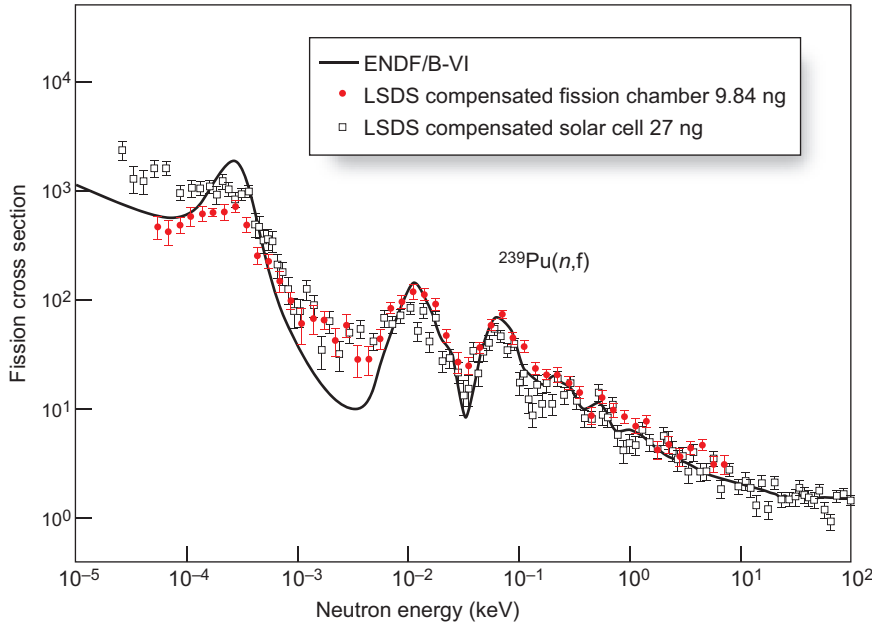


Figure 14. Measuring the Plutonium Fission Cross Section from a 9.87-Nanogram Sample at the LSDS

The measured fission cross sections of plutonium-239 from a 9.87-ng sample of plutonium-239 are in good agreement with the evaluated data, which are based on many other measurements and which are broadened here by the experimental energy resolution of the LSDS. These results demonstrate the capability of the LSDS for measuring the fission cross section of the isomeric state of uranium-235.

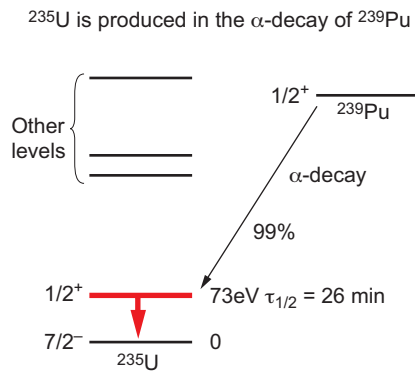


Figure 15. Energy Levels for the α -Decay of Plutonium-239

Uranium-235m is produced in the decay of plutonium-239. The challenge is to separate a few nanograms of uranium from grams of plutonium by chemical means in a short time, before the isomer decays. The half-life of uranium-235m is only 26 min.

interact with the tungsten to produce spallation neutrons. Neutrons scatter in the lead and lose energy slowly, hence “slowing-down” in the name of this spectrometer. Samples and detectors are placed in channels in the lead assembly. We measure reaction rates, especially of neutron-induced fission, as a function of time and therefore of neutron energy—hence the term “spectrometer.” The advantage of this approach is that the neutron flux on a sample is about 1000 times higher than in traditional beam-target experiments (refer back to Figure 2).

Whereas GEANIE and FIGARO require samples of several grams, and DANCE requires samples of a milligram or so, the LSDS can use samples in the nanogram (1 billionth of a gram) range. Measurements of very short-lived isotopes must be done with such small samples because of the intrinsic radioactivity and because often only very small amounts of the materials are available. Consequently, the incident-neutron flux must be much higher to get a measurable signal.

Addressing the Isomer Problem.

An uncertainty regarding the fission performance of a nuclear weapon is the fission of a 26-minute excited state of the uranium-235 nucleus, which can be produced in intense neutron fluxes. Recent theory suggests that the fission rate for this isomeric state of uranium-235 might be up to a factor of 2 less than that for the ground-state (unexcited) nucleus if the incident-neutron energies are low (below 200 keV). In contrast, older theories predicted that the cross section of the isomer might be much higher than that of the ground state. Despite the importance of knowing the relative fission cross sections in this energy range, an experimental measurement has never been made because it is very difficult to make enough of the isomer and complete the measurement in the short time that this state survives before decaying away.

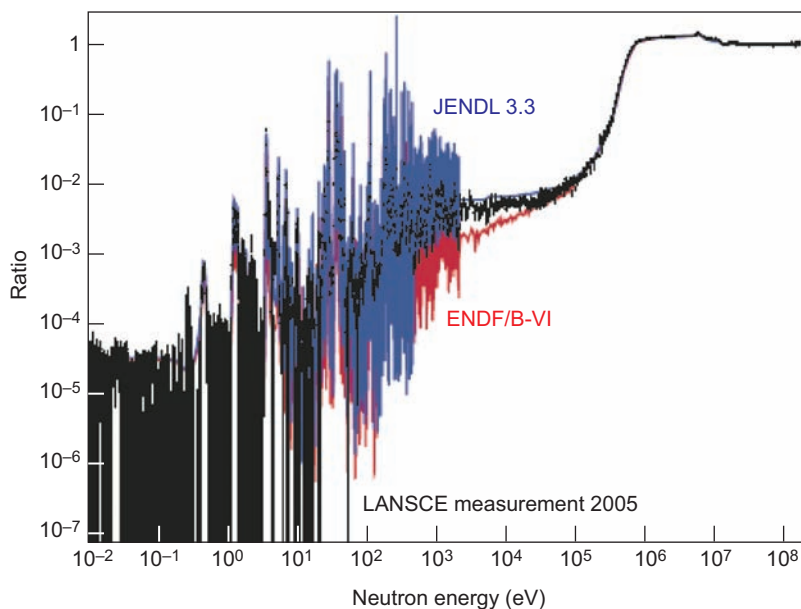


Figure 16. Ratio of Neptunium-237 to Uranium-235 Fission Cross Sections
Note the discrepancy between the data and the values from the ENDF/B-VI file (accepted for use in the United States) in the range from 3000 to 100,000 eV. The ENDF/B-VI file is being updated to correct inaccuracies in this energy range. The JENDL 3.3 values are from the Japanese evaluated data library.

In the past few years, we and our colleagues from the CEA in France (the CEA supplied the lead assembly), the Chemistry Division at Los Alamos, and the Rensselaer Polytechnic Institute have developed the LSDS to measure the fission cross section of the isomeric state of uranium-235 and of other nuclides or isomers that can only be obtained in ultrasmall quantities. This measurement will not only provide data for applications but will be a unique probe into the fission physics of excited states of nuclei.

We have tested the assembly by measuring the well-known fission cross section for plutonium-239 on a very small sample, weighing only 9.8 nanograms (Figure 14). The results were accurate enough to enable plans for measuring the fission cross section of the isomeric state of uranium-235.

This short-lived, excited state of uranium-235 can be isolated by chemical techniques developed in the Los

Alamos Chemistry Division. The process involves taking a sample of plutonium-239 and letting it decay, which it does by alpha-particle emission. Nearly all the decays (99%) populate the isomeric state of uranium-235 (Figure 15). The half-lives of the plutonium-239 parent and the isomer tell us that the equilibrium concentration of the isomer in the plutonium is only 2 parts in a billion. Thus, extreme demands are placed on the separation chemistry, which should exceed 1 part in 10^{10} to enable a clean experiment on the isomer.

For the experiment on the isomer, we will place the sample in the LSDS and measure the fission rate as a function of time to get the energy dependence of the fission cross section, and we will continue to measure that rate as the isomer decays to the ground state of uranium-235, where the cross section is well known. In this sense, the experiment is “self-normalizing,” and we will report the ratio of the

isomer-to-ground-state fission cross sections.

Many other reactions can be investigated with the LSDS, including fission cross sections and reactions that produce an alpha particle. The latter are especially interesting for understanding the formation of the elements in stars and for refining nuclear reaction models in ranges that desperately need more experimental data.

Fission

Improved accuracy for fission cross sections is another significant activity at LANSCE. An advanced fission chamber is being developed to identify the individual fission products, their energies, and their emission angles relative to the incident-neutron direction.

Our present measurements are with a conventional chamber, but with advanced electronics to improve on the techniques used for many years at Los Alamos. An example of the data is given in Figure 16 for the fission cross section of neptunium-237, measured relative to the standard uranium-235 over the full range of incident-neutron energy from thermal energies (0.025 electron volt) to 200 MeV. This work is the beginning of a major program at LANSCE to restart precision measurements of fission and to make significant improvements in the accuracy now required by the weapons program.

New and Unusual Nuclei

Finally, the new Isotope Production Facility (IPF) at LANSCE and the Chemistry Division at Los Alamos are equipped to fabricate the radioactive nuclear targets that can reasonably be measured (see the article “Accelerator Radioisotopes Save Lives” on page 112). These

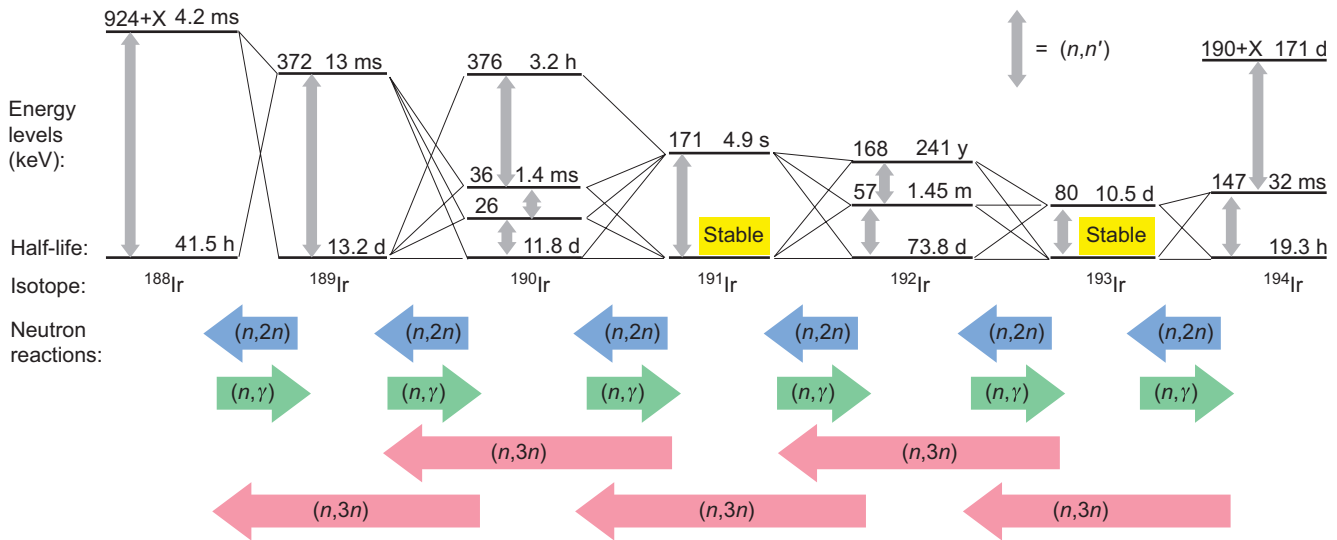


Figure 17. Realistic Network of Neutron-Induced Reactions on Iridium

This network of neutron-induced reactions is more realistic than the one shown in Figure 1. Here, the major isomeric (relatively long-lived) states are also shown as they need to be included in a comprehensive calculation. The energy of some isomeric levels is not known exactly—hence, the “+X” for two of the levels. Reactions on states living more than tens of days can, in principle, be studied with the instruments at LANSCE. The reaction rates on shorter-lived states must be calculated with the best physics models available.

isotopes are appropriate for experiments in our most-sensitive instruments, DANCE and the LSDS. Because the IPF is located on the same site as the nuclear data experiments, transportation of radioisotopes is easy and fast, and nuclei with rather short half-lives can be studied. Although this facility is dedicated to the production of medical radioisotopes, usable quantities of other radioactive isotopes may be produced at the IPF using its 100-MeV, 250-microampere proton beam and the facilities for processing irradiated targets in the Chemistry Division. We are presently working to prepare radioactive samples of arsenic-73 and gadolinium-153 that cause minimal disruption to the medical-radioisotope production program. These isotopes are important in assessing radiochemical diagnostic data from past nuclear tests.

Table II. Institutions in the LANSCE Nuclear Data Program

Instrument/Project	Institutions
GEANIE	Los Alamos National Laboratory (LANL), Lawrence Livermore National Laboratory (LLNL), Idaho National Laboratory (INL), Oak Ridge National Laboratory (ORNL), Commissariat à l'Énergie Atomique (CEA, France), and North Carolina State University (NC State)
FIGARO	LANL and CEA
DANCE	LANL, LLNL, ORNL, INL, Colorado School of Mines, NC State, and FZK Karlsruhe (Germany)
LSDS	LANL, LLNL, CEA, and Rensselaer Polytechnic Institute
Fission	LANL, Institute for Reference Materials and Measurements (European Union), LLNL, and INL
Others	Ohio University, Massachusetts Institute of Technology, University of Kentucky, Kyushu University (Japan), and Harvard University

The Importance of Nuclear Physics

The capabilities described above are used to make direct measurements (or nearly direct) of the cross sections of importance to understanding nuclear-weapon performance. A more detailed look at the processes shows, however, that not all the reactions of possible importance can be investigated even with the significant advances in the LANSCE neutron sources and the associated instruments. Figure 1 above is a simplified picture of the reactions. Other isomers make the situation more complicated as shown in Figure 17, where 98 reactions are indicated (the thin lines and the arrows go in both directions). It will never be possible to measure all these reactions. Some are undoubtedly unimportant, but others may be extremely important. With the physics insights that come from the measurements that we can make, nuclear reaction models are put on a much firmer footing so that their predictions can assess the importance and magnitude of each of these reactions. With the new LANSCE capabilities, we can pin down the physics and the model parameters (optical model, nuclear-level densities, gamma-ray strength functions, fission physics, and others) and extend our present knowledge into reactions on unstable nuclides and isomeric nuclear states.

LANSCE—The Human Element

LANSCE has a dedicated staff of first-rate nuclear researchers who have developed the advanced neutron sources and innovative detectors described here in collaboration with colleagues from the Chemistry Division at Los Alamos and with coworkers from the U.S. and foreign laboratories and universities listed

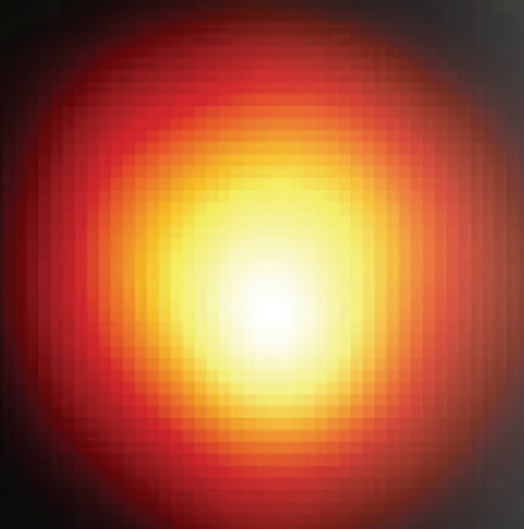
in Table II. This array of human and instrumental assets produces crucial experimental data for use by nuclear theorists in the Applied Physics and Theoretical Physics Divisions at Los Alamos and the wider national and international nuclear physics community to deliver the most-essential nuclear data for making reliable predictions of weapon performance. Nuclear theory is an integral part of this effort because many of the relevant radioactive species have half-lives that are too short to measure in the laboratory even with our advanced instrumentation and the intense neutron sources at LANSCE. The continuing close collaboration among experimentalists, theorists, data evaluators, and applied scientists is essential to the significant advances made and expected in the interpretation of past nuclear-weapon-test data and to the analysis and prediction of weapon performance in the absence of nuclear tests.

Conclusions

Nuclear data measurements for the nuclear weapons program are urgently needed to interpret nuclear test data for improving the calculational models so that they are applicable in a credible way to (1) quantify margins and uncertainties, (2) calculate effects caused by aging of materials and component replacement, and (3) investigate new designs, especially those that might be pursued by a rogue nation or terrorist organization. A steady investment in new types of sensitive detectors over the past few years has made possible relevant experimental measurements that were heretofore impossible. A bright future, with more innovative instruments, lies ahead. ■

Further Reading

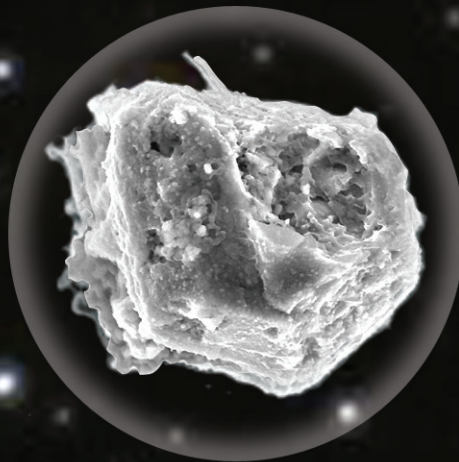
- Bernstein, L. A., J. A. Becker, P. E. Garrett, W. Younes, D. P. McNabb, D. E. Archer et al. 2002. $^{239}\text{Pu}(n, 2n)^{238}\text{Pu}$ Cross Section Deduced Using a Combination of Experiment and Theory. *Phys. Rev. C* **65** (2): 021601.
- Ethvignot, T., M. Devlin, R. Drosch, T. Granier, R. C. Haight, B. Morillon et al. 2003. Prompt-Fission-Neutron Average Energy for $^{238}\text{U}(n, f)$ from Threshold to 200 MeV. *Phys. Lett. B* **575** (3–4): 221.
- Ethvignot, T., M. Devlin, H. Duarte, T. Granier, R. C. Haight, B. Morillon et al. 2005. Neutron Multiplicity in the Fission of ^{238}U and ^{235}U with Neutrons up to 200 MeV. *Phys. Rev. Lett.* **94** (5): 052701.
- Heil, M., R. Reifarth, M. M. Fowler, R. C. Haight, F. Käppeler, R. S. Rundberg et al. 2001. A 4π BaF₂ Detector for (n, γ) Cross-Section Measurements at a Spallation Neutron Source. *Nucl. Instrum. Methods Phys. Res. A* **459** (1–2): 229.
- Rochman, D., R. C. Haight, J. M. O'Donnell, A. Michaudon, S. A. Wender, D. J. Vieira et al. 2005. Characteristics of a Lead Slowing-Down Spectrometer Coupled to the LANSCE Accelerator. *Nucl. Instrum. Methods Phys. Res. A* **550** (1–2): 397.
- Rochman, D., R. C. Haight, J. M. O'Donnell, M. Devlin, T. Ethvignot, and T. Granier. 2004. Neutron-Induced Reaction Studies at FIGARO Using a Spallation Source. *Nucl. Instrum. Methods Phys. Res. A* **523** (1–2): 102.
- Staples, P., and K. Morley. 1998. Neutron-Induced Fission Cross-Section Ratios for ^{239}Pu , ^{240}Pu , ^{242}Pu , and ^{244}Pu Relative to ^{235}U from 0.5 to 400 MeV. *Nucl. Sci. Eng.* **129**: 149.



Stardust and the Secrets of Heavy-Element Production

Rene Reifarth

As they come down from the skies, meteorites bring with them stardust—tiny diamond-like grains, each formed from the material in the interior of a single Red Giant star. Those grains contain heavy elements that were synthesized through the slow neutron-capture process, known as the s-process. The relative abundances of the elements hold the secret of how they were made. Just as new neutron-capture measurements of rare and short-lived elements are needed to benchmark weapon simulations against past nuclear test results, similar measurements are needed to infer the stellar conditions that produced the heavy elements in stardust. DANCE, the unique spectrometer at the Los Alamos Neutron Science Center for measuring neutron capture reactions, is now providing the data for both.



Neutron Capture Physics for Nuclear Weapons and Nuclear Astrophysics

Francis X. Timmes

It might seem odd for weapons scientists to be looking to the stars for information and inspiration. However, stars have long been of interest to Los Alamos researchers because there is a tremendous overlap between the physical processes governing stellar systems and those in nuclear-weapon systems. In fact, many of the scientists currently engaged in theoretical modeling of weapon performance and effects have developed the relevant knowledge and skill sets by working on problems in astrophysics.

Today cutting-edge studies at the Los Alamos Neutron Science Center (LANSCE) and the Theoretical Division are exploiting parallels between the two fields. Nuclear astrophysics, which is largely concerned with the origin of the elements, is being paced by LANSCE experiments that delve into the neutron capture physics of nuclear weapons. The reason is that both the production of heavy elements in stars and the transmutation of heavy elements in nuclear explosions occur through neutron capture reactions. Further, just as weapons scientists infer details of weapon performance from the heavy-element abundances found in the debris from past nuclear tests, astrophysicists hope to infer the conditions inside Red Giant stars from the heavy-element abundances in stellar “debris”—micrometer-sized dustlike grains brought to Earth by meteorites. Provided one has measured the neutron capture processes involved in making the heavy elements, the abundances of those elements in the grains lead directly to predictions of the temperatures at which they were made, the neutron densities, and the abundances of the elements that donate neutrons. The temperatures and neutron donor abundances, in turn, reveal the extent of hydrodynamic mixing between the different layers of the Giant stars. For example, the isotope samarium-151, discussed in this article, is a sensitive barometer of the thermodynamics and hydrodynamics in Giant stars.

Neutron capture measurements at the Detector for Advanced Neutron Capture Experiments (DANCE) at LANSCE are the start of a closed-loop effort to provide verified and validated multidimensional hydrodynamic models of convection and other mixing in the presence of thermonuclear reactions. Neutron capture data from DANCE are fed into stellar models created by the Theoretical Division’s Astrophysics Group. The models are then checked against measurements of isotopic ratios in the “debris” of a Red Giant by external collaborators. Los Alamos leads work in modeling the slow neutron-capture process of nucleosynthesis (known as the s-process) in Giant stars, which has a direct connection to the work involved in understanding the neutron capture physics required to predict the behavior of nuclear weapons.

Since the middle of the 19th century, the spectral analysis of starlight was used to investigate the elemental composition of stars. Most stars have a very similar composition to our sun and lie along the so-called main sequence in the Hertzsprung-Russel diagram, which shows the stellar luminosity versus surface temperature. There is, however, a small but distinctive group of stars off the main sequence that is characterized by red light (which means relatively cool surface temperature) and enormous brightness (luminosity). The diameter of those Red Giant stars is about 50 times bigger than the diameter of our sun. The 1952 discovery of atomic lines from the heavy element technetium in the spectra of Red Giants was the long-desired smoking gun, revealing the site of heavy-element production. The half-lives of all technetium isotopes are much shorter than the billion-year time scales of stellar evolution, which means that the technetium—and therefore most heavy elements—are produced inside the Red Giants. Shortly after this breakthrough discovery, an overall picture of the synthesis of the elements was developed that took into account all available scientific knowledge at that time. The main aspects of this picture are still valid nowadays.

According to our current understanding, only the very light elements (hydrogen, helium, and lithium) were produced during the big bang, the initial explosion from which our universe evolved. Those elements condensed into the first generation of stars, and the most massive ones (more than a hundred times the mass of our sun) evolved on a time scale of millions of years through different burning stages, producing heavier and heavier elements up to iron, the most stable element in the periodic table. After forming an iron core, which cannot support further fusion burning of charged particles, these massive

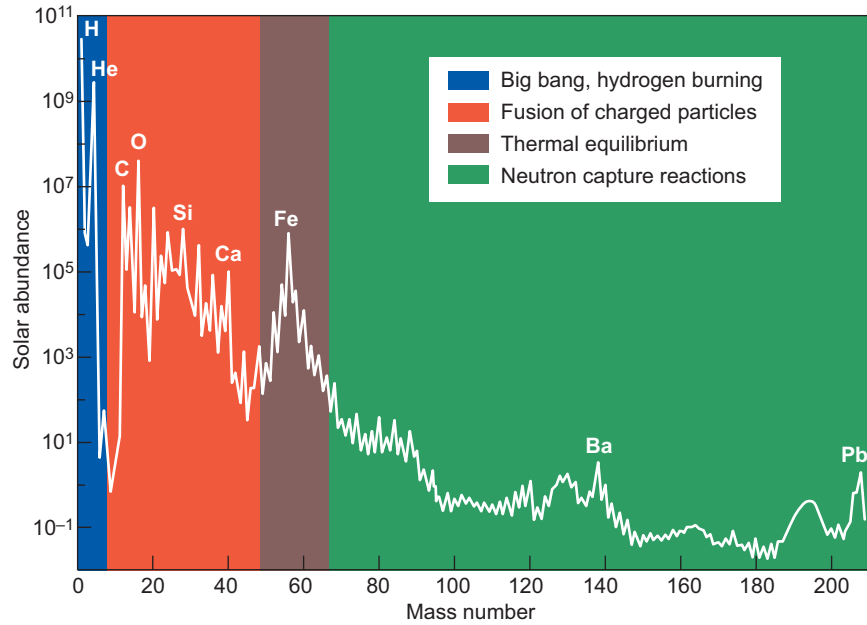


Figure 1. Solar Abundance Distribution and Production Mechanisms
The colored backgrounds in this graph of solar abundances vs mass number indicate the most important mechanisms that produced the elements. Blue and red indicate that most of the elements up to titanium are produced by the fusion of charged particles during the different burning stages of stellar evolution—hydrogen burning (the fusion of hydrogen to helium), helium burning (the fusion of helium to carbon), and so on. At very high temperature and pressure conditions, as during the various stages of compression preceding supernova explosions, production and destruction reactions occur in equilibrium. The very stable iron group is mainly produced in this equilibrium context, hence its high abundance. For elements beyond iron, the enormous Coulomb barrier all but prevents the fusion of charged particles to make heavier elements. Instead, the elements heavier than iron are mainly produced during nuclear processes induced by neutron capture reactions.

stars suddenly collapse under their own weight and then blow off their outer layers in a supernova explosion. During that explosion, heavy elements between iron and uranium were produced in the expanding envelope and blown off into the interstellar medium. The ejected material then served as seed material for new generations of stars, such as, our sun. Only much later did the low-mass stars, which were undergoing very slow hydrogen burning over billions of years, finally evolve to the Red Giant phase and contribute to heavy-element production.

Figure 1 shows a summary of the origin of the elements from the isotopic, or nuclear physics, point of view, which means it focuses on the

nuclear processes that produced the elements and does not contain information about the times when those isotopes were produced. Almost all the elements heavier than iron are produced through neutron-induced processes. There are two major processes, the rapid neutron-capture process (r-process), which takes place in explosive scenarios such as a supernova explosion, and the slow neutron-capture process (s-process), which can be found in Red Giants. Solving the secrets of the s-process through new radiochemical measurements of stardust and new nuclear-data measurements at the Los Alamos Neutron Science Center (LANSCE) is the subject of this article.

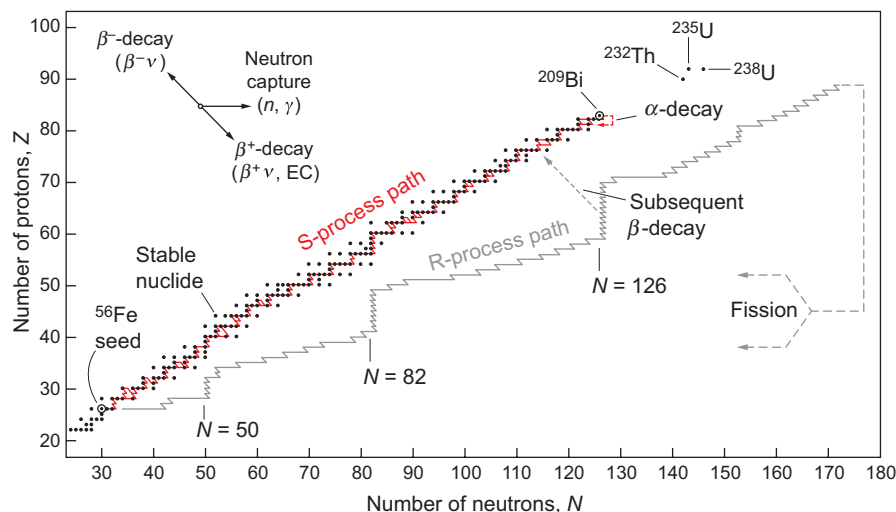


Figure 2. S-Process and R-Process Synthesis of the Heavy Elements
 The s- and r-processes start with the iron peak nuclei as seeds. The s-process path follows the nuclear valley of stability until it terminates in the lead-bismuth region. The r-process drives the nuclear matter far to the neutron-rich side of the stability line and upwards until beta-delayed fission and neutron-induced fission occur and recycle the material back to smaller mass numbers. Only a few isotopes on the proton-rich side of the valley of stability get significant contributions from other processes. (This illustration is reproduced from *Cauldrons in the Cosmos*, C. E. Rolfs and W. S. Rodney, 19888, courtesy of The University of Chicago Press.)

Basics of the S-Process

Figure 2 shows the pathways for making the heavy elements through the s- and r-processes. The horizontal axis is the number of neutrons in an isotope, and the vertical axis is the number of protons. About half of the element abundances from iron to the lead-bismuth group are produced by the s-process, and the other half by the r-process. The two most-important reactions occurring during the s-process are neutron capture (right arrow in Figure 2), in which the mass of the nucleus increases by one unit while the charge stays constant, and beta decay (diagonal arrows in Figure 2), in which the charge of the nucleus increases or decreases by one unit and the mass stays constant. Free neutrons must be available for neutron capture to occur, whereas an unstable nucleus undergoes beta decay spontaneously, emitting an electron and an antineu-

trino as a neutron inside the nucleus changes into a proton (or a positron and neutrino as a proton changes into a neutron).

The s-process starts with an iron seed exposed to free neutrons, and it builds up the elements following the neutron-rich side of the nuclear valley of stability, that is, the region to the right of the stable isotopes in Figure 2. Following neutron capture, the new unstable isotope will almost always beta-decay back to the valley of stability before it can capture another neutron. In contrast, during the r-process, the neutron flux is so high and the neutron capture times so short that a nucleus will almost always capture several neutrons before it undergoes a beta decay. Thus, the r-process follows a path that is shifted farther toward the neutron-rich isotopes. The beta decay half-lives are much shorter for isotopes very rich in neutrons, so that shortly after the neutron source terminates, the products of the r-pro-

cess will beta-decay back to the valley of stability.

The purely phenomenological, classical approach to describing the s-process was formulated even before a detailed understanding of the development of stars was available (Burbidge et al. 1957, Seeger et al. 1965). It assumes that iron, seeded randomly inside stars, is irradiated by neutrons through an exponential distribution of neutron exposure times. This classical approach also assumes a constant neutron density and temperature.

It turns out that the heavy-element abundances in the solar system can be explained only by assuming two different parameter sets for the s-process—a weak component that explains the s-process abundances between iron and strontium and a main component that accounts for the s-process abundances between strontium and lead. The classical model became a useful tool not only for reproducing the s-process abundances, but also for characterizing in an empirical way the physical conditions during the s-process. Meanwhile, the two components of the classical approach were assigned to different stellar scenarios. The weak component was attributed to helium burning in the core of massive stars (10 to 25 solar masses), whereas the main component was attributed to helium burning in a shell around the carbon-oxygen core of low-mass Red Giants (1 to 5 times the mass of the sun)—refer to Figure 3.

Inferring Stellar Conditions from S-Process Abundances

The exact pathway of the s-process depends on the conditions in the star. Starting at the very abundant iron group, all elements up to bismuth could, in principle, be produced by a sequence of reactions in which each neutron capture produces an unstable isotope that quickly decays to the next

higher element through beta decay and then waits for the next neutron capture. If, however, conditions in the star make the rates for neutron capture comparable to the rate of beta decay by a particular isotope, then the s-process path would branch at that isotope with some fraction of that isotope transforming via neutron capture, while another fraction transforms through beta decay. The branching ratio, or relative likelihood, for the different reactions depends on the physical conditions in the interior of the star—temperature, neutron density, and electron density. At higher neutron densities with all other conditions equal, more nuclei of a given isotope would capture a neutron before having the chance to beta-decay than at low neutron densities. Thus, the branching ratios deduced from the isotopic ratios observed in stellar material could provide the tools to effectively constrain modern models of the stars where the nucleosynthesis occurs, provided one knows the fundamental rates, or cross sections, for neutron capture and beta decay.

Evidence of the S-Process in Stardust

At present, the s-process path for the samarium-europium-gadolinium (Sm-Eu-Gd) region shown in Figure 4 is being actively explored. This region is particularly exciting because observational data on the stellar abundances of those isotopes have recently become available from stardust, extremely small diamond-like grains that can be found in meteorites on the earth's surface and are known to be formed in the outer regions of Red Giant stars. Under certain circumstances, such grains survive their long journey through interstellar space and participate in the formation of new stars and their planets. This is the

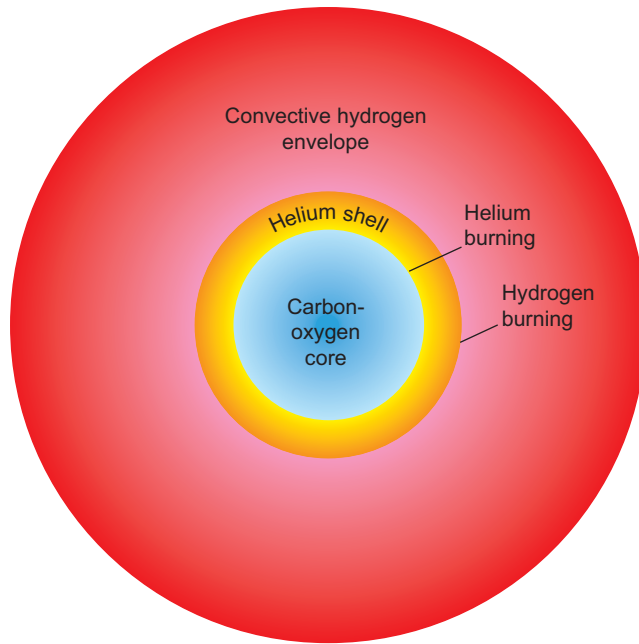


Figure 3. Site of the S-Process in Red Giant Stars

The figure shows a cross section of a Red Giant with its quiescent carbon-oxygen core, a shell of helium surrounding the core in which helium burning creates carbon and oxygen, and an outer envelope in which hydrogen burning creates helium. The helium shell is much thinner than shown in this schematic, and the convective envelope, consisting mainly of hydrogen, is much thicker. In general, the inner shells of stars consist of the burning products of the outer shells.

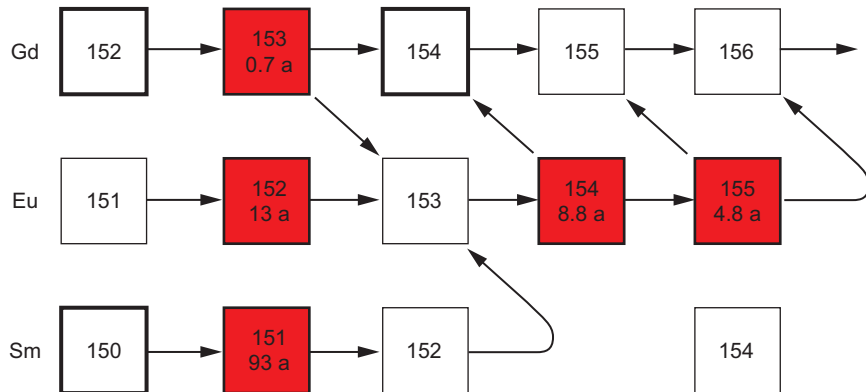


Figure 4. The S-Process Path in the Sm-Eu-Gd Region

The s-process path in the Sm-Eu-Gd region is shown by arrows. This path has branch points at the unstable isotopes (red squares), which have half-lives given in years. All the white squares are stable isotopes. The heavy outlines around samarium-150 and gadolinium-152 and -154 indicate that these stable isotopes are produced only in the s-process. During the r-process, stable neutron-rich isobars (nuclei with the same atomic mass but different atomic number) are made first and halt the beta-decay pathway that would otherwise produce them. Thus, for example, formation of samarium-154 during the r-process prevents formation of gadolinium-154.

reason why we can find them nowadays on earth. Because the grains are extremely small—only a few micrometers in diameter—it was necessary to develop greatly improved experimental equipment to reach the sensitivity needed for isotopic-abundance measurements of several isotopes from a single grain (see Figure 5). Because of these new developments, it is now possible to extract information about all stable isotopes in the Sm-Eu-Gd region from a single grain—hence, from a single star.

At the same time, at LANSCE we have the capability to measure the neutron-capture cross sections of all isotopes on the s-process path in that region, including the radioactive isotopes. Together, the isotopic ratios and neutron-capture cross sections from this region should enable us to constrain current stellar models of the main component of the s-process.

Current Stellar Models of the Main Component of the S-Process

Past precision measurements on the stable isotopes have revealed that the very sensitive branching regions, as for example in Figure 4, cannot be described with the simple classical s-process model but require the complicated physics of thermally pulsing low-mass Asymptotic Giant Branch (AGB) stars, also known as Giants. The mechanism for the s-process involves a series of helium shell flashes and the alternating presence of two neutron sources, as shown in Figure 6. During helium burning, three helium nuclei, called alpha particles, fuse into carbon via the famous triple-alpha process. The AGB stars are not heavy enough to ignite helium burning on a continual basis. Most of the time, these stars burn only hydrogen into helium, converting the inner parts of the envelope into the

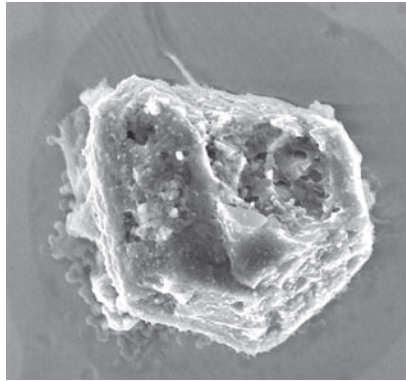


Figure 5. Single Grains from Giant Stars

The scanning electron micrograph is of a silicon-carbon (SiC) grain from the Murchison meteorite, named after the town in Australia where fragments of the meteorite fell in 1969. The grain is approximately 2 micrometers in diameter. Most presolar SiC is believed to have formed in Asymptotic Giant Branch stars (see Figure 6), which are very old Red Giant stars rich in carbon, but some grains have isotopic signatures indicating other stellar sources, such as supernovae and novae. Secondary ion-mass spectrometry is used to determine isotopic ratios in the grains. (This photo is courtesy of Larry R Nittler, Carnegie Institute of Washington, Washington, D.C.)

helium shell (the red layer converts into a yellow layer in Figure 6). But these quiescent phases are interrupted by flashes of helium burning in the helium shell around the core, which last only a few hundred years and convert helium shell material into a carbon and oxygen core (see the yellow region converting into a blue region in Figure 6). During these flashes, energy production of the star is significantly increased, and about 20 to 30 such flashes occur during the life of a Giant star.

The s-process occurs during both the helium flashes and the quiescent periods. Immediately after a helium flash, the convective mixing between the hydrogen and the helium layers introduces hydrogen and elements

such as carbon, neon, and iron into the helium layer. With the fresh supply of hydrogen, proton capture on the always abundant carbon-12 produces nitrogen-13, which beta-decays to carbon-13. Although the temperature is relatively low during this quiescent period, the carbon-13 will fuse with alpha particles and produce neutrons through the reaction $^{13}\text{C}(\alpha, n)^{16}\text{O}$. Now, the main ingredients needed for the s-process are present—free neutrons and an iron seed. The neutron flux, however, ends as soon as all the freshly produced carbon-13 is burnt (see the ends of the horizontal red bars in Figure 6), and the s-process comes to a halt. The heavy-element abundances produced during the quiescent phase are subsequently modified during the next helium flash (dark blue region in the helium shell in Figure 6), when higher temperatures cause marginal activation of the alpha particle reaction with neon, $^{22}\text{Ne}(\alpha, n)^{25}\text{Mg}$, and this new source of free neutrons drives the s-process farther. During and following the helium flash, those freshly produced s-process materials get swept up into the convective hydrogen envelope and are brought to the surface of the Giant star, where they can be seen with telescopes, as was the technetium mentioned above. Because these Giant stars are relatively light but huge, the material brought to the surface by convection can then be carried into the interstellar medium by stellar winds.

During the final stages of the AGB phase, strong stellar winds will blow the entire hydrogen envelope, which had been enriched with elements produced by the s-process, into the interstellar medium. This freshly produced material will not only form new generations of stars and planets, like our sun and earth, but it is imprinted in the micrometer-sized dust grains mentioned above. Such dust grains can be found in meteorites on earth, and their heavy-element abundances contain an

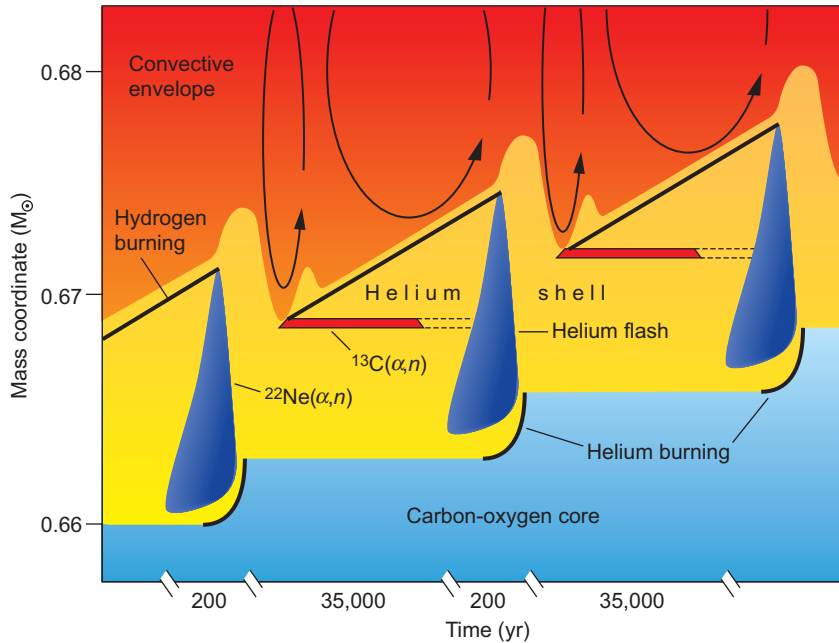


Figure 6. The S-Process during the AGB Phase

The breaks in the time axis illustrate the brevity of the helium shell flashes, only a few hundred years, compared with the duration of the quiescent phases, about 35,000 years. The mass coordinate (in solar masses, where 1 solar mass is the mass of our sun) indicates the extent of the thin helium shell, which is the site of the s-process. The $^{13}\text{C}(\alpha,n)^{16}\text{O}$ reaction is the dominant neutron source during the quiescent period, whereas during the convective helium shell flash, higher temperatures eventually activate the $^{22}\text{Ne}(\alpha,n)^{25}\text{Mg}$ reaction, the neutron source that is important for establishing the abundance patterns of the s-process branchings (Gallino et al. 1998).

almost undisturbed signature of the star in which they were formed. Those abundances, sometimes only a few thousand atoms, can now be revealed because of advancements in experimental techniques.

The Role of Neutron Capture Measurements

As isotopic abundances from the s-process are now observable in stellar grains, neutron capture measurements on the nuclei at the branch points of the s-process are the most-important missing experimental link to further improve our picture of the evolution of Giant stars and, hence, the history of the elements of which we and our world are made. In general, the main uncertainty

in predicting heavy-element abundances arises from uncertainties in the physics of mixing, whether in the long-lasting quiescent phases of Giant stars or the terminating supernova explosions. Data from neutron capture measurements, combined with information from stellar grains, can be used to constrain models of mixing in Giant stars. Fortunately, the required neutron-capture measurements can now be carried out with the Detector for Advanced Neutron Capture Experiments (DANCE) at LANSCE.

The DANCE Array. DANCE is designed as a high-efficiency, highly segmented 4π barium fluoride (BaF_2) detector for detecting the energies of gamma rays emitted by a nucleus following neutron capture. DANCE is located on the 20-meter neutron flight

path 14 (FP14) at the Lujan Neutron Scattering Center at LANSCE. For practical reasons, the detector modules do not really cover the entire solid angle. The design of the detector is such that a full 4π array would consist of 162 crystals of four different shapes, each shape covering the same solid angle—see Figure 7.

Two of the 162 crystals are left out in order to leave space for the neutron beam pipe. This combination of the strong neutron source at LANSCE and the high-efficiency gamma-ray detector DANCE allows us to measure neutron-capture cross sections of radioactive isotopes with half-lives as short as a few hundred days.

During the first year of experiments at DANCE, we measured the s-process branch point at the unstable isotope samarium-151, which has a half-life of 100 years (see Figure 4), as well as other stable isotopes important for nuclear astrophysics. An example is given in Figure 8. Stellar temperatures are on the order of 10^4 electron volts, or 10^8 kelvins. The data show that the uncertainty of the cross section at these energies was approximately a factor of 2, which makes the use of this branch point impossible as a tool to analyze the mixing in AGB stars. Therefore, sensitive high-precision measurements and sophisticated data analysis were needed. In the near future, we will also investigate the remaining radioactive isotopes in the Sm-Eu-Gd region.

The long-term goal of the DANCE collaboration is to perform neutron capture experiments on all feasible radioactive nuclides on the s-process path. This effort will establish an experimental basis for all relevant neutron-capture rates. When these uncertainties are resolved, the unknown parameters in the models, such as mixing parameters, can be adjusted according to the abundance distributions found in presolar grains and telescope-based observations. ■

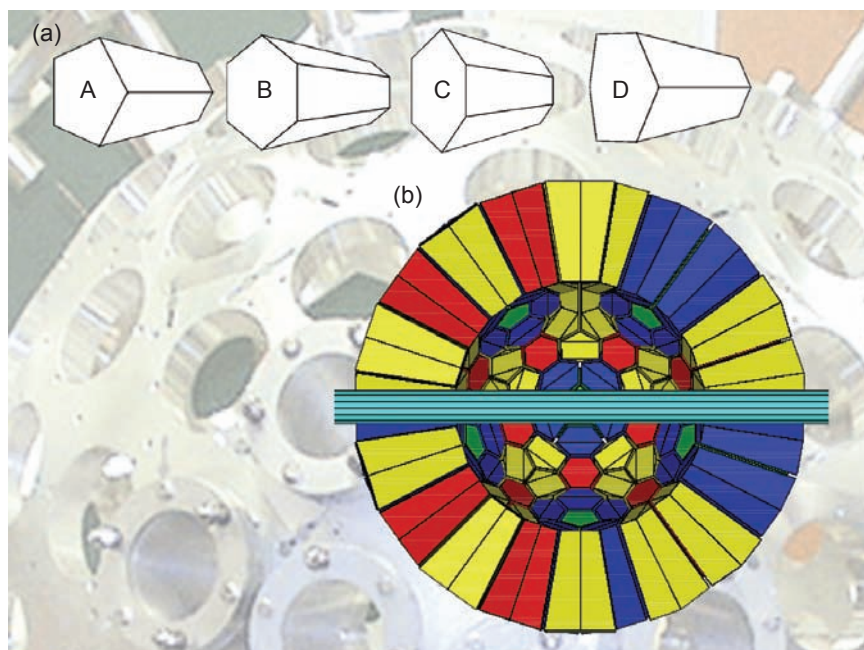


Figure 7. Design and Schematic Views of the DANCE Array
 (a) The design of DANCE, a 160-module array, is based on 12 regular pentagon crystals of type A and requires three differently shaped hexagons, 60 irregular crystals of type B and C, and 30 regular crystals of type D. (b) Each color in the schematic corresponds to a different crystal type (A—green, B—dark blue, C—yellow, and D—red). Only half the sphere of crystals is shown to allow the beam pipe (light blue) to be seen.

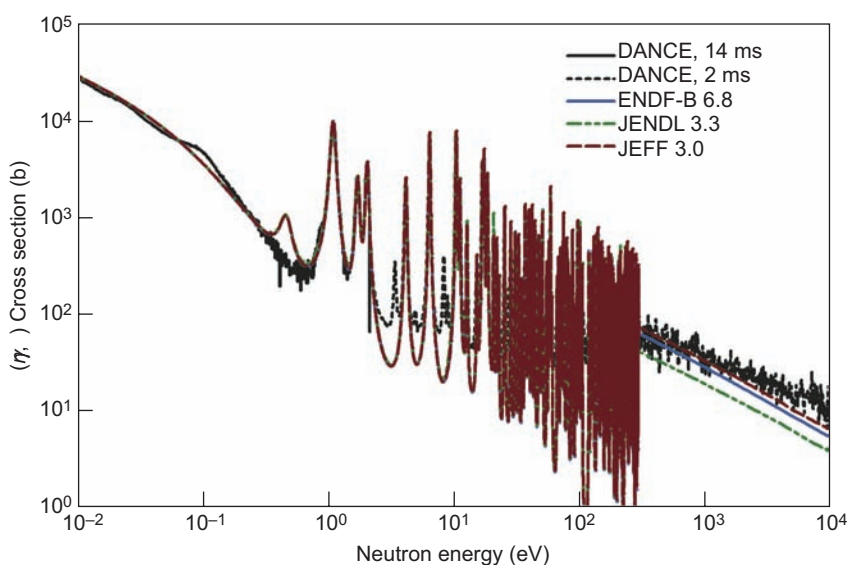


Figure 8. Measurement Performed with DANCE
 A sample of samarium-151 weighing only 0.5 mg was placed in the center of DANCE and irradiated with neutrons. The black curves correspond to the neutron-capture cross section of samarium-151 as a function of neutron energy (preliminary data). The other curves show the recommended values for this reaction from different databases. Especially at energies above 1000 eV, data gained at DANCE help to resolve the big discrepancies between the databases.

Further Reading

- Anders, E., and N. Grevesse. 1989. Abundances of the Elements: Meteoritic and Solar. *Geochim. Cosmochim. Acta* **53** (1): 197.
- Burbidge, E. M., G. R. Burbidge, W. A. Fowler, and F. Hoyle. 1957. Synthesis of the Elements in Stars. *Rev. Mod. Phys.* **29** (4): 547.
- Gallino, R., C. Arlandini, M. Busso, M. Lugaro, C. Travaglio, O. Straniero et al. 1998. Evolution and Nucleosynthesis in Low-Mass Asymptotic Giant Branch Stars. II. Neutron Capture and the S-Process. *Astrophys. J.* **497** (1): 388.
- Lugaro, M., F. Herwig, J. C. Lattanzio, R. Gallino, and O. Straniero. 2003. S-Process Nucleosynthesis in Asymptotic Giant Branch Stars: A Test for Stellar Evolution. *Astrophys. J.* **586** (2): 1305.
- Merrill, P. W. 1952. Technetium in the Stars. *Science* **115** (2992): 484.
- Raiteri, C. M., M. Busso, R. Gallino, and G. Picchio. 1991. S-Process Nucleosynthesis in Massive Stars and the Weak Component. 2. Carbon Burning and Galactic Enrichment. *Astrophys. J.* **371** (2): 665.
- Raiteri, C. M., M. Busso, R. Gallino, G. Picchio, and L. Pulone. 1991. S-Process Nucleosynthesis in Massive Stars and the Weak Component. 1. Evolution and Neutron Captures in a 25 Mass Star. *Astrophys. J.* **367** (1): 228.
- Reifarth, R., F. Kappeler, F. Voss, K. Wisshak, R. Gallino, M. Pignatari, and O. Straniero. 2004. ^{128}Xe and ^{130}Xe : Testing He-Shell Burning in Asymptotic Giant Branch Stars. *Astrophys. J.* **614** (1): 363.
- Reifarth, R., T. A. Bredeweg, A. Alpipar-Vicente, J. C. Browne, E. I. Esch, U. Greife et al. 2004. Background Identification and Suppression for the Measurement of (n, γ) Reactions with the DANCE Array at LANSCE. *Nucl. Instrum. Methods Phys. Res. A* **531** (3): 530.
- Seeger, P. A., W. A. Fowler, and D. D. Clayton. 1965. Nucleosynthesis of Heavy Elements by Neutron Capture. *Astrophys. J. Suppl. Ser.* **11**: 121.



Los Alamos researchers Deniece Korzekwa and Phil Tubesing position a cylindrical graphite funnel over a graphite mold used to cast pieces of uranium alloy. Proper casting helps produce alloy pieces that age gracefully. The upper background shows regions of high niobium content (green) and low niobium content (blue) that make up the complex microstructure of uranium-niobium alloy. The lower background shows a polished, pure uranium sample exposed to air overnight. The colors are produced by the interference of light in the oxide films that form on the microcrystals.

Aging and Deformation of Uranium-Niobium Alloys

Donald W. Brown, Robert E. Hackenberg, David F. Teter, and Mark A. Bourke

One of the major goals of stockpile stewardship is to ensure that weapons in the nation's nuclear stockpile will perform as designed—even as the weapons age. To pursue this goal, we studied the crystal structure of uranium-niobium alloys. Such studies provide insight into how the alloys age and deform under stress. For example, we determined that one of these alloys deforms under stress as shape-memory alloys do, that is, mainly by reorienting its crystalline “twins.” This result can be used in computer models to more accurately predict part performance. Our next step will be to measure changes in the crystal structures of aged alloys as they are subjected to stress and elevated temperatures.

As the nation's nuclear stockpile ages, there are concerns that the properties of the materials in the weapons could degrade to values outside acceptable design limits. Depending on the application, values for properties such as strength, ductility, and hardness may be specified in the design, but these values can change with time. The causes of aging are manifold and inexorable; they include corrosion, oxidation, chemical reactions, radiation damage, and changes in crystal structure. The last of these mechanisms—in which atoms adopt increasingly lower energy states due to thermodynamic considerations—is particularly important for a class of uranium-niobium alloys relevant to the nation's nuclear stockpile. How the crystal structures of these alloys change as a function of composition, aging, and stress is the subject of this article.

Uranium-Niobium Microstructures

Uranium-6 weight% (wt%) niobium (U-6Nb) has several properties that make it desirable for weapon applications. Among them are corrosion resistance and the ability to be heat-treated to obtain strength–ductility combinations that facilitate fabrication. When U-6Nb enters the stockpile, it is thermodynamically metastable, with a majority phase called α'' (a monoclinic distortion of the orthorhombic α -uranium phase characteristic of pure uranium) that maintains a significant supersaturation of niobium owing to the diffusionless martensitic mechanism intrinsic to its formation. The microstructure also exhibits remnants of segregation patterns that develop when the alloy is cast, giving compositional variations at length scales of approximately 100 micrometers of up

to ± 2 wt% niobium about the nominal 6 wt% niobium mean value. This variability in composition and microstructure and its effects on hardness can be seen in Figure 1.

Despite its comparatively complicated microstructure, the alloy's mechanical properties are appropriate for the application at the time of fabrication and insertion into the stockpile—the problem is that the alloy is metastable. The metastability is in the form of niobium supersaturation that is relieved through a diffusion-controlled phase reaction, in which a body-centered-cubic γ_2 phase precipitates. That phase contains more than 50 wt% niobium. The precipitation depletes the remaining matrix phase of niobium, transforming the matrix to α -uranium, which is susceptible to corrosion. Moreover, even before the decomposition reaction reaches a final $\alpha + \gamma_2$ equilibrium,

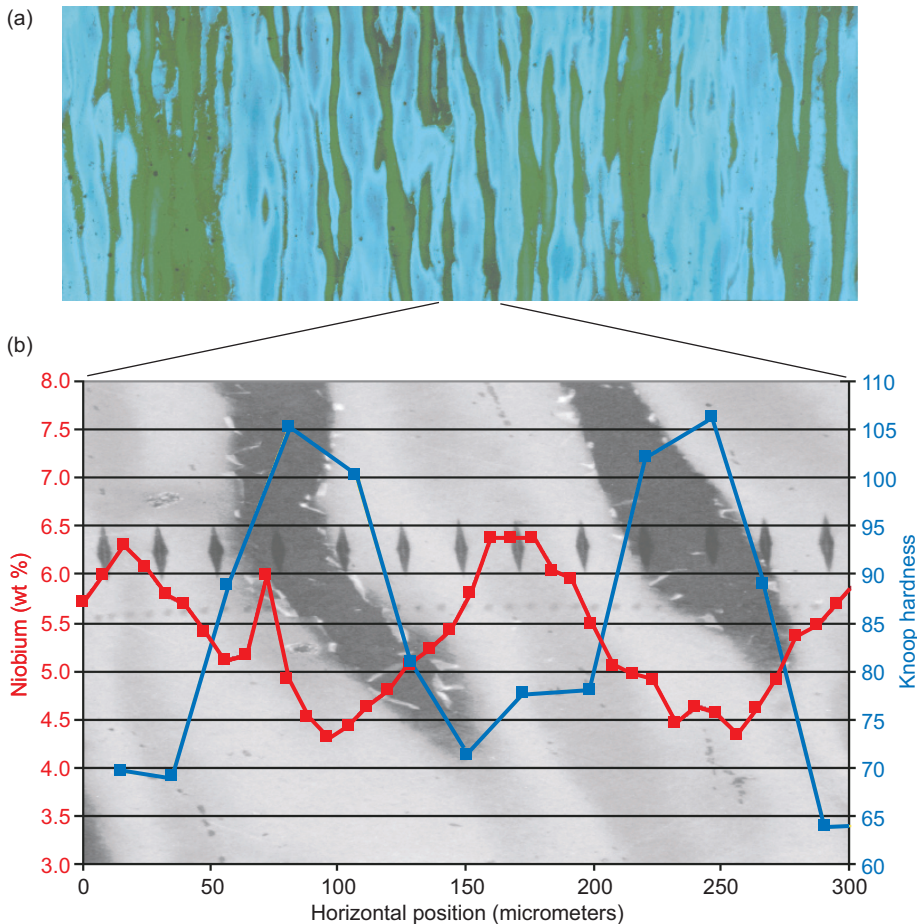


Figure 1. Microstructure and Banding in U-6Nb
 (a) The light microscope image reveals the edges of pancake-shaped bands, with blue and green indicating opposite extremes of compositional variation.
 (b) Two of these bands are magnified in this image, and the composition and hardness traces are superimposed.

other changes occur. For example, the strength increases at the expense of reduced ductility, producing a material that is brittle and unable to deform without cracking. Figure 2 shows the effects of artificial aging at a temperature of 250°C: Aged material exhibits much greater strength but little or no ductility compared with the as-quenched state of the material.

Is Aging a Cause for Concern?

At ambient temperature, the diffusion of niobium is slow—typically

taking years to occur—but whether the diffusion is still rapid enough to cause concern over the decades that make up the anticipated lifetime of a weapon is unclear. Furthermore, at the upper extreme of compositional variation (regions with >6.5 wt% niobium), another metastable martensitic phase, tetragonal γ^0 , can exist. In addition to being stronger than the α'' phase, kinetics studies suggest that γ^0 ages faster than α'' (Eckelmeyer and Thoma 2002), making it possible that premature embrittlement of pancake-shaped regions of high niobium content could occur.

Clearly, an understanding of the

time scales and mechanical implications of the precipitations that take place in uranium-niobium alloy is important to ensure that the alloy's properties remain within design specifications even after decades in the stockpile. Since precipitation is a thermally activated process, exposing the material to elevated temperatures provides one way to accelerate aging. Because of the compositional banding and the likelihood of differential aging rates, a key question is how the aging rate is related to the local niobium content, which varies from 4 to 8 wt%.

Of equal importance is the quantitative relationship between precipitation and mechanical properties. The mechanical response of uranium-niobium alloy (Figure 2) exhibits a relatively unusual double-yielding phenomenon that is symptomatic of the special crystalline mechanisms (occurring in relatively few alloys) that account for plastic deformation. As shown below, these mechanisms prove to be composition dependent and introduce further uncertainty into the question of how aging affects function. At present, there is no rigorous criterion that defines property values beyond which a component will no longer perform its intended function. Further research on the crystallography of the components is required to scientifically inform the development and application of such a criterion.

Why Use Neutrons?

“Engineering performance” is generally defined in terms of bulk properties, but bulk properties are determined by microstructural effects. Thus, as we move from empirical to fundamental models of constitutive behavior, the importance of microstructural evolution during aging and concomitant changes in mechanical properties has been increasingly recognized. Phase, texture, and the

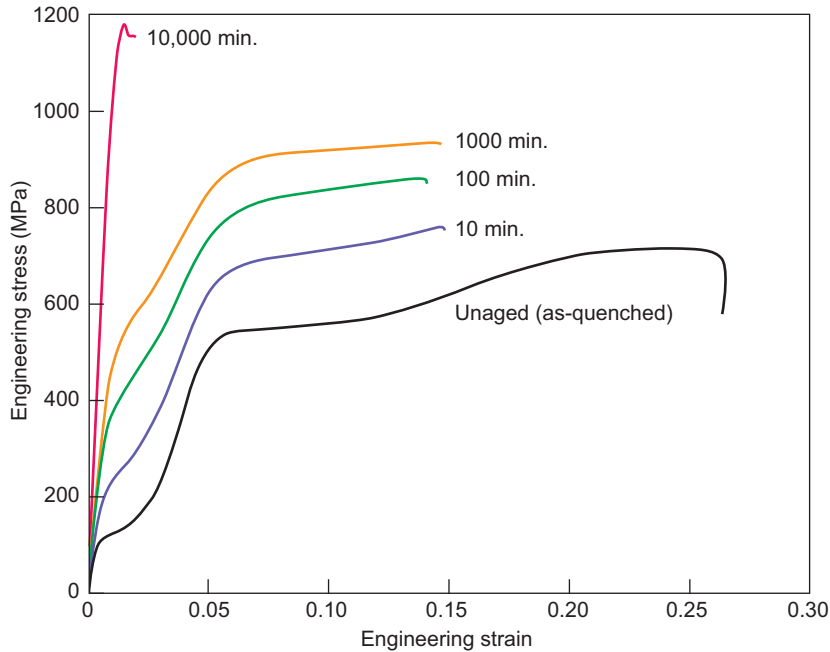


Figure 2. Tensile Stress–Strain Response of U-5.5 wt% Nb (Unbanded) as a Function of Artificial-Aging Time at 250°C

The tests were performed at room temperature after the alloy had been aged at 250°C. As the aging time increases, the stress required to deform the material increases, while the ductility decreases to almost zero for the 10,000-minute-aged material.

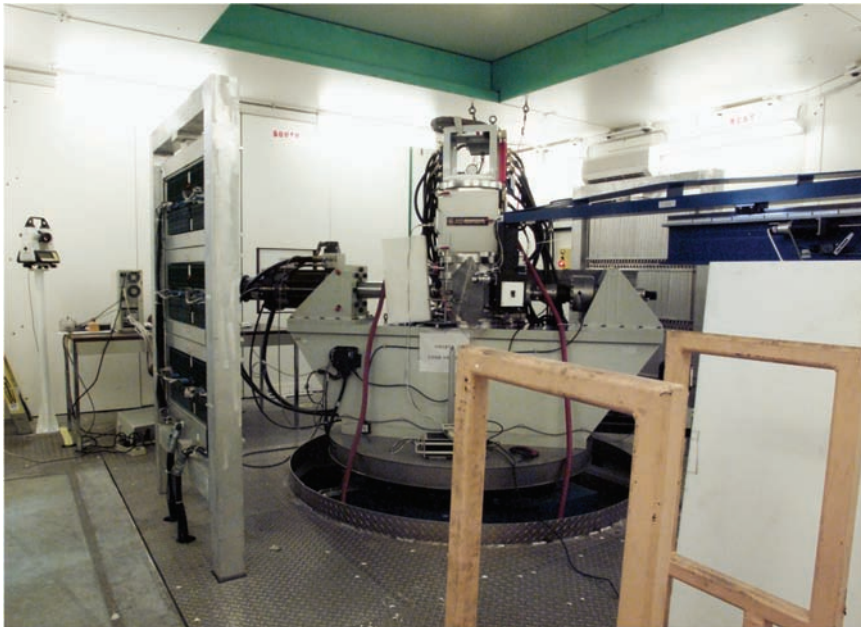


Figure 3. Interior of the SMARTS Experimental Cave at LANSCE
The 250-kN load frame with the 1800°C furnace is mounted in front of the detector panel on the left.

partitioning of strain between different elements of the microstructure are all relevant. To explore their effects, conventional x-ray diffraction has been used for many years to study surfaces, but bulk and in situ measurements are uniquely suited to neutron diffraction. X-rays and electrons penetrate uranium to less than 1 micrometer, whereas neutrons penetrate it to more than 1 centimeter. The larger penetration depth of neutrons provides a key advantage in studying uranium alloys, whose propensity for surface oxidation and mechanical damage makes one uncertain whether surface-sensitive x-ray measurements represent the bulk. In the last few years, two new diffractometers have been commissioned at the Los Alamos Neutron Science Center (LANSCE), SMARTS (Figure 3) and HIPPO. These instruments permit studies of bulk phase, microstructural, and strain response during aging or loading. The results identify the phases and deformation modes and complement conventional characterization by optical and electron microscopy, as well as measurements of heat capacity, electrical resistivity, and dilatometry.

Phase Evolution during Aging

To ensure that trends in martensite transition temperatures and lattice constants could be distinguished by neutron diffraction, a series of 41 compositionally homogeneous uranium-niobium alloys in 0.25 wt% niobium increments were prepared. Figure 4 shows short sections from the neutron diffraction spectra used to identify the phases present at niobium concentrations of 0 to 10 wt%. These data characterize the “baseline” compositions of unaged material. The next step was to evaluate the responses of different compositions at temperatures between 100°C and 300°C. Over this temperature range, measurable precipitation

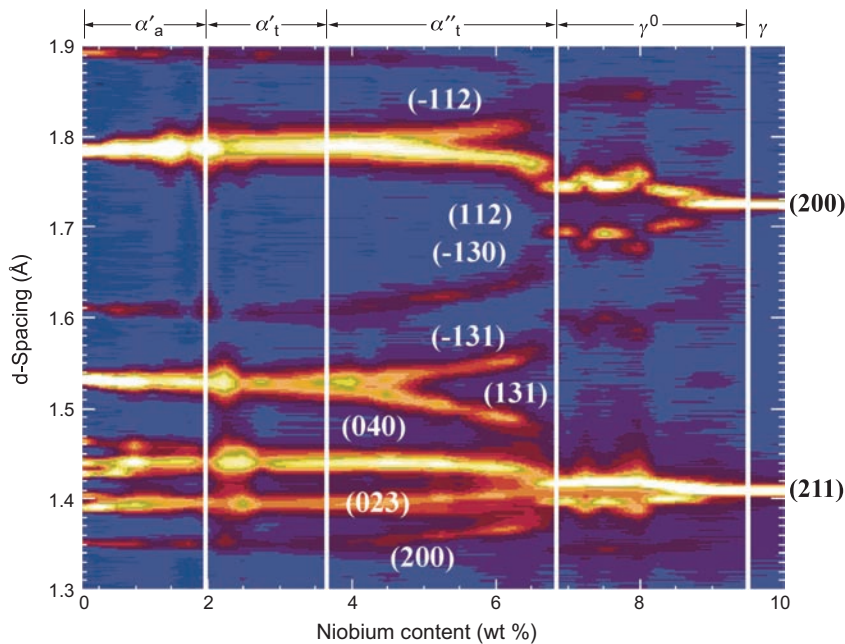


Figure 4. Uranium-Niobium Neutron Diffraction Patterns (1.3 to 1.9 Å) These diffraction patterns are plotted against niobium content. The crystallographic (hkl) planes for the different reflections are labeled. The designations of the different phases are listed above the graph.

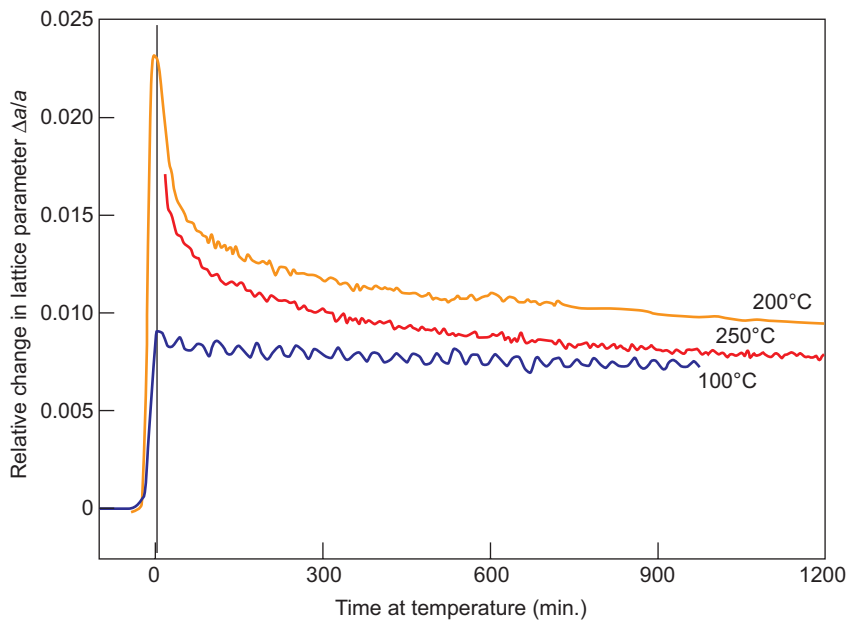


Figure 5. Changes in the U-6Nb's Lattice Parameter vs Dwell Time at Three Temperatures Relative changes in the U-6Nb lattice parameter are plotted for 100°C, 200°C, and 250°C. These changes are attributed to the niobium leaving the solid solution of the majority α'' -phase.

occurs in hours or days (comparable to the time available in a typical neutron-diffraction measurement). In a typical aging experiment, a sample is heated to between 100°C and 300°C and held at constant temperature for approximately 24 hours while neutron diffraction data are collected at 5-minute intervals. During this time, changes in the lattice parameters (obtained from the diffraction data) occur and can be expressed as strains relative to the lattice parameter at the start of the test. Figure 5 illustrates the strain changes of the U-6Nb lattice parameter for three temperatures. The changes in the lattice parameter can be attributed to niobium leaving the solution, and by combining the results from Figures 4 and 5, it is possible to estimate the niobium left in solution. For instance, after 2 hours at 200°C, the niobium content was reduced from 5.75 wt% to roughly 5.25 wt%; after 17 hours, it was further reduced to 4.8 wt%. Since the measurements cannot determine where the niobium goes, the neutron measurements are complemented by other techniques such as transmission electron microscopy.

Different Deformation Mechanisms for 6 wt% and 7 wt% Niobium

The stress-strain responses shown in Figure 2 indicate the complicated nature of the plastic deformation of U-6Nb. Indeed, early versions of the mechanical threshold strength (MTS) model (Chen and Gray 1996), which is widely used to model dynamic materials properties, did not effectively describe the double-yield behavior. The first plateau in U-6Nb is known to be caused by twinning. However, comparable mechanisms for other uranium-niobium compositions are not well understood. For this reason, in situ neutron-diffraction measurements were performed under load for

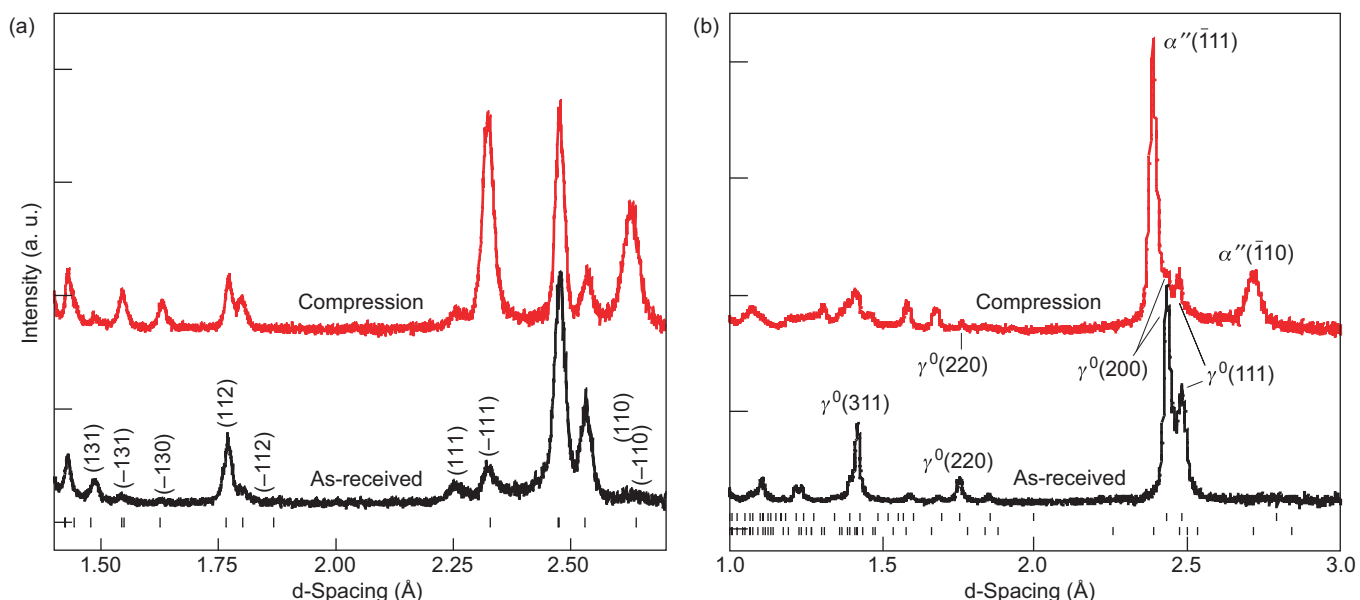


Figure 6. Neutron Diffraction Patterns for U-6Nb and U-7Nb

Plot (a) is for U-6Nb and (b) is for U-7Nb. Both plots show neutron-diffraction patterns for as-received material and after 4% plastic deformation (compression). (a) Changes in peak intensity and the absence of new peaks are an indication of twinning. (b) The presence of new peaks observed in this case is an indication of a phase transformation from γ^0 to α'' .

different niobium compositions. These measurements indicated a significant metallurgical difference between the deformation mechanisms seen in U-6Nb (α'' monoclinic phase) and in U-7Nb (γ^0 tetragonal phase). Figure 6 shows diffraction patterns in the as-received condition and after 4 percent compressive strain for both materials. Figure 6a shows the data for U-6Nb. Changes in peak intensity, indicating rapid texture change, are clear, but no new peaks appear. This behavior is a signature of twinning. However, in Figure 6b, which shows the data for U-7Nb, comparison of the diffraction patterns for the as-received condition and after 4 percent compressive strain show the presence of new peaks, which is symptomatic of a stress-induced phase transformation from γ^0 to the α'' . The understanding obtained from these experiments has led to improving the MTS model by incorporating twinning. This improvement resulted in more faithful modeling of the double-yield stress-strain response of U-6Nb.

Future Measurements

Our current work has established the baseline properties of U-6Nb. The neutron diffraction measurements at LANSCE have added insight to the deformation mechanisms and to the niobium redistribution kinetics. The next steps are to look at the deformation properties of aged material and to quantify the activation energy for aging by analyzing data from a variety of tests. Finally, we wish to link aging-related property degradation to performance. ■

Acknowledgments

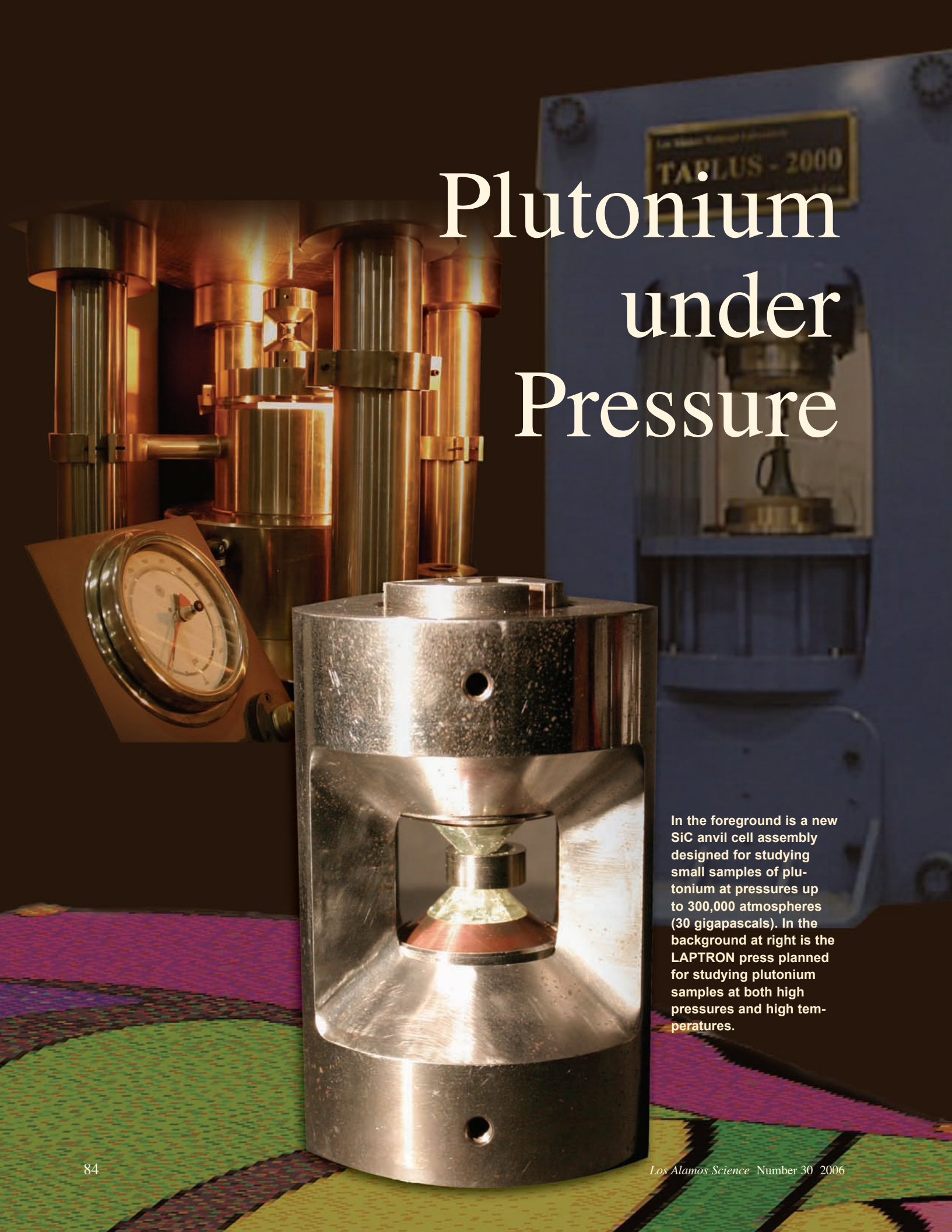
We wish to thank Ann Kelly and Pallas Papin for the metallography and microprobe results, Larry Hults for specimen preparation, Mike Lopez for mechanical testing, Thomas Sisneros for maintaining the neutron diffraction instrumentation and related ancillary equipment, and

Dan Thoma and Rusty Gray for contributions and discussions.

Further Reading

- Chen, S. R., and G. T. Gray III. 1996. Constitutive Behavior of Tantalum and Tantalum-Tungsten Alloys. *Metall. Mater. Trans. A* 27 (10): 2994.
- Eckelmeyer, K. H., and D. J. Thoma. 2002. Age Hardening of U-6% Nb: Kinetic Analysis of Existing Heat Treatment Data and Prediction of Property Changes During Long-Term Storage. Los Alamos National Laboratory document LA-UR-02-7188.

Plutonium under Pressure



In the foreground is a new SiC anvil cell assembly designed for studying small samples of plutonium at pressures up to 300,000 atmospheres (30 gigapascals). In the background at right is the LAPTRON press planned for studying plutonium samples at both high pressures and high temperatures.

Introduction

James L. Smith and George F. Chapline

It is a coincidence that the nuclei of plutonium-239, whose fission properties were predicted before they were used in the atomic bomb, have electrons around it with collective properties that have made this metal difficult to work with for over sixty years. There is no reason that a useful nucleus should be surrounded by badly behaving electrons. As the atomic number—that is, the electric charge on the atomic nucleus—increases, electrons must be added to the electron shells surrounding these nuclei to maintain charge neutrality. The organization and energies of the electrons when the atoms condense into a crystalline form are determined by the rules of quantum mechanics, but unlike nuclear properties, most material properties are too complicated to be predicted directly from quantum mechanics. Among the complications are the occurrence of many different phases and the effects of impurities.

Steel is a difficult material to process because its phase diagram with carbon and other low-level constituents is so complex. But this variety in behavior has a big payoff in allowing us to adjust its strength and properties to the needs of society. Plutonium is also one of the most difficult materials to process and predict for much the same reasons as steel. In both metals, the fact that magnetism can appear or be absent depending on the arrangement of atoms and their spacing leads to the astounding richness of proper-

ties. Steel is usually magnetic, and plutonium is not. They are on opposite sides on the divider between magnetism and non-magnetism, but their complex properties depend on the two metals being close to this crossover. The properties change because, if some electrons contribute to magnetism, they do not participate in holding the metal together. Seemingly insignificant differences in pressure, impurities, processing, and environment lead to major changes in behavior. It takes all of today's best theories, calculations, and experiments even to begin to understand what is going on and to attempt to predict properties more accurately.

At Los Alamos and Lawrence Livermore National Laboratories, a new generation of scientists has joined forces with the veterans in this field and is beginning to produce answers. For the Stockpile Stewardship Program we need to know what plutonium does at all temperatures, pressures, and long times to have some ability to predict the behavior of plutonium outside of what we can measure in laboratory experiments. The new generation has shown that radiation damage in plutonium at low temperatures gives rise to magnetism, and this tendency for electrons to localize around defects affects mechanical properties even at room temperature. The radiation damage experiments have also led to a promising idea for understanding why, under ordinary conditions, plutonium often occurs

in two forms—alpha and delta—with very different properties.

As discussed in the two short articles that follow, the delta form seems to consist of two different quantum phases, a quantum analog of the mixture of water droplets and water vapor that occurs when it rains. The article by Angus Lawson suggests that the phase coexistence in delta plutonium can explain its negative thermal expansion. The article by Albert Migliori shows that the effects of negative thermal expansion on compressibility are not easily explained by single-phase theories. More recently, it has been conjectured that this same kind of phase coexistence may describe the organization of electrons in a solid when they are on the verge of magnetism.

We also need to visualize how the atoms move when the structure changes. Better plutonium samples are needed to understand how radiation damage and impurities come into play, or equivalently, what the starting material really is. It is clear that the study of plutonium will be important for fundamental research and, equally so, for the weapons program for years to come. The new scientists do worry, however, that the increasing bureaucracy of handling plutonium, which is more based on fear than safety, confounds their futures.

Filling the Gap in Plutonium Properties Studies at Intermediate Temperatures and Pressures

Albert Migliori, Alan J. Hurd, Yusheng Zhao, and Cristian Pantea

Pure plutonium exhibits unusual sensitivity to processing, impurities, and aging because its *f*-electrons straddle the boundary between bonding and localization, and plutonium-gallium alloys are unstable to changes in pressure and temperature. Small thermodynamic perturbations, self-irradiation, ingrowth of radiogenic elements, and aging destabilize most plutonium behaviors, while the many structural phases occur within a narrow range of pressures and temperatures (within a few gigapascals and a few hundred kelvins of ambient temperature). This sensitivity and complexity of plutonium and plutonium-gallium alloys make it difficult to obtain reliable measures of the important equation of state (EOS), which describes the relationship among density, temperature, and pressure in a material and therefore serves as input to hydrodynamic calculations. Although an actual full implosion is the most sensitive test of the EOS, such a test benefits enormously if performed on accurately characterized starting materials. It is clear, therefore, that one of our essential functions at the Laboratory is to use the highest-fidelity measurements available to establish the EOS as far up the pressure-temperature (*P-T*) curve as we can manage.

Satisfying this urgent need will support the development of property/performance models, ab initio atomistic computation, Kolski bar and light-gas-gun studies, hydrotests, and more, all of which are aimed at better understanding the connections among aging, physical properties, and weapon per-

formance. Better, more-comprehensive, more-accurate static measurements of plutonium at higher temperatures and pressures than now available can also improve our estimation of margins and uncertainties when applied to new or old computations.

Where Does LANSCE Come in?

The tricky part of any attempt to push static measurements beyond ambient temperature and pressure is that plutonium has two “volumes.” One is a measure of the exact distance between atoms—the crystallographic unit cell. This volume is determined by the most fundamental physics of plutonium and its alloys, and it equals the volume a chunk of plutonium would have if all the atoms sat on the exact positions determined by the crystal structure. This so-called x-ray volume is measured by diffraction of either neutrons or x-rays. But not all atoms sit where they belong. Many are displaced from their exact positions because of impurities, Frenkel-pair formation (Frenkel pairs are composed of a vacancy in the crystal lattice and the displaced atom), radiation damage, dislocations, interstitials, grain boundaries, and vacancies. And in some regions, such as voids produced by helium ingrowth, there just are not any plutonium atoms. So the second volume is determined by a macroscopic measurement of density, such

as weighing the plutonium sample when it is immersed in a fluid.

The difference between these two volumes contains important physics. For example, even in aluminum (Gordon and Granato 2004), a metal with almost none of the complications of plutonium, precise measurements of the difference between these volumes shows a temperature dependence. The dependence occurs because thermal energy can, every once in a while, displace an aluminum atom from its crystallographically correct position, forming a vacancy-interstitial pair. There is a thermal activation energy required for this displacement to happen, and that energy can be found from the difference between the volumes as a function of temperature. In plutonium, we expect the difference to be rich in valuable information and crucial to understanding the way this metal behaves when compressed.

We know how to measure x-ray density at the Los Alamos Neutron Science Center (LANSCE), the Advanced Photon Source (APS) at Argonne National Laboratory, and other facilities where diffraction of x-rays or neutrons is available. However, put plutonium under static pressure, and things get a lot more difficult. X-ray diffraction does not work very well when the low-energy x-rays required have to penetrate the structure of a high-pressure system, so neutron scattering is the technique of choice. But how can one measure the other volume? Radiography is key

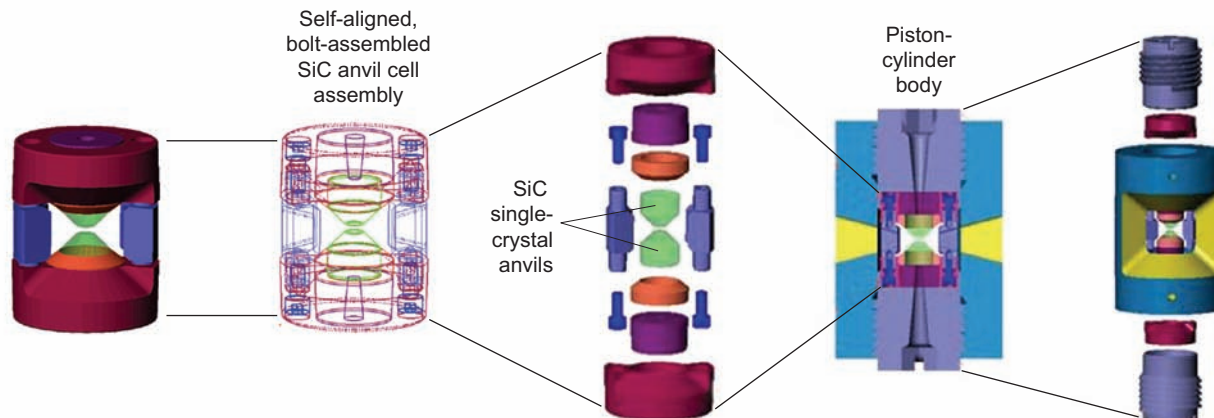


Figure 1. The ZAP Cell, a SiC Anvil Cell Assembly

One of us (Y.Z.) has designed a self-aligning and bolt-turnbuckle cell, which consists of a piston-cylinder body with a SiC (or moissanite) anvil cell assembly at its center (enlarged version is shown at the left of the figure). The SiC cell uses a huge pair of single crystals of SiC, from 5 to 100 carats, to apply pressure on a small sample volume (3~30 mm³). During a test at the LANSCE HIPPO diffractometer, the SiC cell was loaded to a pressure of 30 GPa in the TAP-98 press, and the whole assembly, including the press, was placed inside the HIPPO chamber. The neutron diffraction signal from small iron samples was strong because of the open structure of the SiC anvil cell assembly and the TAP-98 press. High pressures achieved under high hydraulic loading forces (up to 100 tons) can be locked into the inner cell. Through a unique detachment mechanism, the cell can be removed from the press and can then be easily transported to other experimental setups, where the same sample can be studied under identical pressure-temperature (*P-T*) conditions. The optically transparent windows of SiC anvils are particularly useful for measurement of vibrational spectra (Raman and IR) on the same sample under identical *P-T* conditions. The straightforward anvil-sample-anvil setting allows applications of acoustic transmission and ultrasonic interferometry techniques for elasticity measurements at high pressures.

to the measurement. Using neutron radiography techniques available at LANSCE, we can take a dimensionally accurate picture of samples of plutonium while they are in a high-pressure environment and, at the same time, measure the diffraction density.

Pressure Cell for Simultaneous Measurements of Plutonium Properties

Conventional pressure cells are in place at LANSCE, but the silicon carbide (SiC) anvil cell shown in Figure 1 provides a safe, secure environment and an unusually large working space for the plutonium measurements we want to make. A large plutonium sample (millimeters in size) fits in between the two anvils without touching them and thus leaves enough room for a hydraulic

medium to surround it and apply pressure indirectly. Although the pressure in the SiC cell is less than in the conventional diamond cell, inclusion of the hydraulic medium is more important than the higher pressure because no shear stresses or large stress gradients occur in the hydraulic medium and, therefore, the hydrostatic pressure on the sample is accurate and uniform. The stored energy in a SiC cell, as in a diamond anvil cell, is small, and this feature makes any safety issues easy to handle. Large windows in the anvil supports allow neutrons for radiography and diffraction to pass through. Because the large flat SiC anvils themselves are a nearly ideal sound-transmission medium and all the materials involved can withstand temperatures of up to 1800 kelvins and pressures of up to 2 gigapascals, we can conduct the measurements described below.

What Will New Measurements Reveal?

The SiC anvil cell is now operational, and a technique is available to measure the time it takes a sound pulse to traverse a plutonium sample under pressure. The speed of sound in plutonium is a direct measure of the metal's elastic stiffness, and from it the bulk modulus can be derived. The bulk modulus of plutonium gives a measure of its compressibility, and it is the very first quantity theorists compute from an electronic-structure model. It is also, therefore, one of the most important material properties for validating any ab initio or molecular-dynamic model of plutonium. Measurements of bulk modulus in a SiC anvil cell require a technique called pulse-echo ultrasound, an old and widely applied method. But to get the precision we need to see very

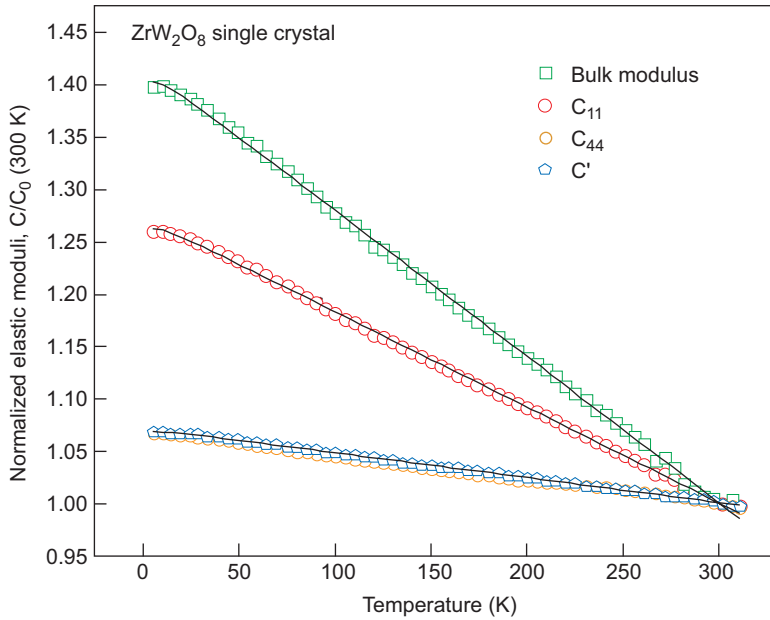


Figure 2. Elastic Moduli of Zirconium Tungstate vs Temperature
 For zirconium tungstate, the softening on warming would be ordinary if it were not for the fact that this material contracts as it warms, and contracting solids usually stiffen.

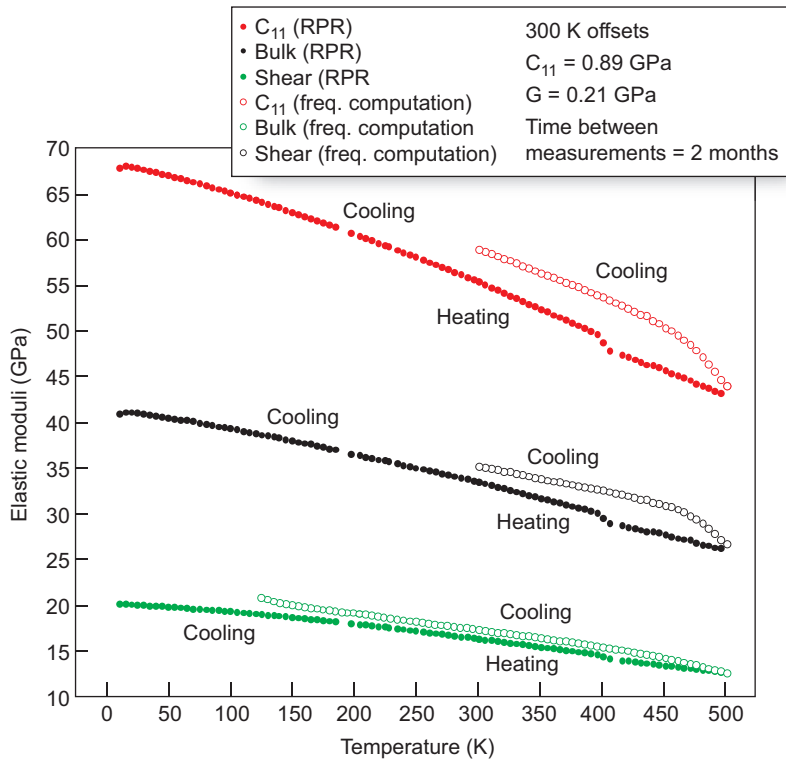


Figure 3. Elastic Moduli of a Plutonium-Gallium Alloy vs Temperature
 One can observe a pronounced softening of the plutonium-gallium alloy above 350 K, where this material, like zirconium tungstate, contracts on warming. A natural prediction is that it must also soften when compressed, a phenomenon not recorded in any of the plutonium databases.

small changes with age, strain, and other parameters, we developed an all-digital signal-processing ultrasound system that enables time-of-flight determination to parts per million, while the sample is hot and compressed. Of course, to get the speed of sound (and bulk modulus), we need not only the time of flight of the sound pulse, but the length of the sample. Here is where radiography and diffraction come in. Using the SiC anvil cell to apply pressure at elevated temperature, radiography to measure length changes, and hence volume, pulse-echo ultrasound to measure time of flight, and neutron diffraction to measure unit-cell volume and structure, we have a tremendously powerful, complete tool, which permits many of the measurements to be done simultaneously. The combination yields both immersion volume and unit-cell volume versus pressure and temperature, basically the two equations of state. Also determined are the thermal expansion coefficient and the bulk modulus (and shear modulus) versus temperature. Within the working envelope of this system, we can also access the liquid state. The liquid phase of metals helps understand shocked metals. Unresolved discrepancies between melting curves derived from shock measurements and those from static experiments have been documented (Luo et al. 2003a, Luo et al. 2003b). Understanding melting and melt structure is fundamental to a material's behavior along a shock Hugoniot. Moreover, the study of high-pressure melting is of interest for density-functional theory and molecular dynamics, which can be incorporated into dynamic simulations of shock.

Implication of New Measurements

If we can implement this set of measurements, we expect to provide

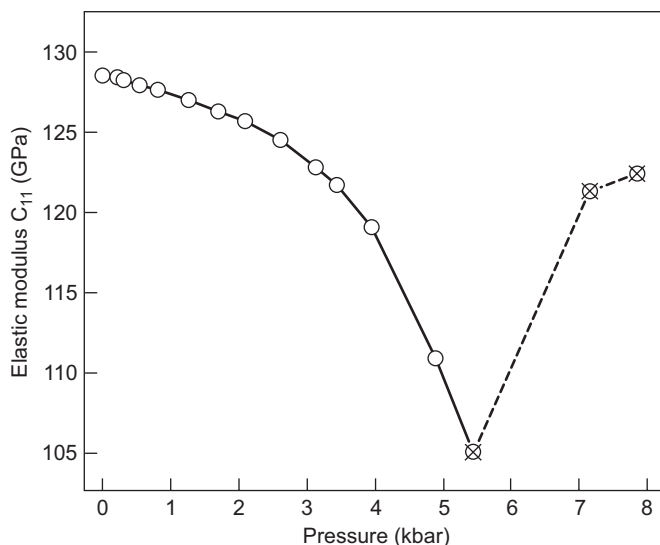


Figure 4. Elastic Moduli of Zirconium Tungstate vs Pressure
We obtained the elastic moduli of zirconium tungstate as we compressed the material. Unlike most solids, this material softens under pressures of up to about 0.5 GPa.

state-of-the-art accuracy of the plutonium EOS over a range of temperatures and pressures heretofore largely ignored at this level of precision. We should also be able to validate extrapolation of aging effects at higher pressures and watch aging in real time at elevated temperatures and pressures. But perhaps there will be some surprises, as well as expansion of the database.

For example, both δ -plutonium (above 375 kelvins) and a zirconium tungstate (ZrW_2O_8) have negative thermal expansion (Figure 2). For plutonium, Angus Lawson has proposed an “invar” model, in which two phases—one is a high-temperature, low-volume phase—are simultaneously present. As temperature changes, more of the low-volume phase appears. Although both phases can have perfectly ordinary properties, the mixture can compensate ordinary thermal expansion, leaving a material that shrinks when heated, and the model works well for plutonium-gallium alloys. But the elastic response of plutonium-gallium is much stranger. We have shown (Drymiotis et al. 2004,

Migliori et al. 1993) that both ZrW_2O_8 and plutonium-gallium soften upon warming in regions where the thermal expansion coefficient is negative (refer to Figures 2 and 3). How can a material get softer as volume decreases? Most conventional models predict that, as a material is compressed and its density increases, it should get stiffer and harder to compress. An even bigger surprise, measured using the SiC anvil cell and the pulse-echo ultrasound system described here, is that ZrW_2O_8 softens when compressed at constant temperature (Figure 4). Can the invar model account for this phenomenon and encompass more than just plutonium, or are other models better at accounting for it? An example would be the Simon-Varma constrained-lattice model (Simon and Varma 2001). What does plutonium-gallium do during the first 2 gigapascals or so of compression at constant temperature? We do not know. If plutonium-gallium also softens, this will be an important new result. We now have the tools for the measurements and plan to find the answer. ■

Further Reading

- Drymiotis, F. R., H. Ledbetter, J. B. Betts, T. Kimura, J. C. Lashley, A. Migliori, et al. 2004. Monocrystal Elastic Constants of the Negative-Thermal-Expansion Compound Zirconium Tungstate (ZrW_2O_8). *Phys. Rev. Lett.* **93** (2): 025502.
- Gordon, C. A., and A. V. Granato. 2004. Equilibrium Concentration of Interstitials in Aluminum Just Below the Melting Temperature. *Mater. Sci. Engin. A* **370** (1–2): 83.
- Hixson, R. S., D. A. Boness, J. W. Shaner, and J. A. Moriarty. 1989. Acoustic Velocities and Phase Transitions in Molybdenum under Strong Shock Compression. *Phys. Rev. Lett.* **62** (6): 637.
- Luo, S.-N., T. J. Ahrens, and P. D. Asimow. 2003a. Polymorphism, Superheating, and Amorphization of Silica Upon Shock Wave Loading and Release. *J. Geophys. Res.—Solid Earth* **108** (B9): 2421.
- Luo, S.-N., T. J. Ahrens, T. Cagin, A. Strachan, W. A. Goddard III, and D. C. Swift. 2003b. Maximum Superheating and Undercooling: Systematics, Molecular Dynamics Simulations, and Dynamic Experiments. *Phys. Rev. B* **68**: 134206.
- Migliori, A., J. L. Sarrao, W. M. Visscher, T. M. Bell, M. Lei, Z. Fisk, and R. G. Leisure. 1993. Resonant Ultrasound Spectroscopic Techniques for Measurement of The Elastic Moduli of Solids. *Physica B* **183** (1–2): 1.
- Migliori, A., and J. L. Sarrao. 1997. *Resonant Ultrasound Spectroscopy: Applications to Physics, Materials Measurements, and Nondestructive Evaluation*. New York: Wiley.
- Shaner, J. W. 1988. Grüneisen Gamma and Acoustic Velocity for Soft Sphere Fluids. *J. Chem. Phys.* **89** (3):1616.
- Simon, M. E., and C. M. Varma. 2001. Dynamics of Some Constrained Lattices. *Phys. Rev. Lett.* **86** (9): 1781.
- Zhao, Y., D. He, J. Qian, C. Pantea, K. A. Lokshin, J. Zhang, and L. L. Daemen. 2005. Development of High P-T Neutron Diffraction at LANSCE. In *Advances in High-Pressure Technology for Geophysical Applications*. Chapter 23, p. 461. Edited by J. Chen, Y. Wang, T. S. Duffy, G. Shen, and L. P. Dobrzinetskaya. Oxford, UK: Elsevier.

Plutonium Magic

Angus Lawson

A mysterious quality of enchantment: “For me the names of those men breathed the magic of the past” (Max Beerbohm).

adj. Of, relating to, or invoking the supernatural:

“stubborn unladen ghost/That breaks his magic chains at curfew time” (John Milton).

Possessing distinctive qualities that produce unaccountable or baffling effects.

Kmetko-Smith Phase Diagram and Magic

The Kmetko-Smith phase diagram (Figure 1) shows how the properties of plutonium metal seem to be “magic” when compared with those of their actinide neighbors in the periodic system. First, plutonium appears in a variety of complex crystal structures not found anywhere else in the periodic system. Second, there is an alarming minimum in the melting point that has significant implications for performance and manufacture. Other anomalous properties, such as the negative thermal expansion observed for the face-centered-cubic (fcc) δ -phase that is stable only at high temperature for the unalloyed metal, have also long been known for plutonium metal, whose behavior has often been construed as magic, in accordance with the last definition above. Finding the reasons for this appearance of magic properties was my goal as a research scientist at Los Alamos.

Zeta

The Kmetko-Smith diagram appeared in print at about the time I started at Los Alamos. My postilion was in the old CMB division (now split off into the Nuclear Materials Technology and Materials Science

and Technology Divisions), and my job was to determine the crystal structure of the ζ -phase (zeta phase) that appears in unalloyed plutonium with the application of modest pressures. I was assigned to the neutron scattering group that had just begun in what is now called the Los Alamos Neutron Science Center (LANSCE). I remained there more than twenty years, but never did succeed in my assigned task. However, I did learn

some other things that help explain the appearance of magic in plutonium (refer to Figure 2).

Pulsed Neutrons and Rietveld Analysis

I began my career in neutron scattering at a good time. I had had previous experience with x-ray diffraction studies of polycrystalline materials,

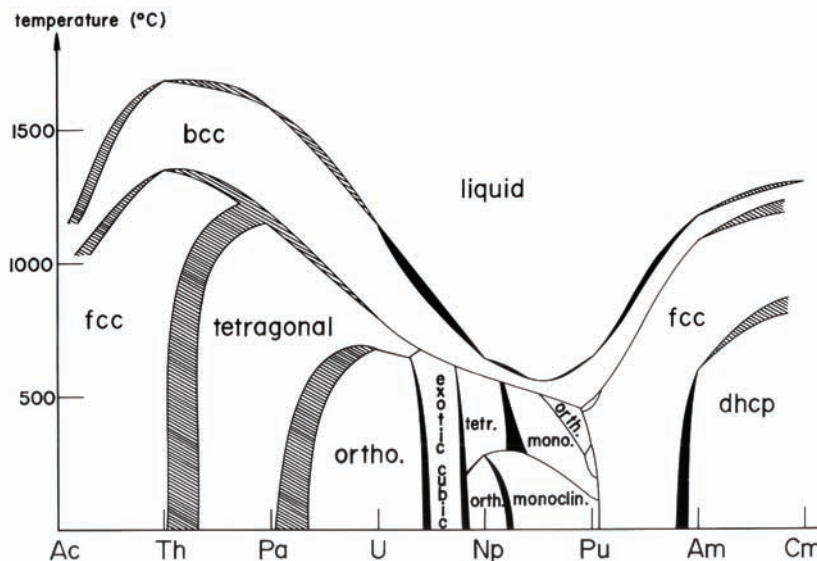


Figure 1. Kmetko-Smith Composite Phase Diagram

This diagram shows how the structures and melting point of the light actinides vary across the periodic table. The deep minimum in melting point is coincident with maximum structural complexity near plutonium’s position.

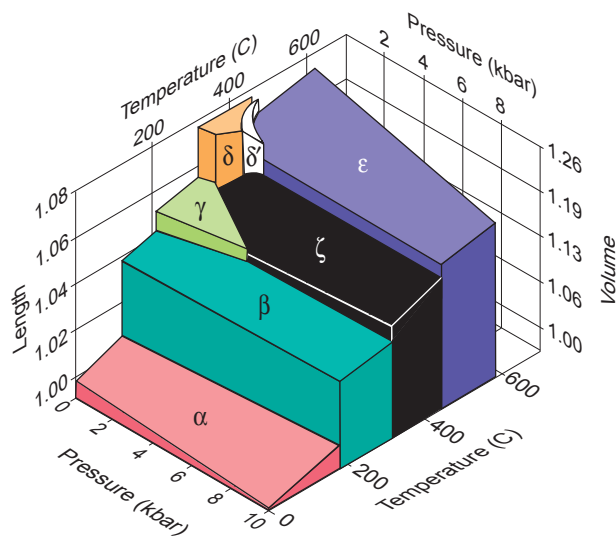


Figure 2. Pressure-Volume-Temperature Diagram for Unalloyed Plutonium Metal (after Morgan)

The ζ -phase is observed at moderately elevated temperatures and pressures, where it replaces the γ - and δ -phases. The crystal structure of the ζ -phase is so far unknown

but there were three technical considerations that made the situation in Los Alamos quite favorable. First, in most circumstances, neutrons are more penetrating than x-rays, so that neutron diffraction data are more representative of the bulk of the specimen. Second, neutron scattering at LANSCE is based on pulsed-neutron diffraction, using neutrons derived from a proton accelerator. This means that the diffraction patterns can be taken at a fixed scattering angle and the resolution of the neutron diffraction is independent of crystallographic d-spacing. Third, a powerful analysis technique, “Rietveld” analysis, was just coming into play. Rietveld analysis provides rapid comparison of the experimentally obtained scattering data with data from a model structure, allowing models to be rapidly compared with reality. The method was soon adapted to the personal computer, which was new then, a development that made its application even more attractive.

Ammonium Fluoride and Uranium at IPNS

The facilities at LANSCE were not ready when I first arrived, so I spent several years traveling to the sister pulsed neutron source, the Intense Pulsed Neutron Source, or IPNS, at Argonne National Laboratory in Chicago. I participated in two experiments there that I construed as warm-ups for the ζ -plutonium problem. First, a group of us determined the crystal structure of a collapsed phase of the nitrogen-deuterium-fluoride compound ND_4F under pressures that were about the same as those required for ζ -plutonium—about 5 kilobars. This experiment was run at room temperature and below rather than at the high temperatures required for ζ -plutonium but was a good introduction to the high-pressure diffraction technique. In a second experiment, a group determined accurately the

crystal structure of β -uranium at high temperatures. This time, no pressure studies, but I learned that high temperatures were in some ways more challenging from the experimental point of view than the modest high pressures required for ζ -plutonium.

First Plutonium Experiment

I conducted my first plutonium experiment at LANSCE on a δ -phase plutonium-aluminum alloy ($\text{Pu}_{0.95}\text{Al}_{0.05}$). An important step was the design of a containment vessel that would keep all radiological contamination safely inside while making minimum contribution to the experimental signal. We managed to get six temperatures between 15 and 260 kelvins before running out of beam time. The results were astonishingly good. We got very precise values of the lattice constants and discovered, perhaps for the first time, that pulsed neutron diffraction combined with Rietveld analysis could give excellent results for the temperature dependence of the thermal motion of the atoms. Rietveld analysis can be used in measurements of atomic thermal motion because that motion causes the diffraction intensities to fall off drastically with d-spacing, and the rate of fall-off, which is a measure of the mean-square atomic thermal displacement, can be determined quite precisely when the Rietveld analysis is applied to diffraction data taken over a range of temperatures. The mean-square displacement is in turn a measure of the material’s elastic stiffness because the interatomic forces responsible for elasticity are in balance with the thermal agitation. The stiffness is expressed by the material’s so-called Debye-Waller characteristic temperature, so we had stumbled on to a good method for determining the elastic properties of plutonium by diffraction methods.

Plutonium Phases at IPNS and LANSCE

The plutonium research then split into two branches. At IPNS, we studied unalloyed plutonium at high temperatures, obtaining data on the α -, β -, γ -, δ -, δ' -, and ϵ -phases. We found that the furnaces available at IPNS did not have sufficiently good temperature control in the region below 600°C and constructed a special furnace with a very long time-constant and excellent temperature stability. A duplicate of this furnace was constructed for use at LANSCE. A separate experiment on unalloyed thorium was also conducted at IPNS. At LANSCE, we completed the study of δ -phase plutonium–5 atomic percent (at. %) aluminum and then concentrated on δ -phase plutonium-gallium alloys. Over a period of ten years, we studied three alloys containing 2, 4, and 6 at. % gallium.

Thermal Atomic Displacements and Melting

A particularly interesting feature of the early high-temperature data was the nonlinear behavior of the mean-square thermal atomic displacement with temperature. Instead of the linear behavior, shown approximately by thorium, we found that the displacement rises faster than linearly for the δ -phase plutonium alloys. Because our methods of measuring the displacement were not yet extensively tested, I was concerned that there was something wrong with the experiment, in particular, that the neutron absorption of plutonium—high even for the nominal plutonium-242 used in our studies—was introducing a bias into the results. After putting these worries to rest, I decided that the cause of the faster-than-linear increase of the atomic displacement with temperature must be the elastic stiffness of the alloy falling sharply with increasing temperature, up to the high-temperature limit

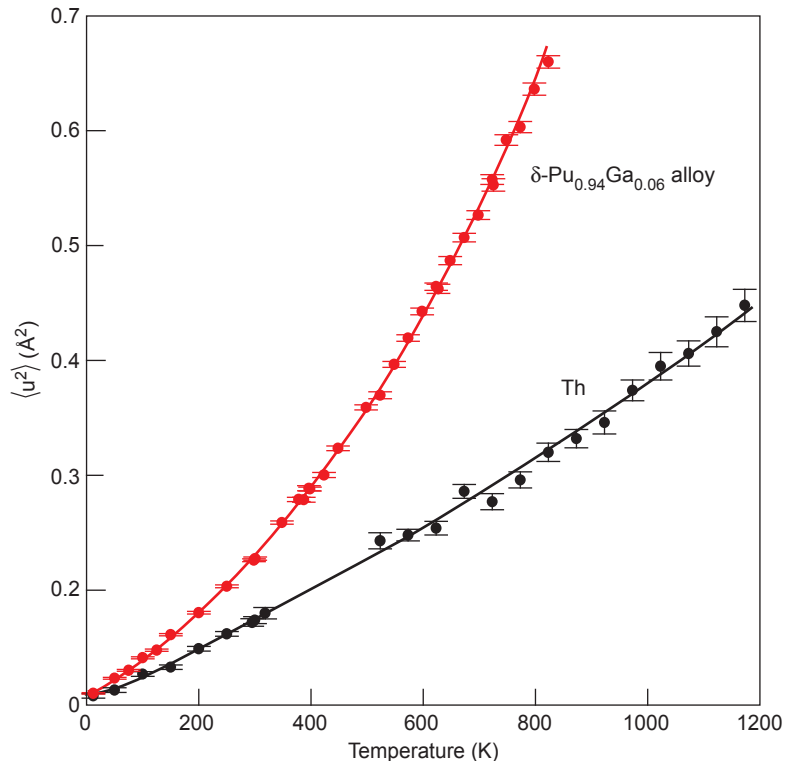


Figure 3. Mean-Square Thermal Atomic Displacement vs Temperature for δ -Phase plutonium and for thorium metal

The atomic displacement measures the increasing thermal agitation with temperature. The increase is approximately linear for most materials, but rises much more quickly for plutonium. This rapid rise explains the low melting point of plutonium, as melting is believed to occur when the displacement reaches about 10% of the interatomic distance.

of the δ -phase stability (see Figure 3).

Suddenly it struck me that this elastic softening behavior was the explanation for the low melting point of plutonium. The Lindemann rule, which goes back to 1910, states that a material melts when its mean-square thermal atomic displacement reaches about 10 percent of the interatomic distance. Although it is impossible to substantiate the Lindemann rule by theory, it is a sensible rule and gives fairly good results. Unfortunately, the rule failed for plutonium and predicted a melting point that was much too high. The problem was that the thermal displacements were estimated by the use of low-temperature elastic constants, and this procedure did not take the high-temperature elastic softening

into account. When the high-temperature softening was taken into account, the melting point predicted by the Lindemann rule was in good agreement with experiment. So I then knew that the low melting point of plutonium was “caused” by high-temperature elastic softening. It should be noted that plutonium does not melt from the fcc δ -phase but rather from the body-centered-cubic (bcc) ϵ -phase; because of the higher temperatures required to access the ϵ -phase, I deliberately chose to ignore this fact.

Zeta and Eta at IPNS

I hadn’t forgotten about the ζ -phase. I now had some experience with high-

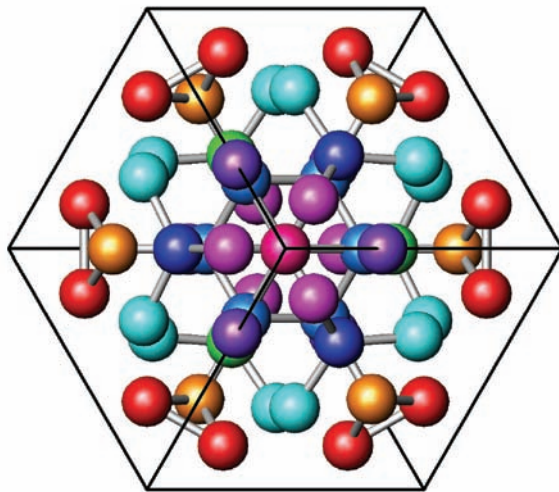
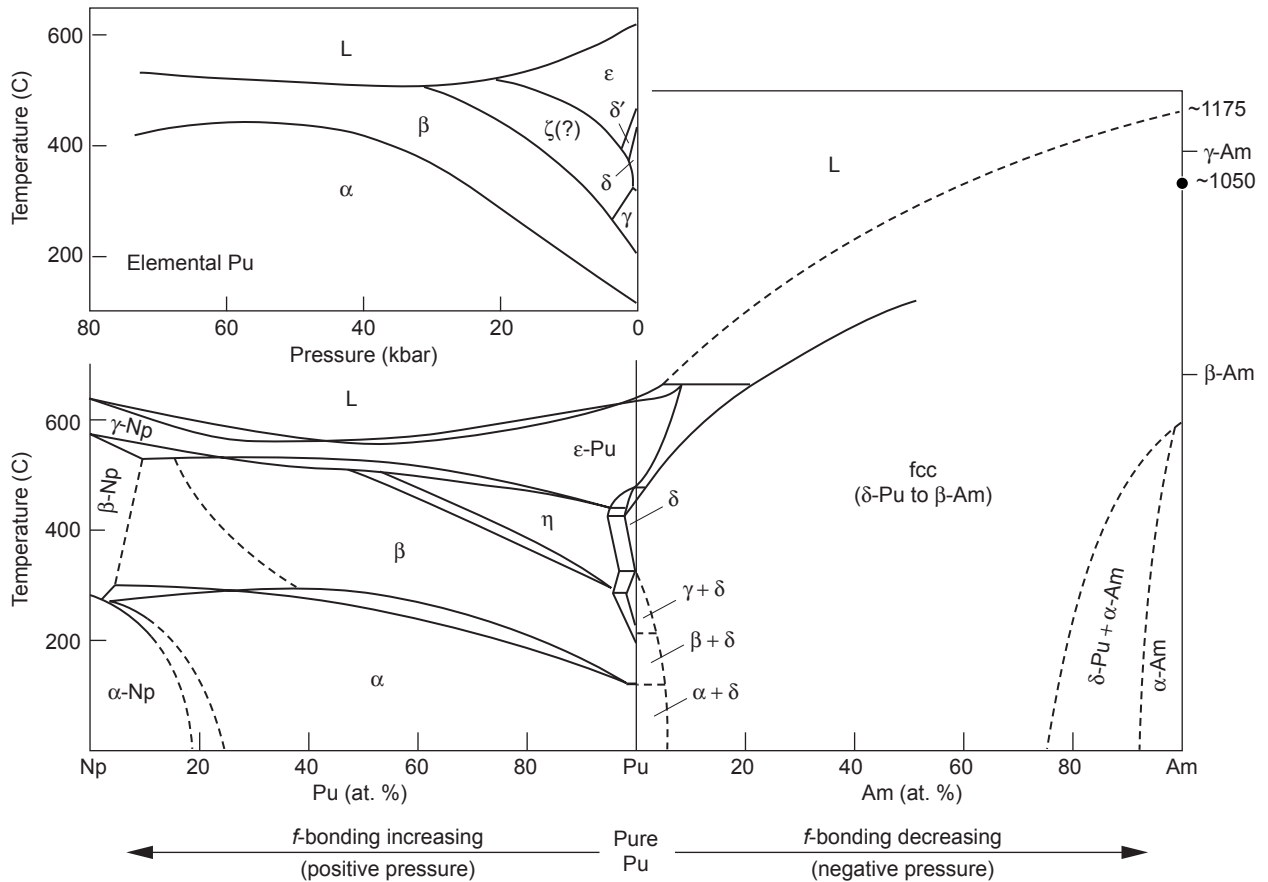


Figure 5. Structure of the ζ -Phase in the Plutonium-Uranium System
 This structure is not the same as the unknown structure of the ζ -phase in unalloyed plutonium, but is found in proximity to the η -phase in the plutonium-uranium system, which is believed to be similar. (The confusing nomenclature is unfortunately fixed by historical happenstance.) The ζ -structure shown has 10 crystallographically distinct plutonium atom types in its 58-atom unit cell and is the most complex structure found so far for a plutonium alloy.

Figure 4. Comparative Phase Diagrams

Reed Elliott observed that the (reflected) pressure-temperature phase diagram of unalloyed plutonium looked just like the ordinary metallurgical phase diagram for plutonium-neptunium. He inferred from this observation that the structure of the ζ -phase for unalloyed plutonium is the same as that of the η -phase in the plutonium-neptunium system. (We are still trying to determine that structure from available data.)

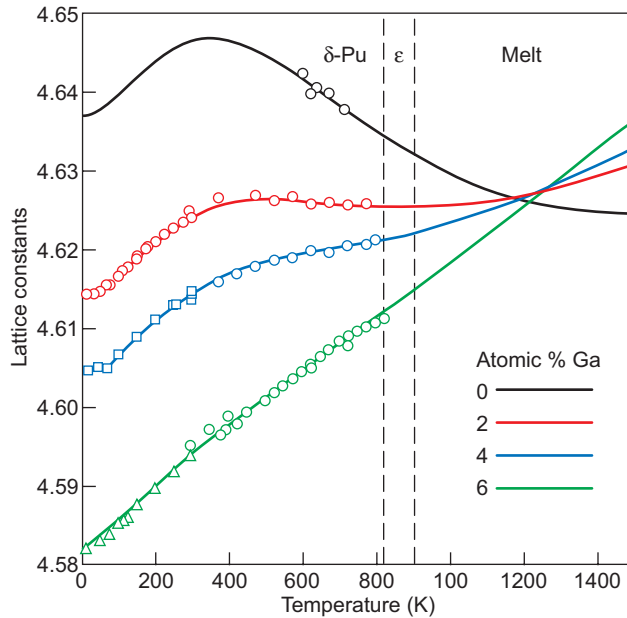


Figure 6. Lattice Constants of Unalloyed δ -Phase Plutonium and Several Plutonium-Gallium Alloys

These data taken by neutron diffraction at LANSCE and IPNS show the gradual transition from negative to positive thermal expansion at high temperatures that is characteristic of δ -plutonium. These data are in good agreement with the x-ray diffraction data published in 1960.

temperature experiments, but I could not find a practical way to do a safe experiment with both high temperatures and high pressures. I decided that the next best thing would be to determine the crystal structure of the η -phase (eta phase) in the plutonium-neptunium system. It had been convincingly demonstrated that alloying with neptunium was equivalent to the application of pressure, so that the determination of the plutonium-neptunium η -phase would also solve the ζ -phase of unalloyed plutonium (see Figure 4). It would certainly be a lot easier.

Experiments were conducted at IPNS on the η -phase of plutonium-neptunium and on the equivalent η -phase of plutonium-uranium, and data were successfully collected on these phases. As a bonus, data were also collected on the ζ -phase of plutonium-uranium (no relation to the ζ -phase of interest). I have so far (after more than ten years) been unable to solve the structure of the equivalent η -phases: They are just

too complicated. The plutonium-uranium ζ -phase was simpler, yet it was still very complicated because of its ten inequivalent actinide atom types in a large unit cell containing 58 actinide atoms (refer to Figure 5). This phase is even more complicated than the α - or β -phase of plutonium. One interesting idea that emerged from this study is that the α - and β -plutonium structures might usefully be construed as intermetallic compounds, just as the complex α -manganese phase, which coincidentally has 58 atoms per cell and 4 distinct atom types, is analogous to the intermetallic titanium-rhenium compound Ti_5Re_{24} .

Thermal Expansion and Invar

For an ordinary metal, the temperature dependence of the stiffness and the thermal expansion are intimately connected through a dimensionless ratio known as the Grüneisen

constant. The Grüneisen constant describes how the elastic stiffness, measured by the Debye temperature, varies with volume. This connection does not hold for δ -phase plutonium because the thermal expansion of unalloyed δ -phase is negative, and the temperature dependence of the volume varies strongly toward more normal positive values as plutonium is alloyed with aluminum or gallium, while the temperature dependence of the stiffness remains essentially constant. This astonishing and magical thermal-expansion behavior of the alloys was published in 1960 and was confirmed much later by the neutron diffraction measurements done at LANSCE (see Figure 6). The plutonium community has wondered for a long time about the magic of the thermal expansion of δ -plutonium.

Charles Edouard Guillaume won the 1920 Nobel Prize in physics for his development of iron alloys with zero and negative thermal expansion that revolutionized the art of metrology. His alloys are generically called “invar,” for invariant volume. A model put forward by Richard Weiss in 1963 explained the invar behavior by postulating the existence of two atomic states for iron, one with lower atomic volume and higher energy, and the other with higher atomic volume and lower energy. The model shows negative thermal expansion because a solid made from a collection of such atoms can access lower volumes at higher temperatures. I applied a similar model to δ -phase plutonium and found that it fit the thermal expansion perfectly. As shown in Figure 7, the energy difference turned out to be 1400 kelvins (or 120 milli-electron volts).

Magic and Invar

What is the connection between the invar thermal expansion and the temperature dependence of the stiffness?

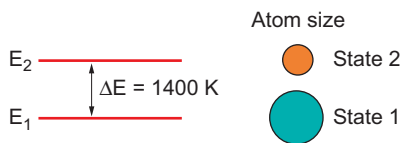


Figure 7. Schematic of the Two-Level Invar Model for δ -Plutonium
The low-volume high-energy state is separated from the high-volume low-energy state by a small energy of 1400 K (or 120 meV).

To answer this question, I constructed a model free-energy function that included the energy of the invar levels. The invar energies have their own Grüneisen constant, which is allowed to vary with gallium content. So there are four model parameters, instead of the two for the normal Debye-Grüneisen solid. This model reproduces all the magic thermomechanical properties of δ -plutonium: the odd behaviors of the thermal expansion, the drastic elastic softening, and the consequent low melting point.

A glimmer of direct observation of the invar levels has been made with inelastic neutron scattering, but results are by no means certain yet. Finally, an identification has been made of the invar levels with the energies that appear in the theoretical dynamic mean-field calculations for δ -phase plutonium. It is perhaps not too early to hope that the origin of the magical properties of δ -plutonium will be found in the two-level invar model. Of course, it remains to be explained why, in terms of f-electron physics, these levels should be stable in the first place. Meanwhile, I will go back to the η -phase and hope that someone will eventually collect data on the magic ζ -phase.

All the pieces of the ζ -phase plutonium puzzle were on the table by 1965. Anyone could have applied Weiss's invar model to plutonium then, but it didn't happen. During my own time at Los Alamos, I was

unaware of the experimental elastic data until after I had completed the thermal displacement measurements at LANSCE. In retrospect, this is probably a good thing, because the effort required to conduct these measurements turned out to be strong motivation for eventually finding the source of plutonium magic in the two-state invar model. ■

Acknowledgment

I thought about listing the names of everyone who helped with this work, but the number of individuals who are owed both my personal thanks and those of the Laboratory must run into the hundreds. Therefore, I listed no one, but I am grateful to them all.

Further Reading

- Calder, C. A., E. C. Draney, and W. W. Wilcox. 1981. Noncontact Measurement of the Elastic Constants of Plutonium at Elevated Temperatures. *J. Nucl. Mater.* **97** (1–2): 126.
- Elliott, R. O., K. A. Gschneidner Jr., and C. P. Kemper. 1961. Thermal Expansion of Some Delta Plutonium Solid Solution Alloys. In *Plutonium 1960*. Edited by E. Grison, W. B. H. Lord, and R. D. Fowler. London: Cleaver-Hume Press.
- Guillaume, C. E. 1897. Recherches sur les Aciers au Nickel. Dilatations aux Températures Elevees; Resistance Electrique. *C. R. Acad. Sci.* **125**: 235.
- Hecker, S. S. 2000. Plutonium and Its Alloys: From Atoms to Microstructure. *Los Alamos Science* **26** (2): 290.
- Lawson, A. C., R. B. Roof, J. D. Jorgensen, B. Morosin, and J. E. Schirber. 1989. Structure of $\text{ND}_4\text{F-II}$. *Acta Crystallogr.* **B45** (3): 212.
- Lawson, A. C., J. A. Goldstone, B. Cort, R. J. Martinez, F. A. Vigil, T. G. Zocco, et al. 1996. Structure of ζ -Phase Plutonium-Uranium. *Acta Crystallogr.* **B52** (1): 32.
- Lawson, A. C., B. Martinez, J. A. Roberts, B. I. Bennett, and J. W. Richardson. 2000. Melting of the Light Actinides. *Philos. Mag.* **B80** (1): 53.
- Lawson, A. C., B. Martinez, J. A. Roberts, J. W. Richardson, and B. I. Bennett. 2000. Atomic Vibrations and Melting in Plutonium. *Los Alamos Science* **26** (1): 190.
- Lawson, A. C., J. A. Roberts, B. Martinez, and J. W. Richardson. 2002. Invar Effect in Pu-Ga Alloys. *Philos. Mag.* **B82** (18): 1837.
- Lawson, A. C., J. A. Roberts, G. Martinez, J. W. Richardson, H. Ledbetter, and A. Migliori, 2003. Applying the Two-State Invar Model to Delta-Phase Plutonium. *JOM* **55** (9): 31.
- Lawson, A. C., J. A. Roberts, B. Martinez, M. Ramos, G. Kotliar, F. W. Trouw, et al. 2004. Invar Model for δ -Phase Pu: Thermal Expansion, Elastic, and Magnetic Properties. Los Alamos National Laboratory document LA-UR-04-6008 (To appear in *Philos. Mag.* 2005).
- Lee, J. A., R. O. A. Hall, E. King, and G. T. Meaden. 1960. Some Properties of Plutonium and Plutonium Rich Alloys. In *Plutonium 1960*. Edited by E. Grison, W. B. H. Lord, and R. D. Fowler. London: Cleaver-Hume Press.
- Lindemann, F. A. 1910. Molecular Frequencies. *Phys. Z.* **11**: 609.
- Morgan, J. R. 1970. New Temperature-Pressure Phase Diagram of Plutonium. In *Plutonium 1970 and Other Actinides*. Edited by W. N. Miner. New York: Metallurgical Society of the American Institute of Mining Metallurgical and Petroleum Engineers.
- Smith, J. L., and E. A. Kmetko. 1983. Magnetism or Bonding: A Nearly Periodic Table of Transition Elements. *J. Less-Common Met.* **90** (1): 83.
- Taylor, J. C., R. G. Loasby, J. D. Dean, and P. F. Linford. 1965. Some Physical Properties of Plutonium at Low Temperatures. In *Plutonium 1965*. Edited by A. E. Kay, and M. B. Waldron. London: Chapman and Hall.
- Taylor, J. C., P. F. T. Linford, and D. J. Dean. 1968. The Low-Temperature Elastic Constants and Specific Heats of Some δ -Phase Plutonium-Gallium Alloys. *J. Inst. Met.* **96**: 178.
- Weiss, R. J. 1963. The Origin of the 'Invar' Effect. *Proc. Phys. Soc.* **82**: 281.

THE ICE HOUSE

Neutron Testing Leads to More-Reliable Electronics

Bruce E. Takala

In 1992, scientist Steve Wender of the Los Alamos Neutron Science Center (LANSCE), working with a team from Boeing, Honeywell, and LSI Logic Inc., discovered that LANSCE's Target 4, the most-intense high-energy neutron source in the world, is an effective tool for testing the vulnerability of computer electronics to single-event upsets induced by cosmic-ray neutrons. That discovery was momentous. Today, companies are literally lining up for neutron beam time at the Irradiation of Chips and Electronics (ICE) House of LANSCE. The effects of neutron irradiation on electronics are not only real but also growing, as electronics become smaller and their vulnerability to neutrons becomes correspondingly higher. Putting electronic devices through their paces helps determine the limits of reliability.





Probably everyone has heard of cosmic rays, but not everyone is aware that cosmic rays affect everyday life. Indeed, secondary neutrons from cosmic-ray showers naturally present in the atmosphere can interact with the memory and logic in electronic systems and cause them to malfunction. Just imagine noticing that the million-dollar digit in your bank account has changed, especially if it has done so in the wrong direction, or traveling in a car or airplane in which the safety system has suddenly failed. Although designers and users of semiconductor electronics have taken steps to avoid potentially catastrophic events, the cause of such events is constantly present and is of increasing concern.

When cosmic rays collide with nuclei in the upper atmosphere, they create a shower of subatomic particles. By the time the cosmic-ray shower reaches aircraft altitudes and below, the uncharged neutrons present are the dominant source of errors in electronics. These neutrons pose little health hazard because the radiation dose is relatively low, but each neutron can interact with silicon and other elements in integrated circuits to deposit charge in localized regions, with potentially disastrous impact on memory and chip function. Such disruptions, potentially caused by a single neutron, are collectively known as single-event upsets (SEUs), and their rate is the largest single contributor to the soft-error rate of modern electronic integrated circuits. (For further information on how SEUs are created, refer to the box “The Origins of SEUs” at right.) Hardware is said to experience soft errors if it malfunctions temporarily and hard errors if it is damaged permanently.

What are the effects that can be so disastrous to electronics? The simplest SEU occurs when a memory or logic location changes its state because of charge deposited by an energetic

The Origins of SEUs

High-energy cosmic rays impacting the upper atmosphere generate a cascade of secondary particles that reach lower altitudes. In general, these high-energy particles are very penetrating and do not stop in exposed electronic devices. Since the energy deposited in the host device is small, the excess charge (electron-hole pairs) generated by electronic ionization is insufficient to cause soft errors. Even though the probability of a collision is very small, these secondary particles can collide with a silicon nucleus in the semiconductor device. When neutrons collide with a silicon nucleus, many different nuclear reactions can occur. Scattering reactions, elastic and inelastic, leave the silicon nucleus intact, but they cause it to recoil. The recoiling nucleus leaves an intense local ionization trail (see reaction 1). In high-energy cases, the collision may lead to a series of direct reactions (intranuclear cascade), whereby individual nucleons (protons or neutrons) or small groups of nucleons (say, an alpha particle, ${}^4\text{He}_2$ —see reaction 2) are ejected from the silicon nucleus or the silicon nucleus may fragment. As the available energy becomes less, a compound nucleus (a neutron may be captured by a nucleus) may be formed that will “boil off” nucleons to reach stability. When the total number of ionization electron-hole pairs collected in a sensitive region of the device exceeds a critical value (which is a characteristic of the device), an SEU is born.

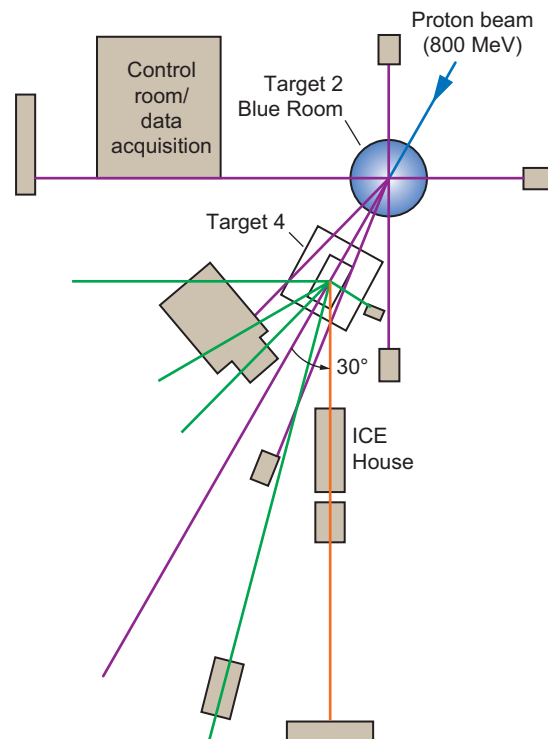
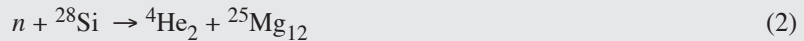
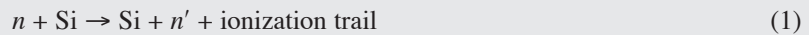


Figure 1. The Beam Lines at the WNR Facility

particle. Sometimes more than one memory location can be affected by a single particle. Latchup is another frequently encountered, although much more serious, soft error, whereby an electrical current arises in an unintended area. The device stops functioning until it is turned off and then on again. Finally, hard errors can permanently damage or even destroy devices by causing them to draw large currents.

History

Following up on what was mostly anecdotal information, Ziegler and Lanford (1979) showed that the products of cosmic rays striking the atmosphere were causing upsets in computer memory. Even though the authors considered those effects only marginally significant, they were quite prophetic in asserting that their observation would be important for future electronic circuits. By 1993, Taber and Normand concluded “that a significant SEU phenomenon exists at airplane altitudes, that it is most likely due to energetic neutrons created by cosmic ray interactions within the atmosphere (NSEU), and that memory error-correction coding is likely to be necessary for most high density avionics memory systems” (1993).

As the SEU phenomenon was increasingly recognized as a problem, a method for rapidly testing device susceptibility to neutron-induced errors was needed. In 1992, scientist Steve Wender of LANSCE, working together with a team from Boeing, Honeywell, and LSI Logic Inc., designed an experiment to demonstrate that neutrons generated at the Weapons Neutron Research (WNR) Facility (Figure 1) could be used as an effective SEU testing tool. The team had recognized that the spectrum of neutrons delivered on one of the beam lines from Target 4, the most-intense

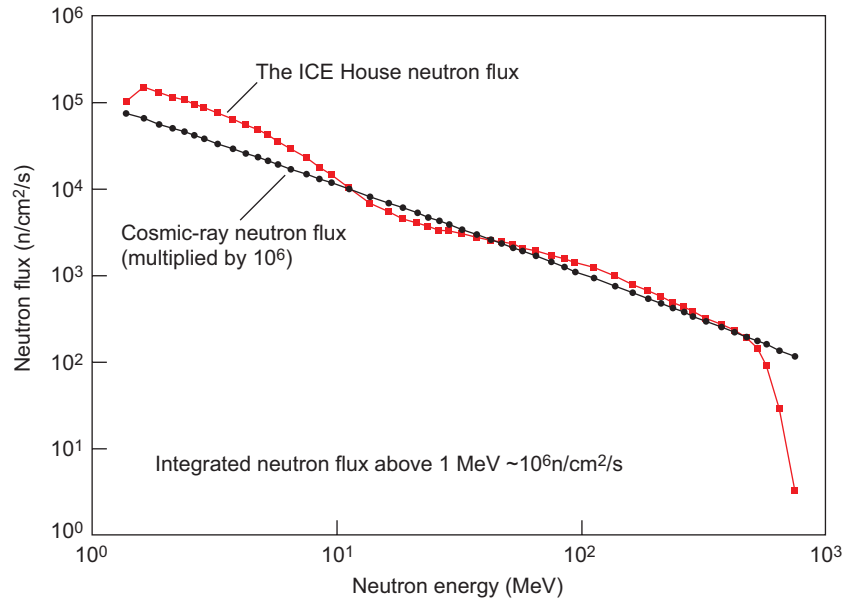


Figure 2. ICE House vs Cosmic-Ray Neutron Spectrum
This plot of neutron intensity vs energy illustrates the high degree of similarity between the ICE House neutron spectrum and the natural atmospheric neutron spectrum from cosmic rays. Significant differences show up only at energies close to 800 MeV.

high-energy neutron source in the world, was quite similar to the neutron spectrum in the atmosphere. The first experiments consisted of small boxes taped to the end of an outdoor beam pipe. Despite the makeshift design, the experiment was highly successful in establishing the proof of principle. None of the participants could have imagined that this simple experiment would eventually result in the busiest beam line at the facility and so many publications at the forefront of the field.

Creating a Neutron Beam Line for Testing Chips and Electronics

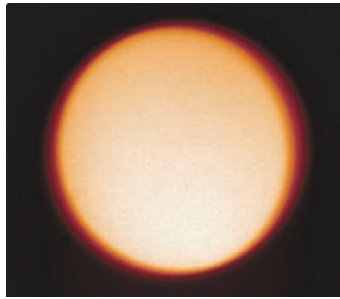
The heart of LANSCE is the 800-million-electron-volt (MeV) half-mile-long linear accelerator producing a pulsed proton beam. Neutrons are produced at LANSCE by directing the

pulses of the proton beam at high-Z neutron-rich targets. The impact of each pulse of protons causes a short burst of neutrons with a wide range of energies (up to 800 MeV) to be released from nuclei in the target and to travel down beam lines. The WNR Facility, first conceived in the early 1970s, is made up of two target areas, Target 2 and Target 4. Target 4 consists of a “bare” tungsten neutron-production target and six instrumented beam lines with detector stations ranging from 10 to 90 meters from the target and at angles of 15° to 90° with respect to the incoming proton beam. The neutron spectrum ranges from a hard (high-energy) spectrum at 15° to a softer (low-energy) spectrum at 90°.

The New Facility

The ICE House (ICE is short for Irradiation of Chips and Electronics)

(a) Upstream



(b) Downstream

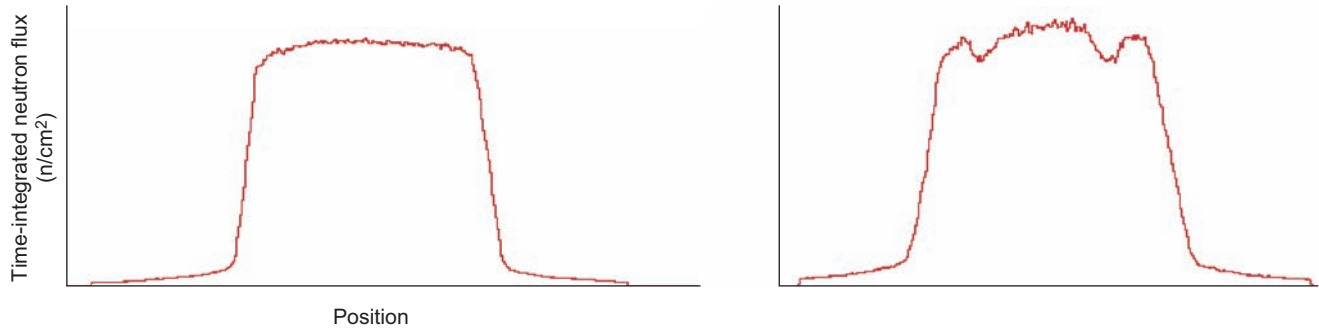
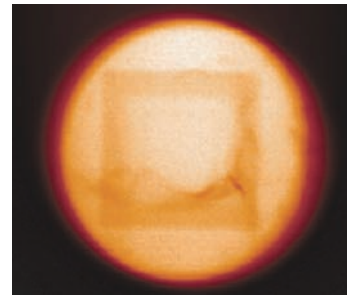


Figure 3. Neutron Radiographs of the ICE House Beam

Image plates of the ICE House neutron beam in (a) and (b) show uniform brightness and sharp edges. Note that the image downstream of the device is a neutron radiograph of the device. The radiographs measure neutron fluence (time-integrated neutron flux). The matching plots show line scans of the radiographs along the horizontal axis, which correspond to a cross section of the beam before and after the beam passes through the device.

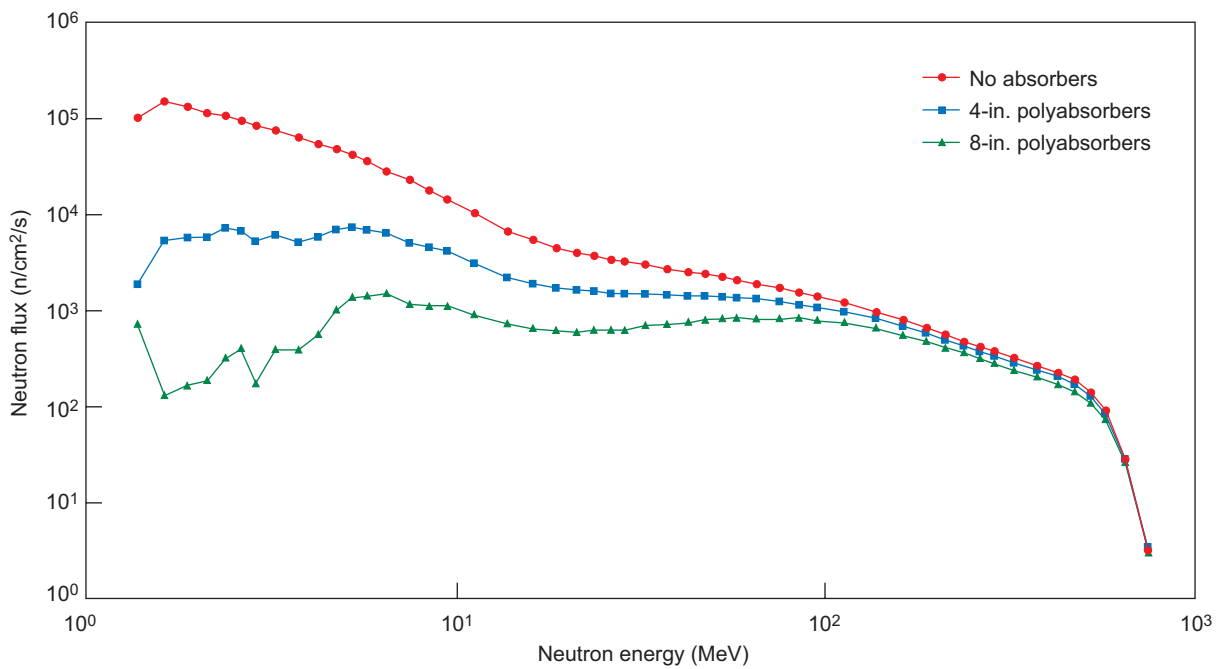


Figure 4. Altering the Neutron Spectrum

As polyethylene is added to the beam, low-energy neutrons are removed, leaving a beam with higher average neutron energy.

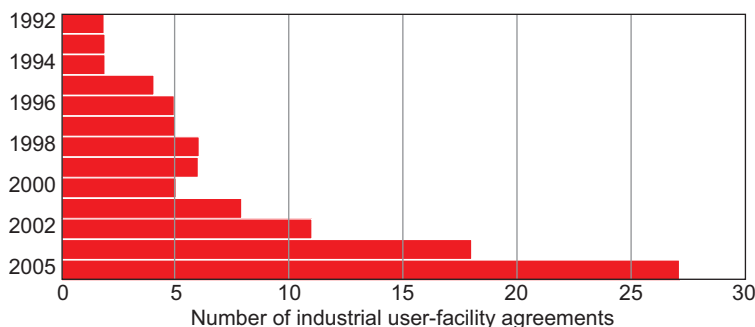


Figure 5. Use of the ICE House by Industry

A remarkable increase in user facility agreements is apparent between 2001 and 2005. (Note that 2004 is not included in this graph because of a Laboratory-wide shutdown.)



Figure 6. International Collaborators at the ICE House

Art Bridge and Bruce Takala (wearing hats) of LANSCE are pictured here with a large team of European and United States collaborators from STMicroelectronics, Commissariat à l'Energie Atomique, Hirez, Motorola, and Trinity Convergence.

is located on the 30° left beam line of the high-energy neutron source at the WNR (Figure 1). At this angle, the neutron spectrum is very similar to the spectrum of neutrons produced in the atmosphere by cosmic rays (Taber and Normand 1993), but the neutron flux at 30° is a million times higher (Figure 2) than the flux of neutrons produced by cosmic rays, depending on altitude. This large neutron flux allows testing of semiconductor devices at greatly accelerated rates, in which one hour of exposure is equivalent to more than 100 years of exposure at aircraft altitudes. By starting a timer when the proton pulse hits

the target and measuring the time the neutrons take to travel the length of the beam line, the number and energy of the neutrons are measured.

No other facility in the world can offer this intensity with a spectrum whose shape matches that of the natural atmospheric spectrum so closely. Because this flux is composed of approximately 35,000 individual neutron pulses caused by the time structure of the accelerator proton beam, the results are still representative of atmospheric results because the probability of multiple neutron events is exceedingly low for individual pulses. The capability of the facility has been suc-

cinctly recognized by the Joint Electron Device Engineering Council (JEDEC), representing about 300 manufacturers and users of electronics. Its published memory-testing standard JESD89 mentions that “The WNR at Los Alamos is the preferred facility” for accelerated neutron-induced SEU testing.

Advantages. The ICE House approach to testing has several advantages over other testing methods.

Unlike heavy-ion tests, during which a device must often have its case material removed and be placed in vacuum to permit particles to reach the sensitive regions of the chip, testing in the ICE House beam permits normal operation of the device in the open air. In fact, because neutrons are not strongly absorbed by the device tested, several devices may be placed in the neutron beam at once, one behind the other. At the experimenters' request, the diameter of the beam spot can also be changed by collimation. As the device under test is moved down the flight path, the beam spot on the device becomes correspondingly wider in diameter. One can choose almost any diameter for the beam spot within the range of 1 to 6 inches. In Figures 3a and 3b, images of neutron beam intensity taken at the ICE House before and after the beam hits the object tested show uniform brightness and sharp edges. The matching plots show line scans of the radiographs along the horizontal axis, which correspond to a cross section of the beam. The plot in Figure 3b clearly indicates that the device has scattered neutrons out of the beam.

In addition, the neutron spectrum can be altered if absorbing material is placed in the beam to reduce the low-energy intensity relative to the high-energy part. Figure 4 shows what happens to the shape of the neutron spectrum when different amounts of polyethylene are added into the neutron beam. By using this method,

Industrial Customers of the ICE House

ABB, Switzerland



Fujitsu, Japan

Motorola, U.S.A.



Advanced Micro Devices, AMD, U.S.A.

Hewlett-Packard, U.S.A.

NEC Electronics, Japan

AeroSpeciale, France

Hirex, U.S.A.



Qinetiq Ltd., U.K.



AerotechTelub, Sweden



Hitachi, Japan

Rockwell Collins, U.S.A.

Agere Systems, U.S.A.

Honeywell, U.S.A.

Saab, Sweden

Alpha Sciences, U.S.A.

Infineon Technologies AG, Germany

Samsung, Korea



Altera, U.S.A.

Intel Corp., U.S.A.



Smiths Aerospace, U.S.A.

BAE, U.K.



iRoc Technologies, France

Sony Corporation, Japan

Boeing, U.S.A.

Lockheed Martin, U.S.A.

STMicroelectronics, Italy and France

Digital Equipment Corporation, U.S.A.

LSI Logic, U.S.A.



Sun Microsystems, Inc., U.S.A.

Dynex Technologies, U.K.

Lucent Technologies, U.S.A.

Texas Instruments, U.S.A.

Eupec, Germany



MBDA Missile Systems, U.S.A.

Trinity Convergence Limited, U.K.

Extreme Networks, U.S.A.

Micron Technology, Inc. U.S.A.

Xilinx, U.S.A.



experimenters determine the relative contributions of higher- vs lower-energy neutrons to the error rate.

The Testers or Who's Who in Electronics

Customers who have brought electronic devices to LANSCE's ICE House make up a who's who of

the global electronic and avionics industries. Testers represent the full spectrum of product manufacturers: from chip producers and board level integrators to consumer product companies. Circuit manufacturers understand the risk posed by cosmic-ray neutrons and try to design around it, so testing at the ICE House is increasingly becoming an international standard for putting new circuits through

their paces. Figure 5 illustrates the sharp growth in the number of user facility agreements between 2001 and 2005. Eight experiments were conducted in 2001, twenty-one in 2002, twenty-eight in 2003, and the numbers of both proposals and industrial participants are continuing to increase at record levels in 2005. The year 2004 is not listed because a Laboratory-wide standdown delayed the start of

the 2004 run cycle until 2005.

A large increase in the number of multicompany collaborations sharing beam time is also notable. Figure 6 is a picture of one of the recent large teams from Europe and the United States. Demand for the test bed has grown so much that we had to come up with a waiting list for beam time. The box “Industrial Customers of the ICE House” on the opposite page lists many of the companies that have so far tested electronic components at LANSCE. A strong international presence is evident. Clearly, the ICE House has developed into a valuable resource for the worldwide electronics community.

The Good News for Consumers and Industry

As more and more companies are testing at the ICE House, the good news for consumers is that their electronic systems end up being more reliable and more secure. Companies come to the ICE House because they must answer a very difficult question: How good is good enough? In general, a typical static-random-access-memory chip (referred to as an SRAM chip in the industry) will generate roughly 1200 soft errors per hour when subjected to the intense neutron flux at the ICE House, which can be as high as a million neutrons per square centimeter per second. For the devices they test, companies hold as proprietary information the exact number of errors per unit of testing time. The Laboratory supplies them with information on the number of neutrons per square centimeter that went through the device during the test. When they are done testing at Los Alamos, companies have data showing the number of errors per neutron. With this information and knowing the neutron flux in the environment in which the system will

operate, they can predict the soft-error rate of the system in the field (an example of testing results is discussed in the accompanying article “Testing a Flight Control System for Neutron-Induced Disturbances” on page 104). Once they know the expected error rate from neutrons, chipmakers can decide if error correction, redundancy, or other protective measures are needed to compensate for the neutron-induced errors. This approach ensures that any unreliability at the device level is compensated for at the system level.

Failure to test has been a costly mistake for some companies. One instance involved a Honeywell component that was failing in the field, but the problem could not be duplicated in the lab. After several failed attempts to diagnose the problem, Honeywell experimenters made an urgent request for ICE House beam time. Their subsequent run in the beam confirmed the problem as a latchup vulnerability of one chip that had been designed with a new type of memory cell. Not only did it cost Honeywell millions of dollars to recall the devices and replace the chip, the company also had to redesign several items that were nearing production. Honeywell has been back to test every year since. According to the company, “The results of these series of experiments will, in large part, drive Honeywell’s future memory architectures and fault-protection methodologies for the next generation of [a new product] now in development.”

The Future

New issues continue to emerge from recent experiments. Neutron-induced effects on field-programmable gate arrays (FPGAs), one of the cutting-edge developments in microelectronics, are being widely studied. The relationship between failure rates

and feature size is hotly debated. Indeed, there are those who believe that the smaller the electronic components, the higher the error rate and that keeping the error rate at tolerable levels could be the ultimate constraint on the size of electronic parts. Wide variations in latchup susceptibility have been observed. Variations depending on orientation (which side of the component is facing the beam), socket type (the type of mounting on the circuit board), and even circuit layout have been demonstrated. “No one’s been able to make this problem go away for key electronic applications; in fact, even the codes people use to predict failure rates are becoming less accurate,” Wender said. “But if somebody eventually comes up with a possible solution, the new design will have to be brought here and tested out.” Neutron-induced SEUs remain a significant threat to semiconductor electronics. Through the new ICE House Facility, LANSCE is uniquely positioned to address this problem for the electronics industry, the nation, and the world.

Further Reading

- Baumann, R. C. Accelerator Needs for Characterization of Radiation Effects in Commercial Semiconductor Technologies. To appear in *Proceedings of the 18th International Conference on the Application of Accelerators in Research and Industry*. (Ft. Worth, TX, October 10–15, 2004).
- Taber, A., and E. Normand. 1993. Single Event Upset in Avionics. *IEEE Trans. Nucl. Sci.* **40** (2): 120.
- Ziegler, J. F., and W. A. Lanford. 1979. Effect of Cosmic Rays on Computer Memories. *Science* **206** (4420): 776.

Testing a Flight Control System for Neutron-Induced Disturbances

Celeste M. Belcastro, Kenneth Eure,* and Richard Hess***

Atmospheric neutrons can cause single-event upsets in the microelectronic devices used in aircraft systems. Reducing the effects of those upsets is most important to the aircraft industry. We tested the robustness of a flight control computer containing our new rapid-recovery architecture by irradiating it in a beam of intense neutrons at the Irradiation of Chips and Electronics (ICE) House in Los Alamos. For a realistic test, the flight control computer was connected in a closed loop to a flight simulator. According to the results, our new architecture enabled the computer to recover from neutron-induced electronic upsets with no loss of flight control.

Individual cosmic rays were first suspected of causing temporary upsets in the electronics of orbiting satellites in 1975 (Binder et al.). By 1979, electronic upsets caused by cosmic rays in the atmosphere, as well as in space, had been studied in detail (Ziegler and Lanford). In 1992, Taber and Normand found that neutrons generated by cosmic rays in the atmosphere can cause “single-event upsets”

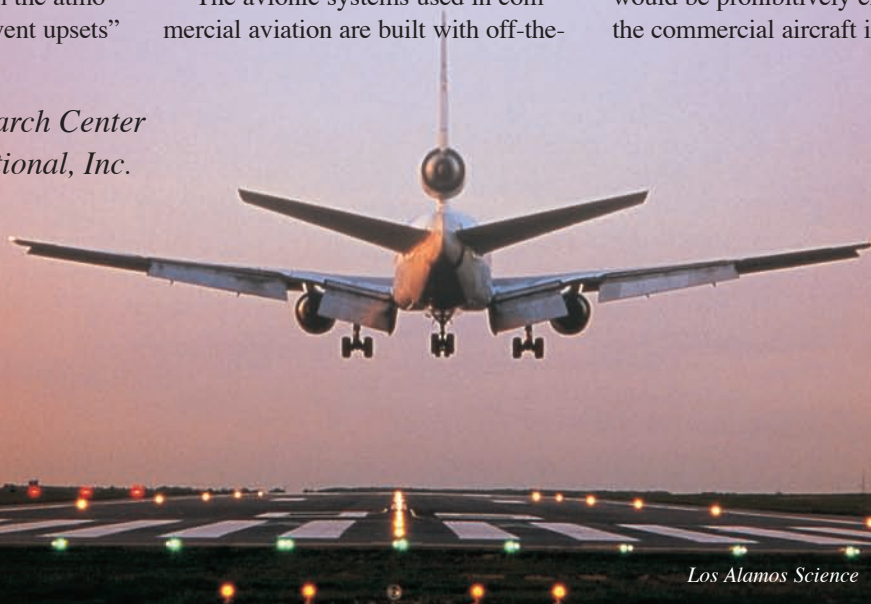
(SEUs) in avionic systems during flight. A Naval Air Systems Command (NAVAIR) Avionics Working Group completed a survey of SEU phenomena and research in 2000 (Chambers). It is now clear that the effects of SEUs may become more severe as the feature sizes and operating voltages of modern microelectronic devices decrease.

The avionic systems used in commercial aviation are built with off-the-

shelf microelectronic devices, which are not specifically designed for the neutron radiation environments in which aircraft fly. Shielding the avionics from atmospheric neutrons in order to overcome radiation effects is not feasible because of the extra weight that would have to be added. Using radiation-hard circuits in those systems would be prohibitively expensive for the commercial aircraft industry.

* *NASA Langley Research Center*

** *Honeywell International, Inc.*



Although the extent of SEUs in avionic systems has not been quantified, it is important to mitigate their potential effects. Our research shows that changing the computer architecture achieves efficiently and cost effectively the required system performance in the presence of atmospheric neutrons.

In the late 1990s, we studied the effects of electromagnetic events, such as lightning and nearby radar, on a flight control computer connected in a closed loop to software simulating the flight of a Boeing 737. For the flight control computer, we developed a new architecture aimed at mitigating the effects of upsets caused by those electromagnetic events (Belcastro 1998a and 1998b, Hess 1997 and 1999, Eure 2001). The new architecture allows a putative flight-control computer to recover its functionality rapidly and is described in the box “A Rollback Rapid-Recovery Computer Architecture” to the right.

In 2002, when the effects of neutron radiation on avionic systems were much discussed in the aviation community, NASA Langley Research Center, the Federal Aviation Administration, Los Alamos Neutron Science Center (LANSCE), Honeywell International, Inc., and Old Dominion University formed a research partnership whose goal has been to study the effects of atmospheric neutrons on flight systems that implement functions whose failure would be catastrophic to the aircraft. We decided to test our new computer architecture developed for studying the effects of electromagnetic events by irradiating the flight control computer with neutrons.

The neutron beam at LANSCE’s Irradiation of Chips and Electronics (ICE) House made these studies possible. The neutrons in the beam have an energy spectrum similar to that of atmospheric neutrons but a million times the intensity. This high intensity

A Rollback Rapid-Recovery Computer Architecture

We tested a new computer architecture to detect and mitigate the effects of “soft” and “hard” faults in a hybrid flight-control computer (Belcastro 1997, Belcastro 1998a). A soft fault occurs when some event (neutron, lightning, and others) unintentionally changes the output of a digital circuit within a computer from “zero” to “one” or vice versa. After the fault, the circuit still functions properly, but the fault introduces an error into the system resulting in anomalous performance. The proper performance of the system will be restored when the change is cleared by placing (for example, by rebooting) the circuit into its proper state. A hard fault occurs when a circuit continues to generate errors because of damage by some event, and proper performance cannot be restored until the circuit is repaired.

At every clock cycle, the fault-detection hardware compares the flight-critical commands computed by the two microprocessors bit by bit (Figure A). If the two commands do not match, they are discarded, and the critical data for a previously computed command are retrieved from protected memory and used instead for computing the new command. Thus, essentially, the flight control computer recovers from the fault by rolling back to a previous command.

Our tests with the LANSCE neutron beam show that a flight control computer with this architecture will recover from SEUs induced by neutrons at the cruise altitudes of commercial airlines.

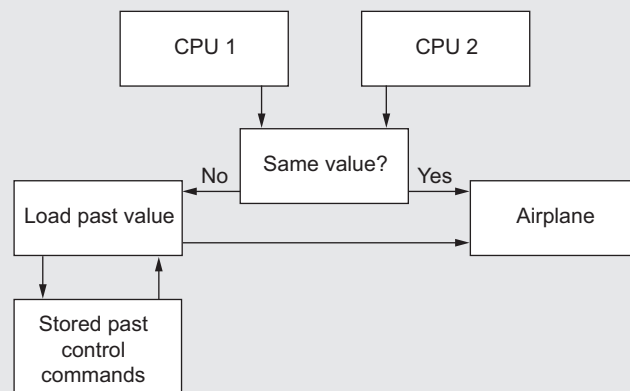


Figure A. Diagram of Rollback Computer Architecture

allows researchers to study neutron-induced SEU effects a million times faster than if the tests were done with natural neutrons in the atmosphere. Dozens of companies, including Honeywell International, Inc., have used the ICE House since 1992 to study the SEU-induced failure rates of individual microelectronic devices

exposed to neutrons (refer to page 96 in the article “The ICE House”). However, ours is the first partnership to have tested the ability of a closed-loop flight control system to recover rapidly from the effects of neutron-induced SEUs. In our experiments at the ICE House, the computer operated successfully while being irradiated.

Testing the Recoverable Flight Control Computer with Neutrons

Test Procedures. We conducted the ICE House experiments between February 20 and February 24, 2004. Figure 1 shows the closed-loop flight control computer positioned in the LANSCE neutron beam at the ICE House. During neutron exposure, the computer controlled the simulated aircraft's ailerons and elevators. Figure 2 identifies these surfaces that control motion. The ailerons control the aircraft's roll and yaw (banking of its wings); the elevators control the aircraft's pitch. The simulated flights were level at 34,000 feet with an option to apply random wind gusts. During the experiments, we recorded the flight conditions provided by the simulation, as well as the commands issued by the flight control computer.

The computer contains microelectronics from the 1990s, whose feature sizes are 1 micrometer or less, an important detail because the smaller the size of the electronics, the higher the SEU rates. As mentioned before, we also used this computer in our studies of electromagnetic events. This computer is a modified version of the computer used in a Boeing 777 Airplane Information Management System (AIMS), and we will therefore refer to it in the rest of this article as the "hybrid" flight-control computer. To use the AIMS computer as a flight control computer, we first stripped it of all AIMS avionic tasks (including flight management, displays, monitoring the airplane's condition, thrust management, digital flight data, and the engine data interface) and then reprogrammed it to conduct flight control commands. The computer has a dual-lock-step architecture, which involves two microprocessors that compute commands simultaneously. If the two computed commands do not match, they are discarded, and

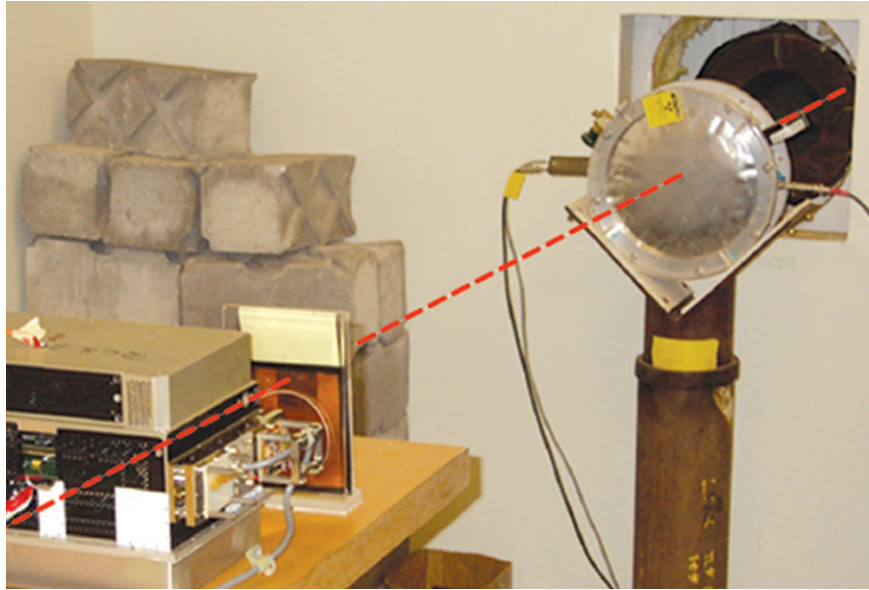


Figure 1. ICE House Tests
The rapid-recovery hybrid flight-control computer is aligned in the neutron beam at the ICE House at LANSCE.

data are retrieved by "rollback" to previously executed commands. Rollback requires additional memory for storage of the previously executed commands. Finally, as we did in our electromagnetic experiments, we connected the computer in a closed loop with software simulating the flight of a Boeing 737 aircraft. (For safety reasons, several flight computers doing the same calculations in tandem are normally used on an actual aircraft.)

For the tests at the ICE House, we replaced the circuit card assembly of the computer's power supply with four external current-limited power supplies. The purpose of these power supplies was to avoid damage to components that might latch up during the experiment. During a neutron-induced single-event latchup, a device gets stuck in a high-current state that could damage it. If the current exceeds the threshold of a current-limiting power supply, the power supply shuts down before the device can be damaged.

We performed 100 tests in which the hybrid flight-control computer was exposed to the neutron beam

and approximately 100 baseline tests in which it was not. Each test lasted 60 minutes unless it was aborted for some reason. Our goals were to measure how many soft faults occurred during a test in which the computer was or was not exposed to the beam and to observe whether the architecture allowed the computer to recover rapidly from any soft faults that occurred during a test. Measuring how frequently a soft fault occurred when a specific portion of the computer was exposed to the neutron beam—whose flux we also measured—allowed us to predict how frequently a fault will occur when that portion of the computer is exposed to the flux of atmospheric neutrons at airline cruise altitudes.

We were able to expose specific groups of the computer's digital circuits during the experiments because the neutron beam's cross section was much smaller than the area of any side of the hybrid flight-control computer. In fact, 11 individual groups, or "positions," were exposed in the tests. Table I provides exposure instructions

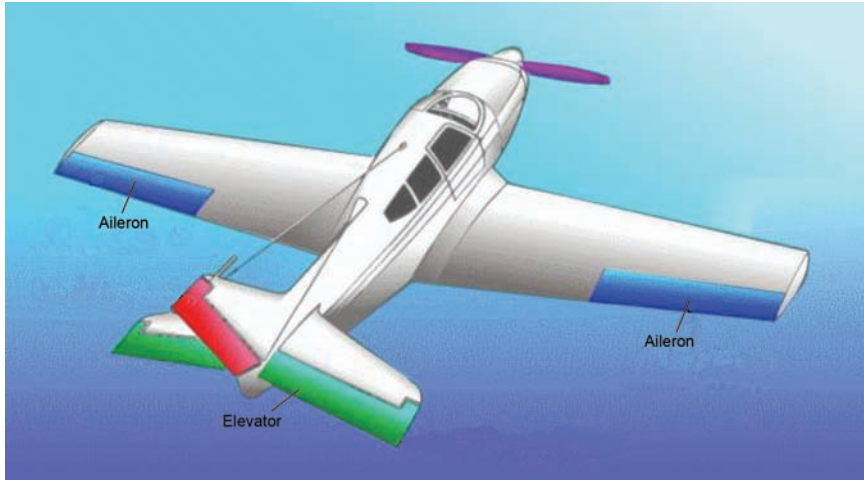


Figure 2. Placement of Ailerons and Elevators
Shown here are the simulated aircraft's ailerons and elevators controlled by the flight control computer during the neutron exposure tests.

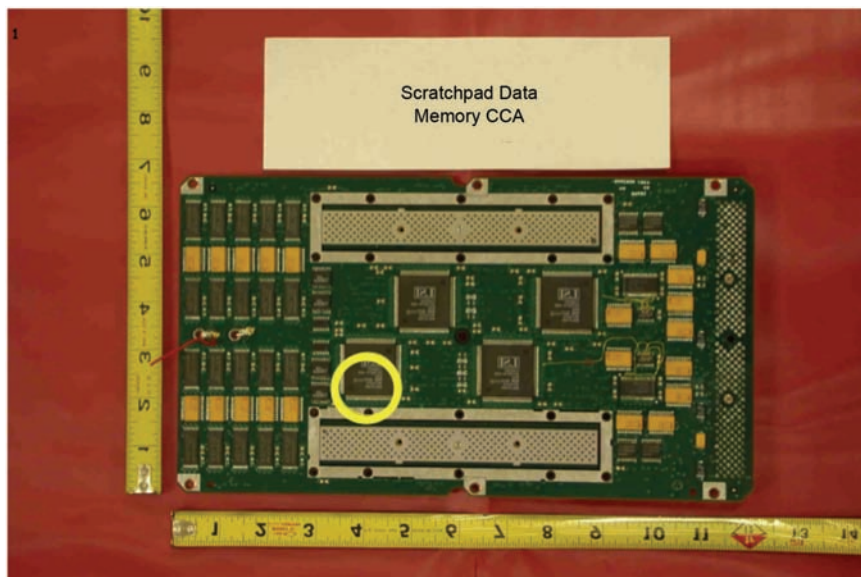


Figure 3. Neutron Beam Exposure for Position 3
For this position, the neutron beam, suggested by the yellow circle, exposed a large portion of the scratchpad data memory in the circuit card assembly (CCA).

for each of the positions of the flight control computer in the neutron beam. Figure 3 is a photograph of the circuit card exposed at position 3.

Our Los Alamos collaborators used Fuji Film image plates to measure the diameter of the neutron beam and a neutron counter to measure the total number of neutrons per square centimeter striking a given position during

the exposure time, or the time-integrated neutron flux. The data obtained from the image plates also allowed us to identify the circuits exposed at each position.

An image plate displays the two-dimensional distribution of the time-integrated neutron flux. When scanned by a laser beam, the image plate emits an amount of light proportional to the

total number of neutrons absorbed at the scan point, an effect called photo-stimulated luminescence. Figures 4a and 4b are false-color images of the data obtained with the image plates. In these images, red indicates high values of time-integrated neutron flux, and purple indicates low values (following the rainbow's color order). This pair of images was obtained by placing an image plate just in front of the spot where the beam entered the flight-control computer and just behind the spot where the beam exited the computer.

Los Alamos collaborators also provided the image plate data in two other forms. Figure 4c shows the image plate data displayed as a black-and-white x-ray image, which allowed us to see exactly which components were illuminated by the neutron beam for a given position. Figure 4d shows horizontal and vertical line scans of the image-plate data, which allowed us to measure precisely the width of the neutron beam in two perpendicular directions.

Knowing the time-integrated neutron flux before the beam entered the flight-control computer for each position allowed us to calculate the probability that an SEU will occur for that position over a given period for the flux of cosmic-ray neutrons at a given flight altitude. We calculated these probabilities from the cross sections measured during the tests, as described below.

Test Results. The measured fluxes of the incident neutron beam were all about a million times the flux of atmospheric cosmic-ray neutrons at an altitude of 34,000 feet. The conditions at the ICE House are therefore ideal for performing accelerated tests of the susceptibility of avionics systems to neutron radiation. As shown in Table I, the total exposure for each position was several hours because we conducted many tests for each position.

Table I also summarizes the

Table I. Exposure Instructions for Computer Positions in the Neutron Beam and Observed Events

Position	Exposure Instructions	Time (h)	Beam Diam. (in.)	Recoveries	Reboots	Lost I/O	Lost Sync.
1	Maximize beam exposure to the RAM ^a on the scratchpad data memory in the CCA ^b .	8.9303	2	2	0	0	0
2	Maximize beam exposure to flash memory on the instruction memory CCA but miss the processor CCA.	7.8761	2	0	0	0	0
3	Target the processor and miss all other chips on the processor CCA.	1.9736	2	1	1	0	0
4	Target the LSI ^c chip next to the processor and miss the processor on the processor CCA.	5.5674	2	0	0	1	0
5	Maximize beam exposure to one CPU ^d on the processor CCA but miss the instruction memory CCA.	2.8312	3	27	1	5	1
6	Same as 5 but target the alternate processor on the processor CCA.	5.1884	2	72	2	3	1
7	Center beam on the first processor.	2.0486	3	12	0	0	0
8	Expose a single CPU on the processor CCA, as much flash memory as possible on the instruction memory CCA, and as many RAMs as possible on the scratchpad data memory in the CCA.	5.8951	3	18	1	2	0
9	Same as 8 but with a 3-inch beam diameter.	2.2188	1	7	0	1	0
10	Same as 8 but with a wider beam to hit the protected rollback area.	5.9294	1	16	1	1	0
11	Same as 5 but with a 3-inch beam diameter.	5.5610	1	145	9	10	6

^aRandom access memory
^bCircuit card assembly
^cLarge-scale integration
^dCentral processing unit

events observed at each position: the number of recoveries during the total exposure, the number of times the flight control computer rebooted, the number of times communication was lost between the flight control computer and the 737 simulator, and the number of times synchronization between the flight control computer and the simulation was lost. When the computer recovered

or rebooted, the simulated flight ended successfully; when communication or synchronization was lost, the flight ended unsuccessfully. The events listed in Table I occurred only when the flight control computer was exposed to the neutron beam. Therefore, all these events were caused in some way by neutron-induced SEUs.

The unsuccessful flights shown

in the table and mentioned above are not relevant to this study because they were caused by the built-in "strike counters," which were part of the AIMS computer and which had not been deactivated before the ICE House tests. The purpose of the strike counters in the AIMS computer was to count the number of times a computer tried to recover within a preset time determined for actual flight

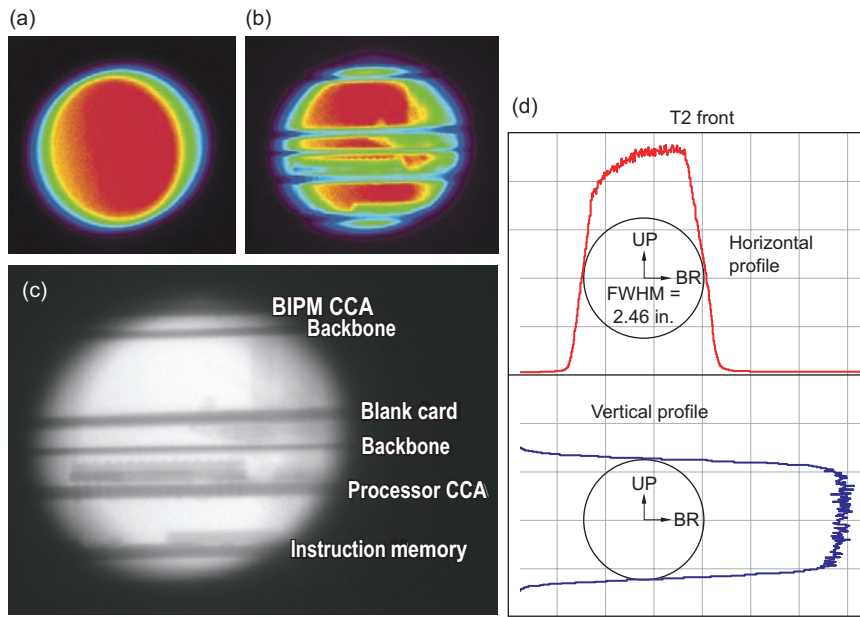


Figure 4. Measuring the Time-Integrated Neutron Flux during ICE House Tests

The false-color images are of the two-dimensional spatial distributions, obtained from image-plate data, of the time-integrated neutron flux (a) entering and (b) exiting the flight-control computer. Red indicates a high value of time-integrated neutron flux; purple, a low value. (c) This “x-ray” display of the image-plate data was obtained from a position just behind the spot where the beam exited the computer. One can see exactly what circuits were exposed to the neutron beam during the test. (d) These line scans of the image-plate data are from a position just in front of where the beam entered the computer. Line scans allowed precise measurements of the beam widths in two perpendicular directions.

conditions and then to shut the computer down by rebooting or stopping it if that number had been exceeded. Because the neutron intensity for the ICE House tests was about a million times that at aircraft cruise altitudes, the rates at which the strike counters rebooted or stopped the computer because of SEUs also increased by about a million times. These artificially high rates do not therefore reflect the actual performance of the rapid-recovery architecture and must be disregarded.

An Example of a Successful Recovery. Figure 5 shows data from a test in which the rapid-recovery architecture successfully mitigated the effect of a neutron-induced SEU. For this test, we selected the flight simula-

tion option of random wind gusts at 1 foot per second. Figure 5a shows the commands sent by the computer (in degrees) to the simulated aircraft’s elevators near the time of the SEU. Figure 5b shows the corresponding commands sent to the simulated aircraft’s ailerons.

The hybrid computer computed new flight-control commands every 50 milliseconds. The time it takes to issue a new command corresponds to a “frame.” Starting at frame 5991, the flight computer began to send the same commands (indicated by constant degrees) because the outputs of its two microprocessors did not agree, indicating the occurrence of a soft fault (for further details on the role of the two microprocessors, see the box “A Rollback Rapid-Recovery

Computer Architecture” on page 105). By frame 5997, however, new computed commands were accepted and sent to the simulated aircraft’s ailerons and elevators, indicating that the computer had recovered from the SEU. The recovery introduced no noticeable perturbations in the flight dynamics while compensating for the neutron-induced error in the control command calculations.

SEU Cross Sections. Table II lists the SEU cross sections (σ), in square centimeters, calculated from our experimental measurements. The probable number of occurrences per unit time divided by the neutron flux [ϕ , in neutrons (n)/cm²·s] for a particular type of event equals the cross section for that type of event—see Equation (1). Thus the number of events equals the cross section times the neutron flux, as shown in Equation (2).

$$\sigma = \text{Number of events per time} / \phi \quad (1)$$

$$\text{Number of events per time} = \sigma \phi \quad (2)$$

Table III lists the probable number of occurrences per flight hour for each type of event. These values were obtained with Equation (1), using the cross sections in Table II and the atmospheric cosmic-ray flux at 34,000 feet of about 1.7 n/cm²·s.

For a commercial transport airplane, one flight year equals 3000 flight hours. Although the values in Table III indicate that SEUs are relatively rare, these rates individually apply to only a portion of one flight-control computer. However, for the air transport fleet, thousands of aircraft fly fully exposed to atmospheric neutrons at any given time. The effects of the SEUs could become significant when the fleet is considered as a whole.

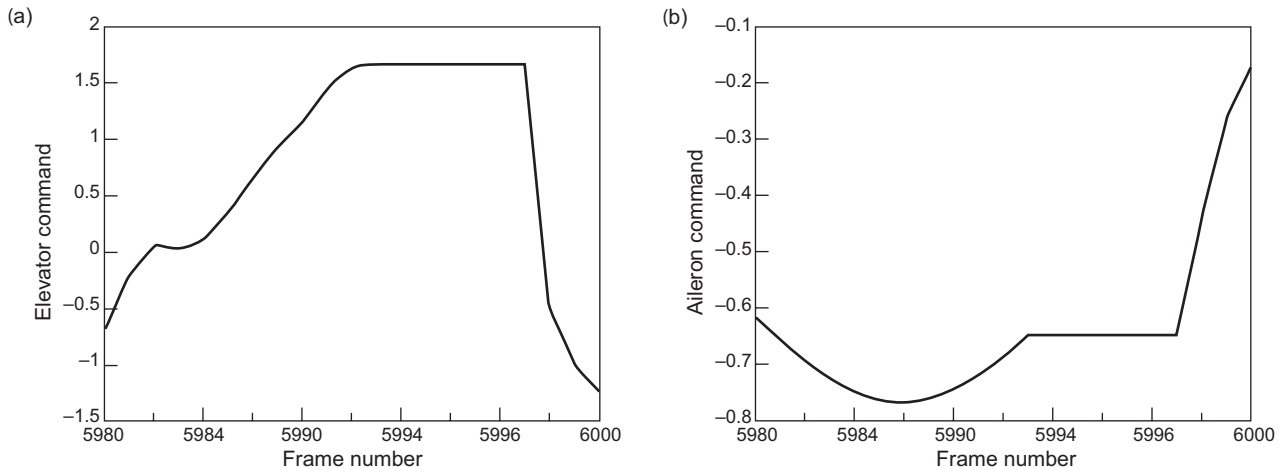


Figure 5. SEU Effects on Flight Control Commands to Elevators and Ailerons

The flight control computer sent commands to the simulation’s elevators (a) and ailerons (b) before, during, and after a neutron-induced SEU. The commands are sent in degrees. New commands are computed every 50 ms, and that amount of time corresponds to a “frame.” The flight command computer began sending the same commands at frame 5991, indicating the occurrence of an SEU at that time. By frame 5997, the flight computer started sending new commands again, indicating that the computer had fully recovered from the SEU.

Table II. SEU Cross Sections for Each Position

Position	$\sigma_{\text{Recovery}} \text{ (cm}^2\text{)}$	$\sigma_{\text{Reboot}} \text{ (cm}^2\text{)}$	$\sigma_{\text{I/O}} \text{ (cm}^2\text{)}$	$\sigma_{\text{Sync.}} \text{ (cm}^2\text{)}$
1	4.28918×10^{-11}	0	0	0
2	0	0	0	0
3	8.80598×10^{-11}	8.80598×10^{-11}	0	0
4	0	0	3.45474×10^{-11}	0
5	1.68654×10^{-9}	6.24644×10^{-11}	3.12322×10^{-10}	6.24644×10^{-11}
6	2.35334×10^{-9}	6.53706×10^{-11}	9.80558×10^{-11}	3.26853×10^{-11}
7	9.55673×10^{-10}	0	0	0
8	5.50792×10^{-10}	3.05995×10^{-11}	6.11991×10^{-11}	0
9	6.36923×10^{-10}	0	9.09890×10^{-11}	0
10	5.57584×10^{-10}	3.48490×10^{-11}	3.48490×10^{-11}	0
11	4.71361×10^{-9}	2.92569×10^{-10}	3.25077×10^{-10}	1.95046×10^{-10}

Future Work

Future experiments will focus on the effects of rollback recovery on closed-loop stability and on exactly which chips and chip sets in the flight control computer are susceptible to neutron-induced SEUs. Identifying these components and subsystems could affect fault-tolerant design strategies if similar components are currently used, or will be used, in avionic systems.

In future work, we will expose an Integrated Modular Avionics (IMA) computer to the ICE House neutron beam. A microwave link will connect the IMA computer in Los Alamos to a flight simulation running at the System and Airframe Failure Emulation Testing and Integration (SAFETI) Laboratory at NASA Langley Research Center in Virginia. During the tests, the IMA computer will run flight management and display software, and the SAFETI

Laboratory will run a simulation of the large transport aircraft for which the IMA computer performs flight management and display functions.

In addition to providing aircraft simulations, the SAFETI Laboratory has a full-scale mockup of an airplane flight deck, so we can close the airplane’s control loop through a human pilot. Such an experiment would determine if a pilot can compensate for upset of the flight management/display system during a simulated flight. ■

Table III. Predicted SEUs per Flight Hour at 34,000 Feet

Position	Recovery	Reboot	Lost I/O	Lost Sync.
1	2.4×10^{-7}	0	0	0
2	0	0	0	0
3	5×10^{-7}	5×10^{-7}	0	0
4	0	0	2×10^{-7}	0
5	9.6×10^{-6}	3.5×10^{-7}	1.8×10^{-6}	3.5×10^{-7}
6	1.3×10^{-5}	3.7×10^{-7}	5.6×10^{-7}	1.9×10^{-7}
7	5.4×10^{-6}	0	0	0
8	3.1×10^{-6}	1.7×10^{-7}	3.5×10^{-7}	0
9	3.6×10^{-6}	0	5.2×10^{-7}	0
10	3.2×10^{-6}	2×10^{-7}	2×10^{-7}	0
11	2.7×10^{-5}	1.7×10^{-6}	1.8×10^{-6}	1.1×10^{-6}

Acknowledgments

John Dimtroff of the Federal Aviation Agency provided timely funding, which expedited this work.

Further Reading

Belcastro, C. M. 1999. Detecting Controller Malfunctions in Electromagnetic Environments: II. Design and Analysis of the Detector. In *Proceedings of the Conference on Control Applications*. (Hawaii, 1999), Vol. 2, p. 1531. Piscataway, NJ: IEEE.

———. 1998a. Ensuring Control Integrity of Critical Systems Subjected to Electromagnetic Disturbances: Problem Overview. In *Proceedings of the American Control Conference*. (Philadelphia, PA, 1998), p. 353. New York: IEEE.

———. 1998b. Monitoring Functional Integrity in Critical Control Computers Subjected to Electromagnetic Disturbances. In *Proceedings of the American Control Conference*. (Philadelphia, PA, 1998), p. 374. New York: IEEE.

———. 1997. Closed-Loop HIRF Experiments Performed on a Fault Tolerant Flight Control Computer. In *Proceedings of the 16th Digital Avionics Systems Conference*. (Irvine, CA, 1997), p. 4.1-40. Piscataway, NJ: IEEE.

Binder, D., E. C. Smith, and A. B. Holman. 1975. Satellite Anomalies from Galactic Cosmic Rays. *IEEE Trans. Nucl. Sci.*, **22**: 2675.

Chambers, R. 2000. "Single Event Upset (SEU) Phenomenon Caused by Low Level/Ground Level Radiation," NAVAIR White Paper.

Eure, K. W. 2001. Fault Detection of a Flight Control Computer in a Harsh Electromagnetic Environment. In *Proceedings of the 20th Digital Avionics Systems Conference*. (Daytona Beach, FL, 2001), Vol. 1, p. 1.E.3-1. Piscataway, NJ: IEEE.

Eure, K., C. M. Belcastro, W. S. Gray, and O. R. González. 2003. Neutron Particle Effects on a Quad-Redundant Flight Control Computer. In *Proceedings of the 22nd Digital Avionics Systems Conference*. (Indianapolis, IN, 2003), Vol. 1, p. 1.B.2-1.

González, O. R., W. S. Gray, and A. Tejada. 2002. Analysis of Design Trade-offs in the Rollback Recovery Method for Fault Tolerant Digital Control Systems. In *Proceedings of the American Control Conference*. (Anchorage, AK, 2002), Vol. 6, p. 4801.

———. 2001. "Analytical Tools for the Design and Verification of Safety Critical Control Systems," International Conference on Lightning and Static Electricity, Seattle, WA, September 11–13, 2001, SAE document 2001-01-2935.

Gray, W. S., O. R. González, and M. Dogan. 2000. Stability Analysis of Digital Linear Flight Controllers Subject to Electromagnetic Disturbances. *IEEE Trans. Aerospace Electron. Sys.* **36** (4): 1204.

Gray, W. S., S. Patilkulkarni, and O. R. González. 2003. Stochastic Stability of a Recoverable Computer Control System Modeled as a Finite-State Machine. In *Proceedings of the American Control Conference*. (Denver, Colorado, 2003), p. 2240.

Gray, W. S., H. Zhang, and O. R. González. 2003. Closed-Loop Performance Measures for Flight Controllers Subject to Neutron-Induced Upsets. In *Proceedings of the 42nd IEEE Conference on Decision and Control*. (Maui, Hawaii, 2003), p. 2465.

Hess, R., and C. M. Belcastro. 2001. "Design and Verification of Robust Architectures for Electronic Systems," International Conference on Lightning and Static Electricity, Seattle, WA, September 11–13, 2001, SAE document 2001-01-2935.

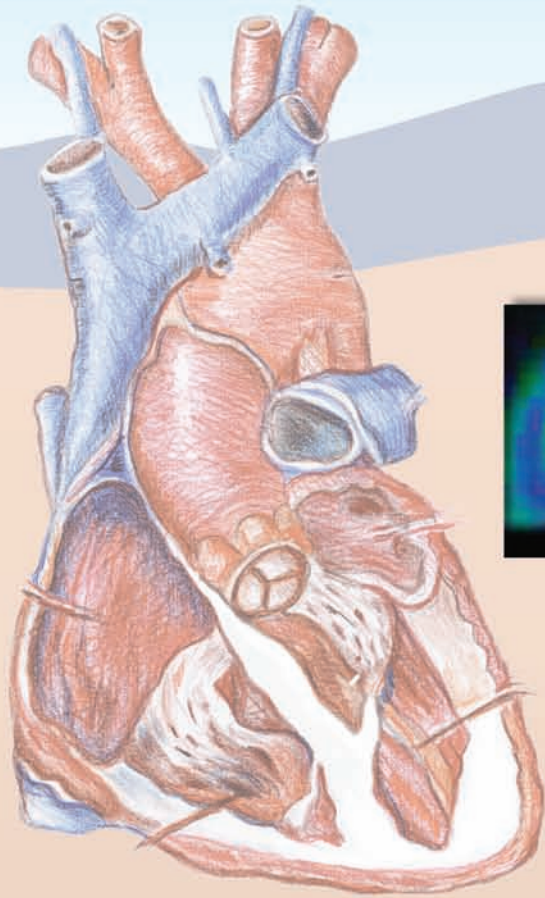
Hess, R. 1999. Options for Aircraft Function Preservation in the Presence of Lightning. In *Proceedings of the 1999 International Conference on Lightning and Static Electricity*. (Toulouse, France, 1999), p. 433.

Hess, R. 1997. Computing Platform Architectures for Robust Operation in the Presence of Lightning and Other Electromagnetic Threats. In *Proceedings of the Digital Avionics Systems Conference*. (Irvine, California, 1997), p. 4.3.9.

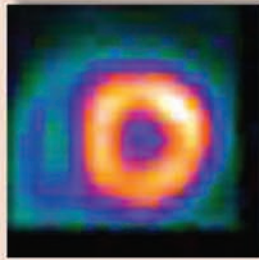
Normand, E., 1996. Single-Event Effects in Avionics. *IEEE Trans. Nucl. Sci.* **43** (2): 461.

Taber, A., and E. Normand. 1992. "Investigation and Characterization of SEU Effects and Hardening Strategies in Avionics," IBM Report 92-L75-020-2, republished as DNA-Report DNA-TR-94-123, Defense Nuclear Agency (February 1995).

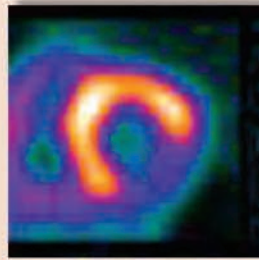
Ziegler, J. F., and W. A. Lanford. 1979. Effect of Cosmic Rays on Computer Memories. *Science* **206** (4420): 776.



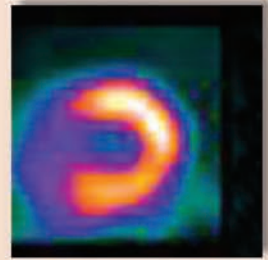
Normal Heart



Single Abnormality



Possible Heart Attack



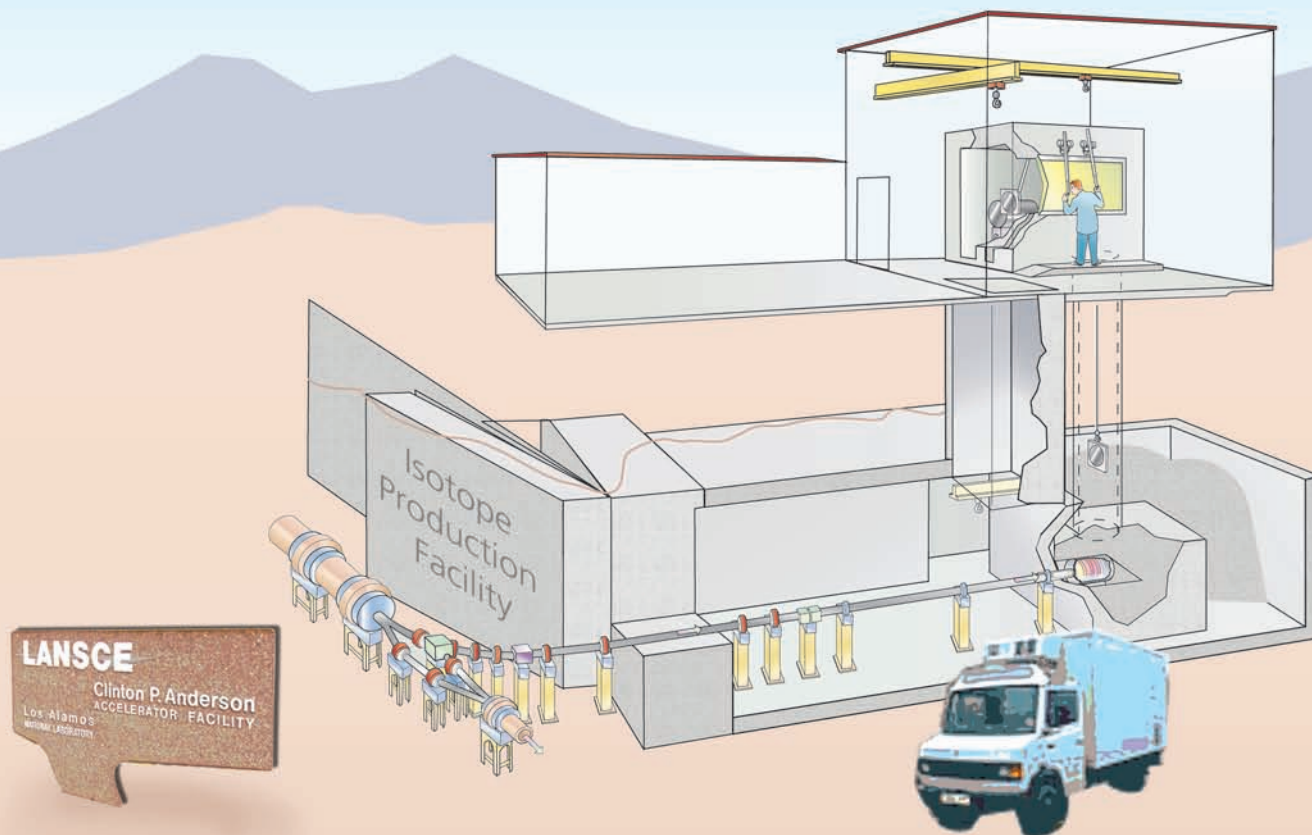
Accelerator Radioisotopes Save Lives

The Isotope Production Facility at Los Alamos

Eugene J. Peterson

On April 11, 2005, the new Isotope Production Facility (IPF) at the Los Alamos Neutron Science Center (LANSCE) delivered its first commercial product, 4.5 curies of the radioisotope strontium-82, to General Electric Healthcare. Strontium-82 is the source for an ideal tracer used in scanning the heart by positron emission tomography. Every month, a supply of 4.5 curies makes it possible for 6,000 patients to receive this potentially life-saving procedure. But strontium-82 is only one of many radioisotopes produced at LANSCE. A whole range of products has been made available by the scores of scientists, engineers, and technicians who have developed new radioisotopes and increasingly sophisticated ways of using them. They have designed the Los Alamos state-of-the-art irradiation facility for an entirely safe, perfectly orchestrated production process. Together with the isotope facility at Brookhaven National Laboratory, the IPF will ensure a steady year-round supply of radioisotopes for medicine, biomedical research, threat reduction, and research into nuclear weapons and fundamental science.





Isotopes of a given element are atoms whose nuclei contain the same number of protons (known as the atomic number, Z) but different numbers of neutrons. Therefore, they are chemically alike but have different atomic masses and different nuclear properties. Every chemical element has one or several isotopes, which can be stable or unstable. Whereas the nuclei of stable isotopes remain unchanged indefinitely, the nuclei of unstable, or radioactive, isotopes disintegrate spontaneously, emitting radiation as they transmute into other isotopes, often of different chemical elements. It is the radiation they emit that makes “radioisotopes” useful for medical applications—both for imaging specific organs for diagnostic purposes and for treatment of diseases such as cancer. Radium was the first isotope used for cancer treatment at the beginning of the 20th century, and its success was much publicized. However, at that time, radioactivity was still a novelty, and some thought that the healing powers of radium

were unlimited. And so, radium was soon advanced as a miracle cure for every ailment and was used indiscriminately. Unfortunately, the long half-life (1600 years) of this radioisotope led to its silent accumulation in the body and, eventually, to numerous deaths. Since that time, it has been known that, to be suitable for medical treatment and imaging, radioisotopes must be short-lived. Short half-lives maximize the radioisotopes’ effectiveness during the limited time of a medical procedure and minimize their side effects to nontargeted organs. Typical half-lives of medical radioisotopes are as long as weeks, days, hours, or even minutes, which means that an administered dose decays away in times of that order (see the box “Radioisotopes: Production, Decay, and Half-Life” on the next page). It is clear that, if the medical procedures they support are to be widely available, medical radioisotopes must be produced artificially on a more or less continuous basis. Today, the demand is increasing as about one in three

hospitalized patients requires a medical procedure involving radioisotopes.

Artificial production of radioisotopes for medicine first began at Berkeley Lab in the 1930s, soon after the invention of the cyclotron. Iodine-131, for example, was produced in small quantities by bombarding tellurium with deuterons, 8 million–electron volts (MeV) in energy, at Berkeley’s 37-inch cyclotron. This radioisotope was used to treat small numbers of thyroid cancer patients. The first large-scale radioisotope production was a spinoff from the development of nuclear energy and nuclear weapons during World War II. In the 1940s, radioisotopes were produced at both nuclear reactors and cyclotrons. Beginning in the 1950s, increasingly high-energy particle accelerators, built by the Department of Energy (DOE) primarily for studies of the fundamental makeup of matter, have also been used to produce radioisotopes for clinical medicine, as well as for research and development. Indeed, since the 1940s, the widespread availability of

medical isotopes and the growth of the radiopharmaceutical industry have been largely a result of successful technology transfer from the DOE and its predecessors, the Atomic Energy Commission and the Energy Research and Development Administration.

Radioisotope Production at Los Alamos

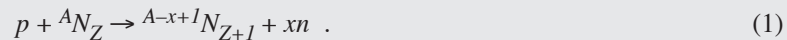
Los Alamos National Laboratory has had a long and prominent tradition in radioisotope production for medicine, biology, and nuclear physics. Beginning in 1974 and up until November 1998, the isotope production station was located at the very end of the proton beam line of what was once the Los Alamos Meson Physics Facility (LAMPF) and later became the Los Alamos Neutron Science Center (LANSCE). There, medium-energy protons—with energies of 800 MeV—were used to irradiate specially designed targets. Following irradiation, the highly radioactive targets were sent to the Laboratory's Chemistry Division, where a special hot-cell facility enables remote handling of the radioactive target materials during chemical separation, processing, and packaging of the radioisotopes of interest. The most important radioisotopes for medicine being produced at Los Alamos were germanium-68, used for calibrating positron emission tomography (PET) scanners; strontium-82, the parent of the very short-lived rubidium-82, used for PET scans of the heart; and the short-lived copper-67, used for research on cancer detection and therapy.

In 1998, as a result of changing programmatic requirements, delivery of the H^+ beam at LANSCE stopped. The Los Alamos Isotope Program would have come to a halt but for the enterprising spirit of the scientists. Through international collaborations,

Medical Radioisotopes: Production, Decay, Source, and Half-Life

Production. An isotope with atomic mass A and atomic number Z , A_ZN , has a nucleus consisting of Z protons and $A-Z$ neutrons held together by the strong force. That isotope can be transmuted to another isotope by bombardment with either protons or neutrons. The nuclear reactions that occur depend on the identity and energy of the incident particle.

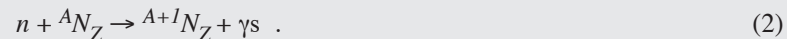
A proton with an energy of up to 100 MeV will typically cause the target nucleus to emit one or more neutrons, producing an isotope of the next higher element (atomic number $Z + 1$) with an atomic mass equal to or lower than that of the original nucleus. The general form of the reaction for one proton absorbed and x neutrons released is



The shorthand for this reaction is ${}^A_ZN(p,xn){}^{A-x+1}_{Z+1}N$. This reaction indicates that protons tend to produce neutron-deficient isotopes.

At higher energies, the protons cause nuclear spallation, in which lighter nuclides break off from the nucleus or from large numbers of neutrons and protons evaporate from the surface.

A neutron with an energy of up to a few million electron volts will typically be captured, producing a heavier isotope of the original element:



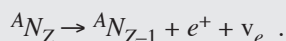
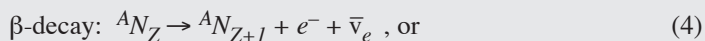
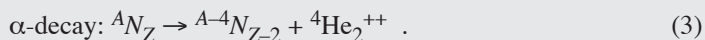
This reaction indicates that neutron capture reactions tend to produce neutron-rich isotopes.

Radioactive Decay. Often the isotopes produced by bombardment with neutrons or protons are radioactive; that is, they are unstable and spontaneously decay, or transmute, to a new isotope through the emission of radiation. Typical radiation emitted in radioactive decay includes alpha particles, which are just helium nuclei (${}^4_2He^{++}$), beta particles, which are either electrons or positrons; gamma rays, which are very high energy x-rays; and neutrinos, which pass through most materials without interacting with them. The energies of alphas, betas, and gammas are typically quite high, and they cause ionization as they pass through matter, which may result in permanent damage, especially to live cells. As shown in Figure A, the two most common decay reactions are alpha and beta decay:

the program continued to be a supplier of germanium-68, strontium-82, and other isotopes with half-lives greater than 15 days in spite of not having its own irradiation facility. Targets were irradiated abroad and returned to the Los Alamos hot cell facility in the Chemistry Division building for chemical separations, purity checks, and delivery of final products to

industrial partners.

In the meantime, a proposal for a new target irradiation facility was put forward and was soon approved for LANSCE. Its construction, funded by the DOE Office of Nuclear Energy, Science, and Technology, was started in 1999 and completed in 2003 at a cost of \$23.5 million. Having been successfully commissioned—all the

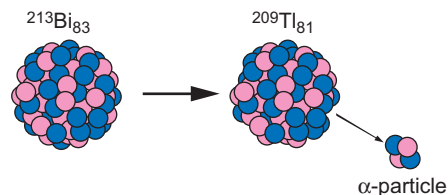


Each radioisotope has a characteristic decay mode and thus emits a particular type of radiation. Radioisotopes that emit alpha particles or electrons are used for cancer treatment because those particles deposit their energy in very short distances. Radioisotopes that emit positrons or gamma rays are used for imaging specific organs and physiological processes. [The positron does not travel far because it annihilates with a nearby electron (its antiparticle), producing two gamma rays that go off in opposite directions and are easily detected by detectors used in PET scanners.]

Radioactivity of a Source. The activity of a radioactive source is a measure of its intensity and is equal to the number of atoms decaying each second. Radioactivity is measured in curies. A curie is the number of decays per second in 1 gram of radium and is equal to 3.7×10^{10} decays per second. The more atoms in the source and the shorter the half-life of the source, the higher its radioactivity.

Radioactive Half-Life. Radioactive decay is a quantum mechanical process; one cannot therefore predict when a particular atom will decay. What can be known is the decay rate, or probability for decay per unit time. That probability is intrinsic to the radioisotope and remains constant in time. Rather than specifying the decay rate of a radioisotope, it is customary to give its half-life T —the time during which an individual atom has a 50 percent chance of decaying. Thus, as shown in Figure B, if there is a collection of identical radioactive atoms, then after one half-life, half of the atoms will have decayed; during the second half-life, half of the remaining half will have decayed, leaving only 25 percent of the original number, and so forth. This exponential fall-off in the number of atoms continues, and after seven half-lives, about 98.8 percent of the original number will have decayed away and become another isotope. Radioisotopes used in medicine are chosen, in part, because they have short half-lives and decay to stable, benign isotopes.

(a) α -Decay of Bismuth-213



(b) β -Decay of Iodine-131

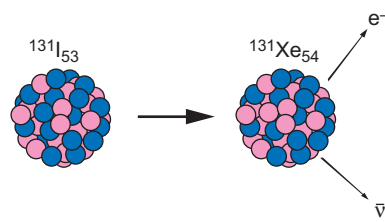


Figure A. Examples of α - and β -Decay

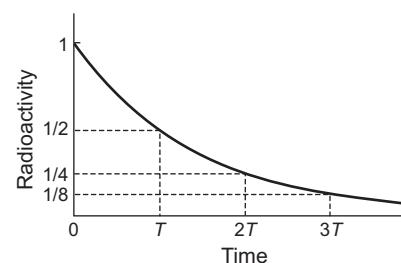


Figure B. Exponential Decay of Radioactivity

design goals were met or exceeded—the new facility became fully operational in the spring of 2004, and the Los Alamos Isotope Program returned to being a self-contained source of radioisotopes, ready to meet the needs of clinical medicine, as well as those of the biomedical, environmental, biological, nuclear physics, nuclear weapons, and homeland security communities.

Design of the New Isotope Production Facility

The Los Alamos state-of-the-art Isotope Production Facility (IPF) was designed to make isotope production more efficient, as well as completely reliable and safe. The new IPF is located near the beginning of the linear accelerator (Figure 1), where

100-MeV protons are diverted to the facility. This lowering of the incident-proton energy from 800 MeV at the old facility to 100 MeV at the new one has resulted in a more efficient process for isotope production.

Bombardment with 800-MeV protons causes nuclear spallation reactions that leave behind a very wide array of isotopes, as protons smash

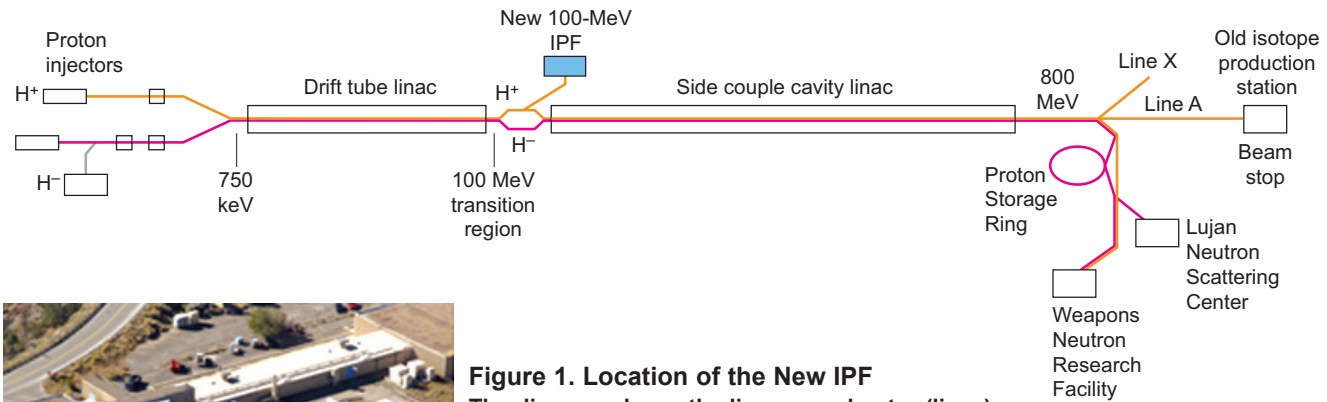


Figure 1. Location of the New IPF
 The diagram shows the linear accelerator (linac) at LANSCE and the locations of both the old isotope production station at the end of the proton beam line and the new IPF, located alongside the accelerator between the Drift Tube Linac and the Side-coupled Cavity Linac. At that point, protons, which have been accelerated to energies of 100 MeV, are diverted to the IPF. The photo shows the exterior of the new IPF.

into target nuclei, sometimes causing chunks of a nucleus to break off and sometimes causing large numbers of neutrons and smaller numbers of protons to evaporate from the nuclear surface. Separating the desired isotopes from the unwanted ones is chemically challenging and time consuming. Only small quantities of the desired isotopes are produced; the radioactive waste, on the other hand, is considerable and must be carefully disposed of. By contrast, when 100-MeV protons hit target nuclei, they release primarily neutrons and occasionally protons and alpha particles, yielding much greater amounts of the desired isotope and lesser amounts of byproduct isotopes and involving a much easier chemical-separation task. Figure 2 illustrates the nuclear reaction processes occurring at 800 MeV and 100 MeV.

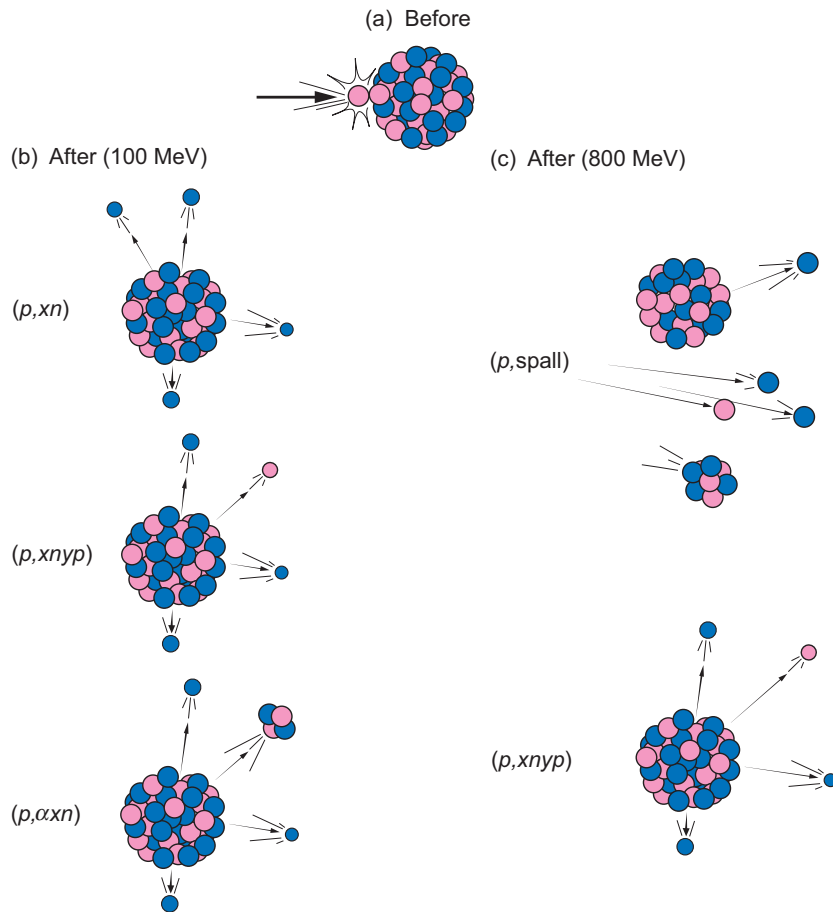


Figure 2. Proton-Induced Nuclear Reactions at 800 and 100 MeV
 (a) At 800 MeV, protons induce spallation reactions that break apart the nucleus into chunks or cause large numbers of neutrons and smaller numbers of protons to evaporate from the nucleus. (b) At energies of up to 100 MeV, protons cause the release of one or several neutrons and sometimes the release of a proton or an alpha particle, in addition to neutrons.

Designing for Safety. The IPF is a radiological facility in which irradiation with protons causes not only the targets but also the environment around the targets to become radioactive. Therefore, our first priority throughout the design and construction phases was to create an environment where workers would be safe during all operations. Ease of pre-

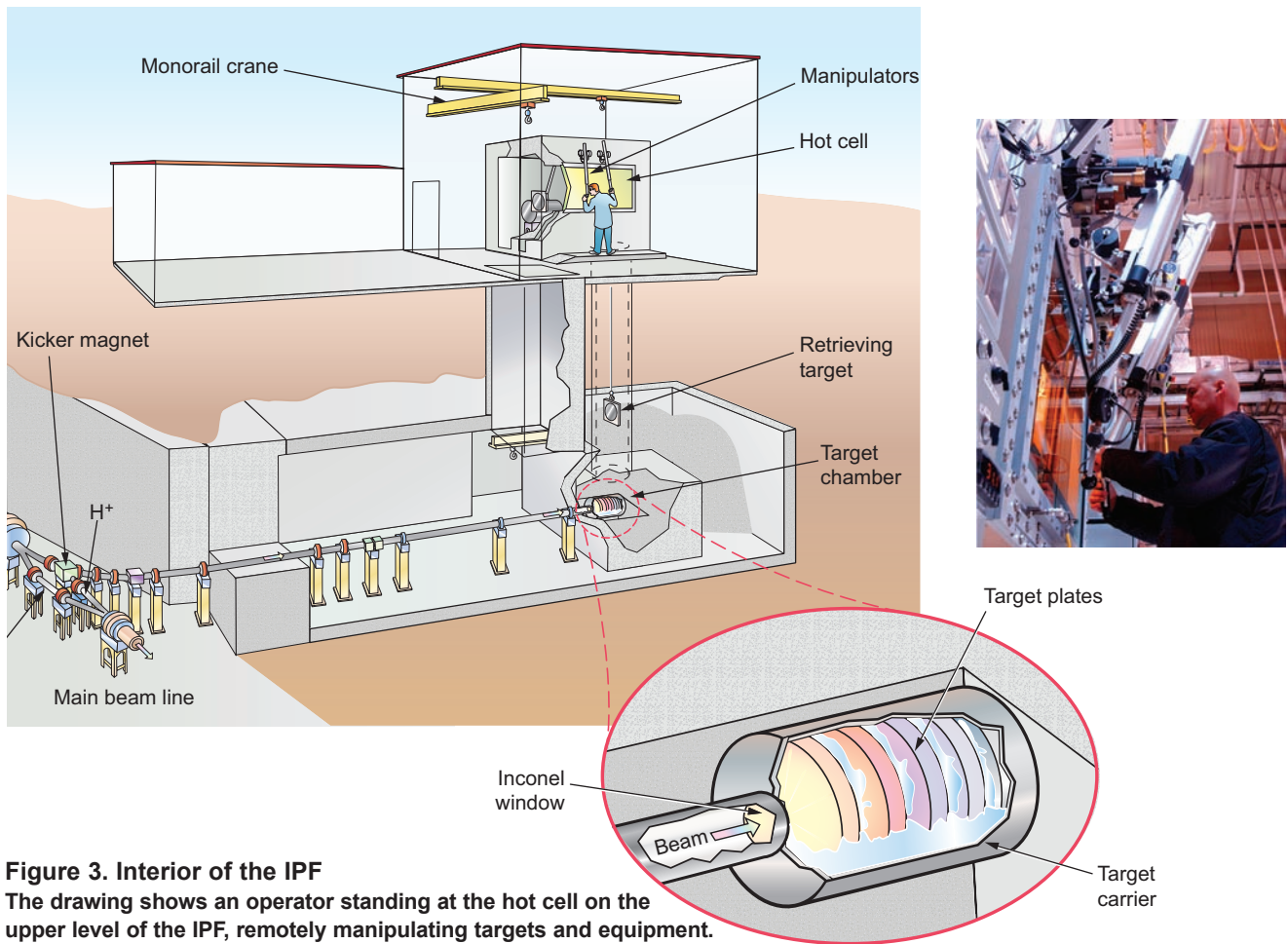


Figure 3. Interior of the IPF

The drawing shows an operator standing at the hot cell on the upper level of the IPF, remotely manipulating targets and equipment. The remote-controlled chain-drive shuttle system is visible, and a stack of targets is in the cave on the lower level, being irradiated with protons. The blowup shows the proton beam entering the target chamber through an inconel window and cooling water flowing through the spaces between the stacked targets. The photo shows a technician remotely manipulating targets in the hot cell.

ventative maintenance and of repair in radiation fields was considered extensively. Although radioisotope production is an inherently dangerous activity, radiation shielding, remote-handling equipment, a closed-loop target-cooling system, and other design features make the facility operationally safe and compliant with all environmental rules and regulations. Moreover, contingency plans ensure that, if anything were to go wrong, safety would not be compromised. For example, multiple safety systems are in place to shut off the proton beam if any facility or irradiation parameters vary from expected values. If an upset condition is detected, the beam is shut

off instantaneously.

Because the proton beam line passes 40 feet underground, the IPF was built on two levels (see Figure 3). Belowground is a thick cave of concrete and lead shielding that houses the targets during irradiation by energetic protons and shields the surroundings from harmful radiation; aboveground is a “hot cell” (an enclosure with windows that shields the upper surroundings from radiation) for the remote handling of both the radioactive targets and the equipment that supports the operation of the beam line. A remote-controlled chain-drive shuttle system connecting the hot cell and the cave is used to

lower targets into the cave for irradiation and raise them back up to the hot cell, where they are put into heavily shielded containers for transport to the Chemistry Division facilities.

Target Configuration for Maximized Production. The target configuration was designed to maximize production of the desired isotopes. It consists of three disc-shaped targets, each 2 inches in diameter. They are stacked in a carrier. Spacers separate individual targets by 5 millimeters (Figure 4). Stacking allows us to vary the energies of the protons impinging on each target from 10 to 90 MeV. The target carrier fits into a

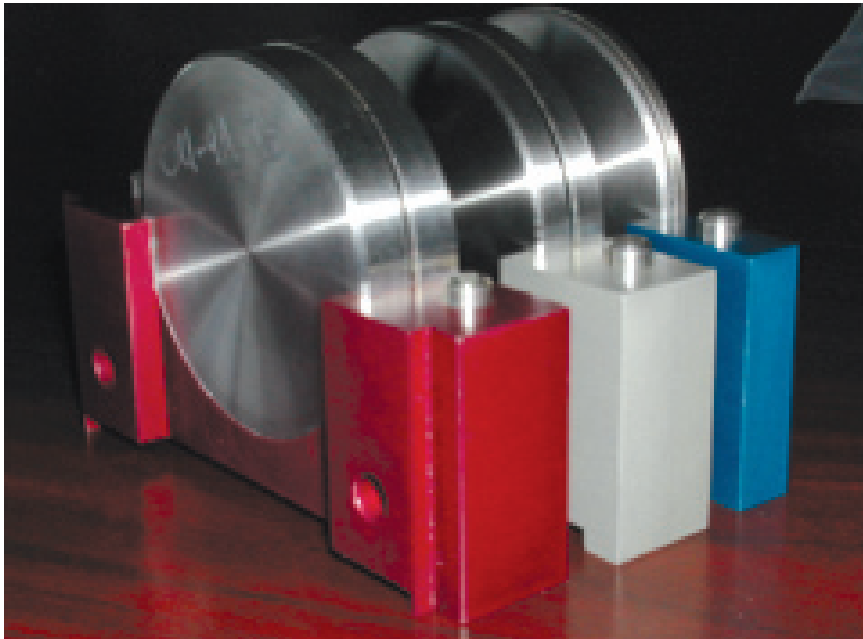


Figure 4. Target Stack and Carrier
Disc-shaped targets of varying thicknesses and compositions are placed in the carrier (shown here without its upper part). The protons travel from left to right through the target stack and lose energy as they undergo Coulomb scattering in the target materials. Protons strike the first (leftmost), second, and third targets in the stack with nominal energies of approximately 90, 65, and 40 MeV, respectively.

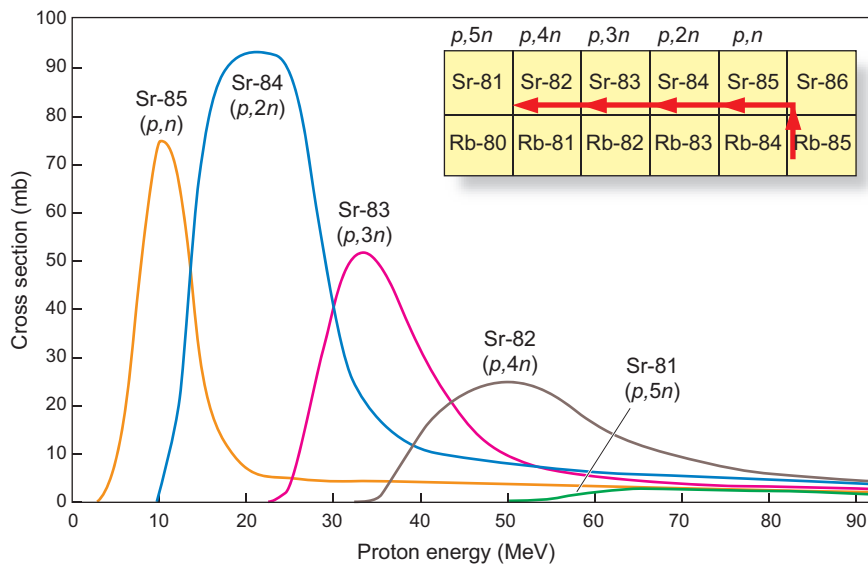


Figure 5. Nuclear Cross Sections for Protons on Rubidium-85
Strontium-82 is made by bombarding with protons the stable isotope rubidium-85. The cross section as a function of energy has a peak at about 50 MeV, and so the rubidium target is placed in the middle of the target stack for maximum production of strontium-82.

target chamber, making a water seal along the chamber walls so that, when the carrier is lowered into the water-cooling loop inside the cave, the full cooling-water stream flows upward along the faces of each target (Figure 3 inset).

During irradiation, 100-MeV protons enter the target chamber through an inconel window and follow successively through the first cooling channel, the first target, the second cooling channel, the second target, the third cooling channel, the third target, and finally, the fourth cooling channel. Target thicknesses are chosen to ensure that protons lose about 20 MeV through Coulomb scattering as they pass through each target. Target positions within the stack are chosen to maximize the rate at which the desired isotope will be produced. For example, when a rubidium-85 target (typically in the form of a chloride) is used to make strontium-82 (the relevant nuclear reaction is $p + \text{Rb-85} \rightarrow \text{Sr-82} + 4n$), it is placed in the middle of the stack because the cross section for that production reaction is greatest for incident protons with energies between 45 and 65 MeV. Figure 5 shows the energy-dependent cross sections for protons incident on rubidium-85 nuclei. Isotope production rates for each target are predicted from Monte Carlo and other calculations and depend on the position in the stack, the reaction cross section, and the target thickness. Irradiation times are determined by those production rate calculations and the amount of material that must be produced to satisfy customer requirements for the isotope.

Closed-Loop Cooling System.

During the irradiation process, heat is generated at an enormous rate. At a maximum proton beam current of 250 microamperes, the energy loss of 20 MeV per proton translates into energy being dissipated into heat at

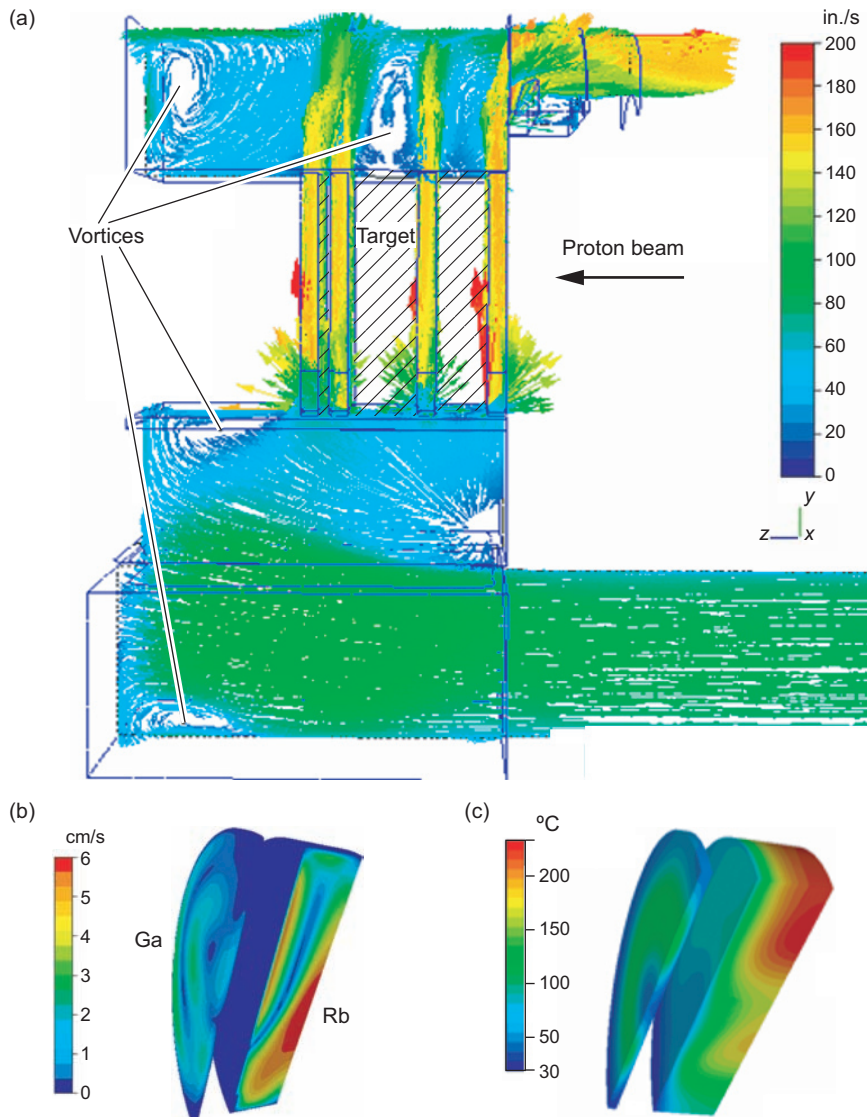


Figure 6. Modeling and Thermal Analysis of the Target-Cooling System This figure shows calculated results for (a) the temperature of the cooling water as it flows past the targets in a closed-loop configuration, (b) the velocity distributions on the faces of the targets, and (c) the temperature distributions on the faces of the gallium and rubidium targets. Similar analyses are performed for each new set of targets.

an average rate of 5 kilowatts per target. If it were not for the cooling system, which was designed to ensure that the targets withstand this maximum rate of heat generation, target and/or encapsulation materials would melt under bombardment and release radioactive material into the cooling system. As an additional precaution against radioactive contamination,

the target-cooling water is circulated in a closed loop to prevent contact with other facility components and the external environment. The final target-cooling configuration is based on extensive modeling using computation fluid dynamics (CFD) and thermoanalysis. For example, calculations showed that sweeping the beam in a circular motion across the

faces of the targets rather than keeping the beam stationary would lower the peak power density, and therefore the thermal effects, on the target by a factor of 2. Calculations also showed that maintaining cooling-water velocities through the channels at values ranging between 2 meters per second (m/s) and 4 m/s would prevent boiling, ensure even flow distribution across all four channels, and maintain adequate cooling of all target and beam window surfaces. Each new target material undergoes CFD modeling and thermoanalysis to determine the optimum combination of beam parameters and cooling-water parameters for material survivability. Figure 6 shows some results from the modeling efforts.

Efficient isotope production at the new IPF is only one step in a carefully orchestrated cycle that begins and ends at Los Alamos. This cycle is presented in the box “The Isotope on Production Cycle” on the next page.

The Los Alamos Products

The Los Alamos Isotope Program fills an important niche in the worldwide market by producing isotopes that are either unavailable or not sufficiently available elsewhere. For example, Los Alamos and Brookhaven, two DOE laboratories, are the only domestic manufacturers of germanium-68, which, as mentioned above, is used as a radiation source to calibrate the detection sensitivity and other instrument parameters of PET scanners. Without germanium-68, the scanners would quickly lose their usefulness in clinical settings.

Los Alamos has also resumed its role as a major producer of strontium-82, the isotope that decays to the very short-lived radiotracer rubidium-82, used for diagnosis of heart disease. In fact, the IPF’s first commercial product was 4.5 curies of strontium-

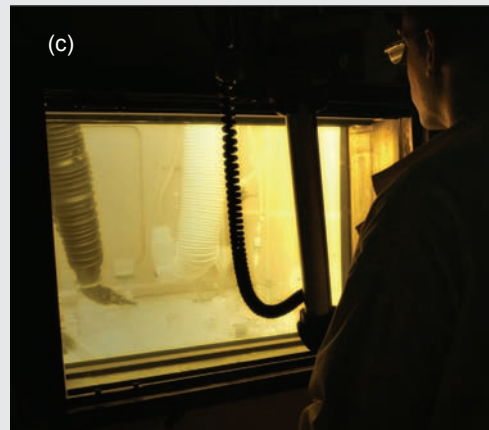
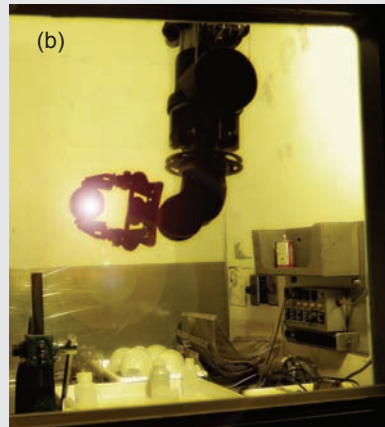
The Isotope Production Cycle

After the targets have been irradiated at the Isotope Production Facility (IPF), they are placed into heavily shielded containers. (a) The container pictured here was specially designed and built in the United Kingdom to ensure safe transport of radioactive materials. It weighs approximately 4 tons and is lifted onto a truck for transport of radioactive targets to the primary Hot Cell Facility at the Laboratory's main radiochemistry site.



Los Alamos workers observe strict safety procedures for placing the irradiated targets into the multipurpose "dispensary" cell, where all materials are received and from which all materials leave the radiochemistry site. This cell is connected to 12 processing cells, where the isotopes of interest are separated from the original target materials and byproducts.

(b) Remote manipulation of an irradiated target inside a processing cell requires considerable skill, which is acquired during rigorous training over a period of two years. The separation processes follow standard chemical procedures, such as ion exchange, solvent extraction, electrochemistry, and distillation. (c) Inside this cell, strontium-82 is being chemically separated from other target materials.



Typically, after initial separation, the chemical solutions containing the desired isotope are further purified in the radiochemistry and analytical laboratories surrounding the Hot Cell Facility. The isotopes are then put in special packages certified for shipment of radioactive material and taken by regular carriers (for example, Federal Express) to their destination. After the radioactive products have outlived their useful life, they are returned to Los Alamos for disposal or recycling. (d) This photo shows a CardioGen-82® generator of the rubidium-82 tracer used in PET scans of the heart. It was returned to the Laboratory after clinical use, and the strontium-82 remaining may be used in the next generator.



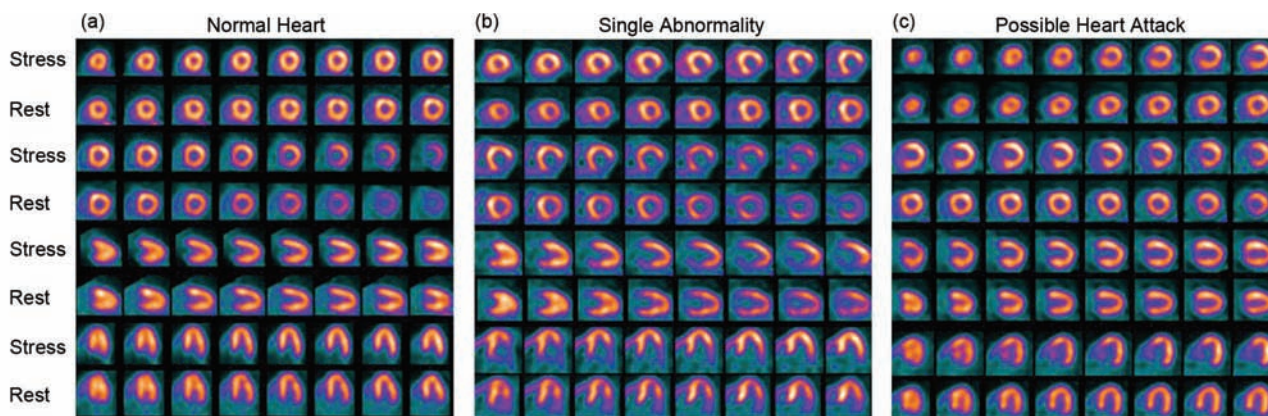


Figure 7. PET Scans of the Heart

These PET scan images of blood flow through the heart show a normal (a), slightly abnormal (b), and severely abnormal (c) heart. The results in (c) indicate the possibility of a heart attack.

82, manufactured at the IPF from a rubidium chloride target. On April 11, 2005, this radioisotope was sent to General Electric Healthcare in South Plainfield, New Jersey, where it was manufactured into approximately 40 biomedical generators, distributed under the trademark CardioGen-82[®]. Those generators produced enough rubidium-82 for 6000 PET scans of blood flow through the heart.

The generator is basically an ion exchange column on which strontium-82 is immobilized. Strontium-82 (with a half-life of 25.4 days) decays continuously to the daughter rubidium-82 (with a half-life of 75 seconds). Right before a PET scan, the proper amount of rubidium-82 is eluted by pumping a specified quantity of saline solution through the generator: Some of the sodium ions in solution exchange places with rubidium-82 ions on the column. The resulting solution containing the rubidium-82 is injected into a patient's bloodstream.

Rubidium, whose chemistry is similar to that of potassium, is preferentially taken up by the heart. As it travels through the bloodstream and the heart, the rubidium-82 ions decay to the stable isotope krypton-82 as they emit a positron. Each positron annihilates with an electron, producing two gamma rays that go off in

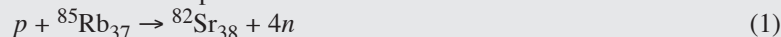
opposite directions. By detecting the gamma rays, the PET scanner can reconstruct where the positron originated, and by recording many such decays, the scanner produces a three-dimensional image of the flow of blood in the heart. This procedure is done fast because, within a few minutes, 99.9 percent of the rubidium injected into the bloodstream has decayed to krypton, which is eliminated as a gas through breathing. Because of the very short half-life of rubidium-82, not only does most of it decay within a few minutes, but so many ions are decaying within a short time that this radiotracer produces a strong signal while it passes through the heart and can easily be detected by PET scanners. (Refer to the box

below for the reactions involved from the production of strontium-82 to the recording of the PET scan.)

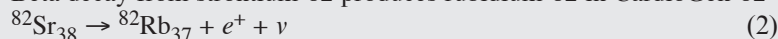
PET studies of myocardial perfusion, or blood flow through the heart, lead to reliable diagnosis of heart function and coronary artery disease (see Figure 7). The PET cardiac procedure distinguishes patients needing further costly intervention from those who do not need such intervention. Translated into economic benefits, the clinical use of the CardioGen-82[®]/PET procedure leads to more than \$10 million in health care economic benefits and untold savings per month through improved cardiac health care. The generator system must be replaced each month because, after one half-life of the strontium-82

Reactions from Isotope Production to Scanning Process

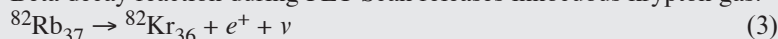
Nuclear reaction produces strontium-82:



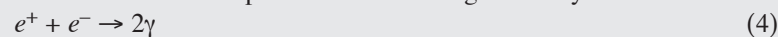
Beta decay from strontium-82 produces rubidium-82 in CardioGen-82[®]:



Beta decay reaction during PET Scan releases innocuous krypton gas:



Positron annihilation produces detectable gamma rays.



Radioisotopes Produced at Los Alamos and Their Applications

Medicine

Isotope	Half-Life	Application
Strontium-82, parent of rubidium-82	25.5 days	Used in cardiac perfusion studies with PET
Germanium-68, positron emitter	270 days	Used in calibration sources for all PET scanners in clinical use
Copper-67, research isotope	2.6 days	Shows promise in cancer detection and treatment
Rhenium-186, research isotope	3.2 days	In high specific activity, potentially strong cancer-cell killer
Arsenic-72, research isotope	26 hours	Used in PET diagnosis and cancer treatment
Arsenic-76, research isotope	26.4 hours	Used in PET diagnosis and cancer treatment
Bromine-77, one of the halogen isotopes	57 hours	Used as versatile tracer label
Lanthanide isotopes, research isotopes		Great potential in medical and biomedical applications

Weapons Applications

Isotope	Half-Life	Isotope	Half-Life	Isotope	Half-Life
Arsenic-73	80.3 days	Europium-149	1 day to 1 year	Tantalum-179	1.8 years
Rubidium-83	86.2 days	Europium-150	36.9 years	Tungsten-181	130 days
Yttrium-88	106.6 days	Terbium-157	>1 year	Gold-195	186 days
Zirconium-88	83.4 days	Terbium-158	>1 year	Bismuth-207	32.2 years
Rhodium-101	5.27 years	Lutetium-173	1.4 years		
Silver-105	1 day to 1 year	Lutetium-174	165 days		

Homeland Security

Isotope	Half-Life	Isotope	Half-Life
Beryllium-7	53.28 days	Strontium-85	64.8 days
Cobalt-56	77.1 days	Cesium-135	2.3 million years
Cobalt-58	70.9 days	Plutonium-237	45.6 days

(that is, approximately 25 days), the generator is considered expired by guidelines from the Food and Drug Administration.

Los Alamos also produces small quantities of radioisotopes whose possible medical applications are in the earliest stages of exploration, and it supports these efforts by charging the user community only a small fraction of the full production costs. In addition, the Laboratory produces isotopes for research in nuclear phys-

ics, biology, nuclear weapons studies, and homeland security. The box above lists a few of the isotopes produced at Los Alamos.

New Tracers, Isotope Availability, and the Future

As the field of nuclear medicine expands and more radioisotopes tailored to solve specific problems are sought, the Los Alamos Isotope

Program is in a good position to increase its contribution to both the production of new radioisotopes and the development of new chelating agents that can bind those isotopes and serve as the delivery system to target organs or target molecules.

The Materials Test Station (MTS), which will be constructed at the end of the linear accelerator, offers several opportunities for Los Alamos to produce an expanded portfolio of isotopes. Targets could be placed in

the intense 800-MeV proton beam reaching the MTS, as well as in the very high flux of spallation fast and slow neutrons that will be generated at the MTS. Irradiation with 800-MeV protons would induce nuclear reactions of the type ($p, xnyp$) and produce neutron-rich isotopes, many of which cannot be produced in a reactor. Irradiation with neutrons at positions available at the MTS can be used to produce large amounts of isotopes, typically produced in reactors, that are not available commercially.

Another opportunity on the horizon is the production of multicurie amounts of high-specific-activity isotopes such as copper-67. Copper-67 (with a half-life of 2.6 days) is a promising medical isotope because it emits an energetic electron (0.6 MeV) that may be useful for cancer therapy, and it also emits a photon that has an energy of 184 kilo-electron volts and can be used to image tumors and assess therapeutic progress. During the 1990s, experiments and a brief human trial supported by the Los Alamos production of copper-67 at LANSCE tested the use of a monoclonal antibody labeled with copper-67 to treat non-Hodgkins lymphoma. The results suggested a high uptake ratio in the cancer tumors relative to the uptake ratio in other tissues. At the time, availability of copper-67 was too sporadic to support continued trials. The new IPF is very well configured to produce multicurie amounts of high-specific-activity copper-67 once isotopically enriched zinc targets are developed that are matched to the range of energies available in the stacked-target configuration of the IPF. In addition, new separation technology must be developed to recycle the enriched target materials, as well as to separate and purify the copper-67 from the target material and irradiation byproducts.

The American Cancer Society estimates that, by the end of 2005, there

will have been 1.4 million new cancer cases and 570,000 deaths from cancer, or 1,500 deaths per day, in the United States. It is obvious that the need for improved methods of early detection and treatment of cancer is acute. Our goal is to combine the Los Alamos expertise in nuclear chemistry and radiochemistry and in the synthesis of molecular inorganic and organometallic complexes with the expertise of the University of California, the University of New Mexico (UNM), and the New Mexico State University in clinical trials and in vivo testing of the stability, biodistribution, and oncological effects of radiopharmaceuticals. The Center for Isotopes in Medicine and the Cancer Research and Treatment Center at UNM will be the focal points for this R&D directed at improved radiotherapy.

In order to develop more-effective therapy agents to target sites in a tumor mass or in cancer cells, we must first develop suitable delivery systems for the radioisotopes, providing the right combination of chemical and biological stability in an easy-to-make ligand. These new ligands would be designed to bind to specific molecular sites in biological systems expressed by tumors/cancer cell lines, thereby becoming potentially unique delivery systems with which to diagnose and treat disease. Designing ligands to bind to specific targets is at the core of how research in nuclear medicine science is being redefined as molecular science. Targets could be any biological molecule found in tissues, individual cells, or genetic material. Once radiolabeled ligands that bind to specific proteins are available, nuclear imaging could monitor specific gene expression (that is, the making of proteins specified by particular genes) and thereby provide greater understanding of developmental biology, cancer induction and pathogenesis, and ultimately, the clinical detection of inherited or acquired

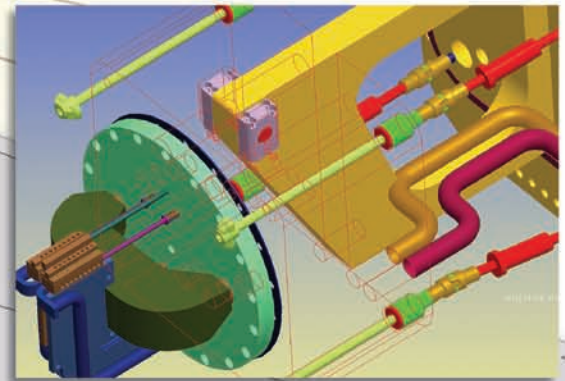
diseases. The capability to image the expression of any gene in any person would likely yield profound health benefits to society. Antisense radiopharmaceuticals (DNA-based targeting agents) analogous to existing chemotherapeutic drugs would be optimized for in vivo imaging by PET or single-photon-emission computed tomography (SPECT).

To date, PET imaging using molecules radiolabeled with fluorine-18 and iodine-124 have been quite promising. We expect that many high-specific-activity and high-purity radioisotope tracers will be available from the new IPF and will be key to advances in science and medicine. Compared with the old isotope station at Los Alamos, the new IPF has doubled its operating period every year with only minimal cost increase. In fact, the facility is designed to operate when the rest of LANSCE goes through maintenance outages. Above all, the efficiency, safety, and reliability of operations at the new IPF ensure domestic and international market demands for most isotopes for years to come. ■

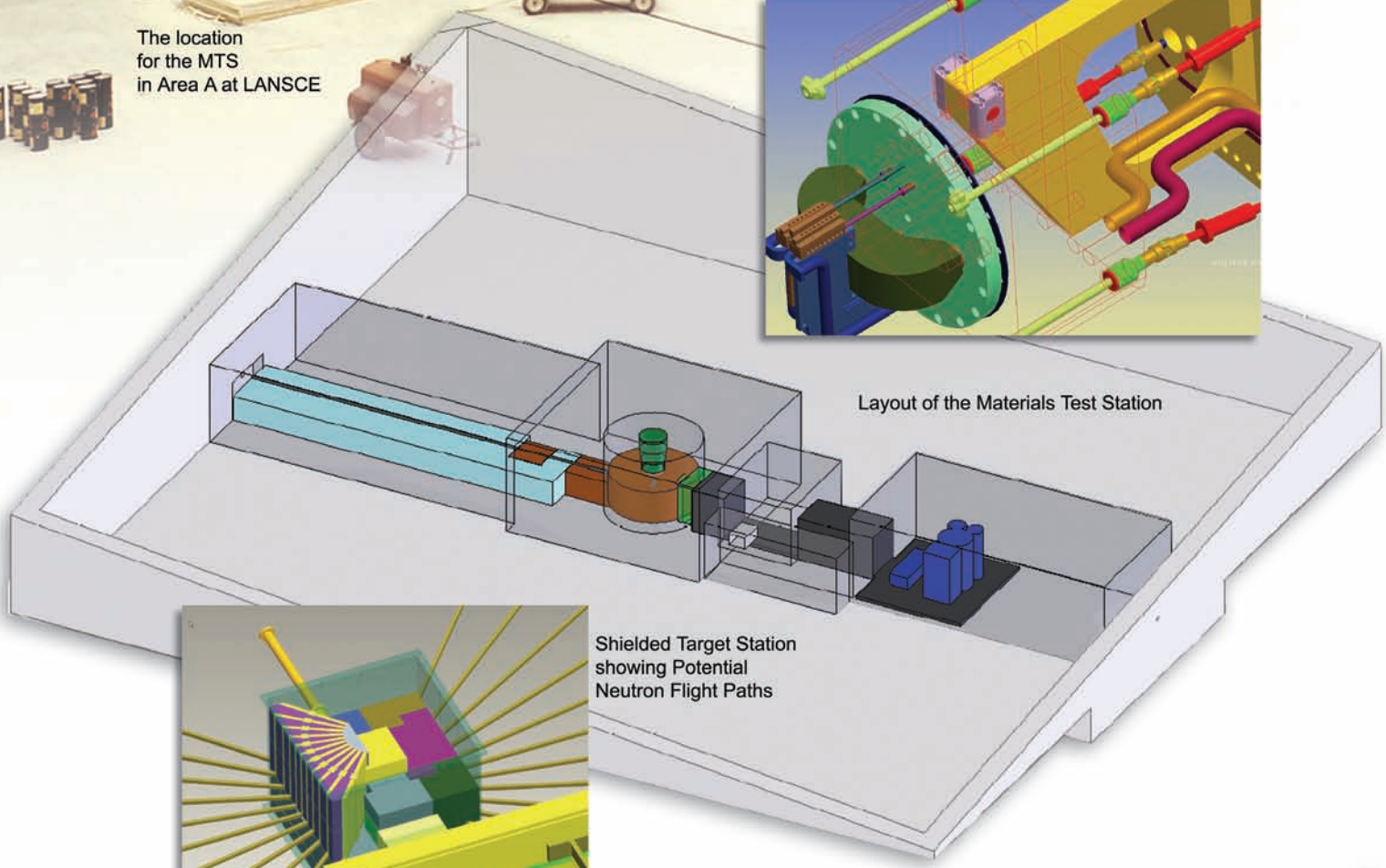


The location for the MTS in Area A at LANSCE

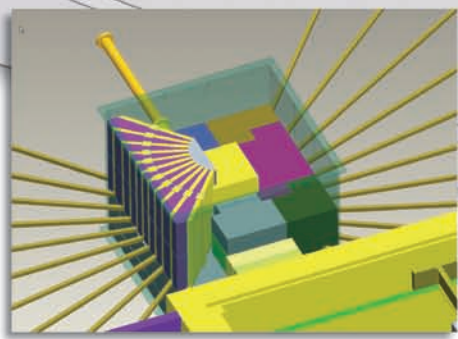
Target Assembly

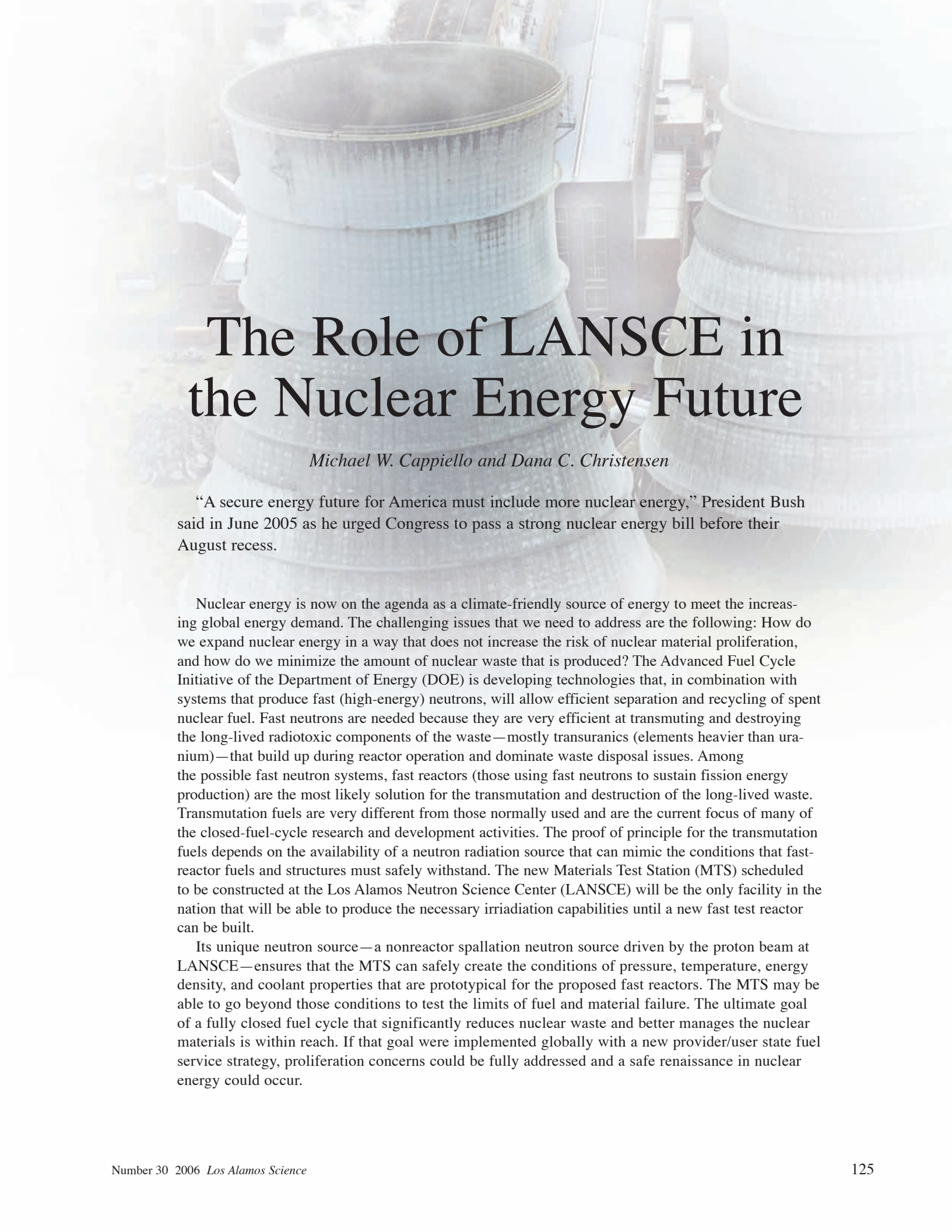


Layout of the Materials Test Station



Shielded Target Station showing Potential Neutron Flight Paths





The Role of LANSCE in the Nuclear Energy Future

Michael W. Cappiello and Dana C. Christensen

“A secure energy future for America must include more nuclear energy,” President Bush said in June 2005 as he urged Congress to pass a strong nuclear energy bill before their August recess.

Nuclear energy is now on the agenda as a climate-friendly source of energy to meet the increasing global energy demand. The challenging issues that we need to address are the following: How do we expand nuclear energy in a way that does not increase the risk of nuclear material proliferation, and how do we minimize the amount of nuclear waste that is produced? The Advanced Fuel Cycle Initiative of the Department of Energy (DOE) is developing technologies that, in combination with systems that produce fast (high-energy) neutrons, will allow efficient separation and recycling of spent nuclear fuel. Fast neutrons are needed because they are very efficient at transmuting and destroying the long-lived radiotoxic components of the waste—mostly transuranics (elements heavier than uranium)—that build up during reactor operation and dominate waste disposal issues. Among the possible fast neutron systems, fast reactors (those using fast neutrons to sustain fission energy production) are the most likely solution for the transmutation and destruction of the long-lived waste. Transmutation fuels are very different from those normally used and are the current focus of many of the closed-fuel-cycle research and development activities. The proof of principle for the transmutation fuels depends on the availability of a neutron radiation source that can mimic the conditions that fast-reactor fuels and structures must safely withstand. The new Materials Test Station (MTS) scheduled to be constructed at the Los Alamos Neutron Science Center (LANSCE) will be the only facility in the nation that will be able to produce the necessary irradiation capabilities until a new fast test reactor can be built.

Its unique neutron source—a nonreactor spallation neutron source driven by the proton beam at LANSCE—ensures that the MTS can safely create the conditions of pressure, temperature, energy density, and coolant properties that are prototypical for the proposed fast reactors. The MTS may be able to go beyond those conditions to test the limits of fuel and material failure. The ultimate goal of a fully closed fuel cycle that significantly reduces nuclear waste and better manages the nuclear materials is within reach. If that goal were implemented globally with a new provider/user state fuel service strategy, proliferation concerns could be fully addressed and a safe renaissance in nuclear energy could occur.

Trends in Global Nuclear Energy—The Role of LANSCE

For decades, the world has recognized that nuclear-material management presents both significant advantages (energy production, health care, industrial growth, and zero greenhouse gas emissions) and significant concerns (nuclear-weapon proliferation and radioactive waste). Today, at least 33 countries utilize nuclear power, and every corner of the globe has been impacted by nuclear medicine. The international growth in nuclear energy is accelerating, along with research and development of closed-fuel-cycle technologies. Closed-fuel-cycle technologies are those that recycle and extract energy from the transuranics, elements heavier than uranium that are produced in reactors by neutron bombardment of uranium nuclei. The need to store nuclear waste for thousands of years stems from the presence of these transuranics. Their elimination through a closed fuel cycle is highly desirable because it would drastically reduce long-term storage requirements.

Closing the fuel cycle also addresses the issue of nuclear material proliferation as one of the major transuranics (plutonium) is recycled and never leaves the system. A new global governance regime, whereby the major industrialized nations provide fuel services to user nations, will allow the safe and controlled expansion of nuclear power to developing countries.

Nuclear Energy: A Sustainable Carbon-Free Energy Source

Globally, burning fossil fuels is the primary source of energy for transportation and electricity. Transportation

requires approximately one-third of the total energy obtained from this source. Such a strong reliance on heavy fossil fuels and the resulting emissions of carbon dioxide are causing global environmental impacts. A transition to noncarbon-emitting technologies is needed now, and nuclear energy is considered one of the primary climate-friendly sources of energy for the future. A recent Massachusetts Institute of Technology report calls for expansion of nuclear power to help solve the pending environmental crisis (Deutch et al. 2003). This study advocates a greatly expanded nuclear-power sector, growing from the current power base of 366 gigawatt-electric (GWe) to a worldwide capacity of 1000 GWe

"Nuclear energy is the only available technology that can replace fossil fuels on a large scale." —Patrick Moore, founder of Greenpeace, keynote address to the American Nuclear Society, November 2005.

by mid-century and eliminating up to 25 percent of carbon emissions. The driving force behind this recommendation is that the "nuclear option should be retained precisely because it is an important carbon-free source of power." The directors of the nation's premier national laboratories have called for a similar expansion of nuclear power, aimed at achieving a sustainable nuclear-fuel cycle to control materials proliferation and waste generation (Six Laboratory Group 2003). The resulting large reduction in carbon emissions makes it imperative that nuclear power play a significant role in the future energy mix.

Consistent with the desire to reduce greenhouse emissions, the transportation sector is aggressively pursuing hybrid vehicle technology as

well as hydrogen fuel cell technology for future vehicles. The problem is that hydrogen is not an energy source, but rather a storage medium. It takes energy to produce hydrogen, and the current method (burning methane in the presence of steam) produces carbon dioxide as a byproduct. Once again, nuclear energy is the front and center option for producing hydrogen cleanly, and the DOE Nuclear Hydrogen Initiative is researching the best and most efficient options for doing so.

The Components of Spent Nuclear Fuel

A major challenge to increased use of nuclear power is the disposition of the spent nuclear fuel, which contributes to long-term radiotoxicity (a potential source of negative health effects in the long term) and thermal heat load in a nuclear-waste repository. In the once-through fuel cycle shown in Figure 1a, a typical nuclear-fuel assembly from a light-water reactor is discharged about 18 months after generating about 41 megawatt-days of energy per kilogram of fuel. It is called "spent" fuel because uranium-235, the fissile isotope of uranium, has been fissioned, or "spent," to the extent that a nuclear chain reaction can no longer be sustained. The composition of the spent-fuel assembly is shown in Figure 1b. A large fraction (95.5 percent) is the original uranium fuel, which exhibits very low radioactivity. The products of uranium fission (primarily cesium and strontium) make up about 3.3 percent of the waste and are intensely radioactive. However, because of their relatively short half-lives, they decay to stable elements in about 300 years and thereafter represent no long-term environmental challenge. Technetium and iodine are long-lived fission products that contribute to long-term radiotox-

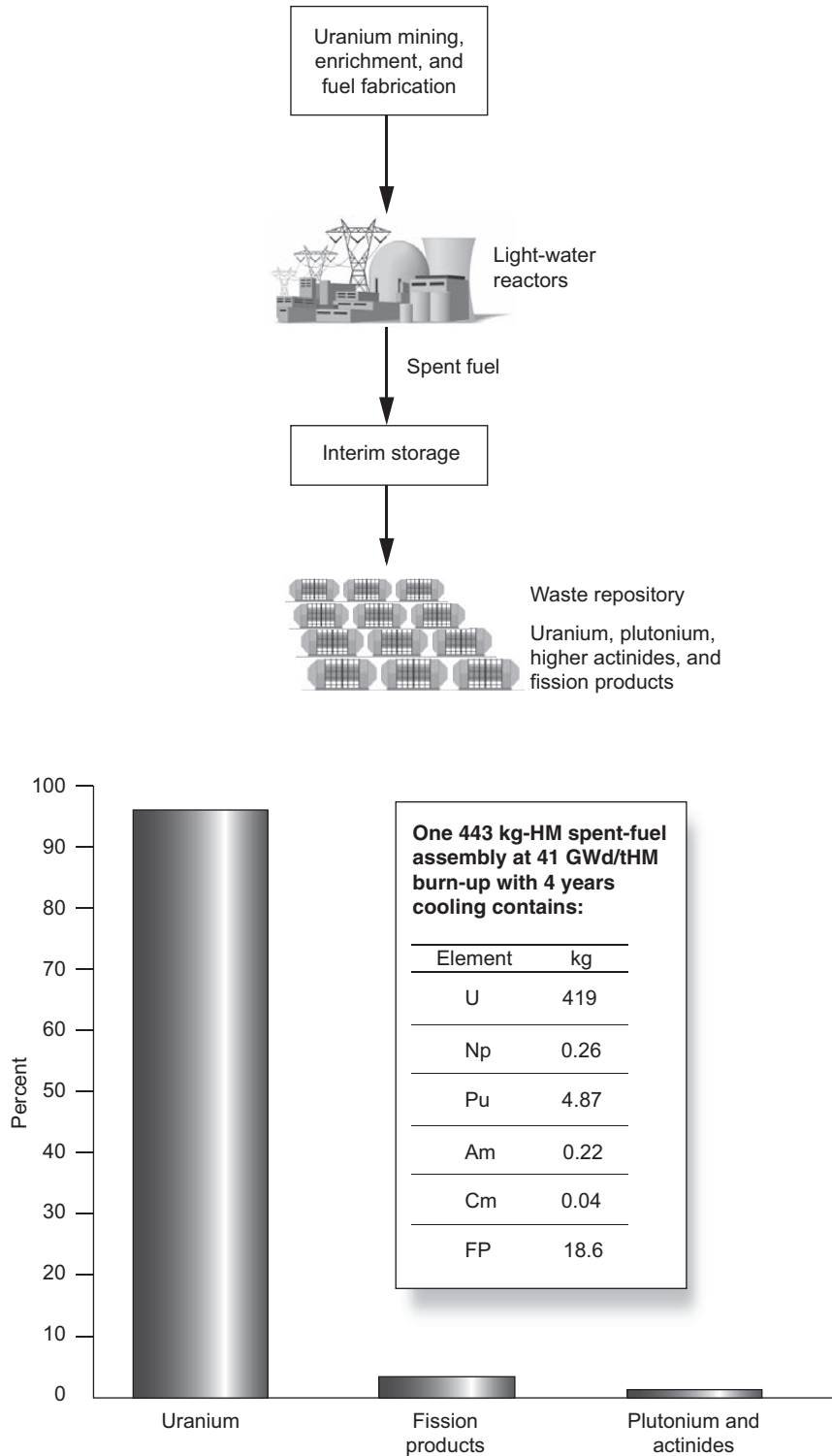


Figure 1. The Once-through Fuel Cycle and Constituents of Spent Fuel
 (a) For the once-through or “open” fuel cycle, spent fuel from light-water reactors is stored and then sent to the repository. (b) Plutonium and the other very long-lived radioactive elements make up only about 1% of the spent fuel from a typical light-water reactor.

icity and therefore must be dealt with separately. During the fuel’s residence in the reactor, transuranic elements (plutonium, neptunium, americium, and curium) are created through neutron interactions with uranium. They make up only about 1 percent of the waste but are radioactive for several hundred thousand years and contribute significantly to the long-term heat load. Essentially, it is this 1 percent fraction of the spent fuel that is the primary challenge of nuclear waste and proliferation.

Because only the transuranics and some fission products require isolation for long periods, opportunities exist for significantly reducing the number of repositories through spent fuel recycling. For example, uranium can be separated and reused or stored; the intensely radioactive fission products can be separated and allowed to decay away; and transuranic elements, which are mostly fissile, can be recycled and fissioned in a neutron environment, providing an important additional source of energy.

Spent Fuel Options: The Once-through Cycle

The current U.S. strategy for nuclear-waste disposal is to send spent fuel directly to the Yucca Mountain underground nuclear-waste repository (to be built in Nevada pending final approval) without processing or recycling (see Figure 2). Initially implemented during the Carter administration, a directive that prohibited reprocessing and plutonium separation essentially required the nuclear industry to adopt the once-through fuel-cycle scheme. Even though this directive was later rescinded by President Reagan, the commercial U.S. nuclear industry has not pursued reprocessing for economic reasons: The current price of enriched uranium is a relatively small fraction



Figure 2. The Planned Nuclear Waste Repository at Yucca Mountain
The planned geologic repository at Yucca Mountain, Nevada, is designed to hold 63,000 tonnes of commercial spent nuclear fuel. A decision on a second repository is needed by 2010 in order to keep pace with the accumulation of waste. The inset suggests the many tunnels belowground that will house the waste.

of the total cost of the reprocessing operation. In the once-through, or “open,” fuel cycle, the requirement to isolate spent fuel for thousands of years derives from the small fraction of long-lived radiotoxic constituents present in the spent fuel assemblies that are left intact at disposition and are not reprocessed or recycled (Figure 1).

Repositories Needed for the Once-through Cycle. Currently, the United States is generating 2100 tonnes of spent nuclear fuel per year. At this generation rate, Yucca Mountain’s legislated capacity (63,000 tonnes) will only hold 30 years’ worth of spent nuclear fuel and this limit will be reached in 2015. Yucca Mountain’s technical limit, as opposed to its legislated limit, is estimated to be two to three times greater, and expanding its legislated limit may offer a solution for additional

spent-fuel disposal in the near term. However, many growth scenarios for nuclear energy would require commissioning similar repositories at a much more frequent rate than every 30 years to dispose of the increasing inventories of spent fuel. As pursued in a once-through fuel cycle, the direct disposal of spent fuel requires geologic formations that can ensure safe containment of nuclear products for millennia. Such environments must protect the biosphere from catastrophic release of transuranics (plutonium, neptunium, americium, and curium) and long-lived fission products. These environments must also be sufficiently robust to deal with long-term heat management issues and to offer protection from possible covert efforts to recover nuclear-weapon materials, such as plutonium.

The disposition of spent fuel is also a global problem. Assuming a conservative energy growth, the

International Atomic Energy Agency (IAEA) estimates that, worldwide, spent-fuel inventories will be greater than 400,000 tonnes by 2020. Direct disposal of this amount of fuel would require seven repositories the size of the Yucca Mountain repository, and none exist today. According to other IAEA projections, by 2050, the installed global nuclear-power capability could be three to six times larger than it is at present. Under such scenarios, as many as 30 Yucca Mountain–equivalent repositories would be needed by mid-century, with the number rising to 100 by century’s end. This is clearly an unsustainable condition.

In the once-through fuel cycle, the fuel discharged from a reactor does not run the risk of being diverted because of its high radiation level resulting from the buildup of fission products. This self-protection feature, however, disappears within

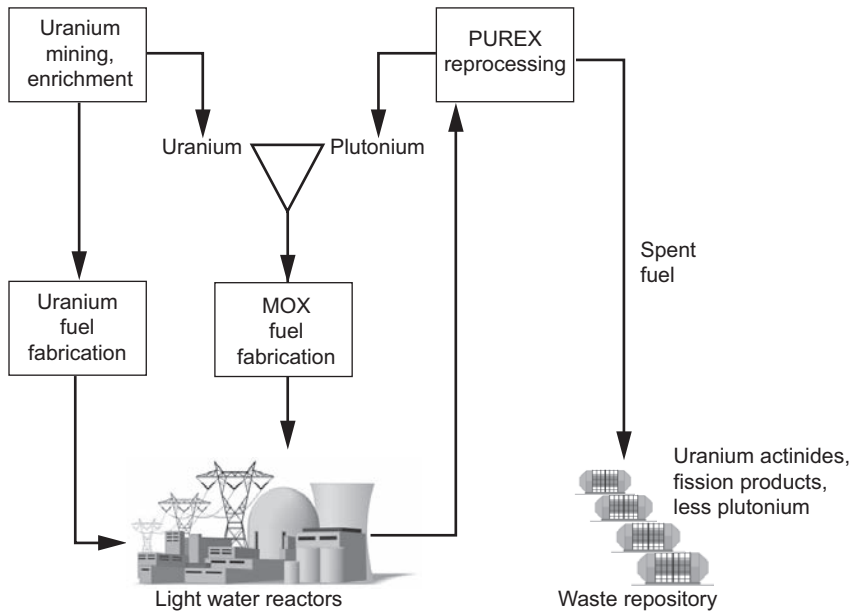


Figure 3. The MOX Intermediate Fuel Cycle
 In the conventional plutonium recycle scheme, spent uranium fuel is reprocessed, and plutonium is extracted and reused in mixed-oxide fuel. France uses this scheme to reduce their waste volume by a factor of 4 over the once-through cycle.

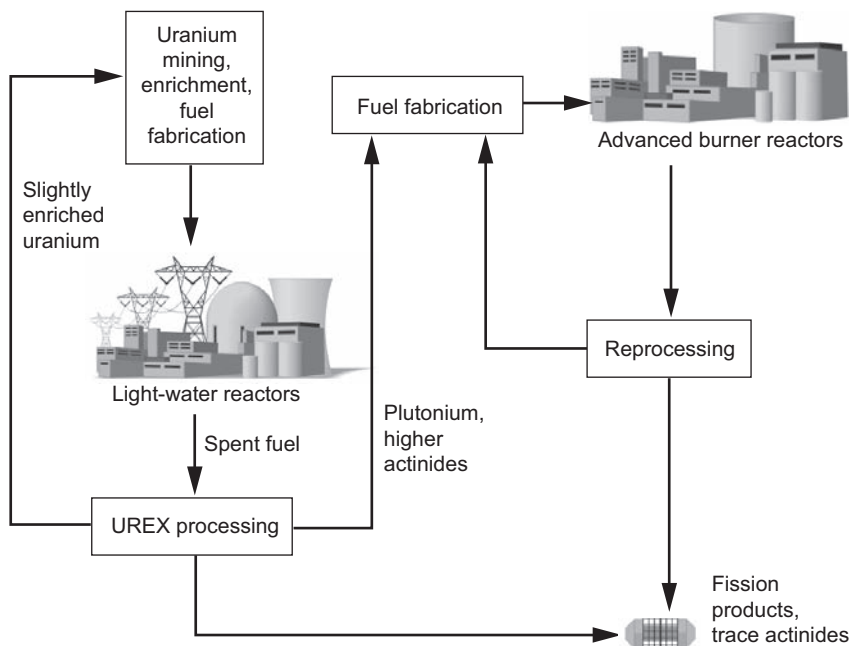


Figure 4. The Closed Fuel Cycle
 In a closed fuel cycle, the transuranics are extracted from the spent fuel and transmuted in fast-spectrum reactors.

about 100 years as the short-lived fission products decay away and the radiation level in the spent fuel drops. After such a period, a large geologic repository containing thousands of fuel elements becomes, literally, a plutonium mine because the plutonium in the spent fuel remains intact for thousands of years. A repository the size of Yucca Mountain would contain more than 600 tonnes of plutonium. Consequently, the only permanent solution to the risk of plutonium being diverted is its destruction.

New Closed-Cycle Technologies to Increase Repository Capacities

The capacity of the Yucca Mountain repository is largely driven by the heat load of the spent fuel. Removal of specific isotopes that dominate the heat load can significantly increase the capacity of the repository. For example, if both the short-lived isotopes of cesium and strontium and the long-lived isotopes of plutonium and americium were removed from the waste, the repository's capacity could be increased by more than a factor of 50. It is therefore important to develop technologies aimed at efficiently separating and then destroying the heat-producing elements in the waste.

An Intermediate Option for Spent Fuel: MOX. The separation of uranium and plutonium from the spent nuclear fuel is a widely known technology already used in several countries. France, Great Britain, Japan, and Russia reprocess their spent fuel and partially recycle it into new fuel. Plutonium is separated from the waste, mixed with uranium to make mixed-oxide fuel (MOX), and then reintroduced as fuel in their reactors (see Figure 3). The world's industrial-scale experience in repro-

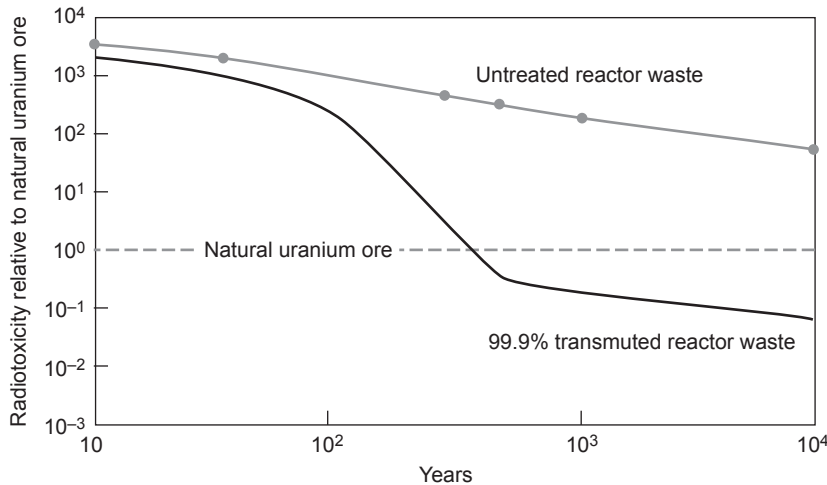


Figure 5. Reduced Radiotoxicity of Transmuted Reactor Waste
 The radiotoxicity of transmuted reactor waste declines precipitously after 100 years and thereby allows repository capacity to increase by a factor of 50. Gains in separation efficiency can increase this value further.

cessing and fabricating MOX comes from those facilities. The resulting high-level waste volume from a single MOX recycle is about a factor of 4 less than that from the once-through system. At the same time, the amount of fissile plutonium is reduced by roughly 20 percent, and in the process, a significant amount of energy is recovered. Recycling the plutonium in a MOX recycle adds only about 2 to 3 percent to the cost of electricity. Although some gains are being made with one MOX recycle, its impact on long-term waste management is limited because most of the high-level transuranic waste remains.

Advanced Fuel Cycle Initiative and the Closed Fuel Cycle. More significant reductions in residual waste can be made with a fully closed fuel cycle (Figure 4). The United States develops partitioning and transmutation technologies aimed at destroying high-level transuranic waste more efficiently under the Advanced Fuel Cycle Initiative (AFCI) of the DOE. Within the AFCI, the DOE is collaborating with other countries to pursue this

goal. Research is being conducted on UREX, a uranium extraction process that does not produce a pure plutonium stream but does efficiently separate uranium and partition fission products and transuranics to minimize waste. An essential feature of the closed fuel cycle is the transmutation of the higher actinides in reactors with fast neutron energy spectra. Robust fuel forms for transuranics are now being developed so that they can be transmuted efficiently. Once the recycled transuranic fuels have been fabricated, reactors with thermal neutron energy spectra (light-water reactors), fast reactors, or accelerator-driven systems can be used for transmutation.

Multiple studies show that the transmutation performance in systems with fast versus thermal neutron energy spectra is fundamentally different. Fast-neutron systems (either fast reactors or accelerator-driven systems) are more “efficient” at destroying actinides because fewer neutrons are lost to the neutron capture reactions that lead to the buildup of higher actinides. Thus, in the closed fuel cycle, the fast system can be uti-

lized for repeated recyclings without concern for the buildup of higher actinides. Thus, as shown in Figure 4, fast reactors are the preferred option for “continuous recycle” fuel-cycle strategies designed to improve waste management and/or resource utilization. The optimal combinations of these technologies depend on country-specific considerations with respect to nuclear energy use and waste management strategies.

Studies funded by the DOE, as well as those conducted in Europe and Japan, indicate that the cost of nuclear energy using a closed fuel cycle (including partitioning of the waste, storage of the fission products, and recycling and transmuting the plutonium and minor actinides) is 10 to 20 percent higher than the cost of electricity using a once-through fuel cycle. However, because of reduced radioactivity, this extra cost is potentially offset by the savings realized by the reduction in the number of repositories (see Figure 5).

Fast-Neutron Testing at LANSCE for Closed-Fuel-Cycle Technologies

The DOE has launched two major programs to explore options for advanced nuclear-energy systems, the AFCI and the Generation IV (GEN-IV), Reactor Program. Both programs are to determine fuel and material performance limits as a first step in designing fast-neutron-spectrum systems that reduce or eliminate transuranics from nuclear waste. These programs will eventually field major system demonstrations for reprocessing and transmutation. The AFCI is tasked with the development of fuels and materials for transmutation in advanced burner reactors. The goal is to develop new fuels, containing significant quantities of actinides,

that can achieve very high burnup,¹ operating safely in a fast-spectrum reactor.

Different fuel forms (such as oxides, metals, or nitrides) will be used, as well as different formulations of constituents. Their success in transmuting long-lived transuranics cannot be judged until they have been irradiated and tested. In addition to actinide-bearing fuels, transmutation also requires development of new advanced structural materials for cladding core components.

Before major systems, such as a new fast-spectrum transmutation reactor, are implemented, the performance of the actinide-bearing fuels and cladding must be proved. A concerted effort is required involving the irradiation of candidates in prototypic environments, postirradiation examinations in hot cells, data analysis, and validation of detailed models that will eventually be used to simulate high-burnup performance (through science-based prediction) and develop the next generation of advanced materials. Reactor core materials must be stable and predictable during prototypic irradiation conditions as well as those that would obtain during design basis accidents. Listed here are several technical issues that affect performance: fuel restructuring and densification, migration of constituents, gas evolution, fuel swelling and fuel-to-cladding interactions, loss of ductility in the cladding, irradiation-induced swelling, gas generation, and creep strength. Only through testing in a prototypic environment can these issues be resolved.

¹ Burnup is the energy extracted per unit mass of nuclear fuel. In typical light-water reactors, burnup is about 50 megawatt-days per kilogram (MWd/kg) in the discharged fuel. Higher burnups (greater than 200 MWd/kg) are possible in fast reactors. Fissile depletion, cladding strain, internal pressure, and fuel-to-clad interaction are the limiting factors used to obtain the maximum burnup of fuels.

DOE's AFCI Materials Test Station at LANSCE. To achieve the goals outlined above within reasonable cost and on schedule, a domestic fast-neutron testing capability is now needed. To fill this major gap, the AFCI has funded the design phase of the Materials Test Station (MTS) at LANSCE. This facility will provide the necessary irradiation capability for performing time-efficient testing. The MTS, combined with the planned refurbishment of the LANSCE accelerator, will provide a long-term reliable irradiation capability. Because of the unique features of its nonreactor spallation neutron source, the MTS can safely provide prototypic coolant, pressure, and temperature conditions of the proposed fast reactors. MTS can also provide a test bed for other DOE programs, including the space reactor and fusion energy systems.

The MTS to Test Safety and Efficiency of Fast Reactor Fuels. From experience, we have learned that all reactor materials undergo profound changes in their important engineering properties because of changes in their crystalline structure. The latter set of changes is caused by long-term neutron irradiation during reactor operation. The performance of fuels and structural materials under neutron irradiation is expected to set the limits for the design of future nuclear-energy systems. These limits can be measured and understood through the irradiation of candidate materials in the proposed MTS at LANSCE, in combination with postirradiation examinations and data analysis. These capabilities will provide validation data for ab initio fuel and material performance models that will be used to design the next generation of high-burnup fuels and radiation-tolerant materials.

To meet research requirements, the MTS will allow irradiating samples in versatile configurations. The facility will provide temperature control

and a choice of coolants. (See the box "Capabilities of the Materials Test Station" on page 136.) The MTS will be placed in a large experimental area at the end of the LANSCE accelerator, where 800-million-electron-volt (MeV) protons will be used to create fast-spectrum neutrons through spallation reactions on a tungsten target. The preconceptual MTS configuration is shown in Figure 6. The spallation target that produces neutrons, the neutron reflector, and the sample irradiation components are all contained in a vacuum vessel that eliminates the production of contaminated air. The initial target configuration will employ water-cooled tungsten technology, which has been used in several other applications at Los Alamos and elsewhere and is well proven.

The spallation target assembly and the sample assembly containing irradiation experiments are introduced horizontally into the vacuum vessel. The sample assembly will provide temperature control to the irradiation experiments, and with future additions, could accommodate special coolant needs with closed loops. Because the MTS is not a reactor, there is no possibility of reactivity feedback effects on the neutron source from the fission neutrons produced in the fuel. The spallation neutron source thus eliminates a potential safety concern and provides the capability to perform controlled run-to-failure tests on advanced transmutation fuels.

The MTS is designed to accommodate an initial proton current of 1 milliamperes on target and has the added ability to handle twice this current. At proton energies of 800 MeV, the initial milliamperes current translates into a beam power of 800 kilowatts. At this design value, a fast-spectrum flux of 1×10^{15} neutrons per centimeter squared per second ($n/cm^2 \cdot s$) is achievable in the central irradiation region (Figure 7). (In a fast-spectrum flux, the energies of the neutrons are greater than 0.1 MeV.)

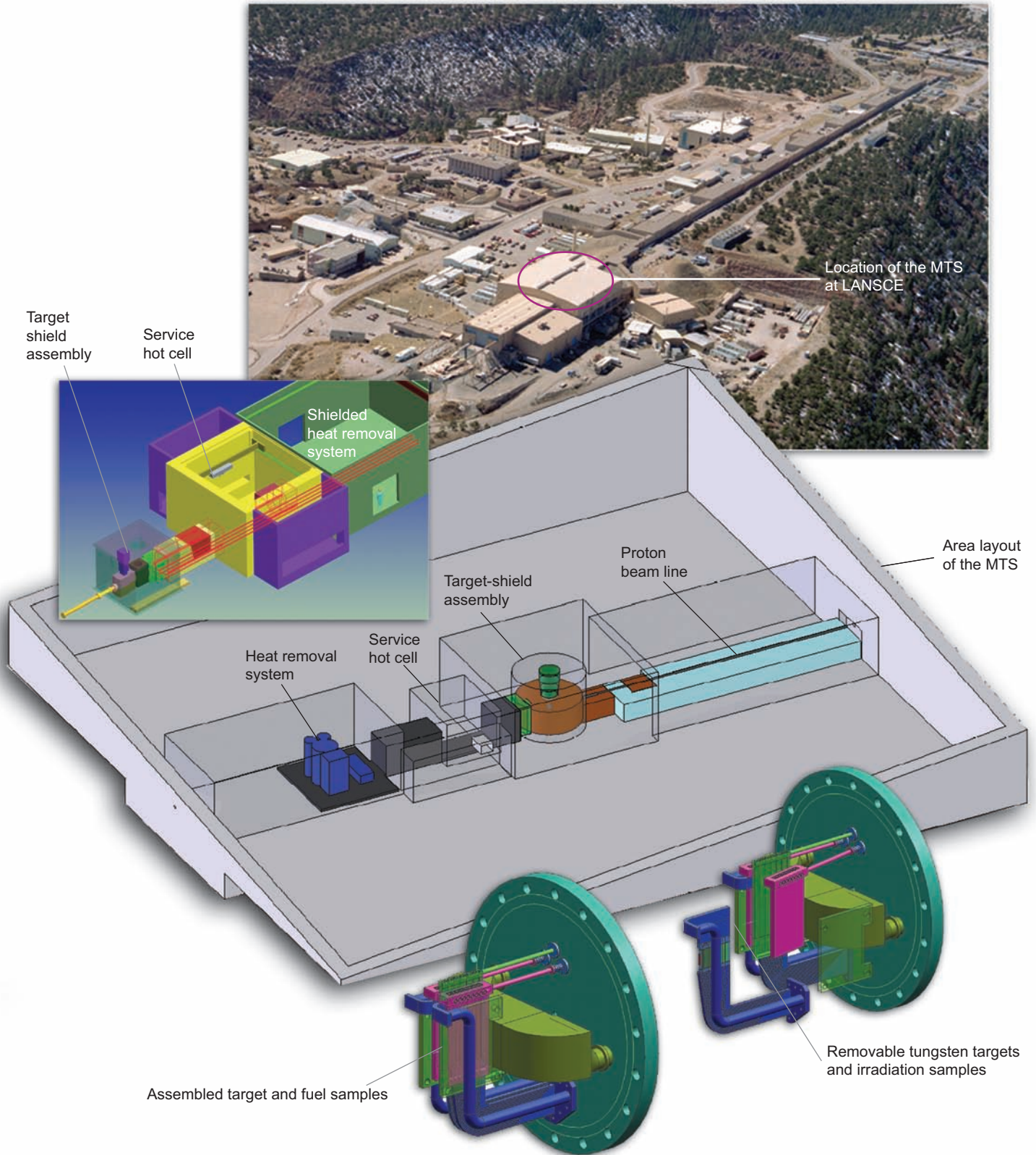


Figure 6. Materials Test Station (MTS) at LANSCE

The preconceptual configuration of the MTS within Area A is shown as well as views of the cooling system, the split target, and experimental assemblies.

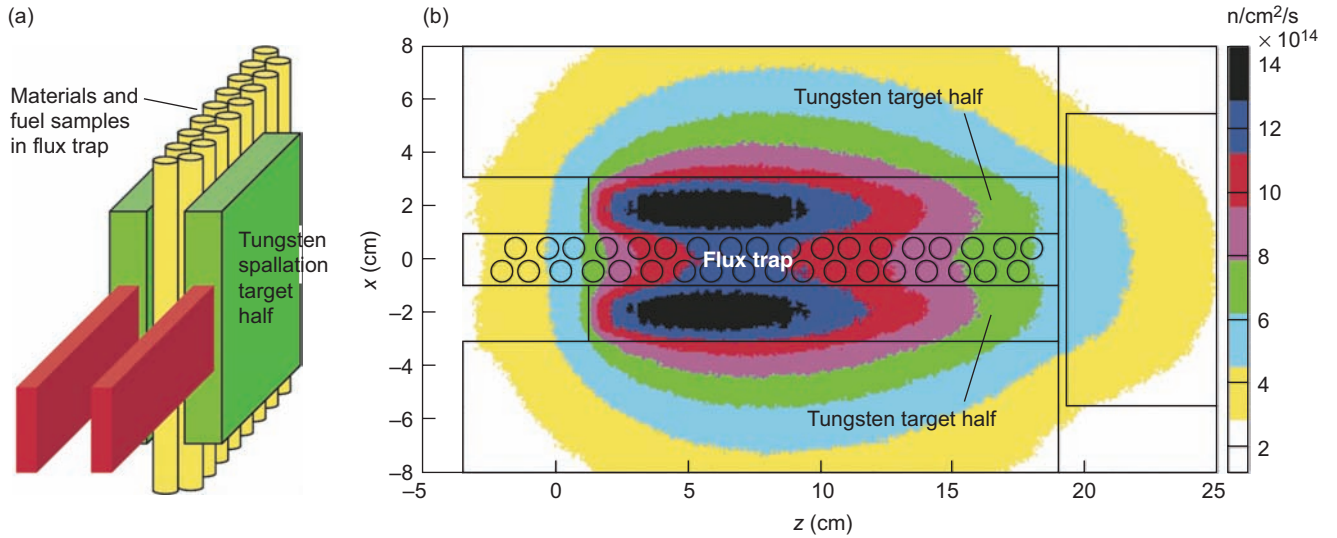


Figure 7. Calculated Neutron Flux in the Split Tungsten Target
 The split tungsten target arrangement shown in (a) and (b) ensures an intense neutron flux in the central flux-trap region, providing experimenters with an environment that is similar to that in a fast reactor.

As shown in Figure 7, the tungsten neutron source is split into two identical target halves. The protons from the LANSCE accelerator are directed equally to the target halves, producing an intense source of neutrons. Each proton striking a tungsten atom releases approximately 15 neutrons. The central flux-trap region, where the neutron flux is most intense, will contain fuel and material samples. Experimental fuel pellets, such as those shown in Figure 8, will be contained in small temperature-controlled “rodlets” that will allow researchers to mimic fast-reactor conditions. More than 200 fuel pellets and 1000 material samples can be irradiated in a given campaign.

Prototypical Fast-Neutron Energy Spectrum at the MTS. The neutron energy spectra of typical fast reactors are compared with the energy spectrum at the future MTS in Figure 9. The Pressurized-Water Reactor (PWR) spectra are typical of commercial power reactors in the United States. Most fission neutrons are “born” with energies between

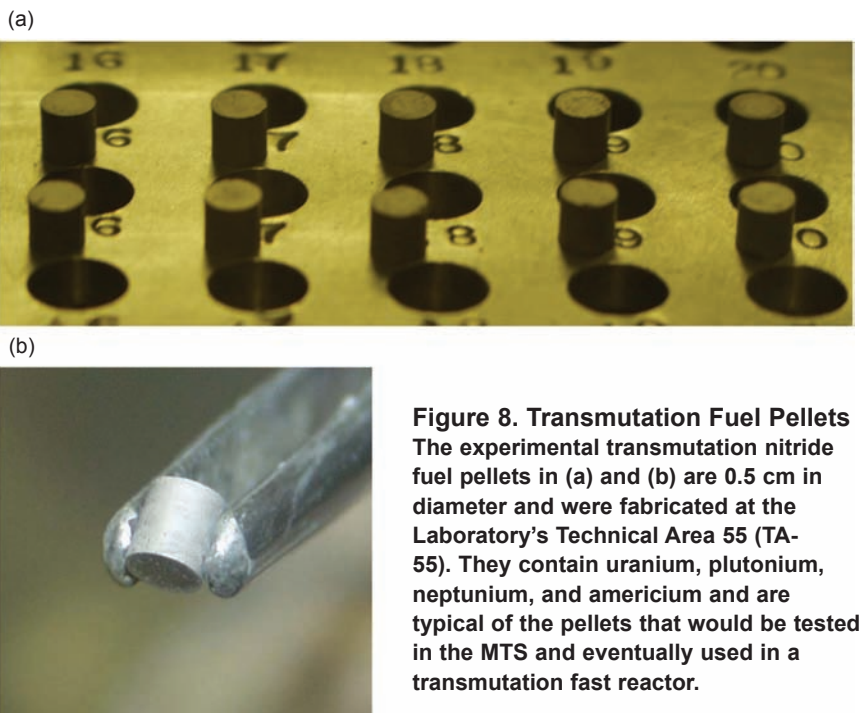


Figure 8. Transmutation Fuel Pellets
 The experimental transmutation nitride fuel pellets in (a) and (b) are 0.5 cm in diameter and were fabricated at the Laboratory’s Technical Area 55 (TA-55). They contain uranium, plutonium, neptunium, and americium and are typical of the pellets that would be tested in the MTS and eventually used in a transmutation fast reactor.

2 and 3 MeV. But as shown, most neutrons in the PWR are in the low-energy range because of slowing-down elastic collisions with the hydrogen in the water coolant. In a typical fast reactor—curve labeled FFTF (for Fast Flux Test Facility)

in Figure 9—the neutron spectrum contains none of the low-energy neutrons because there are no materials present in the reactor core that slow them down (coolants are typically sodium or lead). As mentioned before, the fast-spectrum neutrons are much

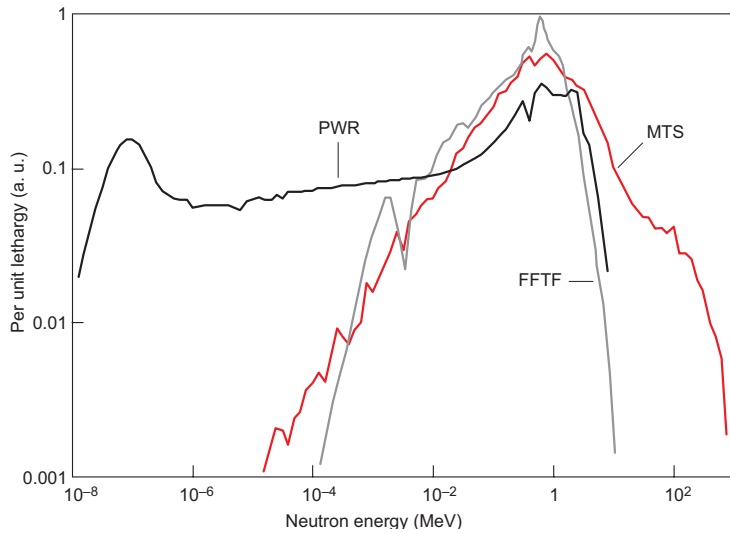


Figure 9. Comparison of Neutron Spectra at the MTS and Existing Fast-Flux Reactors

Neutron flux per unit lethargy is plotted as a function of neutron energy for the MTS and existing fast-flux reactors. Note that the MTS spectrum is very close to that of fast-flux reactors except for a larger contribution at the high-energy end.

more efficient for transmutation and are therefore the focus of our research efforts.

The MTS neutron spectrum is similar to that of a fast reactor, but the MTS has an additional high-energy tail beyond 10 MeV. These high-energy neutrons (about 5 percent of the total number) produce a moderate amount of hydrogen and helium gas in structural materials. Therefore, the ratios of the helium atoms to the displaced atoms in structural materials irradiated at the MTS are higher than those at typical fast-spectrum reactors. Thus the MTS irradiation environment is slightly more severe than that of a fast reactor and therefore will yield conservative results regarding the limits of performance.

Among the domestic facilities currently available, none meet the minimum requirements for fast-spectrum irradiations. Because of the shutdown of FFTF and the Experimental Breeder Reactor II, the only two facilities remaining for irradiations are

the Advanced Test Reactor at Idaho National Laboratory and the High Flux Isotope Reactor at Oak Ridge National Laboratory, both of which are thermal-spectrum reactors (spectra similar to the PWR in Figure 9). These facilities provide some irradiation data but cannot provide the fast-spectrum irradiation environment needed to evaluate fuel performance. Most fission reactions in a fast reactor are induced by neutrons with energies greater than 0.1 MeV, and there are essentially no fissions induced by neutrons in the thermal range. A similar distribution of fissions is observed for the MTS with the addition of some fissions induced by neutrons above 10 MeV from the high-energy tail of the neutron spectrum. In a thermal reactor neutron energy spectrum (in this case a typical light-water reactor), essentially all fissions are induced by thermal neutrons (neutrons with energies less than 0.625 eV). Thus, to investigate the fuel failure mechanisms that affect fast-reactor fuel

performance, such as the fuel-clad interaction, either a new fast test reactor or a facility like the MTS is needed.

The MTS to Begin Operations

in 2009. Given approximately \$60 million in construction funds over the next three years, the MTS will begin materials and fuels irradiation at the 1×10^{15} n/cm²/s level in fiscal year (FY) 2009. With the additional enhancements to the LANSCE accelerator, irradiations at the 2×10^{15} n/cm²/s level will commence in 2012. At this level, each 8-month irradiation campaign will test fuels to 6 percent burnup, which, combined with detailed analysis, will provide the data and information for proof of performance. As shown in Figure 10, these data will directly support the AFCI/Gen-IV research programs and development of the fast-spectrum transmuters.

The GEN-IV Program is developing a fast-reactor technology to achieve significant advances in proliferation resistance and sustainable energy production to meet the long-term energy needs of the country. Several technology options (using gas, lead, or sodium coolant) are being assessed. A selection is expected around 2012 and a demonstration reactor in 2025.

The MTS to Double Its Power with 2012 LANSCE Beam Upgrade.

Enhancements of the beam current at LANSCE (LANSCE-E) are currently being considered for future upgrades beyond the refurbishment stage (LANSCE-R). Studies have shown that the average beam power delivery to MTS can be increased by a factor of 2 over what is currently achievable by doubling the length of the pulses without changing the pulse rate (in other words, by increasing the duty factor). These upgrades could occur as early as 2012. The neutron intensity

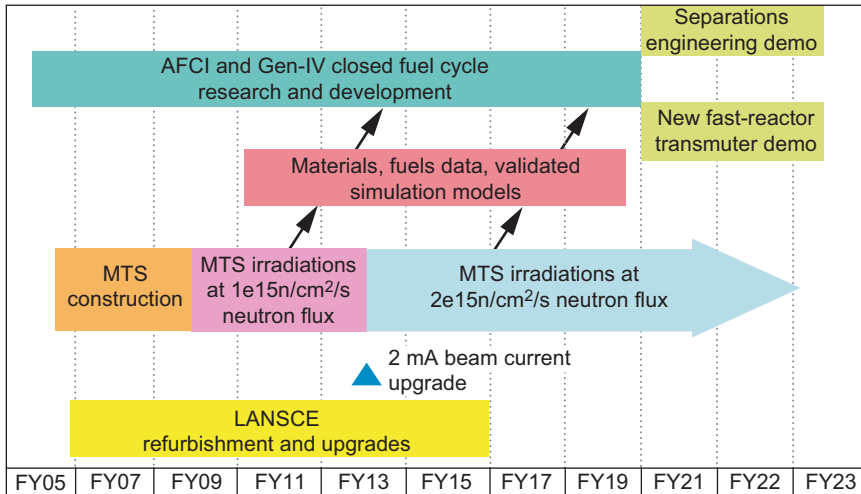


Figure 10. Timeline for the MTS
 The MTS will start operations in FY 2009 at the 800 kW power level, and with an accelerator upgrade in FY 2014, the power level will double. Fuels and materials irradiation data will support the development of the fast reactor transmuter demonstration.

from the spallation target will increase by a similar magnitude (up to 2×10^{15} n/cm²/s), enhancing the irradiation capability at the MTS. The heat removal systems at the MTS will be designed for easy upgrades to accommodate the higher power. The target and sample assemblies are also being designed for easy upgrading.

Conclusions

Global and national energy needs require a safe, efficient, and proliferation-resistant nuclear-energy supply that does not produce greenhouse gases. No single energy resource will meet the future demand in an economically and environmentally acceptable way. We must increase energy efficiency and implement a portfolio of clean energy sources, including nuclear sources. The argument against partitioning and transmutation of materials is that separated plutonium results in a diversion risk. The argument in favor of partitioning and transmutation is that the separated

plutonium is ultimately destroyed, avoiding an inexorable buildup of inventories and a considerable long-term risk for diversion of materials. Closing the fuel cycle with partitioning and transmutation will play a central role in minimizing this risk.

A major challenge to the increased use of nuclear power is global nuclear-material management. Recent world events clearly show that the containment of nuclear-weapon technology is no longer credible because this technology is available to almost any country willing to accept the associated high economic and political costs. Plutonium, an important weapon component, is produced by all nuclear reactors and can be chemically separated from spent nuclear fuel. Thus, it is important to control or avoid producing separated plutonium and enriched uranium that can be used in weapons so that they cannot be diverted for covert use. Managing special nuclear materials in a transparent fashion is essential if nuclear energy is to realize a renaissance.

Unfortunately, it appears that sepa-

rations and enrichment technologies are being pursued in a few countries for nonpeaceful purposes. It is clear that the general know-how for implementing nuclear-material technology exists and is readily available, even under the present import-export control measures of the global Nuclear Suppliers Group. Thus, policies to promote the once-through open cycle as a strategy to prevent nuclear proliferation have not accomplished their intended purpose.

International organizations share U.S. concerns about global nuclear-material management. The Director General of the IAEA, Mohamed El Baradei, published an editorial (ElBaradei 2004) presenting his views on reducing global proliferation risks. They include the need to revisit the limitations of the 1970 Treaty on the Nonproliferation of Nuclear Weapons, to strengthen inspections by the IAEA, and to consider a “multinational approach to the management and disposal of spent fuel and radioactive waste.”

The proposed concept of “supplier and user states” for nuclear energy has significant merit, and the associated details must be fully assessed to determine practical implementation options. This new nuclear governance regime could involve supplier states or regional supply centers that are under strict international control and safeguards.

With careful and judicious planning, a future can be envisioned, perhaps by mid century, in which domestic nuclear power is a significant contributor to a clean energy portfolio, providing half of our nation’s electricity. Globally, an advanced fuel-cycle technology can be fully implemented with a limited number of countries providing fuel services to others while nuclear materials are tracked and managed under strict international control. Partitioning and transmutation are key

elements of the advanced fuel cycle in order to reduce to the maximum the waste needing long-term isolation.

With continued support, LANSCE will play a major role in the development of our nuclear-energy future. With the construction and operation of the MTS, fuels and materials research will be performed that is essential to the implementation of fast-spectrum transmuters and to the closing of the nuclear fuel cycle. The studies at MTS will be a first step in opening up a sustainable nuclear-energy option to the United States.

Acknowledgments

The authors would like to acknowledge Eric Pitcher, Rick Wood, Eric Schneider, Keith Woloshun, Mike James, Jack Edwards, Mahlon Wilson, Stuart Maloy, John Eddleman, Rich Sheffield, Kurt Schoenburg, and Paul Lisowski for their assistance, design information, and analysis of the MTS.

Further Reading

- Deutch, J., E. Moniz, S. Ansolabehere, M. Driscoll, P. E. Gray, J. P. Holdren, et al. 2003. *The Future of Nuclear Power—An Interdisciplinary MIT Study*. Massachusetts Institute of Technology, ISBN 0-615-12420-8. [Online]: <http://web.mit.edu/nuclear-power/>.
- ElBaradei, M. 2004. Nuclear Non-proliferation: Global Security in a Rapidly Changing World. *Peacework Magazine* November issue, p. 4. Philadelphia, PA: American Friends Service Committee. [Online]: <http://www.afsc.org/pwork/0411/041104.htm>
- Six Laboratory Group. 2003. *Nuclear Energy—Power for the Twenty-First Century*. U.S. Department of Energy, Office of Scientific and Technical Information.

Capabilities of the Materials Test Station (MTS)

To be fully certified, the candidate fuels and structural materials of a fast-flux reactor must be proven through testing in a prototypic environment. That is, the new fuels must be characterized, fabricated, and irradiated in a fast-neutron spectrum. Then their performance must be examined for undue damage to fuel cladding and other structural elements and for major restructuring of the fuel. To provide adequate data, the conditions produced at the MTS must mimic the unique and varied conditions in various fast-flux reactor designs, including high power density, very high temperatures, very high radiation doses, and corrosive conditions.

Neutron Fluxes, Volumes, Temperature Controls, and More

The MTS provides the essential attributes necessary for a fast-neutron-spectrum test facility plus the added capability to run experiments in prototypic coolants.

The most important parameter, the neutron flux, which determines the rate of fission in the fuel, and therefore the power density and temperature, must be at least 10^{15} neutrons per square centimeter per second (n/cm^2-s) to equal the flux at which typical fast-reactor systems operate. The MTS achieves this level with the LANSCE accelerator delivering 1 milliamperere of current. With a doubling of the current in 2012, twice the neutron flux, $2 \times 10^{15} n/cm^2-s$, will be achieved in the flux trap.

Another important parameter is the ratio of fast to thermal neutrons—the flux of fast neutrons (energies greater than 0.1 MeV) divided by the flux of thermal neutrons (energies less than 0.625 eV). In typical fast reactors there are essentially no thermal neutrons, and the fast-to-thermal ratio is 75,000 or greater. The MTS achieves this ratio so that most fissions and structure damage observed in a test come from fast neutrons. This will test the mechanical integrity of the fuel/cladding system.

Regarding radiation damage to structures, it is desirable to achieve 10 displacements per atom (dpa) per year or higher because most changes in structure performance occur at this level. The helium generation rate is another parameter pertaining to radiation damage. In fast reactors it ranges from 0.2 to 0.5 atom parts per million (appm) He for each displacement per atom (dpa). For fusion systems this is closer to 10. For Accelerator Driven Systems, structures directly in the proton beam may endure 150.

The MTS achieves 10 dpa per year initially and 20 dpa per year after the LANSCE upgrade. The generation rate for helium is variable and ranges from 0.5 to 20 appm/dpa, thus making the MTS a unique environment for researchers.

High irradiation temperatures must be achieved for both the fuel and structures, and as shown Table I, the relevant range is quite large. Testing

Table I. Characteristics of the MTS

Attribute	Value
Fast neutron flux	1×10^{15} n/cm ² /s – 2×10^{15}
Fast to thermal ratio	75,000
dpa per year	10
Helium generation to dpa ratio in structures	0.5–10 appm He/dpa
Irradiation temperature fuel	1000°C–2000°C
Irradiation temperature structures	350°C–600°C
Active control of structure temperature	Yes, within 10°C
Fuel power density	Up to 1600 W/cc
Fuel pellet diameter	0.5–1.0 cm
Fuel pellet stack height in rodlet	5–10 cm
Fuel irradiation volume	200 pellets
Fuel material	Oxide, nitride, metal, dispersion
Fuel to clad bond	Helium, sodium, or lead
Coolant closed loops	Sodium, lead, or helium

at higher structure temperatures (up to 600°C) and higher fuel temperatures (2000°C) is desirable. The MTS meets those conditions, as well as the ability to control the temperature during irradiation.

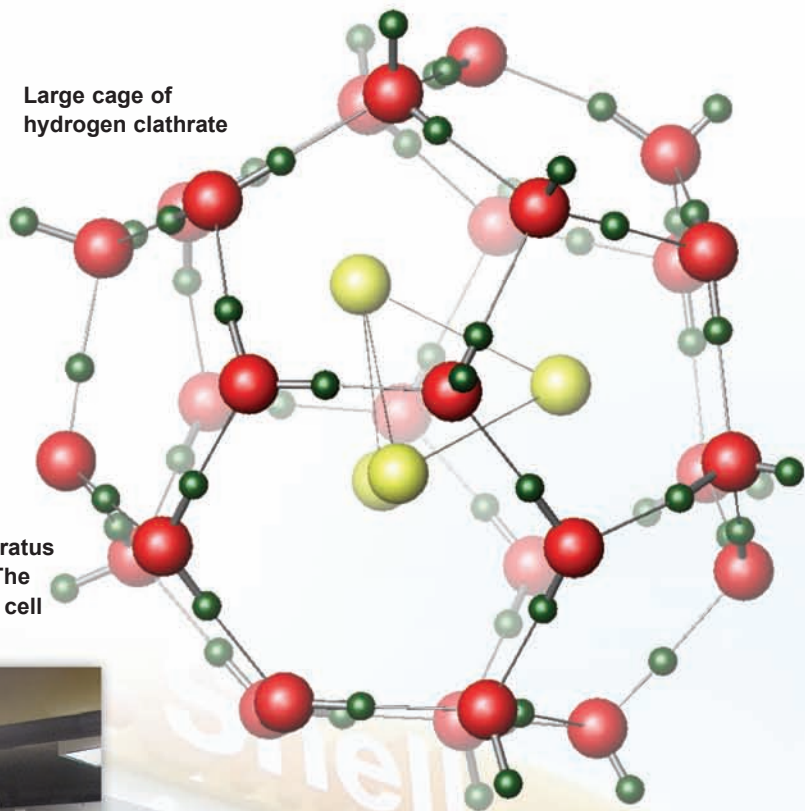
Most fast reactor and transmutation fuels have small diameters (~0.5 centimeter) and operate at high power densities—up to 1000 watts per cubic centimeter (W/cc). The MTS has the ability to test fuels at power densities up to 1600 W/cc, if needed.

The typical rodlets used for fuel tests will have a 2-inch (5-centimeter) fuel pellet stack. A relatively uniform flux over this height is desirable so that the different pellets experience similar irradiation conditions. Experimenters need to be able to irradiate 30 to 40 pellets (each roughly 5 millimeters in diameter by 5 millimeters in height) in the peak flux region. The MTS meets these volume and size requirements easily. Also the MTS has the capability to run some fuel tests to failure, allowing the absolute limits of the fuel integrity to be explored in defining the performance envelope.

The ability to test a variety of fuel types and fuel-to-cladding bonds is required because these features affect performance. The materials and fuels shown in Table I are those that currently require testing, although researchers may want to test other configurations in the future. The MTS can accommodate these needs and operate with several test-material configurations simultaneously.

Finally, the coolant types and the temperatures of prototypic corrosion and environmental conditions for cladding and structures tested at the MTS should cover the range of possibilities of the different fast-spectrum systems. To meet these needs, the MTS design includes the capability for closed coolant loops to provide flowing coolant conditions for corrosion studies under prototypic irradiation conditions. Most likely, the closed loops will be used for liquid-metal coolants, such as lead alloys or sodium, although helium gas is also a possibility.

Large cage of hydrogen clathrate



Konstantin Lokshin works on the apparatus we used to study hydrogen clathrate. The inset is a closeup of the high-pressure cell in which the clathrate formed.



Background photo: (Copyright Shell Hydrogen—www.shell.com/hydrogen)



Storing Hydrogen in Crystalline Molecular Cages of Water

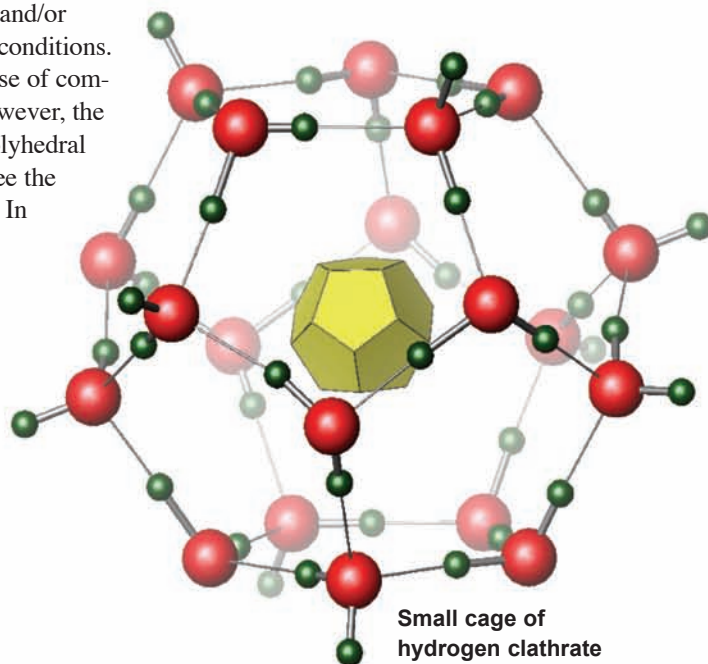
Konstantin A. Lokshin and Yusheng Zhao

Under certain conditions, water mixed with gas will form crystalline cages of water molecules with the gas trapped inside. These “cage compounds”—called clathrate hydrates or simply clathrates—can occur naturally, often under extreme conditions. In fact, methane clathrate, which is found worldwide in ocean floor sediments and permafrost, is believed to contain the largest source of hydrocarbons on Earth. Our studies at the Los Alamos Neutron Science Center show that hydrogen clathrate can trap hydrogen at mass fractions rivaling those of the best materials for hydrogen storage. In addition, we have found a way to capture hydrogen in hydrogen clathrate in as little as a few minutes or less and release it at least as quickly. Neutron diffraction at various pressures and temperatures determined the complete crystal structures of the two types of cages that form in hydrogen clathrate. The results allowed us to revise previous estimates of the numbers and positions of the hydrogen molecules trapped in each type of cage. Our neutron-diffraction studies provide benchmarks for future work on hydrogen clathrate, which could play a significant role in a hydrogen economy.

At certain pressures and temperatures, a mixture of water and a gas can crystallize into an icy solid known as a clathrate hydrate. Some clathrate hydrates form at pressures up to thousands of atmospheres and/or temperatures less than 0°C; others form at more moderate conditions.

The crystal structures of clathrate hydrates, just like those of common ice, consist of hydrogen-bonded water molecules. However, the water molecules in the clathrate hydrates typically form polyhedral cages in which gas molecules can be physically trapped (see the ball-and-stick models on the opening pages of this article). In fact, a significant fraction of the cages must be filled with guest molecules to stabilize the clathrate structure.

Because clathrate hydrates can store large volumes of gas, they are thought to have played a significant role in the development of the solar system. Clathrate hydrates probably formed in the early solar nebula, trapping volatile gases in icy solids that later aggregated, along with other primordial materials, into planets, moons, and other bodies. Clathrate hydrates could also be important on Mars, where the large relative abundance of carbon dioxide (CO₂) in the atmosphere, large deposits of subsurface ice, and very low surface temperatures could result in huge amounts of CO₂ clathrate on or near the surface. Such deposits may be responsible for the violent explosions of CO₂ gas and rapid water production that occur when Martian landslides suddenly



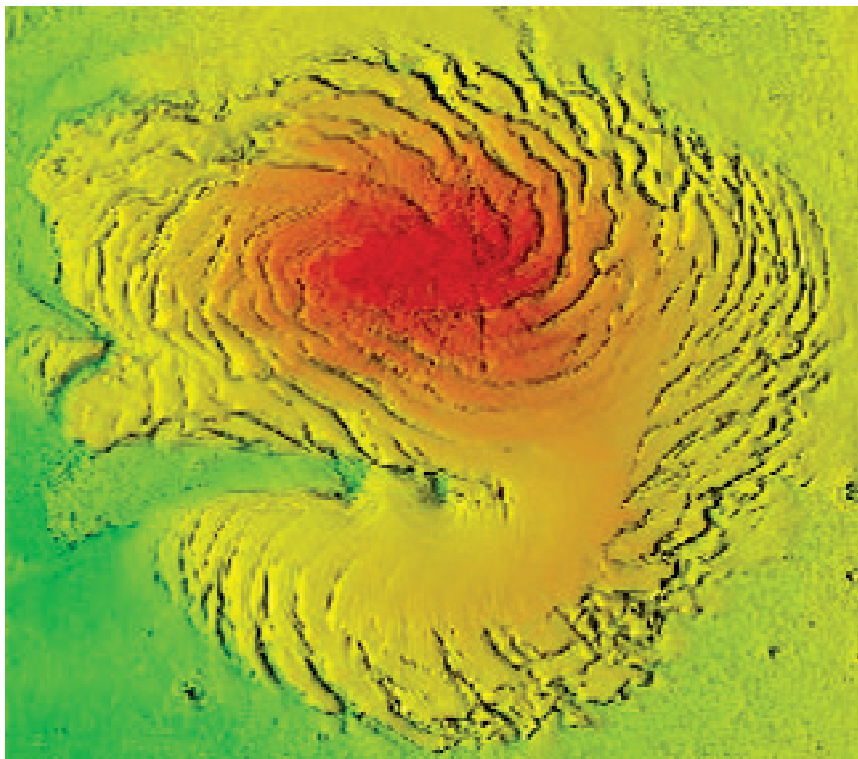


Figure 1. Possible Evidence for CO₂ Clathrates on Mars
 Deposits of carbon dioxide clathrate could be responsible for the “volcanic” blowout shown in this photo of the north pole of Mars. This image was taken by the laser altimeter on the Mars Orbiter spacecraft. (Courtesy of Jon Pelletier, University of Arizona.)

release pressure, possibly leading to the “volcanic” blowouts and deep gully plows seen on the surface of Mars (Figure 1).

On Earth, clathrate hydrates containing mostly methane are found in ocean floor sediments and in permafrost. In fact, it is thought that clathrate hydrates contain the largest source of terrestrial hydrocarbons, which has sparked interest in methane clathrate hydrate, in particular, as a potential source of fossil fuel. Clathrate hydrates also play an unexpected role in the use of existing sources of fossil fuel. In arctic regions, hydrocarbon clathrates form in and can obstruct exploration wells and natural-gas pipelines—a serious problem for the petroleum industry.

Our recent neutron-diffraction studies at LANSCE suggest that hydrogen

clathrate could also play a role in our energy future. They show that hydrogen clathrate can reversibly store and release molecular hydrogen at a mass fraction of up to 3.77 percent at atmospheric pressure. This fraction is significantly higher than those possible with the magnesium nickel and lanthanum nickel hydrides, Mg₂NiH₄ (3.59%) and LaNi₅H₆ (1.37%), which are among the best available hydrogen-storage materials. Our studies also show that hydrogen clathrate can store significant quantities of molecular hydrogen in

¹ This description refers to the structure’s symmetry and relates to a simple face-centered-cubic lattice as follows. For a simple lattice, if the origin of the unit cell’s coordinate system is placed at a particular atom, the same type of atom will be seen in each corner of the unit cell and in the center of each face of the unit cell. For cubic structure II, the origin of the coordinate system is placed instead at the structure’s center of inversion, which is at the center of a small cage.

as little as a few minutes or less and release it as fast or faster.

These properties could lead to a hydrogen storage system that could figure prominently in a hydrogen economy. But to develop such a system requires a detailed understanding of how hydrogen clathrate traps molecular hydrogen at various pressures and temperatures. Our neutron-diffraction studies have provided this information, whose main points are summarized in Figure 2.

Previous Studies of Hydrogen Clathrate

Hydrogen clathrate was discovered in 1999 by Yuri Dyadin’s group during studies of mixtures of water and molecular hydrogen at various temperatures and pressures (Dyadin et al. 1999). These studies involved the use of differential thermal analysis, in which one measures the temperature of a sample that is evenly heated or cooled at a constant rate and plots this temperature as a function of time. Thus, differential thermal analysis allows measuring the heat capacity of a sample as a function of temperature, especially changes near phase transitions. Dyadin’s group used this technique to detect the presence of hydrogen clathrate at 1000 to 4000 atmospheres and 0°C to 10°C.

Using x-ray and neutron diffraction, Mao’s group showed (Mao et al. 2002) that this clathrate’s framework structure is the so-called “cubic structure II,” a face-centered-cubic structure.¹ The unit cell is made up of 8 large polyhedral cages (hexakaidodecahedra) and 16 small polyhedral

cages (pentagonal dodecahedra), as shown in Figure 3. Known for more than 50 years, structure II is the framework structure of about one-half of all small-molecule hydrates known. In hydrogen clathrate, there are 136 water molecules in each unit cell, and each polyhedral cage has an oxygen atom at each vertex and a hydrogen atom on each edge.

Because they were unable to use their neutron-diffraction data to determine the numbers and positions of the hydrogen molecules in each type of cage, Mao's group used Raman spectroscopy to estimate the amount of hydrogen trapped in the clathrate and then inferred that the small and large cages hold up to two and four hydrogen molecules, respectively. However, with Raman spectroscopy, one cannot directly measure the amount and distribution of the hydrogen molecules in the clathrate.

Los Alamos Studies of Hydrogen Clathrate

In 2002, in collaboration with Mao's group, we began neutron diffraction studies of hydrogen clathrate, using LANSCE's High-Pressure Preferred-Orientation (HIPPO) diffractometer. For these studies, we built a special setup that allowed us to take advantage of the three-dimensional geometry of the diffractometer to obtain data of samples synthesized in situ under hydrostatic pressure over a range of temperatures (Figure 4). We made the pressure cell of aluminum alloy because aluminum is transparent to neutrons. The pressure cell can apply pressures between 1 and 7000 atmospheres and temperatures between 4 and 300 kelvins to a sample with a volume of up to 5 cubic centimeters.

The flux of thermal neutrons available at HIPPO, approximately 2.4×10^7 neutrons per centimeter squared

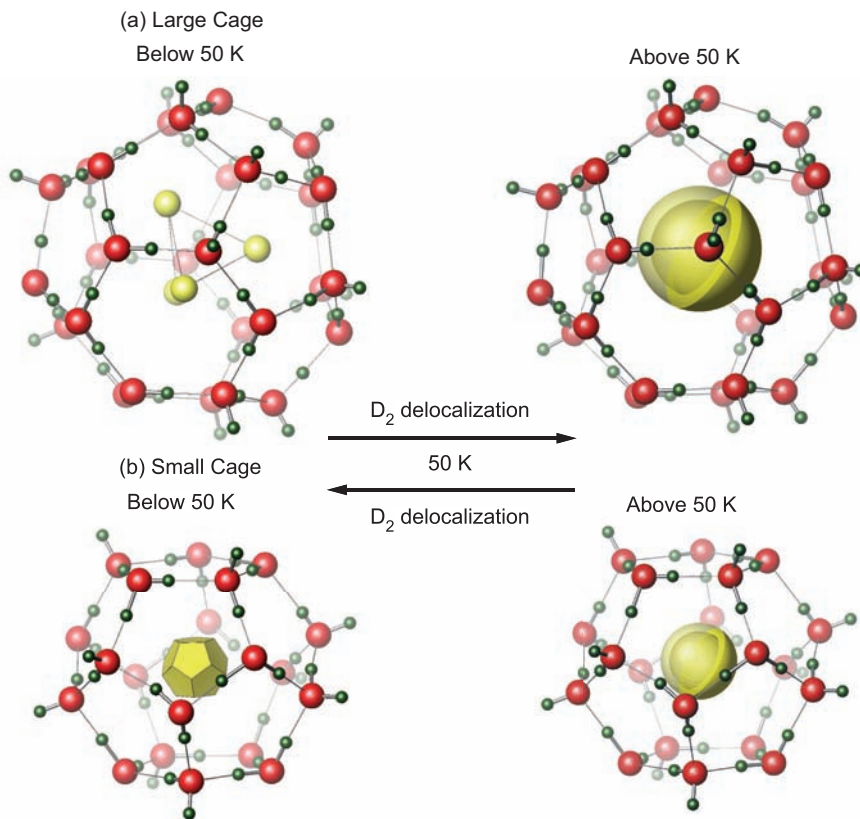


Figure 2. A Summary of Our Main Results

Two types of polyhedral cages are found in crystals of hydrogen clathrate. (Figure 3 shows how the cages are arranged in the clathrate's unit cell.) The red spheres are oxygen atoms in the hydrogen-bonded water molecules that form the cages. The small dark-green spheres are hydrogen atoms in the water molecules. The hydrogen molecules trapped inside the two types of cages are yellowish green. Our studies show that a large cage can hold up to four hydrogen molecules, and a small cage holds one hydrogen molecule. (a) Our studies also show that below 50 K, the four hydrogen molecules in a large cage form a stationary tetrahedral cluster with each hydrogen molecule pointing to the center of one of the cage's hexagonal faces. At higher temperatures, the tetrahedron rotates at the cage's center, the four hydrogen molecules are delocalized, and their density distribution is nearly spherically symmetrical. (b) Below 50 K, the hydrogen molecule in a small cage takes one of 20 orientations, describing a dodecahedron. At higher temperatures, the hydrogen molecule also rotates at the cage's center, and its density distribution also becomes nearly spherically symmetrical. (Reprinted with permission from K. A. Lokshin et al, *Phys. Rev. Lett.*, 93, p. 125503-2, 2004. Copyright 2004 by the American Physical Society.)

per second ($n/cm^2 \cdot s$), is the highest in the world.² This flux, together with the diffractometer's high detection efficiency and the pressure cell's

comparatively large sample volume, allowed us to obtain high-quality neutron diffraction data in less than a minute—the shortest known time for a neutron diffraction measurement.

To further enhance the quality of the neutron diffraction data, we synthesized the clathrate using deuterated water (D_2O) instead of

² Thermal neutrons are used for neutron diffraction studies of solids because the neutron wavelengths are comparable to interatomic spacings in crystalline materials.

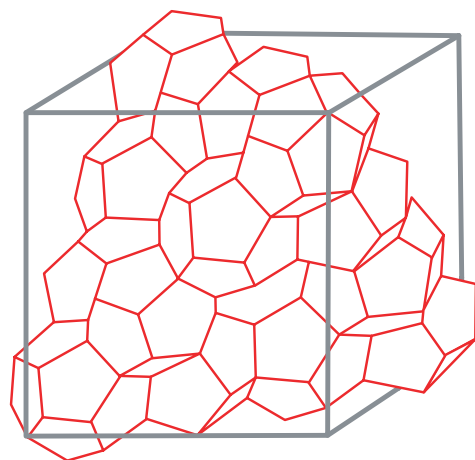


Figure 3. The Unit Cell of a Cubic Structure-II Clathrate
The unit cell consists of 136 water molecules, which form 16 small polyhedral cages (pentagonal dodecahedra) and 8 large polyhedral cages (hexakaidodecahedra).

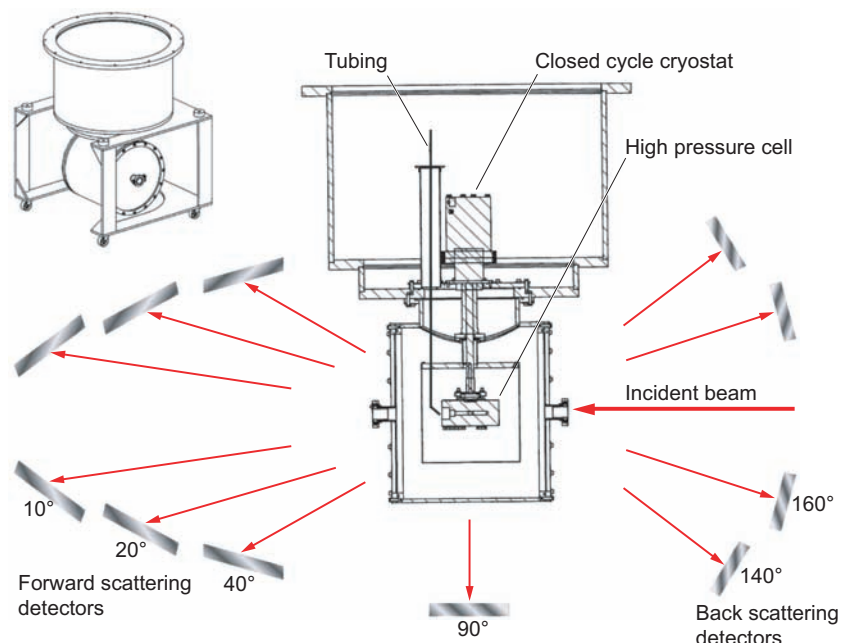


Figure 4. Hydrostatic Pressure Cell and Experimental Setup for Our Neutron-Diffraction Measurements
We synthesized deuterated samples of hydrogen clathrate inside the high-pressure cell and then measured the samples' crystal structures with neutron diffraction. The horizontal orientation of the cell and the complex detector geometry of the HIPPO diffractometer allowed fast collection of diffraction data from the sample without introducing scattering from impurities in the surroundings, which would degrade the quality of the data. (Reprinted with permission from *Rev. Sci. Instrum.*, 76, p. 063909-2 (2005). Copyright 2005, American Institute of Physics.)

water (H_2O), and molecular deuterium (D_2) instead of molecular hydrogen (H_2). Replacing H_2 with D_2 improves the quality of neutron diffraction data by dramatically

decreasing the high background caused by the large incoherent scattering of neutrons by hydrogen atoms. Many studies have shown that substituting D for H in a com-

pound does not significantly affect its size or structure.³

To determine the numbers and positions of the hydrogen molecules, we applied a special addition to our “Rietveld refinement” of the data. Rietveld refinement analyzes the shapes and intensities of the Bragg peaks in x-ray or neutron diffraction data to provide information about structure, the average vibrational displacements of atoms from their lattice positions, and other phenomena. To use Rietveld refinement to locate deuterium molecules, we needed the neutron-scattering form factors for D_2 . But at the time of our analysis, no one had calculated these form factors. To complete the analysis, we modeled D_2 's form factors and used them in the Rietveld refinement assuming that the spatial distribution of D_2 in the cages was either localized (stationary) or spherically delocalized (rotating). It took us approximately one year to complete the refinement after collecting the data.

Details of the Trapped Deuterium Molecules

In the end, Rietveld refinement allowed us to extract, at a given pressure and temperature, the numbers and positions of the hydrogen molecules held in each type of cage (Lokshin et al. 2004). Figure 5 shows the number of deuterium molecules we measured in the large and small cages as a function of temperature for pressures of 1 and approximately 2000 atmospheres. (We use “bar” and “atmosphere” interchangeably since

³ However, an “isotope effect” is sometimes seen in the compound's physical or physiochemical properties, such as a clathrate's thermal-decomposition temperature. In fact, we measured a difference of about 5 to 10 kelvins at 1 atmosphere for the thermal-decomposition temperature of hydrogen clathrate made with H_2 compared with hydrogen clathrate made with D_2 .

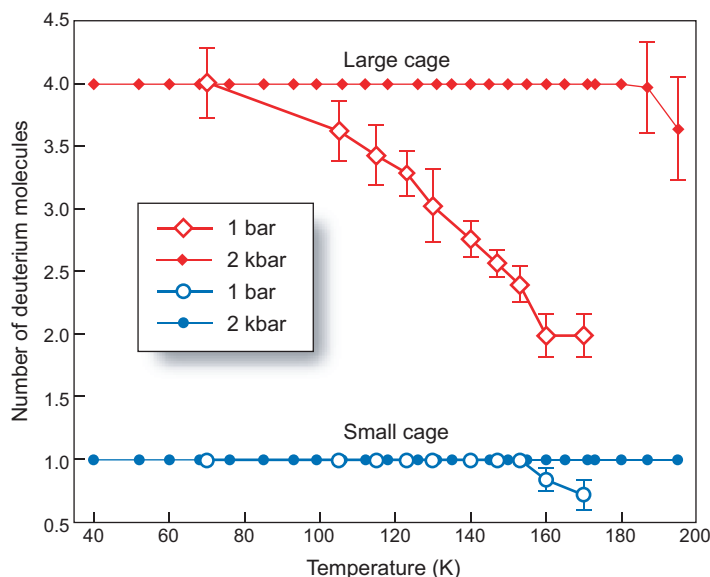


Figure 5. Number of Deuterium Molecules in Large and Small Cages
 The large cages start losing deuterium molecules above 70 K at 1 atm and above 190 K at approximately 2000 atm. Similar behavior is observed for the small cages. As the temperature increases, high pressure is required to stabilize the clathrate for maximum deuterium-molecule occupancy. These data also show that all the cages are filled with the maximum number of hydrogen molecules for temperatures less than 70 K at 1 atm and less than 190 K at approximately 2000 atm. When all the cages are filled with the maximum number of hydrogen molecules, the mass fraction of the stored hydrogen is 3.77%, rivaling the mass fractions of the best hydrogen-storage materials. For reference, at 1 atm, liquid nitrogen boils at 77 K, and dry ice evaporates at 195 K. (Reprinted with permission from K. A. Lokshin et al, *Phys. Rev. Lett.*, 93, p. 125503-2, 2004. Copyright 2004 by the American Physical Society.)

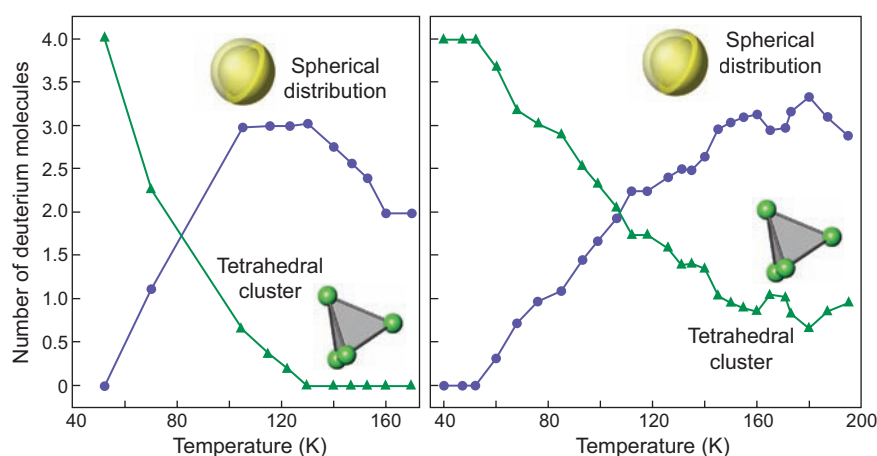


Figure 6. Spatial Distributions of Deuterium Molecules in Large Cages
 These data are plotted as a function of temperature at 1 atm and approximately 2000 atm. (Reprinted with permission from K. A. Lokshin et al, *Phys. Rev. Lett.*, 93, p. 125503-3, 2004. Copyright 2004 by the American Physical Society.)

1 atmosphere equals 1.01325 bars.) The large cage was found to hold 2 to 4 deuterium molecules, depending on the pressure and temperature. At low temperatures, a deuterium molecule is located at each vertex of a tetrahedron centered inside the cage. The deuterium molecules are 0.293 nanometer from each other and 0.180 nanometer from the center of the cage. Each deuterium molecule points toward a center of one of the hexagons formed by the oxygen atoms of the large cage.

For the small cage, we measured a maximum occupancy number of only one deuterium molecule. Rietveld refinement determined that the neutron scattering density of this molecule is statistically distributed between 20 positions that point to the oxygen atoms in the dodecahedral cage. For both types of cages, Rietveld refinement determined the distance between the oxygen and deuterium molecules to be 0.334 nanometer.

We also found that the hydrogen molecules in both types of cages become localized below 50 kelvins. Below this temperature, the four hydrogen molecules in a large cage form a stationary tetrahedron, as mentioned before. Above 50 kelvins, the tetrahedron rotates at the cage's center, so that the average spatial distribution of the four hydrogen molecules is nearly spherically symmetrical and the molecules are delocalized (Figures 2 and 6). A hydrogen molecule trapped in a small cage below 50 kelvins aligns along one of 20 directions. Above 50 kelvins, the molecule rotates at the cage's center, again leading to an average spatial distribution that is nearly spherically symmetrical.

Remarkably, the closest distance between any two hydrogen molecules in the tetrahedron is at least 30 percent less than the closest distance between any two hydrogen molecules in solid hydrogen at 1 atmosphere. This result tells us that the molecular

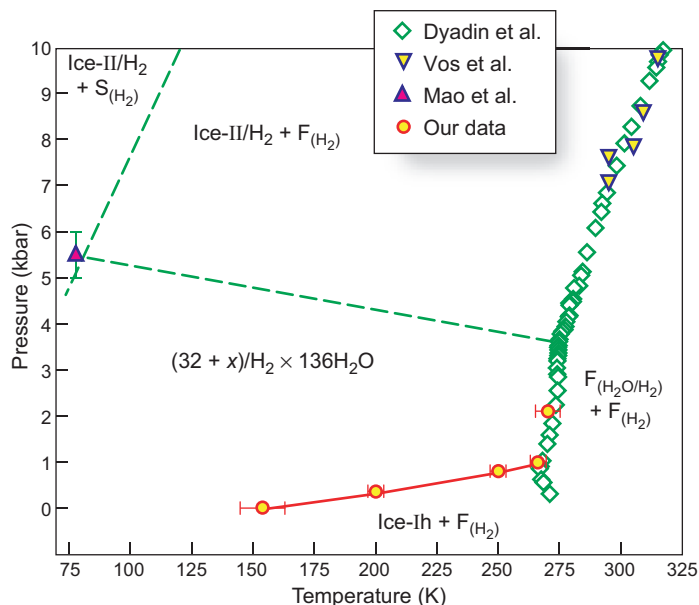


Figure 7. The Phase Diagram for Hydrogen Clathrate

This diagram includes experimental results from Yuri Dyadin’s group, Mao’s group, and the Los Alamos group. The region where the clathrate forms stably is bounded by the temperature and pressure axes, the nearly horizontal green dashed line, the line formed by the green diamonds (the melting curve), and the lower red solid line. All these results were obtained with mixtures that included an excess of hydrogen. “F” refers to fluid (water or liquid hydrogen). “S” refers to solid hydrogen. “ $(32 + x)\text{H}_2 \times 136\text{H}_2\text{O}$ ” refers to the 136 water molecules in a unit cell of hydrogen clathrate, plus the $32 + x$ hydrogen molecules trapped in cages, where x varies from 0 to 16.

framework surrounding the hydrogen molecules affects the local density of the molecules. It also suggests that it may be possible to store molecular hydrogen at higher densities by using an appropriate framework, not necessarily the framework provided by a clathrate’s cages.

The Phase Diagram for Hydrogen Clathrate

Figure 7 is the hydrogen–water phase diagram. This plot shows all the pressure–temperature regions and their boundaries where water and hydrogen molecules form stable crystalline phases. Figure 7 combines our experimental data with the data of the Dyadin and Mao groups that pertain

to the phase transitions of hydrogen clathrate. All measurements were made with mixtures that included an excess of hydrogen.

The stable-clathrate region is bounded by the temperature and pressure axes and three experimentally determined curves. Within the stable-clathrate region, no ice phases are present—only clathrate and excess hydrogen. The three bounding curves are the following: (1) The melting curve (the line formed by the green diamond symbols) is where the clathrate [labeled “ $(32 + x)\text{H}_2 \times 136\text{H}_2\text{O}$ ”] is in equilibrium with a water solution of gaseous hydrogen [denoted as “ $\text{F}(\text{H}_2\text{O}/\text{H}_2)$,” where F stands for fluid]. (2) The high-pressure boundary line (the lower, dashed green line) is where the clathrate is in equilibrium

with a solution of gaseous hydrogen in ice-II (labeled “ice-II/ H_2 ”). The ice-II/ H_2 phase was found to be stable from 7 to 20 kilobars. (3) The low-pressure boundary line (solid red line) is where the clathrate is in equilibrium with ice-Ih. Several points on this line are from our measured data: 163 kelvins at 1 bar, 200 kelvins at 0.35 kilobar, and 265 kelvins at 1.0 kilobar.

Fast Synthesis

We made our first neutron-diffraction measurements of the hydrate with starting mixtures of liquid D_2O and gaseous D_2 . In those experiments, the clathrate formed very slowly. (Sometimes, water did not fully convert to the clathrate after several days.) We initially attributed this effect to the small surface area of the liquid D_2O exposed to the gaseous D_2 and decided to increase the surface area by starting with a mixture of gaseous D_2 and powdered ice instead of water. The particles in the powdered ice had diameters of about 500 micrometers. To our surprise, the clathrate formed extremely quickly with powdered ice (Figure 8)—a result of extreme importance for developing a viable hydrogen-storage system. [This hydrogen storage (release) method could involve, for example, going from lower (higher) pressure to higher (lower) pressure at a constant temperature across the red line shown in Figure 7.]

We also prepared hydrogen clathrate from a chunk of ice-Ih with a mass of about 1 gram and a volume comparable to the volume of water used for clathrate synthesis. The diffraction patterns taken during the synthesis of hydrogen clathrate at 250 kelvins and 1.5 kilobars are shown in Figures 8(d)–(f). The formation of clathrate from the chunk of ice was complete in about 1.5 to 2 hours, which is slower than the synthesis from powdered ice but at least 100 times faster than the synthesis

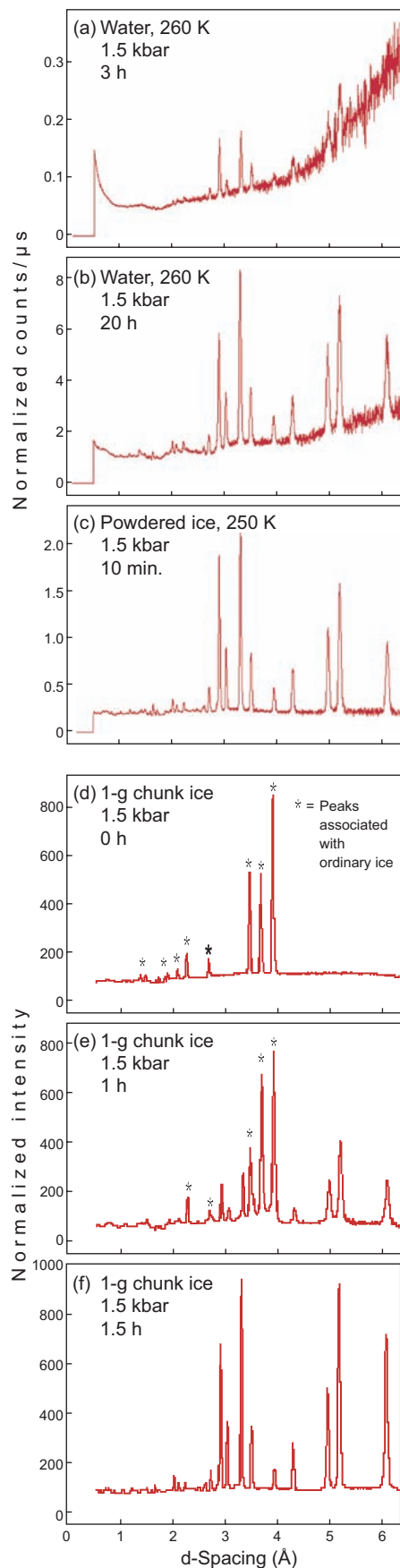


Figure 8. Neutron Diffraction Data for Hydrogen Clathrate Formed in Different Ways

A comparison of plots (a) and (b) with plot (c) reveals that hydrogen clathrate forms more slowly from water than from powdered ice. It also forms somewhat slowly from chunk ice, as shown in (d) through (f). The asterisks denote peaks associated with ordinary ice. When all these peaks disappear, the sample is 100% hydrogen clathrate.

from water. We also found that fast clathrate formation did not occur when we used (bulk) amorphous ice—prepared by chilling water at a pressure of 2.2 kilobars—as the starting material.

Thus, the fast synthesis of hydrogen clathrate from ice cannot be explained only by the difference between the reaction surface areas of powdered ice and water. We believe fast synthesis could occur because ice-Ih is more porous than water. In fact, ice-Ih is much less dense (9 percent less) than water because ice-Ih contains many small cavities. These cavities could be large enough for hydrogen molecules to enter under pressure. We believe that the penetration of the cavities by molecular hydrogen promotes the conversion of ice-Ih to clathrate hydrate.

Conclusions

Until recently, hydrogen clathrate did not appear to have much practical value. It was hard to make, and some of its most important properties were unknown. The clathrate could be synthesized only at pressures of many thousands of atmospheres and/or low temperatures, and it could take several days or more to complete the synthesis. In addition, the precise amounts of molecular hydrogen that could be stored in the material at various pressures and temperatures were unknown.

However, our recent neutron-diffraction studies show that hydrogen clathrate has the potential for use as a practical hydrogen-storage medium. Our studies show that the hydrate can be synthesized in a few minutes from ordinary powdered ice. And when synthesized at 1 atmosphere and liquid-nitrogen temperatures, the clathrate has an H₂ mass fraction of 3.77 percent, rivaling the mass fractions of the best hydrogen-storage materials. Most important, we have measured the numbers and positions of the hydrogen molecules stored in both types of the clathrate's molecular cages at various pressures and temperatures. This information is essential for benchmarking future studies of this and related clathrates and could be used to develop hydrogen storage systems with significant potential for enabling a hydrogen economy. ■

Further Reading

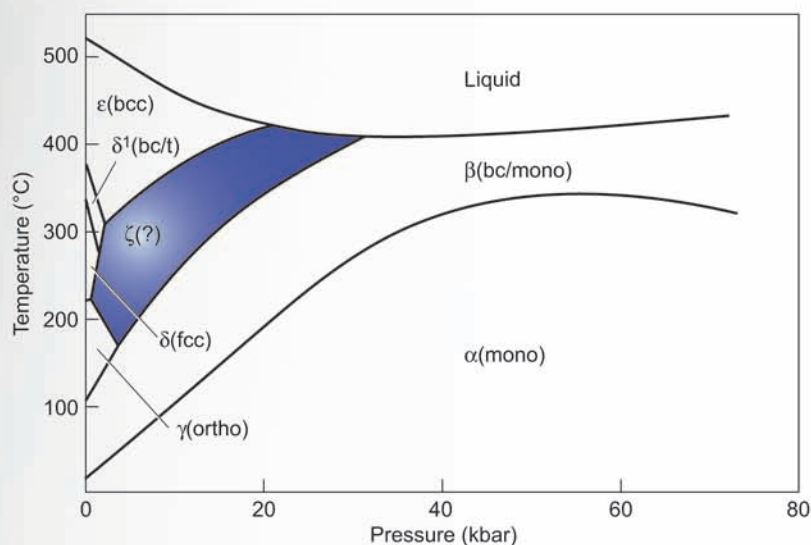
- Dyadin, Y. A., E. G. Larionov, A. Y. Manakov, F. V. Zhurko, E. Y. Aladko, T. V. Mikina, and V. Y. Komarov. 1999. Clathrate Hydrates of Hydrogen and Neon. *Mendeleev Commun.* **5**: 171.
- Lokshin, K. A., Y. Zhao, D. He, W. L. Mao, H.-K. Mao, R. J. Hemley et al. 2004. Structure and Dynamics of Hydrogen Molecules in the Novel Clathrate Hydrate by High Pressure Neutron Diffraction. *Phys. Rev. Lett.* **93** (12): 125503-1.
- Lokshin, K. A., and Y. Zhao. 2005. Advanced Setup for High-Pressure and Low-Temperature Neutron Diffraction at Hydrostatic Conditions. *Rev. Sci. Instrum.* **76**: 063909-1.
- Mao, W. L., H.-K. Mao, A. F. Goncharov, V. V. Struzhkin, Q. Guo, J. Hu et al. 2002. Hydrogen Clusters in Clathrate Hydrate. *Science* **297**: 2247.
- Sloan, E. D. 1998. *Clathrate Hydrates of Natural Gases*. Second Edition. New York: Marcel Dekker.

Introduction to Materials and Bioscience Neutron-Scattering Research

Alan J. Hurd and Dale W. Schaefer

So confident were Manhattan Project scientists about their understanding of the nucleus that the gun concept for detonating a nuclear explosion was never tested before “Little Boy” was deployed against Japan in World War II. The implosion detonation concept, however, required testing at the Trinity Site in New Mexico on July 16, 1945. In the implosion bomb, conventional explosives drive the nuclear explosion by rapidly assembling and then compressing a plutonium “pit.” Implosion was used in “Fat Man,” the second and last nuclear device exploded in war. The issues leading up to Trinity involved not only the nuclear properties of plutonium but also its chemistry and metallurgy. Plutonium had to be manufactured, isolated, and purified; its phase behavior (Figure 1) had to be determined; and the desirable phases had to be stabilized (Hammel 1995 and 2000). Equally challenging problems regarding the behavior of conventional high explosives had to be solved. These issues fall in the realm of materials science, the study of the properties of condensed matter, for which neutron scattering is a unique and precise probe even though those properties are largely independent of the nucleus.

Figure 1. Plutonium at High Pressure and Temperature
The complicated phase diagram of plutonium was a major issue in working with the metal for the Trinity test. Just weeks before the test, the desirable δ -phase was stabilized by proper alloying. The ability to probe the properties of metals with high atomic weights in extreme environments is one of the important characteristics of neutron scattering. Indeed, much materials science remains to be done; even the structure of one high-pressure plutonium phase is still unknown.



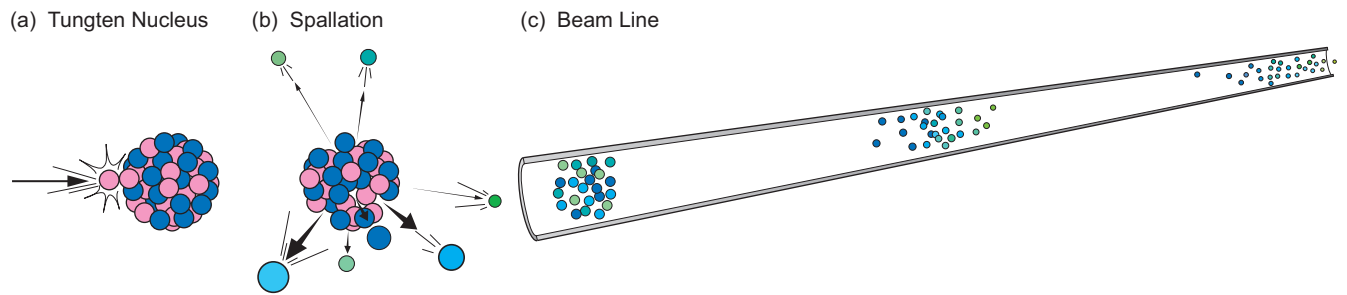


Figure 2. Spallation Neutrons

When a pulse of energetic protons (pink) hits a tungsten target, each proton that collides with a tungsten nucleus as in (a) causes the nucleus to release tens of neutrons with different energies, represented by different colors in (b). Neutrons traveling in a particular direction move along a beam line (c). The resulting pulse of neutrons is very short, but as the pulse travels down the beam line, the higher-energy neutrons travel faster, the pulse stretches out in space, and the arrival times of the neutrons serve to identify their energies and wavelengths.

The Manhattan Project illustrates that critical technologies are often limited by the availability of appropriate materials. This situation is unlikely to change. According to national studies of the last 30 years, the properties of 21st century materials must exceed those of today's materials by large margins. The projected mid-century "end-of-oil" challenge, for example, will elicit new hydrogen-storage materials, more-efficient solar cells, better nuclear fuels, and improved nuclear-reactor materials. In addition, the nuclear-weapon stockpile requires reliable prediction of materials aging to maintain deterrence without testing. Finally, the world faces emerging threats fueled by terrorism that demand significant materials advances. If history is a reliable guide, advances in materials research will be needed to meet these challenges.

Given the central role of materials science "in the beginning" and the importance of materials in emerging technologies, it is not surprising that materials science enjoyed an important position in the research portfolio of Los Alamos National Laboratory. Less obvious is the evolving role that subatomic particles, such as the neu-

tron and proton, play in Los Alamos materials research.

Role Reversal

Conceived by Louis Rosen as a facility to explore nuclear structure, the Los Alamos proton accelerator was originally dubbed the Los Alamos Meson Physics Facility (LAMPF). LAMPF provided the proton beam for many discoveries in the realm of medium-energy nuclear physics, but eventually evolved into a source of protons and neutrons serving the needs of the materials science community at Los Alamos, at other Department of Energy laboratories, and now across the community of external users (see Figure 17 on page 16 of this volume). LAMPF was renamed the Los Alamos Neutron Science Center (LANSCE) in 1995.

As part of this evolution, the Lujan Neutron Scattering Center (Lujan Center) at LANSCE was built to study the properties of materials using the neutron as a probe. At the Lujan Center, protons are slammed into a tungsten target (Figure 2), and the resulting nuclear reactions produce

copious quantities of neutrons that are then directed to 16 beam lines instrumented to explore the structure and dynamics of materials. At LANSCE, neutrons serve materials science as well as nuclear physics research.

Why Neutron Scattering?

The properties of materials are controlled by the positions and motions of atoms. The body of information regarding the position of atoms is called structure, and the information regarding motion is called dynamics. Although other techniques measure structure and dynamics, the neutron has a number of properties that make neutron scattering a unique probe for materials research.

First of all, neutrons are "poor, uneducated, and easy to command." Using moderators, devices that change the neutron energy spectrum, spallation neutrons can be cooled to match the structural length scales and the excitation energies of dynamics in materials. Although some techniques require thermal neutrons, the current emphasis throughout the world is on cold neutrons, which are useful for

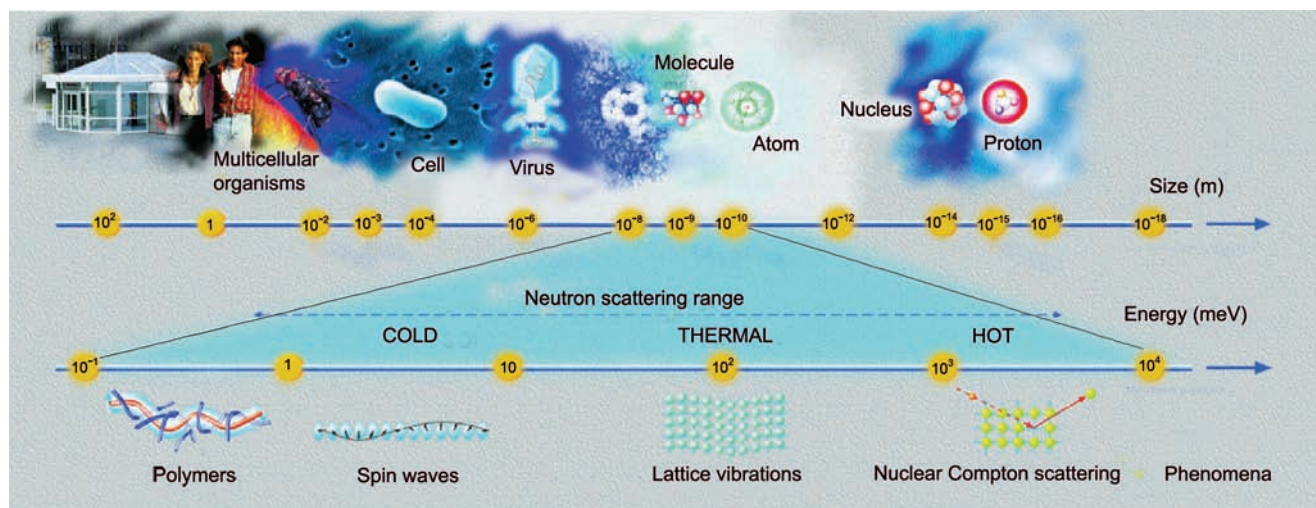


Figure 3. Neutron Energy Spectrum

A cold-neutron energy spectrum (the range is depicted on the energy axis) is best for scattering from polymers, large molecules, biological systems, and other soft materials. LANSCE plays a leading role in cold-neutron peak flux and instrumentation. Long-pulse technology will substantially enhance Lujan Center capabilities in soft matter and bio materials. (This figure was adapted from "The European Spallation Source Project Report" 2002.)

probing large-length-scale structures and low-energy excitations characteristic of soft matter, such as polymers, liquid crystals, colloids, and biological materials (Figure 3). In fact, the interest in cold neutrons and in long-pulse sources, which use cold neutrons efficiently, matches the rapidly growing interest in soft-matter research.

Many experiments can be accomplished only with neutrons. Because neutrons are more penetrating than x-rays, one can probe samples inside high-pressure vessels, refrigerators, and furnaces, or measure deeply buried structures in a bulk material (see the article "Plutonium under Pressure" on page 84 and Figure 1). Neutrons scatter more strongly from some isotopes than others of the same element, which makes isotopic labeling a major advantage as described below. Neutrons are also magnetic, and they are therefore particularly suited to the study of magnetism (see the article "Origins of Spin Coupling across Interfaces" on page 178). The predicted existence of magnetism in plutonium, for example, is important to the electronic

structure of this metal and therefore to its equation of state, a very important factor in weapons physics. Low-energy neutrons match well the spectrum of excitations that underlie the physics of plutonium's electronic structure.

In 1986, the world learned about an entirely new phase of matter signaled by high-temperature superconductivity. Neutron scattering played a central role in understanding high-temperature superconductivity because, unlike x-rays, neutrons are adept at probing magnetic structure and crystal excitations and excel at probing compounds containing high atomic numbers. Nevertheless, the elucidation of high-temperature superconductivity is not yet completed after 20 years (see the article "Unraveling the True Atomic Structures of Exotic Oxides" on page 152).

Because the neutron scattering power of atoms is isotope dependent, labeling techniques are widely employed to sort out complex structures and dynamics (see the article "The Hydrophobic Effect—Why Do Raindrops Slide off Leaves?" on page

164). Hydrogen and deuterium, which are nearly invisible to x-rays, are easily located with neutrons.

Emerging Opportunities: Soft Matter and Bioscience

Starting with the 1975 National Academy of Sciences report "Materials and Man's Needs," the emergence of soft matter as a discipline was anticipated by numerous studies exploring the future direction of materials science. Encouraged by the National Nanotechnology Initiative and the remarkable progress in molecular biology over the last 5 years, soft matter currently dominates hiring in physical sciences at research universities across the world (National Science Board 2004).

The evolution of national security priorities at the Laboratory tracks the emergence of soft matter as a discipline. The traditional focus on metallurgy and condensed matter physics has shifted toward the chem-bio-radiological threats characterizing the period after the 9/11 terrorist attacks

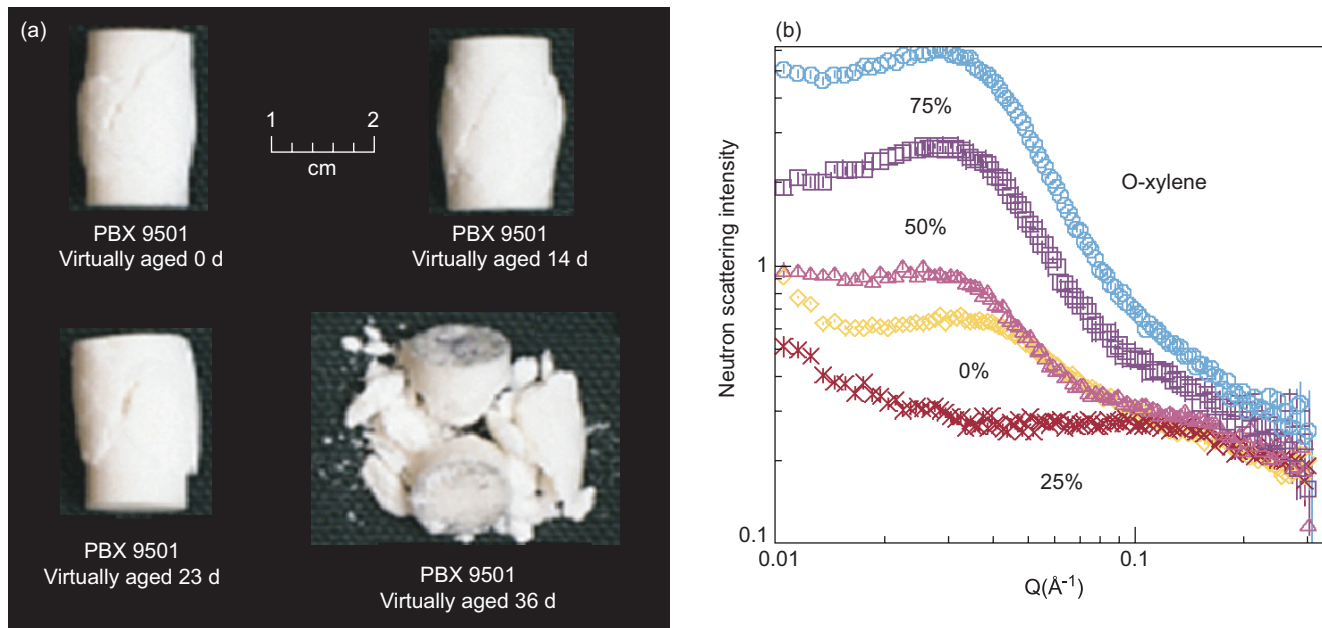


Figure 4. High Explosives Age

(a) The insensitive high explosive PBX 9501 exhibits degradation upon artificial, or virtual, aging. That is why PBX 9501 is being replaced by PBX 9502 and other formulations in the stockpile. Neutron scattering studies are being used to identify the keys to aging. (b) EstaneTM, a polymer binder, is the subject of intense research on aging. Ortho-xylene dissolves part of the EstaneTM binder. By using a series (0% to 100%) of deuterated o-xylene, one changes the scattering contrast between the hard and soft domains without changing the chemistry or structure. At 25% deuterated o-xylene, the hard domains of EstaneTM are seen to match. Future studies of aged EstaneTM will be based on the power of contrast variation to look at hard and soft domains independently.

on the United States. The emphasis on maintaining the current nuclear stockpile and developing robust materials for refurbishment also evokes a host of new materials issues. The aging of high explosives in weapon systems, for example, is a topic of intense study, and neutron scattering allows researchers to distinguish physically different parts within these complex polymer molecules (Figures 4a and 4b). These new priorities underlie the growth of soft-matter research, including biosciences, at Los Alamos.

Nanotechnology is another distinguishable area of materials research enjoying worldwide expansion. The corresponding field of nanomaterials refers to matter organized on nanometer- (10^{-9} meter) length scales. Large-scale organization distinguishes nanomaterials from molecular materials, whose properties are determined

by short-range molecular bonding.

The preferred synthesis path for soft nanomaterials is bottom-up self-assembly, whereby specific short-range interactions are engineered into complex precursor macromolecules. These short-range forces induce long-range order by cooperative physical interactions. Nanomaterials share many characteristics with soft materials in that the essential structural features occur on supramolecular scales and the corresponding dynamics are found at low energy.

Even weapons materials have nanoscale features important to their health and function. Inside neutron tubes, erbium tritide targets, when bombarded with accelerated deuterons, produce copious neutrons via a nuclear reaction. Because the tritium decays in time to helium, which ruins the tube's vacuum, the target films are designed to retain helium. When

retention is low, tube lifetime is low. Owing to its high acuity for light elements, neutron scattering has proved to be effective in determining the mechanisms of helium retention and release. Figure 5 shows small-angle, neutron scattering results that indicate helium buildup along preferred lattice directions. Strategies to adjust the microstructure (grain boundaries) can then be proposed to mitigate the aggregation of helium.

The recurring theme in this discussion of soft matter and biomaterials is large-scale structure. This theme elicits a new perspective on neutron-scattering instrumentation. The long-pulse spallation source, for example, is a new concept recently demonstrated at LANSCE that meets the need to measure structure and dynamics of soft matter and to do bioscience research.

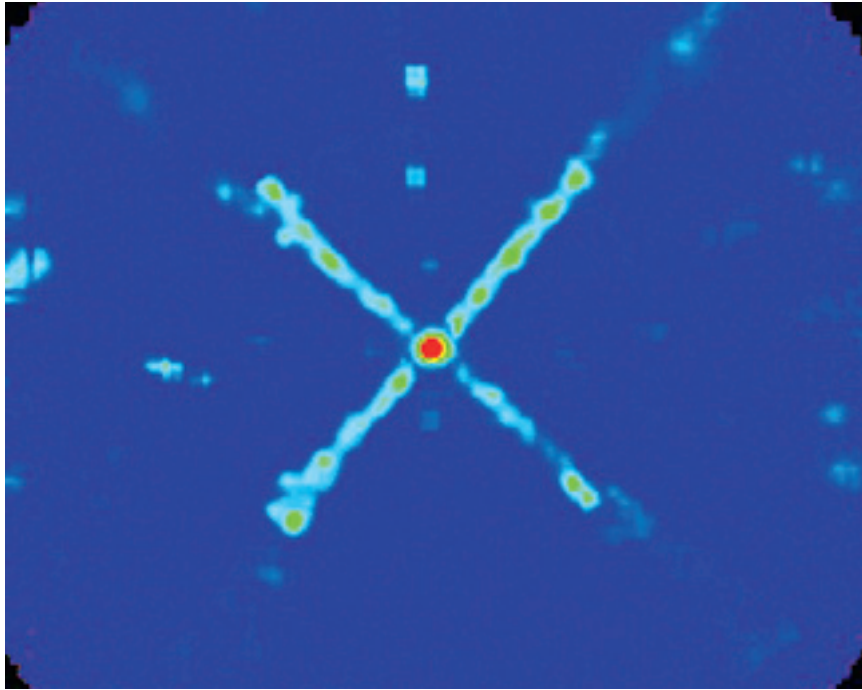


Figure 5. Scattering in Erbium Tritide

This remarkable pattern of small-angle neutron scattering demonstrates that helium released by the radioactive decay of tritium collects preferentially along planes in the lattice. This mechanism limits helium retention by films, thereby shortening neutron tube lifetime. (This image is courtesy of James Browning of Sandia National Laboratories, Albuquerque, NM.)

Long-Pulse Spallation Technology

The demonstration of neutron production from proton beams by spallation in the 1970s offered new hope for a source more intense than fission reactors. Using time-of-flight techniques, pulsed neutrons can be sorted by energy and can be used one by one. In contrast, energy discrimination at steady-state sources requires filtering out an overwhelming fraction of the neutrons.

The challenge for the future is to build neutron sources that combine the efficiency of pulsing with enhanced time-average flux (see Figure 16 on page 15 of this volume). This goal can be achieved using long-pulse spallation source (LPSS) technology. The long-pulse technique circumvents the limitations of the short-pulse spallation source (SPSS) approach, which will be pushed close to its technical limit at the Spallation Neutron Source (SNS) currently under construction at Oak Ridge National Laboratory. The beauty of the LPSS is that the instruments most useful for soft matter and bioscience research can achieve much higher data rates while the instruments optimized for hard materials are only slightly compromised.

Short-pulse spallation sources are limited by the proton beam energy that can be delivered in a single proton pulse. The limit is imposed by both accelerator technology (space charge limits in ring accelerators) and target degradation. In linear accelerators, long, energetic proton pulses can be produced that are far from the space charge limit. Moreover, by comparison with the SPSS, long pulses avoid the target material problems because energy deposition is spread over a much longer time (see Figure 6). Such pulses still afford reasonable velocity definition for long-wavelength neutrons.

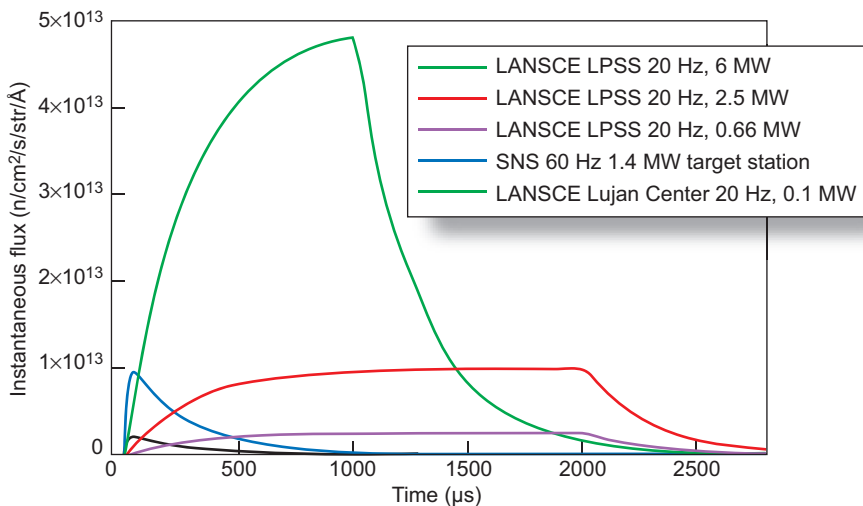


Figure 6. Cold-Neutron Line Shapes for Various Pulsed Sources

In long-pulse neutron sources, proton energy is deposited in the spallation target over a much longer period, which mitigates target degradation. The integrated neutron flux of the LPSS pulses is fully used in applications requiring moderate wavelength resolution, such as small-angle scattering. In applications requiring short-wavelength resolution (for example, medium- and high-resolution diffraction), pulse-shaping choppers will be used to produce pulses with variable lengths, including shorter ones than those available at the SPSS. The 6-MW calculation (green curve) represents the ultimate LPSS potential at LANSCE.

(Ferenc Mezei, Los Alamos National Laboratory, personal communication, June 2005.)

The above considerations imply that LPSS technology can provide neutrons with more than an order of magnitude higher brilliance than the neutrons produced by the SPSS. LPSS can also surpass continuous reactor sources in terms of time average flux and provide superior performance in most applications of neutron beam research.

Conclusions

There is little doubt that basic and applied research in materials and bioscience will define the Los Alamos science portfolio for the foreseeable future regardless of whether the Laboratory's mission emphasizes nuclear weapons, threat reduction, or energy. Solving the structure property puzzle for 21st century materials will require characterization tools that keep pace with advances in synthesis. For 60 years, neutron scattering has been an indispensable technique for materials characterization. In the budding world of nanomaterials, biomaterials, and soft materials, neutron sources optimized for the study of supramolecular structures and collective motions are required. LPSS technology matches this requirement by exploiting long-wavelength low-energy neutrons. Compared with short-pulse instruments, LPSS instruments will yield large performance gains in the study of soft matter and biomaterials.

Further Reading

- Commission on Engineering and Technical Systems, National Research Council. 2000. *Summary Record of the Workshop on Polymer Materials Research: August 30–31, 1999, Woods Hole, Massachusetts*. Washington, DC: The National Academies Press.
- Committee on Advanced Energetic Materials and Manufacturing Technologies, National Research Council. 2004. *Advanced Energetic Materials*. Washington, DC: The National Academies Press.
- Committee on Alternatives and Strategies for Future Hydrogen Production and Use, National Research Council, National Academy of Engineering. 2004. *The Hydrogen Economy: Opportunities, Costs, Barriers, and R&D Needs*. Washington, DC: The National Academies Press.
- Committee on Condensed-Matter and Materials Physics, National Research Council. 1999. *Condensed-Matter and Materials Physics: Basic Research for Tomorrow's Technology*. Washington, DC: The National Academies Press.
- Committee on Materials Research for Defense After Next, National Research Council. 2003. *Materials Research to Meet 21st Century Defense Needs*. Washington, DC: The National Academies Press.
- Committee on National Laboratories and Universities, National Research Council. 2005. *National Laboratories and Universities: Building New Ways to Work Together—Report of a Workshop*. Washington, DC: The National Academies Press.
- Committee on Science, Engineering, and Public Policy. 1975. *Materials and Man's Needs: Materials Science and Engineering—Volume II, The Needs, Priorities, and Opportunities for Materials Research*. Washington, DC: The National Academies Press.
- Committee of Soldier Power/Energy Systems, National Research Council. 2004. *Meeting the Energy Needs of Future Warriors*. Washington, DC: The National Academies Press.
- ESS Council. 2002. *The European Spallation Source Project*. Complete Edition (Volumes I–IV), ISBN 3-89336-299-1. Germany: Druckerei Plump OHG.
- ESFRI Working Group on Neutron Facilities. 2003. *Medium to Long-Term Future Scenarios for Neutron-Based Science in Europe* [online]: http://neutron.neutron-eu.net/n_documentation/n_reports
- Hammel, E. 1995. Plutonium Metal: The First Gram. *Los Alamos Science* **23**: 162.
- . 2000. The Taming of “49”—Big Science in Little Time. *Los Alamos Science* **26**: 48.
- National Science Board. 2004. *Science and Engineering Indicators 2004*. Two volumes. Arlington, VA: National Science Foundation (Volume 1, NSB 04-1; Volume 2, NSB 04-1A).
- Organizing Committee for the Workshop on Energy and Transportation, Committee on Challenges for the Chemical Sciences in the 21st Century, National Research Council. 2003. *Energy and Transportation: Challenges for the Chemical Sciences in the 21st Century*. Washington, DC: The National Academies Press.
- Proceedings of the 2000 National Materials Advisory Board Forum, National Research Council. 2001. *Materials in the New Millennium: Responding to Society's Needs*. Washington, DC: The National Academies Press.
- Solid State Sciences Committee, National Research Council. 1987. *Advancing Materials Research*. Edited by P. A. Psaras and H. D. Langford. Washington, DC: The National Academies Press.
- U.S. Department of Energy's Environmental Management Science Program, National Research Council. 2000. *Research Needs in Subsurface Science*. Washington, DC: The National Academies Press.



Unraveling the True Atomic Structures of Exotic Oxides

*Thomas Proffen and Takeshi Egami**

High-temperature superconductors (HTSCs) and certain oxides with unusual magnetic properties, such as LiNiO_2 , are promising technological materials. But to understand their electronic or magnetic properties, one must know how these materials are constructed at the atomic and slightly larger length scales. A new technique for analyzing neutron-diffraction data—coupled with the high-quality data provided by LANSCE's high-resolution neutron powder diffractometer—has led to the discovery of totally unexpected nanoscale domains in LiNiO_2 and to an apparent confirmation of the presence of nanoscale structural inhomogeneities in HTSC cuprates. These inhomogeneities could play a key role in high-temperature superconductivity.

* *University of Tennessee*



In 1912, Bragg discovered a law relating a crystal's structure to the diffraction pattern produced when the crystal is illuminated by x-rays. Since then, scientists have been able to determine the atomic structures of increasingly complex materials. Diffraction patterns produced by illuminating crystalline powders with x-rays or neutrons, called powder diffraction, have been a large part of that revolution in materials science, and the data analysis technique for powder diffraction data known as full profile refinement, or Rietveld analysis, is now routine. This technique reveals many features of the structure including lattice parameters, atomic positions, or atomic displacement parameters. However, Rietveld analysis determines only the average long-range structure of the material, because only the intensities and positions of the diffraction pattern's peaks—the “Bragg” peaks—are analyzed. The simple example shown in Figure 1 reveals the limitations of Rietveld analysis.

Figure 1a shows two artificial, two-dimensional structures that have one atomic site per unit cell, and identical site occupancies of 30 and 70 percent for atoms of type A (in light blue) and B (in purple), respectively. (The site occupancy for a given type of atom is the fraction of the atomic sites occupied in the lattice by that atom type.) The only difference between the two structures is the atomic ordering. Whereas the two types of atoms in the right lattice are randomly distributed, the arrangement of atoms in the left lattice exhibits “chemical” short-range order: The A atoms are clustered together. Figure 1b shows the powder-diffraction patterns generated by computer simulation for these two artificial lattices. Rietveld analysis of the two patterns yields identical results for both structures because the intensities and positions of the Bragg peaks are the same. This is no sur-

prise, since the “average” structures of both lattices are the same. Rietveld analysis cannot distinguish between the two structures, and this article would end here if we could not obtain additional information from the diffraction data.

In fact, the difference between the two structures is clear in the diffuse-scattering signal shown in the inset of Figure 1b. This signal, which consists of the comparatively small intensity fluctuations between the Bragg peaks, contains information about the chemical short-range order that is revealed in the structures' pair distribution functions (PDFs), shown in Figure 1c. A PDF is simply the Fourier transform of the total-scattering pattern, which includes both Bragg and diffuse scattering. The chemical short-range order is apparent in the difference between the two PDFs shown in Figure 1c. However, diffuse scattering can reveal not only chemical short-range order but also any deviation from the average structure of a sample. In fact, the PDF method was originally used to study glasses and liquids, which have no long-range order.

The Pair Distribution Function

The PDF gives the probability of finding an atom at a distance r from another atom. In other words, the (primary) information contained in the PDF is the distribution of the bond lengths between all the atoms in a sample. Because it is obtained from the total-scattering pattern, the PDF contains structural information over a range of length scales. In fact, the ability to provide structural information at different length scales is one of the PDF's great strengths.

For example, consider the C_{60} molecules (“buckyballs”) shown in Figure 2. A single buckyball is shown

in Figure 2a. Buckyballs can form crystals with long-range order, as shown in Figure 2b. At room temperature, the individual balls within the crystal rotate (nearly) freely with respect to each other. The plot of total-scattering data shown in Figure 2c was used to obtain the PDF results plotted in Figure 2d. The PDF results reflect the rotation of each of the buckyballs. The C-C pairs within each molecule produce sharp peaks in the PDF for distances smaller than the buckyball diameter (~ 0.7 nanometers). The PDF is broad and nearly featureless at larger distances because there are only weak correlations between the molecules. For a detailed summary of these results, see Takeshi Egami and Simon Billinge (2003).

The Neutron Powder Diffractometer (NPDF)

Because the PDF is the Fourier transform of the scattering data, the PDF's resolution is determined by the maximum momentum transfer Q of the measurement. In most cases, a synchrotron source providing high-energy x-rays or a spallation neutron source such as that at LANSCE is used to perform experiments that will be analyzed with PDFs. The advantages of using neutrons over x-rays are discussed elsewhere in this issue. Neutrons are the probe of choice for samples containing light elements (e.g., hydrogen or lithium) or samples with adjacent elements in the periodic table, for example nickel and copper. The only instrument dedicated to studying disordered materials with the neutron PDF technique is the NPDF at LANSCE's Lujan Neutron Scattering Center (Figure 3). The diffractometer's large range of Q values enables one to detect local structural distortions of ~ 0.01 nanometer, and its high Q values provide usable PDF data for atom-atom distances of more

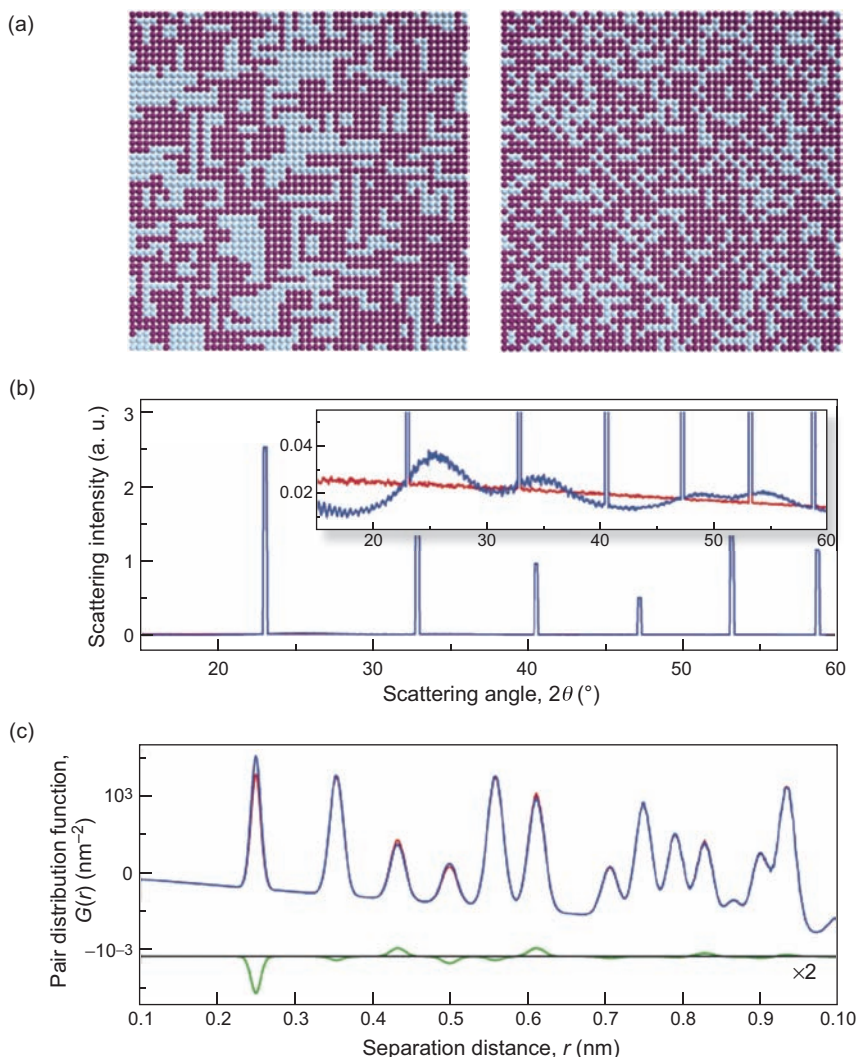


Figure 1. Understanding the Information Contained in Diffraction Data (a) These panels show two artificial, two-dimensional lattices. Each consists of 50×50 atomic sites, with one atomic site per unit cell. Each site is occupied by an A atom (light blue) or a B atom (purple). The site occupancies for the A and B atoms are the same for both lattices. The site occupancy for a given type of atom is the fraction of the atomic sites occupied by that atom type in a lattice. In this case, the site occupancies for the A and B atoms are 30% and 70%, respectively. The structures differ in the short-range ordering of the A atoms. In the left lattice, the A atoms are clustered together; in the right lattice, they are distributed randomly. (b) This panel shows powder diffraction patterns for the two structures. The intensities and positions of the Bragg peaks are identical in both cases because Bragg scattering reveals only the average long-range structure of the material, which in this case is determined by the site occupancies of the A and B atoms. However, the diffuse scattering in the inset clearly shows the difference between the two structures. The blue curve is for the lattice on the left; the red curve is for the lattice on the right. (c) The PDFs in the bottom panel were obtained from the total-scattering data, that is, data for both Bragg and diffuse scattering. The PDFs contain information about the short-range structural ordering, as shown in the differences between the two PDFs. The difference between the two curves, enlarged by a factor of 2, is also shown in this panel (green curve).

than 20 nanometers. A typical measurement with the NPDF takes 3 to 8 hours, depending on sample size.

The NPDF is available for experiments through the User Program at the Lujan Neutron Scattering Center. Applications for beam time are accepted twice a year or through fast-access proposals at the LANSCE webpage (<http://www.lansce.lanl.gov>). Below we discuss some exciting results from recent experiments performed with the NPDF.

Example I: Nickelate with Nanoscale Domains

Although lithium nickelate has a simple chemical formula, LiNiO_2 , the compound's behavior is complex and mysterious. Lithium nickelate consists of layers of Li^+ ions sandwiched between slabs of NiO_2 (see Figure 4). When lithium is deficient (that is, there are vacancies at some of the crystal's lithium sites), lithium ions can move within the lattice, making the compound a fast ionic conductor. But LiNiO_2 's magnetic properties are intriguing as well because the Ni^{3+} ions form triangular networks in the NiO_2 slabs. For those interested in special magnetic order, a triangular network of ions with magnetic moments, or spin, is like a bone to a dog—an ideal playmate. That is so because spin ordering can be frustrated, or blocked from occurring, if the exchange interaction between spins is negative.

In spin ordering, the ions' magnetic spins adjust their orientations to lower the compound's total magnetic energy. Any mechanism or property that prevents this lowering is said to "frustrate" the magnetic ordering. Let us assume that the individual spins of three Ni^{3+} ions form a triangle and are connected through a negative exchange interaction. Here, a negative exchange interaction means that the

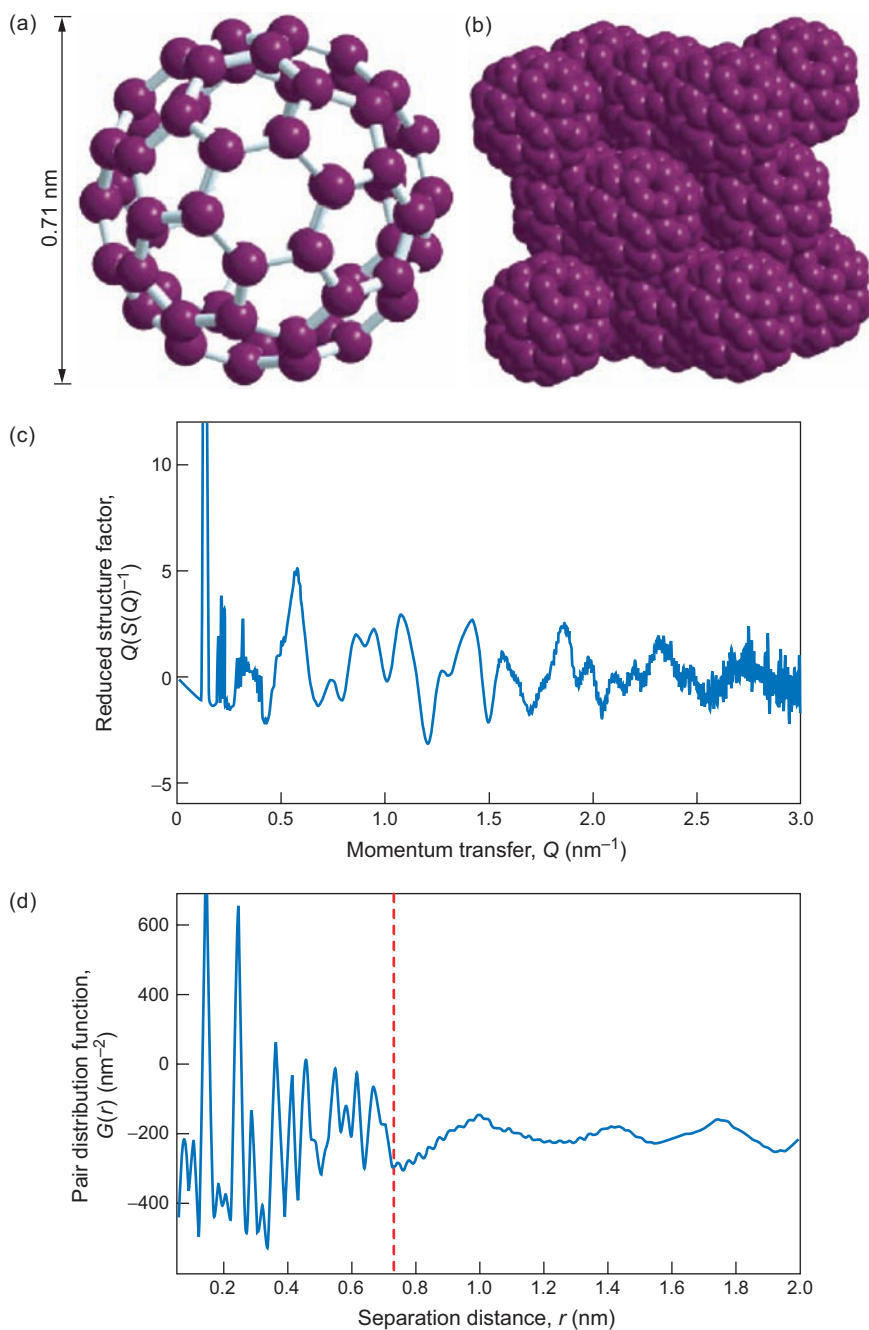


Figure 2. Buckyball Crystals

Buckyballs, or molecules of C_{60} , shown in (a) can form crystals with long-range order (b). We Fourier-transformed the normalized neutron-scattering intensity of a C_{60} crystal (c) to obtain the PDF (d). The PDF shows sharp peaks for distances smaller than the diameter of a single C_{60} molecule; the diameter is indicated by the red vertical dashed line. These peaks correspond to the C–C distances within a single buckyball. For larger distances, there are no sharp peaks, indicating that, at room temperature, there are almost no correlations between C atoms in different C_{60} molecules. [The data are from Egami and Billinge (2003).]

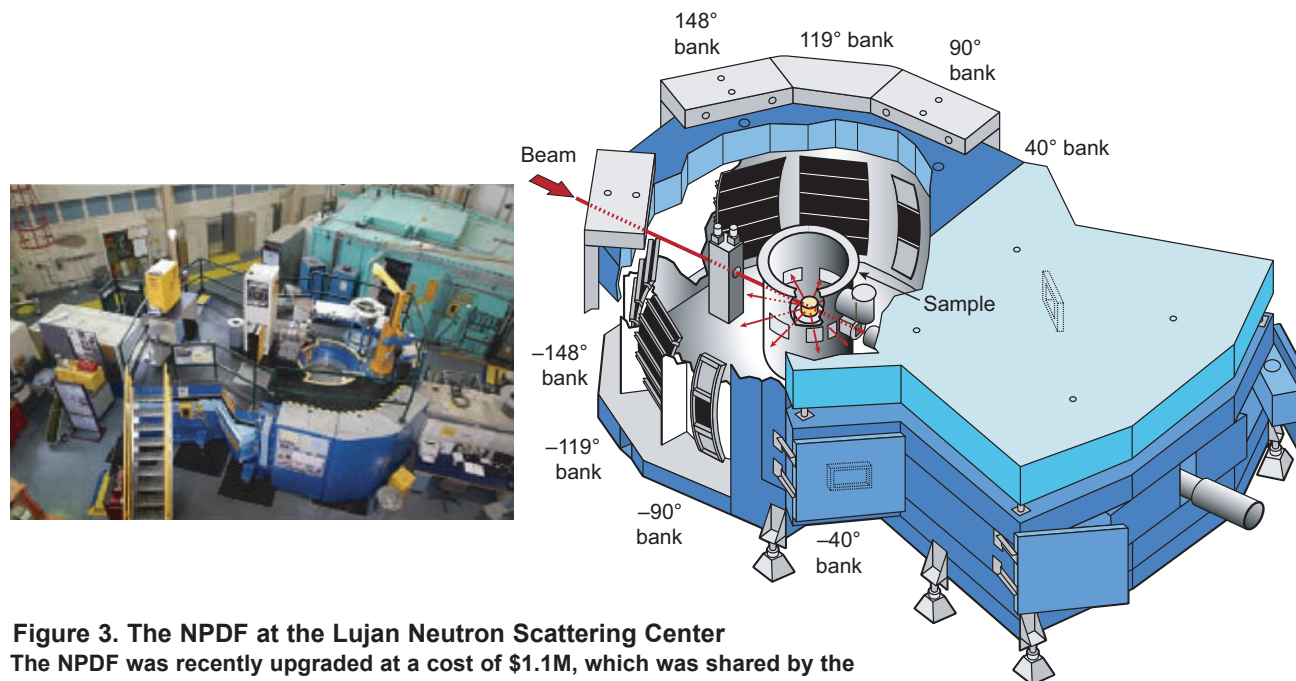


Figure 3. The NPDF at the Lujan Neutron Scattering Center
 The NPDF was recently upgraded at a cost of \$1.1M, which was shared by the National Science Foundation, several academic institutions, and Los Alamos National Laboratory. Now among the world's leading diffractometers, the NPDF is dedicated to studies of the atomic structure of complex materials.

preferred, or lowest-energy, state (the ground state) of the compound should be an antiferromagnetic spin configuration—one in which neighboring spins are antiparallel. However, if we let two of the triangle's spins be antiparallel, as shown in Figure 5, then the third spin would not know which way to point, and the transition to an antiferromagnetic state would be frustrated. Philip W. Anderson suggested (1973) that the quantum-mechanical ground state of such a system could be the resonating valence bond (RVB) state made of dynamic spin-singlet (or antiparallel-spin) pairs. The RVB state shows no phase transition to antiferromagnetic order. Indeed, LiNiO_2 shows no magnetic transition, even though Ni^{3+} clearly has a nonzero spin, $S = \frac{1}{2}$. But there is no credible confirmation of the RVB state in LiNiO_2 . The true spin ground state of this compound remains a mystery.

The ordering of the electronic orbitals of the Ni^{3+} ions seems to

be frustrated as well. A Ni^{3+} ion is a so-called Jahn-Teller (JT) ion. Such ions prefer the local atomic environment to be distorted in order to minimize the electronic energy. Each Ni^{3+} ion is surrounded by six oxygen ions, forming a NiO_6 octahedron. Ni^{3+} has seven d-electrons. Six of these electrons fill the three orbitals designated as t_{2g} , so that their total angular and spin momenta are zero, which is to say that their spatial distribution is spherically symmetric (that is, it has no preferred direction). The last d-electron goes into one of the two orbitals designated as e_g , which have z^2 and $x^2 - y^2$ symmetry, respectively. In a lithium nickelate crystal with cubic symmetry, the two orbital states would have the same energy and would therefore be called "degenerate." But if the O_6 octahedron becomes distorted, the degeneracy is lifted, and the energy level of one state decreases, and that of the other is raised. (As the degeneracy is

lifted, the original states also become new states.) In this distorted environment, the seventh electron takes on the lower energy state. Indeed, in the crystal of a sister compound, NaNiO_2 , the NiO_6 octahedra are JT distorted, and the collective JT distortion across the crystal causes it to distort macroscopically. However, there is no hint of crystal distortion in LiNiO_2 . Hence, it has been argued that the orbital ordering of the e_g state in LiNiO_2 is also frustrated, and therefore LiNiO_2 forms an "orbital" glass state (Chung et al. 2005) in which the d-electrons in the e_g orbitals have no long-range order; that is, they are randomly oriented.

The results we have obtained with the NPDF suggest a different arrangement state (Chung et al. 2005) as shown in Figure 6. To perform our experiments, we loaded a powder of LiNiO_2 in a vanadium can (vanadium is "transparent" for neutrons and often used as container material for neutron

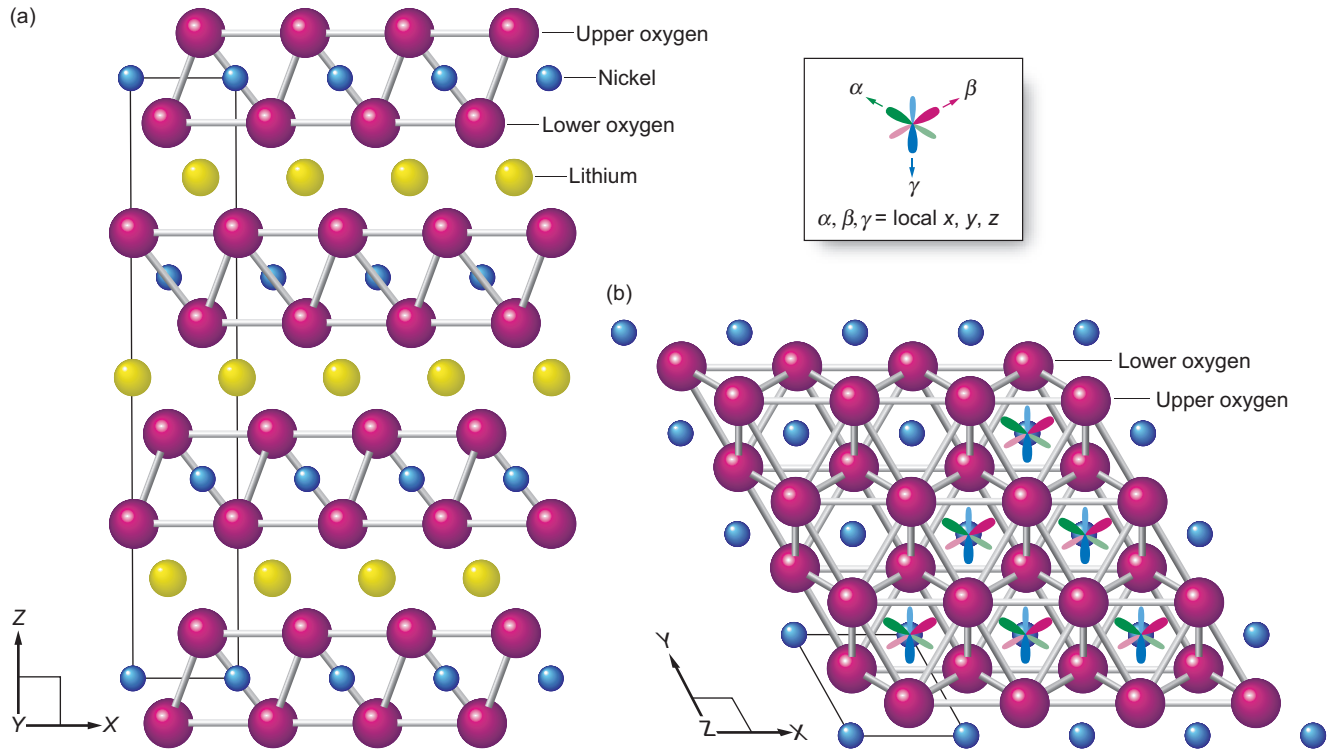


Figure 4. The Crystal Structure of Lithium Nickelate (LiNiO_2)

LiNiO_2 consists of layers of Li^+ ions sandwiched between slabs of NiO_2 . (a) This side view of LiNiO_2 shows that the thin solid lines connecting four nickel sites define the boundary of a unit cell. (b) The Ni^{3+} ions form a triangular network within each NiO_2 slab, making for an interesting magnetic ordering of the compound, as discussed in the text and shown in Figure 5. Each Ni^{3+} ion has seven d-electrons, six of which form spherically symmetrical orbitals. The orbital of the seventh d-electron can point in one of three orthogonal directions, shown as α , β , and γ . The collinear, double-lobed structures represent the possible orientations of the seventh d-electron. Using the PDF method to analyze NPDF data taken on LiNiO_2 , we have determined the local ordering of the seventh d-electron orbitals to be as shown in Figure 7.

diffraction) and measured the powder diffraction at various temperatures. We then Fourier-transformed the scattering results to obtain the PDFs. As mentioned, the NPDF's high resolution allows us to determine the PDF for separation distances of up to 20 nanometers, which is a factor of 4 higher than results obtained elsewhere so far—refer to Figure 6a. From the PDF, we see that the nearest-neighbor environment of Ni^{3+} (out to 0.25 nanometer) is indeed JT distorted. Notice the shoulder on the blue curve

on the high- r side of the first PDF peak in Figure 6b. That shoulder represents the longer Ni–O bond and indicates the JT distortion. However, by modeling the medium-range order (between approximately 0.5 and 2 nanometers), we found that the local JT distortions are not collinear but point in three directions perpendicular, or “orthogonal,” to each other (refer to Figure 7). Below about 375 kelvins, the local JT distortions form three sublattices corresponding to the three directions. Because the local distor-

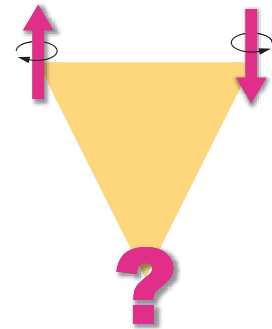


Figure 5. Frustrated Magnetic-Spin Ordering

This drawing shows how an antiferromagnetic system with a magnetic spin at each vertex of a triangle cannot lower its magnetic energy by orienting the neighboring spins so that they are antiparallel. This drawing applies to the magnetic spins of the Ni^{3+} ions in LiNiO_2 , which form a triangular network, as shown in Figure 4.

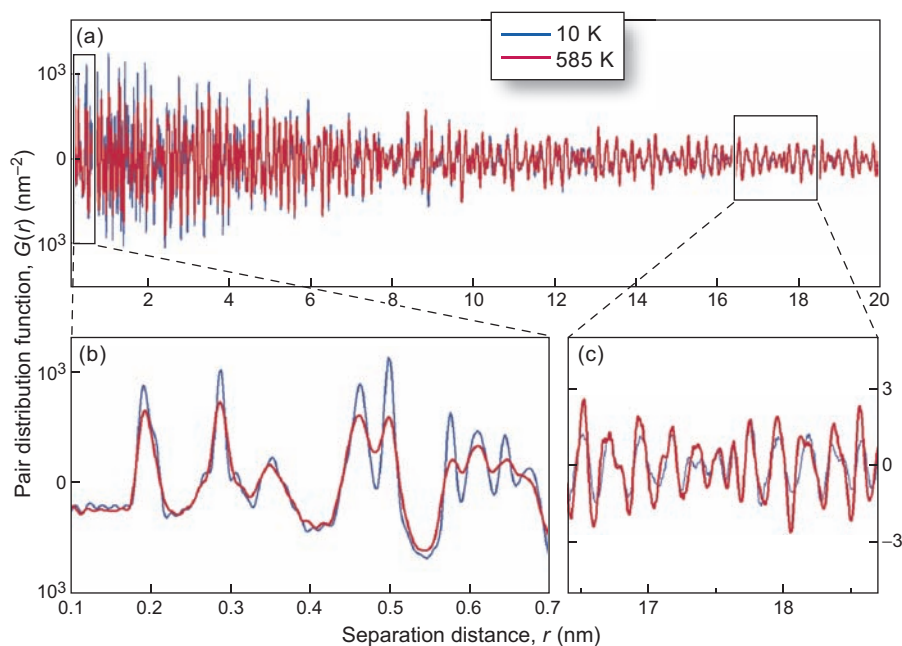


Figure 6. PDFs of LiNiO_2

These plots are from data of LiNiO_2 taken with the NPDF at 10 K (blue curves) and 585 K (red curves). (a) The full range of the data is shown for atom-atom separation distances of up to 20 nm. (b) In the low- r (near-neighbor) region, the PDF peaks broaden as the temperature increases. (c) In the high- r (far-neighbor) region, the opposite occurs, providing direct evidence for the existence of nanoscale domains, which decrease the crystal's long-range order.

tions are orthogonal, there is no macroscopic distortion.

The PDF results also surprised us in another respect. Because the PDF measures atomic correlations, its peaks usually become sharper at low temperatures as thermal vibrations diminish. Indeed, the peaks at short distances for LiNiO_2 's PDFs do exactly that. However, the peaks at distances larger than 8 or 9 nanometers actually become broader at lower temperatures—refer to Figure c. This feature is observed because the local JT distortions are orthogonal, so that the inversion symmetry of the NiO_2 plane is lost, and the plane wants to curve. [In a lattice with inversion symmetry, an atom present at point (x,y,z) has a corresponding atom present at point $(-x,-y,-z)$.]

The result is that domains about 10 nanometers in size form below 375 kelvins. The orbital ordering of the three sublattices is preserved within a domain, and the curvature reverses at a domain boundary (Chung et al. 2005). The formation of the nanodomains frustrates the long-range ordering of the orbital orientations.

Our PDF analysis of NPDF data has furthered our understanding of LiNiO_2 's atomic structure, as well as of its electronic structure through the JT distortion, and may help us understand anomalous experimental observations of the compound's magnetic spin susceptibility. Understanding the material's magnetic interactions could in turn help us develop new technological materials.

Example II: Possible Electronic Inhomogeneity in Superconducting Cuprates

Cuprates that exhibit high-temperature superconductivity (HTSC) are another example of intriguing oxides with local complexity. When the HTSC phenomenon was discovered in 1986 (Bednorz and Müller), many theorists predicted it would be understood fairly quickly because they claimed to already know, more or less, what was going on—although they could not agree on exactly which theory was right. History has since shown how wrong they were and how complex the phenomenon is.

One of the most intriguing complexities of the high-temperature cuprate superconductors is the pronounced inhomogeneity of their electronic structure. This inhomogeneity is baffling, since electronic disorder will scatter and break the Cooper pairs, which are the charge carriers that produce superconductivity. On the other hand, there are many superconductors whose structures are strongly disordered. For instance, some amorphous metallic alloys, such as niobium-boron (Nb-B), are superconducting. But the length scale of the structural disorder (atomic scale) for Nb-B is quite different from its superconducting coherence length (tens or hundreds of nanometers). By contrast, the superconducting coherence length of high-temperature cuprate superconductors is only a few nanometers, and these cuprates appear to have structural inhomogeneities with a similar length scale. The presence of these structural inhomogeneities was first suggested by indirect measurements (Egami and Billinge 1996), although most workers in the field dismissed the inhomogeneities as merely “dirt” (that is, unwanted impurities introduced during sample making) irrelevant to HTSC, or as byproducts of strong coupling at best. Recently,

however, several beautiful images of nanoscale structural inhomogeneities, which were obtained by scanning tunneling microscopy (STM), have appeared in the literature (Pan et al. 2001, Lang et al. 2002, McElroy et al. 2003). It has therefore become more difficult to ignore the possibility that structural inhomogeneities could be an integral part of HTSC. And yet, because STM is a surface probe, the inhomogeneity observed by STM may be considered a surface phenomenon.

To investigate the possibility that structural inhomogeneities are integral to HTSC, we examined a series of high-temperature cuprate superconductors, namely, $\text{La}_{2-x}\text{Sr}_x\text{CuO}_4$ (LSCO), with the NPDF. The parent compound, $x = 0$, is a charge transfer insulator (Zaanen 1985) with long-range antiferromagnetic order. Replacing La^{3+} with Sr^{2+} dopes, or introduces holes into, the system, and these cuprates show HTSC for $0.06 \leq x \leq \sim 0.25$. We obtained PDFs of powdered LSCO samples with x varying from 0 to 0.3. Figure 8 shows the PDFs at $T = 10$ kelvins as functions of distance r and composition x . These PDFs show that the long-range structure (larger than 2 nanometers) varies smoothly with x , while there are anomalous structural variations at distances smaller than 2 nanometers. In particular, deviations from the average structure, as determined by Rietveld analysis, are stronger below 2 nanometers. Although we are still analyzing the details, the results obtained with the NPDF thus far appear to be consistent with those of the STM studies and to indicate that the inhomogeneities exist within the volumes of the materials, not just at their surfaces. At present, however, we do not know what kind of structural deviations exist in these samples. It will be interesting to see how accurately data obtained with the NPDF and analyzed by the PDF technique allow determining the real structures of these strange

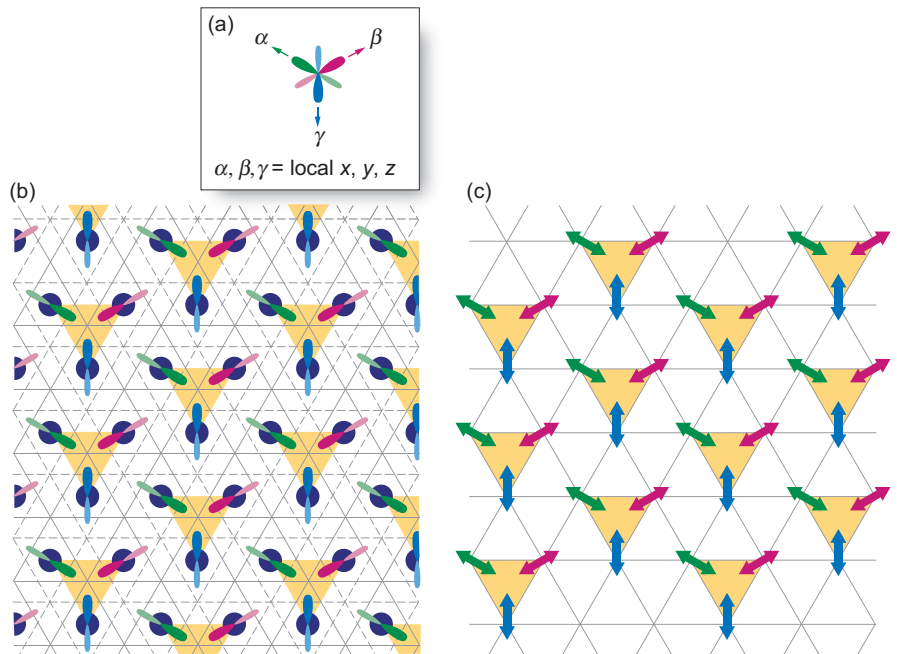


Figure 7. PDF Results for Local Orbital Ordering

(a) A three-dimensional perspective is shown of the three possible orientations of the seventh d-electron orbitals for a single Ni^{3+} ion. (b) Illustrated here is the local ordering of the seventh d-electron orbitals of the Ni^{3+} ions in LiNiO_2 . The dark blue circles are the Ni^{3+} ions. The solid and dashed lines are the upper and lower oxygen planes, respectively (see also Figure 4). We deduced this ordering by comparing PDFs obtained from NPDF measurements of LiNiO_2 with the PDFs of several models of the orbitals' possible orientations. Our analysis shows that this ordering extends over nanoscale domains with sizes of ~ 10 nm. (c) The double-headed arrows indicate the three possible orientations of the orbitals in a particular domain and correspond to three different sublattices (each sublattice corresponds to a differently colored double-headed arrow). In fact, the orbitals for the three sublattices are not in a single plane but are orthogonal, which is why the crystal is not macroscopically distorted—unlike LiNiO_2 's sister compound, NaNiO_2 . In (b) and (c), the orbitals appear to be in a single plane because of the top-view perspective.

and complex cuprates.

We also studied $\text{Na}_{0.3}\text{CoO}_2 \cdot 1.4\text{H}_2\text{O}$, another strange oxide superconductor, a cobaltate that incorporates water molecules in its structure. This cobaltate has the same structure as LiNiO_2 except for the intercalated water (Takada et al. 2003). For our neutron-diffraction studies of this cobaltate, we replaced hydrogen with deuterium to better see the locations of the water molecules. Results indicate that the

water molecules are strongly modified in this compound, but further analysis is needed to understand the implications of this new finding.

It is likely that such nanoscale, multilevel complexities are not uncommon in complex oxides. No doubt, in the future, there will be many opportunities for using the PDF technique on NPDF data to help solve the structural mysteries of other interesting compounds. ■

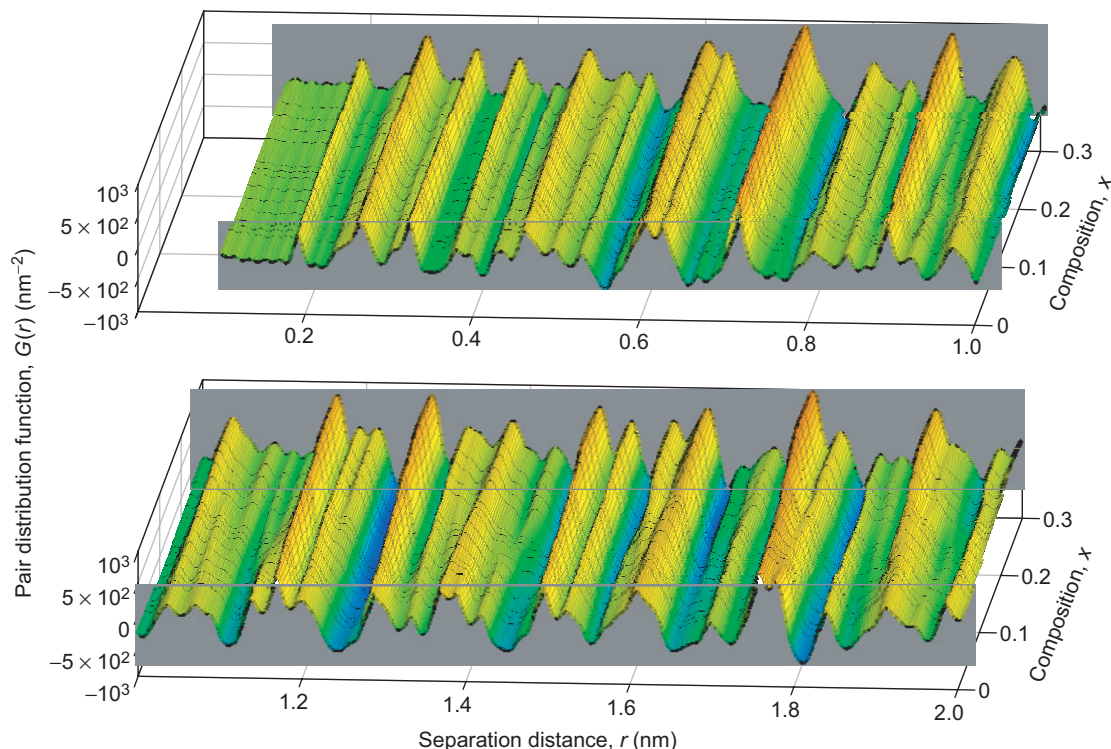


Figure 8. PDFs of $\text{La}_{2-x}\text{Sr}_x\text{CuO}_4$, a High-Temperature Superconductor, as a Function of Composition x All data were taken at $T = 10$ K. Rietveld analysis of the total scattering data suggests that the long-range structure varies smoothly with composition, but these PDF results clearly show structural inhomogeneities to a separation distance of 2 nm. Although some studies had provided similar results, these are the first systematic studies revealing such inhomogeneities, which could be an integral part of high-temperature superconductivity.

Further Reading

- Anderson, P. W. 1973. Resonating Valence Bonds: A New Kind of Insulator? *Mater. Res. Bull.* **8**: 153.
- Bednorz, J. G., and K. A. Müller. 1986. Possible High T_c Superconductivity in the Ba-La-Cu-O System. *Z. Phys. B* **64**: 189.
- Chung, J.-H., Th. Proffen, S. Shamoto, A. M. Ghorayeb, L. Croguennec, W. Tian et al. 2005. Local Structure of LiNiO_2 Studied by Neutron Diffraction. *Phys. Rev. B* **71**: 064410.
- Egami, T., and S. J. L. Billinge. 1996. Lattice Effects in High- T_c Superconductors. In *Physical Properties of High Temperature Superconductors V*. Edited by D. M. Ginsberg. River Edge, NJ: World Scientific.
- . 2003. *Underneath the Bragg Peaks: Structural Analysis of Complex Materials*. Amsterdam: Pergamon.
- Lang, K. M., V. Madhavan, J. E. Hoffman, E. W. Hudson, H. Eisaki, S. Uchida, and J. C. Davis. 2002. Imaging the Granular Structure of High- T_c Superconductivity in Underdoped $\text{Bi}_2\text{Sr}_2\text{CaCu}_2\text{O}_{8+x}$. *Nature* **415**: 412.
- McElroy, K., R. W. Simmonds, J. E. Hoffman, D. H. Lee, J. Orenstein, H. Eisaki et al. 2003. Relating Atomic-Scale Electronic Phenomena to Wave-Like Quasiparticle States in Superconducting $\text{Bi}_2\text{Sr}_2\text{CaCu}_2\text{O}_{8+x}$. *Nature* **422**: 592.
- Pan, S. H., J. P. O'Neal, R. L. Badzey, C. Chamon, H. Ding, J. R. Engelbrecht et al. 2001. Microscopic Electronic Inhomogeneity in the High- T_c Superconductor $\text{Bi}_2\text{Sr}_2\text{CaCu}_2\text{O}_{8+x}$. *Nature* **413**: 282.
- Takada, K., H. Sakurai, E. Takayama-Muromachi, F. Izumi, R. A. Dilanian, and T. Sasaki. 2003. Superconductivity in Two-Dimensional CoO_2 Layers. *Nature* **422**: 53.
- Zaanen, J., G. A. Sawatzky, and J. W. Allen. 1985. Band Gaps and Electronic Structure of Transition-Metal Compounds. *Phys. Rev. Lett.* **55** (4): 418.

Pair Distribution Function for Nanoparticle Studies

Thomas Proffen, Katharine L. Page, Ram Seshadri*, and Anthony Cheetham*

* UC Santa Barbara

Composed of only a few thousand atoms, a nanoparticle can have unique optical, electronic, magnetic, or chemical properties. Such properties are enabling new types of biosensors, drug delivery methods, lubricants, and solar cells and are intimately related to the nanoparticles' structures. However, the preferred tools for measuring the structures of bulk materials—conventional diffraction methods with x-rays or neutrons—often give poor-quality information when applied to nanoparticles. Using the pair distribution function (PDF) method to analyze neutron-diffraction data obtained with the neutron powder diffractometer, we have obtained high-quality structural measurements of gold nanoparticles. These measurements can be used to validate atom-level computer models of nanoparticles and to characterize their structures.

The obvious difference between nanoparticles and their bulk counterparts is size. Because of the nanoparticles' tiny size, conventional diffraction methods often fail to yield accurate measurements of their structure. Those methods assume an infinitely periodic system, which does not work with nanosizes. By contrast, the pair distribution function has no periodicity requirement and thus no

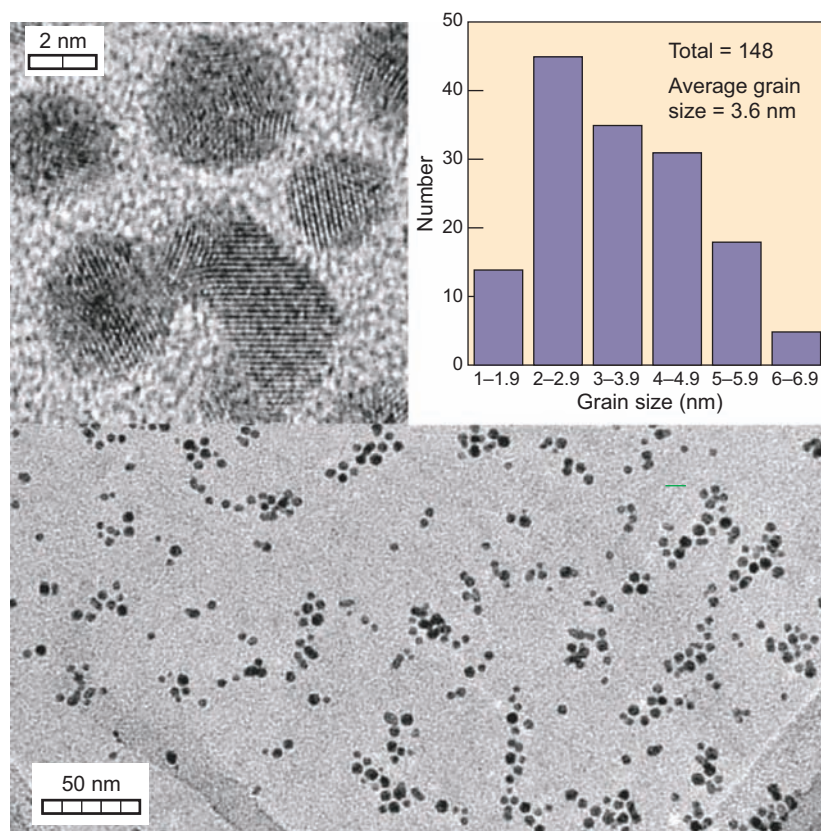


Figure 1. Transmission Electron Micrograph (TEM) of Gold Particles Individual gold nanoparticles are shown in this TEM. The inset is a high-resolution TEM of a few nanoparticles. (b) The histogram shows the particle size distribution. The nanoparticles' mean diameter is ~3.6 nm.

limitation on particle size.

Another difference is that the number of atoms on the surface of a bulk material is small compared with the number of atoms in the core.

By contrast, a nanoparticle's surface atoms can comprise up to 20 percent of its atoms. Again, since the PDF does not require periodicity, it is an ideal method for studying differences

between the surface and core structures of a nanoparticle.

To demonstrate the PDF's ability to measure nanoparticle structure, we took diffraction data with the neutron powder diffractometer (NPDF) on fluoroethyl-capped gold nanoparticles and on a bulk gold sample. We then Fourier-transformed the diffraction data to obtain the PDFs. Figure 1 shows a transmission electron micrograph (TEM) of the individual gold nanoparticles and a histogram of the particle size distribution; the average size is about 3.6 nanometers. Neutron-scattering experiments usually require large samples; this experiment required 1.5 grams of nanoparticles. The measurement lasted for about 15 hours.

Figure 2 shows the experimental PDFs for bulk gold (a) and gold nanoparticles (b). The PDF for bulk gold decreases with r , the atom-atom separation distance, because of the NPDF's finite resolution. However, atom-atom correlations (the small peaks) are clearly visible for large values of r . By contrast, the PDF peaks for the nanoparticles diminish at much smaller r values because there are no atom-atom pairs separated by more than the particle diameter (the vertical dashed line in Figure 2). Because we determined the PDF to atom-atom distances of 10 nanometers—much larger than the nanoparticles' diameters—the PDF provides all atom-atom separation distances of the nanoparticles.

Figure 3 shows the PDFs from experimental data for gold nanoparticles at two temperatures. The peaks at ~ 0.28 nanometer correspond to the closest distance between the gold atoms and confirm previous findings that gold nanoparticles have slightly smaller unit cells than bulk samples do. The sharpness and symmetry of the peaks also show that there is no significant relaxation of the structure near the nanoparticle's surface. The

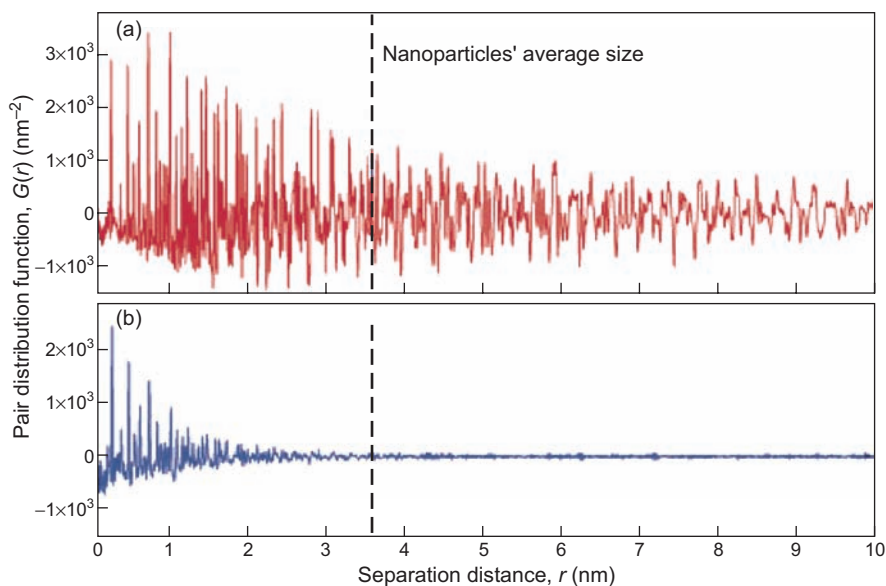


Figure 2. PDFs of Bulk and Nanoparticle Gold Samples

The PDFs of a bulk gold sample and a nanoparticle gold sample to an atom-atom distance (r) of 10 nm are shown in (a) and (b), respectively. The data were taken with NPDF spectrometer at LANSCE. The dashed line marks the nanoparticles' average size. The bulk sample shows atom-atom correlations over the full range of atom-atom separation distances. The PDF peaks decrease with r because of the NPDF's finite resolution. By contrast, there are PDF peaks for the nanoparticle sample only out to the nanoparticles' mean diameter.

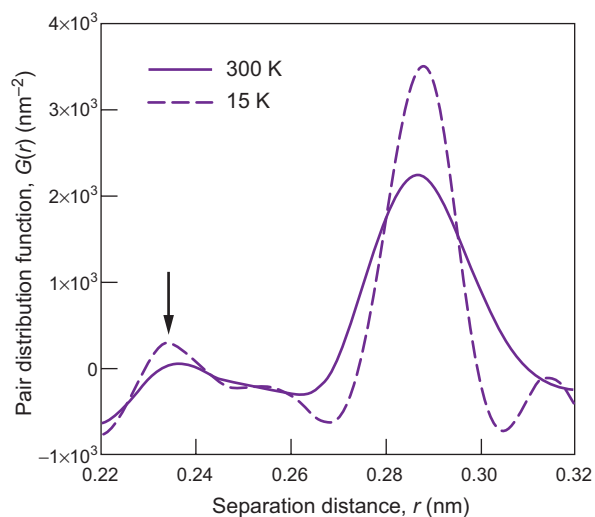


Figure 3. PDFs for Gold Nanoparticles as a Function of Temperature

The PDFs [$G(r)$] at small atom-atom separation distances (r) for experimental data are shown for two temperatures. The small peaks indicate the distance between surface gold atoms and the sulphur atoms in the nanoparticle coating. The large peaks indicate the nearest-neighbor distance between the gold nanoparticles.

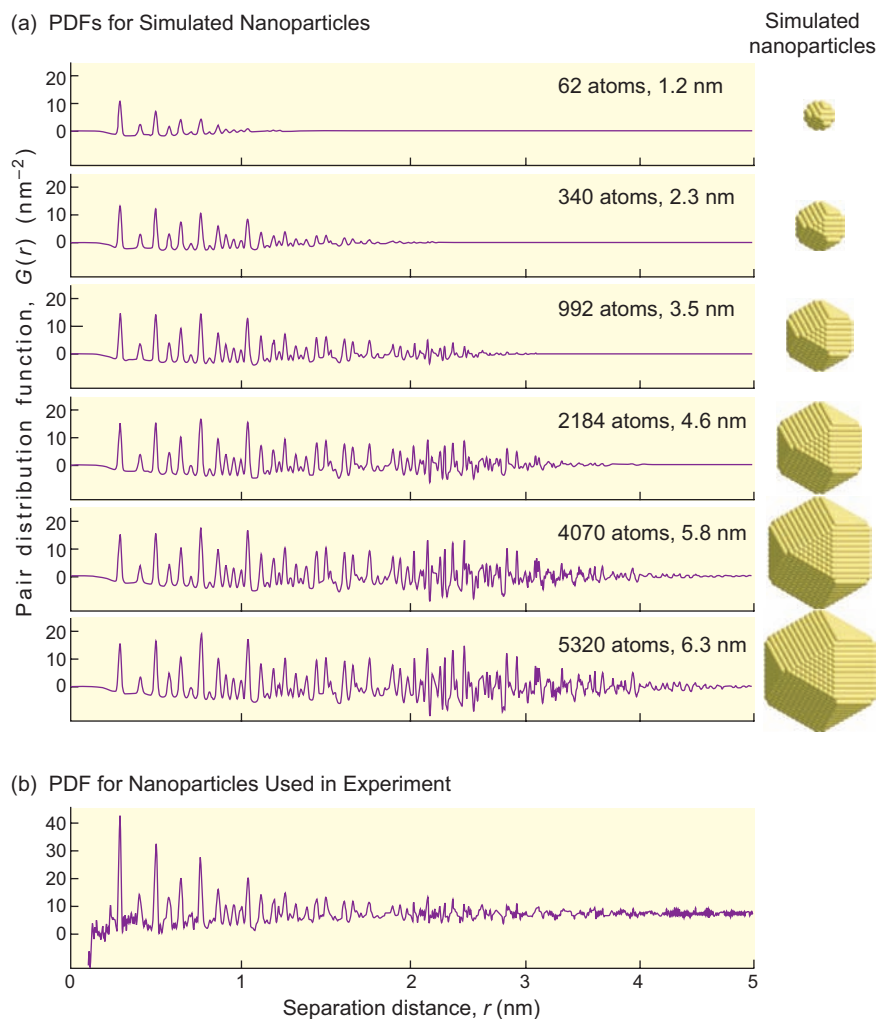


Figure 4. PDFs Calculated for Simulated and Real Gold Nanoparticles (a) Shown here are PDFs for simulated cuboctahedral gold nanoparticles whose sizes are between 1.2 and 6.3 nm. (b) This PDF of gold nanoparticles was calculated from experimental data and is also shown in Figure 2(b). The data were obtained with the NPDF spectrometer.

arrow corresponds to the closest distance between the surface gold atoms and the sulfur atoms in the thiol capping the nanoparticles. This peak is sharper at lower temperatures because thermal vibrations are reduced.

The next step in these studies will be to refine the experimental PDFs with a structural model. One usually starts refining a model based on the lattice parameters and the positions of the atoms in the bulk material (gold,

in this case). The refinement yields structural parameters, which are then compared with the results from the bulk material. In many cases, the PDF contains evidence of disorders (for example, structural distortions at the nanoparticles' surfaces, which contain significant fractions of the atoms in the nanoparticles' structures). These deviations from the average structure are hidden to the Rietveld analysis, and describing them requires

modifications to the atomic model. A detailed discussion of what is involved is beyond the scope of this article, but the interested reader can refer to Page et al. (2004).

Although the experiments used to obtain PDFs are usually quite straightforward, it is often fairly difficult to do computer simulations at the atomic level and compare them with the experimental data. A bulk specimen will contain about 10^{23} atoms or more—well beyond the simulation capabilities of state-of-the-art computers. But since a typical nanoparticle might contain only a few thousand atoms, a complete nanoparticle can be modeled on a computer. Figure 4 shows the PDFs obtained with computer models for cuboctahedral gold nanoparticles of different sizes. High-quality experimental PDFs obtained with instruments such as the NPDF can be used to validate computer simulations of nanoparticles. The PDF method in general and especially as applied to nanoparticles will continue to play a significant role in advancing our knowledge of complex materials.

Further Reading

- Egami, T., and S. J. L. Billinge. 2003. *Underneath the Bragg-Peaks: Structural Analysis of Complex Materials*. Amsterdam; Boston: Pergamon.
- Page, K. L., Th. Proffen, H. Terrones, M. Terrones, L. Lee, Y. Yang, et al. 2004. Direct Observation of the Structure of Gold Nanoparticles by Total Scattering Powder Neutron Diffraction. *Chem. Phys. Lett.* **393** (4–6): 385

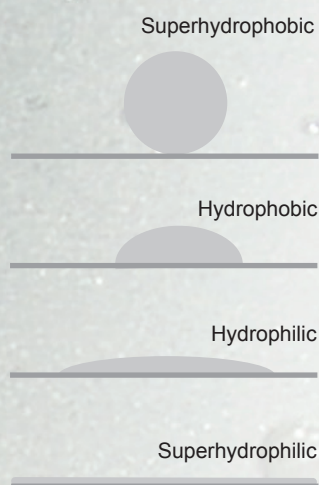
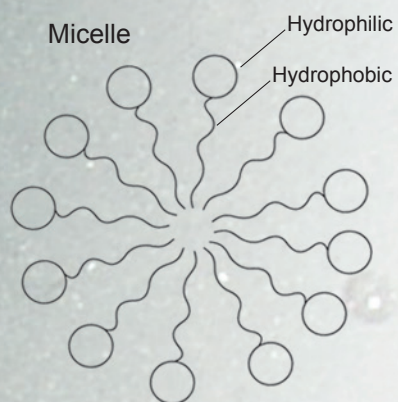
The Hydrophobic Effect

Why Do Raindrops Slide off Leaves?

Dhaval A. Doshi, Erik B. Watkins, Jacob N. Israelachvili, and Jaroslaw Majewski

Many interesting phenomena occur at the surface where two materials meet, and for biological and chemical processes, one of these two materials is often water. Using neutron reflectometry to look at the interface between water and a hydrophobic surface, scientists at the Los Alamos Neutron Science Center have confirmed that water literally hovers above the hydrophobic (or water-hating) surface on a very thin, low-density water layer. The thickness of that layer is about a million times smaller than a millimeter, and it changes with the type and concentration of gas present in the liquid. The presence of a water-depleted layer at hydrophobic surfaces may have implications for many processes—from protein folding and formation of lipid membranes, relevant to biology, to new technologies for water purification and fuel cells.





In nature, surfaces range from hydrophilic (water-loving) to hydrophobic (water-hating) or, more exactly, from superhydrophilic to superhydrophobic. The contact angle between a water droplet and the surface goes from much less than 90° for hydrophilic surfaces to much more than 90° for superhydrophobic surfaces. The latter are typically very rough. Examples include butterfly wings and the leaves of many plants. Amphiphilic molecules have hydrophilic, or polar, heads and hydrophobic, or hydrocarbon, tails. In water, they tend to assemble into closed micelles with the hydrophilic heads on the surface and the hydrophobic tails in the interior. Detergents fall into this category, enclosing dirt particles as they form micelles in water.

The interplay between water and a hydrophobic surface is found everywhere in nature. Water molecules, which tend to stick together because of the large electrical dipole forces between them, segregate from nonpolar molecules such as oil and other hydrocarbons.¹ Raindrops roll off a silane-treated windshield, and the lotus leaf is self-cleaning because of this property.

Life exists in and depends on the vicinity of water. As a result, most biological processes, to one extent or another, are shaped by the interaction between biological molecules and water. Proteins, the tiny biological machines inside our bodies, are built out of parts that are hydrophobic and hydrophilic (having an affinity for water). The way the proteins are shaped and function depends on the intricate interplay of these different parts and the water environment that surrounds them.

In engineering contexts, the hydrophobic interaction influences a wide range of phenomena, including the behavior of small particles in solution, the self-assembly of molecules into bigger complexes, the way detergents clean our clothes, oil recovery processes, the manufacture of nonstick surfaces, mineral extraction and separation, anticorrosive layers, and water flow through small pores in hydrophobic membranes. Understanding the way water flows through such pores holds the key to designing materials and processes for future water purification systems, for fuel cell membranes, and for microfluidic devices. Thus, understanding the interface between water and the hydrophobic layer (hereafter referred to as “the water-hydrophobic interface”) bears

¹ Dipole forces are created by the separation of negative and positive charges. Nonpolar molecules are those in which there are no separate concentrations of charges.

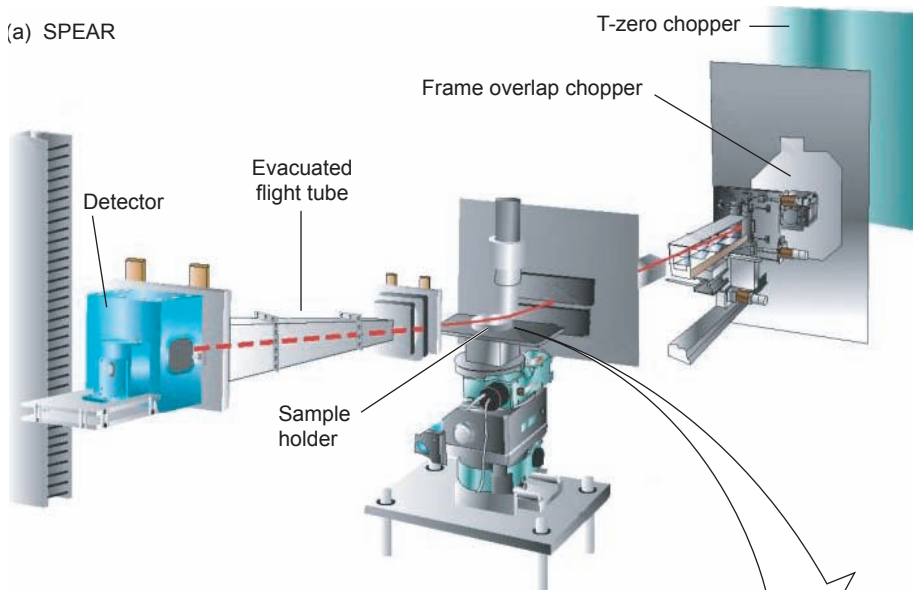
not only on biological questions, such as the origin of life, but also on our future water and energy resources, which affect our national security.

But what exactly happens at a water-hydrophobic interface? Are there structural changes at the molecular level that produce the hydrophobic effect? That question has been debated for over 50 years. Yet despite the ubiquitous presence of the hydrophobic effect, its range and origin have not been resolved. A new wrinkle was added to the debate when Jacob Israelachvili and Richard Pashley (1984) discovered a long-range attractive force between two hydrophobic surfaces submerged in water. That attractive force, called the hydrophobic interaction, extends tens of nanometers (one nanometer is one billionth of a meter). Early theoretical models suggested that, at the hydrophobic-water interface, the structure of water changes to a less-dense, more-ordered phase akin to ice. More recently, images from experiments done with an atomic force microscope suggested that submicroscopic water-vapor bubbles, 50 to 500 nanometers in diameter and 5 to 50 nanometers in height, are present on some hydrophobic surfaces (Attard 2003). But the atomic force microscope is an invasive tool, introducing an additional interface into the system and additional doubts in the results.

In our recent experiments, we used a noninvasive neutron-reflectivity technique to study the water-hydrophobic interface and found a tiny cushion of low-density water between the hydrophobic surface and the bulk liquid. The water-depleted cushion appears to be only about 1 nanometer thick and decreases in thickness a few tenths of a nanometer when the water is degassed. We postulate that the layer is made of density fluctuations rather than a fixed density distribution. Instead of a constant slab of water vapors next to the surface,

Figure 1. Neutron Reflectometry Experiments at LANSCE

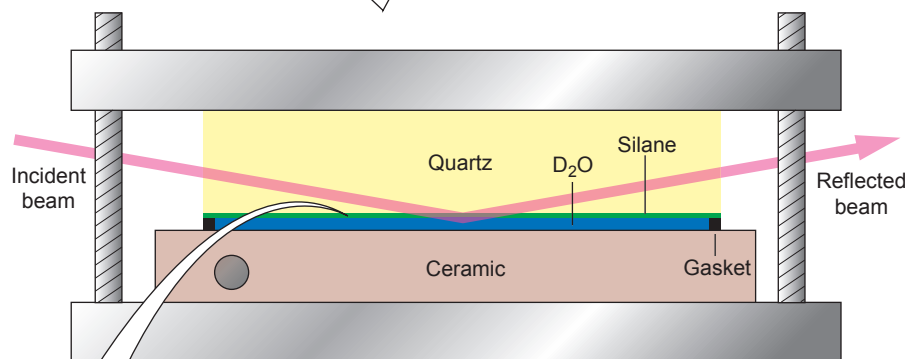
(a) SPEAR



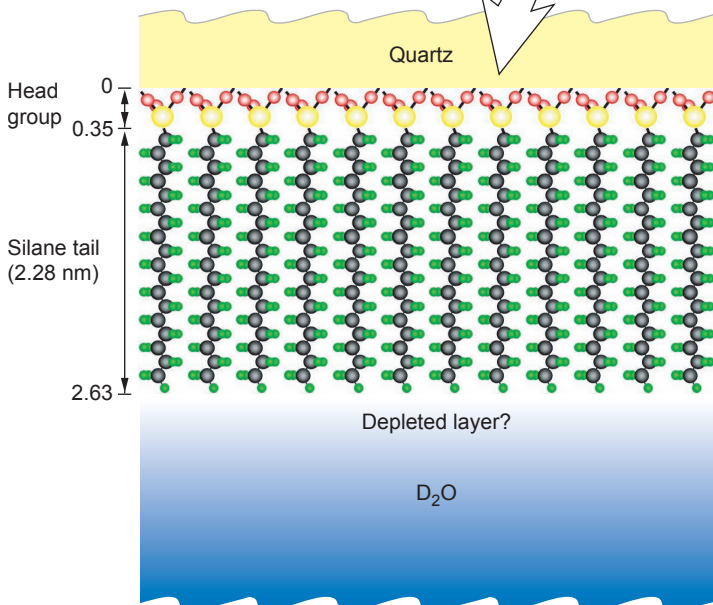
(a) The diagram shows a neutron beam being reflected from our sample at SPEAR, the Surface Profile Analysis Reflectometer at LANSCE. SPEAR is ideally suited for studies of thin (0.5 to 300 nm) organic and inorganic layers in different environments. The instrument uses an unpolarized neutron beam. Two choppers define a typical neutron wavelength range of 0.15 to 1.6 nm. Because the beam is inclined to the horizon at a very small angle (0.9°), the instrument can measure reflectivity from liquid-air interfaces. With SPEAR, good statistics can be obtained even for very low reflectivity in only 3 to 4 h.

(b) This blowup of the sample cell's interior shows the quartz-silane layer on top, a ceramic base on the bottom, and a gasket between them. It is through an inlet in the ceramic base that D_2O is injected into the enclosed space created by the gasket. The red swath indicates the path of the incident and reflected neutrons. The beam is about 1×10 mm and reflects from the quartz-silane and silane- D_2O interfaces.

(b) Side View of Sample Cell



(c) Sample



(c) This sample blowup shows the monolayer of silane molecules, each one containing a head group and an 18-carbon-chain octadecyl-trichlorosilane (OTS) tail. These molecules were deposited according to a prescribed procedure on a quartz substrate (Maoz and Sagiv 1984). Initial x-ray reflectivity measurements in air indicate that the silane portion of the monolayer has a thickness of $t_{hc} = 2.28 \pm 0.05$ nm, which is very close to the theoretical length for fully stretched octadecyl chains. Also shown is the adjacent layer of deuterated water with a low-density region at the hydrophobic interface.

we picture a dynamic interface at which water repeatedly touches and leaves the hydrophobic surface. Our results are consistent with recent measurements of the drag produced by flow past hydrophobic surfaces and promise to enable further quantitative understanding of hydrophobic phenomena.

Measuring the Hydrophobic-Water Interface with Neutron Reflectometry

Before our measurements, experimental evidence had generated much controversy concerning the nature and behavior of water when it meets a hydrophobic surface. Neutron reflectivity experiments at other laboratories suggested the existence of a “water-depleted,” “dewetting,” or “precursor gas” layer with a thickness of 1 to 4 nanometers and a mean density of 85 to 90 percent that of water. However, the systems studied were made of thick or multicomponent layers that complicated the interpretation of the results (Schwendel et al. 2003, Steitz et al. 2003). At the same time, x-ray studies were also inconclusive (Jensen et al. 2003). Disagreements regarding the accuracy of neutron and x-ray reflectivity measurements have been outlined by Phillip Ball (2003).

To understand the properties of the water-hydrophobic interface, we conducted neutron reflectivity experiments on a simple sample, containing a very thin hydrophobic layer and a water layer with high scattering contrast between the two. Figure 1 shows a schematic of our experiment at the SPEAR neutron reflectometer at the Los Alamos Neutron Science Center (LANSCE). The figure also shows details of the cell that houses the sample and the sample itself. From top to bottom, our sample consists of a highly polished quartz crystal, an atomically flat (2.28-nanometer-thick)

self-assembled monolayer of silane molecules chemically attached to the quartz, and a layer of deuterated water (D_2O)—that is, water (H_2O) in which each hydrogen atom is replaced by its heavier isotope, deuterium—to create high contrast relative to the hydrophobic silane layer. The contrast we are interested in is between the neutron scattering-length densities (SLDs) of the system’s components. The SLD depends on the density of the material, as well as on how well the material’s atoms scatter neutrons. Both the quartz layer and the D_2O layer scatter neutrons strongly, whereas the silane layer scatters neutrons weakly. Therefore, the silane layer becomes easily discernible by neutron reflectivity.

During the experiment, incident neutrons with varying wavelengths bombard the sample at glancing angles. When they reach an interface where the density changes, more exactly, where the neutron SLD changes, some are refracted as they enter the next medium, and the remainder are reflected from the surface. The interference pattern resulting from reflections from two or more surfaces reveals the distances between those surfaces, as explained in the box “Measuring Reflectivity” on page 170. In our experiment, we were able to detect not just abrupt changes in density, but also gradual changes at the hydrophobic silane-water interface. Given the high resolution of SPEAR, changes to the density profile as small as one hundredth of a nanometer could be resolved. We repeated the reflectivity experiment using the same hydrophobic layer but with water samples containing different dissolved gases.

One might wonder why we use neutrons rather than x-rays to image a buried hydrophobic-water interface. The primary reasons are that neutrons can traverse centimeter distances in a material before and after being

reflected and can sense differences in density between a hydrophobic layer and a deuterated water layer.

Experimental Results

As an example, Figure 2a shows three reflectivity curves corresponding to our hydrophobic system in contact with water under three different conditions: naturally aerated, degassed, and argon bubbled water, respectively. Because the system is extremely simple—a low neutron-scattering region (hydrocarbon molecules and water-depleted layer) is sandwiched between two high-scattering regions (quartz and deuterated water)—trends can be deduced directly from the data. In particular, the average thickness d of the low neutron-scattering region can be deduced from the values of the momentum transfer Q_z at which the reflected neutron intensity reaches a minimum (Kjaer 1994). The thickness is given by $d = 2\pi/Q_{z,\min}$ (refer to the box “Measuring Reflectivity”). Figure 2a shows minima at three different Q_z values corresponding to the different types of dissolved gas in the deuterated water. In all three cases, the thickness of the low-reflectivity region is larger than the maximum thickness of the hydrocarbon molecules. We interpret that increase as the presence of a low-density D_2O region adjacent to that layer. Such a low-density D_2O region would have a reflectivity well below that of deuterated water and thus would appear to increase the thickness of the hydrocarbon layer.

To obtain a more detailed density profile for the low neutron-scattering region, we developed a model of the density profile and determined the free parameters by fitting the data. Figure 2b shows the layers of constant thickness and scattering-length density used to describe the hydrocarbon chains and the region of

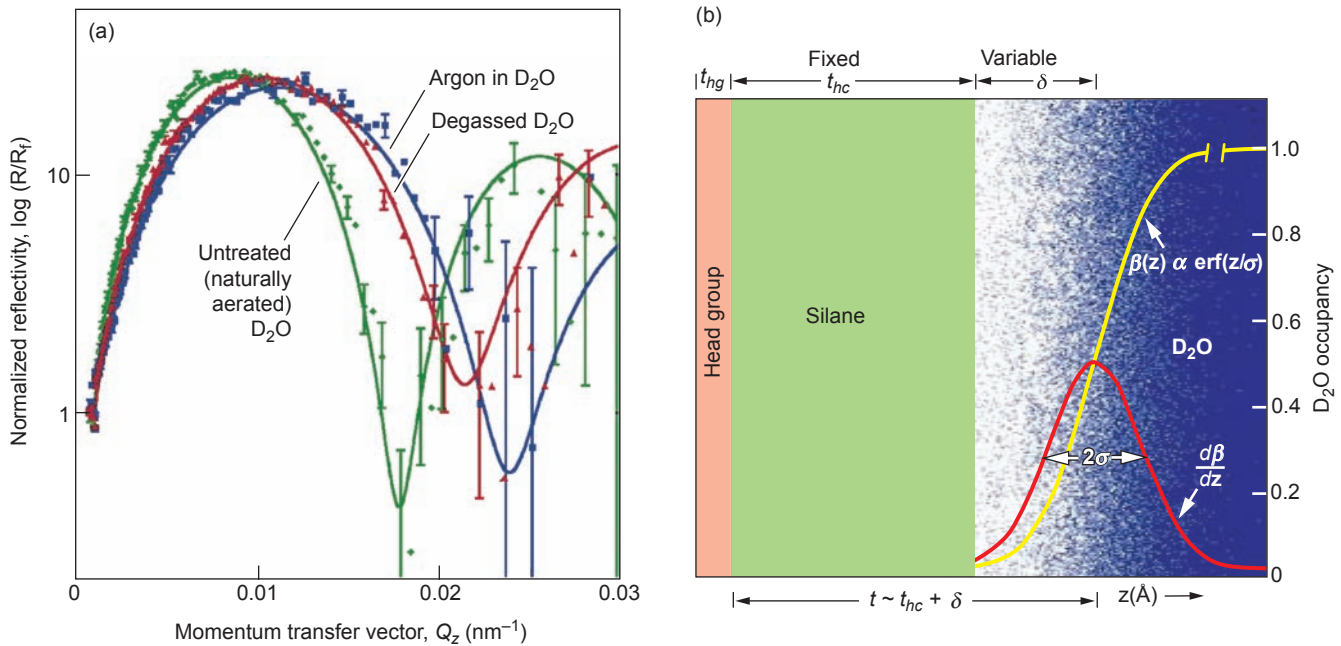
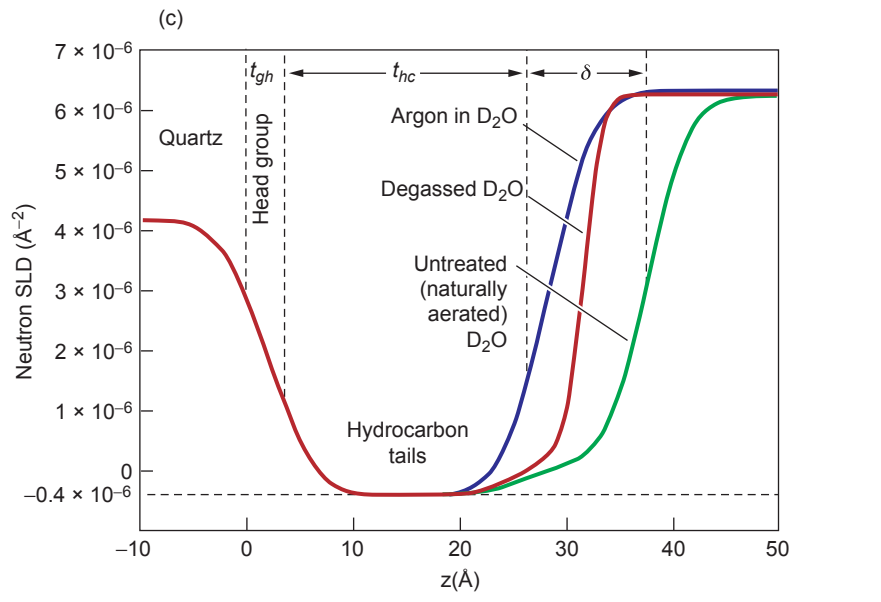


Figure 2. Reflectivity Results and SLD Profiles for Three Cases

(a) Shown here are normalized reflectivity curves for the silane layer in contact with three different D₂O layers: naturally aerated (green), degassed (red), and argon-bubbled (blue) D₂O. The thickness of the reflecting layer can be deduced directly from the value of Q_z at which the reflected intensity has a minimum value, or $t = 2\pi/Q_{z,\min}$. In all three cases, the thickness of the low-density region is greater than that of the silane layer. Also, the low reflectivity layer decreases in thickness from naturally aerated, to degassed, and then to argon-bubbled D₂O. The solid curves represent fits to the reflectivity data using our variable slab-model of the SLD profile of the sample described in (b). Note that we plot Fresnel-normalized reflectivity R/R_F vs Q_z to compensate for the sharp decrease in the reflectivity with increased momentum transfer Q_z, as described by Fresnel's law: $R_F \propto Q_z^{-4}$. Representative error bars are based on the error propagation of the Poisson statistics.

(b) The simple model for the SLD profile of the sample specifies constant widths for the head group of the silane chains and the silane hydrocarbon tails. The model allows a variable width for the reduced-density D₂O layer and



specifies a sigmoidal density profile of the form $\text{erf}(z/\sigma)$ for the average in-plane scattering-length density $\beta(z)$ (yellow curve). The sigmoidal profile is the integral of the Gaussian with full width 2σ that describes the interfacial profile (orange curve). The mid-point of the sigmoidal curve is offset by δ from the hydrocarbon-water interface. The yellow curve shown here and the blue background density represent the SLD profile that best fit the reflectivity data for the naturally aerated layer shown in (a).

(c) The plots of the in-plane average coherent scattering length density (SLD) profiles $\beta(z)$ correspond to the neutron reflectivity fits (solid curves) shown in (a). The lines at $z = 0$ and $z = 2.63$ nm represent the average positions of the silane monolayer. The line at 3.76 nm represents the 50% water density (midpoint of the sigmoidal profile) for naturally aerated D₂O.

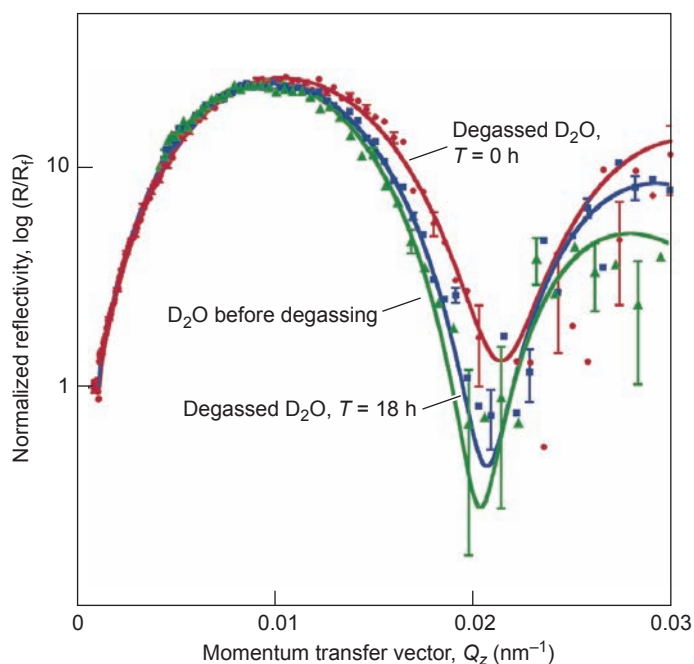


Figure 3. Reversibility of the Effects of Aeration

These neutron reflectivity curves for naturally aerated D_2O , vacuum degassed D_2O , and the degassed sample after allowing air to diffuse back into the D_2O for 18 h show that the effects of aeration on the thickness of the reduced-density layer are reversible.

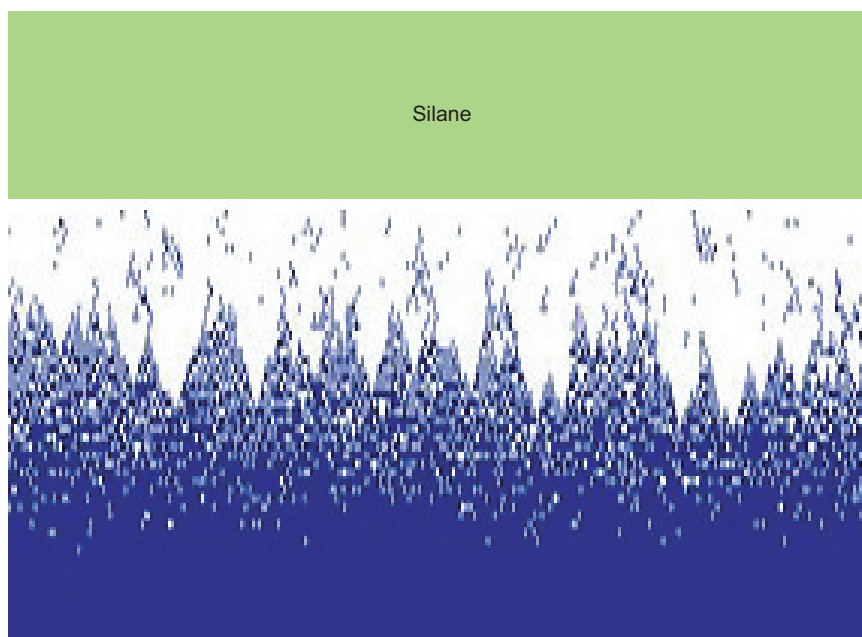


Figure 4. Density Fluctuation of the Reduced-Density Region

Our experiments suggest that the depleted-water region consists of a water surface with fluctuating density. The image shown here is dynamic, showing waves of water that tap on the hydrophobic surface.

variable thickness δ used to describe the region of reduced water density. More exactly, the reduced-water-density region was represented by an S-shaped (sigmoidal) density function with a variable width σ and variable midpoint distance δ measured from the silane surface. At δ , the water density is half the bulk value. The results of fitting this model to the data yield the solid curves in Figure 2a. The curves in Figure 2c display the scattering length density profiles obtained from fitting the neutron reflectivity data for each case in Figure 2a.

The values of δ indicate that the low-scattering region is always well above the 2.28-nanometer thickness of the hydrophobic layer. Because the hydrocarbon chains are fully extended, there appears to be a layer of reduced water density from 0.2 to 1.1 nanometers. Deuterated water bubbled with argon had the smallest reduced-density layer; the largest was for naturally aerated D_2O , whereas D_2O bubbled with carbon dioxide fell in between. To test for reversibility, we removed some of the dissolved gas from D_2O and allowed air to diffuse back in, while performing neutron reflectivity measurements. Figure 3 shows the results from this study. The shift of the position of $Q_{z,\min}$ in the normalized reflectivity back toward the original position (before degassing) 18 hours after reexposing the sample to air clearly demonstrates the effects of changing the dissolved gas concentration and the reversibility of the depleted-water-layer phenomena.

A Dynamic Interpretation

These neutron reflectivity measurements provide new clues for understanding how water behaves when it is next to a hydrophobic material. We provide an atomic-scale density profile for a simple hydrophobic surface immersed in water and observe a

Measuring Reflectivity

Neutron reflectometry is a powerful tool used to study the structure of thin, layered films. By elastically scattering a beam of neutrons off the surface of a sample, we can acquire information about the thickness, roughness, coverage, and material composition of a sample's layers perpendicular to the reflecting surface. Just like light waves, neutron waves reflect off the layer interfaces and can interfere constructively or destructively. The result is a refraction pattern analogous to the rings of color one sees when a thin layer of oil floats on top of water (refer to Figure A). By observing how the wavelength of the neutrons and their angles relative to the sample affect the reflected intensity, one can deduce the thickness and composition of the sample's layers.

We must turn to the physics of waves to understand how neutron reflectometry works. Each neutron can be described as a wave with a wavelength corresponding to its momentum. This relationship is defined by the de Broglie formula, $\lambda = h/p$, where p is the neutron's momentum, λ is the neutron's wavelength, and h is the Planck constant. Figure B shows an incident neutron reflecting from the top and bottom of a thin layer. The difference in path length between the two reflected (scattered) waves is shown in red. According to Bragg's law, constructive interference between two scattered waves will occur when the difference in path length between the two is an integral number of wavelengths. We can calculate that path length difference to show that constructive interference between neutron waves occurs when $n\lambda = 2d \sin(\theta)$, where θ is the neutron's incident angle and d is the distance between reflecting interfaces in the sample. So, the interference of neutron waves from a particular sample depends on both the wavelength λ and the angle θ . The momentum transfer vector, \mathbf{Q} , is the difference between the incident and the reflected wave vectors. For reflectivity measurements, it is always in the direction normal to the reflecting surfaces and is referred to as Q_z . It combines the λ and θ variables in the form $Q_z = 4\pi \sin(\theta)/\lambda$. The reflectivity R is defined as the ratio of the number of neutrons reflected from the sample to the number of incident neutrons. By measuring a sample's reflectivity over a range of Q_z , information about the sample can be obtained for different length scales. For simple systems, the Q_z spacing between minima in the reflectivity is related to the sample's thickness by the equation $\Delta Q_z = 2\pi/d$.

In neutron reflectometry, neutrons approach the sample at a very shallow angle (0.5° to 2.0°) and are reflected from it with the same outgoing angle. For reflectivity experiments at SPEAR, the angle θ is fixed, and the incoming neutrons have a range of wavelengths and, therefore, a range of Q_z values. Plotting the intensity of reflected neutrons versus the momentum transfer Q_z , one sees an interference pattern (refer to Figure C). It looks like a series of peaks and valleys corresponding to constructive and destructive interference of neutron waves reflected from the interfaces within the sample. This interference pattern resides on the envelope of the Fresnel curve, which is the reflectivity of a perfectly sharp interface. Because the Fresnel curve decreases sharply with increasing Q_z , reflectivity data are often displayed divided by this decreasing envelope. Using a modeling process, this information can be converted into a density profile that describes the structure of the sample.

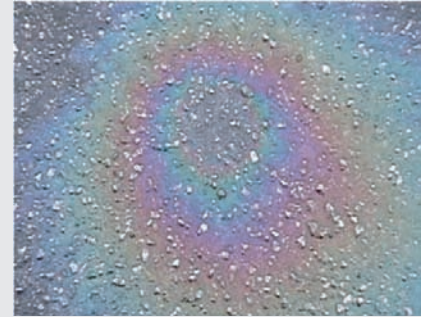


Figure A. Reflections from an Oil Film on Water
The varying thickness of the oil film creates rings of color.

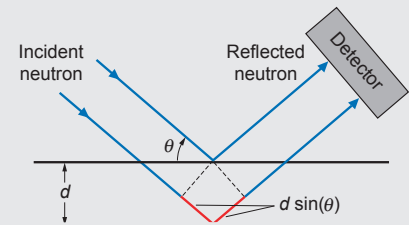


Figure B. Neutron Reflection from a Layer of Thickness d
The red lines show the path length difference between reflections from upper and lower surfaces.

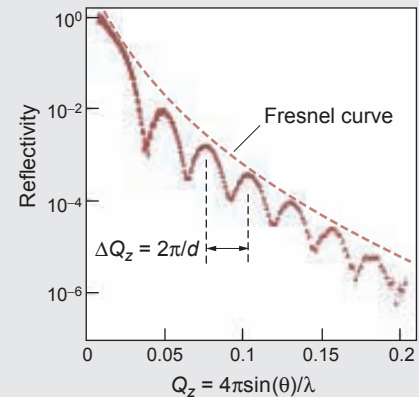


Figure C. Reflected-Neutron Intensity vs Momentum Transfer
The distance between peaks yields a layer of thickness d .

depleted-water region extending from 0.2 to 1.1 nanometers from the surface. Further, the extent of this depleted region was found to depend on both the concentration and type of gas dissolved in the water. Some of our more-recent studies point to additional factors that influence the extent of the depleted-water region, including pressure, temperature, and salt concentration.

A possible description of the depleted-water region is that it is made up of large, flat pockets of water vapor. However, such nanobubbles would have to cover 90 percent of the surface and have an average height less than 1.1 nanometers; under those conditions, the internal pressure of the nanobubbles would be too high for them to be thermodynamically stable. Therefore, such a picture of static bubbles does not make good physical sense. Instead, we suggest that this region consists of a water surface with a fluctuating density (refer to Figure 4). One can imagine a much more dynamic scene, where tentacles and waves of water dance upon the hydrophobic surface. ■

Acknowledgments

This work was supported by Los Alamos National Laboratory and by the U.S. Department of Energy Office of Basic Energy Science.

Further Reading

- Attard, P. 2003. Nanobubbles and the Hydrophobic Attraction. *Adv. Colloid Inter. Sci.* **104** (1–3): 75.
- Ball, P. 2003. How to Keep Dry in Water. *Nature* **423** (6935): 25.
- Baptiste, A., A. Gibaud, J. F. Bardeau, K. Wen, R. Maoz, J. Sagiv, and B. M. Ocko. 2002. X-ray, Micro-Raman, and Infrared Spectroscopy Structural Characterization of Self-Assembled Multilayer Silane Films with Variable Numbers of Stacked Layers. *Langmuir* **18** (10): 3916.
- Christenson, H. K., and P. M. Claesson. 2001. Direct Measurements of the Force between Hydrophobic Surfaces in Water. *Adv. Colloid Inter. Sci.* **91** (3): 391.
- Cottin-Bizonne, C., B. Cross, A. Steinberger, and E. Charlaix. 2005. Boundary Slip on Smooth Hydrophobic Surfaces: Intrinsic Effects and Possible Artifacts. *Phys. Rev. Lett.* **94** (5): 056102.
- Granick, S., Y. Zhu, and H. Lee. 2003. Slippery Questions about Complex Fluids Flowing Past Solids. *Nature Mater.* **2** (4): 221.
- Israelachvili, J. N., and R. M. Pashley. 1984. Measurement of the Hydrophobic Interaction between Two Hydrophobic Surfaces in Aqueous Electrolyte Solutions. *J. Colloid Interface Sci.* **98** (2): 500.
- Jensen, T. R., M. Ø. Jensen, N. Reitzel, K. Balashev, G. H. Peters, K. Kjaer, and T. Bjørnholm. 2003. Water in Contact with Extended Hydrophobic Surfaces: Direct Evidence of Weak Dewetting. *Phys. Rev. Lett.* **90** (8): 086101.
- Kjaer, K. 1994. Some Simple Ideas on X-ray Reflection and Grazing-Incidence Diffraction from Thin Surfactant Films. *Physica B* **198** (1–3): 100.
- Lauga, E., M. P. Brenner, and H. A. Stone. 2005. Microfluidics: The No-Slip Boundary Condition. (To appear as Chapter 15 in *The Handbook of Experimental Fluid Mechanics*. Edited by J. Foss, C. Tropea, and A. Yarin. New York: Springer-Verlag.)
- Leung, K., A. Luzar, and D. Bratko. 2003. Dynamics of Capillary Drying in Water. *Phys. Rev. Lett.* **90** (6): 065502.
- Maoz, R., and J. Sagiv. 1984. On the Formation and Structure of Self-Assembling Monolayers.—I. A Comparative ATR-Wettability Study of Langmuir-Blodgett and Adsorbed Films on Flat Substrates and Glass Microbeads. *J. Colloid Interface Sci.* **100** (2): 465.
- Meyer, E. E., Q. Lin, and J. N. Israelachvili. 2005. Effects of Dissolved Gas on the Hydrophobic Attraction between Surfactant-Coated Surfaces. *Langmuir* **21** (1): 256.
- Pratt, L. R., and D. Chandler. 1977. Theory of the Hydrophobic Effect. *J. Chem. Phys.* **67** (8): 3683.
- Schwendel, D., T. Hayashi, R. Dahint, A. Pertsin, M. Grunze, R. Steitz, and F. Schreiber. 2003. Interaction of Water with Self-Assembled Monolayers: Neutron Reflectivity Measurements of the Water Density in the Interface Region. *Langmuir* **19** (6): 2284.
- Steitz, R., T. Gutberlet, T. Hauss, B. Klösgen, R. Krastev, S. Schemmel et al. 2003. Nanobubbles and Their Precursor Layer at the Interface of Water against a Hydrophobic Substrate. *Langmuir* **19** (6): 2409.

Anticorrosion Coatings

Can They Be Made without Chromium?

Dale W. Schaefer, Guirong Pan, and Wim vanOoij

Chromium is a surprisingly common ingredient in anticorrosion coatings such as the paint pretreatment being sprayed on the airplane fuselage below. Even the stainless steel cutlery that most of us use daily has a native coating of chromium oxide. But the Strategic Environmental Research and Development Program is looking for an alternative because chromium ions are a serious health threat when inhaled or ingested by metal workers during metal coating and stripping. Recent neutron reflectometry studies at the Los Alamos Neutron Science Center explore whether thin films of silane could afford equivalent corrosion protection.

Technicians must wear complete protective clothing as they apply chromate conversion coating to a commercial aircraft. The chromate must be recovered from the overspray.



The 2000 David and Goliath film *Erin Brockovich* pits the heroine, Brockovich, against corporate giant Pacific Gas and Electric (PG&E). The film is based on one of the most lucrative legal cases in history (\$333 million). The suit revolves around hexavalent chromium (Cr^{6+}) used by PG&E to control corrosion in cooling towers in its Hinkley, CA, compressor station. PG&E would periodically treat the surface of the cooling coils and release the chromium-containing wastewater into ponds leading to contamination of the Hinkley air and groundwater. Like most heavy metals, Cr^{6+} is toxic and a suspected carcinogen, the release of which is regulated by the Environmental Protection Agency and the Occupational Safety and Health Administration, as well as state agencies.

In spite of its toxicity, Cr^{6+} remains an essential ingredient in the metal finishing industry for corrosion control. No substitutes perform as well as Cr^{6+} , particularly at high temperature. Cr^{6+} is used as a metal pretreatment and is also found in slightly soluble pigments in paint primers (Figure 1). When Cr^{6+}

comes in contact with most metals, it forms a passive oxide layer called a chromate conversion coating (CCC), which is resistant to most types of corrosive attack. If the oxide layer is scratched, chromium leaches from the pigment and heals the damage.

Chromium oxide itself is not harmful. Health concerns arise primarily during coating application and removal. In fact, chromium oxide exists as protective film on stainless steels, which most of us put in our mouths every day in the form of stainless steel tableware. During application of paint pretreatment, however, soluble salts of chromium are used, which are hazardous. Workers must be protected and recovery costs of the overspray are high (see photo on opposite page). Airborne hazards also exist when the coating is stripped.

Silane Anticorrosion Coatings

Because of the above considerations, the Strategic Environmental Research and Development Program (SERDP) (www.SERDP.org) funds an

extensive research effort to develop alternatives to chromate coating systems used in the Department of Defense. The goal is to completely eliminate Cr^{6+} without introducing other hazardous substances or air pollutants. The SERDP at the University of Cincinnati, for example, exploits inorganic silane polymers deposited from solutions of water-soluble precursors. Bis-type silanes (Figure 2) are particularly effective. These silanes are water soluble and polymerize to corrosion-resistant coatings.

Two alternative coating systems are under development at Cincinnati (Figure 1). In the “silane” system, highly crosslinked silane polymers replace the chromate conversion coating. In the “superprimer” system, silanes are incorporated into water-soluble epoxy and urethane polymer precursors. These precursors cure through crosslinking to a protective film that replaces both the chromate conversion coating, as well as the pigment-containing primer. Figure 3 compares the corrosion performance of conventional chromate-pretreated aluminum alloy with that of the same

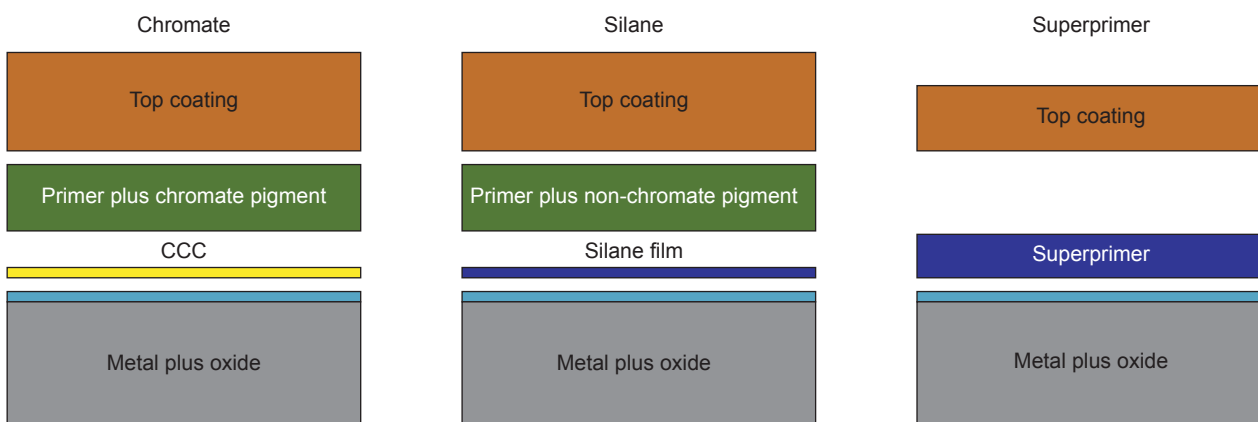


Figure 1. Schematic of Chromate and Silane-Based Coating Systems

(a) In the chromate system, chromium salts are used in the chromate conversion coating (CCC) and in the pigments in the primer. These pigments slowly leach chromium, which heals any damage to the CCC. (b) In the silane system, the CCC is replaced by a silane film and nonchromate corrosion inhibitors are used in the primer. (c) In the superprimer concept, the silane and primer are combined in a one-step superprimer.

material coated with a silane film.

As part of the SERDP, the Cincinnati team collaborates with scientists at Los Alamos and Sandia National Laboratories to elucidate the properties, protection mechanism, and vulnerabilities of silane-based protective coatings. This research exploits the Surface Profile Analysis Reflectometer (SPEAR) at the Manuel Lujan Jr. Neutron Scattering Center (see the article “the Hydrophobic Effect— Why Do Raindrops Slide off Leaves?” on page 164 for a description of SPEAR). One of the issues we investigated is the so-called mixed-silane effect. As part of this effort, we discovered some unexpected properties of hydrophobic silanes, namely, that they are not particularly hydrophobic.

The Mixed-Silane Effect

The mixed-silane effect is observed in mixtures of the two bis-silanes shown in Figure 2. These silanes exhibit contrasting behavior, traceable to the bridging group (the amine group NH vs the sulphur group S₄). Corrosion tests show that bis-amino silane does not offer good corrosion protection on either aluminum alloys or galvanized steel. The more hydrophobic bis-sulfur silane, on the other hand, is slow to react, has poor wetting properties, and is not effective on galvanized steel. Interestingly, a bis-sulfur/bis-amino (3/1) mixture shows enhanced performance compared with the two individual silanes and provides protection for many metals including aluminum alloys and galvanized steel.

To study the films using neutron reflectivity, the silanes are spin-coated on silicon substrates from prereacted silane solutions. Spin-coating is a procedure to produce a very uniform film. A solution containing the silanes is spread in excess on a silicon wafer of the type used in the electronics indus-

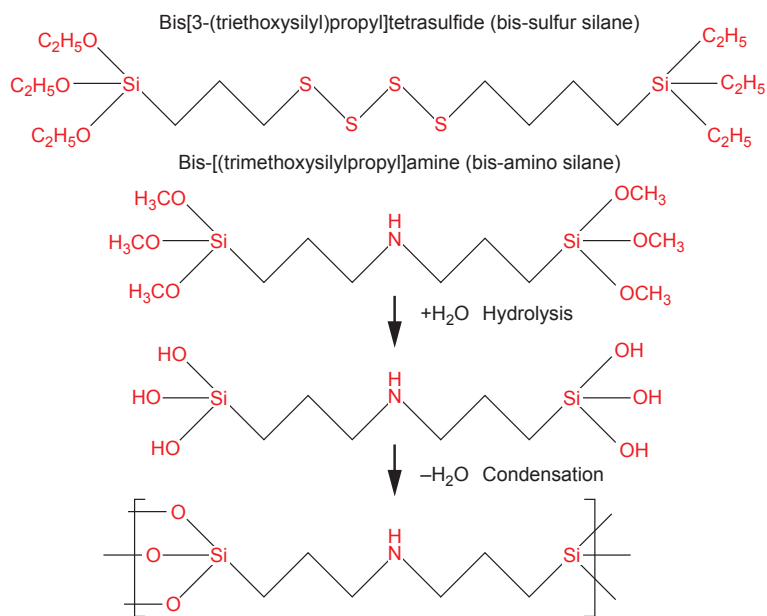


Figure 2. Two Bis-Silanes for Silane-Based Protective Films
Bis-silanes have six alkoxy groups that undergo hydrolysis and condensation to form silicon-oxygen-silicon (Si–O–Si) bonds, leading to a highly crosslinked film. These reactions are shown for the bis-amino compound. In their polymerized state, bis-sulfur is hydrophobic and bis-amino is hydrophilic. Water-soluble mixtures of these two silanes lead to effective protective films.

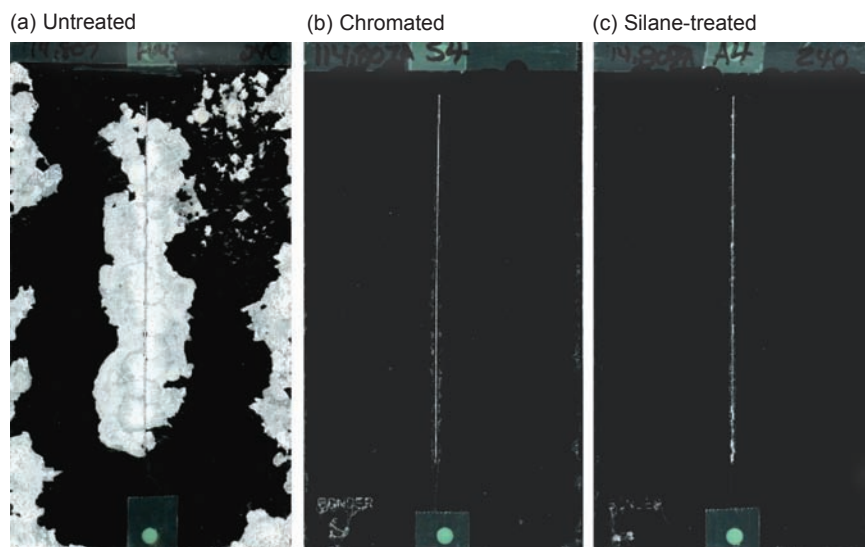


Figure 3. Responses of Aluminum Surfaces to Corrosive Salt Spray
Aluminum alloy (5005) coupons with different surface coatings were exposed to 240 h of copper-accelerated acetic-acid salt spraying. All three panels had a polyurethane powder-paint overcoat. The silane panel was pretreated with a 3/1 mixture of the bis-sulfur and bis-amino silane. The chromated panel (b) shows less scratch corrosion than the silane-treated panel (c). The self-healing character of the chromate conversion coating is responsible for this effect.

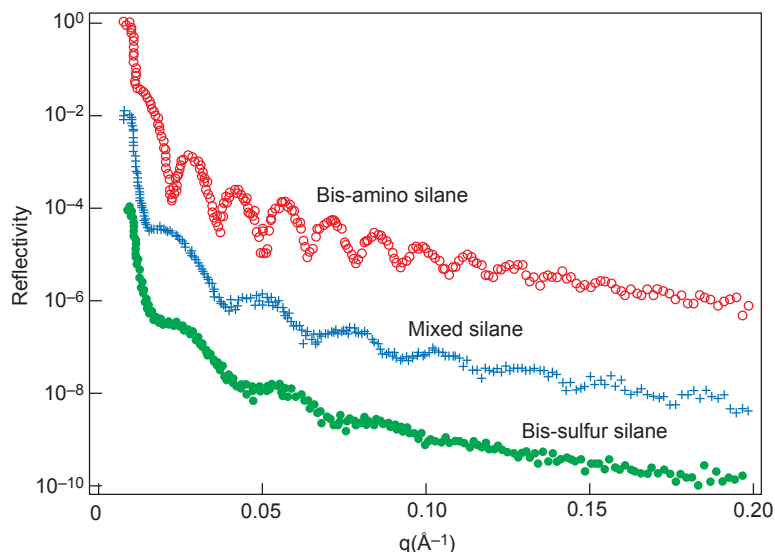


Figure 4. Reflectivity Curves for As-prepared Bis-Amino, Bis-Sulfur, and Mixed Silane

For clarification, the reflectivity curve of mixed silane is suppressed by 10^2 , and the reflectivity curve of bis-sulfur silane is suppressed by 10^4 . The thickness of the films can be calculated from the distance between the fringes, Δq , as $2\pi/\Delta q$. The fringes are the most distinct in the bis-amino film, indicating this film is the smoothest. Bis-sulfur is the thinnest and roughest. The mixed film shows intermediate behavior.

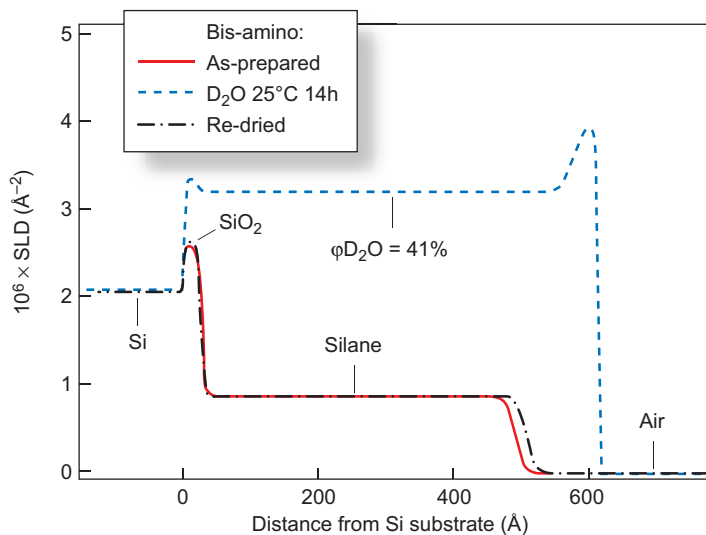


Figure 5. Scattering-Length-Density (SLD) Profiles for Dry, Water-Conditioned, and Redried Bis-Amino Films Coated on Silicon

These profiles were obtained assuming a layered model and then inverting neutron reflectivity data. From the SLD of the dry film (solid red curve), we know the film is fully condensed, or crosslinked. After exposure to D_2O vapor for 14 h, the blue curve is obtained. The SLD of the swollen film is now much higher due to absorption of D_2O , whose SLD is six times larger than that of the dry film. The volume fraction ϕ of D_2O in the film is calculated from the SLD to be 41%. That is, 41% of the volume is occupied by D_2O even though the film swells by only 25%. This high water content is due to the hydrophilic nature of the NH group in the bridge (Figure 2). The film returns almost to the pristine state on redrying, showing that there is no chemical alteration due to water exposure at room temperature.

try. Then the wafer is spun up to 2000 revolutions per minute to strip off the excess solution, leaving a silane film a few hundred angstroms thick. One angstrom is 10^{-10} meter.

Figure 4 compares the neutron reflectivity curves for bis-sulfur, bis-amino, and a 3/1 mixture of the two. The data are plotted as reflectivity (fraction of the neutron beam reflected) vs momentum transfer, q . Momentum transfer is chosen as the independent variable rather than the reflection angle because there is no unique reflection angle at a pulsed neutron source where neutrons with a range of wavelengths impinge on the sample. Also, in the Fourier transform that approximately relates reciprocal-space data (Figure 4) to real-space mass distribution (as in Figure 5), q is the variable conjugate to the spatial coordinate, z , where z is the distance normal to the silicon wafer surface and therefore through the thickness of the film.

Simple observation of the curves in Figure 4 reveals that there is nothing special about the mixed silane. For example, the spacing of the mixed-film fringes, which reveals the film thickness, lies between that of the two neat films. What is really of interest, however, is the response of the films to water. To examine this issue, the films in Figure 4 were exposed to water vapor, and neutron reflectivity was used to examine water penetration. The films were studied dry, in the presence of water vapor and in the redried state. Comparison of the data for the as-prepared and redried films reveals whether the films are chemically modified by exposure to water vapor.

Dry-Film Properties

If the dry as-prepared bis-amino reflectivity data in Figure 4 are inverted, the neutron scattering-length-density (SLD) profile in Figure 5 (red line) is obtained. The

SLD is the neutron scattering power of a material. In Figure 5, for example, the thin oxide layer has a higher SLD than either the substrate or the silane film. Because neutron scattering involves nuclear forces, there is no simple relationship between the SLD and the mass density. Nevertheless, the SLD is calculable for any substance of known composition and density. From the measured SLD of the dry film in Figure 5, for example, we know that the film is fully crosslinked, since all partially crosslinked candidates have a lower calculated SLD. That is, all the alkoxy groups ($\text{CH}_3\text{O-Si}$) in the dry film have hydrolyzed and condensed to form silicon-oxygen-silicon (Si-O-Si) bonds.

Water Barrier Properties

In spite of the fact that the bis-amino film is fully condensed, it swells dramatically in the presence of water vapor (blue line in Figure 5). Heavy water (D_2O , deuterium oxide) is used for this experiment because its SLD is six times greater than that of the dry film, so it is very visible to neutrons. From the SLD of the “wet” film, we calculate that D_2O occupies 41 percent of the volume. This high water content is due to the hydrophilic nature of the NH bridging group. It is interesting that the film thickness increases by only 25 percent, so some of the D_2O must invade free volume present in the dry film. If the film is redried, the SLD profile returns to the dry state (black curve), indicating that no D_2O is retained in the film and no chemical reactions occur to chemically incorporate deuterium in the film.

Another interesting aspect of bis-amino films is the hydrophilic layer at the silane-air interface. This layer is revealed in Figure 5 by the peak in the SLD at the air interface of the wet film. This peak is only observed in films containing bis-amino. This feature could be due to restructuring

of the film surface in the presence of water vapor.

Bis-sulfur films are more hydrophobic, as can be seen in Figure 6. In this case, the water-conditioned film absorbs 7.8 volume percent water, still a surprisingly large number for a hydrophobic coating. We have also studied thicker films and find that water always penetrates the film. Apparently, the protective character of silane films does not depend on strict water-barrier properties.

From the SLD of the dry bis-sulfur film, we calculate that it is less crosslinked than the bis-amino film, even though the latter absorbs four times as much water. At least 11 percent of the bis-sulfur alkoxy groups do not condense at room temperature. Having found that the bis-sulfur is more water-resistant and less crosslinked than bis-amino, we conclude that the nature of the bridging group is more important than the crosslink density in controlling the water barrier properties.

Mixed Films

So what is it about the mixed film that exhibits superior properties in corrosion tests? It turns out that all the properties of the mixed film lie between those of the bis-amino and bis-sulfur films (Figure 7). The SLD, water uptake, film thickness, and film roughness are just the weighted average of the neat-film values. The water content of the wet mixed film, for example is 12.6 percent compared with 7.8 percent for bis-sulfur and 41 percent for bis-amino. The mixed film, however, does show the same hydrophilic layer at the air interface found in the neat bis-amino film. This layer provides a clue regarding the improved performance of the mixed film.

The mixed silane effect is probably related to the buffering and catalytic effect of the amine group on the bis-

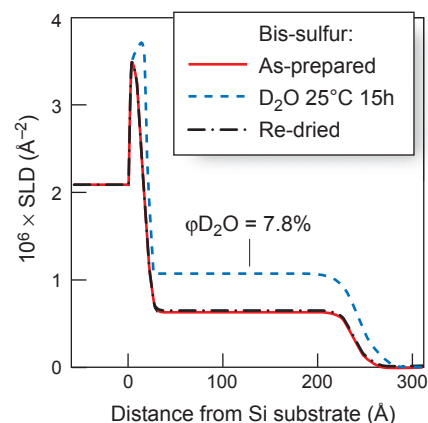


Figure 6. SLD Profile for Bis-Sulfur
Bis-sulfur is hydrophobic, leading to less water absorption than bis-amino. Nevertheless, water penetrates all the way to the oxide surface on the silicon wafer. No deuterium-rich layer is observed at the air-side surface although there is some modification at the wafer-film interface.

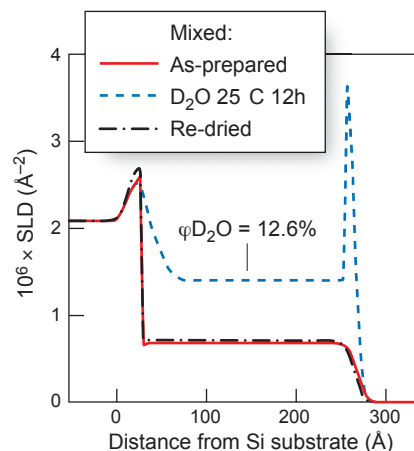


Figure 7. SLD Profile for Mixed Silane
The 12.6% water content in the mixed-silane film lies between that of bis-amino and bis-sulfur. The peak in the SLD at the air interface is seen only for films containing bis-amino. The amino groups must alter the near-surface region in such a way as to attract water. The modified surface also improves bonding to primer overcoats.

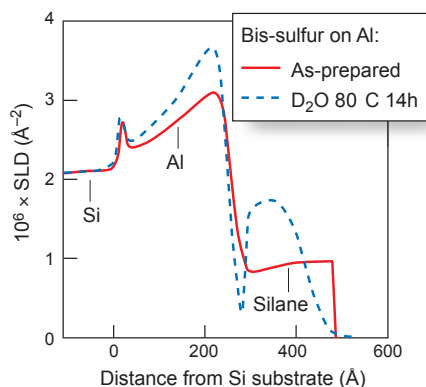


Figure 8. SLD Profile for Bis-Sulfur on Aluminum Aluminum is sputter-deposited on a silicon wafer, and then the surface is spin-coated with silane. The highly distorted profiles are attributed to an etching effect of the acidic bis-sulfur on the aluminum and its native oxide. The increased SLD in the aluminum region is attributed to absorption of D₂O in a porous aluminum oxide layer.

amino moiety. That is, the amine group catalyzes the condensation of bis-sulfur, leading to more crosslinked films as the film ages. This polar (hydrophilic) group also improves the wettability of the mixed silane and moderates the acidic nature of the bis-sulfur. The wettability issue is relevant at both the metal–silane and the silane–air interfaces. Regarding the metal interface, wetting films form more-uniform coatings. At the air interface, the presence of the amino-induced hydrophilic layer enhances bonding to primers and paints.

The buffering effect of bis-amino on bis-sulfur can be appreciated by considering the SLD profile of bis-sulfur on aluminum rather than silicon. To study film on aluminum, we first sputter-deposit aluminum on the silicon wafer and then spin-coat the silane film. The reflectivity data are difficult to fit, and the resulting SLD profile is highly distorted (Figure 8). Because the natural pH of bis-sulfur solutions is acidic, the aluminum sur-

face is etched by the coating solution. In the mixed silane, however, bis-sulfur is buffered by the amino group of bis-amino, and excellent films are obtained on aluminum. The mixed-silane effect, therefore, is not due to any special barrier properties of the film, but to the interaction of the film with both the substrate and overcoat.

Processing Conditions

We are investigating a number of other issues regarding silane-based protective coatings. Given that silanes are not rigorous water barriers, we want to know if polymer-silane superprimers have better water-barrier properties. We are also investigating issues related to curing and aging of the films. Finally, given that water penetrates all water-borne silanes, it is likely that the corrosion inhibition is related to control of transport of ionic species such as chloride. Monitoring chloride by neutron reflectivity is very challenging, however, because it is present at low concentration. Nevertheless, we can explore how films degrade in the presence of such aggressive ions.

Conclusions

The elimination of Cr⁶⁺ in the metal finishing industry is a multibillion-dollar challenge. Our research shows that the protection of metals is a complex problem that is not fully understood. Regardless of which alternative to Cr⁶⁺ is selected, a thorough understanding of the properties and vulnerabilities of the alternative will be required. Neutron reflectivity will continue to provide critical data on the morphology and water response of candidate metal-protection systems. ■

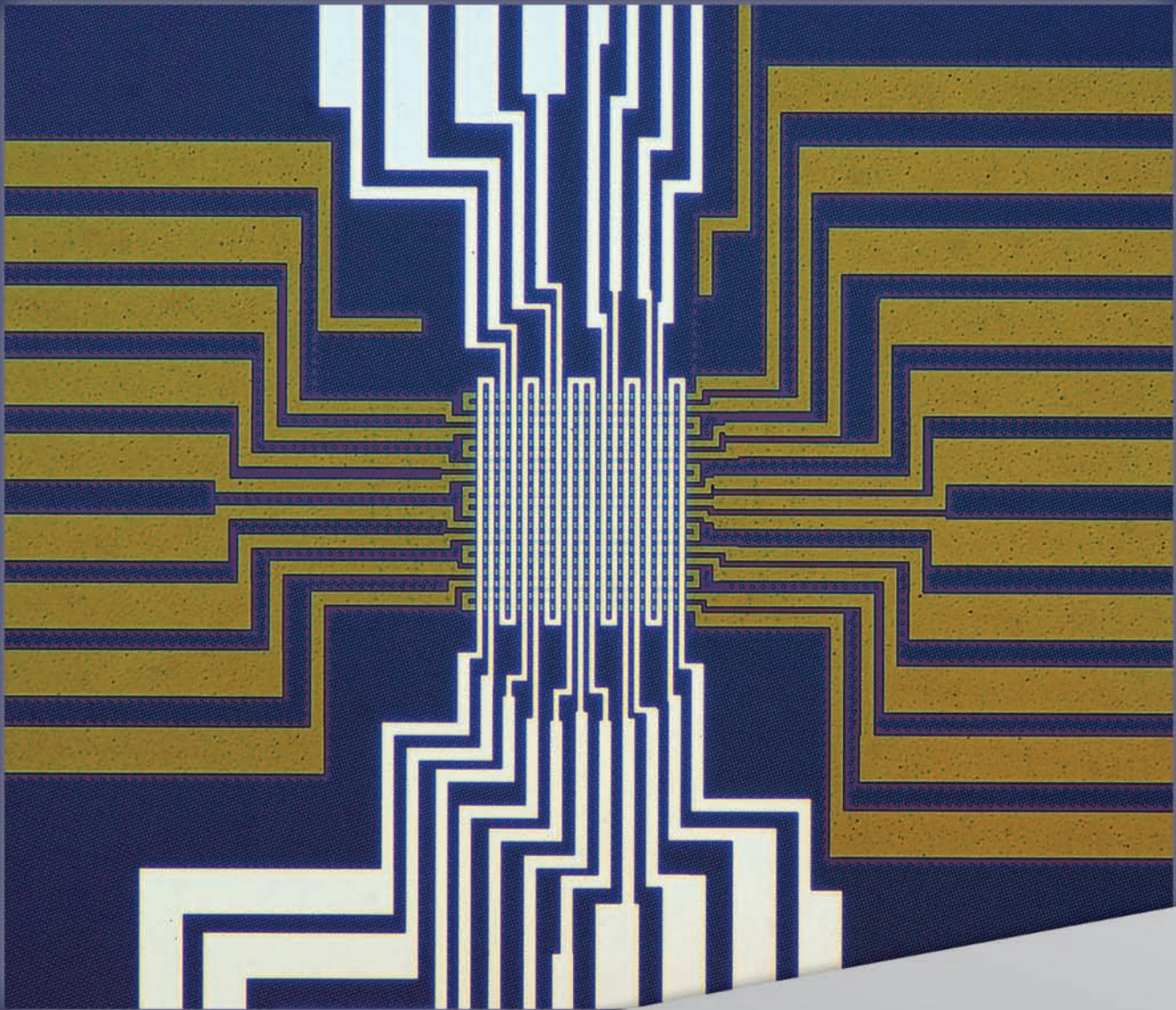
Further Reading

- Kent, M. S., W. F. McNamara, D. B. Fein, L. A. Domeier, and A. P. Y. Wong. 1999. Water Adsorption in Interfacial Silane Layers by Neutron Reflection: 1. Silane Finish on Silicon Wafers. *J. Adhes.* **69** (1–2): 121.
- Kent, M. S., W. F. McNamara, P. M. Baca, W. Wright, L. A. Domeier, A. P. Y. Wong, and W. L. Wu. 1999. Water Adsorption in Interfacial Silane Layers by Neutron Reflection: 2. Epoxy Plus Silane Finish on Silicon Wafers. *J. Adhes.* **69** (1–2): 139.
- Pan, G. R., H. Yim, M. S. Kent, J. Majewski, and D. W. Schaefer. 2003. Neutron Reflectivity Investigation of Bis-Amino Silane Films. *J. Adhes. Sci. Technol.* **17** (16): 2175.
- . 2004. Effect of Bridging Group on the Structure of Bis-Silane Water-Barrier Films. In *Proceedings of the Fourth International Symposium on Silanes and Other Coupling Agents*. Netherlands: VSP.
- Plueddemann, E. P. 1991. *Silane Coupling Agents*. 2nd ed. New York: Plenum Press.
- Roe, R. J. 2000. *Methods of X-ray and Neutron Scattering in Polymer Science*. New York: Oxford University Press.
- Russell, T. P. 1996. On the Reflectivity of Polymers: Neutrons and X-rays. *Physica B* **221**: 267.
- van Ooij, W. J., and T. Child. 1998. Protecting Metals with Silane Coupling Agents. *CHEMTECH* **28** (2): 26.
- Yim, H., M. S. Kent, J. S. Hall, J. J. Benkoski, and E. J. Kramer. 2002. Probing the Structure of Organosilane Films by Solvent Swelling and Neutron and X-ray Reflection. *J. Phys. Chem. B* **106** (10): 2474.
- Zhu, D. Q., and W. J. van Ooij. 2004. Enhanced Corrosion Resistance of AA 2024-T3 and Hot-Dip Galvanized Steel Using a Mixture of Bis-[triethoxysilylpropyl]tetrasulfide and Bis-[trimethoxysilylpropyl]amine. *Electrochim. Acta* **49** (7): 1113.

Origins of Spin Coupling across Interfaces

*Michael Fitzsimmons and Sunil K. Sinha**

** University of California, San Diego*



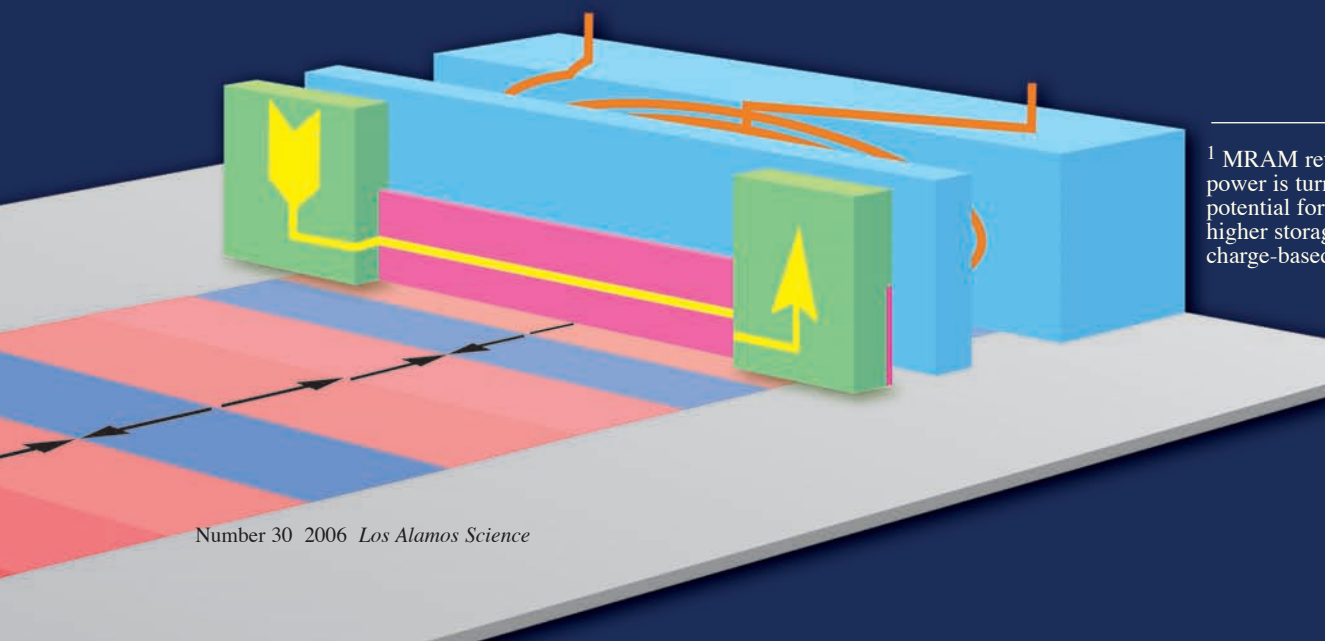
The tiny “read head” in a computer hard drive is a multilayered magnetic-thin-film structure. Essential to its operation is a ferromagnetic thin film whose magnetization is held fixed through a phenomenon known as exchange bias. Magnetic coupling of the “fixed” layer to an adjacent antiferromagnetic layer establishes the bias. The fixed layer provides a reference point for a second “free” ferromagnetic layer in the read head which enables it to discriminate between 1s and 0s magnetically stored on the hard-drive disk. We used x-rays at the Advanced Light Source and then polarized neutrons at the Los Alamos Neutron Science Center’s ASTERIX spectrometer to probe the origin of exchange bias in a model ferromagnetic-antiferromagnetic thin-film system. We found an interesting interplay between loose and pinned spins near the ferromagnetic-antiferromagnetic interface, which motivated us to develop a new model of exchange bias to explain its magnitude and sign.

Currently, microelectronic devices use the electron’s charge for their operation and for the most part ignore the electron’s “spin” (intrinsic angular momentum), or intrinsic magnetic moment. However, new types of microelectronic devices are now emerging that use the electron’s spin (or magnetic moment), together with its charge.

Compared with conventional devices, these “spintronic” devices have the potential advantages of nonvolatility, increased data-processing speed, decreased electrical-power consumption, and increased integration densities. Although a whole range of spintronic devices is being studied and developed, the read head in a computer hard drive, also called a “spin-

valve head,” is already widely used. Another spintronic device, magnetic random access memory (MRAM), is poised to replace the charge-based RAM now used in computers.¹ Both spin-valve heads and MRAM employ the magnetic properties of layered thin films to influence electron transport through the films and thereby read magnetically stored data.

At left is a micrograph of a magnetic random access (MRAM) circuit. MRAM is nonvolatile RAM poised to replace the electronic RAM now used in computers (reprinted courtesy of International Business Machines Corporation, Copyright 2000). Below is a schematic of the spin-valve that reads data stored on computer hard drives. Both devices use exchange bias provided by thin antiferromagnetic layers.



¹ MRAM retains data when the power is turned off and has the potential for higher speeds and higher storage densities than charge-based RAM.

For both computer read heads and MRAM, the thin film nanostructure essential in reading magnetically stored data consists of two closely spaced ferromagnetic thin films, one a “free” layer and the other a “fixed” layer (Figure 1). The magnetization of the free layer can be changed by the fringe fields of magnetically stored bits, whereas the magnetization of the fixed layer is engineered to remain constant. In a read head, for example, a change in the magnetization of the free layer relative to the fixed layer changes the read head’s resistance, and the resulting change in voltage is used to discriminate between stored 1s and 0s [see the box “Giant Magnetoresistance (GMR) in a Hard-Drive Read Head” on page 182].

The magnetization in the fixed layer can be held constant in different ways, but the most common method is called “exchange bias.” An antiferromagnetic layer placed next to the fixed layer shifts, or biases, the fixed layer’s hysteresis curve (Figure 2) through magnetic, or spin exchange, coupling between the two layers. The exchange bias in the fixed layer ensures that only extremely large external magnetic fields can change that layer’s magnetization, whereas relatively small external magnetic fields can only change the free layer’s magnetization. Our studies have focused on the details of how exchange bias works.

How Antiferromagnets Produce Exchange Bias

The “Old” Picture. An antiferromagnet is said to consist of nominally equal numbers of atoms whose spins point in opposite directions. (An atom’s spin is produced mainly by the spins of its outer electrons.) Thus, the net magnetization of an antiferromagnet is nominally zero, which means an external magnetic field does not affect

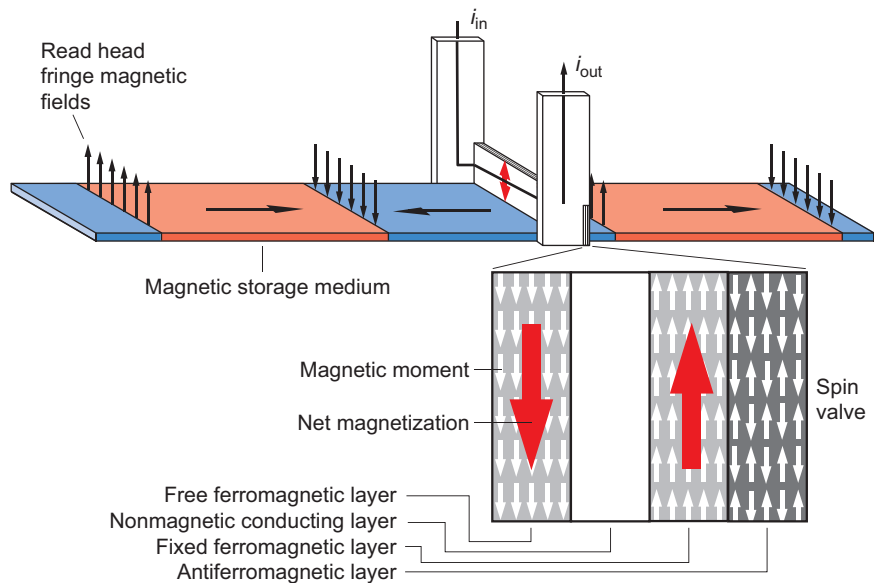


Figure 1. Operation of a Spin-Valve Read Head

A spin-valve read head consists of four conducting nanolayers: an antiferromagnetic layer, a “fixed” ferromagnetic layer, a nonmagnetic conducting layer, and a “free” ferromagnetic layer. As the spin valve passes over the magnetic bits on the hard-drive disk, for fixed current through the spin valve, the voltage across the spin valve changes because of a magnetic interaction with the net magnetic fringe fields between a 0 and a 1 or between a 1 and a 0. Specifically, those fringe fields cause the magnetization in the free layer of the spin valve to align parallel to them while the magnetization in the fixed layer of the spin valve remains in a fixed direction. A change in the free layer’s magnetization causes the resistance (and thus the voltage) across the spin valve to change. The resistance is low when the magnetizations of the free and fixed layers are parallel, and it is high when they are antiparallel, as described in the box on page 182. The magnetization in the fixed layer is held constant by the exchange bias established through magnetic coupling with the adjacent antiferromagnetic layer, whose microscopic origin is still debated. The nonmagnetic conducting layer provides a conducting path between the free and fixed layers.

the net magnetization. However, in practice, a relatively small number of “uncompensated” spins in an antiferromagnet are not canceled by opposite spins. Strongly coupled to nearby spins in the antiferromagnetic layer, the uncompensated spins are seemingly “frozen” and do not easily respond to an external applied magnetic field. But the uncompensated spins are also coupled to the spins in the adjacent ferromagnetic layer. That coupling across the antiferromagnetic–ferromagnetic interface produces the exchange bias by inhibiting the response of the ferromagnetic

material to applied fields.

However, this model raises several questions. (1) Why is the exchange bias two to three orders of magnitude smaller than that predicted by a simple calculation assuming a perfectly smooth interface? (2) Where exactly are the uncompensated spins? (3) How do the uncompensated spins couple to the ferromagnetic spins? We performed a series of experiments to try and answer these questions.

Los Alamos Studies. In early experiments, we showed that the exchange bias produced by an anti-

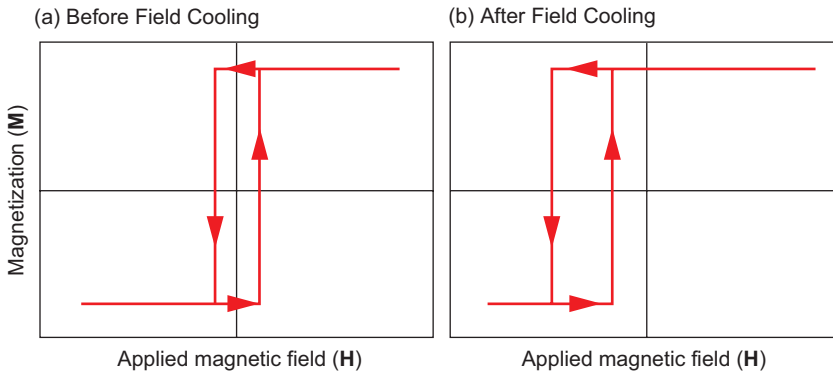


Figure 2. Exchange Bias in a Ferromagnetic-Antiferromagnetic Two-Layer System

These plots show the hysteresis curves (magnetization vs applied magnetic field) of a ferromagnetic thin film in contact with a second film that changes from paramagnetic to antiferromagnetic when cooled below its Néel temperature. The curves are for temperatures (a) above and (b) below the Néel temperature. (The arrows indicate whether the applied field is being increased or decreased.) After cooling, the ferromagnetic layer's hysteresis curve is shifted along the magnetic field axis from being centered at 0 to being centered at a higher absolute value. "Exchange bias" refers to this effect and to the magnitude of the shift. The fixed layer in a spin-valve read head is exchange-biased to make its magnetization impervious to the small fields of the storage medium. The fixed layer thus provides a reference point that allows the nanostructure in Figure 1 to discriminate between the 1s and 0s stored on a hard drive.

ferromagnetic iron fluoride (FeF_2) nanolayer grown with minimal crystal strain is small (Fitzsimmons et al. 2002). However, dramatic increases of exchange bias using the same ferromagnetic and antiferromagnetic materials have been realized when the antiferromagnetic layer (FeF_2) is grown on magnesium fluoride (MgF_2) single crystals. Because of the large lattice mismatch between FeF_2 and MgF_2 , misfit dislocations are formed in the FeF_2 (Figure 3) that partially relieve the crystal strain across the FeF_2 - MgF_2 interface. These dislocations and unrelieved misfit strain are sources of uncompensated magnetization in the FeF_2 antiferromagnetic that promote large exchange bias.

The exchange bias model system studied in our new experiments consisted of a ferromagnetic layer over an antiferromagnetic layer with the two sandwiched between two nonmagnetic

layers (Figure 4). The nonmagnetic substrate layer was a single crystal of MgF_2 . The other layers, in the order in which they grew onto the nanostructure, were a 36.6-nanometer-thick, single-crystal layer of FeF_2 ; a 4.1-nanometer-thick layer of cobalt, which is ferromagnetic; and a 5.0-nanometer-thick layer of aluminum, which is nonmagnetic.

In all the experiments, we subjected the sample to a magnetic field parallel to the [001] direction of the FeF_2 crystal before cooling the sample well below its Néel temperature of 78.4 kelvins (the temperature below which the FeF_2 is antiferromagnetically ordered). The [001] direction is along the "easy" magnetization axis.²

² The magnetic moments in an antiferromagnetic crystal prefer to align parallel or antiparallel to a crystal direction called the easy axis.

We first used circularly polarized, resonant soft-x-ray reflectometry to measure the magnetization as a function of depth. The x-ray measurements provided the magnitude of the magnetization component along the direction of the incident x-ray beam in an element-specific manner (namely, that arising separately from the cobalt and iron atoms). We then used polarized-neutron reflectometry to measure the depth dependence of both the magnitude and direction of the magnetization in the sample. For both the x-ray and the neutron measurements, the spatial resolution was 1 nanometer.

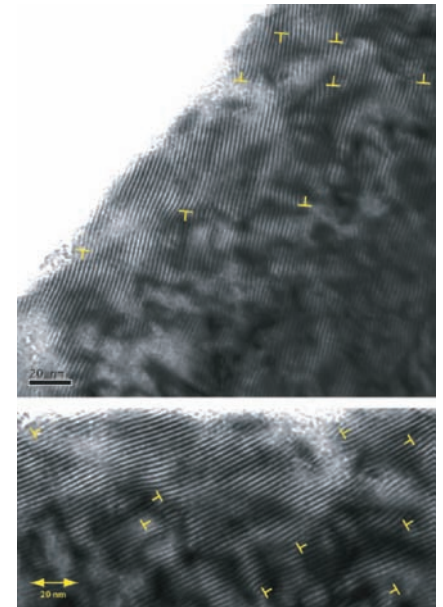


Figure 3. Transmission Electron Micrograph of the Dislocations in the FeF_2 Layer

The dislocations (yellow symbols) were produced by growing the FeF_2 layer on a MgF_2 substrate with a slightly smaller lattice spacing than the FeF_2 layer. The dislocations arise in order to partially relieve misfit strain across the FeF_2 - MgF_2 interface. The dislocations and unrelieved misfit strain are sources of uncompensated magnetization in antiferromagnetic FeF_2 .

Giant Magnetoresistance (GMR) in a Hard-Drive Read Head

Brian H. Fishbine

Giant magnetoresistance (GMR) was first observed independently by Baibich et al. (1988) and Binasch et al. (1989). They found the resistance of a structure of alternating nanolayers of iron and chromium decreased by as much as 50 percent when the magnetizations in all the iron nanolayers were aligned. The effect was called “giant” because it is much larger than the other effects of magnetization on the resistance of ferromagnetic materials known at the time.

Figure A shows how GMR works. Driven by a voltage produced by an electric field perpendicular to the layers, electrons travel successively through a ferromagnetic layer, a nonmagnetic conducting layer, and a second ferromagnetic layer. Each layer is nanometers thick at the most. The electrical resistance of the layered nanostructure is low when the magnetic fields in the two ferromagnetic films are parallel and high when the fields are antiparallel. The GMR effect is analogous to that observed when aligned polarizers pass light but crossed polarizers do not.

In a conducting ferromagnetic transition metal, approximately equal numbers of free electrons have spins parallel or antiparallel to a given direction. The first ferromagnetic layer allows electrons whose spins are parallel to that layer’s magnetization to pass through easily. If the magnetization of the second ferromagnetic layer is parallel to that of the first layer, the same electrons also pass easily through the second ferromagnetic layer, and the resistance of the layered nanostructure will be low. However, if the magnetic fields of the two layers are antiparallel, electrons with either spin will not pass through the nanostructure easily, and the electrical resistance will be high.

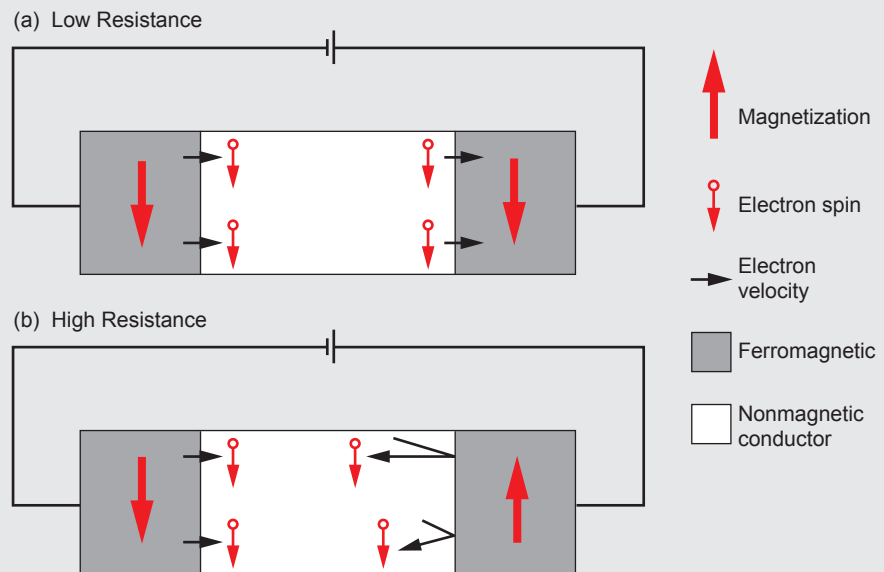


Figure A. Spin-Dependent Electron Transport in a GMR Nanostructure

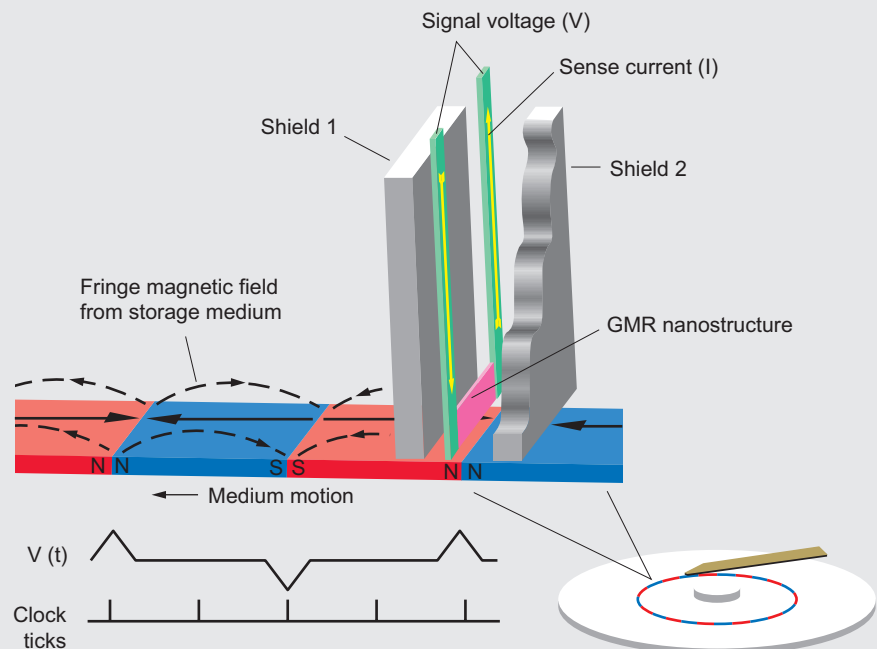


Figure B. The Spin-Valve Read Head in a Computer Hard Drive

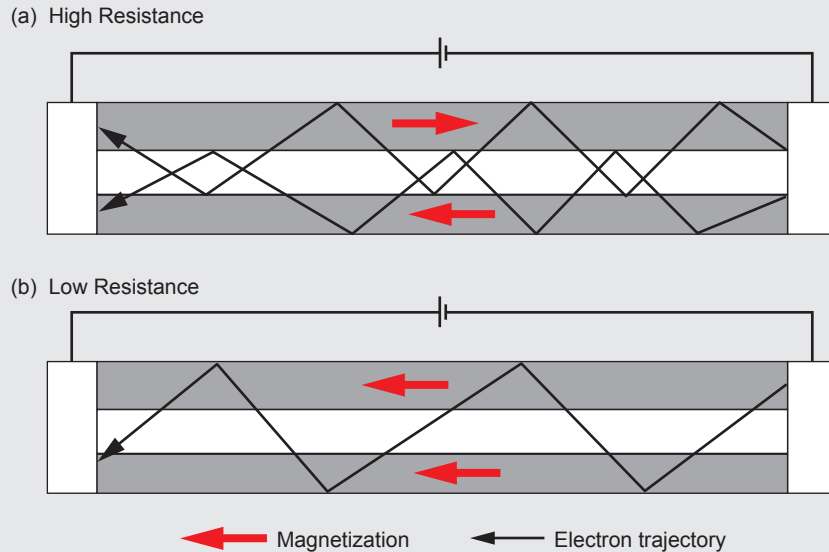


Figure C. The Geometry of the GMR Nanostructure in a Spin-Valve Read Head

Figure B shows how the GMR, or spin-valve, read head in a hard drive works. As the hard-drive disk rotates, the bits stored on it pass under the read head's GMR nanostructure at a distance of 10 nanometers or less. The bits' magnetic fields can change the magnetization of the nanostructure's "free" layer but not the magnetization of the nanostructure's "fixed" layer, which is held constant (either up or down) by the nanostructure's antiferromagnetic layer. Through the GMR effect, the resistivity of the nanostructure's layers depends on whether the magnetizations in the two ferromagnetic layers are parallel or antiparallel. Thus, the resistivity depends on the bits' magnetic fields. A constant current flows through the layers, so the voltage across them is determined by the bits' magnetic fields; data are read by measuring this voltage. The two shields ensure that the nanostructure responds only to the magnetic fields at the bit boundaries, where the magnetic fields from two adjacent bits cancel or are mainly perpendicular to the hard drive disk. The bit values are determined from the voltages measured at the clock ticks. As shown, a bit passes under

the GMR nanostructure every two clock ticks. The three layers shown in Figure C are the heart of the GMR nanostructure. A spin-valve read head has an additional layer (not shown), which stabilizes the fixed layer (see Figure 1 in the main article).

In Figure C, the current is generally parallel to the nanostructure's layers, which is the case with actual read heads but differs from the situation depicted in Figure A. As in Figure A, however, changes in resistance result from changes in how the electrons scatter from the conductor-ferromagnet interfaces as the magnetizations of the ferromagnetic layers change. We also note that the GMR effect works even if magnetizations in the ferromagnetic layers are perpendicular to the current rather than parallel to it as shown in Figure C.

GMR's high sensitivity to magnetic fields allows a read head to read small bit volumes, which translate to high storage densities.

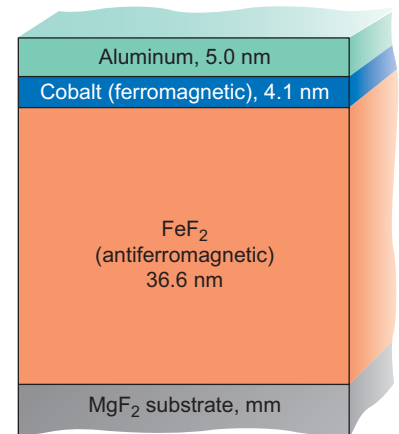


Figure 4. Model System for Studying Exchange Bias

The model system consists of a ferromagnetic cobalt layer in contact with a single-crystal FeF_2 layer. The FeF_2 layer becomes antiferromagnetic when cooled below its Néel temperature of 78.4 K.

We performed the x-ray measurements at the Advanced Light Source at Lawrence Berkeley National Laboratory. Circularly polarized x-rays tuned to the x-ray absorption L-edges of first cobalt and then iron were used. The difference in the reflected x-rays for left and right circular polarization at the L-edge of a magnetic atom is proportional to the magnetization involving that element. First, we applied a magnetic field of 796 kiloamperes per meter (kA/m) parallel to the FeF_2 's [001] direction and cooled the sample to 20 kelvins. Then, we took x-ray reflectometry measurements at a single angle of incidence and reflection while gradually varying the magnitude and reversing the direction of the applied magnetic field. That procedure allows us to measure the projection of the magnetization along the direction of the incident x-ray beam as a function of applied magnetic field. Using this procedure, we measured the hysteresis curves of the ferromagnetic

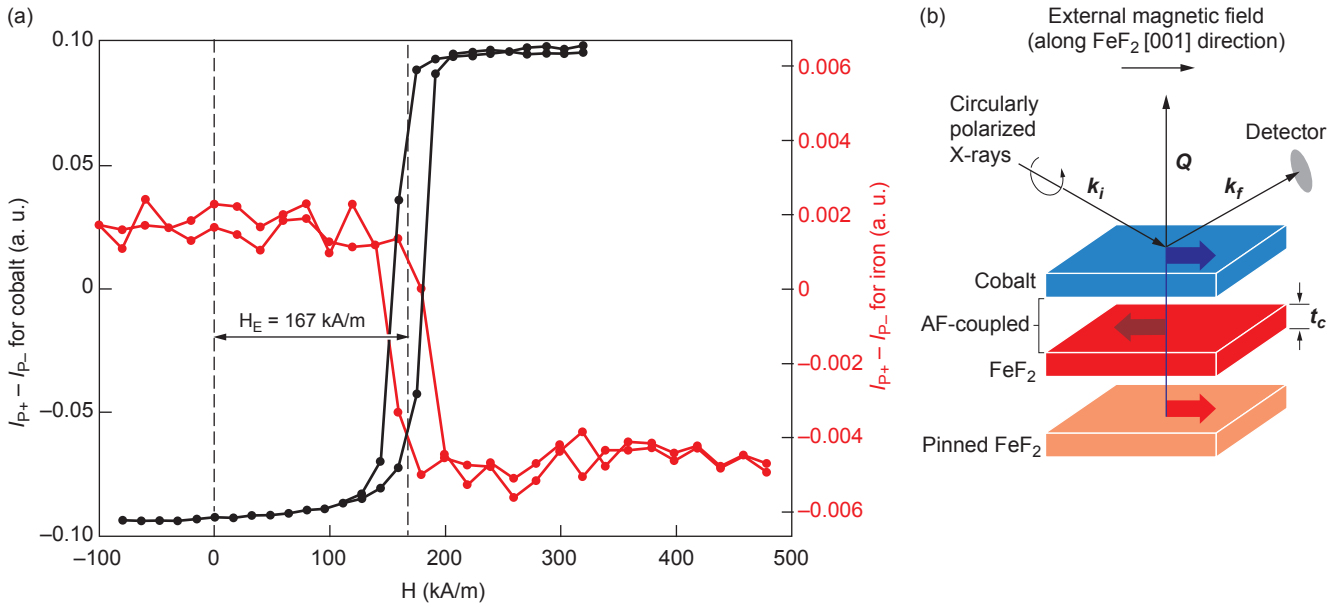


Figure 5. Hysteresis Curves for the Cobalt and Iron Spins

(a) These hysteresis curves were obtained by tuning the incident x-ray energy to the absorption edges of cobalt or iron. I_{P+} and I_{P-} are the intensities of, respectively, the left and right circularly polarized x-rays reflected from the model nanostructure. The offset of 167 kA/m is the exchange bias, a key parameter for a spin-valve read head or an MRAM cell. Note that, in this system, the exchange bias is positive, unlike the negative exchange bias in conventional systems. This result is due to the cobalt and iron spins across the interface being oppositely coupled. (b) This schematic shows the region of the sample near the cobalt– FeF_2 interface. In the cobalt layer (blue), the magnetization follows the external field. In the FeF_2 layer (red), the iron spins are antiparallel to the cobalt spins (believed to be a consequence of antiferromagnetic coupling across the interface); in the orange layer, the iron spins are pinned along the initial direction of the magnetization. In these experiments, the applied external magnetic field was always parallel or antiparallel to the FeF_2 [001] direction and varied in magnitude. The arrows indicate the projections of the magnetizations along the direction of the incident x-rays, which in (b) is shown parallel to the applied magnetic field. We measured the thickness t_c of the red slab to be 2 to 3 nm. (Reprinted with permission from S. Roy et al., *Phys. Rev. Lett.*, 95, p. 047201–2, 2005. Copyright 2005 by the American Physical Society.)

cobalt layer and the antiferromagnetic FeF_2 layer, respectively, as shown in Figure 5. An exchange bias of 167 kA/m in both layers is apparent in the figure. These measurements lead us to conclude that the cobalt and iron spins are likely to be coupled magnetically.

In a second set of x-ray measurements, we applied a field of 796 kA/m parallel and then antiparallel to the [001] direction of the FeF_2 layer and in each case measured the magnetization of the cobalt and iron spins as a function of scattering angle. From those data, we extracted the separate magnetizations of the cobalt and iron spins as functions of depth (Figure 6), from which we conclude that cobalt and unpinned iron spins are antiparal-

lel across the ferromagnetic/antiferromagnetic interface.

From these results, we concluded that a large applied magnetic field caused the cobalt spins to align with the field whereas the uncompensated iron spins near the FeF_2 –cobalt interface rotated in a direction opposite to the cobalt spins because of a strong antiferromagnetic coupling across the interface between those two types of spins.

We then employed reflectometry with polarized neutrons to determine the direction, as well as the magnitude, of the magnetization in both layers. The neutron measurements were performed at the ASTERIX spectrometer at LANSCE. We first applied a magnetic field of 438 kA/m in the

[001] direction of the FeF_2 layer while cooling the sample to 10 kelvins. Then, we took neutron scattering data after rotating the sample about its surface normal until the applied field was parallel to the FeF_2 's [110] direction. This procedure intentionally twisted the magnetization in the sample. By examining where the magnetic twist occurred we could identify where the magnetization of the sample was pinned. Figure 7 shows the direction and the magnitude of the sample's magnetization as a function of depth determined from our polarized neutron measurements. While the magnetization in the cobalt layer and near the cobalt– FeF_2 interface is twisted, the net magnetization inside the nominally antiferromagnetic FeF_2

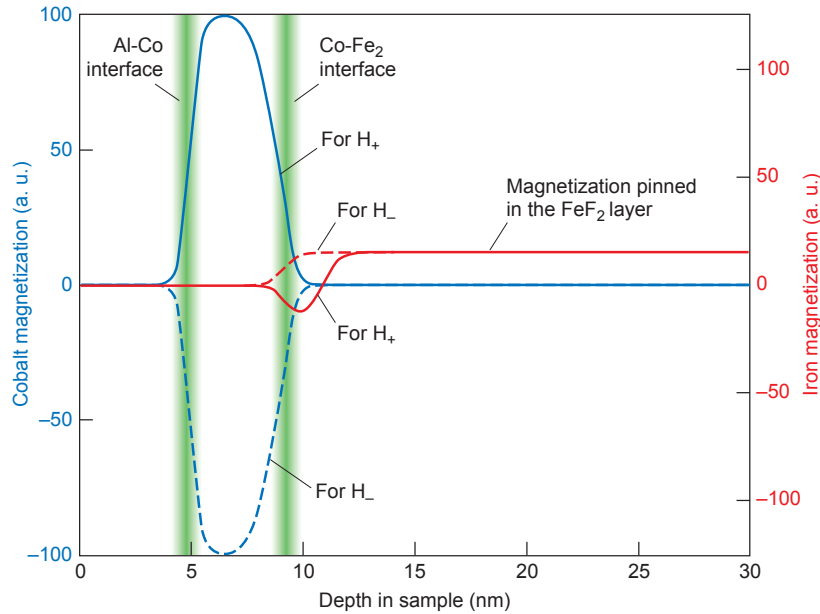


Figure 6. Magnetization Depth Profiles from Resonant-X-Ray Reflectometry
The depth profiles of the cobalt and iron magnetizations were measured for two values of applied magnetic field, $H_+ = +796$ kA/m and $H_- = -796$ kA/m. The measurements were taken after the sample had been initially magnetized in a field $H_{FC} = 796$ kA/m at 20 K along the [001] direction of the FeF_2 crystal. The pinned iron spins in the FeF_2 layer reflect the initial magnetization. The unpinned iron spins in the FeF_2 layer point opposite to the cobalt spins, indicating an antiferromagnetic coupling across the cobalt- FeF_2 interface. (Reprinted with permission from S. Roy et al, *Phys. Rev. Lett.*, 95, p. 047201-2, 2005. Copyright 2005 by the American Physical Society.)

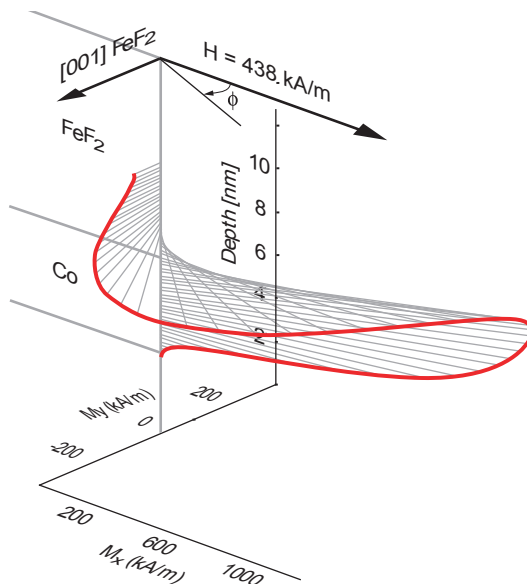


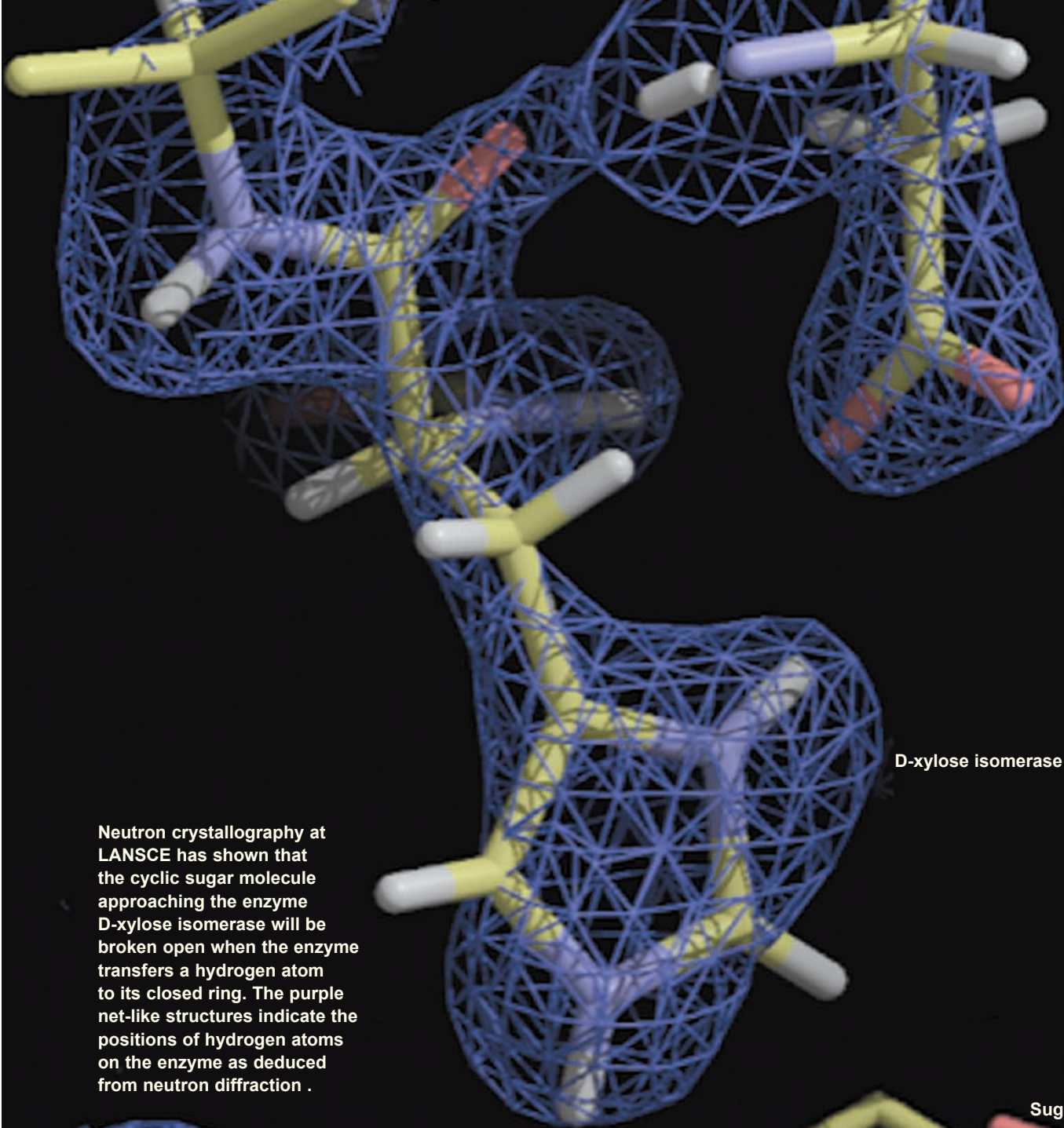
Figure 7. Magnetization Depth Profile from Polarized-Neutron Reflectometry
The depth profile of the magnetization in the cobalt- FeF_2 sample exhibited a twist with respect to the applied field of 438 kA/m because the magnetization inside the FeF_2 layer was pinned or frozen in the [001] FeF_2 direction (parallel to the direction of the field applied to the sample during cooling to 10 K) while the field applied after pinning the magnetization was perpendicular to the [001] direction. (Reprinted with permission from S. Roy et al, *Phys. Rev. Lett.*, 95, p. 047201-3, 2005. Copyright 2005 by the American Physical Society.)

layer was apparently pinned along a particular crystallographic axis, namely, that of the initial magnetization of the sample. In other words, the pinned magnetization could not be moved by the applied magnetic field. We suggest that the net magnetization is due to piezomagnetism, that is, strain-induced magnetization, in FeF_2 and to uncompensated magnetization of misfit dislocations.

The combination of our x-ray scattering study (in which the orientations of unpinned cobalt and iron spins near the interface was identified) and neutron scattering study (in which location of pinned magnetization was identified) enabled us to develop a model of the exchange bias mechanism. Because the loose and pinned iron spins prefer to point in the same direction, the pinned spins inside the antiferromagnet inhibit the response of the loose iron and cobalt spins to small applied magnetic fields. The inhibited response of cobalt spins to the magnetic field is manifested as exchange bias. These somewhat unexpected results go a long way toward yielding a clearer picture of the microscopic origins of exchange bias.

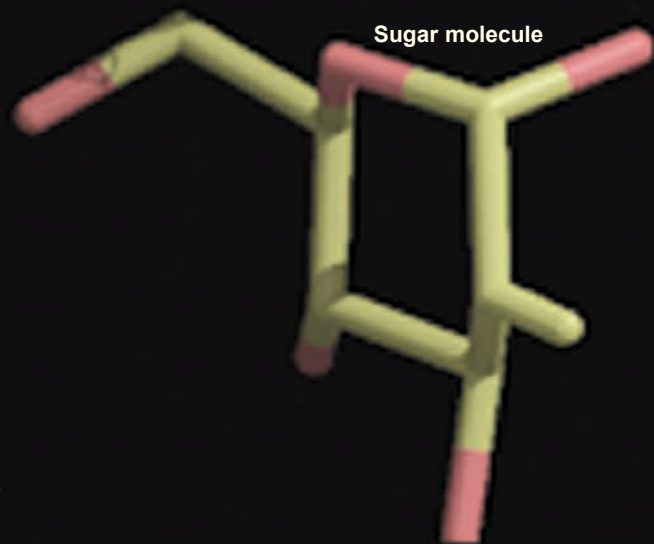
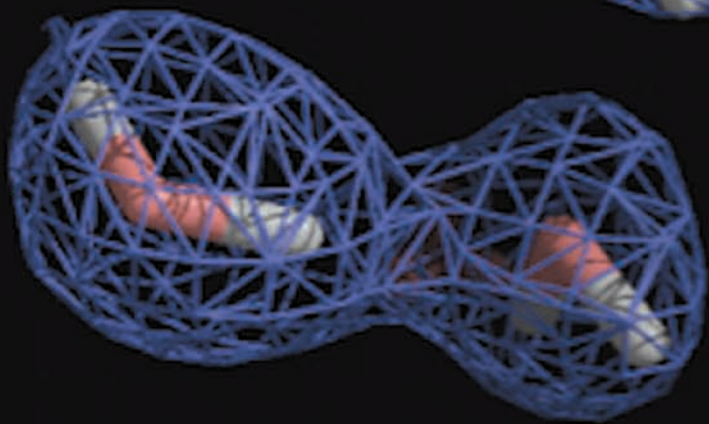
Further Reading

- Baibich, M. N., J. M. Broto, A. Fert, F. N. Van Dau, and F. Petroff. 1998. Giant Magnetoresistance of (001)Fe/(001)Cr Magnetic Superlattices. *Phys. Rev. Lett.* **61**: 2472.
- Binasch, G. P. Grünberg, F. Saurenback, and W. Zinn. 1989. Enhanced Magnetoresistance in Layered Magnetic Structures with Antiferromagnetic Interlayer Exchange. *Phys. Rev. B* **39**: 4828.
- Fitzsimmons, M. R., C. Leighton, J. Nogués, A. Hoffmann, Kai Liu, C. F. Majkrzak, et al. 2002. Influence of In-Plane Crystalline Quality of an Antiferromagnet on Perpendicular Exchange Coupling and Exchange Bias. *Phys. Rev. B* **65**: 134436.
- Roy, S., M. R. Fitzsimmons, S. Park, M. Dorn, O. Petravic, I. V Roschein, et al. 2005. Depth Profile of Uncompensated Spins in an Exchange Bias System. *Phys. Rev. Lett.* **95**: 047201.



D-xylose isomerase

Neutron crystallography at LANSCE has shown that the cyclic sugar molecule approaching the enzyme D-xylose isomerase will be broken open when the enzyme transfers a hydrogen atom to its closed ring. The purple net-like structures indicate the positions of hydrogen atoms on the enzyme as deduced from neutron diffraction .

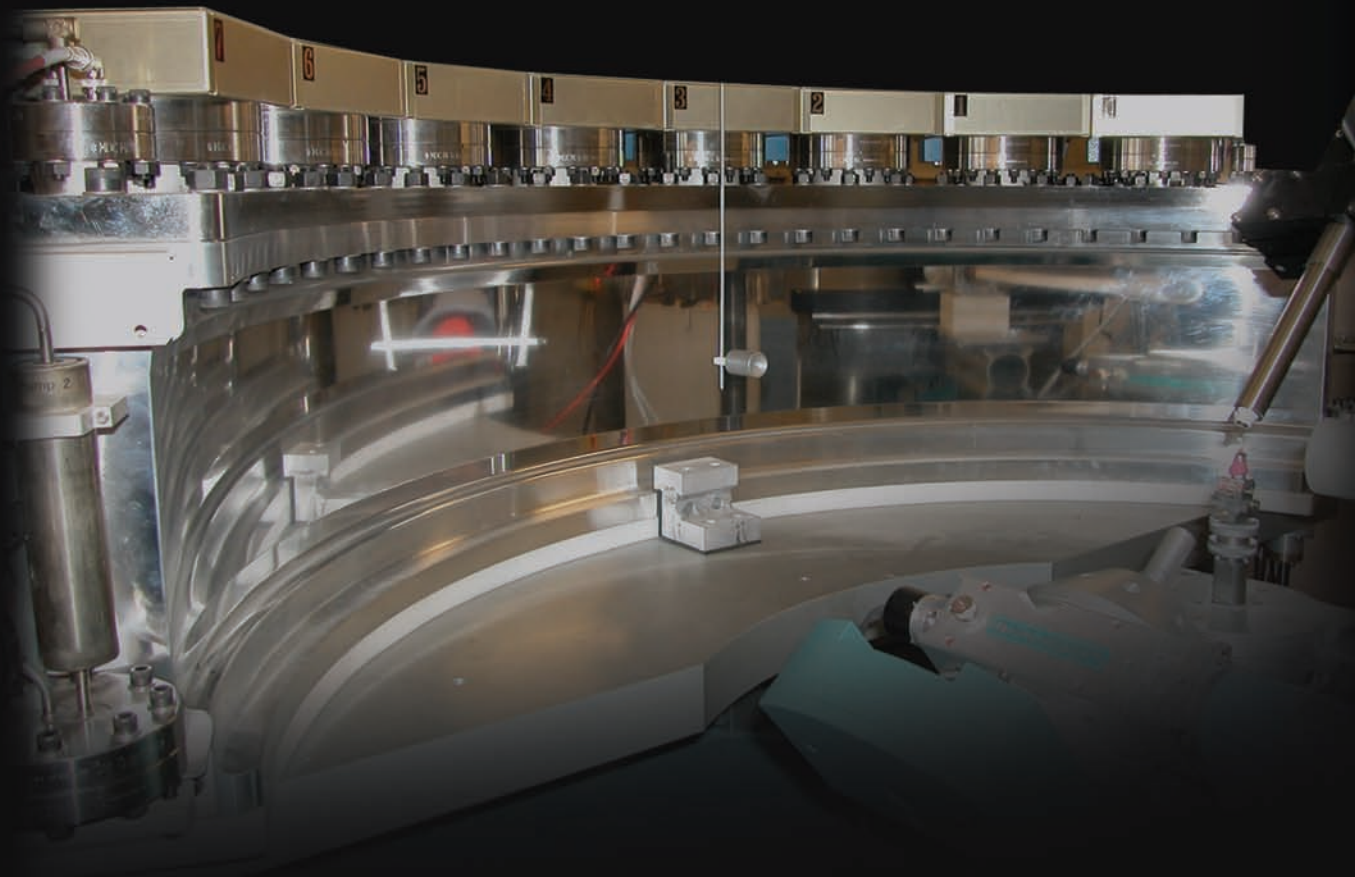


Sugar molecule

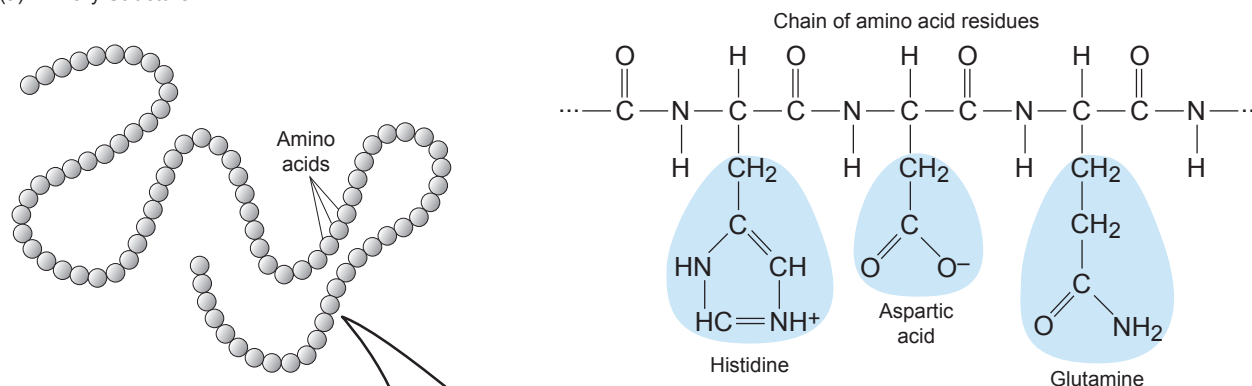
Finding out How Enzymes Work

Paul A. Langan

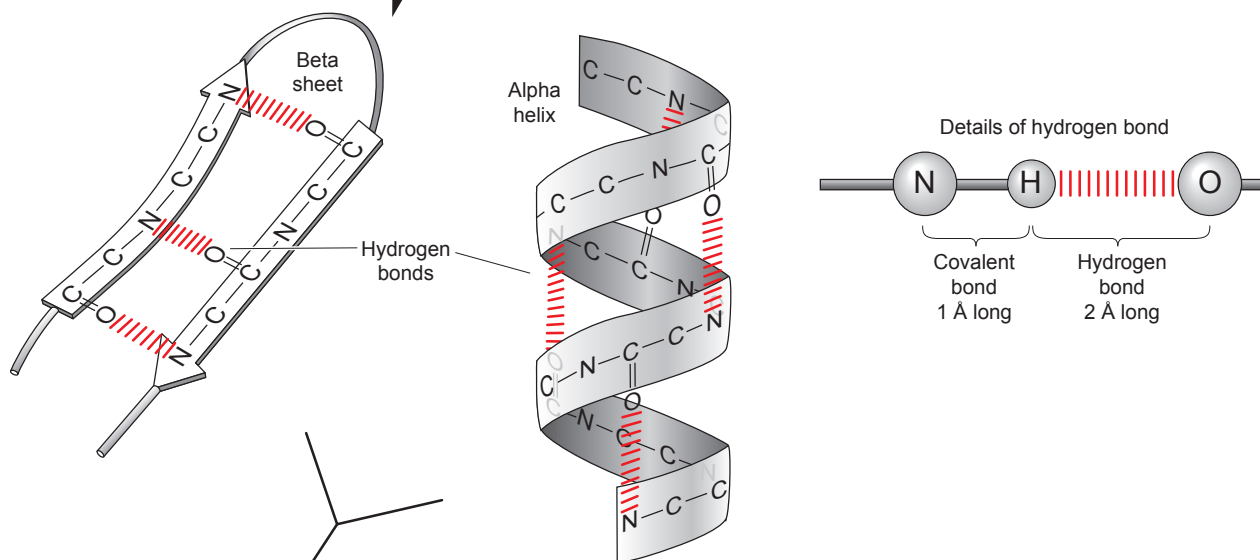
The new Protein Crystallography Station at LANSCE is making it possible to pinpoint the biochemical steps involved in enzyme reactions. That knowledge should improve our overall understanding of cellular processes and of how defective and pathogenic enzymes affect our health. It should also enable the design of more effective drugs and therapeutics for treating disease.



(a) Primary Structure



(b) Secondary Structure



(c) Tertiary Structure



Figure 1. Protein Structure

Proteins are constructed from individual building blocks known as amino acids. The amino acids polymerize, or join together, to form long chains of amino acid residues. (a) Shown here are a cartoon of the primary chainlike structure of a protein and an expanded view, showing three amino acid residues—histidine, aspartate, and lysine—strung on the protein backbone. (b) The secondary structure is the folding of the chain into either (1) beta sheets, in which segments of the amino acid chain, represented by ribbonlike arrows, lie parallel or antiparallel to each other and are held in place by hydrogen bonds (red dashed lines) connecting the backbones of the segments or (2) alpha helices, a helical winding of the chain held in place by a scaffold of hydrogen bonds parallel to the axis of the helical winding and again connecting the backbones of parallel portions of the chain. (c) The tertiary structure is a single chain folded into alpha helices, beta sheets, and intervening loops to form a complicated structure with clefts, barrels, pockets, and cages.

Within each of the microscopic cells that make up our bodies, specialized protein molecules, called enzymes, are frantically working away shuffling atoms about in chemical reactions that make those cells come alive. Energy production, cell growth, cell division, and other essential life processes involve thousands of such reactions, many with their own specialized enzymes, interconnected through complex pathways and networks. Like all proteins, an enzyme is created by linking small molecules, called amino acids, into a long chain. About twenty kinds of amino acids, each with different chemical properties, are found in our cells. Many of these amino acids—for example, aspartic acid, glutamine, and lysine—are found in food supplements. Each type of enzyme is composed of a different sequence of tens, sometimes hundreds, of amino acids, and that sequence determines how its chain folds into a unique three-dimensional shape with features such as helices, barrels, sheets, loops, pockets, clefts, and cages (Figure 1). The shape of an enzyme is key to understanding how it works, and understanding how enzymes work is key to understanding cellular life processes.

The Structure-Function Relationship

The shape of a molecule, which scientists call its structure, can be revealed using a technique called x-ray crystallography, developed in the last century. Over the past 50 years or so, x-ray crystallography has been used to reveal the structure of a number of enzymes. These structures, together with information from their chemical analysis, have led to a clear set of ideas about how an enzyme might work. The essential job of an enzyme, speeding up a particular chemical reaction, can be

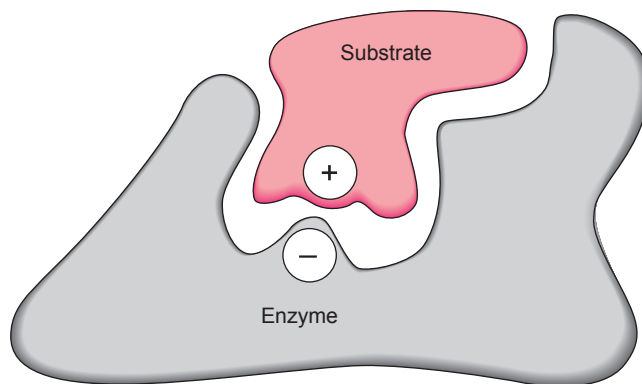


Figure 2. Enzyme-Substrate Binding

An enzyme begins its catalytic function by binding a particular substrate to its active site. The two fit together like a lock and key. In addition to shape, a unique pattern of attractive forces and hydrogen bonds makes the active site highly selective for one particular substrate.

thought of as involving two steps: binding a chemical that the enzyme will work on, called a substrate, and then pushing the chemical reaction to occur, called catalysis. Binding takes place at an active region of the surface of the enzyme where the enzyme and substrate have complementary shapes. The substrate fits into the active site like a key in a lock (Figure 2). However, the lock-and-key model is not enough to explain binding; attractive forces are needed to hold the substrate in place. These forces include electrostatic attractions between oppositely charged groups and also chemical bonds that are mediated by hydrogen atoms, called hydrogen bonds. The unique pattern of these interactions makes the active site of an enzyme highly selective for its particular substrate.

During catalysis, as the atoms in the enzyme and substrate begin to react with each other to weaken old bonds and to begin to form new bonds, the reacting atoms must overcome forces that tend to push them apart. Pushing atoms together into a momentary transition state through which the reaction must pass requires energy. This extra energy can be thought of as a hill or barrier that

must be climbed before the reaction can take place. A key insight, made by the famous chemist Linus Pauling in the early years of studying enzymes, is that enzymes bind the transition state better than the substrate, and this process reduces the height of the energy hill. More recently, scientists have mapped out other possible routes for ascending the energy hill. One of these is based on the idea that binding a substrate on the surface of an enzyme reduces its entropy (the amount of freedom to move) and increases its free energy, and that this free energy can be used to climb the energy hill. It has even been proposed that small particles such as electrons and hydrogen atoms can tunnel through the energy hill rather than climb over it, by using quantum physical processes. These ideas on substrate binding and catalysis have led to a number of medical advances, particularly in the design of new drugs and therapeutics.

Protein Structure and Drug Design

At present, x-ray crystallographic studies of enzymes are mostly con-

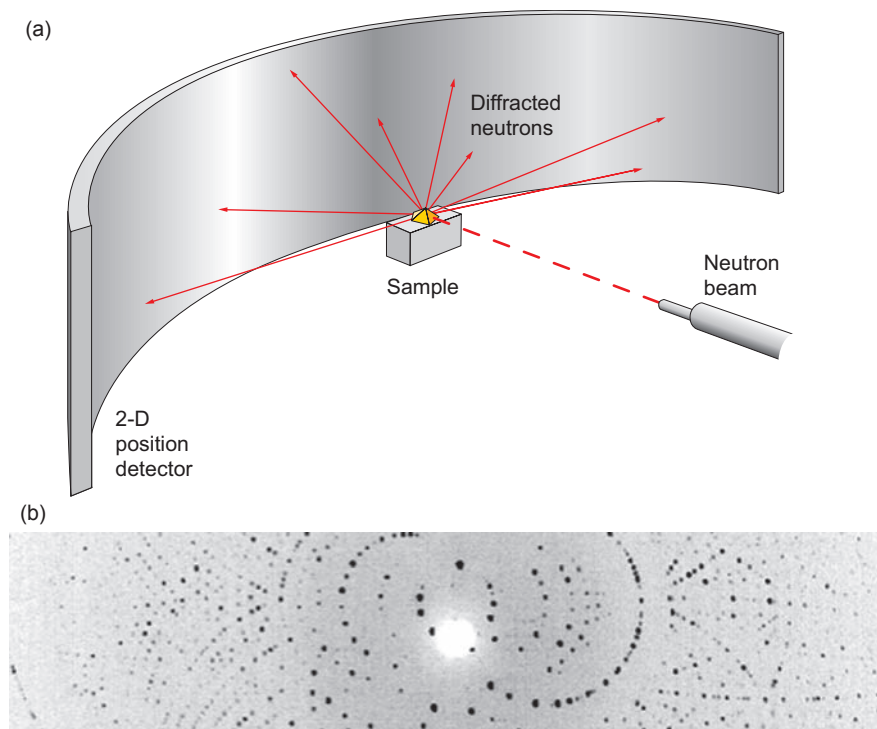


Figure 3. Diffraction
(a) In a neutron diffraction experiment at the LANSCE Protein Crystallography Station (PCS), a protein crystal is placed in a neutron beam, and the diffracted rays are recorded on a large two-dimensional electronic detector. **(b)** This diffraction pattern of the protein D-xylose isomerase taken at the PCS shows a regular array of diffraction peaks. These peaks are analyzed to reveal the location of hydrogen atoms in the protein structure.

ducted at large central synchrotron x-ray sources that are used by many groups of visiting scientists and that are powerful enough to visualize the structure of thousands of enzymes a year. As a result of the Human Genome Project and its spinoffs, the amino acid sequence of any enzyme that is encoded in a gene can now be read, and then that enzyme can be synthesized for study even if it has never been seen before and its function is completely unknown. There is great hope that, by revealing the structure of all proteins and enzymes, we will begin to understand how they work in detail and that this awareness will provide an overall understanding of cellular processes and of how defective or pathogenic enzymes can affect our health. Understanding how

enzymes work in greater detail may also provide further clues about how they could be improved or modified for medical applications or for applications in industries such as food, agriculture, and remediation.

One of the most powerful benefits of our improved understanding of how enzymes work has been to the design of new drugs and therapeutics. Many diseases, such as cancer, involve enzymes that don't work properly or that are not produced or regulated properly. Drugs can bind to an enzyme and stop it from working in at least two ways: competitive inhibition and noncompetitive inhibition. In competitive inhibition, a drug competes with the substrate to bind at the active site of the enzyme. The goal is to design a drug that binds

more strongly in the active site than the enzyme's natural substrate. A drug is designed to bind in a region next to the active site in noncompetitive inhibition. The drug prevents substrate binding by distorting the shape of the active site, so that the key no longer fits the lock. Structure-based drug design has already produced several life-saving drugs, such as Fortovase[®], Norvir[®], Crixivan[®], Viracept[®], Agenerase[®], Trusopt[®], Relenza[®], Celebrex[®], Vioxx[®], and Thymitaq[®] that are vital for people with health problems such as AIDS, arthritis, glaucoma, flu, and cancer. Many more drugs are in the pipeline.

Deciphering Function with Neutrons

Despite these advances, a limitation in using x-rays to study enzymes is that they only reveal the enzyme's "skeleton." Although x-rays "see" the atoms of carbon, oxygen, sulfur, and nitrogen that connect up the skeleton of a protein, they have a much harder time seeing the smaller, more-mobile atoms of hydrogen that are attached to this skeleton and that make up the water molecules that surround and interact with the protein. The reason for this observation is that x-rays interact primarily with the electrons surrounding the nucleus of an atom; the more electrons an atom has, the stronger its interaction with x-rays. With only one electron, a hydrogen atom is usually invisible to x-rays. This limitation is severe because hydrogen atoms—whether they are involved in folding the enzyme or binding the substrate, whether they are shuffled about during catalysis or take part in interactions of the enzyme with its aqueous environment—are crucial to enzyme function. Without knowledge of where the hydrogen atoms are in an enzyme and how they are moved about during binding and catalysis, it is difficult to

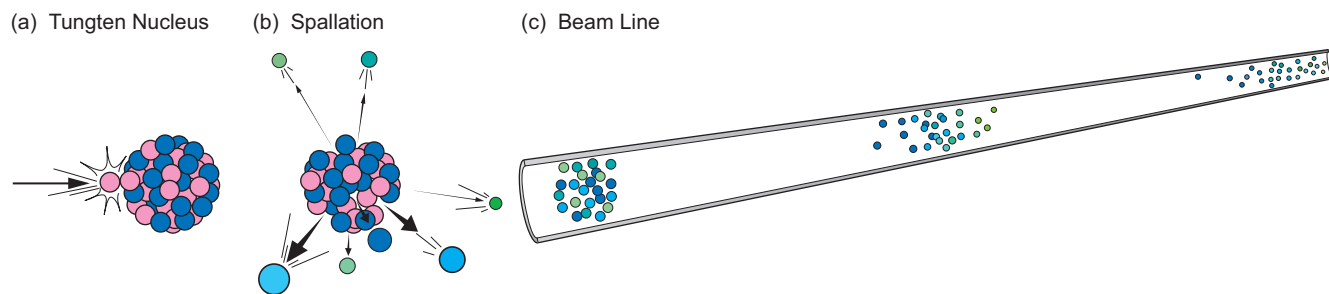


Figure 4. Spallation Neutrons

(a) When an energetic proton hits the nucleus of a heavy atom, (b) the nucleus releases tens of neutrons with different energies. (c) The resulting pulse of neutrons is very short, but as the pulse travels down the flight path toward the experiment, the higher-energy neutrons travel faster, the pulse stretches out in space, and the arrival times of the neutrons serve to identify their energies. This temporal separation of neutrons by energy allows collection of separate diffraction patterns, each corresponding to a different neutron energy (or wavelength).

know how an enzyme works in detail and how to design a drug that will bind more effectively.

In order to solve the problem of finding hydrogen atoms, neutron crystallography has been developed and applied to study enzymes over the past 40 years. Like x-ray crystallography, neutron crystallography can be used to reveal structure by a process called diffraction. A sample made from crystallized protein molecules is placed in a beam of neutrons, and the atoms scatter neutrons out of the beam. Because the protein molecules are packed in a very regular way in the crystal, neutrons are scattered strongly only in certain directions and make a pattern of spots, called a diffraction pattern, when they are recorded on a detector (Figure 3). The diffraction pattern is then used to work out the structure of the protein. However, whereas x-rays are scattered by the electrons surrounding the nucleus of an atom, neutrons are scattered by the nucleus itself through a nuclear force called the strong interaction. The nucleus of a hydrogen atom, and in particular that of its deuterium isotope, interacts with neutrons very efficiently. Neutron crystallography is therefore a powerful probe for locating hydrogen atoms in enzymes, especially if the hydrogen atoms have been replaced by deuterium atoms.

Progress in applying neutron crystallography to studying enzymes has been slow because it is difficult to produce neutrons in large numbers. Neutron beams are relatively weak compared with x-ray beams, and therefore large crystal sizes are required to scatter enough neutrons to record a clear diffraction pattern. Crystals for studies at x-ray sources are typically a fraction of a millimeter in size, and it can be difficult to grow them larger. When Los Alamos scientist Benno Schoenborn performed the first neutron study of a protein back in 1968 at a nuclear reactor run by Brookhaven National Laboratory, he had to spend several months collecting data from a crystal that was about half the size of a dime. In the years following this pioneering experiment, a number of technical advances at nuclear reactors in the United States, Japan, and Europe provided more facilities for neutron protein crystallography and pushed the required crystal sizes down below 1 millimeter and the time needed to collect neutron diffraction data down to a few days. However, there is little prospect of any further large increase in the flux of reactor neutron sources because of inherent limitations in the nuclear process called fission that is responsible for the production of neutrons.

At another type of neutron source that Los Alamos National Laboratory has been at the forefront of developing, called a spallation source, there are fewer flux limitations. Spallation sources, like the one run by Los Alamos Neutron Science Center (LANSCE), produce neutrons by bombarding a metal target with pulses of high-energy subatomic particles, called protons. Showers of neutrons with a range of energies come off the target in bursts 20 times a second. At the target, the duration of each pulse or burst of neutrons is very short, but as the neutrons travel down beam lines, the pulses become longer because neutrons with different energies travel at different speeds (Figure 4). The low-energy neutrons cannot keep up with the high-energy neutrons in the same pulse. As a result, neutrons of different energies are detected in a diffraction pattern at different times. Being able to record diffraction patterns that change in time is a big advantage for neutron crystallography. Although the current spallation neutron source run by LANSCE produces fewer neutrons than a large nuclear reactor, the time structure of the neutron beam allows the neutrons to be used more efficiently and with much lower noise levels. There is also the possibility of upgrading the spallation source in the future to produce much higher neutron fluxes.



Figure 5. The Los Alamos Protein Crystallography Station

The Los Alamos PCS is the only resource of its kind in North America and the first to be built at a spallation neutron source. Data collection from small (millimeter-sized) crystals is possible at the PCS because of the use of time-of-flight methods, together with a number of technological innovations, including a large cylindrical neutron detector and a special neutron moderator that, in effect, increases the neutron flux on the sample.

The New Protein Crystallography Station (PCS)

In order to demonstrate the advantages and potential of spallation neutron sources for protein crystallography, Los Alamos scientists Benno Schoenborn and the author have designed and built a PCS at LANSCE (Figure 5). By carefully tailoring the incoming neutron pulses and optimizing detection of those that are diffracted, a state-of-the-art user facility has been created for the national and international structural biology community. Since its commissioning in 2002, the PCS has remained the only resource for neutron crystallography studies of enzymes in North America and the first in the world to be built at a spallation neutron source. The PCS project is funded by the office of Biological and Environmental Research of the U.S. Department of Energy. Up to twenty scientific teams visit Los Alamos every year to use

the PCS. Although the PCS has been in operation for only two years, those teams, mostly from universities in the United States, have broken new ground by looking at a number of enzymes never studied before with neutrons. And for some of these, they have been able to pin down specific information on important enzymatic reactions and on how drugs bind to enzymes. The two examples that follow are illustrative of these developments.

Solving the Mechanism of Xylose Isomerase

D-xylose isomerase is an enzyme that a number of bacteria use to convert one type of sugar to another (D-xylose to D-xylulose) through a process called hydrogen atom transfer. Not only is this enzyme responsible for a crucial step in the sugar metabolic pathway, and therefore the growth, of a number of bacteria, but

it is also used in the food industry to catalyze the conversion of glucose to fructose. A mixture of glucose and fructose, in the form of high-fructose corn syrup, is a high-powered sweetening agent used as a sugar replacement, and D-xylose isomerase has become one of the largest volume commercial enzymes of today. One of the first experiments on the PCS was carried out by a team of visiting researchers from the Fox Chase Cancer Research Center and the University of Tennessee, which is paving the way for scientists to learn exactly how D-xylose isomerase works.

Through previous x-ray diffraction studies, researchers know how the heavier atoms—carbon, oxygen, and nitrogen—make up the molecular structure. The enzyme looks like a barrel or cup with a long handle attached (Figure 6). The walls of the barrel are made from panels of amino acid chains that are folded into sheets on the inside and helices on the outside. At the bottom of the barrel is the active site where the sugary transformation takes place. We know that two metal atoms, usually magnesium atoms, are present in the active site and are important for binding the sugar substrate and also for catalysis. The chief mystery with D-xylose isomerase is where the hydrogen atoms are located in the active site and how they are shuffled during binding and catalysis.

From an industrial point of view, understanding the details of how D-xylose isomerase works could provide clues on how reaction rates could be made faster and higher fructose concentrations achieved, as well as on improving other areas of the production process. However, as team leader Gerry Bunick puts it, “it’s not simply to create a more corn-syrupy world: Better understanding of that particular hydrogen-atom transfer process could lead to improved and better targeted medicines and advances in nanotech-

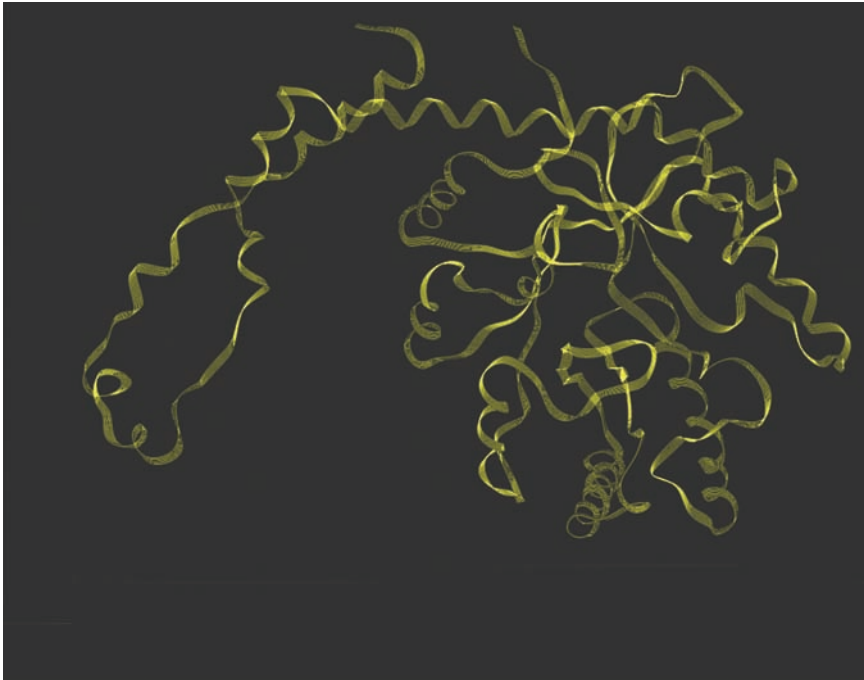


Figure 6. Structure of D-xylose Isomerase
Xylose isomerase, an enzyme responsible for the crucial first step in the metabolism of sugar by bacteria, looks like a cup with a long handle. The active site for the metabolic reactions is deep inside, at the bottom of the cup.

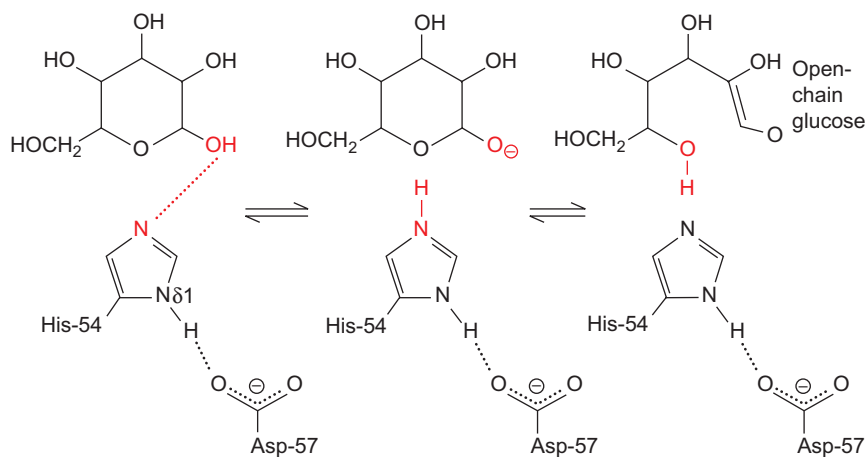


Figure 7. Assumed Initial Steps of Sugar Metabolism by Xylose Isomerase

To break apart the ring of cyclic glucose, D-xylose isomerase was thought to catalyze the transfer of a hydrogen atom from one oxygen in the ring to another. This hypothesis could not be confirmed with x-ray crystallography because none of the details concerning the hydrogen-bonding arrangement of water molecules or the presence of water ions are visible to x-rays.

nology.” In particular, the Fox Chase members of the team are interested in the roles of magnesium and water in

the function of the enzyme—knowing where the hydrogens are located is a key to understanding those processes.

That knowledge will be useful in working with magnesium-containing enzymes that are important to cancer research.

X-ray crystallography has suggested a general pathway for the chemical reaction that involves a number of distinct steps. There are two steps where hydrogen transfer is involved in the catalytic mechanism. One involves opening the ring of the cyclic sugar into a straight chain that the enzyme can then isomerize. The second step involves the transfer of a hydrogen atom between neighboring carbon atoms on the extended sugar chain.

A key histidine amino acid residue in the D-xylose isomerase active site, labeled His54 in Figures 7 and 8, is thought to play a role in opening the sugar ring. The important part of this residue is a flat ring made up from three carbon and two nitrogen atoms. Histidines are unusual because they can have a number of different possible electronic states, depending on whether the nitrogen atoms, labeled N δ 1 and N δ 2, have an attached hydrogen atom or not. Before sugar binds to D-xylose isomerase, the active site is filled with a network of ordered water molecules. One of those water molecules hydrogen bonds to N δ 2 of His54. A water molecule has two hydrogen atoms and an oxygen atom, and knowing whether one of the hydrogen atoms or the oxygen atom is bonding to His54 is important. If N δ 2 does not have an attached hydrogen atom, then it must bond to a hydrogen atom of a water molecule. Therefore, when the sugar substrate displaces water molecules in order to bind in the active site, N δ 2 must bond to a sugar hydrogen atom (Figure 7). Alternatively, if N δ 2 does have an attached hydrogen atom, then it must bond to the oxygen atom of a water molecule, or when sugar is bound, to the oxygen atom of the sugar ring (Figure 8).

For the first experiment on the PCS, crystals of D-xylose isomerase

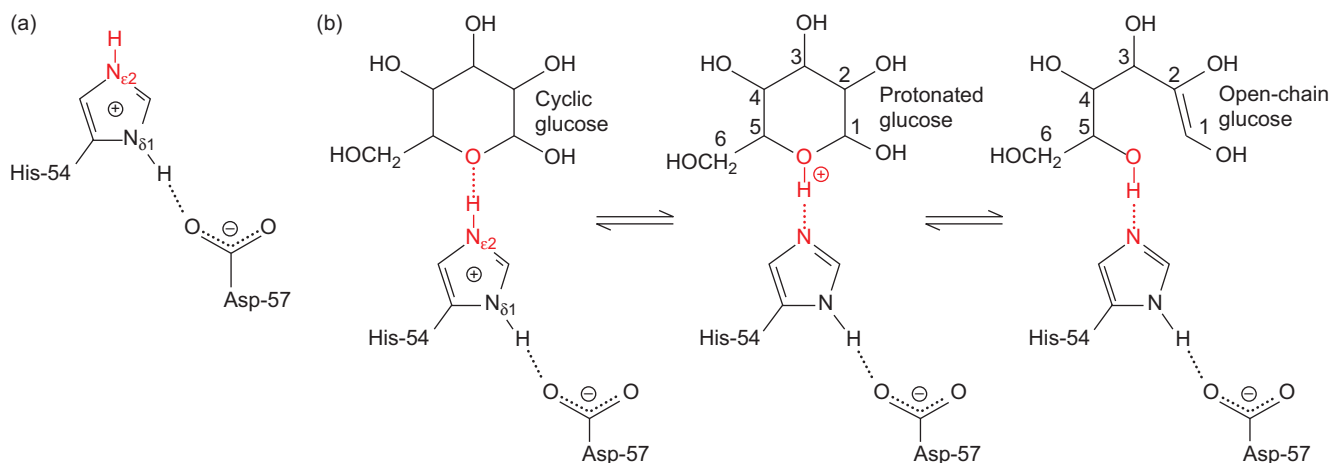


Figure 8. Neutron Results for Breaking the Ring in Cyclic Glucose

(a) The hydrogen atom on $N_{\epsilon 2}$ in the His54 residue in D-xylose isomerase is deduced from neutron crystallography at the PCS. (b) The hydrogen on $N_{\epsilon 2}$ first forms a bond with the oxygen on the sugar ring, then it is transferred to that oxygen because His54 is configured to act like an acid, and finally, by that transfer, it causes the sugar ring to break. This mechanism, revealed by neutron diffraction, should be compared with the one shown in Figure 7.

were prepared with no sugar present. The neutron diffraction patterns that were recorded have allowed the visiting researchers to pinpoint where the hydrogen atoms are in the active site. $N_{\epsilon 2}$ is found to have an attached hydrogen atom that bonds to the oxygen of a water molecule, and what is more, $N_{\delta 1}$ is also found to have an attached hydrogen atom and to be hydrogen-bonded to one of the other amino acid residues (Figure 8). This type of arrangement leads to the hydrogen atom on $N_{\epsilon 2}$ being very reactive, and it can be easily given up to another molecule in a chemical reaction. The importance of this finding is that it immediately reveals the mechanism for breaking the sugar ring. As shown in Figure 8, the oxygen atom in the sugar ring forms a bond with the hydrogen on $N_{\epsilon 2}$. However, the His54 is configured to act as an acid and to transfer the hydrogen atom on $N_{\epsilon 2}$ to the sugar ring oxygen atom, an event that breaks the sugar ring open. A number of other important observations have been made that will be crucial in clearing up details of subsequent reaction steps.

The next experiments on the PCS,

which are already underway, involve preparing crystals of D-xylose isomerase with the sugar bound in the active site in order to unravel the details of the second step, in which hydrogen atom transfer is involved in enzyme mechanism. What has been achieved so far is a breakthrough not only from a scientific point of view, but also from a technical point of view. At the time of this experiment, D-xylose isomerase was the largest enzyme ever to have been studied to high resolution using neutron crystallography, an achievement that made the cover of the Winter 2002 issue of the *American Crystallographic Association Newsletter* and also the “Search and Discovery” section of the journal *Physics Today*. As Bunick puts it, “In the case of light elements such as hydrogen, x-rays diffract very weakly. What we were able to do with neutron beams in comparison exceeded everyone’s expectations.”

DHFR and Antitumor Therapy

Yet another experimental team from the University of Tennessee, this

time led by Chris Dealwis, has been studying a similarly large enzyme, dihydrofolate reductase (DHFR). This enzyme binds a small molecule called dihydrofolate and then helps to convert it to tetrahydrofolate, commonly called folic acid, a B vitamin. Before DHFR can shuffle hydrogen atoms about on folic acid, it must bind a helper or cofactor molecule called NADPH. Many metabolic pathways in the cell, in particular those involved in generating the components of proteins and the genetic material DNA, amino acids, and nucleotides, require DHFR along with its cofactor as a specialist enzyme. Blocking the activity of DHFR interrupts the cell’s ability to produce DNA and ultimately leads to cell death. X-ray diffraction has shown that the enzyme has two domains with a large cleft where the domains join. NADPH and dihydrofolate have shapes that fit snugly into different pockets in the cleft.

Several drugs have been discovered that block the action of DHFR, and this effect has been of great use in antitumor therapy. On its first visit to Los Alamos last year, the experimental team collected neutron data from DHFR with the anticancer drug meth-

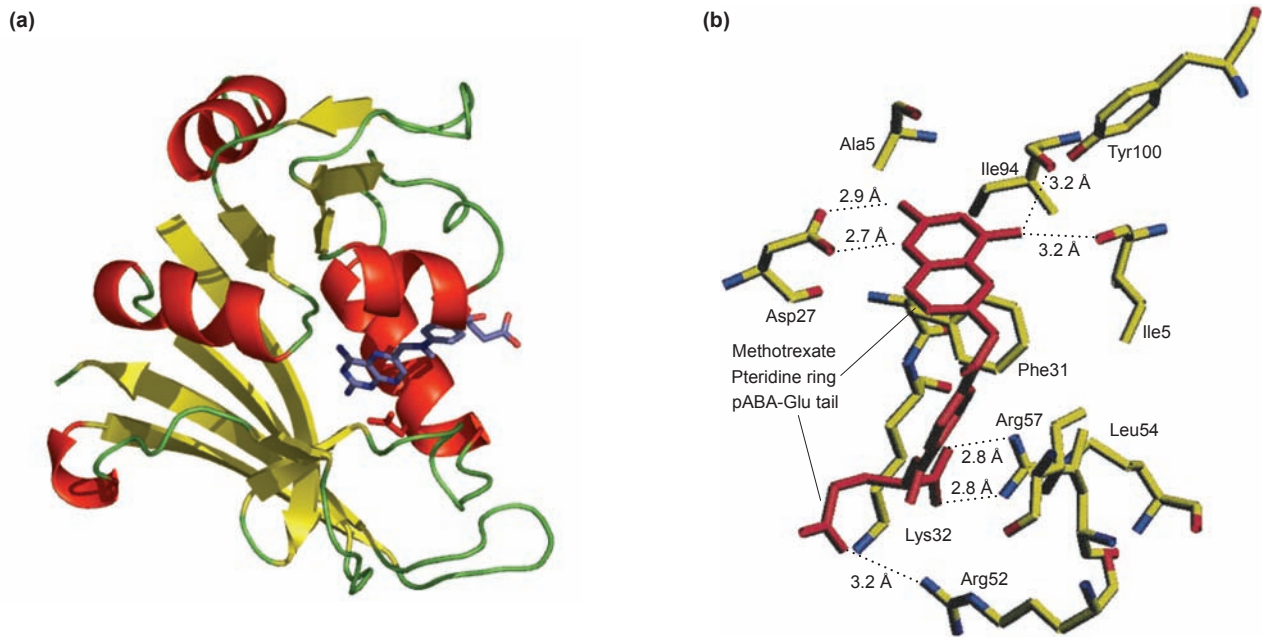


Figure 9. Dihydrofolate Reductase with Methotrexate Bound

(a) This diagram shows the structure of DHFR with the anticancer drug methotrexate bound to the active site. This structure was determined using neutron diffraction. (b) A detail of the binding of methotrexate to the active site is shown. Neutron data are revealing the hydrogen bonds that produce the tight binding of these two.

methotrexate bound (Figure 9). Information on where the hydrogen atoms are around methotrexate when it is bound to the enzyme will provide insight that may be key in guiding future anticancer drug design. Unfortunately, the initial diffraction patterns were too weak to allow hydrogen atoms to be visualized. At about 250 times smaller than an inch, the crystals, although large enough for synchrotron x-rays, were too small for neutrons. One of the team members, Brad Bennett, investigated two approaches to overcoming this problem: trying different ways to grow larger crystals and replacing all the hydrogen atoms in DHFR by deuterium atoms, a process called deuteration.

Deuteration makes crystals scatter neutrons up to 10 times more strongly and reduces background noise because deuterium scatters neutrons more efficiently than hydrogen. A biological deuteration laboratory is now in operation at LANSCE churning out deuterated proteins for the PCS user

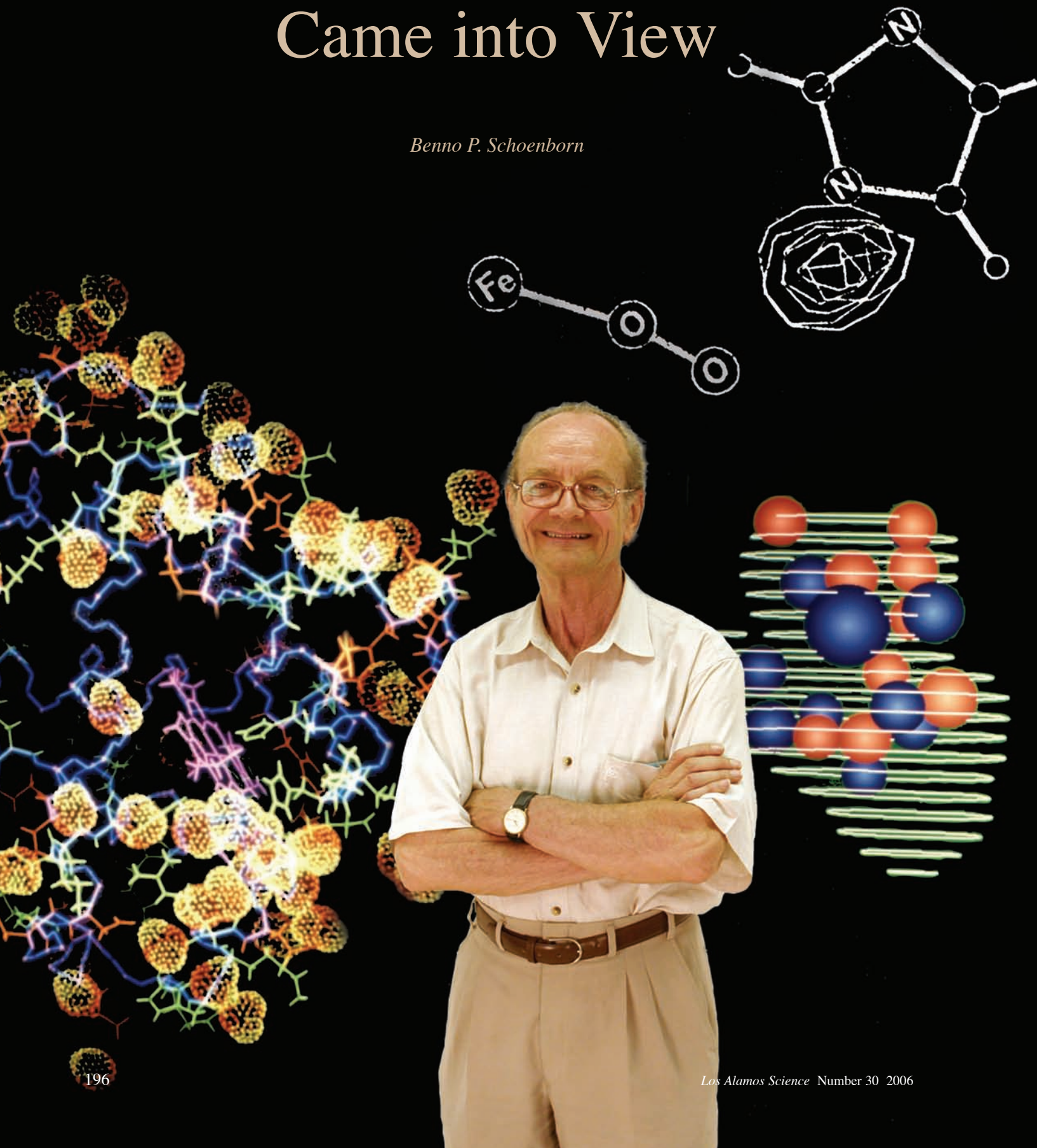
program. DHFR was the first protein to be produced at this facility in a pilot project carried out by Bennett in April 2004. Bennett's efforts in crystal growth and deuteration allowed strong neutron-diffraction patterns to be collected in March 2005, and these data are now providing crucial information about why methotrexate binds so strongly to the enzyme. In fact, by directly visualizing individual protons in the binding site the researchers have found one particular hydrogen atom that they think is key to the binding strength of the drug, an important result for future drug design, which is currently being published in the scientific literature.

The experiments on D-xylose isomerase and dihydrofolate reductase are just two examples from a number of enzymes that have been studied on the PCS so far. Although an increasing number of enzymes are now being studied by neutron protein crystallography, this emerging technique in itself will never be sufficient to deter-

mine an enzyme's mechanism or to get a drug to market. It is much more efficient to determine the skeleton of an enzyme structure using synchrotron x-ray or nuclear-magnetic-resonance techniques. However, only neutron protein crystallography can provide the complementary information about how hydrogen atoms are shuffled about this skeleton during enzyme reactions. Structure-based drug design is not one but a collection of technologies that include molecular biology, computational chemistry, bioinformatics, and structural genomics. Los Alamos has provided the nation with a new and unique capability, spallation neutron protein crystallography, that is developing into another, complementary technology in structure-based drug design. However, the role of the PCS goes beyond drug design to providing information on the biochemical steps that underpin our overall understanding of cellular processes and of how defective and pathogenic enzymes affect our health. ■

How Single Hydrogen Atoms Came into View

Benno P. Schoenborn



Forty Years Devoted to Neutron Techniques for Structural Biology

The father of neutron protein crystallography and contrast matching recounts his pioneering efforts to make neutrons a powerful tool in structural biology. The new Protein Crystallography Station at LANSCE—where scientists can finally pinpoint the specific hydrogen atoms that an enzyme moves to accomplish its catalytic work—marks the culmination of Benno's extraordinary achievements.

The first mention of using neutron scattering to investigate hydrogen bonding in proteins occurred in the spring of 1965, during a tea time discussion I had with Herman Watson, Uli Arndt, John Kendrew, and Chris Nobbs at the MRC Laboratory in Cambridge, England. I had just finished studying the binding of the inert gas xenon, an anesthetic, to the protein myoglobin and was trying to calculate the binding energies (Schoenborn et al. 1965). Thirty-two atoms were surrounding the xenon atom at van der Waals bonding distances, and structural assumptions suggested that most were likely to be hydrogen atoms. But that was only a guess. Clearly, a map depicting actual hydrogen atom locations was needed. We discussed a number of options for obtaining those locations, but only neutron diffraction was a possibility and a distant one at that because neutron sources have very low fluxes. Subsequent discussions with neutron-scattering experts at the Atomic Energy Research Establishment (Harwell, U.K.) were rather disappointing, and I shelved the idea at that time.

In 1967, during a seminar I gave on the binding of xenon to proteins at the Biochemistry Department at the University of California, Berkeley, I mentioned the neutron approach to mapping hydrogen atoms, and Prof. Daniel Koshland suggested I try to obtain some time on the neutron beam at the High-Flux Beam Reactor at the Brookhaven National Laboratory (BNL). On Koshland's recommendation and with help from Werner Hirs, I obtained a position at BNL and took another leave of absence from University of California, San Francisco, on what many considered a wild goose chase.

I was immediately faced with the problem that neutron sources have low fluxes and that, therefore, big crystals would be needed to obtain a measurable signal in a reasonable amount of time. Fortunately, millimeter-sized crystals are quite easy to grow for sperm whale myoglobin (this protein is the primary oxygen-carrying molecule of muscle tissue). In mid 1968, I obtained a few days of beam time at Walter Hamilton's single-crystal diffractometer, a monochromatic instrument with a single-

neutron detector and one of the first computer-controlled data acquisition systems. Before making the diffraction measurement, I soaked the crystal in deuterated buffer (D_2O) to reduce incoherent background scattering from hydrogen atoms. It was already known that soaking would cause D_2O to replace water (H_2O) molecules in the crystal and that some

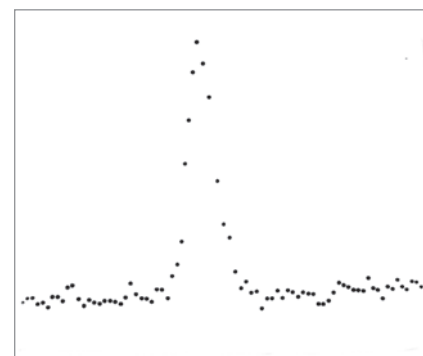


Figure 1. First Peak from Neutron Diffraction on a Protein Crystal To collect this first reflection (6-0-3) from a single crystal of myoglobin, we used a single-crystal diffractometer on the High-Flux Beam Reactor at BNL. The vertical axis is the scattered intensity, and the horizontal axis is the scanning angle.

hydrogen atoms within the protein structure might be replaced by deuterium atoms as well. After a few hours of playing with the automation, we found the first Bragg reflection (refer to Figure 1), which turned out to be the 6-0-3 plane. Even with the large 25-cubic-millimeter crystal, it took 1 minute to collect each data point in Figure 1, and 15 points were needed to scan the width of a single reflection peak. It became obvious that completing the entire map would take an enormous amount of time. Over the next year, I was able to collect 4800 reflections and demonstrate that protein crystallography with neutrons was indeed possible and that hydrogen atom locations with a 2-angstrom resolution could be determined easily (Schoenborn 1969).

Expanding the Use of Neutrons in Structural Biology

I soon realized that the different neutron-scattering lengths of deuterium ($b = +6.65$) and hydrogen ($b = -3.71$) could be used to enhance contrast in neutron diffraction and neutron-scattering studies of biological structures, especially if only gross features were to be determined. This idea is analogous to the use of heavy (high Z) atoms to enhance contrast in x-ray scattering. By using different percentages of D_2O and H_2O in the solvent, one can match the average scattering-length density of the solvent to one or another component of a structure. The component then looks like the solvent and fades into the background whereas the components of different scattering-length density stand out.

I did the first diffraction experiment using contrast (or density) matching in collaboration with Donald Casper. It was on frog sciatic nerves. After soaking the excised nerve in

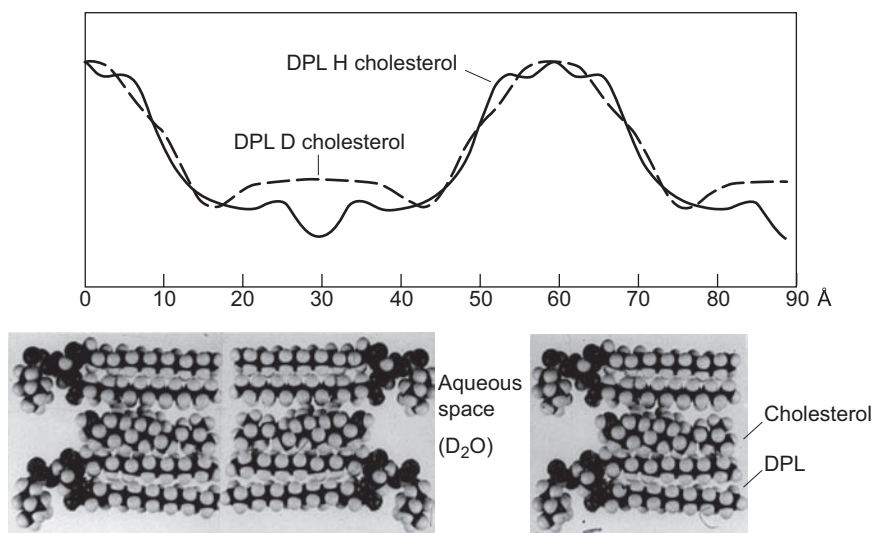


Figure 2. Neutron Scattering Data for a Reconstituted Membrane Results are shown of the measured neutron-scattering density as a function of distance through a reconstituted membrane of dipalmitoyl lecithin with and without cholesterol. (Reprinted from *Chem. Eng. News*, January 24, 1977, 55, pp 31–41. Published 1977 American Chemical Society).

D_2O and mounting it, we observed an extraordinarily large signal, of about 80 percent of the collimated incident beam. At first, we looked for a leak in the shielding and collimation since we were working very close to the direction of the incident beam. We found nothing wrong and eventually realized that we were observing a very intense 2-0-0 Bragg reflection. The reflection was caused by constructive interference from the membrane bilayer structure, which approximated a positive neutron-scattering layer (D_2O) next to a negative neutron-scattering layer composed of one carbon and two hydrogen atoms (nCH_2). The two layers were of about equal thickness. This work led to the development of and a patent for multilayer monochromators (Schoenborn et al. 1974), which select single-energy neutrons and x-rays and are therefore widely used now in x-ray and neutron-diffraction equipment. Similar principles are used today in studying surface layers with neutron reflectometry. (For example, see studies of the

hydrophobic effect on page 164 of this volume.)

The technique of combining diffraction experiments with H_2O/D_2O exchange through soaking was soon used by some scientists to elucidate membrane structures such as the one shown in Figure 2 (Zaccai et al. 1975) and large biological complexes, including the structure of filamentous bacteria. A novel use of hydrogen/deuterium exchange, which involved extracting and perdeuterating whole proteins and then reinserting them into ribosomes, was proposed by Donald Engelman and Peter Moore. Together, we were hoping to elucidate the structure of ribosomes, the complex biological machines that manufacture proteins from genetic instructions (Moore et al. 1974). Perdeuterating means producing the protein in vivo by using genes cloned in *E. coli* and deuterated water and nutrients at every step. Figure 3a illustrates our strategy for perdeuterated proteins in neutron scattering studies of the ribosome structure. Our strategy reached

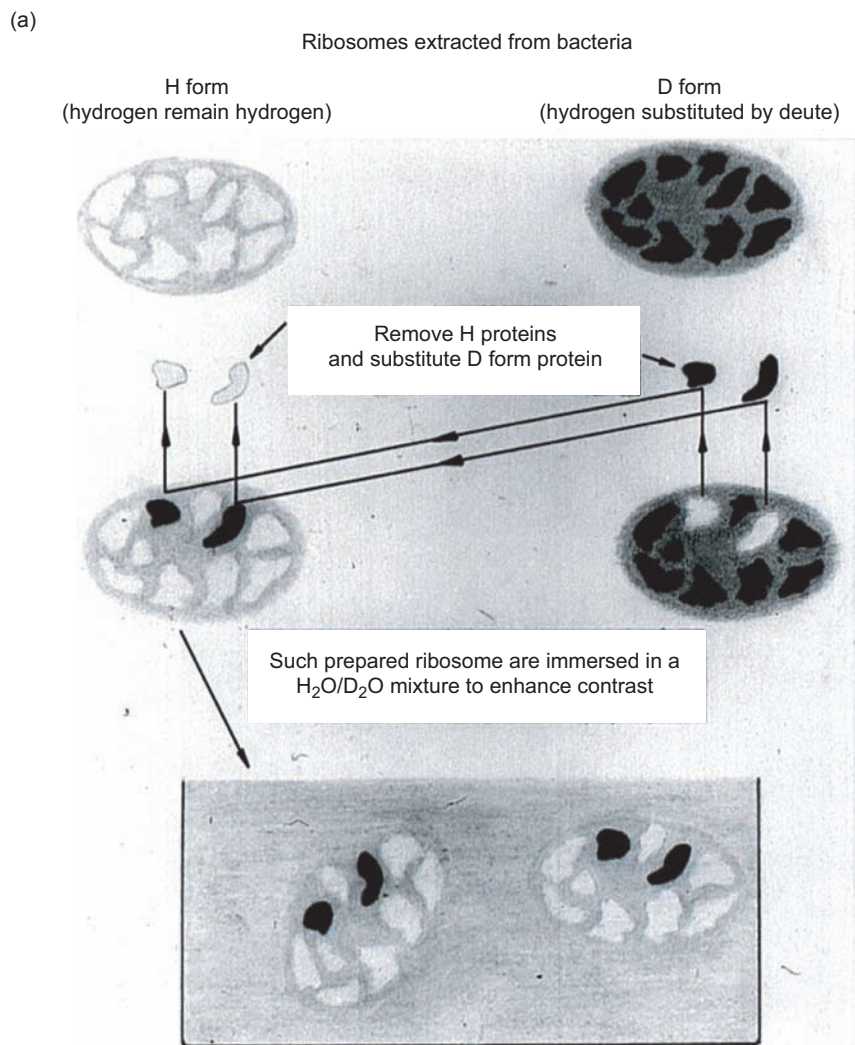


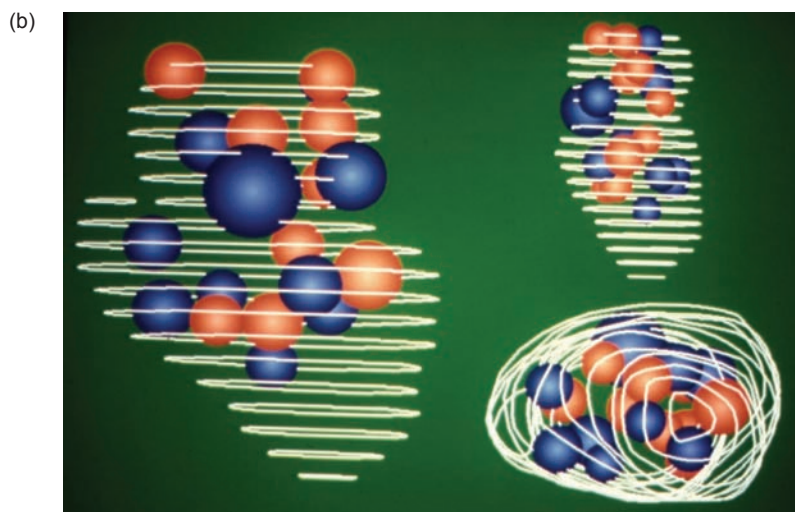
Figure 3. Strategy for Determining Protein Arrangement in the 30S Ribosomal Subunit

(a) Shown here schematically is the removal of pairs of proteins, their reinsertion in a perdeuterated form, and then the use of contrast matching and small-angle neutron scattering to make their sizes and relative positions visible in the 30S ribosomal subunit of *E. coli*. (b) Three orthogonal views are shown of the low-resolution structure of the 30S ribosomal subunit. (Courtesy of *Neue Zuercher Zeitung*, April 18, 1979, #89.)

fruition 13 years later, when we completed the structure of the ribosomal subunit shown in Figure 3b (Capel et al. 1987).

With the rapid growth of neutron science in structural biology during the 1970s and 1980s, the nuclear reactor sources at BNL and the Institut Laue-Langevin in Grenoble, France, emerged as two major centers of activity.

Seeing Hydrogen Atoms with High-Resolution Neutron Diffraction. Once two-dimensional (2-D), position-sensitive detectors had been developed, we were able to use high-resolution neutron diffraction at BNL to reveal hydrogen atom positions on both the protein and the solvent. We were also able to distinguish nitrogen from carbon or oxygen because of their different scattering lengths. Our neutron-diffraction data on the positions of nitrogen atoms in proteins were used to resolve ambiguities in x-ray diffraction studies, particularly the orientation of



the amino acid residues known as histidines (see Figure 4). To reduce background scattering during data collection and enhance the localization of exchangeable hydrogen atoms, we exchanged the H₂O solvent in most single crystals with D₂O, using a soaking procedure similar to that for the membrane studies. This soaking exchange procedure allowed us to observe the exchange rate of labile hydrogen atoms. Labile hydrogen atoms that do not exchange indicate some structural stability in a given region. Structural studies as a function of soaking times give insight into diffusion effects within proteins. Thus we realized almost immediately that H₂O/D₂O exchange could provide some information on protein dynamics and enhance protein-solvent contrast in diffraction and small-angle neutron-scattering experiments.

The solvent analysis in myoglobin resolved a major controversy between nuclear magnetic resonance (NMR) studies that showed only three water molecules bound to myoglobin and x-ray studies that showed over 80 bound water molecules. The neutron studies proved that, indeed, only three water molecules are bound to the protein with three hydrogen bonds, which makes them irrotationally bound, that is, they are unable to rotate. All other water molecules exhibit only two or fewer hydrogen bonds and thus can rotate, tumble, and jump about (see Figure 5). Studies with x-rays reveal only the central oxygen atom of water molecules and therefore cannot provide any indication of permanent binding. By contrast, NMR studies locate only irrotationally bound water molecules.

Need for Improved Instrumentation

Collecting neutron-diffraction data had a very slow start because the low flux at neutron reactors made it

time-consuming. Because increasing the flux was not a real possibility, it seemed that developing improved instrumentation would be the only way to increase data collection. The 2-D position-sensitive detectors previously discussed are an example of improved instrumentation. They allow studying macromolecules such as myoglobin routinely. It seemed that increased data-collection rates would be possible only by improved instrumentation, particularly by increasing detector coverage. But then another possibility opened up. In the 1990s Tom Kitchens and John Browne, then Physics Division Leader, invited me to Los Alamos, and I became aware of the power of spallation neutron sources to provide dramatic increases in usable neutron flux. Following that visit, I slowly developed plans for a protein station at a spallation source. With the help of Morton Bradbury of Los Alamos, these ideas were presented to the Department of Energy's Office of Health and Environmental Research and eventually led to the development of the Protein Crystallography Station (PCS) at LANSCE (Schoenborn 1996).

Designing a PCS for a Spallation Neutron Source

One way to increase neutron flux and thus increase data-collection rates is to apply the Laue diffraction technique, which uses white radiation instead of monochromatic radiation. Unfortunately, this technique increases the background significantly and degrades data quality. Therefore, it has limited use at reactor-based installations. The Laue technique can, however, be advantageously tailored to spallation neutron sources at accelerators, which produce extremely short bursts, or pulses, of spallation neutrons having a broad range of

energies. As the neutrons in a pulse travel down the beam line to the spectrometers, they develop a time-dependent wavelength spread with the shortest-wavelength (highest-velocity) neutrons arriving first and the longest-wavelength (lowest-velocity) neutrons arriving last. Data can be collected as a function of time, yielding sequential diffraction data sets at increasing wavelengths and each set mimicking a monochromatic diffraction experiment (Schoenborn 1992).

Maximizing Neutron Flux.

Maximizing flux and reducing background were the main criteria guiding the design of a protein crystallography station for LANSCE. Neutrons having relatively low energies (long wavelengths) suitable for diffraction experiments of all kinds are typically produced by sending the high-energy spallation neutrons through a moderator containing light elements such as water. The interactions with those light elements cause the neutrons to slow down. The typical moderators at LANSCE contain poison layers (elements that absorb neutrons) and decoupling layers to maintain a pulse containing a narrow band of neutron wavelengths for high-resolution diffraction experiments. Unfortunately, this narrow wavelength bandwidth is achieved at the expense of the neutron flux.

Our calculations showed, however, that high-wavelength resolution is not necessary for protein crystallography. Rather, a wavelength bandwidth of ± 0.12 angstrom is ideal for protein crystallography. This wavelength bandwidth is determined by the typical disorder (mosaic) in protein crystals of $\pm 0.1^\circ$. To achieve this broader bandwidth, we studied the placement of poison layers surrounding the moderator by performing Monte Carlo calculations with the Lahet code (Schoenborn 1992, 1996). The backscattering moderators at

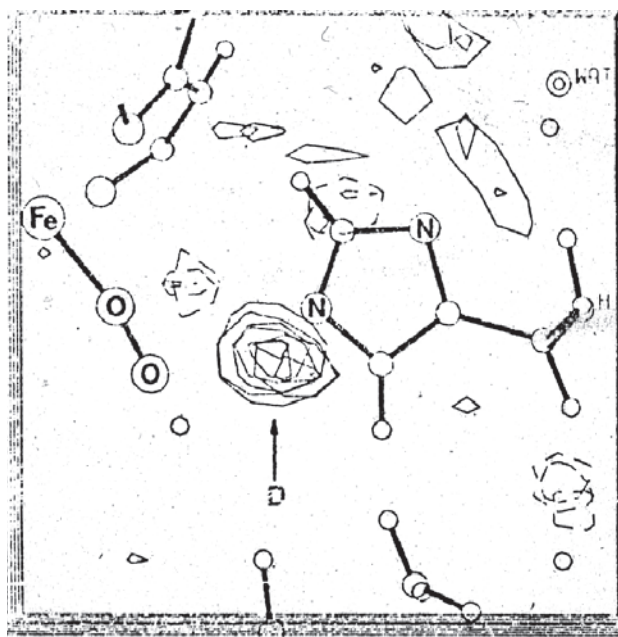


Figure 4. Single Hydrogen Atom Binding Oxygen to Myoglobin
A neutron-density map (fine lines) is superimposed on a ball-and-stick model of a histidine residue in oxygen-carrying myoglobin. The map shows a hydrogen atom bound to the nitrogen atom of the histidine residue and indicates a hydrogen bond between an oxygen atom and the histidine. These structural data were the first to reveal the biological role of a specific hydrogen bond.

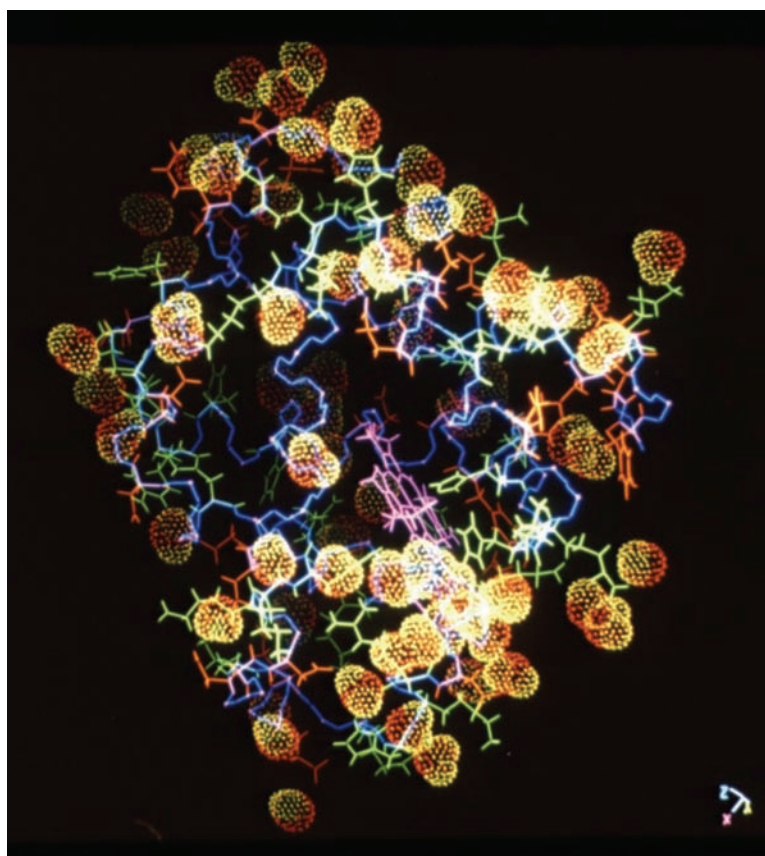


Figure 5. Water Molecules on Myoglobin
This neutron-density map showing 87 water and ion molecules (space-filling dotted clusters) are superimposed on the surface structure of myoglobin. The iron (heme) group is purple; the backbone is blue; the acidic residues of the amino acid are orange; and the basic residues of the amino acid are green

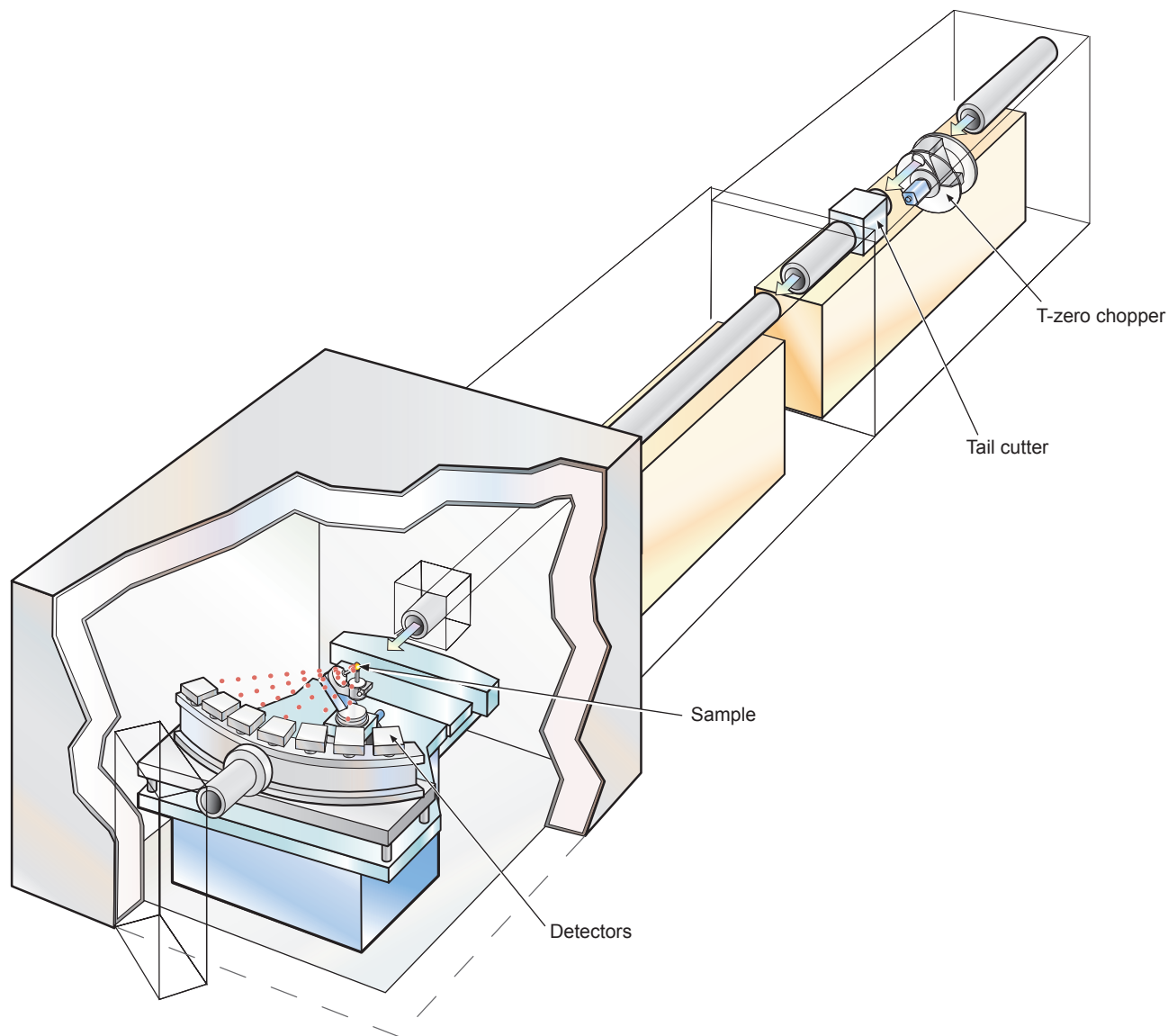


Figure 6. The Protein Crystallography Station at LANSCE

This drawing shows the layout of the PCS at LANSCE's Lujan Center. The large cylindrical position-sensitive detector was built by the Instrumentation Division at the BNL for the PCS at LANSCE. This collaboration marked the beginning of a productive relationship with the Instrumentation Division.

LANSCE were thus modified to produce pulses with a broader bandwidth and increased flux. With a pulse frequency of 20 hertz, a 28-meter flight path allows us to collect data between 0.6 and 7 angstroms with 96 time slices and a bandwidth of about ± 0.1 angstrom. With a required beam divergence of $\pm 0.1^\circ$, this 28-meter flight path allows the complete view of the moderator; that is, it collects all neutrons within the given angular

divergence. The beam line consists of a conical focusing tube with beam-defining apertures placed at calculated distances aimed at maximizing neutron flux at the given divergence. The beam tube itself is lined with boron poly inserts to minimize beam scattering and thus background. A large concrete shield surrounds the evacuated beam tube to reduce room background. To avoid any crystal and detector damage a beam chopper

eliminates the front end of the pulse with its fast neutrons and gamma radiation. Radiation with wavelengths longer than 7 angstroms is eliminated by a second disk on the chopper.

Minimizing Background.

Background radiation on the detector arises from a number of contributors: room background, air scattering from the direct beam, crystal scattering from incident radiation not in

the diffraction (Bragg) condition, and incoherent scattering from hydrogen atoms.

Room background radiation has been minimized by a well-shielded beam pipe and experimental hut. Both are lined with boron poly and steel. Air scattering from the direct beam can be reduced by minimizing the air gap between the neutron collimator, the crystal, and the detector. A helium or argon gasbag between the crystal and the detector is unfortunately not easy to achieve without structural elements interfering with diffracted beams. Protein crystals often contain more than 50 percent water, which produces large incoherent scattering from the hydrogen atoms. As discussed earlier, this incoherent scattering can be eliminated by soaking the crystal in heavy water to exchange most labile hydrogen atoms in the proteins and replace all hydrogen atoms in water with deuterium. The ultimate background-elimination scheme involves the exchange of all hydrogen atoms by perdeuterating the protein (Shu et al. 2000). Modern biochemical techniques have been perfected to allow perdeuteration of most proteins if the clone of the corresponding gene is available. We have now established a deuteration laboratory at LANSCE to produce fully deuterated proteins.

Operation of the PCS. This first neutron PCS based on the previously-described design using time-of-flight techniques has now been operating as a user facility for nearly three years and has produced superb data for a number of proteins, notably D-xylose isomerase and dihydrofolate reductase (see Figure 6 as well as the preceding article “Finding out How Enzymes Work” on page 186). ■

Acknowledgments

I wish to acknowledge the numerous students and colleagues that made the described work possible. I thank Paul Langan and Gayle Greene for major contributions in the development and fabrication of the Protein Crystallography Station at Los Alamos National Laboratory.

Further Reading

- Capel, M. S., D. M. Engelman, B. R. Freeborn, M. Kjeldgaard, J. A. Langer, V. Ramakrishnan, et al. 1987. A Complete Mapping of the Proteins in the Small Ribosomal Subunit of *Escherichia-Coli*. *Science* **238** (4832): 1403.
- Cheng, X., and B. P. Schoenborn. 1990. Hydration in Protein Crystals. A Neutron Diffraction Analysis of Carbonmonoxymyoglobin. *Acta Crystallogr.* **B46**: 195.
- Engelman, D. M., and P. B. Moore. 1972. A New Method for the Determination of Biological Quarternary Structure by Neutron Scattering. *Proc. Natl. Acad. Sci. U.S.A.* **69** (8): 1997.
- King, G. I., N.-M. Chao, and S. H. White. 1984. Neutron Diffraction Studies on Incorporation of Hexane into Oriented Lipid Bilayers. In *Neutrons in Biology*. Edited by B. P. Schoenborn. New York: Plenum Press.
- Moore, P. B., D. M. Engelman, and B. P. Schoenborn. 1974. Asymmetry in the 50S Ribosomal Subunit of *Escherichia-Coli*. *Proc. Natl. Acad. Sci. U.S.A.* **71** (1): 172.
- Phillips, S. E. V., and B. P. Schoenborn. 1981. Neutron Diffraction Reveals Oxygen-Histidine Hydrogen Bond in Oxymyoglobin. *Nature* **292**: 81.
- Schoenborn, B. P. 1969. Neutron Diffraction Analysis of Myoglobin. *Nature* **224** (5215): 143.
- . 1992. Multilayer Monochromators and Supermirrors for Neutron Protein Crystallography Using a Quasi-Laue Technique. *Proc. SPIE Int. Soc. Opt. Eng.* **1738**: 192.

- . 1996. A Protein Crystallography Station at the Los Alamos Neutron Scattering Center (LANSCE). Los Alamos National Laboratory document LA-UR-96-3508.
- Schoenborn, B. P., D. L. D. Caspar, and O. F. Kammerer. 1974. A Novel Neutron Monochromator. *J. Appl. Crystallogr.* **7**: 508.
- Schoenborn, B. P., H. C. Watson, and J. C. Kendrew. 1965. Binding of Xenon to Sperm Whale Myoglobin. *Nature* **207** (4992): 28.
- Shu, F., V. Ramakrishnan, and B. P. Schoenborn. 2000. Enhanced Visibility of Hydrogen Atoms by Neutron Crystallography on Fully Deuterated Myoglobin. *Proc. Natl. Acad. Sci. U.S.A.* **97** (8): 3872.
- White, S. H., and M. C. Wiener. 1996. Fluid Bilayer Structure Determination—Joint Refinement in ‘Composition Space’. In *Neutrons in Biology*. Edited by B. P. Schoenborn and R. B. Knott. New York: Plenum Press.
- White, S. H., G. I. King, and J. E. Cain. 1981. Location of Hexane in Lipid Bilayers Determined by Neutron Diffraction. *Nature* **290**: 161.
- Zaccai, G., J. K. Blasie, and B. P. Schoenborn. 1975. Neutron-Diffraction Studies on Location of Water in Lecithin Bilayer Model Membranes. *Proc. Natl. Acad. Sci. U.S.A.* **72** (1): 376.

Overview of Fundamental Physics at LANSCE

Martin D. Cooper and W. Scott Wilburn

Experiments to elucidate fundamental physics have had a long history and are expected to have an exciting future at the Los Alamos Neutron Science Center. This overview discusses a selection of past, current, and future experiments exploring the validity of the standard model of strong and electroweak interactions and possible physics beyond that model. It concludes with a look at how current experiments are stimulating plans for the future. The current experiments are then further described in the short articles that follow.

Experiments to elucidate the fundamental physics of elementary particles at the Los Alamos Neutron Science Center (LANSCE) began about 30 years ago, when the facility was called the Los Alamos Meson Physics Facility (LAMPF) and its operation had just recently begun. At that time, the Standard Model describing the known phenomenology of elementary particle physics (Figure 1) was still in the making. Groundbreaking high-precision experiments were performed at LANSCE to explore the symmetries and dynamics of the Standard Model, especially the electroweak part, which unifies the description of the weak and electromagnetic forces. LAMPF produced a very intense source of muons and neutrinos (from the decay of pi mesons, also called pions), ideal for testing the new electroweak theory and for exploring the limits of the observed family symmetry.

Today, the spotlight at LANSCE has shifted to neutrons and to studies aimed at discovering physics not explained by the Standard Model—such as the prevalence of matter over antimatter in our universe. Although relatively old by most standards, LANSCE remains a premier facility for conducting state-of-the-art experiments. Its proton beam

power has remained one of the highest in the world. The intense flux of neutrons released when those protons strike a heavy-metal target continue to make possible very high precision measurements, as well as searches for rare processes predicted by theories that go beyond the standard model. Los Alamos National Laboratory has also built up a unique cadre of first-rate scientists with the desire and know-how to design and perform these difficult experiments, including the suppression of myriad systematic effects that could wipe out the signals of interest.

Fundamental physics is the study of the four known forces in nature. In order of strength, they are the strong (nuclear) force that binds neutrons and protons (nucleons) into a nucleus and is responsible for nuclear reactions such as fission and fusion; the electromagnetic force that governs all of chemistry and everything from light waves to magnets; the weak force that induces radioactive decay; and the gravitational force that binds the universe together. When physicists try to write a mathematical description of the forces, they need to know their strengths, their behavior as a function of distance between affected objects, and the transformation properties under symmetry operations.

The Standard Model is a quantum mechanical description of the strong, weak, and electromagnetic forces. It divides the known elementary particles in nature into those that carry the force and those that are affected by the force (Figure 1). For example, the electromagnetic force between two charged particles is described as an exchange of photons between them; in other words, the photons carry the force. Similarly, the weak force is carried by the W and Z bosons, and the strong force is carried by the gluons. The particles affected by the forces are the quarks and the leptons. The quarks make up the hadrons—neutrons, protons, and other heavy particles—that interact primarily through the strong force and less strongly through the other three forces. In contrast, the leptons (light particles including the electron, its neutrino partner, and their heavier cousins) are unaffected by the strong force in the same way that neutral particles such as the neutron and the neutrino are immune from electric attraction or repulsion. The fact that the elementary particles interact differently greatly assists in separating the properties of the forces. Figure 1 shows a diagram of how the quarks and leptons are grouped in three families, or generations, with each family composed of two quarks and two

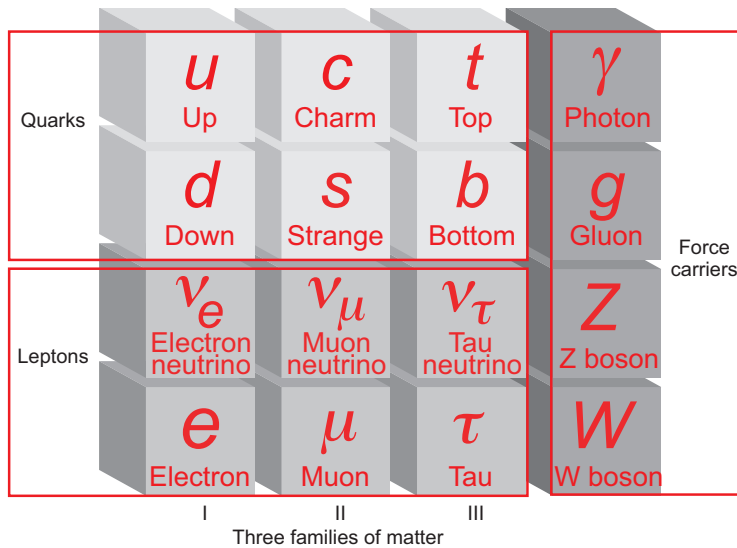


Figure 1. The Standard Model Illustrated

The fundamental particles are divided into those that are affected by the strong and electroweak forces, the quarks and leptons, and those that mediate, or carry, the forces. The quarks and leptons are arranged to illustrate their periodic character, or family structure. Families II and III have been shown to be reproductions of family I but with increasing mass. Within each family, the quarks and leptons are arranged from the heaviest on top to the lightest on the bottom to indicate the way the heavier particles decay through the electroweak force. A number of discoveries remain to be made that will reveal whether this picture is complete or whether extensions to the Standard Model are required.

leptons. The lightest family comprises the up and down quarks (that make up the neutron and the proton) and the electron and its partner, the electron neutrino. The other two families have identical properties (quantum numbers) except for being heavier particles and carrying a family identity. One of the great mysteries of the Standard Model is why there is a threefold reproduction of the basic family structure.

Examples of Past Experiments

The historical record at LANSCE contains many significant experiments. The four examples described below demonstrate the strengths of the facility today.

Testing the Family Symmetry.

The family symmetry arises from the

observation that the number of members of a given family remains constant (where particles of a family have family number +1 and antiparticles have family number -1). Thus, particles of one generation do not transform into particles of another generation unless another family member is created. For example, a muon from family II cannot decay into an electron without the emission of a muon neutrino to conserve the number of family II members or without the emission of an electron antineutrino to conserve the number of family I members. Thus, the decay $\mu^- \rightarrow e^- + \nu_\mu + \bar{\nu}_e$ occurs in nature. This apparent conservation law has no known physical basis, and the recent discovery of neutrino oscillations in which electron neutrinos can transform into muon and tau neutrinos and vice versa proves it is not exact. However, though the family symmetry is broken,

the violation is extremely small. The archetype process that appears to be forbidden is the decay of a muon into an electron and a gamma ray.

In 1978, it was known that $\mu \rightarrow e + \gamma$ does not occur at the level of two decays in 10^8 . Physicists have good reason to believe that the Standard Model is incomplete, and many models of its extension predict that $\mu \rightarrow e + \gamma$ should happen at measurable levels. A series of experiments were mounted at LANSCE between 1978 and 1995 to search for $\mu \rightarrow e + \gamma$ with ever-increasing sensitivity. All these experiments took advantage of the intense beams of muons extracted from the Stopped Muon Channel. They shared some common features based on the unique signature of $\mu \rightarrow e + \gamma$, the detection of a gamma ray and an electron with precisely half the energy of the muon mass, the electron and the gamma ray traveling back to back in opposite directions and being coincident in time. All the experiments used electron and gamma-ray detectors that provided good resolution of energy, time, and position of the decay products. Each successor experiment improved the resolutions to more sensitively isolate the $\mu \rightarrow e + \gamma$ process from a variety of backgrounds. The final experiment, known as MEGA, improved the sensitivity to one decay in 10^{11} , three orders of magnitude better than the 1978 value. These investigations by Los Alamos staff and many university collaborators severely constrain the types of extensions to the Standard Model that observation tolerates.

Measuring the Strength of the Weak Hadronic Force. Physicists have determined that the symmetry properties of the forces are the keys to understanding the forces. For example, the weak force violates mirror symmetry, or parity, the symmetry that postulates that a process and its mirror image should be equally likely. In fact, this “parity violation” by the weak force is observed to be as large

as possible. Because parity violation is unique to the weak force, measuring the degree of parity violation in a given process can be used to identify the influence of the weak force in the presence of the dominant strong force. The TRIPLE collaboration (a team from Los Alamos and many other institutions) used that approach to determine the strength of the weak force between hadrons (neutrons and protons) in heavy nuclei. That measurement is of great interest as a check against the best calculations to see if the complicated effects of the strong force can be accounted for properly.

The team measured the cross section for polarized epithermal neutrons (spins pointing in one direction and energies of approximately 1 electron volt) to undergo resonant absorption in heavy nuclei. Such neutrons are absorbed by populating many unstable states in compound nuclei. Varying the direction of neutron polarization resulted in the effects of the weak force becoming apparent. The depletion of the neutron beam by the target depended on the direction of the neutron spins relative to their direction of motion, a violation of mirror symmetry. Because so many nuclear states exhibited parity violation, the extracted strengths for the weak interaction could be treated statistically. Such an analysis allowed for the extraction of the parameters that characterize the average weak interaction in heavy nuclei. Good agreement was achieved with measurements in other systems. J. David Bowman of Los Alamos National Laboratory received the Bonner Prize in nuclear physics for this work.

Measuring Alpha, the Strength of the Electromagnetic Force. The strength of the electromagnetic force is measured by the fine structure constant, alpha. One of the most accurate ways of measuring that constant is in an atom made of leptons because the

strong interaction plays no role in such a system. An atom with this property is muonium, in which a positive muon binds an electron to make a neutral atom. Muonium has been extensively studied by a LANSCE collaboration led by Yale University and the University of Heidelberg. To extract alpha, the team measured the hyperfine splitting of muonium energy levels when placed in a magnetic field.

Muonium was produced by taking the lowest-energy positive muons from the Stopped Muon Channel and stopping them in krypton gas. A small fraction of the muons would capture electrons and form muonium. The stopping region was contained in a microwave cavity whose frequency was adjusted to populate the hyperfine states with a preselected direction of muon spin. The weak decay of the polarized muons produced an asymmetric angular distribution of electrons due to parity violation, which reflected the relative population of the hyperfine states. The energy separation of the states was determined by adjusting the frequency of the microwave cavity for a resonance condition. The precise measurement of the energy splitting allowed the extraction of alpha with a precision of 58 parts per billion, competitive but not quite as good as the value of alpha obtained by other methods. Such precise measurements have led to the most stringent tests of quantum electrodynamics.

Detecting Neutrino Oscillations. There have been a series of experiments to study neutrino properties at LANSCE. The most recently completed was the Large Scintillating Neutrino Detector (LSND). The LSND project invented a novel technique of mixed Cerenkov and scintillation light detection to separate the neutrino signal from backgrounds. LSND reported neutrino oscillations arising from a (squared) difference in mass between two neutrino species of approximately (1 electron volt)². This result has been

highly controversial because the current three-neutrino model allows for only two independent mass differences, which have been established in solar and atmospheric oscillation experiments and disagree with the LSND value. If proven correct by experiments elsewhere, LSND would have discovered the existence of a fourth neutrino with revolutionary properties. Such a particle would induce a dramatic change to the Standard Model, possibly destroying the categorization represented in Figure 1.

Current Experiments

LANSCE has evolved into a world-class neutron facility since 1995, and three high-profile neutron experiments are currently underway that build on past experience in fundamental physics.

An Ultracold-Neutron (UCN) Source and Measurements of Neutron Properties. UCNs are neutrons with such low energies that they can be held in a bottle—energies below 200 billionths of an electron volt or 200 nano-electron volts (neV). The bottle walls can be made from material, magnetic fields, or the gravitational force. All three confinement methods of UCNs are being exploited at LANSCE. Such low-energy neutrons are very hard to produce in great numbers. A new technique, known as the super-thermal method, is being pioneered at LANSCE. The method scatters cold neutrons from very cold (5 kelvins) solid deuterium. The cold neutrons lose energy and become UCNs exciting phonons (vibrational waves) in the solid deuterium. A prototype of the facility produced a world record in UCN density.

The UCN facility is currently being commissioned to measure the decay properties of polarized neutrons. These ultralow-energy neutrons allow us to search with increased sensitivity for significant deviations from Standard

Model predictions that could indicate the existence of new particles and modify our understanding of the weak force. This experiment is due to take data next year. The facility will also be used to make a more precise measurement of the neutron lifetime. The neutron lifetime is an essential component of determining the weak interaction between quarks. Its value also has implications for the cosmological origin of the light elements.

Neutron Electric Dipole Moment.

Determining the value of the neutron electric dipole moment (EDM) has long been considered a seminal experiment. The existence of this quantity at values greater than predicted by the Standard Model requires further violations of time reversal symmetry, which would have important consequences for modern theories of particle physics such as supersymmetry and for the origin of the matter–antimatter asymmetry of the universe. Los Alamos is leading the development of a new technique to improve experimental sensitivity to the EDM by two orders of magnitude. An extensive research and development program has been underway to demonstrate the feasibility of this goal. Several parts of the demonstration have taken place at various neutron sources at LANSCE.

Strength of the Weak Hadronic Force between Two Nucleons. The strength of the hadronic weak interaction remains a puzzle because of conflicts among the methods for determining it. A direct and definitive method for measuring the strength of the weak hadronic force in the neutron–proton system is underway at LANSCE’s Lujan Center. The method takes cold neutrons from the cold source, polarizes them, and has them captured in a hydrogen target. By looking at the asymmetry in gamma-ray production associated with deuteron formation, the quantity of interest is extracted with little theo-

retical uncertainty.

These three efforts have the current staff in fundamental physics fully engaged for the near term. As described below, the next generation of scientists has an exciting future awaiting them at LANSCE.

Future Directions

LANSCE has a long tradition of evolving its capabilities to take advantage of changes in facility operations. Four areas of fundamental nuclear physics—nuclear astrophysics, cold neutron physics, ultracold neutron physics, and neutrino physics—are currently being evaluated. They are well matched to upgrades under consideration for LANSCE. Facility improvements being sought for materials science research and advanced proton radiography for nuclear weapons research would naturally lead to enhanced capabilities in nuclear astrophysics and fundamental physics with cold neutrons.

As the current UCN source achieves its full potential, producing UCN densities of approximately 100 per cubic centimeter (cc), it will be used to perform the UCNA experiment, which will measure the electron asymmetry in polarized-neutron beta decay. Further upgrades will then be explored. Increases in the flux of protons delivered to the facility, improvements in UCN production efficiency, and use of novel production targets may ultimately provide UCN densities of approximately 1000 per cc for multiple simultaneous experiments. Such an apparatus would be a true UCN user facility and would open new opportunities for testing the Standard Model of electroweak physics using neutrons.

We know that neutrinos have mass from the observations that they are created and destroyed as states of definite “flavor” (electron, muon, or tau type) but propagate as states with definite mass. Because the flavor and mass

states are not perfectly aligned, neutrinos can change flavor as they propagate through vacuum or matter, a process that would not be possible if neutrinos were massless. These flavor oscillations were possibly glimpsed in the LSND experiment at LANSCE and have since been definitively seen in solar and atmospheric neutrino experiments. Mapping out the full set of fundamental neutrino parameters will require new experiments with more intense fluxes of neutrinos than have previously been available. These parameters are the mass differences between neutrino types, angles that describe the degree of mixing between flavors, and a possible charge-parity symmetry (equivalent to time reversal symmetry) violating phase that may be related to the differing amounts of matter and antimatter in the early universe.

Very intense, pulsed beams of neutrinos can be produced with existing technology by directing proton beams with megawatt power onto material targets to produce an intense source of pions and then focusing those pions with electromagnetic horns. Construction of the requisite “proton driver” in the United States has been recommended in a recent American Physical Society report. Several national laboratories in the United States, Europe, and Japan are pursuing such a facility; however, a decision to build a U.S. facility has not yet been made. If LANSCE were to upgrade the power of its existing proton beam, an improvement that is also sought for other areas of research, a proton driver would be a natural extension. A study will be conducted in the near future to evaluate the scientific case for building this facility at LANSCE. ■

Electric Dipole Moment of the Neutron

Martin D. Cooper

The search for physics beyond that encompassed by the Standard Model has been a major research theme since the Standard Model was formulated. Even though physicists are convinced that the model is incomplete, it is the Standard Model's remarkable success that no new physics has been found besides neutrino oscillations. At high energies, experiments are designed to look for new particles. At low energies, precise experiments are designed to look for processes that are not allowed in the Standard Model. The searches are equally important and often indirectly probe energies not reachable by direct particle-production experiments. An important example is the search for the electric dipole moment (EDM) of the neutron. Since the theoretical predictions for the size of the neutron EDM are so small, the gap between the Standard Model predictions ($10^{-31} e \cdot \text{cm}$, where $e = -1.6 \times 10^{-19}$ coulomb) and current experimental sensitivity ($6 \times 10^{-26} e \cdot \text{cm}$) is the territory for new discoveries. New theories that can account for the matter–antimatter asymmetry, such as supersymmetry, predict values for the neutron EDM in this range.

The neutron is a particle with spin, a quantum mechanical concept analogous to the neutron being a top rotating around an axis through its center. The neutron EDM may be pictured as a separation of positive and negative charges along the spin axis—see Figure 1a. Those charges must add to zero because the neutron has no net charge. The EDM is measured in units of separation distance for a unit of charge. Experiments already limit that separation distance in the neutron to an incredibly small size. For

example, if the neutron were the size of the earth, the maximum separation allowed would be less than 10^{-5} meter (approximately one-tenth the diameter of a human hair). New experimental techniques, however, allow that limit to be improved by another factor of 100. Such sensitivities allow testing some important theoretical extensions of the Standard Model.

The three most popular ideas that will be tested are the possible violation of time reversal symmetry by the strong force, the existence of supersymmetry, and the origins of the matter–antimatter asymmetry in the universe. Time reversal is the symmetry in nature predicting that physics should remain the same whether time runs forward or backward. For certain mesons called kaons, which are made of a strange quark and a down anti-quark, this symmetry is broken by the weak force. There is no known reason, however, forbidding the strong force from violating time reversal symmetry as well. Yet, previous EDM experiments have shown that time reversal symmetry is nearly perfect for neutrons. Theoreticians have some ideas why the effect might be small, but it is important to further test those ideas. Supersymmetry, a popular theory that invents a whole new set of particles needed to solve inconsistencies in the Standard Model, predicts a nonzero neutron EDM within the range of the next generation of experiments. The observed matter–antimatter asymmetry of the universe could be explained by a time reversal asymmetry, but the asymmetry observed with kaons is believed to be insufficiently large. A new phenomenon appears to be needed. A new EDM search could discover the needed source of time rever-

sal that could explain this big mystery of our universe.

Because the neutron has spin (and therefore a magnetic moment that points in the same direction as the spin), the neutron feels a torque in a uniform magnetic field, \mathbf{B} (Figure 1). If the spin direction is perpendicular to the magnetic field, the neutron will precess about the magnetic field direction. In the same way, if the neutron has an EDM, it will precess about an electric field, \mathbf{E} . The difference is that the spatial transformation properties of magnetic and electric fields are different so that the existence of an EDM violates time reversal symmetry. An EDM experiment consists of measuring the precession rate of an ensemble of neutrons in a weak magnetic field and searching for a very small change in the precession rate when a strong electric field is applied parallel to the magnetic field.

The figure of merit for neutron EDM experiments is $E(N\tau)^{1/2}$, where N is the number of neutrons in the ensemble, and τ is the time they are under the influence of the fields. Based on this formula, the ideal experiment maximizes the strength of the electric field, the number of neutrons in the measurement region, and the time the neutrons remain in the bottle. The new techniques for improving the EDM measurement sensitivity involve producing ultracold neutrons (UCNs) in a bottle that can store them for a time approaching the natural decay time of the free neutron (~ 900 seconds) and placing the bottle inside a region where the static electric and magnetic fields are uniform and parallel, as described above. UCNs can be bottled if the container has walls built of a material that repels the neutrons.

UCNs are copiously produced in the bottle by cold neutrons if the bottle is filled with low-temperature ultrapure liquid helium-4 (which has spin 0).

The change in precession rate due to the electric field is so small that fluctuations in the magnetic field could mimic an EDM signal. In order to eliminate this systematic effect, another species with a similar response to a magnetic field (that is, a similar magnetic moment) but without an EDM is placed inside the measurement volume. Helium-3, a light isotope of helium, has the same spin as the neutron. Moreover, it can exist inside the liquid helium and occupy the same space as the neutrons. The helium-3 atoms provide a control measurement to reduce many systematic effects.

The quantity of helium-3 must be controlled carefully because helium-3 atoms absorb neutrons. The amount needs to be quite small to keep the neutron storage time long, about one helium-3 atom for every 10^{10} helium-4 atoms. However, the helium-3 absorption is highly spin-dependent and provides for the method of measurement. If both the neutrons and the helium-3 atoms are polarized (that is, the spins of each species are separately aligned), the neutrons are absorbed only when the spins of the neutron and helium-3 are pointing opposite to each other. As the magnetic moments of the two species differ by 10 percent, they oscillate between being aligned and antialigned. Thus, the neutron absorption rate is proportional to the beat frequency of the two rates of precession. When the neutrons are absorbed into a helium-3 nucleus, the positively charged reaction products (a tritium nucleus and a proton) scintillate in the liquid helium, emitting light in the hard ultraviolet. That light can be observed with a photosensitive detector if it is wavelength-shifted into the visible spectrum by scattering from an

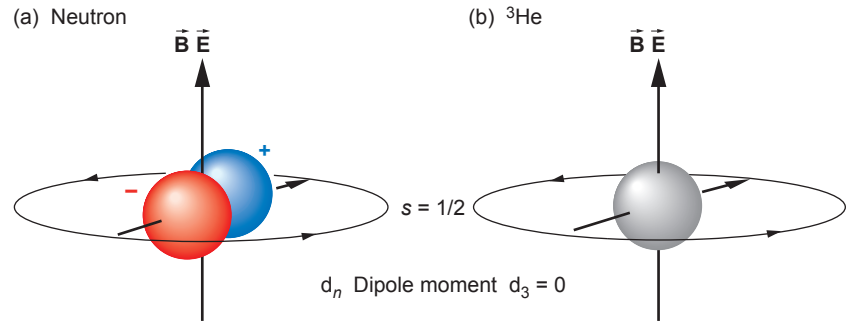


Figure 1. Possible Electric Dipole Moment of the Neutron

The neutron has a net charge of zero. A dipole moment would appear as a separation between a positive and negative charge along the spin axis of the neutron, as illustrated in (a). Helium-3, shown in (b), is known to have no EDM. The spin axes of both neutrons and helium-3 nuclei precess in the applied magnetic field B but at different rates. Applying an electric field E changes the precession rate of the neutrons in proportion to their EDM but not that of the helium-3 nuclei.

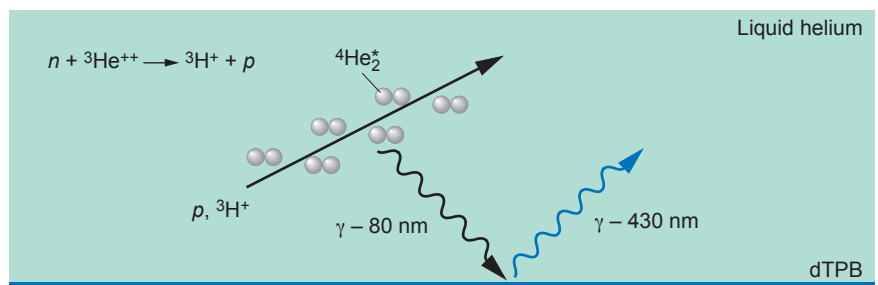


Figure 2. Detection of Neutron Absorption by Helium-3

The capture of a neutron by a helium-3 nucleus creates a proton and a hydrogen-3 nucleus (tritium). The energy from these particles excites helium molecules to higher energies, which then de-excite by emitting very short wavelength ultraviolet photons. Interaction with a deuterated-TPB organic fluor lining converts those ultraviolet photons into visible photons, which can be more readily detected.

organic fluor lining on the surface of the measurement cell. That detection process is illustrated in Figure 2. The other piece of the experimental signal is a direct measurement of the precession rate of helium-3, which is accomplished by detecting the magnetization of the helium-3 with a superconducting quantum-interference device. In summary, the experiment consists of measuring the characteristic frequencies of two oscillating signals: one from the scintillation light produced

by neutron absorption and one from the precession of the helium-3 nuclei. The signal for a nonzero EDM is a slight shift in the absorption frequency when the strong electric field is applied (Figure 3).

The apparatus to produce the conditions described is quite complicated and is shown as an engineering schematic in Figure 4. The essential parts are labeled. The final experiment requires the most intense source of neutrons available, and this experi-

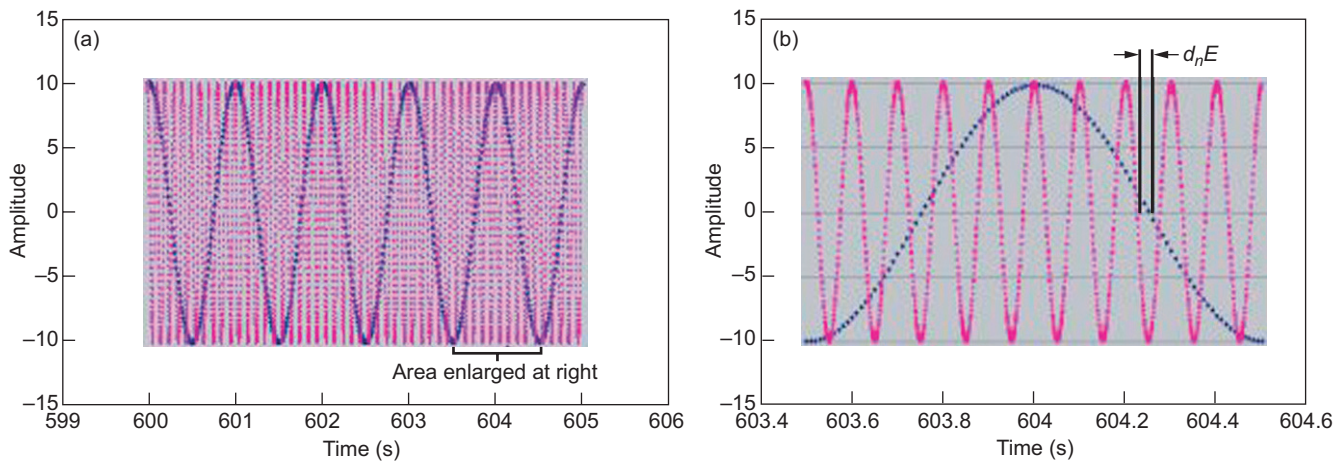


Figure 3. Signals Measured in the EDM Experiment

(a) The expected oscillation signals correspond to the helium-3 spin precession rate (fast) and the neutron absorption signal (slow). (b) The two signals are shown on an expanded scale, and the small shift in frequency that would be produced by a neutron EDM in the presence of an applied strong electric field is indicated schematically.

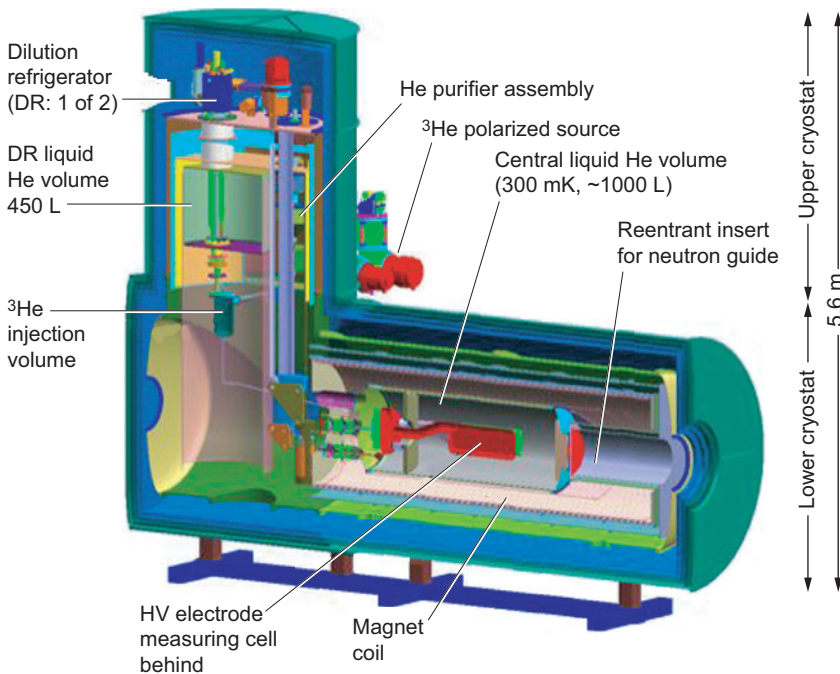


Figure 4. Current Design Concept for the Neutron EDM Experiment
This cutaway view shows the major components of the experiment.

ment will eventually be operated at the new Spallation Neutron Source under construction at Oak Ridge National Laboratory in Tennessee. However, there is a great deal of innovation involved in the method described, and the experimental team has engaged in an extensive research and development program to verify

that all the ideas will work. Much of the developmental work is being performed at the Los Alamos Neutron Science Center (LANSCE).

The figure of merit for EDM experiments required a long storage time. A measurement of the storage time for UCNs in a cryogenic bottle coated with wavelength shifter is

one of many experimental tests that are required to establish the feasibility of the experiment. This storage time measurement is well suited to LANSCE because the facility has an intense new source of UCNs that is being assembled for another experiment (see the article “Neutron β -Decay and Precision Tests of the Standard Model” on page 214). The idea is to take UCNs from the source, place them in the appropriate bottle, and see how many come out after some interval of time. By making a series of measurements for different times between loading and counting the neutrons, one measures the storage time. After extracting the effects of natural decay and other losses of neutrons, the partial lifetime induced by the bottle walls can be measured.

The project plan calls for all the auxiliary measurements to be completed by the end of 2006. At that time, construction can begin within a year. The Department of Energy has recently given the first stage of approval to the experiment. The experiment should be ready to acquire data at the Spallation Neutron Source in 2012. The real excitement will begin if those data indicate a nonzero value for the EDM of the neutron. ■

The NPDGamma Experiment

W. Scott Wilburn

Nuclear interactions between nucleons (protons and neutrons) involve both the strong and weak forces. Because the strong nuclear force is 10 million times stronger than the weak nuclear force, the weak force between nucleons is difficult to study and is not well understood. A tool for separating the two is the parity symmetry because the strong force preserves this symmetry and the weak force breaks it. The NPDGamma Experiment (Figure 1) is designed to study the weak force acting between neutrons and protons by observing violation of the parity symmetry in the capture of neutrons by protons, which results in the production of a deuteron (hydrogen-2 nucleus) and a gamma ray: $n + p \rightarrow d + \gamma$. Parity symmetry requires that the probability of the gamma ray being emitted in the direction of the neutron spin axis is equal to the probability of its being emitted in the opposite direction (Figure 2). Although the weak interaction between nucleons is fundamentally due to the exchange of W and Z bosons between quarks, nucleons are such complicated objects that computing the weak-interaction dynamics between them is impossible in the foreseeable future. One of the main problems with carrying out such a computation is that the quarks interact through the strong force. Consequently, the weak interaction must be calculated in the framework of an effective model of the strong interaction. Measurement of parity violation in the two-nucleon system provides an important test of theoretical calculations of the weak interaction in the nonperturbative quantum chromodynamic (QCD) regime.



Figure 1. The NPDGamma Experiment at LANSCE

The neutron beam enters from the left via a neutron guide enclosed by the stainless steel pipe, and the neutrons are polarized in the helium-3 polarizer (blue). Also shown is the array of 48 CsI detector crystals (right side). The reddish brown coils surrounding the apparatus generate a magnetic field to preserve the neutron polarization.

In one model of the weak force between nucleons, the force is carried by mesons traveling between the two. The NPDGamma experiment measures the contribution of the longest-range meson, the pion. This contribution has never been directly measured; it has only been inferred from effects in more-complicated systems, which have produced contradictory interpretations. Values of the weak pion-nucleon coupling have been extracted from two types of experiments. Interpretation of parity violation measurements of fluorine-18 gives an upper limit on this coupling that is significantly smaller than the value predicted by theory. Contradicting this result is a

measurement of the anapole moment of cesium-133, which has been interpreted to give a value for the weak pion-nucleon coupling that is several times larger than the theoretical prediction. In contrast to both of these experiments, NPDGamma measures this effect in the two-nucleon system, so it is free from the uncertainties inherent in a nuclear many-body calculation.

In the NPDGamma experiment, when a neutron is captured to form a deuteron (the nucleus of a deuterium atom also called heavy hydrogen), a 2.2-million-electron-volt (MeV) gamma ray is emitted in the process to conserve energy. As mentioned above, parity symmetry requires

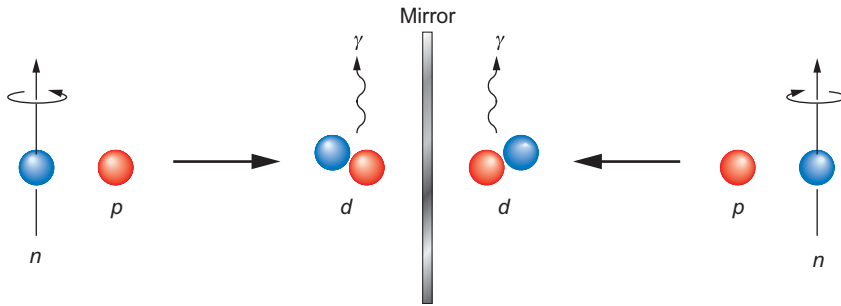


Figure 2. Parity Violation in the NPDGamma Experiment

Parity violation in the experiment is illustrated by comparing the reaction to its mirror image. In the reaction (left), a spin-polarized neutron combines with a proton to form a deuteron and a gamma ray. The gamma is shown being emitted in a preferential direction compared to the neutron spin axis. When the process is viewed in a mirror (right), the neutron appears to be spinning in the opposite direction, but the gamma ray is emitted in the same direction. The neutron spin direction can be restored by flipping the mirror image from top to bottom, but then the preferential direction for gamma-ray emission is reversed. This example shows that, if there is a preferential direction for gamma-ray emission relative to the neutron spin axis, then parity (mirror image) symmetry is violated.

that the probability of the gamma ray being emitted in the direction of the neutron spin axis is equal to the probability of its being emitted in the opposite direction (Figure 2). If there is any difference (asymmetry) in the two probabilities, it is due to the weak force, and the size of the difference is proportional to the relative contribution of the weak force compared to with the strong force to this process. This effect is expected to be small, approximately 50 parts per billion (ppb). The ultimate goal of NPDGamma is to measure parity violation in neutron-proton capture with a precision of 10 ppb.

The NPDGamma experiment, shown conceptually in Figure 3, starts with a beam of cold neutrons produced at LANSCE. The neutrons are guided by reflection from highly polished, specially prepared surfaces to the experimental cave, where they are spin-polarized in preparation for the measurement. The neutrons pass through a 30-liter liquid hydrogen target, where approximately 60 percent of the neutrons are captured by the

protons inside the hydrogen atoms. The 2.2-MeV gamma rays from those reactions are detected in cesium iodide (CsI) crystals surrounding the target.

The neutrons have to be spin-polarized, that is, they must have all their spins pointing in the same direction, so that we can tell the relative probability of the gammas being emitted parallel and antiparallel to the spin direction. The method of neutron polarization used by the NPDGamma experiment relies upon the spin dependence of the interaction of neutrons with helium-3 nuclei. Both neutrons and helium-3 nuclei have spin $\frac{1}{2}$. When the spins of a neutron and a helium-3 nucleus are oriented in opposite directions, the probability of the helium-3 capturing the neutron is very high. When the spins are oriented in the same direction, the probability is thousands of times lower. If the unpolarized neutrons pass through enough polarized helium-3, the neutron beam becomes polarized in the same direction. The helium-3 nuclei are polarized by shin-

ing circularly polarized laser light on a glass cell containing helium-3 atoms and a small amount of rubidium. The rubidium atoms with spin in one direction preferentially absorb the laser light, which leads first to polarized rubidium atoms. Collisions between the rubidium and helium-3 atoms transfer the polarization to the helium-3 nuclei. This polarization technique was perfected by the NPDGamma team.

The 48 gamma-ray detectors surrounding the liquid-hydrogen target are cubes of crystalline CsI measuring 15 centimeters on a side (Figure 4). When gammas strike the crystals, flashes of blue light are produced by a process called scintillation. This light is viewed by vacuum photodiodes, which convert the light to an electrical current. This current is converted to a voltage and amplified in specially designed low-noise electronics. The detector electronics are so quiet that “noise” in the electrical signals is actually due to the statistical fluctuations in the number of gammas arriving at a given time. Finally, the signals from many events are digitized and stored in computers. The low-noise electronics have also been developed by the NPDGamma team.

Because the detector sensitivities can never be matched accurately enough to detect a 50-ppb difference in the rates between different detectors, a technique called neutron spin reversal is employed. The neutrons are produced by the LANSCE accelerator in pulses spaced 50 milliseconds apart. Each pulse of neutrons starts with spins polarized in the vertical direction (up) by passing through the helium-3 cell. An asymmetry of approximately 2 percent is seen between the top and bottom CsI detectors because of differences in detector sensitivity. On the next pulse, a neutron spin flipper can be energized to rotate the spins by 180° (down). While the 2 percent asymmetry caused by

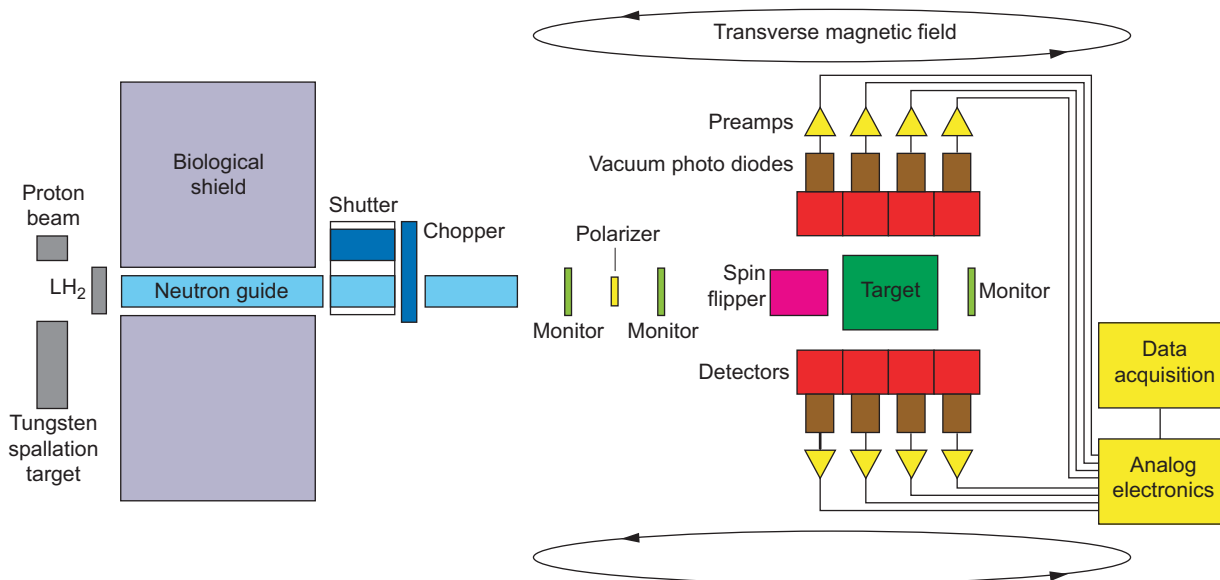


Figure 3. Conceptual Drawing of the NPDGamma Experiment

This drawing shows the major components of the NPDGamma Experiment. Neutrons are produced by the LANSCE proton beam striking a tungsten spallation source and are slowed to low energies by a cold hydrogen moderator. They are guided to the experiment and polarized by passage through a helium-3 polarizer. A spin flipper can periodically reverse the polarization of the neutrons before they are captured by the liquid hydrogen target. CsI crystals surround the target to detect the gamma rays produced in the NPDGamma reaction.

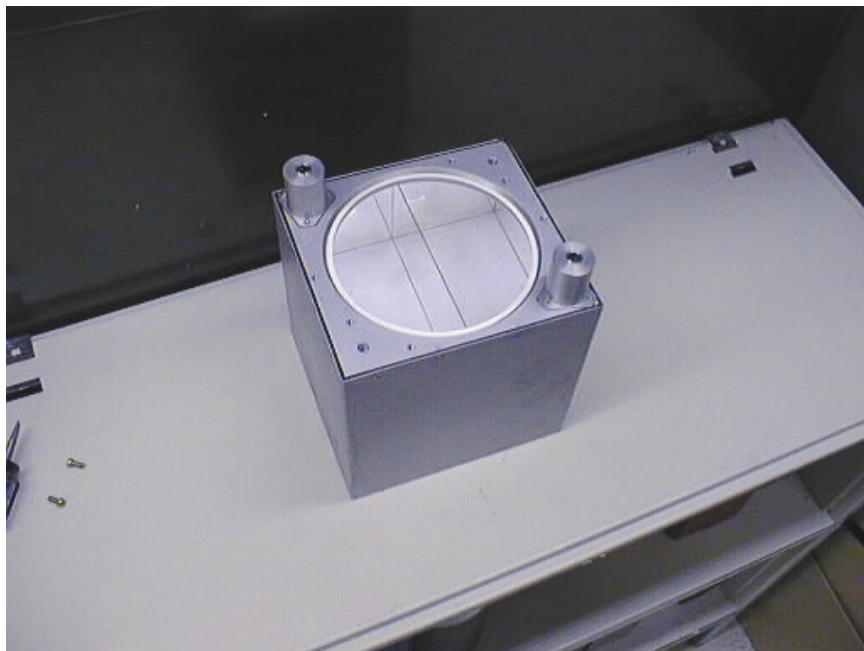


Figure 4. CsI Crystal for Detecting Gamma Rays

The photo shows one of 48 CsI crystals used to detect gamma rays in the NPDGamma experiment. Each crystal is approximately 15 cm on a side.

detector sensitivities remains the same, the 50-ppb asymmetry expected from parity violation reverses sign. Subtracting the asymmetries from the two pulses cancels the first (instrumental) effect and enhances the second (physics) effect.

In an attempt to measure such a small physics effect, many instrumental effects must be considered and minimized. These include parity violation from neutron capture on materials other than hydrogen, changes in beam properties or detector sensitivities with spin reversal, and electronic noise due to the operation of the spin flipper. All those effects have been considered in the design of the NPDGamma experiment and careful controls have been demonstrated to reduce these effects to less than 10 ppb. ■

Neutron β -Decay and Precision Tests of the Standard Model

Takeyasu Ito and J. David Bowman

The neutron, the simplest nucleus that undergoes β -decay, is an ideal system with which to study the weak interactions of the Standard Model. In neutron β -decay, the neutron, made up of three quarks (udd), decays to a proton (uud), an electron (also called a beta particle), and an electron antineutrino: $n \rightarrow p + e^- + \bar{\nu}$ an antineutrino. At the quark level, one of the d quarks in the neutron decays to a u quark inside the neutron, emitting a W particle, which further decays into an electron antineutrino and an electron. The transformation of the d quark into a u quark inside the neutron creates a particle made up of uud , which is a proton.

In the Standard Model, the neutron β -decay process can be described using very few parameters. By performing precision measurements on various aspects of this decay, one can determine values for those fundamental parameters that best describe the experimental results. They can then be compared with or combined with the parameter values that best describe other processes governed by the same weak force. In this way, one can perform precision tests of the validity and consistency of the Standard Model.

One test of consistency is to check that the experimental values for the elements of the CKM (Cabibbo-Kobayashi-Maskawa) matrix maintain the unitarity of the matrix. The CKM matrix is a set of nine numbers that describes the mixing between the mass and the weak eigenstates

of the quarks. These numbers can be determined by measuring the rate at which hadrons (particles made of quarks and/or antiquarks) undergo weak decay (for example, the rate of neutron β -decay) and comparing that to the decay rate of the muon. Testing to see if the CKM matrix is unitary, in particular, whether it satisfies the condition

$$|V_{ud}|^2 + |V_{us}|^2 + |V_{ub}|^2 = 1 \quad (1)$$

tests various aspects of the Standard Model, including the following: the possible existence of more than three generations of quarks, the validity of the quark-lepton universality of the strength of the charged weak interaction, and the existence of possible new physics through the small radiative corrections that need to be applied in extracting the CKM elements from the observed decay rates of hadronic systems and the muon.

The value of $|V_{ud}|$ can be determined from the A coefficient in neutron β -decay (which characterizes the angular correlation between the neutron spin and the direction into which the electron is emitted) and the neutron lifetime. As seen in Figure 1, the value of $|V_{ud}|$ determined in that way has a large uncertainty because of widely varying values of λ deduced from measuring A . In addition, the most recent and precise result for $|V_{ud}|$ (deduced from the Perkeo II measurement of β) disagrees with the gray band, the value predicted when

the experimental results for $|V_{us}|$ and $|V_{ub}|$ determined from kaon decay and B -meson decay are inserted in the unitarity condition—Equation (1). Furthermore, those two values of $|V_{ud}|$ are inconsistent with the result for $|V_{ud}|$ from nuclear β -decay. It is not clear whether these discrepancies are caused by some erroneous measurements or by some new physics. A measurement of A with a much higher precision ($\delta A/A \sim 0.2$ percent) is needed to resolve this situation.

New Approach—Ultracold Neutrons

All previous measurements of A were done using beams of cold neutrons from nuclear reactors. These neutrons have velocities of a few hundred to several hundred meters per second (m/s), or temperatures of a few tens of kelvins. In general, these experiments have the following problems: (1) the halo in the beam acts as background radiation; (2) the supermirror used to polarize the neutrons is basically magnetized iron and therefore acts as an additional source of gamma-ray background; (3) the supermirror polarizer typically limits the neutron polarization to 98–99 percent. Most of these difficulties can be overcome by using ultracold neutrons (UCNs) instead of cold neutrons. Ultracold neutrons have velocities less than 8 m/s (which correspond to millikelvin temperatures). Having such low velocities,

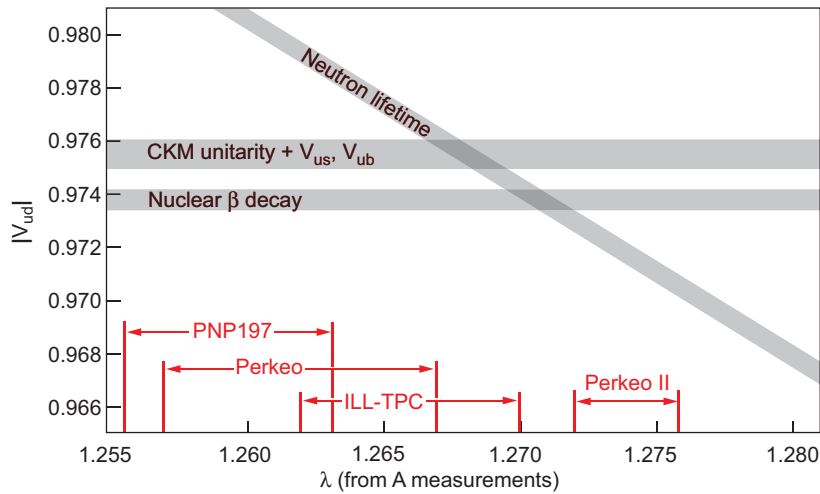


Figure 1. Current Experimental Status of the Determination of $|V_{ud}|$
 The measurements of the A -coefficient in neutron β -decay determine the value of λ , the ratio of two different nucleon coupling constants of the weak interaction. The results from four recent experiments are shown by the four brackets along the λ axis. The combination of a λ -measurement (or A -measurement) and a neutron lifetime measurement determines the value of $|V_{ud}|$. Also shown are the $|V_{ud}|$ determination from nuclear β -decay and the $|V_{ud}|$ determination from kaon and B -meson decays and the assumption of CKM unitarity. Currently, nuclear β -decay provides the most precise experimental determination of $|V_{ud}|$. However, it is inconsistent with the value obtained from kaon and B -meson decays and the assumption of CKM unitarity. In principle, neutron β -decay can provide a theoretically cleaner determination of $|V_{ud}|$ than nuclear β -decay. However, the value of $|V_{ud}|$ determined from neutron β -decay has a large uncertainty because of the large uncertainty in the value of λ . In addition, the most recent (and most precise) λ -measurement (Perkeo II) yields a value of $|V_{ud}|$ inconsistent with the values from two other methods.

they can be totally externally reflected from the surface of selected materials. Therefore, it is possible to transport UCNs over long distances and store them in an area well shielded from background radiation. In addition, with such small velocities, the potential energy associated with the interaction of the magnetic moment of the neutron can easily be made comparable to the kinetic energy of the neutron. Therefore, by simply passing neutrons through a region with a large magnetic field (>6 teslas), one can filter out neutrons with one spin state, thereby making them 100 percent spin-polarized. Such properties of UCNs allow designing and performing a much improved A -coefficient measurement.

Solid-Deuterium Superthermal UCN Source

The traditional approach to the production of UCNs was to obtain neutrons from a reactor and cool them down by passing them through a moderator such as liquid hydrogen. The principal difficulty with such an approach is that neutrons from reactors typically have energies 13 orders of magnitude higher than UCNs, and even the neutrons that are cooled by the moderator have energies 4 orders of magnitude too high. Therefore, the fraction of neutrons that have low enough velocities to be UCNs is very

small, about 1 in a million even in the case of neutrons cooled by a 20-kelvin liquid-hydrogen moderator.

A new approach adopted by a team of physicists from Los Alamos and other institutions for the new UCN source at the Los Alamos Neutron Science Center (LANSCE) is (1) to use neutrons from a spallation source and (2) to cool the neutrons through a superthermal process that uses solid deuterium as the moderator (Figure 2). In a spallation neutron source, a beam of protons from an accelerator strikes a target made of heavy metal such as tungsten, and neutrons are knocked out and boiled off from the atomic nuclei. By operating the accelerator in a pulsed mode, one can limit the emission of background radiation, which interferes with precision measurements, to the period in which the beam pulse strikes the target. This is a big advantage of spallation sources over reactor sources, which generate continuous background radiation. In the superthermal process, the modera-

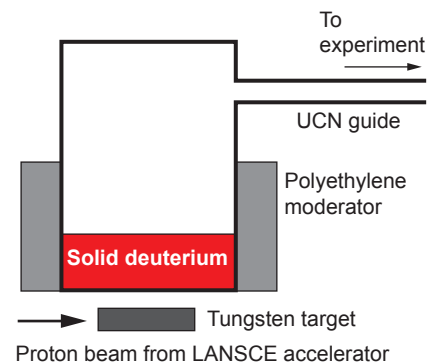


Figure 2. Schematic of the LANSCE Spallation-Driven Solid-Deuterium Superthermal Source
 The neutrons are produced by spallation when the LANSCE 800-MeV proton beam strikes the tungsten target. Then the produced neutrons are “cooled” by the cold polyethylene moderators and then further cooled by the superthermal process in solid deuterium to become ultracold. The UCNs are guided to the experiment through the UCN guides.

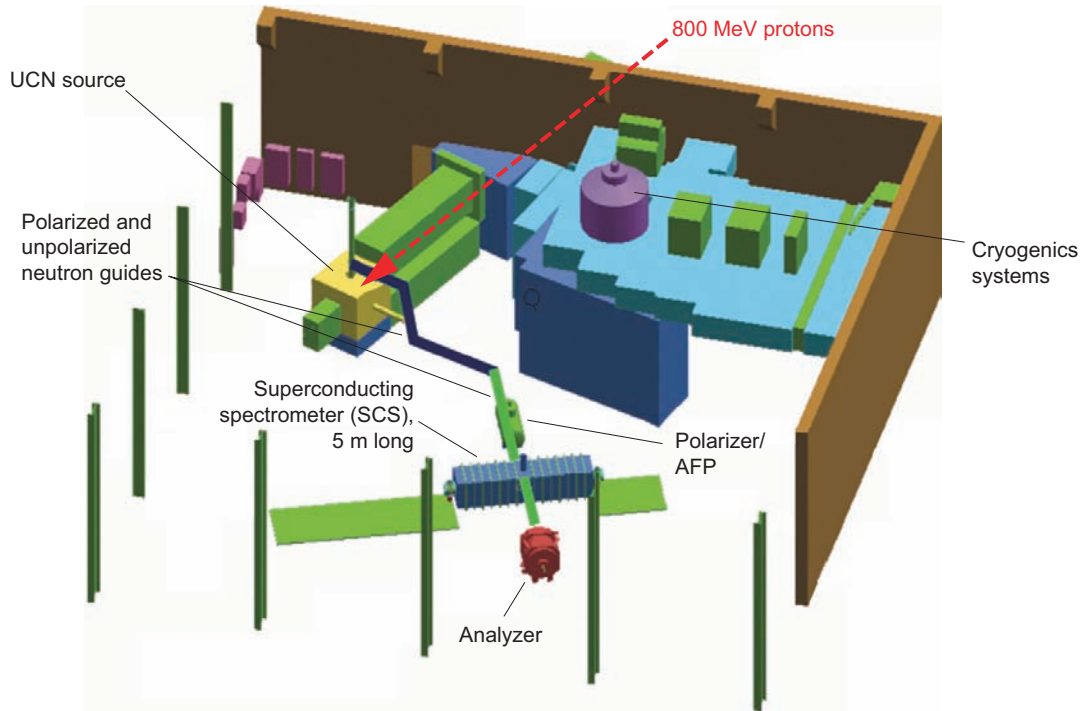


Figure 3. Schematic of the UCNA Experiment in Area B

UCNs are produced in the spallation-driven solid-deuterium superthermal source by the 800-MeV proton beam from the LANSCE linac. UCNs are guided to the experiment through the UCN guides. UCNs are polarized by going through a 7-T magnetic field and are then sent to the decay volume in the superconducting spectrometer (SCS). The neutron spin can be flipped by adiabatic fast passage (AFP). The superconducting coils create a 1-T magnetic field in the decay volume, which serves as the holding field for the neutron spin and as the guiding field for the electrons. The electrons from neutron decay are guided toward the electron detectors mounted at each end of the decay volume.

tor and the neutrons do not come to a thermal equilibrium. Rather the input flux of cold neutrons is efficiently converted to UCNs by exciting vibrations (phonons) in the solid deuterium. The reverse process, whereby a UCN absorbs energy from a phonon, can be suppressed by keeping the temperature of the deuterium relatively low (~5 kelvins). To demonstrate that this UCN production mechanism indeed works, we have built a prototype UCN source and used it to achieve the world record for the UCN density: approximately 140 UCNs per cubic centimeter.

The UCNA Experiment

The UCNA experiment aims to measure the *A*-coefficient with a pre-

cision of 0.2 percent (Figures 3 and 4). In general, *A*-coefficient measurements are performed by letting spin-polarized neutrons decay in a volume in the presence of a uniform magnetic field and counting the number of decay electrons emitted parallel, N_+ , and the number emitted antiparallel, N_- , to the neutron spin. The asymmetry, which is the difference of the two divided by the sum, is related to the *A* coefficient, as shown in the following expression:

$$\text{Asymmetry} = \frac{(N_+ - N_-)}{(N_+ + N_-)} = A\beta P/2, \quad (2)$$

where β is the electron's velocity and P is the degree of spin polarization of the neutron. As can be seen from this expression, it is important to determine the degree of neutron polarization with

high precision to obtain the value of *A* with high precision. Also, in order to determine the value of the asymmetry reliably, it is important to minimize the background in the electron detector.

As mentioned above, UCNs produced by the spallation-driven solid-deuterium superthermal source at LANSCE provide a high degree of neutron spin polarization and a low-background environment. In addition, this experiment has various new features, including very sensitive, multiwire, proportional chambers that complement plastic scintillation detectors for electron detection. In the previous experiments, one serious source of uncertainty was a class of events in which the decay electron is emitted in one direction, strikes the detector in that direction, gets bounced back by it, and gets detected by the other

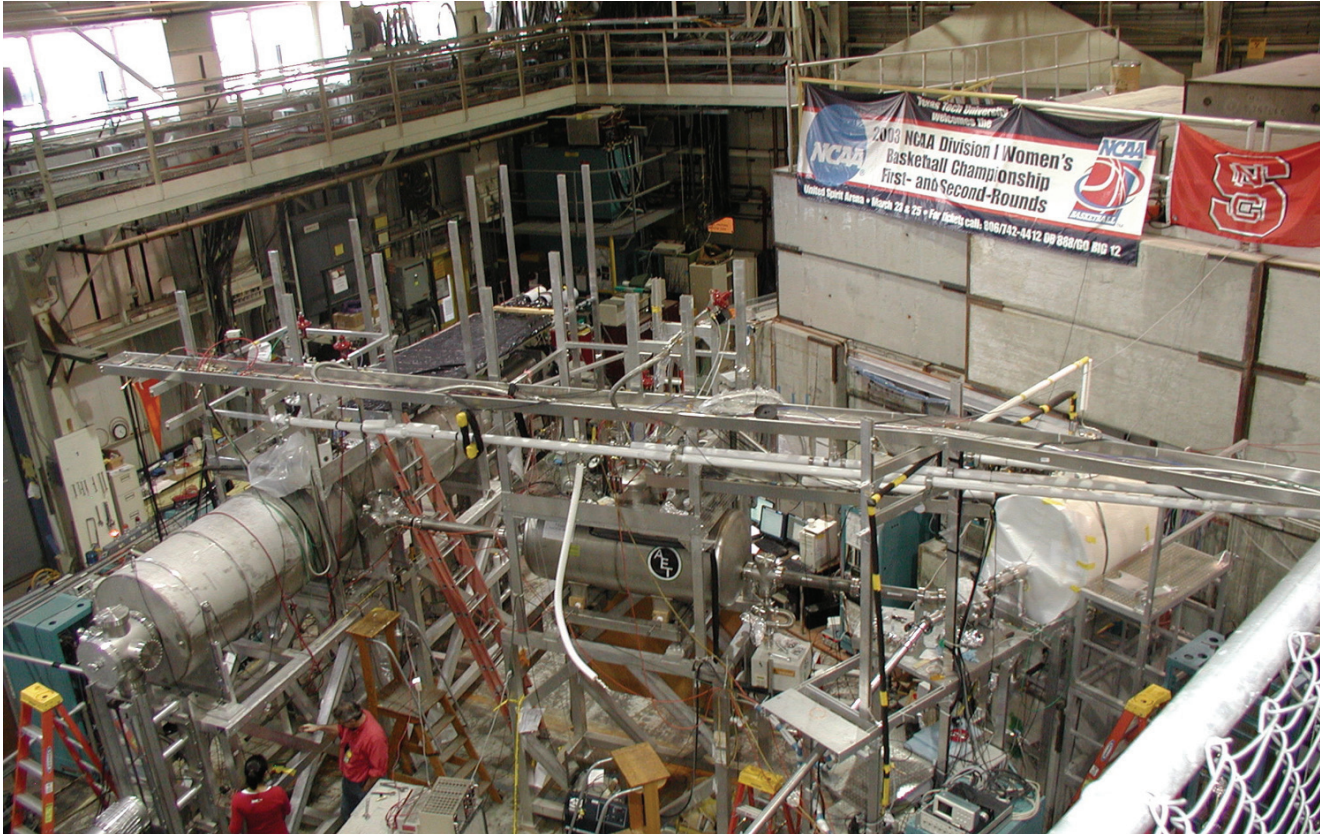


Figure 4. The UCNA Experiment in Area B

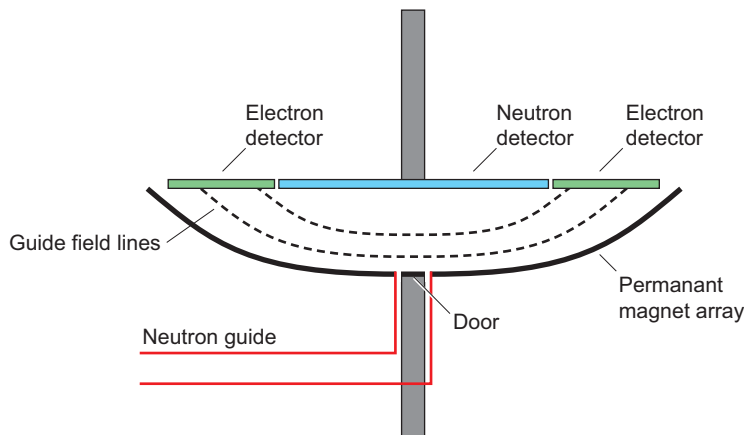


Figure 5. Schematic of the LANSCE Neutron Lifetime Experiment. Neutrons are trapped in vacuum in a tub-shaped trap by magnetic and gravitational fields. Permanent magnets covering the bottom of the trap provide the magnetic field. The trap design forces the motion of the neutrons to be chaotic to eliminate quasistable trajectories. The detector array is lowered periodically to absorb any neutrons that have enough energy to leave the trap.

detector. Obviously, if the electron leaves a signal below the detection limit on the first detector, we are led to an erroneous value for the asymmetry in Equation (2). The use of multiwire proportional counters, which are far more sensitive to small signals than plastic scintillators, will help us reduce the uncertainty in measuring the asymmetry in Equation (2).

This experiment is currently under commissioning at Area B of LANSCE. We plan to start taking physics data in 2006.

A New Neutron Lifetime Experiment at LANSCE

The neutron lifetime is a key input in determining the value of $|V_{ud}|$ from the neutron decay (Figure 1). In addition, it has an important implication

for understanding Big-Bang nucleosynthesis, the production of various nuclear elements in the early universe.

In general, to measure the lifetime of a subatomic particle, one needs to measure either the intensity of the decay products emitted from a sample of the particles in question or the exponential decay of the emission rate of the decay products (which is equivalent to the exponential decay of the number of surviving particles). For the first approach, one needs to know the number of particles in the sample. For the second approach, one needs to ensure that radioactive decay is the only mode by which particles in the sample are lost. The fact that the neutron has no electric charge makes either approach very challenging. In the first approach, measuring the intensity of the decay products, one typically uses a beam of neutrons as the sample (beam method), but knowing the number of neutrons has proved to be a major challenge because it is very difficult to measure the neutron beam intensity accurately. In the second approach, measuring the exponential decay of the emission rate or the number of surviving particles, one typically traps the neutrons in a material bottle (trapping method), but controlling and understanding neutron loss caused by the material wall interaction has been a daunting task.

It is possible, however, to trap neutrons without a material bottle by using the magnetic force and/or the gravitational force. In an inhomogeneous magnetic field, neutrons feel a force that pushes them either toward or away from a region with stronger a field depending on the orientation of spin. By arranging the magnetic field so that it becomes stronger as one goes away from the center of the trap, one can trap neutrons at the center because the magnetic force pushes them toward the weaker field region. The trapped neutrons do not interact with any material, and hence β -decay

is the only mechanism through which the trapped neutrons can disappear.

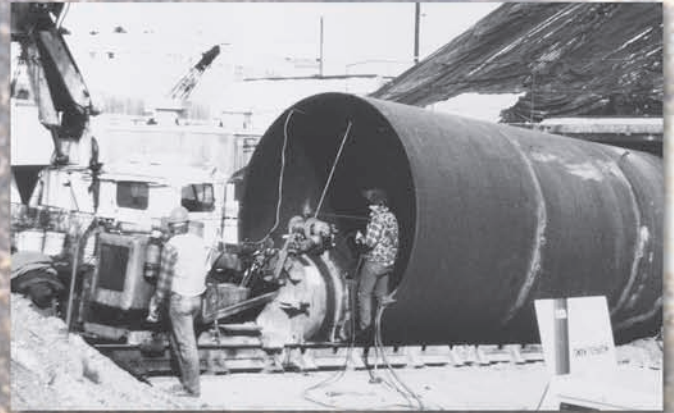
In a new lifetime measurement currently under development at LANSCE, neutrons will be trapped in vacuum in a trap made of magnetic and gravitational fields (Figure 5). The arrays of permanent magnets covering the tub-shaped surface at the bottom of the trap provide the magnetic field, which falls off exponentially as the distance from the surface. This magnetic field provides the force to trap neutrons horizontally and the force to keep the neutrons from escaping from the bottom of the trap. Gravity provides the force to keep the neutrons from escaping from the top of the trap. The solid-deuterium UCN source will be used as the source of neutrons. The electrons from neutron β -decay will be guided by the magnetic field lines toward the electron detectors.

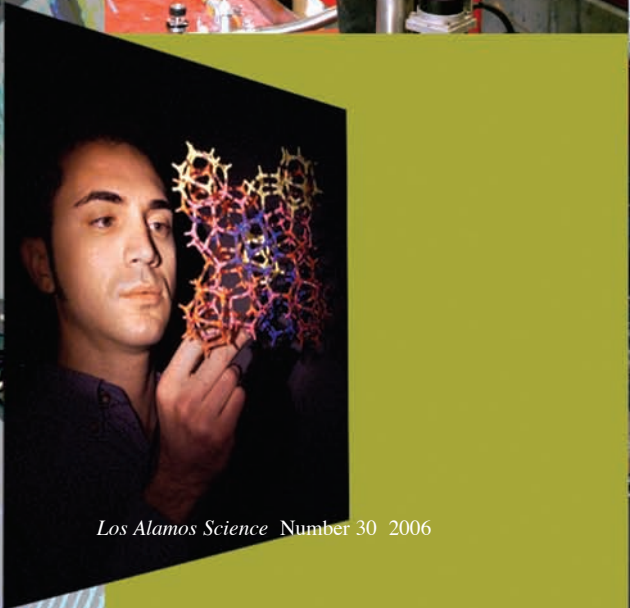
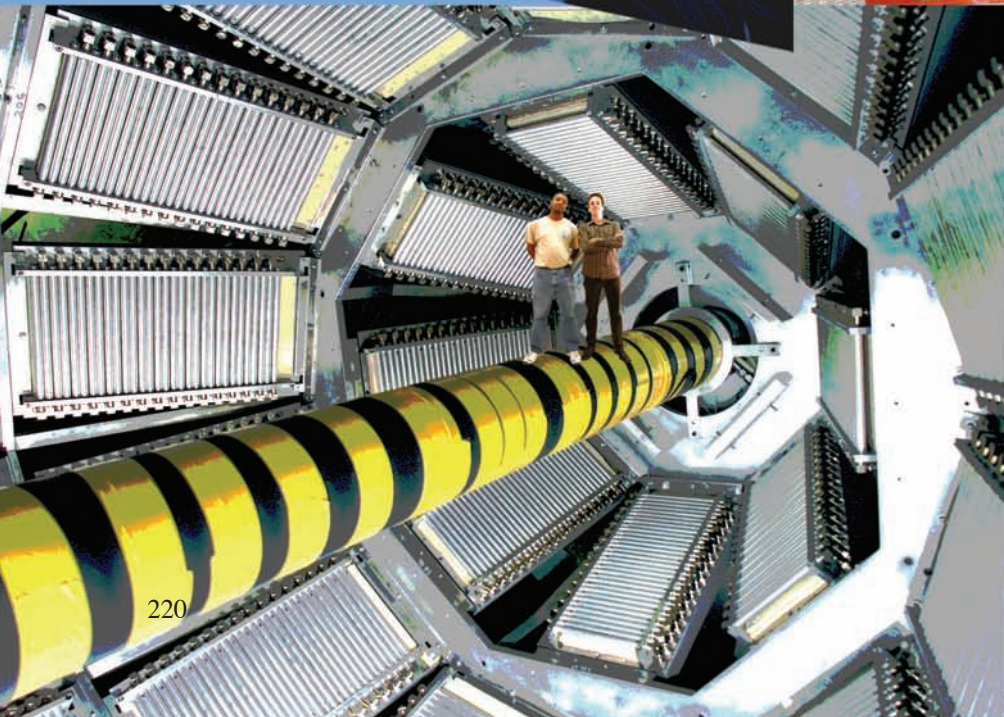
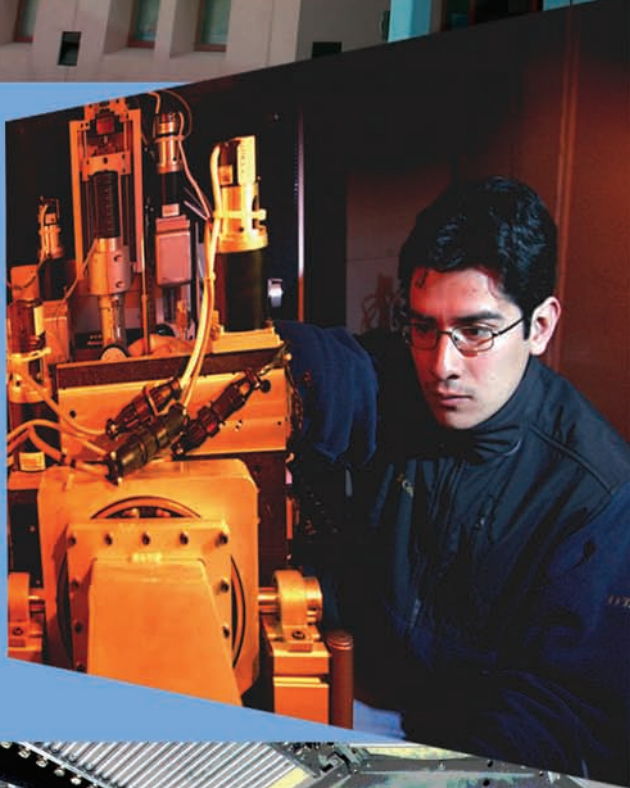
This experiment is notable for its ability to address the issue of marginally trapped neutrons. Marginally trapped neutrons have enough energy to leave the trap but are following quasistable orbits and may therefore remain in the trap for times comparable to the neutron lifetime. Such neutrons can cause the measured lifetime to deviate from its true value by providing an extra mechanism through which neutrons in the trap can disappear. In this experiment, this loss mechanism is prevented by the “chaotic-cleaning” method. The trap is designed in such a way that the motion of the neutrons in the trap is chaotic to eliminate quasistable trajectories. During the cleaning period of the experiment, the detector array is lowered so that any neutrons that have enough energy to leave the trap are forced to collide with the detector array and be absorbed in 2 to 3 seconds.

Once the solid-deuterium UCN source reaches its full potential, a neutron lifetime measurement with an accuracy of 10^{-4} is possible with this apparatus. ■

Further Reading

- The EDM Collaboration. 2002. A New Search for The Neutron Electric Dipole Moment. Los Alamos National Laboratory document LA-UR-02-2331. [Online]: http://p25ext.lanl.gov/edm/pdf.unprotected/EDM_proposal.pdf
- The EDM Collaboration. 2005. A New Search for The Neutron Electric Dipole Moment, Report: Recent Progress and Design Changes. Los Alamos National Laboratory document LA-UR-05-0829. [Online]: http://p25ext.lanl.gov/edm/pdf.unprotected/EDM_Pre-prop_Update_final.pdf
- Freedman, S., and B. Kayser. 2004. Joint Study on the Future of Neutrino Physics: The Neutrino Matrix. [Online]: <http://www.aps.org/neutrino/>
- Page, S. A., J. D. Bowman, R. D. Carlini, T. Case, T. E. Chupp, K. P. Coulter et al. 2005. Measurement of Parity Violation in NP Capture: The NPDGamma Experiment. *J. Res. Natl. Inst. Stand. Technol.* 110: 195.





The User Program at LANSCE

Serving the Nation and the Laboratory

Allen Hartford, Jr.

“ . . . we had to convince people that, in contrast to the rest of the Laboratory, [the Los Alamos Meson Physics Facility, LAMPF] would be open to all interested users. Users are involved in determining policy for upgrading the facility, for new beam lines, and for experimental programs, and of course, they are primarily and heavily involved in advising on the allocation of beam time. Although the users do not make the final decisions, they advise us on what scientific priorities should be assigned to various proposals. . . . LAMPF provides a great arena where faculty and students can together teach and practice the art and science of solving interdisciplinary problems. The very large number of publications and doctoral theses based on research at LAMPF attests to its excellence as an educational tool and, in a larger sense, as an educational environment.”

—Louis Rosen, Founder of LANSCE



For about 30 years, the 800-million-electron-volt (MeV) accelerator and its attendant facilities at Technical Area 53 (TA-53, often referred to as “the mesa”) at Los Alamos National Laboratory have been a resource to an international community of scientific researchers. During its heyday, the Los Alamos Meson Physics Facility (LAMPF), as it was originally called, hosted about 1000 users per year. In 1977, the first pulsed spallation source was commissioned. Beginning in 1985, with the completion of the Proton Storage Ring (PSR) that compresses proton pulses from 750 microseconds to a quarter of a microsecond, the emphasis at TA-53 shifted to neutron science, and the facility became known as the Los Alamos Neutron Scattering Center and more recently (1995) as the Los Alamos Neutron

Science Center (LANSCE) to reflect the broad base of research being conducted. In 2001, a Memorandum of Understanding among three branches of the Department of Energy (DOE)—the National Nuclear Security Administration (NNSA), the Office of Science (SC), and the Office of Nuclear Energy (NE)—and the Laboratory officially designated LANSCE as a national user facility.

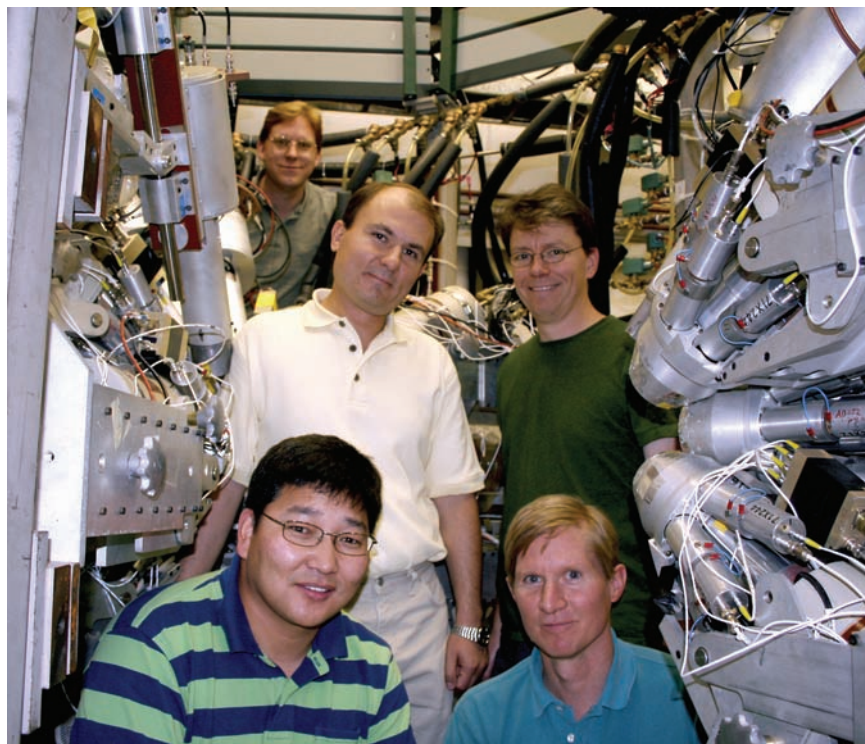
Several key events have occurred during the last 20 years that have fostered the growth of the user program at LANSCE. In 1986, the Office of Basic Energy Sciences in the SC began providing funding for a formal user program in neutron scattering. In the same year, construction of a new experimental area, including office space, was begun and was completed in 1988. In 1996, the SC transferred responsibility

for LAMPF to the Defense Programs (DP) of the DOE. Beginning in 1997, the SC, in partnership with the DP, began investing in the development of new instruments. Today, there are 14 active flight paths; seven are new since 2000 and two have been substantially upgraded.

Today, users conduct research at three major facilities at LANSCE: the Lujan Neutron Scattering Center (Lujan Center), the Weapons Neutron Research Facility (WNR), and the Proton Radiography (pRad) Facility. A nascent capability in ultracold neutrons (UCN) will be available to users in the near future. In the 2003–2004 run cycle at LANSCE, both the WNR and the Lujan Center achieved significant milestones by exceeding 500 users each for the first time. In 2005, the number of user visits at the Lujan Center was greater than during the previous run cycle. Proton radiography is a smaller effort in terms of users but is a vital element of the research conducted at LANSCE because of its focus on and contributions to the Laboratory’s programmatic mission in stockpile stewardship.

Importance of the User Program

The spectrum of capabilities available at LANSCE is not replicated anywhere else. Neutrons in the energy range from micro–electron volts to hundreds of million–electron volts are available, along with an array of instruments and detectors to utilize and analyze them. At the low end of the energy spectrum, ultracold and cold neutrons will allow fundamental physics studies, such as measurements of the electric dipole moment of the neutron with unprecedented accuracy and of the parity symmetry breaking in the weak interaction. Moderated neutrons in the milli-electron-volt to



Pictured here are GEANIE users, together with LANSCE staff. Left (front to back): Dugersuren Dashdorj—North Carolina State University and Lawrence Livermore National Laboratory (LLNL), postdoctoral fellow—Nikolaos (Nick) Fotiades—LANSCE, staff—and Robert (Rob) Macri—LLNL, postdoctoral fellow. Right (front to back): Ron Nelson and Matt Devlin—LANSCE, staff.

the electron-volt range are used at the Lujan Center with 12 spectrometers dedicated to research in materials science, condensed matter physics, structural biology, geoscience, and chemistry. Two beam lines in the Lujan Center are used for investigations in neutron nuclear science (including the aforementioned studies of parity violation). At the WNR, unmoderated neutrons (spanning energies from kilo–electron volts to million–electron volts) are used in nuclear science research, as well as in irradiating semiconductor devices, to understand the effects of cosmic-ray-induced neutrons. The WNR permits accelerated testing of these effects because the energy spectrum of the neutrons is similar to that produced by cosmic rays, but 5 orders of magnitude more intense.

These myriad capabilities and the LANSCE mandate as a national user facility attract a diverse array of users, both in terms of their research interests and their institutional affiliations. Most users come from universities, other national and federally funded laboratories, and industry. Because many of the university users are graduate students or postdoctoral researchers, LANSCE makes important contributions to the education and development of the country’s next generation of scientists. Researchers from other federally funded laboratories conduct work that ranges from fundamental science to programmatic efforts, thus helping to ensure that the

nation maintains a leading position in areas necessary for its continued well being. Among the results of industrial research at LANSCE are technological innovation and improvement in product reliability.

The demand for access to neutron sources is clear; LANSCE receives many more high-quality proposals than can be accommodated on the available beam lines and spectrometers. To respond to this demand, the country has invested in the construction of yet another facility, the Spallation Neutron Source (SNS) in Oak Ridge, Tennessee. Many of the scientists coming to LANSCE are introduced for the first time to neutron scattering. The Lujan Center, in particular, makes researchers aware of the versatility and power of this technique. Thus, LANSCE plays a pivotal role in training scientists who will continue to incorporate neutron scattering into their research and who will become part of the expanding user community.

The constant influx of users to LANSCE and the interactions with them benefit the Laboratory directly. Users help keep the Laboratory in touch with members of the external scientific community, who bring new perspectives and fresh ideas with them. In addition, many of the Laboratory’s scientists have the opportunity to collaborate with the users and thus continue to be engaged in forefront research that hones their skills. A significant number of

students and postdoctoral researchers who become familiar with the Laboratory through their experiences at LANSCE become part of the permanent workforce, joining many different technical organizations and making important contributions to the Laboratory’s principal missions.

How Are Experiments Selected?

Individuals or teams who wish to conduct experiments at LANSCE must submit proposals. Calls for proposals are typically issued twice for each run cycle of the accelerator. Three program advisory committees (PACs) for materials, nuclear physics, and pRad have been established to evaluate the proposals. Each committee is further subdivided into subcommittees that evaluate proposals in specific areas. For materials and nuclear physics, most of the PAC members are from outside the Laboratory, many of them from the academic community. Because pRad is focused on the nuclear weapons program, most of the members of the PAC are from Los Alamos, Sandia, and Lawrence Livermore National Laboratories.

Scientific merit is the principal criterion for judging all the proposals submitted for beam time at LANSCE. Programmatic relevance is also considered in evaluating mission-driven proposals. Because proposals for pRad

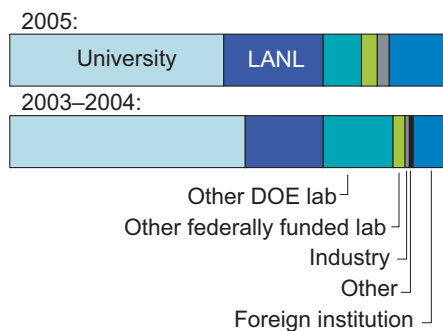


Figure 1. Lujan Center Users—Institutional Affiliations



Figure 2. WNR Users—Institutional Affiliations



“I like to send my students to LANSCE because things are working smoothly. In the last three years, in particular, the beam line has been reliable, and the software is very well set up.”

—Simon Billinge (right), Professor, Michigan State University



“The NPDF is exactly the instrument I need for my work. Being the world’s best diffractometer of its kind, the NPDF generates data of exceptional quality. This time, I’ll be using the NPDF for 12 full days. I’m up all the time, keeping an eye on the experiments and changing samples, but it’s all worth it!”

—Emil Bodzin (left), Postdoctoral Fellow, Michigan State University



“The WNR is a unique high-intensity neutron source for the study of nucleon–nucleon physics over a broad range of energies. It has allowed many graduate and undergraduate students to experience firsthand the design, construction, performance, and analysis of nuclear physics experiments.”

—June Matthews, Professor, Massachusetts Institute of Technology (MIT), and Director, MIT Laboratory for Nuclear Science





“Professor Peter Littlewood, director of the Cavendish Laboratory at Cambridge University, recommended that I use pair distribution function (PDF) to study the most fundamental nature of polycrystalline manganites. LANSCE has a very good setup for using the PDF—perhaps it’s the best place in the world for experiments that use this method for very small scale ordering. Working with the people at LANSCE has been an extremely positive experience.”

—Susan Cox (left), PhD Student, Cambridge University, United Kingdom



“LANSCE uses new technologies to answer controversial questions in biology. To do functional genomics, we need to know, for example, the locations of key hydrogen atoms. The Protein Crystallography Station at the Lujan Center gives us the power to look for those key hydrogen bonds.”

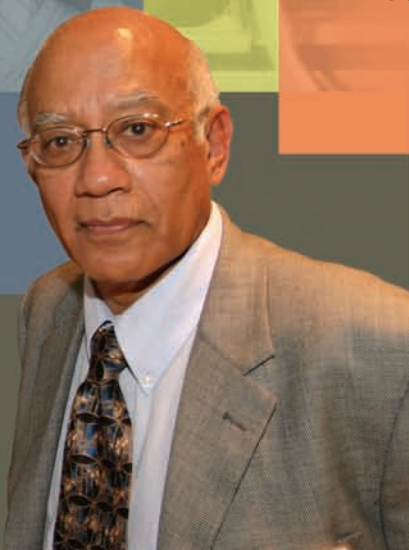
—Chris Dealwis (above), Assistant Professor, University of Tennessee



“This was my first experience of LANSCE, and I would describe it as impressive. The neutron flux is high, and the furnace can be used at temperatures as high as 1250°C. We need such high temperatures for our inelastic-neutron-scattering experiments. In 10 days of beam time, we conducted 30 runs ”

—Rebecca Stevens, PhD Student, Caltech

Sunil K. Sinha (right), Professor, University of California, San Diego



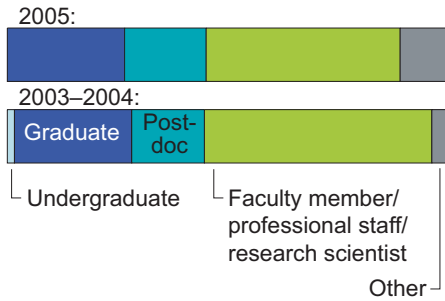


Figure 3. Lujan Center Users—Positions

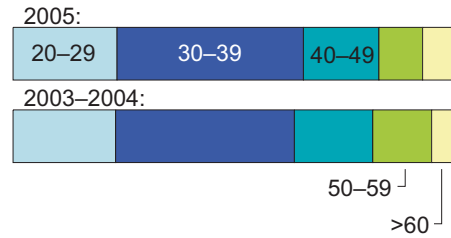


Figure 4. Lujan Center Users—Age Distribution (years)

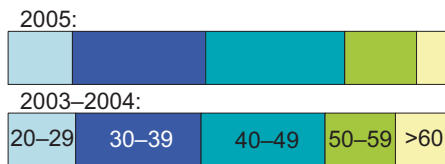


Figure 5. WNR Users—Age Distribution (years)

are highly focused on addressing programmatic requirements, mission relevance is an important factor in their overall evaluation. A measure of the overall high quality of all the proposals is that, for most of the beam lines and flight paths, we are unable to accommodate all the proposals recommended by the PACs.

Who Are the Users?

The users at the Lujan Center and the WNR are different in several respects, including the institutions they represent, their age distribution, and the number of students and postdoctoral researchers. Figures 1 and 2 show the differences in the institutional affiliation of the users at the Lujan Center and the WNR, respectively, for the 2003–2004 and 2005 (from February through September) run cycles.

Approximately half of the users at the Lujan Center are affiliated with universities, whereas most WNR users come from industry. The types of research conducted at the two facili-

ties determine this obvious difference. The WNR enjoys growing numbers of users from the semiconductor industry, who test their latest devices for robustness against neutron-induced upsets. For instance, in the 2003–2004 and 2005 (through September) run cycles, 24 and 23 semiconductor manufacturers conducted experiments, respectively. Of these organizations, 15 were users during both run cycles, including major companies such as Advanced Micro Devices, AMD, Intel Corp., Sun Microsystems, Texas Instruments, and Xilinx.

By contrast, a relatively small fraction of the total number of users (approximately 10 percent) were members of the academia, who conducted nuclear science research at the WNR. These small numbers are likely related to a gradual decline in enrollment in this area at many universities. This trend concerns the Laboratory because of the Laboratory’s ongoing need for nuclear scientists to support its primary mission.

At the Lujan Center, approximately 45 percent of the users are students and postdoctoral researchers conduct- ing publishable research of a more

fundamental nature (Figure 3).

The relative youth of the users is a remarkable strength of the user program at LANSCE. As shown in Figures 4 and 5, over 60 percent of the Lujan Center users and approximately 45 percent of the WNR users were below the age of 40 for both run cycles. Maintaining a strong component of students, postdoctoral researchers, and early-career scientists is a priority for LANSCE because we are fulfilling a mandate to help train and advance the next generation of scientific leaders, some of whom will join the Laboratory’s staff.

Research Breadth and Diversity at LANSCE

A rather remarkable range of science is covered at LANSCE. Studies in materials science and engineering, geoscience, nanoscience, bioscience, condensed matter physics, chemistry, and soft matter are pursued at the Lujan Center. Resources available there allow research into systems subjected to extreme conditions, such as high pressure, high magnetic fields, high and low temperatures, large deformations, and extreme stress, many of these often in combination. Identification of a superhard carbon phase that results from squeezing carbon nanotubes to 75 gigapascals at room temperature (Wang et al. 2004) and the formation of a new clathrate molecule that efficiently stores hydro-

gen molecules (Loshkin et al. 2004) are only two examples of exciting new research from the high-pressure capability at the Lujan Center. Los Alamos scientists and external collaborators worked together on these projects. In addition, texture data for plutonium obtained on the high-pressure preferred-orientation (known as HIPPO) diffractometer at the Lujan Center have benefited weapons designers because grain alignment gives information about metallurgical structure and, hence, mechanical behavior.

At the WNR, research is conducted in areas such as nuclear structure, fission cross sections, neutron-induced reactions, neutron resonance spectroscopy, and neutron-induced failures in semiconductor devices. Researchers at the WNR have recently made important contributions to the nuclear weapons program by measuring neutron-capture and inelastic-reaction cross sections of radiochemical diagnostics—materials that were introduced into nuclear devices to measure performance during the nuclear-testing period. This information is being used to reevaluate archival nuclear data and to refine computational models. Improved measurements of fission cross sections are being conducted for both the nuclear weapons program and for evaluating advanced nuclear-reactor designs. Recently, a lead slowing-down spectrometer that increases neutron flux by over 3 orders of magnitude was developed to conduct measurements of very short-lived isotopes on very small samples. The size of the samples is determined by their high radioactivity and small abundance. Using smaller than 10-nanogram samples, LANSCE researchers recently conducted a proof-of-principle experiment, whose results were in good agreement with previous measurements of the plutonium-239 fission cross section. Another instrument, the Fast Neutron-Induced Gamma-Ray Observer (FIGARO), is used to mea-



Thierry Granier has been a user at the WNR for several years. Thierry works at the Commissariat à l'Énergie Atomique (CEA) at Bruyères-Le-Châtel, France, and periodically comes to Los Alamos to use the FIGARO and LSDS instruments for fission measurements.

sure neutron inelastic reactions and fission, the former being important for neutron transport calculations.

Proton radiography has proved to be a versatile technique for imaging dynamic events with high spatial resolution on submicrosecond time scales. It has been successfully used to investigate high-explosive detonation and burn, hydrodynamics and shock physics, and materials damage and spall, all-important phenomena in nuclear weapons.

Conclusions

The user facilities at LANSCE will continue to contribute to the science of the Laboratory for years to come. Materials research and neutron nuclear science are important elements of many of the Laboratory's programmatic responsibilities in national security, energy security, and basic research. Industrial research at both the WNR and the Lujan Center helps maintain the competitiveness of U.S. industry. Proton radiography is making important contributions to the certification of our nation's nuclear weapons stockpile in an era with no

underground testing.

As a national user facility, LANSCE keeps the Laboratory in direct and permanent contact with the external scientific community, thus contributing to the Laboratory's scientific vitality. In addition, LANSCE exposes students and postdoctoral researchers to career opportunities at the Laboratory. Over 1200 people have joined the Laboratory in the last 25 years after having had a stint at LAMPF or LANSCE. Indeed, many of those people have contributed to the Laboratory's core mission. ■

Further Reading

- Lokshin, K. A., Y. Zhao, D. He, W. Mao, H.-K. Mao, R. J. Hemley et al. 2004. Structure and Dynamics of Hydrogen Molecules in the Novel Clathrate Hydrate by High Pressure Neutron Diffraction. *Phys. Rev. Lett.* **93**: 125503.
- Wang, Z., Y. Zhao, K. Tait, X. Liao, D. Schiferl, C. Zha et al. 2004. A Quenchable Superhard Carbon Phase Synthesized by Cold Compression of Carbon Nanotubes. *Proc. Natl. Acad. Sci. U.S.A.* **101**: 13699.

Los Alamos National Laboratory, an affirmative action/equal opportunity employer, is operated by the University of California for the U.S. Department of Energy under contract W-7405-ENG-36. All company names, logos, and products mentioned herein are trademarks of their respective companies. Reference to any specific company or product is not to be construed as an endorsement of said company or product by the Regents of the University of California, the United States Government, the US Department of Energy, nor any of their employees. The Los Alamos National Laboratory strongly supports academic freedom and a researcher's right to publish; as an institution, however, the Laboratory does not endorse the viewpoint of a publication or guarantee its technical correctness.

